Rate Determination in Metal Nanoparticle Synthesis and Catalysis

Sushila Marie Marlow

Department of Chemical Engineering

University College London

Submitted for the degree of Doctor of Philosophy

2023

I, Sushila Marie Marlow, confirm that the work presented in this thesis is my own. Where information has been derived from other sources, I confirm that this has been indicated in the thesis.

Acknowledgements

This thesis was written with the help of many people, some of whom I will acknowledge here, and to all of whom I am deeply indebted. First, I would like to thank my supervisor, Ryan Wang, for his support, ideas and guidance with my research. I would also like to acknowledge the EPSRC grant which allowed my to conduct my research and the support of Diamond Light Source (DLS) and SPring-8 in allowing me to attend beamtimes, particularly I20-EDE and the BAG beam access which helps so many researchers.

This work would not have been possible without my collaborators, beamline scientists and the team of technicians and researchers at UCL and DLS who helped with training me and improving my understanding of the results, in particular Luke Keenan, Hiroyuki Asakura, Alberto Alvarez Fernandez, Matt Darby, Hao Gu and Jay Yan for their notable contributions. In addition I should express my gratitude to the other present and past members of the MCL, Bolun Wang, Liqun Kang, Ruoyu Xu, Yifei Ren, Xuze Guan, Zhipeng Wang, Junrun Feng, Lin Sheng, Manxi Gong, Qiming Wang, Daniel Wan, Lu Chen, Yiyun Liu and others for sharing knowledge, discussions, beamtimes, lab times and friendship with me.

On a more personal note, I thank my family, house mates and friends in London and abroad. I dedicate this project to my husband Matteo, my parents and to Shri Mataji.

Abstract

This research explores the role of reaction rates and intermediate species in the synthesis and catalysis of transition metal nanoparticles using high-resolution *in situ* spectroscopic techniques. Experimental measurement of time-resolved data during a reaction, though challenging, affords fundamental insights into the reaction mechanisms, transient states and nanoparticle behaviour, as a foundation for theoretical calculations.

The projects presented advance the measurement and analysis of *in situ* data, at the limits of time-resolution and elemental-detection. After the introduction (Chapter 1) and scientific background (Chapter 2), Chapters 3 to 7 reveal the rates of synthetic reduction and electrochemical oxidation of Pd, Pt-Pd and Cu nanoparticles, obtained primarily from *in situ* X-ray absorption spectroscopy.

First, a 500 ms-time-resolved study of CTAC-capped Pd nanoparticle growth (Chapter 3), with a series of temperatures and seed solutions, measured the growth profile, activation energy and, for the first time, the formation of soluble Pd(0)-Cl intermediates.

Applied in Chapter 4, Pt-Pt coordination number alloyed in a Pd nanoparticle matrix was studied as a descriptor for Oxygen Reduction Reaction activity. Extreme ratio Pt_1Pd_{493} nanoparticles containing Pt dimers, inhibited Pt oxidation and increased atomic efficiency.

The role of the surfactant during growth was studied in Chapter 5, where CTAB-induced faceted Pd nanoparticle morphology did not significantly form soluble Pd(0)-Br, due to the Pd-ligand interaction and exhibited a different growth profile.

A 1.27 ms-resolved study of early-stage Cu nanoparticle formation captured the effect of intermediate Cu^{1+} species and hydrazine-complexation in determining morphology (Chapter 6).

Lastly, the rate of electrochemical oxide-formation at a Cu surface was observed with µs-resolution (Chapter 7), with the aim of enhancing CO_2RR activity.

The driving principle behind this research is that such detailed experimental measurements of nanoparticle synthesis and catalytic behaviour, is a necessary foundation for the 'rational design' of catalysts over more costly and laborious trial-and-error.

(299 words)

Impact Statement

Transition metal nanoparticles are finding an ever-broadening spectrum of scientific, commercial, and industrial applications. Studied here are the synthetic mechanisms of formation and their potential application in two catalytic reactions, both of which are important in reducing dependence on fossil fuels and creating a sustainable future for the planet, in fuel cells and in the capture of carbon dioxide and its transformation into useful organic compounds.

Heterogeneous nanoparticles, where small quantities (sometimes single atoms) of expensive catalyst are attached to an inert substrate, are the future of catalytic materials as they use less material, lower energy consumption and increase reaction efficiency. The *in situ* observation of nanoparticle behaviour in such materials can allow understanding of the catalysis, degradation and electrochemical behaviour, to improve efficiency in applications such as fuel cells.

The underlying mechanistic chemistry of nanoparticle catalysis is also furthered with this research by studying the rates of formation of final and intermediary products during both the formation and activity of catalytically relevant nanoparticles (mainly Pt, Pd and Cu), using advanced high-time-resolution *in situ* techniques. These nanoparticles are already commercially used and could be improved with increased morphology control.

Understanding these mechanisms will better enable us to develop more efficient catalysts through ‘rational design’ rather than by hit-and-miss, trial-and-error techniques, saving time, money and materials along with a better product.

Measurement with a wide array of characterization tools, at increasingly high time-resolutions, incorporating a large variation of reaction parameters (temperature, concentration, etc.) has provided new glimpses inside nanoparticle

formation and catalysts at work. Hitherto unmeasured intermediate forms such as Pd(0) growth species have been detected. Our understanding of the mechanisms involved has been broadened; and this evidence has been used to confirm existing theories of nucleation, particle formation and catalytic pathways but has also indicated possible other explanations. We believe that such studies will continue to shape the scientific understanding of nanoparticles at a fundamental level.

More detailed characterization, coupled with precise rate determination and better understood catalytic pathways, will enable the selection, design and creation of improved materials for existing applications and may suggest new fields in which these materials can be used.

Industrially, this work will help in the rational design of nanoparticles. We are learning how the morphology of nanoparticles affects catalytic activity; and we are learning how to precisely tailor their size and shape to maximise efficiency. Apart from those mentioned, there are a growing number of applications where choosing the best catalyst (based not just on efficiency but also on cost and availability), designing nanoparticles and optimising material and energy consumption will be greatly beneficial.

There is still much to learn about the behaviours, growth mechanisms and possible applications of metal nanoparticles, especially in the fields of health and the environment. The advancement of nanoscience and cutting-edge technologies such as new and larger synchrotrons will grant us an even closer look inside particle formation and catalytic reactions in real time. (485 words)

Contents

Acknowledgements **3**

Abstract **4**

Impact Statement **6**

Contents **8**

List of Abbreviations *15*

List of Unit Prefixes *18*

List of Units *19*

Chapter 1. Introduction and Literature Review **20**

1.1 Chemical Rate Determination *23*

1.2 Metal Nanoparticles in Electrocatalysis *26*

1.2.1 Oxygen Reduction Reaction 30

1.2.2 *In situ* and Time-Resolved ORR Measurements 38

1.2.3 Cu oxidation in CO_2 Reduction Reaction (CO_2RR) 41

1.2.4 Rate Determination: Cu Oxidation 43

1.3 Growth of Metal Nanoparticles in Solution *44*

1.3.1 Nucleation Theories 48

1.3.2 Growth Theories 52

1.3.3 Reshaping After Growth 58

1.4 Synthetic Conditions During Chemical Precipitation Growth *61*

1.4.1 Synthetic Control Mechanisms 62

1.4.2 Size Control 64

1.4.3 Shape Control 66

1.4.4 *In situ* Characterization 68

1.5 Scope of Thesis *74*

1.6 Aims and Objectives *78*

1.7 References *80*

Chapter 2. Characterization Principles and Methodology **98**

2.1 Introduction *98*

2.2 Synchrotron-based Characterization *99*

2.2.1 XAS 103

2.2.2 High Resolution XANES 119

2.2.3 Valence-to-Core XES 120

2.2.4 SAXS 122

2.2.5 Summary 123

2.3 Lab-based Characterization *125*

2.3.1 XPS 125

2.3.2 XRD 126

2.3.3 Electron Microscopy 128

2.3.4 Energy Dispersive Spectroscopy 129

2.3.5 Electron Paramagnetic Resonance 130

2.3.6 UV-vis 133

2.3.7 Nitrogen Sorption Isotherms (with BET) 134

2.3.8 MP-AES 135

2.4 Chemical Precipitation Growth Rate Measurements *137*

2.4.1 Adapting Synthesis Procedures 137

2.4.2 Time-Resolved *Ex situ* Measurements 139

2.4.3 *In situ* EPR Setup 141

2.4.4 *In situ* XAS and SAXS Flow-Cell Design (SFM-4000) 142

2.5 Electrochemical Setup *145*

2.5.1 Three-electrode cell setup 146

2.5.2 ORR Catalytic Evaluation 149

2.5.3 Cu Oxidation Evaluation 153

2.5.4 *In situ* Cell Design and Setup 153

2.6 Chemical Rate Determination 156

2.6.1 Rate of Reduction and Formation of Intermediate Species 157

2.6.2 Activation Energy and Arrhenius Equation 158

2.6.3 Rate of Electrochemical Oxidation 160

2.7 Sources of Error 160

2.7.1 Experimental Measurements 161

2.7.2 Reproducibility 162

2.7.3 Data Analysis 163

2.8 References 166

Chapter 3. Millisecond-Resolved *in situ* XAS and SAXS Study of CTAC-Capped Pd Nanoparticle Growth 172

3.1 Introduction 173

3.2 Results and Discussion 177

3.2.1 Observing Nanoparticle Growth 177

3.2.2 Pd^0-Cl in Temperature-Controlled Growth 180

3.2.3 Bypassing Nucleation with Seeded Growth 183

3.2.4 Discussion 187

3.3 Outcomes 188

3.4 Experimental Details 189

3.4.1 Porous Pd Nanoparticle Synthesis 189

3.4.2 Lab-Based Characterization 190

3.4.3 Synchrotron Characterization 191

3.4.4 Large Dataset Analysis 193

3.4.5 Calculating Pd^0-Cl Content 196

3.5 Supplementary Information 200

3.5.1 TEM Images and *ex situ* Characterization....200

3.5.2 Temperature-Controlled XAS and SAXS Results....203

3.5.3 Seed-Controlled XAS and SAXS Results....213

3.6 References....220

Chapter 4. Engineering the Pt-Pt Coordination Environment to Study Activity for Oxygen Reduction Reaction....224

4.1 Introduction: A model catalyst to test the O-O dissociation....225

4.2 Results and Discussion....227

4.2.1 Structure and Identification of Pt dimers in the Pd matrix....227

4.2.2 Electrochemical Behaviour of Pt Dimers and Clusters....237

4.2.3 Structure-Activity Relationship and Reaction Pathways of Pt Oligomers and Clusters....240

4.2.4 *In situ* XAS results....244

4.3 Outcomes....247

4.4 Experimental Methods....248

4.4.1 Nanoparticle Synthesis....248

4.4.2 Lab-Based Characterization....249

4.4.3 Electrochemical Testing....250

4.4.4 Modelling: DFT Calculation Setup and Parameters....251

4.4.5 Beamline Setup and Data Analysis....253

4.5 Supporting Information....256

4.5.1 TEM Additional Images....256

4.5.2 Electrochemical Method and Results....259

4.5.3 Beamlines B18 (DLS) and BL01B1 (SPring-8)....260

4.5.4 XAS Analysis and Fit Results....261

4.5.5 DFT Definitions and Figures....269

4.6 References....277

Chapter 5. The Role of Surfactants in Pd Nanoparticle Growth: CTAB versus CTAC. .282

5.1 Introduction 283

5.2 Results and Discussion 285

5.2.1 Faceted Pd Nanoparticle Growth 286

5.2.2 Br^- Ligand-Mediated Growth Profile 289

5.2.3 Rate of Temperature Controlled Reduction 290

5.2.4 Role of AA Concentration in Growth Rate 293

5.2.5 Surfactant Effect: CTAB versus CTAC 296

5.3 Outcomes 300

5.4 Experimental Details 301

5.4.1 Faceted Pd Nanoparticle Synthesis 301

5.4.2 Nanoparticle Imaging 301

5.4.3 Synchrotron Characterization 302

5.4.4 Data Analysis 303

5.5 Supplementary Information 305

5.5.1 TEM Images and Measurements 305

5.5.2 XAS Analysis and Fit Results 306

5.6 References 315

Chapter 6. The Role of Intermediates in Cu Nanoparticle Growth 317

6.1 Introduction 318

6.2 Results and Discussion 321

6.2.1 Expected Reduction Mechanisms and Characterization 321

6.2.2 Cu Standards and Solvents: H_2O versus DMF 323

6.2.3 Ascorbic Acid: Two Stage Reduction 329

6.2.4 Beam Induced Reduction: *In situ* TEM 344

6.2.5 Hydrazine: Ligand Substitution 346

6.3 Outcomes 355

6.4 Experimental Methods *357*

6.4.1 Nanoparticle Synthesis 357

6.4.2 Lab-Based Characterization 358

6.4.3 Synchrotron Characterization 361

6.4.4 Data Analysis 366

6.5 Supplementary Information *371*

6.5.1 Standards 371

6.5.2 TEM Images of AA Reduction 372

6.5.3 XAS Results AA Reduction 374

6.5.4 $Cu(OAc)_2$/DMF/AA 384

6.5.5 TEM images of N_2H_4 Reduction 389

6.5.6 $Cu(OAc)_2$/DMF/N_2H_4 390

6.6 References *391*

Chapter 7. Rate of Electrochemical Cu Oxidation with Fast-Switching 396

7.1 Introduction *397*

7.2 Results and Discussion *399*

7.2.1 Electrochemical Behaviour 400

7.2.2 Rate of Cu Oxidation 402

7.3 Outcomes *411*

7.4 Experimental Methods *413*

7.4.1 Cu Foil and Electrochemical Setup 413

7.4.2 Beamline Setup 414

7.4.3 Data Analysis 414

7.5 References *416*

Chapter 8. Conclusions 418

8.1 Research Summary *418*

8.1.1 Pd Nanoparticle Growth with CTAC 418

8.1.2 Pt-Pd Alloy Nanoparticles in ORR 419
8.1.3 Pd Nanoparticle Growth with CTAB 421
8.1.4 Cu Nanoparticle Growth 422
8.1.5 Cu Oxidation 423
8.2 Outcomes and Challenges 424
8.3 Future Work 426
Chapter 9. Additional Materials 430
9.1 List of Figures 430
9.2 List of Tables 435
9.3 Academic Activities 438
9.4 Publications with Authorship Contributions 440
9.5 Bibliography 441
9.6 References 442

List of Abbreviations

AA	L-Ascorbic Acid
AC	Alternating Current
AES	Auger Electron Spectroscopy
AFM	Atomic Force Microscopy
BCC	Body Centred Cubic (Crystal Structure)
BET	Brunauer-Emmet-Teller
BF-STEM	Bright Field -STEM
CCD	Charge Coupled Device
C.N.	Co-ordination Number
CNT	Classical Nucleation Theory
CO_2RR	Carbon Dioxide Reduction Reaction
CTAB/CTAC	Cetyltrimethylammonium Bromide / Chloride
CV	Cyclic Voltammetry
DAWN	Data Analysis WorkbeNch Software
DFT	Density-Functional Theory
DI (water)	Deionised
DLS	Diamond Light Source (Harwell, UK)
EDE	Energy Dispersive EXAFS
EDX or EDS	Energy Dispersive X-ray Spectroscopy
EELS	Electron Energy-loss Spectroscopy
EIL	Electrochemical Innovation Laboratory, UCL Chemical Engineering
EIS	Electrochemical Impedance Spectroscopy
EPR or ESR	Electron Paramagnetic Resonance Spectroscopy
EXAFS	Extended X-ray Absorption Fine Structure Spectroscopy
FEFF8	Code for calculating X-ray absorption structures
FCC	Face Centred Cubic (Crystal Structure)
FTIR	Fourier Transformed Infrared Spectroscopy
GI-XRD	Grazing Incidence X-ray Diffraction Spectroscopy
HAADF-STEM	High Angle Annular Dark Field – Scanning Transmission Electron Microscopy

HERFD-XANES or HR-XANES	High Energy Resolution Fluorescence Detected -XANES
HR-TEM	High Resolution -TEM
LCF	Linear Combination Fitting
LN_2	Liquid Nitrogen
LSV	Linear Sweep Voltammetry
MALDI-TOF MS	Matrix Assisted Laser Desorption Ionisation Time-of-Flight Mass Spectroscopy
MCL	Materials and Catalysis Laboratory, UCL Chemical Engineering
MP-AES	Microwave Plasma – Atomic Emission Spectroscopy
NP	Nanoparticle
OER	Oxygen Evolution Reaction
ORR	Oxygen Reduction Reaction
NXES	Non-resonant (normal) X-ray Emission Spectroscopy
PEM (FC)	Proton Exchange Membrane (Fuel Cells)
PVP	Poly-Vinyl-Pyrrolidone
QXAFS	Quick X-ray Absorption Fine Structure Spectroscopy
RHE	Reversible Hydrogen Electrode
RXES	Resonant X-ray Emission Spectroscopy
SAXS	Small Angle X-ray Scattering
SBCA	Spherically Bent Crystal Analyser
SEM	Scanning Electron Microscope
STEM	Scanning Transmission Electron Microscope
TEM	Transmission Electron Microscopy
UCL	University College London
UV-vis	Ultra-Violet-visible Spectroscopy
VtC	Valence to Core XES
% V/V	Volume Concentration (Volume per Volume)
WAXS	Wide-angle X-ray Scattering
WF	Watzky-Finke (Theory of Nanoparticle Growth)
% W/W	Weight Concentration (Weight per Weight)
XAFS	X-ray Absorption Fine Structure

XANES	X-ray Absorption Near Edge Structure Spectroscopy
XAS	X-ray Absorption Spectroscopy
XES	X-ray Emission Spectroscopy
XFEL	X-ray Electron Free Laser Spectroscopy
XPS	X-ray Photoelectron Spectroscopy
XRD	X-ray Diffraction Spectroscopy

Sample Naming Conventions

Chapter	Sample Code	Description
Ch. 3	Pd^0-Cl	Palladium(0) with chlorine coordination
Ch. 4	Pt/C	Platinum NP on a carbon support
	Pt_xPd_y/C	Platinum-palladium alloy NP on a carbon support with Pt:Pd ratio of x:y
	PtNi/C	Platinum-nickel alloy NP on a carbon support
	PtCo/C	Platinum-Cobalt alloy NP on a carbon support
Ch. 5	Pd^0-Br	Palladium(0) with bromine coordination
Ch. 6	$Cu(OAc)_2/H_2O$	Copper acetate dissolved in H_2O
	$Cu(OAc)_2$/DMF	Copper acetate dissolved in DMF
	$Cu(OAc)_2/H_2O$/AA	Copper acetate dissolved in H_2O, reduced by ascorbic acid
	$Cu(OAc)_2$/DMF/AA	Copper acetate dissolved in DMF, reduced by ascorbic acid
	$Cu(OAc)_2$/DMF/N_2H_4	Copper acetate dissolved in DMF, reduced by hydrazine
Ch. 7	$Cu^{2+}\leftrightarrow Cu^0$	Square-wave cycling between Cu^{2+} and Cu^0
	$Cu^{1+}\leftrightarrow Cu^0$	Square-wave cycling between Cu^{1+} and Cu^0
	$Cu^{1+}\leftrightarrow Cu^{2+}$	Square-wave cycling between Cu^{1+} and Cu^{2+}

List of Unit Prefixes

Prefix	Symbol	Meaning
Tera-	T	10^{12}
Giga-	G	10^{9}
Mega-	M	10^{6}
Kilo-	k	10^{3}
Deci-	d	10^{-1}
Centi-	c	10^{-2}
Milli-	m	10^{-3}
Micro-	μ	10^{-6}
Nano-	n	10^{-9}
Pico-	p	10^{-12}
Femto-	f	10^{-15}

Note: Lists of Tables and Figures are provided in the Additional Materials (Chapter 9) to assist navigation.

List of Units

Unit	Symbol	Equivalent
Ampere	A	-
Angstrom	Å	10^{-10} m
Arbitrary Units	a.u.	-
Atomic Mass Units	amu	1.66×10^{-27} kg
Atomic Percentage	at%	-
Degrees Celsius	°C	K – 273.15
Coulomb	C	A·s
Dollars (USD)	$	-
Gauss	G	10^{-4} T
Gram	g	10^{-3} kg
Joule	J	$kg.m^2.s^{-2}$
Kelvin	K	-
Litre	L	10^{-3} m^3
Metre	m	-
Minute	min	60 s
Molar	M	$mol.L^{-1}$
Mole	mol	-
Ohm	Ω	$kg.m^2.s^{-3}.A^{-2}$
Papers	pp	-
Parts per Million	ppm	10^{-6}
Pascal	Pa	$kg.m^{-1}.s^{-2}$
Percentage	%	-
Pounds (GBP)	£	-
Radian	rad	-
Second	s	-
Tesla	T	$kg{\cdot}s^{-2}{\cdot}A^{-1}$
Electron Volt	eV	1.602×10^{-19} J
Weight Percentage	wt%	-
Revolutions per Minute	rpm	-
Volt	V	$kg.m^2.s^{-3}.A^{-1}$

Chapter 1. Introduction and Literature Review

Nanoparticles with high surface area are being widely adopted in catalysis due to their improved activity and material efficiency, showing promise for chemistry in a sustainable future. A large body of research has shown that the shape and size of nanoparticles plays a key role in catalytic activity, selectivity, durability, and other properties. Thus, the ‘rational design’ of nanomaterials has emerged as an important strategy for their optimisation and commercial adoption, with potential benefits including increased material efficiency, reduced costs, higher selectivity, reduced energy use and better resistance to degradation.

The ideal process of ‘rational design’ of enhanced nanomaterials for a catalytic reaction would broadly have two stages –first, the identification of catalytic active sites (with selection of the desired nanoparticle morphology that maximises these sites) and, second, the optimisation of synthetic procedure to control and predict the formation of the required nanoparticle morphology (Figure 1.1). In practice, both stages of nanocatalyst development are experimentally iterated through trial-and-error, learning from the results, until a better material is found.

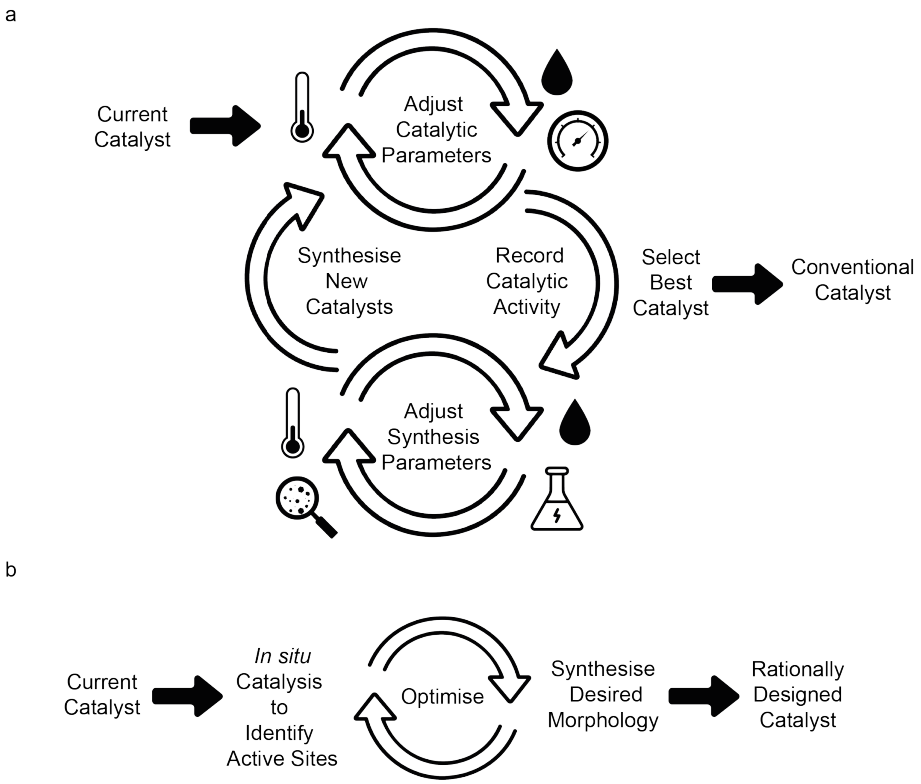

Figure 1.1 ***Conventional and Rational Catalyst Design Routes.*** *(a) The process currently followed for the optimisation of catalysts, requiring high quality trial-and-error elimination of catalysts (b) the ideal flow method for the rational design of improved catalysts, which would require less trial-and-error.*

The extensive literature studying nanomaterials for catalysis generally describes experiments spanning one or both of catalyst synthesis and catalytic application. For example, a typical study about the effect of nanoparticle size on a catalytic reaction might synthesise or model a range of nanoparticle sizes and catalytically test them to identify the optimal size.[1-6] Or, to study the effect of growth conditions on nanoparticle morphology, a single reaction parameter (e.g., temperature) could be varied during synthesis, while keeping other parameters constant, to record the shape and size of the resulting nanoparticles.[7-11] This knowledge is valuable as a foundation for theoretical understanding, identifying relevant factors and optimising industrially-applicable catalysts but it is hard to draw major scientific conclusions due to the range and volume of results. Moreover, the

intricate interplay of kinetics and thermodynamics often renders the underlying reasons for modified behaviours unclear.[12,13]

This highlights the need in catalytic chemistry and nanoparticle synthesis for the experimental understanding of not only 'what' the result of a reaction is, but also 'how?' and 'why?'. This is challenging to prove practically, and often the only way to find the solutions is using *in situ* characterization techniques to observe changes during a reaction and relate them to chemical or physical behaviours in the system. In fact, catalysis is a perfect example of the value of *in situ* measurements, as it was previously accepted that catalysts (which are, by definition, not consumed or chemically changed at the end of a reaction) did not chemically interact with reactants during a reaction, but *in situ* experimental results have demonstrated the importance of a catalyst's intermediate states and interactions with chemical species, confirming that catalysts may chemically and physically change during a reaction.[14]

The fundamental understanding of nanoparticle synthesis (in this case, studied as growth from solution) and the mechanisms of catalytic activity seem to be limited by the experimental observation of their behaviour. We believe that measuring these processes *in situ* and determining the reaction rates and intermediate species, is a stepping-stone towards the rational design of highly active nanocatalyst materials. While a defined set of rules for such design may not be achieved, we believe that the methodologies applied during this research, and the results obtained will contribute to a deeper understanding.

This chapter will outline the important concepts, existing literature and identified challenges to the experimental study of chemical rate determination in nanoparticle electrocatalysis and the precipitated growth of nanoparticles. Based

on this discussion, a summary of the structure and aims of the thesis will be set out.

1.1 Chemical Rate Determination

The determination of the reaction rate, by recording the progress of a chemical reaction over time, is imperative in both understanding and optimising reaction conditions. Reaction rate, or chemical kinetics, has been a fundamental measurement in chemistry since the first rate measurement experiments by Wilhelmy in Germany and Harcourt in the UK, more than 150 years ago.[15,16] The mathematical description of rate (Equation 1.1) is a scientific description of the progress of a reaction, and remains largely unchanged to this day.

$$Rate = \frac{Change\ in\ concentration\ of\ reactants\ or\ products}{Time} \qquad \textit{Equation 1.1}$$

Experimental measurements of the rate of reactions have been the foundation for theories describing the pathways and stages of nanoparticle growth as well as catalytic processes.[17,18] However, the physical limitations of experimental measurements and characterization tools is also the bottleneck in forming a deeper, scientifically-justified theory.[19,20] This limitation highlights the importance of advanced and reliable characterization tools for gathering *in situ* data, as an observational basis to build the fundamental scientific understanding of chemistry.

Progress in the development and availability of advanced characterization tools has therefore been swift in recent years. Initially, changes accompanying the reaction such as temperature shift or concentration of gases evolved were the only metrics available to measure reaction progress.[21] These experimental methods are still effective today and are widely used. However, a good

understanding of the reaction mechanism is needed in many cases to interpret these changes, since the formation of relevant intermediates or transient states may remain undetected. Modern tools have allowed more direct measurements of chemical and physical changes in reactants and products using X-rays and light scattering. While these advanced methods sometimes give a clearer understanding of the reaction steps, it is generally a combination of complementary techniques that is most reliable in providing a result (discussed in Chapter 2).

These technological advancements, including more sensitive detection techniques and data processing, have made rate determination and *in situ* experiments increasingly available and popular in the scientific literature since the 1990s (rate = 150 pp/year, Figure 1.2). At the time of writing, facilities such as the X-ray electron free laser (XFEL) can record chemical processes at the femtosecond time scale[22] despite numerous physical challenges and system limitations. However, in many cases this resolution is not necessary, since the time-scales of interest vary with the reaction mechanisms studied.

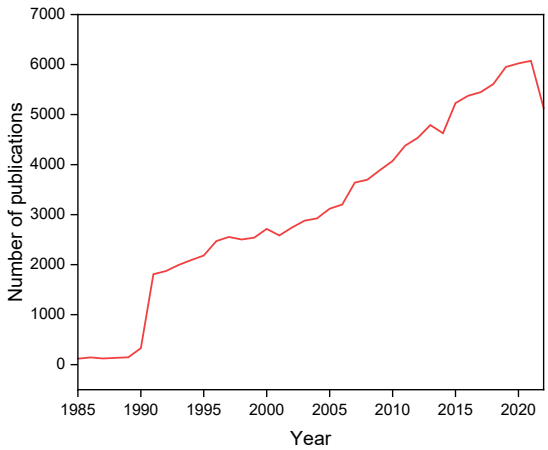

Figure 1.2 ***'Rate determination' Literature Survey.*** *Graphical representation of the number of papers available on Web of Science under the keyword "rate determination" (y-axis) and the year of publication (x-axis).*

Alongside scientific interest, the determination of reaction rate is an important diagnostic tool. In this work the effects of reaction conditions and catalyst materials on reaction rate and the implications for the nanoparticle formation are studied. These tools can give insights into why a certain nanoparticle shape forms or which catalyst sites are most active, allowing us to adjust and improve the materials or synthesis procedure, as necessary.

Already, reaction rates reported in the literature have proved valuable in finding clues to the chemistry occurring during a reaction.[23,24] There have been numerous reports of the rates of reaction at a catalyst surface, since the primary role of a catalyst is to adjust the rate of a reaction to form a desired product quickly and selectively.[25] In fact, catalysis is one of the areas which has benefitted most from *in situ* measurements since the precise role of a catalyst during catalysis is often not understood, although its effects are well-known.[26]

Another feature that reaction rate determination may provide is the ability to select ideal parameters for a reaction to occur. In the case of nanoparticle growth, the rate of the reaction can determine the shape and size of the particles formed, which is already clearly shown for the case of anisotropic particles forming at higher rates. Like catalysts, these systems are complex where reaction pathways and external reaction conditions may have intricate relationships with the reaction rate.

For example, the relationship between temperature and reaction rate is shown in the Arrhenius equation (Equations 1.2 and 1.3), where k represents the reaction rate, E_a activation energy, R Boltzmann constant and T temperature (K). It was proposed in 1889 by Svante Arrhenius, starting from an equation by van't Hoff relating temperature and equilibrium constants, and fitted with experimental data.[27]

$$k = Ae^{-\frac{E_a}{RT}} \qquad \textit{Equation 1.2}$$

$$ln(k) = ln(A) - \frac{E_a}{RT} \qquad \textit{Equation 1.3}$$

An empirical approach has been instrumental in confirming the relationship.[27] This indicates that factors which affect the rate, will directly affect the activation energy, and therefore the degree of completion of the reaction at a given temperature.

It has been the work of various studies to distinguish these parameters of interest, such as the catalyst surface changes or the effect of temperature on nanoparticle growth to assist in modelling and better understanding these systems.[28] The tools available for measuring the rate applied in this work are further discussed in Chapter 2, which expands on the scientific workings and the current state of research.

1.2 Metal Nanoparticles in Electrocatalysis

Catalysis is the acceleration of a reaction by a material which is not permanently changed at the end of the reaction.[29] This presents a particularly interesting case for rate-determination, as the primary role of a catalyst is to influence the reaction rate, without changing the equilibrium. By lowering the activation barrier to a reaction, catalysis may lead to faster reaction times, improved yields, selective reaction products, and reduced energy costs.[29,30] Thus, catalysis, by reducing chemical waste and energy use, is considered one of the twelve principles of 'green chemistry'.[31]

In heterogeneous catalysis, as studied here, the surface of a catalyst is where the reaction occurs and is therefore the region of scientific interest and potential

improvement. Catalyst materials are often expensive and degrade over time, especially in extreme industrial reaction conditions.[32-34] The key to reducing the cost and increasing the efficiency of these reactions is in improving the activity, stability and degradation resistance of the catalyst surface, or finding cheaper alternative materials.

One solution to maximise material use in catalysis is the application of "nanomaterials", which have an extremely high surface area to volume ratio. In recent years great research efforts in both industry and academia, have been dedicated to the study of nanoparticle synthesis for increased catalytic performance. These are supported by large investments, as exemplified by the UK in 2019 producing "at least one billion dollars' worth of catalyst" according to a UKRI report.[35] The same report goes on to describe catalysis as a $34 billion industry, and list 'CO_2' and 'fuel cells' among the key catalytic challenges studied in the UK for clean growth.[35] A similar interest is found in academia, where more than a million papers (1,031,522 based on a Web of Science search) have been published mentioning nanoparticles. Many of these works discuss preparation for a catalytic reaction *via* photocatalysis, electrochemistry or directly in catalysis, as shown in Figure 1.3. Of these numerous works on nanoparticles, the materials which stand out in the field of catalysis are the platinum group metals, where nanoscaling is a method to cut down on expensive material costs and tune selectivity.

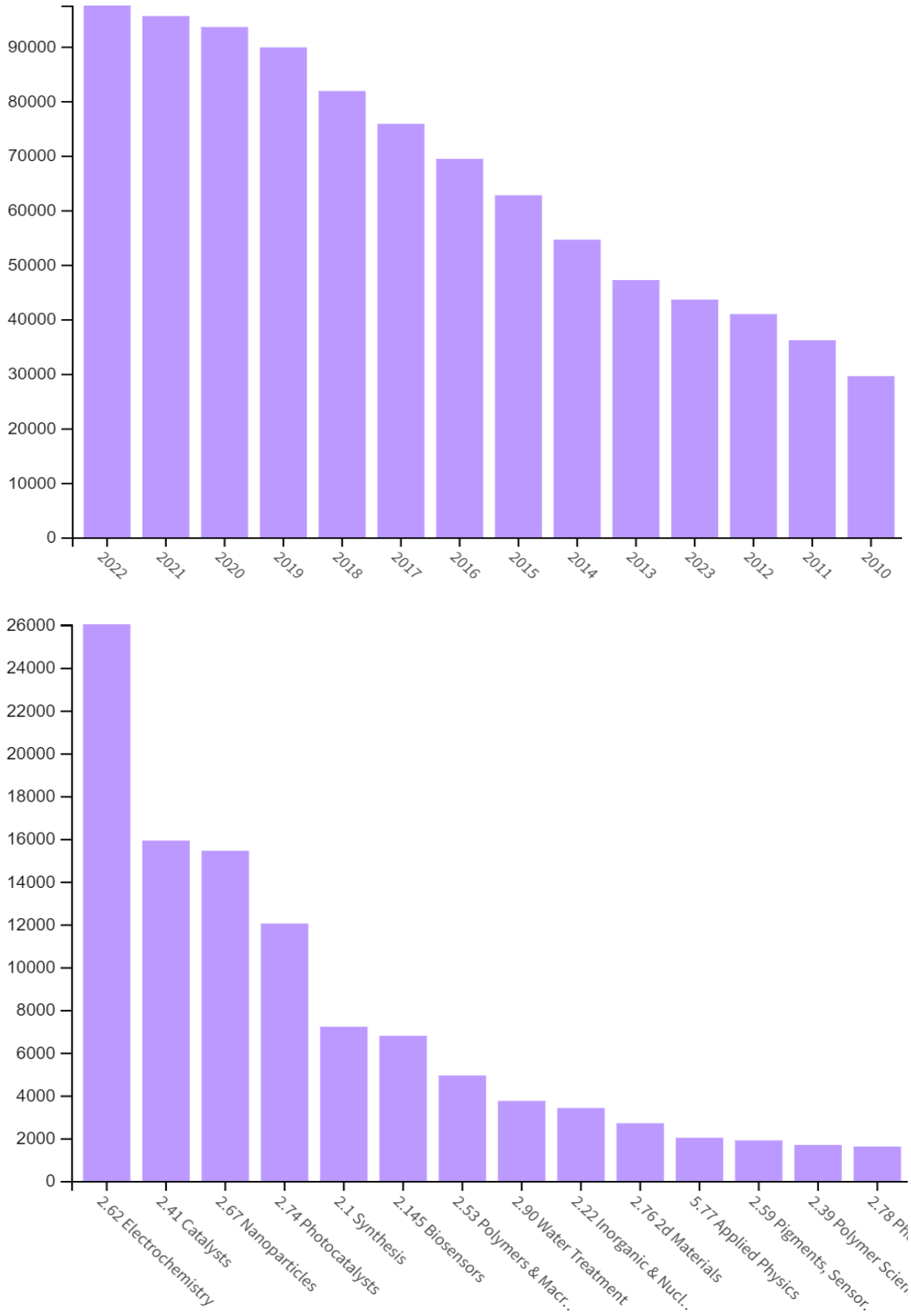

Figure 1.3 ***"Nanoparticle" Literature Survey.*** *(a) Number of papers with keyword "nanoparticle" has increased with publication year. (b) 'Platinum group metal nanoparticle' mentions by topic show high numbers in electrochemistry and catalysis.*

Nanoparticles are classified only by their size (usually 1 nm to 100 nm, in this work including up to 500 nm) and can be made of any solid or liquid material. In this work, the term nanoparticle will refer to metal nanoparticles unless otherwise specified, since metals are widely used in electrocatalysis and catalysis.

At the nanoscale, materials often have different chemical and physical properties to their bulk, making them attractive for applications like catalysis in which these properties can be exploited. The unique features achieved in metal nanoparticles include high surface area, reactive facets, size-tuned behaviour, and range of possible materials and shapes.[36-38] Currently the disadvantages of nanoparticles are the scaling of the production, expensive synthetic processes, and the degradation/loss of activity over time.[33,39,40]

Metal nanoparticles are already industrially applied in a range of reactions, including oxygen reduction, hydrogenation, and reductive coupling.[41-46] While these materials are active catalysts, the mechanisms by which they work are little understood. Through more detailed characterization in recent years, it appears that understanding the complex relationship between activity and structure is the cornerstone to the design of superior catalytic materials.[47] The reaction pathway followed may be controlled by the material properties of the catalyst, such as the shape, size, crystallinity and synergy between the alloyed metals. The catalytic behaviour of these nanoparticles are also difficult to predict, affected by factors such as surface area,[4,48] active site availability,[5,49] strain effect,[50] electronic interactions (affecting d-band energy and ligand interaction),[36] support interactions[51,52] and oxidative resistance.[32]

Currently, the world is heavily reliant on fossil fuels for energy and the high-volume synthesis of chemicals. To achieve independence from fossil fuels, clean energy must be made from renewable resources and the production of chemicals

based on non-critical materials. Electrochemistry is valuable in both applications, creating green electricity from chemical energy, and using green electricity to produce useful chemicals. In this work, the oxygen reduction reaction (ORR) in hydrogen fuel cells is an example of the former, and the carbon dioxide reduction reaction (CO_2RR), of the latter. The use of transition metals in these reactions and their chemical oxidation will be investigated, to give meaningful information about the catalytic reaction mechanisms involved.

The current state-of-the-art catalysts and mechanistic understanding of their catalytic activity are discussed in the following sections, to give context to this work.

1.2.1 Oxygen Reduction Reaction

Hydrogen has been promoted as an alternative to fossil fuels, especially in the transport sector, where hydrogen fuel cells can be used to power vehicles. Of the technologies available, Proton Exchange Membrane (PEM) fuel cells are the most widely adopted due to their compact, lightweight, and solid-electrolyte design. In a PEM fuel cell, electrical energy and water are produced through the controlled reaction between anodic H^+, passing through a proton exchange membrane, to combine with O^{2-} formed at the cathode. This produces electricity through the movement of electrons with only H_2O as a by-product.

Widespread use of commercially available fuel cells is restricted by their expense, and deactivation, among other challenges to the hydrogen economy. This high cost is often attributed to the use of 10 to 30 g of platinum per vehicle (at around £23 per gram), for example in the commercially available Toyota Mirai.[53] As an environmentally-friendly energy technology, the use of platinum is also

undesirable as it is a ‘critical material’ due to supply risks and intensive processing.

A majority of the Pt required for a PEM fuel cell is used in the cathode, where the oxygen reduction reaction occurs. This is to compensate for the slower cathodic reaction caused by multiple factors including the relatively low concentration of O_2 in air (20%), blocking of O_2 reduction sites and slow electron transfer kinetics. To reduce Pt use, a body of research has emerged to better understand the reaction mechanism and limitations, as well as engineering active and stable catalysts for the oxygen reduction reaction (ORR).

The ORR at the Pt surface in the cathode follows either the two electron or four-electron pathway, following the dissociative or associative mechanism (Figure 1.4). Both mechanisms have different rate determining steps, making their identification and control important for catalyst development. Generally, the four-electron pathway is preferred since it does not lead to the formation of corrosive H_2O_2 as a by-product of the reaction.

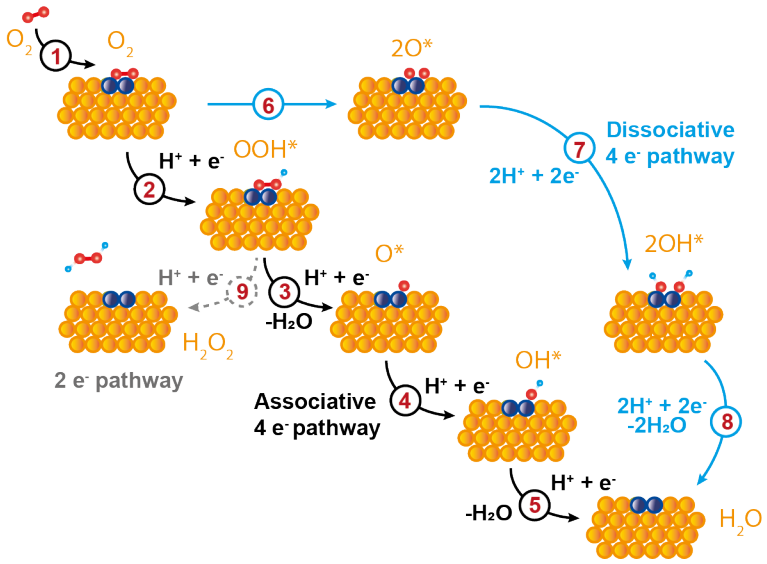

Figure 1.4 ***Oxygen Reduction Reaction Pathways.*** *Three possible reaction pathways followed during the oxygen reduction reaction occurring at the cathode of a fuel cell. The dissociative pathway is given by steps 1, 6, 7 and 8 (blue arrows), associative pathway in steps 1, 2, 3, 4, and 5 (black arrows) and two-electron pathway in step 9 (grey, dashed arrow). The number of protons and electrons involved in each step are indicated alongside.*

In step 1, the gaseous oxygen is adsorbed onto the catalyst surface.

$$O_2(gas) \rightarrow O_2^*(ads) \qquad \textit{Step 1, Equation 1.4}$$

Then the reaction may follow one of three pathways:

Associative 4e$^-$ pathway:

$$O_2^* + (H^+ + e^-) \rightarrow OOH^* \qquad \textit{Step 2, Equation 1.5}$$

$$OOH^* + (H^+ + e^-) \rightarrow O^* + H_2O \qquad \textit{Step 3, Equation 1.6}$$

$$O^* + (H^+ + e^-) \rightarrow OH^* + H_2O \qquad \textit{Step 4, Equation 1.7}$$

$$OH^* + (H^+ + e^-) \rightarrow H_2O \qquad \textit{Step 5, Equation 1.8}$$

Dissociative 4e$^-$ pathway:

$$O_2 \rightarrow 2O^* \qquad \textit{Step 6, Equation 1.9}$$

$$2O^* + (2H^+ + 2e^-) \rightarrow 2HO^* \qquad \textit{Step 7, Equation 1.10}$$

$$2HO^* + (2H^+ + 2e^-) \rightarrow 2H_2O \qquad \textit{Step 8, Equation 1.11}$$

Associative 2e$^-$ pathway:

$$O_2^* + (H^+ + e^-) \rightarrow OOH^* \qquad \textit{Step 2, Equation 1.12}$$

$$OOH^* + (H^+ + e^-) \rightarrow H_2O_2 \qquad \textit{Step 9, Equation 1.13}$$

Based on these reaction steps, theoretical and experimental works have focused on finding activity descriptors and materials properties which can be maximised to reduce the reaction barriers of the desired pathway. For instance, the identification of the *d*-band centre and calculated overpotential as descriptors in the determination of active catalysts has allowed the theoretical selection of metals and alloys for testing.[54] Another factor describing activity is the adsorption of reacting species (such as *O and *OH) on the catalyst surface, which could be enhanced by material selection and a nanoparticle morphology with active site access and optimised facets.[55,56] Further works calculate similar activity descriptors for a range of cluster sizes, down to single atoms.[3,57,58]

Despite testing a wide range of metal and non-metal combinations with various support materials and morphologies, platinum remains the most efficient elemental catalyst material, as corroborated by theoretical calculations.[54,59] Increasing the surface area of Pt and alloying are two effective strategies for reducing platinum use, with 2 nm diameter Pt/C nanoparticles and PtNi/C and PtCo/C alloy nanoparticles already adopted commercially.[60] Both strategies may be adopted to fine-tune the catalytic behaviour.

To compare materials, a higher half-wave potential and mass activity during the ORR in an acidic medium is desirable for an active catalyst. The benchmark for activity is generally commercially available 20 wt% Pt/C (Vulcan), which has a

half-wave potential of ~0.84 V[61] and mass activity around 0.21 $A.mg_{Pt}^{-1}$ (current produced by platinum mass loading).[62]

Nanoparticle Morphology

The high degree of control in nanoparticle synthesis has allowed for a wide range of catalyst shapes and sizes, through the modification of synthesis parameters. In general, a high surface area leads to high catalytic activity but may also increase effects of degradation mechanisms such as leaching, agglomeration and ripening.[63] Optimal morphologies have been reached through a combination of experimental trials and theoretical models. Activity has been attributed variously to increased access of reactants to active sites,[64,65] higher surface area and greater number of active sites,[66] preferred active metal coordination at edges and crystal facets,[67] neighbouring atoms affecting *d*-states and electronic structure,[68-70] and more.[64]

Nanoparticle shape influences the exposed facets, and the degree of coordination of active sites *via* surface area. Since the catalytic reaction occurs at the surface, an increase in surface area may lead to more exposed active sites and higher activity. Particles with extremely high surface areas have therefore been designed. For example, ultra-jagged Pt nanowires have shown an extremely high mass activity of 13.6 $A.mg_{Pt}^{-1}$.[48] This activity is attributed to the undercoordination of Pt atoms, with coordination values of 6 to 9.[48] The role of undercoordination has been controversial since theoretically Pt(111) surfaces should show higher activity than undercoordinated Pt edges,[2,66] but the enhancement only in cases of concave defects has been suggested by Calle-Vallejo et al.[71]

Faceted growth has received particular interest and has assisted in identifying key descriptors for ORR in Pt.[55,72] For example, theoretical evidence shows that

in ORR the Pt(111) facet has higher activity than the Pt(100) facet.[56] The same result is observed experimentally for ORR[73,74] and with hydrogen oxidation reaction (HOR) on single crystals which may translate to ORR activity.[75,76] This increase in activity may be caused by lowered binding energy of reacting species on the Pt(111) surface.[2] To design a catalyst based on this insight, an ideal particle shape would maximise the active Pt(111) facet exposure. To test this, octahedral Pt nanoparticles with a majority of Pt(111) have been designed and found to be highly effective for ORR.[55,74]

The size of nanoparticles, particularly in “regular shapes” has been an area of wide interest, controlling the surface area to volume ratio and edge sites to surface sites ratio. Indeed, due to the unpredictability of metals at the nanoscale, testing nanoparticles sizes down to clusters and single atoms has shown the effects on the chemical properties of the metal surface.[2,66] From size-control experiments, 1.1 nm has been found to be the optimal size for the efficient use of Pt in spherical particles, with mass activity of 0.87 ± 0.14 $A.mg_{Pt}^{-1}$.[77]

Pd nanoparticles are also widely studied for ORR. Pt has a higher activity than Pd, typically exhibiting mass activity values around 0.17 to 0.25 $mA.\mu g_{Pt}^{-1}$ while commercially available Pd catalysts have a mass activity of less than 0.1 $mA.\mu g_{Pd}^{-1}$.[50,78-81] While Pt has the advantage of being more active, Pd is resistant to CO poisoning and has high stability. Although the exact mechanism of ORR is still under investigation, literature predicts that Pt and Pd catalysts follow a similar reaction route.[81,82] Thus, papers citing the reaction mechanisms of ORR on Pd catalysts follow the same two electron and four electron transfer routes as shown for Pt catalysts.[81]

Alloying

Alloying has been shown to afford numerous advantages, such as poison-resistance, durability and tuning of chemical behaviour. It has also been highly effective in reducing precious metal use and has led to the commercial adoption of PtNi and PtCo nanoparticles in PEM fuel cells.[83-86] Research has shown that both the distribution of the metals within the alloy and the ratio between alloyed metals are significant in these materials, aside from their morphology.[87] Similar to Pd alloys, Pt atoms dispersed in Co and Ni experimentally maintain their high activity, while using less Pt.[55,87,88] Comparisons of highly dispersed structures and core-shell configurations of Pt distribution, have favoured the formation of a core-shell where Pt is preferentially present at the surface.[80,88] Since only the surface is exposed to the reactants, concentrating Pt at the surface is most reasonable, to lower Pt use. Effective alloy metals alongside Pt include Ni, Co, Pd, Cu, Au and Fe.[41,89-91]

At the surface, the interaction between Pt and alloyed metals can enhance activity, meaning that alloys with higher Pt loadings do not always show higher activity. A work by Thanasilp and Hunsom shows that the ideal ratio between Pt and Pd in an alloy was 1:2 for the given system.[92] For similar experiments with PtNi, the optimal Pt:Ni ratio was 1:1,[93,94] although Pt_3Ni_1 has shown high durability.[95]

Pt/Pd alloys are believed to show high activity due to the electron transfer from Pd to Pt, and the adjustment of Pt *d*-band centre by alloying.[81,96] Xu et al. have also shown that the presence of Pd in Pt-Pd/C alloy makes Pt increasingly resistant to passivating oxidation and has a high activity.[32] Highly active Pd alloys have been formed with transition metals such as Pt[82], Fe,[97] Mo[50] and more, giving

activities as high as 16.37 mA.μg_{Pd}^{-1}, although most values are closer to or below those observed in Pt.[50]

The fluctuating price and limited reserves of Pd,[33] have lowered interest in Pd catalysts in recent years.[33,81] However, all material alternatives to Pt are worth pursuing for the collection of scientifically valid options in case of a change in circumstances. The high value of Pt and Pd shows the need for improved activity where less material will be required in future. The properties exhibited in alloys undergo a drastic change when metal atoms are isolated, or in small clusters such as in single atom alloys.

“Single atom alloys”, in which a single atom of an active metal (like Pt) is surrounded by and alloyed with a less active host (like Pd or Ni), have unique chemical properties on account of lattice insertion effects and the modification of the electronic states. This could ideally lead to high activity with extremely low Pt loading. These materials have been mainly studied through density functional theory (DFT) modelling, due to the difficulty in synthesis and conclusive characterization. Since models predict high activity in these materials for a range of reactions including ORR, experimental investigations are of considerable interest. A work by Zhang et al. showed that Pt atoms dispersed in a Pd matrix were highly active for ORR, comparable to that of a commercial catalyst.[57] Such investigations are extending to non-noble metal hosts, and improved stability of isolated sites. However, it should be mentioned that the experimental proof of the presence of single sites are generally localised and may not exclude the possible presence of nanoparticles within the material, which could influence activity.

Theoretically, in a single atom alloy, each platinum atom could be 100% efficient for ORR, without competing with neighbouring active sites. The stability and poison resistance are determined by the host material which makes up the bulk

of the catalyst, and its interaction with the active metal. In general, it is found that migration and agglomeration under extreme conditions such as those of an applied catalytic reaction are the most common problems in highly distributed alloys. The *d*-band energy, crystal packing structure and bond length of the host metal tune the catalytic behaviour. These properties of single atoms with highly discrete energy levels can be achieved to a lesser degree by a small cluster of atoms (<10 for example) forming isolated active sites within an alloy. Such small clusters would still show adjustment in *d*-states, have narrow energy bands compared to bulk material, and are more likely to form experimentally.

For the ORR, these materials may potentially favour a different reaction pathway since the chemical properties of the active sites have been adjusted. Studies show that the reaction pathway in single atom alloys and on Pt and Pd single atoms may follow the $2e^-$ pathway and produce H_2O_2.[98,99] This is contrary to the results from theoretical calculations which predict high $4e^-$ pathway ORR activity in Pd/Au single atom alloy.[58] Similar behaviour may be observed in extreme ratio alloys, so the study of these materials and ORR pathways may identify chemical properties which can enhance activity and lead to the development of improved catalyst materials.

1.2.2 *In situ* and Time-Resolved ORR Measurements

Many of the advancements in ORR catalyst materials have been achieved through trial-and-error testing under various nanoparticle shapes, sizes, alloy compositions and materials. The theoretical understanding of the descriptors for ORR which can be used to predict active materials has emerged in the last 20 years, based on the work by Norskov et al. in 2004.[100] The reaction mechanisms and understanding of a material can also only be understood by reconciling

theoretical knowledge with experimental results. Thus, *in situ* characterization is important in reactions such as ORR which are widely studied.

Research works in recent years have applied advanced characterization to record the changes undergone by various conformations of catalyst nanoparticles *in situ* during ORR. These results aim to deduce the chemical reaction pathway as well as mechanisms of passivation, dissolution, and aggregation.[32] Alongside an applied potential, techniques including X-ray diffraction (XRD),[49,101] X-ray absorption spectroscopy (XAS),[89,102,103] Raman spectroscopy,[104,105] Fourier transform infrared spectroscopy (FT-IR),[106-108] transmission electron microscopy (TEM),[109,110] and atomic force microscopy (AFM)[111] have been used to measure the physical and chemical changes at the catalyst surface.[49] *In situ* time-resolved XAS has been notably applied in catalysis and electrocatalysis due to the versatile information obtained with a non-destructive method.[103,112-114] Of these works, a number have focused on determining the reaction mechanism while others have studied the catalyst deactivation. It can be noted that deactivation studies usually focus on the changes in nanoparticle morphology and aggregation,[115] surface species[32] and metal dissolution[39] which may occur simultaneously and impact activity.

To determine the reaction mechanism, it is current practice to measure either the intermediates/products or activity descriptors, such as chemisorption or electronic states, during ORR. Intermediates are effective in determining the $2e^-$ pathway, where H_2O_2 evolved can be quantified (usually with a rotating ring disk electrode), and thereby distinguished from the $4e^-$ pathway.[116] However, the $4e^-$ pathway may follow a combination of associative and dissociative mechanisms, which are difficult to distinguish. *In situ* IR spectra captured by Nayak et al. identified three oxygen-containing intermediates adsorbed on Pt/C,

corresponding to adsorbed superoxide (OOH_{ad}), hydroperoxide ($HOOH_{ad}$), and weakly adsorbed oxygen ($O_{2,\ ad}$).[117] The majority of OOH_{ad} and $HOOH_{ad}$ below 0.8 V suggests an increased contribution from the association pathway at lower potentials. This result further illustrates the difficulty in distinguishing these two reaction pathways, since they often occur simultaneously.

Inconclusive experiments can be combined with theoretical calculations to infer the reaction pathways or the causes of enhanced performance. The higher activity for de-alloyed Pt_1Co_1 nanoparticle in comparison with pure Pt catalyst was studied by Jia et al. with a combination of *in situ* XAS, ex-situ TEM, and FEFF8 calculations.[118] Experimental results combined with FEFF8 calculations, showed that the higher catalyst activity of de-alloyed Pt_1Co_1 nanoparticle for ORR could be attributed to tuned *d*-band energy influenced by ligand effects and compressive-strain.[118]

The oxidation at the surface of platinum during ORR cycling causes passivation and lowers activity, and is therefore undesirable.[119] The rate of formation of this PtO_2 and the surface oxidative species have given insights into the degradation of different types of catalysts. Xu et al. looked at Pt surface oxide species and intermediates using the X-ray absorption near-edge structure difference (Δμ-XANES) technique during *in situ* ORR on Pt-Pd alloy, to distinguish between the configurations of oxygen atoms on the Pt surface.[32,119,120] Through this study, it was determined that the Pt oxidative passivation was reduced with Pd alloying.

These insights have brought us closer to finding optimal materials and eliminating materials which are not effective. The search for durable active catalysis is ongoing, to achieve Pt mass in a PEM fuel cell (10 - 30 g) less than or equal to that in a diesel car's catalytic converter (8 - 10 g).[60]

1.2.3 Cu oxidation in CO_2 Reduction Reaction (CO_2RR)

A major by-product of fossil fuel consumption and contributor to global warming, carbon dioxide (CO_2) can be a building block for the production of valuable organic compounds. In the efforts towards a more sustainable "closed carbon cycle", technologies for the capture and utilisation of CO_2, such as the electrocatalytic CO_2 reduction reaction (CO_2RR), are receiving increased attention.

Many products can be formed from CO_2RR, but the production of lower hydrocarbons (C_1) such as CH_3OH and CH_4, are not currently cost effective. The production of higher hydrocarbons with two or more carbon atoms (C_{2+}) is of more scientific interest and commercial viability. Catalysts of interest for CO_2RR include Ag and Au, but Cu is particularly significant for the formation of C_2 products.[121]

Copper is currently the only heterogeneous catalyst effective in producing hydrocarbons and alcohols, converting CO_2 to products with more than two electron transfers.[121] Although it is the most widely studied catalyst for the CO_2RR, with a Cu catalyst these reactions still require significant overpotentials.[122,123]

As a chemical reaction, the general CO_2RR at the cathode can be written as

$$xCO_2 + nH^+ + ne^- \rightarrow product + yH_2O \qquad \textit{Equation 1.14}$$

While at the anode, the oxygen evolution reaction (OER) occurs.

The activity of Cu is attributed to its unique quality among metals that the adsorption energy is negative for *CO but positive for *H.[121] Copper for CO_2RR is often studied as a single crystal sheet but has more recently been developed as nanoparticles and Cu alloys to tune activity and selectivity. For the electrochemical reaction, the two major factors identified to affect reaction

products formed on a copper surface are facets present[124,125] and the oxidation state of surface Cu.[126] However, it should be noted that these two factors are not unrelated, as certain facets may be more conducive to creating particular oxidised Cu species.[125]

As the formation of C_{2+} products requires the adsorption and interaction of intermediate species, the facets favouring these adsorptions are investigated. DFT studies have shown that the Cu(100) and Cu(211) facets favor C_{2+} product formation, over Cu(111).[124] Experimentally, the evidence to support this has been consistent with the theory, with the majority of research surrounding stepped facets of varying complexity.

It should also be noted that the presence of oxidised Cu species, rather than the facet structure, or their combination, may lead to preferred product formation.[124] A work by Chou et al. has shown that the mixture of Cu(0) and Cu(I) at the surface could lead to a mixture of CO_{atop} and CO_{bridge} adsorption and increase the yield of C_{2+} products.[126] Increased formation of C_1 products was observed in the case of majority Cu(0) or Cu(I) indicating that the relationship between activity and oxidation states may be complex.[126] Alternatively, highly selective Cu(II) oxide nanosheets have been grown which show high ethylene and ethanol formation. Studies comparing oxidation states often include variations in crystal facets, supporting the idea that these factors are intertwined. The control of the Cu oxidation state at the surface has previously been achieved by square-wave cycling.[127]

Based on the literature, the importance of the control of oxidation states at a Cu surface for CO_2RR is clear. The rate of formation and ability to switch between oxidation states, is of scientific interest and could be directly applied to pre-

treatments of CO_2RR catalysts. Methodologies and developments in the time-resolved observation of Cu oxidation rates and species will be further discussed.

1.2.4 Rate Determination: Cu Oxidation

The recording of CO_2RR on a Cu surface has shown surface species changes and indicates that the Cu_2O is the active species for the formation of useful reactants.[128] However, the selectivity of C_{2+} products is complicated and pure Cu_2O is not effective in the absence of Cu^0, with computational studies showing a synergistic relationship between Cu^+ and Cu^0 for CO_2 activation and C-C coupling.[122,129] *In situ* observations in this area are relatively few and remain challenging for CO_2RR systems where the selectivity of products is unpredictable. There have already been numerous works discussing the rates of catalyst oxidation and degradation in CO_2RR and the selective formation of the products. A work by Lai et al. uses an online mass spectrometer to measure the products formed during the reaction and relate them to the measured electrochemical data.[130] The formation of oxide species at the Cu surface was also studied with *in situ* XAS and *in situ* Raman to monitor the species formed.[131-133] An *in situ* grazing incidence-XRD (GIXRD) study by Scherzer et al. showed the transient oxidation states of Cu oxidation, and determined that further *in situ* investigations are required even for a simple oxidation reaction.[134]

These effects of shape, size and surface species on the nanoparticle activity during catalysis highlight the importance of controlling these features. Chemical behaviours such as oxidation state may depend on the surface facets and enhance or decrease activity dramatically. Time-resolved studies offer valuable insight into the relationships between these factors and the reaction mechanisms. Once a certain desirable physical or chemical trait is determined, optimisation

can be performed by making the trait more available. An understanding of the synthetic procedures to obtain such materials is the practical next step in their optimisation, so that the desired shapes and sizes can be rationally designed.

1.3 Growth of Metal Nanoparticles in Solution

In both described electrocatalyst systems, the surface morphology and oxidation states have been found to play an important role in defining catalytic activity. Once the optimal morphology of the catalyst for a given reaction is determined, it is necessary to have a suitable method of synthesis. This can only be achieved through an understanding of the effect of reaction rates and mechanisms on catalyst morphology.

The synthesis of catalytic nanoparticles, less than 100 nm in size, has received particular attention, as designed nanomaterials are being applied and optimised for commercial applications. Diverse strategies have been developed to create a range of nanomaterials, controlling shape and size. However, the development of synthetic techniques for nanoparticle production has outpaced the theoretical understanding and ability to predict mechanisms and morphology control.[135,136] These predictions can only be formed based on experimental study of the growth of nanoparticles in diverse systems. Many of the same advanced characterization tools used to identify the catalytic active sites, are applied to observe nanoparticle growth processes *in situ.*

Synthetic procedures for nanoparticles can be broadly classified as top-down or bottom-up methods (Figure 1.5). The ‘top-down’ approach favours the breakdown of larger particles to nano-size. In contrast, the ‘bottom-up’ techniques take advantage of physical and chemical properties to grow particles of a defined

shape and size. Bottom-up synthesis techniques are the most widely used in research, largely due to their high degree of morphological control. Common examples of bottom-up synthetic techniques include chemical vapour deposition, sol-gel, precipitation, and hydrothermal synthesis.

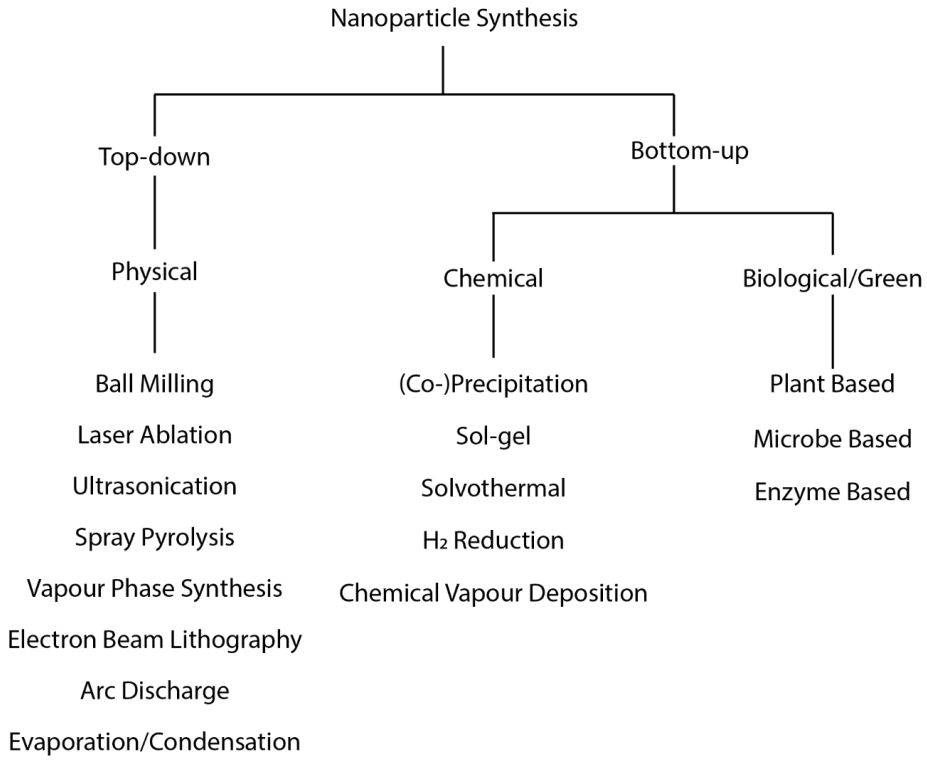

Figure 1.5 ***Summary of Nanoparticle Synthesis Methods.*** *Systematic diagram showing the classification of popular synthesis methods used for the formation of nanoparticles. These are broadly distributed into physical methods (red), chemical methods (blue) and biological methods (green). These are labelled to indicate the more popular methods in recent publications.*

Of these, growth *via* chemical 'precipitation' or 'co-precipitation' is one of the most popular bottom-up synthesis techniques, due to the ease of use, versatility of materials and high crystallinity of structures formed.[137,138] In this work, chemical 'precipitation' refers to the synthesis technique during which one (or more) metal salt solutions is mixed with a reducing agent in the liquid phase to induce the precipitation of crystalline metal nanoparticles. A surface agent is typically added

to prevent agglomeration and achieve a controlled morphology. In many cases, chemical precipitation can be performed under mild reaction conditions and with simple materials.

Growth *via* chemical precipitation is often classified into stages, based on defined chemical and physical changes. In this work, the four stages of growth will be described as reduction, nucleation, growth and reoxidation. The reduction stage includes the chemical change of oxidation state of the metal, generally from a higher oxidation state to metallic, which occurs at the beginning of the reaction. 'Nucleation' describes the first formation of solid species in solution, while 'growth' describes the addition of reduced metal atoms to existing nuclei. Finally, the 'reoxidation stage', typically observed at longer reaction times, involves the reshaping, oxidative etching or redissolution of nanoparticles in solution.

Challenges to the wide-spread adoption of chemical precipitation growth include the dependence on surface active agents (surfactants), the reaction scalability, the use of harsh chemicals and the difficulty in predicting nanoparticles formed under different conditions. Surfactants, although necessary to prevent clustering and control morphology, are often difficult to remove and can be detrimental for catalytic applications since they block the catalytically active surface. Surfactant removal has been achieved by nanoparticle washing after growth, application of heat after nanoparticle formation and electrochemical surface activation. In addition, continuous flow reactors are under development for increased synthetic output and the use of mild chemicals and reaction conditions is being promoted. However, a challenge remaining is the unclear relationship between the reaction conditions and the growth behaviours of nanoparticles.

Currently, there exist multiple theories for the growth of nanoparticles in solution, based on experimental findings gathered at the time. A factor which has

particularly influenced this increased interest and understanding of the growth is the use of advanced characterization tools, giving experimental observations which were previously impossible to achieve. Theoretical descriptions of nucleation and growth *via* chemical precipitation, previously assumed to be correct, are now being revised as new observations come to light.

The chemical and physical experimental evidence has been the key to recent advances in growth theories.[136] The first significant contribution to chemical kinetics is attributed to Harcourt,[139] although Wilhelmy performed the first quantitative study in 1850.[140] These laid the foundation for modern studies using *in situ* advanced characterization tools.

For the growth of nanoparticles, various theories have formed over the years, aiming to determine the mechanisms of growth from kinetic data. In 1900, Ostwald began forming theories of growth in solutions, applicable to a wide range of solution growth systems, most notably the concept of Ostwald ripening.[141] The LaMer theory of burst nucleation was developed around the 1950s based on his work with sulphur, and described the nucleation and growth stages of a reaction as two separate processes.[21] The shape control was later attributed to the theory of Ostwald ripening of selective growth and dissolution. Contrary to LaMer's assumption of separate nucleation and growth, in 1997 Watzky and Finke suggested that constant simultaneous slow nucleation leading into autocatalytic growth was a more likely explanation for the growth profiles observed experimentally.[18]

To form a better understanding of the differences in these theories, the salient points and evidence supporting them are discussed, starting with classical theories before following chronological developments. A particular emphasis is

put on the assumptions made by each theory, as these are usually the limitations of the system.

1.3.1 Nucleation Theories

Nucleation is the first step of growth, in which solid nuclei form the templates for crystal growth.[17] It can also be described in terms of thermodynamics as the formation of a low free energy phase with an organised structure from a high free energy phase, like a solution. Thus, nucleation is defined by the first appearance of a thermodynamically stable solid phase. Depending on the conditions, the nucleation time can have a difference of orders of magnitude, with small particle sizes between the angstrom (10^{-10} m) and nanometre (10^{-9} m) scales.[142] As such, the nucleation process is difficult to study and little understood.

Nucleation processes may be classified based on the nucleating site. During 'primary nucleation', nuclei form directly from solution. This can be homogeneous where the nucleation occurs spontaneously in clear solution, or heterogeneous where the nucleation occurs at a foreign surface such as an impurity, dust particle or on the vessel walls.[143] The contrary of 'primary nucleation' is 'secondary nucleation', in which growth occurs on pre-existing solid materials. For controlled secondary nucleation, pre-formed nuclei are used as templates for particle growth and are termed 'seeds'. Various theories have emerged to find a reasoning behind the nucleation process of which the classical nucleation theory has historically been the most popular.

Classical nucleation theory aims to find the nucleation rate, based on the free energy for formation of nuclei. A key achievement of this theory has been the ability to explain and calculate the large variation in time-scales of nucleation.[142] Homogeneous nucleation is not as common as heterogeneous nucleation but provides a simpler system as a foundation of the theory.

Classical Nucleation Theory

To begin with, for the prediction of nucleation rate, R, defined as the number of nucleation events per unit volume per unit time, in classical nucleation theory (CNT), can be given by

$$R = (\rho Z j)\ exp\left(-\frac{\Delta G_{crit}}{k_B T}\right) \qquad \textit{Equation 1.15}$$

where k_BT is the thermal energy and ΔG_{crit} is the Gibb's free energy of the system, above which nucleation occurs.[17]

In the pre-exponential factor, ρ is the number density of molecules, which is effectively the number of possible nucleation sites available (every molecule in the case of homogeneous nucleation). j is the rate of attachment of molecules, for which the upper-bound is limited by the diffusion on the nucleus. It can, however, be much slower than the diffusion. Z, the Zeldovich factor is included because the probability that a potential nucleus eventually forms a crystal is less than one. Thus, the rate of nucleus formation is Zj instead of simply j.

The remaining factor that will determine the nucleation rate is the free energy. The free energy increase in formation of an additional surface (surface free energy) is balanced by the free energy decrease of formation of a solid species (bulk free energy). The change in free energy is given by:

$$\Delta G = 4\pi r^2 \gamma + \frac{4}{3}\pi r^3 \Delta G_v \qquad \textit{Equation 1.16}$$

Where r is the radius of the nucleus, γ is the interfacial tension and ΔG_v is the energy difference between the nucleated phase and the solution (Figure 1.6).[17] This can be given in terms of the supersaturation (S), the molar volume (v), temperature (T) and Boltzmann's constant (k_B) by:

$$\Delta G_v = \frac{-k_B T\ ln\ (S)}{v} \qquad \textit{Equation 1.17}$$

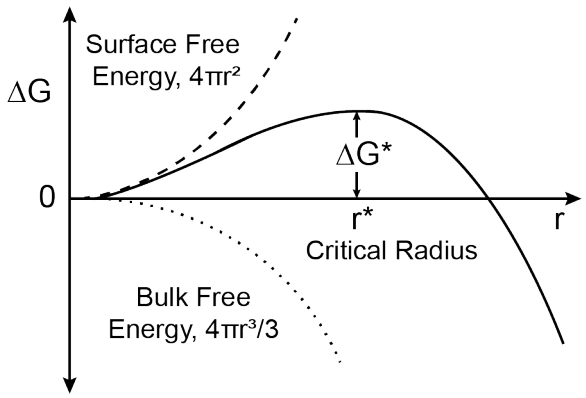

Figure 1.6 ***Free Energy with Nanoparticle Radius.*** *Diagram showing the contribution of the surface free energy ($4\pi r^2$) and bulk free energy ($4\pi r^3/3$) to the resulting free energy (ΔG), with increase in particle radius (r). ΔG^* represents the highest ΔG value and r* the corresponding radius. Redrawn based on Thanh et al., 2014.*[17]

The free energy decreases after a 'critical' radius, r*, corresponding to the time when the derivative of ΔG is zero. The critical radius is the particle radius above which the nuclei have higher probability of remaining in the solid phase without redissolving.

$$r_{crit} = \frac{-2\gamma}{\Delta G_v} = \frac{2\gamma v}{k_B T\, ln\,(S)} \qquad \textit{Equation 1.18}$$

This critical radius can be used to calculate the critical free energy for homogeneous nucleation:

$$\Delta G_{crit}^{homo} = \frac{4}{3}\pi\gamma r_{crit}^2 \qquad \textit{Equation 1.19}$$

This value can be included in the initial rate of nucleation equation to give:

$$Rate = R = (\rho Z j) exp\left(-\frac{\Delta G_{crit}}{k_B T}\right) = (\rho Z j) exp\left(-\frac{16\gamma^3 \pi v}{3\, k_B^3 T^3\, ln(S)}\right) \qquad \textit{Equation 1.20}$$

This gives a prediction for the nucleation rate during homogeneous growth of spheres.

For heterogeneous nucleation, which occurs at an existing surface, the contact between the solution and surface must be considered. The heterogeneous rate is generally orders of magnitude higher than homogeneous nucleation, so a factor φ is included when calculating the free energy of heterogeneous nucleation.

$$\Delta G_{crit}^{hetero} = \varphi \Delta G_{crit}^{homo} \qquad \textit{Equation 1.21}$$

This factor of φ is related to the contact angle θ by

$$\varphi = \frac{(2+cos\,\theta)(1-cos\,\theta)^2}{4} \qquad \textit{Equation 1.22}$$

This is the desired method of nucleation in 'seed-mediated' growth, often applied in nanoparticle synthesis. However, it should be noted that in most cases, homogeneous and heterogeneous nucleation occur indistinguishably in parallel.[19]

The limitations for application of the classical nucleation theory are whether the assumptions made match with the system studied. First, the assumption that the inside of a nucleus is a bulk incompressible fluid, and that the interfacial tension of the nuclei is like a similar macroscopic surface has been questioned. The second assumption is that particles grow or shrink only by the addition or loss of single particles or atoms, rather than clusters. This may be more unlikely in cases near the critical point, as the number of clusters joining may be significant. Lastly, the assumption of spherical particles also becomes less probable as nuclei grow. Therefore, these models can only be fitted to experimental data and first-principles prediction is rarely accurate.

In recent years, additional criticisms of the application of CNT to transition metal systems have appeared. In the 2021 review by Whitehead et al., concerns are raised that the classical nucleation theory ignores the effect of surface ligands, applies a thermodynamic calculation to a kinetically limited reaction and that

metal systems are too large to follow this theory.[144] Thus, new 'non-classical' theories have emerged, allowing a better understanding of the more likely pathways.

Non-Classical Nucleation

In response to data collected and the doubt cast on the classical nucleation theories, various other ideas have emerged, which are classified simply as 'non-classical' nucleation theories.[145,146] None of these has been proven to be universal and the collection of reliable experimental evidence is challenging. The size of a critical radius depends on the reaction conditions which shift the equilibrium of solid nuclei.[147]

An example of the type of system addressed by non-classical theory is the case where nanoclusters form during the pre-nucleation, giving rise to local energy minima. This can lower the nucleation barrier, allowing nucleation at supersaturation levels lower than predicted by the classical theory.[148]

While the details of the non-classical theories are not discussed here, the measurement of data for nucleation is extremely challenging due to a lack of consensus about the rate of nucleation and the size of the critical nucleation radius.

1.3.2 Growth Theories

LaMer "Burst Nucleation"

LaMer theory is one of the most prominent theories about growth since its publication in the 1950s. Despite its name, the theory does not provide any mechanism for nucleation with the assumption that this stage is 'instantaneous'. The nucleation and growth stages are separated, with 'burst nucleation' occurring

after a critical supersaturation is reached, generally assumed to be *via* classical nucleation theory. After nucleation the supersaturation level is lowered, and the diffusion-controlled growth stage occurs.

To be precise, this process is often divided into three portions: (I) A rapid increase in the supersaturation or concentration of free monomers in solution; (II) the 'burst-nucleation' significantly reduces the concentration of free monomers in solution at an "effectively infinite" rate and after which, there is almost no nucleation occurring; (III) diffusion-controlled growth occurs, where monomers are added to existing particles. The three stages are shown in Figure 1.7 where the concentration of the monomers is plotted as a function of time, although it should be noted that stage II should be instantaneous. This gives an understanding of how a monodisperse particle size could be achieved as all nuclei are the same size before diffusion growth occurs.

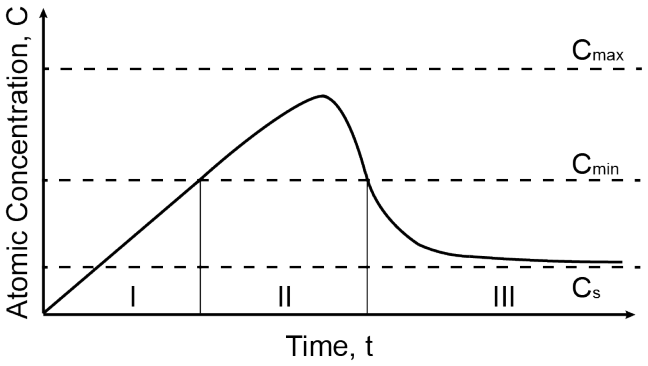

Figure 1.7 ***Stages and Concentration Profile of LaMer Growth.*** *Theoretical representation of the change in atomic concentration of M^0 atoms (y-axis) over time (x-axis), based on the LaMer theory of growth. The nucleation occurs around a critical supersaturation of the solid species. Redrawn based on You and Fang.*[149]

For the characterization tools available at the time, the LaMer theory laid down an impressive foundatiosn for the theory of nanoparticle growth which is today

being built upon and improved. However, its limitations should also be acknowledged. One of the major assumptions, which is not practically possible, is that nucleation is instantaneous. The theory also states the case that nucleation no longer occurs after this stage, which is contrary to recent accounts.[150] In addition, homogeneous nucleation is assumed, although this is rarely possible in experimental setups, and agglomeration of clusters is not accounted for.

A valuable technique for verification of the model would be the *in situ* measurement of monomer species and nanoparticle size distributions, for comparison with the modelled rates. The LaMer theory describes changes in the supersaturation of monomer species, but this is rarely, if ever, measured experimentally or reported, as it is challenging to record. The concept of experimental observation of monomer species will be further discussed in this work.

Classical Growth Theory

The theory of the growth of spherical particles by diffusion later developed into the classical growth theory. It describes the diffusion of monomer particles to a spherical surface, assuming even distribution in the bulk. There are two main limiting factors based on this theory – the reduction to monomers and the diffusion of monomers to a surface. It should be noted that there is no clear consensus on whether the reduction occurs directly at the surface or if the monomers are formed in solution and then migrate to join a crystal lattice, and this may vary with reaction conditions. Fick's first law is used to solve the rate of diffusion against the rate of the surface reaction.[17]

$$J = 4\pi x^2 D \frac{dC}{dx} \qquad \textit{Equation 1.23}$$

Where J is the flux of monomers in a spherical plane with radius x, D is the diffusion coefficient and C is the concentration at distance x. In the case of a

nanoparticle surface (Figure 1.8), δ is the distance from the surface to the bulk monomer solution. The concentration of monomers in the bulk (C_b) and at the interface (C_i) can be entered into the same equation.

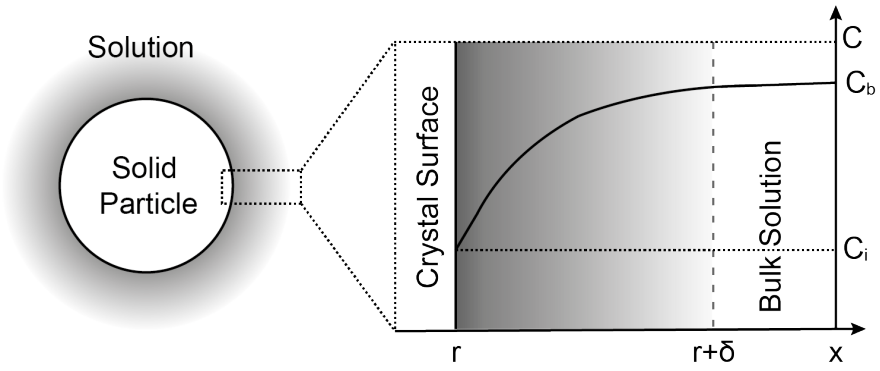

Figure 1.8 ***Classical Growth Theory.*** *The variables used in the calculation of classical growth are defined, showing the surface of the nanoparticle where growth occurs (r), and the concentration profile of the surrounding solution from interface (C_i) to bulk (C_b), until a distance x. Redrawn based on Thanh et al., 2014.*[17]

$$J = \frac{4\pi Dr(r+\delta)}{\delta}\,(C_b - C_i) \qquad \textit{Equation 1.24}$$

This formula can be substituted to find two limiting factors to growth, either the diffusion of monomers to the surface or the rate of reduction to form monomers directly at the surface.[17] Distinguishing between these two pathways of growth is difficult to achieve experimentally, since localised measurements are rare, favouring averaged results. The experimental exploration of monomer diffusion (solution reduction) versus surface reduction will be further discussed in this work, assuming the simplified model of classical growth.

Finke-Watzky Two-Step Mechanism

A more recent theory for the formation of nanoparticles in solution was proposed by Watzky and Finke in 1997, following the two steps of 'continuous nucleation' and 'autocatalytic growth'.[151] The characteristic 'sigmoidal'-shaped curve of the WF two-step mechanism has since been observed to fit well with nanoparticle growth *via* chemical precipitation of other transition metals with a range of reducing agents.[150,152-154] In its simplified form, the reaction can be said to contain two stages, where A is the initial metal precursor and B is the reduced metallic product.

$$A \rightarrow B \qquad \textit{Equation 1.25}$$

$$A + B \rightarrow 2B \qquad \textit{Equation 1.26}$$

Although the first evidence for this theory was collected for hydrogen reduction of iridium nanoparticles, subsequent publications show that it can be applied to the growth of a range of transition metals including Au, Pt, Pd, Ag and Cu nanoparticles.[150,152,155-157] The growth pattern for WF growth is characterised by 'sigmoidal' shape, caused by a rapid initial rate which slows as the reaction proceeds (Figure 1.9).[154] This shape is characteristic of continuous nucleation occurring simultaneously with growth.

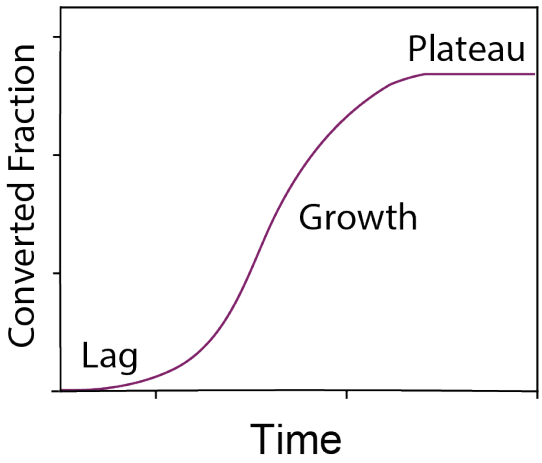

Figure 1.9 ***Sigmoidal Finke-Watzky Two-Step Growth.*** *The Finke-Watzky two step mechanism describes continuous nucleation, with simultaneous growth via ripening and aggregation of nucleating species. Auto-catalytic growth occurs, in which the rapid growth is triggered by the presence of metallic species.*

A valuable insight gained from the same research is that "a reaction mechanism is only as good as the data that could be gathered for it."[158] The improvement of characterization tools and experimental design can shed further light on these mechanisms of growth. Direct or indirect observations of the chemical and/or physical changes in particles or in the surrounding system are necessary to complement and confirm existing theories, as unpredictable behaviours and intermediates may be detected.

Proposed Multi-Step Mechanisms

The WF two-step and three-step mechanisms have been described as "deliberately simplistic" so that they could be applied to a wide range of systems.[159] This two-step mechanism has been further refined to give the three-step and four-step mechanisms which are adjustments made to more accurately match experimental results.[159] The three-step mechanism has the same fundamental understanding of growth, except that the rate of the growth of

smaller particles may be faster than the rate of growth of large particles, leading to monodispersity, similar to LaMer's theory. This can be given as the following equations:

$$A \rightarrow B\ (k_1) \qquad \textit{Equation 1.27}$$

$$A + B \rightarrow C\ (k_2) \qquad \textit{Equation 1.28}$$

$$A + C \rightarrow 1.5C\ (k_3) \qquad \textit{Equation 1.29}$$

The reaction rate of $k_2 > k_3$, allows smaller particles to grow faster than large particles and increases monodispersity. This model has been backed up with disproof-based analysis where, by attempting to disprove a range of models, the correct mechanism can be selected.[159] The development of further reaction stage models, such as four-step mechanisms may prove more realistic to fit with the reaction results, as growth processes likely occur simultaneously.[160]

1.3.3 Reshaping After Growth

After the chemical reduction and growth of nanoparticles, it is common for restructuring processes to take place by which the shape and size of the particles continue to evolve over time. These can include stages of coarsening, dissolution, agglomeration, or coalescence, among others. These are briefly discussed, with a focus on the experimental evidence which can be collected to distinguish these processes.

Ostwald Ripening and Digestive Ripening

The LaMer theory in the 1950s introduced the idea that growth of monodisperse particles could occur through the preferential growth of smaller particles, also stating that the particles would preferentially re-dissolve, when the monomer supersaturation is too low. This was not further discussed until the introduction of

the similar process of Ostwald ripening, that is shown to play a large role in the shape and size regulation during nanoparticle growth. Ostwald ripening is a phenomenon observed in many crystallisation systems, including nanoparticle growth,[161] by which smaller particles may redissolve into solution while larger particles may continue to grow *via* diffusion (Figure 1.10).[162]

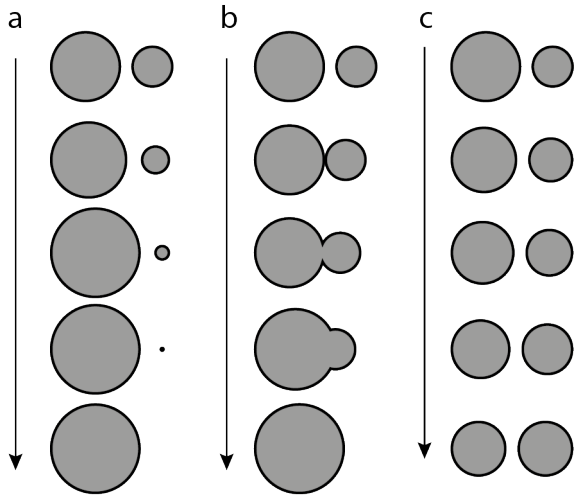

Figure 1.10 ***Nanoparticle Ripening and Coalescence.*** *(a) The growth of large particles at the expense of smaller particles via diffusion in solution, is shown here to describe the Ostwald ripening process. As shown, ripening may continue until the smaller particle is completely dissolved and only the larger remains. (b) Coalescence occurs when two particles are fused together to form a single larger particle. (c) The process of digestive ripening leads to the formation of monodisperse particles. Redrawn based on Kregar et al., 2020.*[163]

An *in situ* observation of Ostwald ripening has been published using time-resolved liquid TEM.[164] It has also been observed, using the same method for core-shell growth of CdSe that ripening is defect mediated and is not due to the large particle absorbing the smaller particle.[165]

Digestive Ripening is the opposite of Ostwald ripening, where the smaller particles grow at the expense of larger ones.[166] It follows a similar process of

dissolution and diffusion, allowing a polydisperse system to become monodisperse. It has been reported for nanoparticles of Ag,[166] Pd,[167] Au[168] and alloys including core-shell Au-Pd.[169]

It should be noted that although there have been various citations of the Ostwald and digestive ripening being observed, after considerable research on the topic Polte points out that there is little convincing experimental evidence to prove this, especially in distinguishing it from coalescence and agglomeration.[19]

Coalescence and Attachment

Coalescence and oriented attachment are effectively the same process and are both largely ignored by the simplified growth theories. It is generally accepted that these processes occur but their mode of growth, distinguishing features and effect on the reaction rate are little understood. Intraparticle growth, in which a controlled growth occurs between two smaller particles to form a large single particle, may also compete with Ostwald ripening processes under specific conditions.[17]

Coalescence has a significant contribution and is often mentioned in texts describing nanoparticle formation. Published works theoretically model coalescence[170] to fit with existing *in situ* experimental studies.[171] However, it has been challenging to separate these features from the damage caused by characterization techniques, such as *in situ* TEM, small angle X-ray scattering (SAXS) and XRD.[171] Temperature has a strong effect on the coalescence behaviour, as well as surfactant materials.[172]

Oxidative Etching

A final method of reshaping worth mentioning is oxidative etching, as observed in the formation of porous nanoparticles.[173] Such a mechanism occurs in reactions where nanoparticles with a regular structure are reoxidised to form a

more irregular surface. This has particularly been observed in the presence of chloride ions, where dissolution along the nanoparticle surface is possible at longer reaction times. This phenomenon has previously been used to control nanoparticle morphology.[174-176]

1.4 Synthetic Conditions During Chemical Precipitation Growth

The importance of nanoparticle morphology control has been made clear in the previous sections. Morphology is largely determined by the synthetic conditions of growth. However, a direct control of morphology would require a definitive understanding of the growth mechanisms and results. A unified growth theory effective for all systems may not exist; such a complex reaction may depend on a wide range of reaction descriptors. Still, a deeper understanding through the gathering of controlled observations leads towards the final goal of a 'rational design' and could well be applied to systems in which similar trends are observed. Nucleation and growth theories aim to ultimately find the relationship between the reaction rates and reaction conditions to the control of nanoparticle shape and size. Factors such as temperature,[8,28,177], solvent,[178-182] seeded growth,[74,178,183-186] reducing agents,[187-189] surfactant ligands,[153,182,190-193] and concentrations[10,152,194-196] are among the most widely studied. For a given metal salt, these major factors can be classified as affecting the rate of chemical precipitation growth of metal nanoparticles through either kinetic control or surface control, as outlined in Figure 1.11.

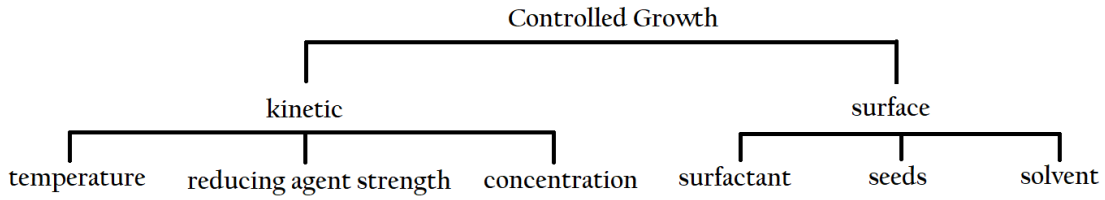

Figure 1.11 ***Growth Control Parameters.*** *Methods of controlling growth, classified under kinetical and surface controls. These outline the parameters of interest and areas to monitor during growth experiments in this thesis.*

Kinetic control and surface controlled growth may occur simultaneously, and both contribute to the nanoparticle formed. However, both modes of control can be distinguished by observing the reaction mechanism, allowing the dominating factors to be extrapolated from experimental results. This understanding can contribute towards the goal of rational design, controlling the shape and size to one day optimise nanoparticle catalysts, and save valuable time and resources. In addition, this is a key area of chemistry in which further experimental evidence is required to support the proposed theories. The availability of reliable time-resolved experimental data remains limited in cases of nanoparticle growth and catalysis, although recent advances have increased interest in such studies.

1.4.1 Synthetic Control Mechanisms

Nanoparticles tend to agglomerate to larger nanoparticles and reduce their high surface area, unless steps are taken to maintain their nanostructure. Therefore, during chemical growth of nanoparticles, kinetic and thermodynamic factors play a large role in determining the morphology of materials formed. Kinetic controls are implemented by controlling the reaction rate, such that the equilibrium-favoured results are not reached, like in diffusion-limited growth from high reduction rates. In contrast, thermodynamic controls alter the equilibrium of the

system, and the energetic favourability of an outcome. For example, adding chemicals which adjust the surface energy and strain while keeping the other reaction parameters constant may change the stable nanoparticle shape at equilibrium. The kinetic and thermodynamic effects are not mutually exclusive for a single reaction control. Reaction parameters such as temperature have both a kinetic effect and a thermodynamic effect on the system, making the prediction of behaviour highly complex, even for a single parameter. It is the design of experimental observation *in situ* that can elucidate the real behaviour for comparison with models.

As shown in the examples given, the surfactant, presence and shape of seed solutions and the interaction of the solvent with the metal salt also affect the rate of the reaction, but locally rather than for the entire system. The ligand coordination with the surface may also affect the rate of the reaction at certain sites to determine morphology. These factors which control the growth through the interaction or design of the nanoparticle surface have been labelled as ‘surface control parameters’.

As there is a multitude of multi-disciplinary literature describing the synthesis of particles, factors like capping agent, temperature and reducing agents used have a well-understood effect on the nanoparticles formed. Yet the reason why or how is not clear from a theoretical standpoint and the changes over the course of the reaction are not widely reported. With the goal of preferentially producing the active sites for catalysis, this information would be valuable to optimise catalyst design. Thus, the fundamental study of nanoparticle formation under different conditions can complement papers that produce highly active catalysts, and lead to material improvements.

For industrial applications as catalysts, the scale-up of chemical precipitation growth is under investigation. Most colloidal systems are dilute, to allow precise control of nanoparticles formation, without agglomeration. However, largescale batch production, continuous flow reactors and systems with increased concentration have been suggested for industrial production of nanoparticles, including Pd and Cu.[197-201] In this work, relatively high concentrations of metal salts are used, to meet characterization requirements and to study scaled-up production.

Alongside chemical and physical effects of the reaction components, the mixing rate and method should be considered. As the rate of mixing is not negligible on the time-scales proposed in this work, the mixing time must be accounted for during the recorded reaction, rather than attributing changes directly to the rate of the reaction itself. However, the non-negligible mixing rate is a physical limitation of the reaction systems and will affect real-life applications, as well as experiments. Most reactions are controlled simply by optimising the conditions for mixing at the beginning of the reaction, or by ignoring the effect of this property by keeping it constant.

1.4.2 Size Control

Control of nanoparticle size is mainly based on kinetic control and the rate of diffusion. From the growth theories, it is intuitive that at lower reaction rates, there will be fewer number of particles formed but with a higher average size (rate limited), while at high reaction rates, a larger number of small and increasingly anisotropic particles are formed (diffusion limited). This rate can be controlled by the reaction temperatures, concentrations of reducing agent and strength of reducing agent, all of which when low, reduce the reaction rate.[28,193,202] Equally,

to decrease reaction rate, an additional inhibiting agent or accelerant can be added.

These cases are directly predicted by theories of nanoparticle growth and are widely observed in the literature. For transition metal particles, the effects of temperature on particle size were seen for Pd, Ag and Au showing consistently smaller particles at high temperatures.[8,9,28] Reducing agent concentration was varied by Kim et al., among others, to show the result of smaller particles and increased reduction rate.[203] In addition, numerous studies exist comparing the effects of strong reducing agents such as $NaBH_4$ with weak reducing agents like ascorbic acid and citric acid.[188,189] If chlorine is evolved during a reaction, the presence of chloride ions in the system may act as an inhibitor or an etching agent and slow the rate of the reaction.[173]

In addition to these direct effects on nanoparticle size, the capping agent has also been shown to change the rate of the reaction at certain sites of the particle where it is absorbed. By slowing the reaction rate, surfactants could lead to an increase in overall particle size, but there have also been contrary reports of surfactants limiting particle size, by blocking growth at the surface.[10,192,204]

A final factor in the size of nanoparticles formed is the reaction solvent. The rate of diffusion of the reactants may depend on the solvent viscosity, boiling point, polarity and the chemical species interacting with the reactants and intermediates. Inorganic solvents like H_2O can be compared with organic solvents like alcohols and dimethyl formamide (DMF). For example, a study by Hao et al. showed that increasingly polar solvents maintained a narrower size distribution.[205] The effect of the solvent is addressed in this work, in that ligands in the solvent may interact with the metal atoms, determining the size and shape of particles formed.

1.4.3 Shape Control

The control of shape is dependent on the kinetics and diffusion but has an additional controlling influence from surface-controlled factors. As mentioned, anisotropic growth is more likely in cases of fast kinetics and a diffusion limitation, leading to de*via*tions from spherical particles with minimal surface area. In the case of shape control, the specific growth of certain facets or preferred morphologies can be determined by chemically controlled or blocked surfaces. Both of these factors are harnessed for catalyst development, where high surface area, with selected facets, can lead to high activity and greater number of active sites.

Among the most widely used methods of shape control are surfactants (surface active agents), as previously mentioned. Surfactants generally consist of a long chain body with a cationic or anionic head species at one end (Figure 1.12 a). These materials interact, through the surfactant head, with a metal surface to locally control the growth rate and direction. The structure of the surfactant and strength of the ligand have both been found to determine shape.[11,204,206,207]

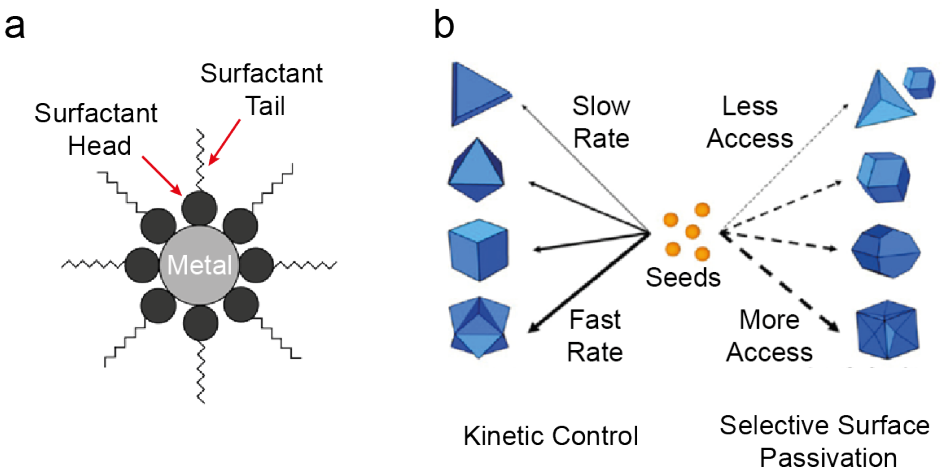

Figure 1.12 ***Controlling Nanoparticle Morphology.*** *Two modes of nanoparticle morphology control are shown through (a) A schematic of the ligand interaction and surface blocking configuration of surfactant molecules (black circles with tails) around a metal atom (grey), controlling the growth facets. (b) Routes for nanoparticle morphologies obtained by initiating (Ag) growth on crystalline (Au) seeds show that two morphology determining factors are the kinetic control (rate) and the surface control (such as with surfactants). Redrawn based on Langille et al., 2012.*[208,209]

Another commonly used method, is the introduction of pre-formed “seeds”. These seeds often already have a crystal structure which can contribute to the shape of the nanoparticles grown around them (Figure 1.12 b). Seeds have also been used to create more uniform shape and size distributions, by taking advantage of the controlled nucleation.

The solvent and dissolved intermediates may also have an impact on shape. In cases such as copper nanoparticle growth the dissolved gases affect the intermediates formed leading to oxide species formation and eventually the particle shape, while anaerobic growth has allowed faceted growth.[210,211]

The shape of nanoparticles have also been controlled after growth using etching techniques. In particular, for the growth of porous Pd nanoparticles, chloride etching for long periods of time are responsible for increasing surface area.[173]

It can be observed from this summary that the control of nanoparticle shape and size are usually interdependent, being determined by the same reaction parameters.

1.4.4 *In situ* Characterization

Rate determination of growth of nanoparticles in solution is already a large and growing field of research which continues to bring fundamental insights into the chemistry of nanoparticle reduction for synthesis. Pushing the limitations of the characterization tools available and applying them to a wide range of systems is necessary, to advance the scientific understanding of the underlying reaction mechanisms. Major innovations in recent years have allowed the application of advanced characterization at increasingly high time-resolution, by developing methods to observe previously undetected chemical changes, analysis techniques to study large datasets, and lastly, determining the rates of chemical reactions at resolutions which have not been measured before. The rate of intermediate formation and nanoparticle growth during chemical reduction, especially at the early stages of the reaction remain unknown for a range of reactions, due in part to the difficulty of experimental observation.

Determination of the chemical reduction rate generally records the change of either reactants or products over time. However, a more complete observation would record the consumption of reactants, formation of intermediates and synthesis of products simultaneously. For a simple system without intermediates, this does not provide significant benefit, since either the reactants or products

would directly indicate the rate. Such a complete observation becomes important in cases where there is a complex or unclear reaction mechanism with contributions from the formation of intermediates, or rate-affecting reaction conditions.

Lab-based techniques for monitoring nanoparticle growth generally record reduction rate *via* consumption (by mass/volume) of reactants or formation of products, later determining the nanoparticles formed. With the advancement of characterization tools, minor physical and chemical changes can be exploited to follow the reaction, such as variations in light/x-ray absorption and scattering, colour, and electronic states. *In situ* techniques have been widely used for characterising nanoparticle growth, often with high time-resolution to catch the fast reaction kinetics at the early stages.[165,177,212-219] In this work, the term *'in situ'* refers to any characterization performed under reaction conditions, while '*operando*' is used to specifically refer to cases where the catalytic performance is recorded simultaneously with the characterization under reaction conditions.

Spectroscopy has emerged as a frontrunner in time-resolved analysis, as the study of the absorption of radiation, such as light, is often "non-destructive" and rapid. Of the spectroscopic tools available, a range of chemical information during nanoparticle growth has been obtained using *in situ* XAS, alongside complementary techniques. Although it has found applications in diverse fields, this thesis focuses on the application of time-resolved *in situ* XAS for the study of the synthesis of nanoparticles from solution and the rate of oxidation. The use of XAS has allowed the direct observation of oxidation state changes during reduction. Characterization tools for rate determination vary in complexity and parameters measured, so this section will outline the major advances in relation to the methods explored.

In this work we focus on the use of time-resolved experiments for the monitoring of the growth of a nanoparticle from solution *via* chemical reduction. This has been performed previously for various reaction systems including Au,[165,216,218] Pt,[212,214] Pd,[195,220,221] Rh[220,222] and Ag.[156,166,223,224]

The use of complementary techniques to corroborate the findings allows for more reliable results. Systems with recorded *in situ* techniques can be confirmed with secondary *in situ* characterization, or *ex situ* observations which uphold the scientific results. In the literature, the most common characterization tools applied to study metal growth from solutions *in situ* are XAS, ultraviolet-visible spectroscopy (UV-vis), SAXS and TEM. For example, it was shown that during the formation of shape-controlled rhodium nanoparticles the combination of XAS, XRD, matrix-assisted laser desorption ionization – time of flight mass spectrometry (MALDI-TOF MS), TEM and UV-vis indicate $RhBr_3$ as growth precursor, Rh_4 as nuclei formed and elucidates the role of Br at the Rh surface.[222] The *in situ* characterisation tools applied over the course of this research include XAS, SAXS, electron paramagnetic resonance (EPR) and UV-vis alongside temporal observations of X-ray emission spectroscopy (XES), microwave-plasma-atomic emission spectroscopy (MP-AES) and TEM, which are discussed further in Chapter 2. Due to the difference in behaviours observed, and since each route has its limitations, a combination of characterization tools, both *in situ* and *ex situ*, is most reliable and therefore selected according to the system.

In situ UV-vis measurements are often run for single-batch reactions, although continuous flow systems have also been successfully conducted.[218,225,226] Under ideal set-up and reaction conditions, UV-vis measurements can achieve time-resolutions at the millisecond scale, making it particularly useful in observing metal nucleation and growth.[227] While effective for dilute systems, UV-vis has

limited capabilities for measuring high metal salt concentration solutions. This is generally applicable with growth *via* chemical precipitation used for the synthesis of nanoparticles since they are often dilute by nature (below 10 mM metal content) to aid in the dispersion of nanoparticles and reduce agglomeration.

In situ SAXS is one of the more reliable methods to show the formation of solid particles but does not give information about the chemical changes in the solution. The formation of crystalline regions and concentration, as well as the size and size distribution can be analysed.[228] The effectiveness of *in situ* SAXS in understanding reaction mechanism was shown in the case of Au nanoparticles grown *via* citrate synthesis, where coalescent growth was observed to lead to monodispersity.[229] A work by Mozaffari et al. also proved that the LaMer mechanism was not likely during Pd nanoparticle growth, where nucleation and growth stages overlapped.[195]

In situ TEM would potentially be the most direct method of observing nanoparticle formation.[230] However, it is challenging to measure due to factors influencing the growth such as the reductive effect of the beam, beam damage, the formation of bubbles and the use of the reducing agent in a confined space may also limit growth during *in situ* TEM measurement. Samples may be recorded with and without the beam to assess the degree of damage to the precursor solution, but beam damage cannot be ruled out entirely. Thus, literature often describes beam induced reduction with *in situ* TEM, rather than the addition of a reducing agent.[231,232] Nanoparticle growth has also been studied with *in situ* XRD, observing the formation of crystal facets, but usually for temperature or beam induced reduction, rather than chemical reduction.[233,234]

In situ EPR gives information about the presence and chemical changes to species in solution, although it is only active in cases where unpaired electrons

are present. *In situ* EPR has previously been used to observe the formation of Fe_3O_4 nanoparticles in solution and would also be active for a range of Cu species in the 2+ oxidation state.[235]

In situ XAS has also been applied to capturing nanoparticle growth, especially of Au, Ag and Pt nanoparticles.[136,223,236,237] XAS allows the non-destructive simultaneous capture of oxidation state information and metal coordination, although this may be challenging in cases where concentrations are low. Beam damage and reduction of the sample during *in situ* XAS measurement can be compensated by increasing attenuation. *In situ* XAS is high versatile and is therefore often combined with SAXS,[237] UV-vis,[223] and other *in situ* and *ex situ* characterisation techniques, to capture growth systems. The growth of Pd and Cu nanoparticles have both been measured previously with *in situ* XAS, achieving mechanistic information which supports the experiments performed in this work.[219,221,238-240]

Clearly the importance of *in situ* techniques in studying nanoparticle synthesis are being more widely recognised, and measurements are becoming accessible for public use. Some techniques are available on the lab scale such as SAXS, lab based XAS, XPS and XRD, while the development of analysis programmes has made synchrotron techniques interpretable by a wider range of researchers. At the time of writing, the time-resolution achieved with XAS is not as high as has been achieved with other characterisation tools such as SAXS and UV-vis in the field of nanoparticle growth, measured at the ms to µs-scale.[228] However, other less common and challenging *in situ* techniques such as TEM and EPR were measured at the minute-scale.[115,232,241] The lower time-resolution of *in situ* XAS measurements can be variously attributed to beam damage with high flux, use of dilute solutions or the recent advancements and limited availability of highly time-

resolved XAS recording technologies. XANES results have also been more widely reported for high time-resolution (with large datasets), since the fitting of XANES data is more straightforward than the extended X-ray absorption fine structure (EXAFS) refinement. As a result, *in situ* XAS results of changes occurring over shorter time-scales for nanoparticle growth, such as milliseconds, have often remained unmonitored, potentially missing experimentally formed intermediate stages.

For instance, the paper by Yao et al. studying Rh growth achieves a time-resolution of 6.6 s and other papers have consistently given results with more than 1 to 2 s between readings.[136,220,222] A technique to increase measurement time used by Polte et al. with *in situ* XAS was increasing the length scale for a microfluidic flow cell so that the distance translates to reaction time.[217] Another approach, applied less often in the literature, is the measurement of lower-quality high time-resolution data, and merging datasets of repeated cycles of the same reaction to improve data quality. This requires a highly reproducible reaction but can give an improved signal-to-noise ratio with a small time-scale.[242] This has the added benefit of monitoring the reproducibility of the reaction, and is explored in this work (Chapter 6). Thus, the fastest times for growth data recording remains at the ms time scale and does not include the understanding of the coordination numbers.

In this work, the study of nanoparticle growth is achieved at a time scale which has not been achieved before. Significance is given to the precautions surrounding these measurements, ensuring that they are sufficient to obtain useful chemical information about the system. Furthermore, methodologies are outlined to analyse and interpret the data obtained. Based on the extensive literature and the considerable gap in experimental observation of nanoparticle

growth data to prove existing theories, we believe such *in situ* techniques can and should be applied a wide range of systems. This can contribute towards determining the reaction properties and simplify the methodology for reporting and understanding the behaviour of nanoparticles in various reactions.

1.5 Scope of Thesis

This thesis serves to investigate the rates of metal nanoparticle reduction and catalytic oxidation, with an interest in applications for a greener and lower emission future. Based on the literature, it appears that there is a gap in the knowledge about the early stages and rates of growth mechanisms of nanoparticles. This could be solved by the development of high time-resolution characterization and data analysis, which is explored in this thesis, to obtain fundamental chemical knowledge about the system. This high time-resolution and *in situ* monitoring of chemical changes is also applied to study the rates of oxidation in electrocatalysts. The improvement in these techniques and the analytical tools available, as well as the useful fundamental information which can be interpreted fits into the existing literature and advances the field of nanoparticle growth and catalysis.

Chapter 2 will discuss the key techniques and underlying science used in this work. This will supplement the understanding of the later chapters studying the growth and give an overview of the experimental procedures.

The other chapters of the thesis are approximately ordered based on the time-resolution of XAS measurements achieved, with the exception of Chapter 3 (Table 1.1). These measurements are used to calculate the reaction rates,

following the continuous advancement to high time-resolution and the increase in information which can be obtained at each stage.

Table 1.1 ***Time-Resolution of in situ Measurements by Chapter.*** *The highest time-resolution achieved for spectroscopic measurements in each chapter of this work varies by more than six orders of magnitude. Time-scales are selected based on the experimental conditions, characterization tools and reaction rate limitations.*

Chapter	System	Time-resolution Achieved
3	Pd Growth with CTAC	0.5 s (500 ms)
4	Pt-Pd Alloy ORR	600 s (10 min)
5	Pd Growth with CTAB	0.5 s (500 ms)
6	Cu Growth with PVP	0.00127 s (1.27 ms)
7	Cu Foil CO_2RR, 1 s switch	0.0021 s (2.1 ms)
7	Cu Foil CO_2RR, 10 ms switch	0.00021 s (210 μs)

The synthesis of nanoparticles are introduced first, in chapters studying different external effects on the nanoparticle growth systems – temperature, reducing agent concentration, seeded growth, surfactant, solvent and reducing agent. Each synthesis is followed by research on the potential applications of such nanoparticles.

The growth of Pd nanoparticles, detailed in Chapters 3 and 5, is studied by varying reaction conditions of temperature, reducing agent concentrations, surfactants and seed content. These projects will apply time-resolved spectroscopy to observe the rate of the reaction under different surfactant conditions using a combination of characterization tools including *in situ* XAS, SAXS, and time-resolved *ex situ* TEM imaging. The growth profiles are studied

to find the activation energy of the reaction, the effect of growth rate on the resulting particles and the presence of intermediate species during the reaction. The reaction results are compared with the expected profiles from the literature.

Chapter 4 describes the use of Pt-Pd alloys, synthesised with the same Pd growth procedure as catalysts for the oxygen reduction reaction. The effectiveness of seeded growth in the formation of Pt sites within a Pd matrix and the effect of Pt-Pt coordination number (C.N.) on the mass activity of the catalyst is recorded. The catalytic activity as well as mechanism in these low C.N. Pt alloys is of particular interest for the oxygen reduction reaction (ORR). XAS is used to monitor the changes in C.N. and the catalyst oxidation state changes during electrochemical cycling. Although partly inconclusive, this is supplemented with a density functional theory (DFT) study of the system, to explain the behaviour observed.

Chapter 6 observes the growth of Cu nanoparticles with extremely high time-resolution *in situ* XAS. This is combined with a Valence-to-Core (VtC) XES study of the Cu-ligands during the reaction, as well as an *in situ* EPR study of the rate of formation of nanoparticles. The growth of copper is studied for three systems, with and without the presence of water, and under the influence of two different reducing agents. This observation aims to elucidate the importance of an oxygen-free environment in avoiding the formation of Cu^{1+} intermediate and the reaction intermediates formed. The nanoparticle morphology formed may also be determined by the rate of change of reaction stages. The observation of the growth of Cu nanoparticles using Energy Dispersive EXAFS technique is a step below the highest time-resolution possible at the XFEL but allows a detailed capture of the real-time growth of nanoparticles. This technique can be applied

to the growth of different materials and to catalytic systems which have reproducible behaviour.

Chapter 7, the final study, captures the electrochemical oxidation of Cu nanoparticles with microsecond-resolution to see the rate of reduction and oxidation in a system where physical mixing is not a limitation. Such oxidation is considered valuable for the activation of the Cu surface for the CO_2RR.

1.6 Aims and Objectives

The aim of this PhD thesis is to use advanced characterization tools to determine valuable rate information about chemical systems and use this to understand the effect on the reaction mechanism. Highlighting the importance of fast, *in situ* observation of reactions, spectroscopic characterisation techniques are applied in two diverse systems – to measure the rate of formation of transition metal nanoparticles (Cu, Pd and Pt) from precipitates, and the rate of electrochemical oxidation under an applied potential. Therefore, this thesis aims to capture rate information during both reduction and oxidation, and compare reactions caused by liquid-mixing with electrochemical cycling, occurring on different time-scales. The rate determination should be supported with a general understanding of the reaction systems, with the final goal of optimisation. Through this work, we hope to highlight the use of advanced characterization, applicable to diverse chemical processes, to elucidate the underlying chemistry. Some of the general goals set out while conducting this research were to:

1. Increase the time-resolution of *in situ* characterization used to observe catalytic oxidation and growth mechanisms in metal nanoparticles.
2. Combine characterization techniques to observe complementarity and gain new understanding of the reaction mechanism.
3. Synthesise a range of nanomaterials which could be applied to improve catalytic activity in environmentally relevant reactions of ORR and CO_2RR.
4. To find chemically significant information about the reaction, such as the intermediate species formed during a reaction and the activation energy of their formation.

5. To draw conclusions about the nanoparticles formed such as growth rates, activation energy and growth mechanism which could aid in the future synthesis of more active, rationally designed catalyst materials.

Based on these, three major research objectives set out for nanoparticle growth studies are to:

1. Design a range of experiments to study the effects of temperature, reducing agent concentration, seeded growth, surfactant, solvent and selected reducing agent during the chemical precipitation of catalytically useful nanoparticles (Cu and Pd).
2. Determine and compare the rate of reduction and activation energy measured experimentally at each growth condition, to quantify the effects of reaction parameters.
3. Assign or confirm a reaction mechanism for each reduction pathway, based on the collection of complementary characterization data.

To study electrochemical surface oxidation behaviour, the three specific research objectives set out were to:

1. (For the PtPd alloy) Determine the role of small Pt clusters in comparison to bulk materials during ORR and thereby suggest their ORR reaction pathway.
2. (At a metallic Cu surface) Develop a method of surface oxidation control using electrochemical switching which could be applied during CO_2RR and determine the highest time-resolution where Cu oxidation could be recorded.
3. Record the rate of oxidation at the catalytic surface within an electrochemical reaction setup using time-resolved *in situ* XAS.

1.7 References

1 Yano, H. *et al.* Particle-size effect of nanoscale platinum catalysts in oxygen reduction reaction: an electrochemical and 195Pt EC-NMR study. *Phys Chem Chem Phys* **8**, 4932-4939, http://dx.doi.org/10.1039/b610573d (2006).

2 Perez-Alonso, F. J. *et al.* The effect of size on the oxygen electroreduction activity of mass-selected platinum nanoparticles. *Angew Chem Int Ed Engl* **51**, 4641-4643, http://dx.doi.org/10.1002/anie.201200586 (2012).

3 Wang, L. *et al.* Porous Carbon-Supported Gold Nanoparticles for Oxygen Reduction Reaction: Effects of Nanoparticle Size. *ACS Appl Mater Interfaces* **8**, 20635-20641, http://dx.doi.org/10.1021/acsami.6b02223 (2016).

4 Nesselberger, M. *et al.* The particle size effect on the oxygen reduction reaction activity of Pt catalysts: influence of electrolyte and relation to single crystal models. *J Am Chem Soc* **133**, 17428-17433, http://dx.doi.org/10.1021/ja207016u (2011).

5 Zhen, S. *et al.* Accessing the Nature of Active Sites and Particle Size Effect for Reduction of Carbon Dioxide over Copper-Based Catalysts. *The Journal of Physical Chemistry C* **127**, 4975-4983, http://dx.doi.org/10.1021/acs.jpcc.2c08950 (2023).

6 Zhou, W. *et al.* Pd particle size effects on oxygen electrochemical reduction. *International Journal of Hydrogen Energy* **39**, 6433-6442, http://dx.doi.org/10.1016/j.ijhydene.2014.01.197 (2014).

7 Suarez-Lopez, R., Puntes, V. F., Bastus, N. G., Herves, C. & Jaime, C. Nucleation and growth of gold nanoparticles in the presence of different surfactants. A dissipative particle dynamics study. *Sci Rep* **12**, 13926, http://dx.doi.org/10.1038/s41598-022-18155-2 (2022).

8 Tran, M., DePenning, R., Turner, M. & Padalkar, S. Effect of citrate ratio and temperature on gold nanoparticle size and morphology. *Materials Research Express* **3** http://dx.doi.org/10.1088/2053-1591/3/10/105027 (2016).

9 Abbas, G., Kumar, N., Kumar, D. & Pandey, G. Effect of Reaction Temperature on Shape Evolution of Palladium Nanoparticles and Their Cytotoxicity against A-549 Lung Cancer Cells. *ACS Omega* **4**, 21839-21847, http://dx.doi.org/10.1021/acsomega.9b02776 (2019).

10 Lee, S., Cho, H., Kim, H. J., Hong, J. W. & Lee, Y. W. Shape- and Size-Controlled Palladium Nanocrystals and Their Electrocatalytic Properties in the Oxidation of Ethanol. *Materials (Basel)* **14** http://dx.doi.org/10.3390/ma14112970 (2021).

11 Wu, Z., Yang, S. & Wu, W. Shape control of inorganic nanoparticles from solution. *Nanoscale* **8**, 1237-1259, http://dx.doi.org/10.1039/c5nr07681a (2016).

12 Yao, Q., Wang, C., Wang, H., Yan, H. & Lu, J. Revisiting the Au Particle Size Effect on TiO2-Coated Au/TiO2 Catalysts in CO Oxidation Reaction. *The Journal of Physical Chemistry C* **120**, 9174-9183, http://dx.doi.org/10.1021/acs.jpcc.5b12712 (2016).

13 Marks, L. D. & Peng, L. Nanoparticle shape, thermodynamics and kinetics. *J Phys Condens Matter* **28**, 053001, http://dx.doi.org/10.1088/0953-8984/28/5/053001 (2016).

14 Catalysis as it goes. *Nature Catalysis* **1**, 165-166, http://dx.doi.org/10.1038/s41929-018-0050-4 (2018).

15 Shorter, J. A. G. Vernon Harcourt. *Journal of Chemical Education* **57**, 411-416, http://dx.doi.org/10.1021/ed057p411, (1980).

16 Farber, E. Earyle Studies Concerning Time in Chemical Reactions. *Chymia* **7**, 135-148, (1961).

17 Thanh, N. T., Maclean, N. & Mahiddine, S. Mechanisms of nucleation and growth of nanoparticles in solution. *Chem Rev* **114**, 7610-7630, http://dx.doi.org/10.1021/cr400544s (2014).

18 Watzky, M. A. & Finke, R. G. Nanocluster Size-Control and "Magic Number" Investigations. Experimental Tests of the "Living-Metal Polymer" Concept and of Mechanism-Based Size-Control Predictions Leading to the Syntheses of Iridium(0) Nanoclusters Centering about Four Sequential Magic Numbers. *Chemical Materials* **9**, 3083-3095, (1997).

19 Polte, J. Fundamental growth principles of colloidal metal nanoparticles – a new perspective. *CrystEngComm* **17**, 6809-6830, http://dx.doi.org/10.1039/c5ce01014d (2015).

20 Whitehead, C. B., Özkar, S. & Finke, R. G. LaMer's 1950 Model for Particle Formation of Instantaneous Nucleation and Diffusion-Controlled Growth: A Historical Look at the Model's Origins, Assumptions, Equations, and Underlying Sulfur Sol Formation Kinetics Data. *Chemistry of Materials* **31**, 7116-7132, http://dx.doi.org/10.1021/acs.chemmater.9b01273 (2019).

21 La Mer, V. K. Nucleation in Phase Transitions. *Industrial and Engineering Chemistry* **44**, 1270-1277, (1952).

22 Rivas, D. E. *et al.* High-temporal-resolution X-ray spectroscopy with free-electron and optical lasers. *Optica* **9** http://dx.doi.org/10.1364/optica.454920 (2022).

23 Worrell, B. T., Malik, J. A. & Fokin, V. V. Direct Evidence of a Dinuclear Copper Intermediate in Cu(I)-Catalyzed Azide-Alkyne Cycloadditions. *Science* **340**, 457-460, http://dx.doi.org/doi:10.1126/science.1229506 (2013).

24 Connors, K. A. *Chemical kinetics: the study of reaction rates in solution*. (Wiley-VCH Verlag GmbH, 1990).

25 Zhang, M., Wang, M., Xu, B. & Ma, D. How to Measure the Reaction Performance of Heterogeneous Catalytic Reactions Reliably. *Joule* **3**, 2876-2883, http://dx.doi.org/10.1016/j.joule.2019.11.005 (2019).

26 Wisniak, J. The History of Catalysis. From the Beginning to Nobel Prizes. *Educación Química* **21**, 60-69, http://dx.doi.org/10.1016/s0187-893x(18)30074-0 (2010).

27 Laidler, K. J. The development of the Arrhenius equation. *journal of Chemical Education* **61**, 494-498, http://dx.doi.org/10.1021/ed061p494, (1984).

28 Jiang, X. C., Chen, W. M., Chen, C. Y., Xiong, S. X. & Yu, A. B. Role of Temperature in the Growth of Silver Nanoparticles Through a Synergetic Reduction Approach. *Nanoscale Res Lett* **6**, 32, http://dx.doi.org/10.1007/s11671-010-9780-1 (2010).

29 Hagen, J. *Industrial catalysis : a practical approach*. (Wiley-VCH, 1999).
30 Catlow, C. R., Davidson, M., Hardacre, C. & Hutchings, G. J. Catalysis making the world a better place. *Philos Trans A Math Phys Eng Sci* **374** http://dx.doi.org/10.1098/rsta.2015.0089 (2016).
31 Anastas, P. & Eghbali, N. Green chemistry: principles and practice. *Chem Soc Rev* **39**, 301-312, http://dx.doi.org/10.1039/b918763b (2010).
32 Xu, R. *et al.* Improving the ORR performance by enhancing the Pt oxidation resistance. *Journal of Catalysis* **416**, 311-321, http://dx.doi.org/10.1016/j.jcat.2022.10.025 (2022).
33 Smiljanić, M. *et al.* Electrochemical Stability and Degradation of Commercial Pd/C Catalyst in Acidic Media. *The Journal of Physical Chemistry C* **125**, 27534-27542, http://dx.doi.org/10.1021/acs.jpcc.1c08496 (2021).
34 Popovic, S. *et al.* Stability and Degradation Mechanisms of Copper-Based Catalysts for Electrochemical CO(2) Reduction. *Angew Chem Int Ed Engl* **59**, 14736-14746, http://dx.doi.org/10.1002/anie.202000617 (2020).
35 Lynch, M. K. UK Catalysis Market Study Summary. *Enabled Future Limited, UKRI* (2020).
36 Liu, Z., Zhao, Z., Peng, B., Duan, X. & Huang, Y. Beyond Extended Surfaces: Understanding the Oxygen Reduction Reaction on Nanocatalysts. *J Am Chem Soc* **142**, 17812-17827, http://dx.doi.org/10.1021/jacs.0c07696 (2020).
37 Ma, R. *et al.* A review of oxygen reduction mechanisms for metal-free carbon-based electrocatalysts. *npj Computational Materials* **5** http://dx.doi.org/10.1038/s41524-019-0210-3 (2019).
38 Lang, P., Yuan, N., Jiang, Q., Zhang, Y. & Tang, J. Recent Advances and Prospects of Metal-Based Catalysts for Oxygen Reduction Reaction. *Energy Technology* **8** http://dx.doi.org/10.1002/ente.201900984 (2019).
39 Beermann, V. *et al.* Real-time imaging of activation and degradation of carbon supported octahedral Pt–Ni alloy fuel cell catalysts at the nanoscale using in situ electrochemical liquid cell STEM. *Energy & Environmental Science* **12**, 2476-2485, http://dx.doi.org/10.1039/c9ee01185d (2019).
40 Pandey, G. & Jain, P. Assessing the nanotechnology on the grounds of costs, benefits, and risks. *Beni-Suef University Journal of Basic and Applied Sciences* **9** http://dx.doi.org/10.1186/s43088-020-00085-5 (2020).
41 Greeley, J. *et al.* Alloys of platinum and early transition metals as oxygen reduction electrocatalysts. *Nat Chem* **1**, 552-556, http://dx.doi.org/10.1038/nchem.367 (2009).
42 Nijamudheen, A. & Datta, A. Gold-Catalyzed Cross-Coupling Reactions: An Overview of Design Strategies, Mechanistic Studies, and Applications. *Chemistry* **26**, 1442-1487, http://dx.doi.org/10.1002/chem.201903377 (2020).
43 Jammi, S. *et al.* CuO Nanoparticles Catalyzed C−N, C−O, and C−S Cross-Coupling Reactions: Scope and Mechanism. *The Journal of Organic Chemistry* **74**, 1971-1976, http://dx.doi.org/10.1021/jo8024253 (2009).
44 Choudhary, A., Sharma, V., Sharma, S., Sharma, N. & Paul, S. Pd nanoparticles supported on magnetic CoTiMgLDH with enhanced catalytic activity in Suzuki cross-coupling and reductive degradation of dyes.

Applied Organometallic Chemistry **37** http://dx.doi.org/10.1002/aoc.7112 (2023).

45 Wang, Y., Zhao, D., Rodríguez-Padrón, D. & Len, C. Recent Advances in Catalytic Hydrogenation of Furfural. *Catalysts* **9**, 796, (2019).

46 Anand, S., Pinheiro, D. & Sunaja Devi, K. R. Recent Advances in Hydrogenation Reactions Using Bimetallic Nanocatalysts: A Review. *Asian Journal of Organic Chemistry* **10**, 3068-3100, http://dx.doi.org/10.1002/ajoc.202100495 (2021).

47 Li, C. *et al.* Structure-activity collective properties underlying self-assembled superstructures. *Nano Today* **42**, 101354, http://dx.doi.org/https://doi.org/10.1016/j.nantod.2021.101354 (2022).

48 Li, M. *et al.* Ultrafine jagged platinum nanowires enable ultrahigh mass activity for the oxygen reduction reaction. *Science* **354**, 1414-1419, http://dx.doi.org/doi:10.1126/science.aaf9050 (2016).

49 Zhao, J., Lian, J., Zhao, Z., Wang, X. & Zhang, J. A Review of In-Situ Techniques for Probing Active Sites and Mechanisms of Electrocatalytic Oxygen Reduction Reactions. *Nanomicro Lett* **15**, 19, http://dx.doi.org/10.1007/s40820-022-00984-5 (2022).

50 Luo, M. *et al.* PdMo bimetallene for oxygen reduction catalysis. *Nature* **574**, 81-85, http://dx.doi.org/10.1038/s41586-019-1603-7 (2019).

51 Kang, L. *et al.* Adsorption and activation of molecular oxygen over atomic copper(I/II) site on ceria. *Nat Commun* **11**, 4008, http://dx.doi.org/10.1038/s41467-020-17852-8 (2020).

52 Carlos Calderón, J., Ndzuzo, L., Bladergroen, B. J. & Pasupathi, S. Catalytic activity of carbon supported-Pt-Pd nanoparticles toward the oxygen reduction reaction. *Materials Today: Proceedings* **5**, 10551-10560, http://dx.doi.org/10.1016/j.matpr.2017.12.387 (2018).

53 Yoshida, T. & Kojima, K. Toyota MIRAI fuel cell vehicle and progress toward a future hydrogen society. *Electrochemical Society Interface* **24**, 45, (2015).

54 Nørskov, J. K. *et al.* Origin of the Overpotential for Oxygen Reduction at a Fuel-Cell Cathode. *The Journal of Physical Chemistry B* **108**, 17886-17892, http://dx.doi.org/10.1021/jp047349j (2004).

55 Stamenkovic, V. R. *et al.* Improved oxygen reduction activity on $Pt_3Ni(111)$ via increased surface site availability. *Science* **315**, 493-497, http://dx.doi.org/10.1126/science.1135941 (2007).

56 Duan, Z. & Wang, G. Comparison of Reaction Energetics for Oxygen Reduction Reactions on Pt(100), Pt(111), Pt/Ni(100), and Pt/Ni(111) Surfaces: A First-Principles Study. *The Journal of Physical Chemistry C* **117**, 6284-6292, http://dx.doi.org/10.1021/jp400388v (2013).

57 Zhang, L. *et al.* Pt/Pd single-atom alloys as highly active electrochemical catalysts and the origin of enhanced activity. *ACS Catalysis* **9**, 9350-9358, http://dx.doi.org/10.1021/acscatal.9b01677 (2019).

58 Darby, M. T. & Stamatakis, M. Single-atom alloys for the electrochemical oxygen reduction reaction. *Chemphyschem* **22**, 499-508, http://dx.doi.org/10.1002/cphc.202000869 (2021).

59 Tian, F. & Anderson, A. B. Effective reversible potential, energy loss, and overpotential on platinum fuel cell cathodes. *The Journal of Physical Chemistry C* **115**, 4076-4088, http://dx.doi.org/10.1021/jp1100126 (2011).

60 Pollet, B. G., Kocha, S. S. & Staffell, I. Current status of automotive fuel cells for sustainable transport. *Current Opinion in Electrochemistry* **16**, 90-95, http://dx.doi.org/10.1016/j.coelec.2019.04.021 (2019).

61 Ruan, M., Liu, J., Song, P. & Xu, W. Meta-analysis of commercial Pt/C measurements for oxygen reduction reactions via data mining. *Chinese Journal of Catalysis* **43**, 116-121, http://dx.doi.org/https://doi.org/10.1016/S1872-2067(21)63854-8 (2022).

62 Garsany, Y., Baturina, O. A., Swider-Lyons, K. E. & Kocha, S. S. Experimental methods for quantifying the activity of platinum electrocatalysts for the oxygen reduction reaction. *Analytical Chemistry* **82**, 6321–6328, http://dx.doi.org/10.1021/ac100306c (2010).

63 Chen, M. Y., Li, Y., Wu, H. R., Lu, B. A. & Zhang, J. N. Highly Stable Pt-Based Oxygen Reduction Electrocatalysts toward Practical Fuel Cells: Progress and Perspectives. *Materials (Basel)* **16** http://dx.doi.org/10.3390/ma16072590 (2023).

64 Bevilacqua, N. *et al.* Impact of catalyst layer morphology on the operation of high temperature PEM fuel cells. *Journal of Power Sources Advances* **7** http://dx.doi.org/10.1016/j.powera.2020.100042 (2021).

65 Taylor, S., Fabbri, E., Levecque, P., Schmidt, T. J. & Conrad, O. The Effect of Platinum Loading and Surface Morphology on Oxygen Reduction Activity. *Electrocatalysis* **7**, 287-296, http://dx.doi.org/10.1007/s12678-016-0304-3 (2016).

66 Shao, M., Peles, A. & Shoemaker, K. Electrocatalysis on platinum nanoparticles: particle size effect on oxygen reduction reaction activity. *Nano Lett* **11**, 3714-3719, http://dx.doi.org/10.1021/nl2017459 (2011).

67 Li, K. *et al.* The oxygen reduction reaction on Pt(111) and Pt(100) surfaces substituted by subsurface Cu: a theoretical perspective. *Journal of Materials Chemistry A* **3**, 11444-11452, http://dx.doi.org/10.1039/c5ta01017a (2015).

68 Xu, R. *Structure-activity relationship of porous materials for energy conversion and storage* Doctor of Philosophy thesis, University College London, (2020).

69 Wang, X. X., Sokolowski, J., Liu, H. & Wu, G. Pt alloy oxygen-reduction electrocatalysts: Synthesis, structure, and property. *Chinese Journal of Catalysis* **41**, 739-755, http://dx.doi.org/10.1016/s1872-2067(19)63407-8 (2020).

70 Wu, D., Shen, X., Pan, Y., Yao, L. & Peng, Z. Platinum Alloy Catalysts for Oxygen Reduction Reaction: Advances, Challenges and Perspectives. *ChemNanoMat* **6**, 32-41, http://dx.doi.org/10.1002/cnma.201900319 (2019).

71 Calle-Vallejo, F. *et al.* Why conclusions from platinum model surfaces do not necessarily lead to enhanced nanoparticle catalysts for the oxygen reduction reaction. *Chemical Science* **8**, 2283-2289, http://dx.doi.org/10.1039/c6sc04788b (2017).

72 Li, Y. & Liu, Z. F. Solvated proton and the origin of the high onset overpotential in the oxygen reduction reaction on Pt(111). *Physical Chemistry Chemical Physics* **22**, 22226-22235, http://dx.doi.org/10.1039/d0cp04211k (2020).

73 Gómez-Marín, A. M. & Feliu, J. M. New insights into the oxygen reduction reaction mechanism on Pt(111): a detailed electrochemical study.

ChemSusChem **6**, 1091-1100, http://dx.doi.org/10.1002/cssc.201200847 (2013).

74 Hornberger, E. *et al.* Seed-Mediated Synthesis and Catalytic ORR Reactivity of Facet-Stable, Monodisperse Platinum Nano-Octahedra. *ACS Applied Energy Materials* **4**, 9542-9552, http://dx.doi.org/10.1021/acsaem.1c01696 (2021).

75 Markovića, N. M., Sarraf, S. T., Gasteiger, H. A. & Ross, P. N. Hydrogen electrochemistry on platinum low-index single-crystal surfaces in alkaline solution. *Journal of the Chemical Society, Faraday Transactions* **92**, 3719-3725, http://dx.doi.org/10.1039/FT9969203719 (1996).

76 Schmidt, T. J., Ross, P. N. & Markovic, N. M. Temperature dependent surface electrochemistry on Pt single crystals in alkaline electrolytes: Part 2. The hydrogen evolution/oxidation reaction. *Journal of Electroanalytical Chemistry* **524-525**, 252-260, http://dx.doi.org/https://doi.org/10.1016/S0022-0728(02)00683-6 (2002).

77 Garlyyev, B. *et al.* Optimizing the Size of Platinum Nanoparticles for Enhanced Mass Activity in the Electrochemical Oxygen Reduction Reaction. *Angew Chem Int Ed Engl* **58**, 9596-9600, http://dx.doi.org/10.1002/anie.201904492 (2019).

78 Kim, H. Y. *et al.* Activity Origin and Multifunctionality of Pt-Based Intermetallic Nanostructures for Efficient Electrocatalysis. *ACS Catalysis* **9**, 11242-11254, http://dx.doi.org/10.1021/acscatal.9b03155 (2019).

79 Zhu, X., Amal, R. & Lu, X. N,P Co-Coordinated Manganese Atoms in Mesoporous Carbon for Electrochemical Oxygen Reduction. *Small* **15**, e1804524, http://dx.doi.org/10.1002/smll.201804524 (2019).

80 Wang, L. *et al.* Plating Precious Metals on Nonprecious Metal Nanoparticles for Sustainable Electrocatalysts. *Nano Lett* **17**, 3391-3395, http://dx.doi.org/10.1021/acs.nanolett.7b00046 (2017).

81 Wang, T. *et al.* Palladium alloys used as electrocatalysts for the oxygen reduction reaction. *Energy & Environmental Science* **14**, 2639-2669, http://dx.doi.org/10.1039/d0ee03915b (2021).

82 Zhang, X., Wang, J. & Zhao, Y. Enhancement Mechanism of Pt/Pd-Based Catalysts for Oxygen Reduction Reaction. *Nanomaterials* **13**, 1275, (2023).

83 Yang, Z., Wang, J. & Yu, X. The adsorption, diffusion and dissociation of O_2 on Pt-skin $Pt_3Ni(111)$: a density functional theory study. *Chemical Physics Letters* **499**, 83-88, http://dx.doi.org/10.1016/j.cplett.2010.09.021 (2010).

84 Huang, J., Ding, C., Yang, Y., Liu, G. & Cai, W.-B. An alternate aqueous phase synthesis of the Pt_3Co/C catalyst towards efficient oxygen reduction reaction. *Chinese Journal of Catalysis* **40**, 1895-1903, http://dx.doi.org/10.1016/s1872-2067(19)63338-3 (2019).

85 Shen, X. *et al.* Deconvolution of octahedral Pt_3Ni nanoparticle growth pathway from in situ characterizations. *Nature Communications* **9**, 4485, http://dx.doi.org/10.1038/s41467-018-06900-z (2018).

86 Sassin, M. B., Garsany, Y., Gould, B. D. & Swider-Lyons, K. E. Fabrication Method for Laboratory-Scale High-Performance Membrane Electrode Assemblies for Fuel Cells. *Anal Chem* **89**, 511-518, http://dx.doi.org/10.1021/acs.analchem.6b03005 (2017).

87 Wang, Y. J. *et al.* Carbon-supported Pt-based alloy electrocatalysts for the oxygen reduction reaction in polymer electrolyte membrane fuel cells: particle size, shape, and composition manipulation and their impact to activity. *Chem Rev* **115**, 3433-3467, http://dx.doi.org/10.1021/cr500519c (2015).

88 Xiong, Y., Xiao, L., Yang, Y., DiSalvo, F. J. & Abruña, H. D. High-loading intermetallic Pt_3Co/C core–shell nanoparticles as enhanced activity electrocatalysts toward the Oxygen Reduction Reaction (ORR). *Chemistry of Materials* **30**, 1532-1539, http://dx.doi.org/10.1021/acs.chemmater.7b04201 (2018).

89 Kaito, T. *et al.* In Situ X-ray Absorption Fine Structure Analysis of PtCo, PtCu, and PtNi Alloy Electrocatalysts: The Correlation of Enhanced Oxygen Reduction Reaction Activity and Structure. *The Journal of Physical Chemistry C* **120**, 11519-11527, http://dx.doi.org/10.1021/acs.jpcc.6b01736 (2016).

90 Zhang, L., Lee, K. & Zhang, J. The effect of heat treatment on nanoparticle size and ORR activity for carbon-supported Pd–Co alloy electrocatalysts. *Electrochimica Acta* **52**, 3088-3094, http://dx.doi.org/10.1016/j.electacta.2006.09.051 (2007).

91 Zhou, M. *et al.* Quantitative Analysis of the Reduction Kinetics Responsible for the One-Pot Synthesis of Pd-Pt Bimetallic Nanocrystals with Different Structures. *J Am Chem Soc* **138**, 12263-12270, http://dx.doi.org/10.1021/jacs.6b07213 (2016).

92 Thanasilp, S. & Hunsom, M. Effect of Pt: Pd atomic ratio in Pt–Pd/C electrocatalyst-coated membrane on the electrocatalytic activity of ORR in PEM fuel cells. *Renewable Energy* **36**, 1795-1801, http://dx.doi.org/10.1016/j.renene.2010.10.024 (2011).

93 Chou, S.-W. *et al.* Uniform size and composition tuning of PtNi octahedra for systematic studies of oxygen reduction reactions. *Journal of Catalysis* **309**, 343-350, http://dx.doi.org/10.1016/j.jcat.2013.09.008 (2014).

94 Do, C. L., Pham, T. S., Nguyen, N. P., Tran, V. Q. & Pham, H. H. Synthesis and characterization of alloy catalyst nanoparticles PtNi/C for oxygen reduction reaction in proton exchange membrane fuel cell. *Advances in Natural Sciences: Nanoscience and Nanotechnology* **6** http://dx.doi.org/10.1088/2043-6262/6/2/025009 (2015).

95 Colón-Mercado, H. R., Kim, H. & Popov, B. N. Durability study of Pt3Ni1 catalysts as cathode in PEM fuel cells. *Electrochemistry Communications* **6**, 795-799, http://dx.doi.org/10.1016/j.elecom.2004.05.028 (2004).

96 Wu, J. *et al.* Understanding Composition-Dependent Synergy of PtPd Alloy Nanoparticles in Electrocatalytic Oxygen Reduction Reaction. *The Journal of Physical Chemistry C* **121**, 14128-14136, http://dx.doi.org/10.1021/acs.jpcc.7b03043 (2017).

97 Shao, M.-H., Sasaki, K. & Adzic, R. R. Pd−Fe Nanoparticles as Electrocatalysts for Oxygen Reduction. *Journal of the American Chemical Society* **128**, 3526-3527, http://dx.doi.org/10.1021/ja060167d (2006).

98 Shen, R. *et al.* High-Concentration Single Atomic Pt Sites on Hollow CuSx for Selective O2 Reduction to H2O2 in Acid Solution. *Chem* **5**, 2099-2110, http://dx.doi.org/10.1016/j.chempr.2019.04.024 (2019).

99 Yang, S., Tak, Y. J., Kim, J., Soon, A. & Lee, H. Support Effects in Single-Atom Platinum Catalysts for Electrochemical Oxygen Reduction. *ACS*

Catalysis **7**, 1301-1307, http://dx.doi.org/10.1021/acscatal.6b02899 (2017).

100 Nørskov, J. K. *et al.* Origin of the overpotential for oxygen reduction at a fuel-cell cathode. *Journal of Physical Chemistry B* **108**, 17886-17892, http://dx.doi.org/10.1021/jp047349j (2004).

101 Drnec, J. *et al.* In-Situ x-Ray Diffraction Study of Pt(111) Oxidation during Oxygen Reduction Reaction (ORR). *ECS Meeting Abstracts* **MA2015-01**, 1747, http://dx.doi.org/10.1149/MA2015-01/30/1747 (2015).

102 Morris, D. J. & Zhang, P. In situ X-ray Absorption Spectroscopy of Platinum Electrocatalysts. *Chemistry–Methods* **1**, 162-172, http://dx.doi.org/10.1002/cmtd.202000069 (2021).

103 Yamamoto, N. *et al.* Investigation of hydrogen superoxide adsorption during ORR on Pt/C catalyst in acidic solution for PEFC by in-situ high energy resolution XAFS. *Journal of Power Sources* **557** http://dx.doi.org/10.1016/j.jpowsour.2022.232508 (2023).

104 Dong, J. C. *et al.* Direct In Situ Raman Spectroscopic Evidence of Oxygen Reduction Reaction Intermediates at High-Index Pt(hkl) Surfaces. *J Am Chem Soc* **142**, 715-719, http://dx.doi.org/10.1021/jacs.9b12803 (2020).

105 Wang, Y. H. *et al.* In situ Spectroscopic Insight into the Origin of the Enhanced Performance of Bimetallic Nanocatalysts towards the Oxygen Reduction Reaction (ORR). *Angew Chem Int Ed Engl* **58**, 16062-16066, http://dx.doi.org/10.1002/anie.201908907 (2019).

106 Mondal, S. *et al.* In Situ Mechanistic Insights for the Oxygen Reduction Reaction in Chemically Modulated Ordered Intermetallic Catalyst Promoting Complete Electron Transfer. *J Am Chem Soc* **144**, 11859-11869, http://dx.doi.org/10.1021/jacs.2c04541 (2022).

107 Kunimatsu, K., Yoda, T., Tryk, D. A., Uchida, H. & Watanabe, M. In situ ATR-FTIR study of oxygen reduction at the Pt/Nafion interface. *Phys Chem Chem Phys* **12**, 621-629, http://dx.doi.org/10.1039/b917306d (2010).

108 Nesselberger, M. & Arenz , M. In Situ FTIR Spectroscopy: Probing the Electrochemical Interface during the Oxygen Reduction Reaction on a Commercial Platinum High-Surface-Area Catalyst. *ChemCatChem* **8**, 1125-1131, http://dx.doi.org/10.1002/cctc.201501193 (2016).

109 Dai, S., Zhang, S., Graham, G. W. & Pan, X. In situ Scanning Transmission Electron Microscopy with Atomic Resolution under Atmospheric Pressure. *Microscopy Today* **27**, 16-21, http://dx.doi.org/10.1017/s1551929519000439 (2019).

110 Rudneva, M. *et al.* In situ transmission electron microscopy imaging of electromigration in platinum nanowires. *Microsc Microanal* **19 Suppl 5**, 43-48, http://dx.doi.org/10.1017/S1431927613012300 (2013).

111 Kolagatla, S., Subramanian, P. & Schechter, A. Catalytic current mapping of oxygen reduction on isolated Pt particles by atomic force microscopy-scanning electrochemical microscopy. *Applied Catalysis B: Environmental* **256** http://dx.doi.org/10.1016/j.apcatb.2019.117843 (2019).

112 Nagasawa, K. *et al.* Performance and durability of Pt/C cathode catalysts with different kinds of carbons for polymer electrolyte fuel cells characterized by electrochemical and in situ XAFS techniques. *Physical Chemistry Chemical Physics* **16**, 10075-10087, http://dx.doi.org/10.1039/c3cp54457e (2014).

113 Nagamatsu, S.-i. *et al.* Structural and electronic transformations of Pt/C, Pd@Pt(1 ML)/C and Pd@Pt(2 ML)/C cathode catalysts in polymer electrolyte fuel cells during potential-step operating processes characterized by in-situ time-resolved XAFS. *Surface Science* **648**, 100-113, http://dx.doi.org/10.1016/j.susc.2015.10.053 (2016).

114 Newton, M. A. & Dent, A. J. in *In-situ Characterization of Heterogeneous Catalysts* 75-119 (2013).

115 Gocyla, M. *et al.* Shape Stability of Octahedral PtNi Nanocatalysts for Electrochemical Oxygen Reduction Reaction Studied by in situ Transmission Electron Microscopy. *ACS Nano* **12**, 5306-5311, http://dx.doi.org/10.1021/acsnano.7b09202 (2018).

116 Ni, L., Theis, P., Paul, S., Stark, R. W. & Kramm, U. I. In situ 57Fe mössbauer study of a porphyrin based FeNC catalyst for ORR. *Electrochimica Acta* **395** http://dx.doi.org/10.1016/j.electacta.2021.139200 (2021).

117 Nayak, S., McPherson, I. J. & Vincent, K. A. Adsorbed Intermediates in Oxygen Reduction on Platinum Nanoparticles Observed by In Situ IR Spectroscopy. *Angew Chem Int Ed Engl* **57**, 12855-12858, http://dx.doi.org/10.1002/anie.201804978 (2018).

118 Jia, Q. *et al.* In Situ Spectroscopic Evidence for Ordered Core–Ultrathin Shell Pt1Co1 Nanoparticles with Enhanced Activity and Stability as Oxygen Reduction Electrocatalysts. *The Journal of Physical Chemistry C* **118**, 20496-20503, http://dx.doi.org/10.1021/jp507204k (2014).

119 Sasaki, K., Marinkovic, N., Isaacs, H. S. & Adzic, R. R. Synchrotron-Based In Situ Characterization of Carbon-Supported Platinum and Platinum Monolayer Electrocatalysts. *ACS Catalysis* **6**, 69-76, http://dx.doi.org/10.1021/acscatal.5b01862 (2015).

120 Gatewood, D. S. *et al.* Characterization of Ligand Effects on Water Activation in Triarylphosphine-Stabilized Pt Nanoparticle Catalysts by X-ray Absorption Spectroscopy. *The Journal of Physical Chemistry C* **112**, 4961-4970, http://dx.doi.org/10.1021/jp709588c (2008).

121 Nitopi, S. *et al.* Progress and Perspectives of Electrochemical CO(2) Reduction on Copper in Aqueous Electrolyte. *Chem Rev* **119**, 7610-7672, http://dx.doi.org/10.1021/acs.chemrev.8b00705 (2019).

122 Wang, X. *et al.* Morphology and mechanism of highly selective Cu(II) oxide nanosheet catalysts for carbon dioxide electroreduction. *Nat Commun* **12**, 794, http://dx.doi.org/10.1038/s41467-021-20961-7 (2021).

123 Jia, Y., Li, F., Fan, K. & Sun, L. Cu-based bimetallic electrocatalysts for CO2 reduction. *Advanced Powder Materials* **1** http://dx.doi.org/10.1016/j.apmate.2021.10.003 (2022).

124 Jiang, K. *et al.* Metal ion cycling of Cu foil for selective C–C coupling in electrochemical CO2 reduction. *Nature Catalysis* **1**, 111-119, http://dx.doi.org/10.1038/s41929-017-0009-x (2018).

125 De Gregorio, G. L. *et al.* Facet-Dependent Selectivity of Cu Catalysts in Electrochemical CO(2) Reduction at Commercially Viable Current Densities. *ACS Catal* **10**, 4854-4862, http://dx.doi.org/10.1021/acscatal.0c00297 (2020).

126 Chou, T. C. *et al.* Controlling the Oxidation State of the Cu Electrode and Reaction Intermediates for Electrochemical CO(2) Reduction to Ethylene.

J Am Chem Soc **142**, 2857-2867, http://dx.doi.org/10.1021/jacs.9b11126 (2020).

127 Giziński, D. *et al.* Nanostructured Anodic Copper Oxides as Catalysts in Electrochemical and Photoelectrochemical Reactions. *Catalysts* **10** http://dx.doi.org/10.3390/catal10111338 (2020).

128 Yang, P. P. *et al.* Protecting Copper Oxidation State via Intermediate Confinement for Selective CO(2) Electroreduction to C(2+) Fuels. *J Am Chem Soc* **142**, 6400-6408, http://dx.doi.org/10.1021/jacs.0c01699 (2020).

129 Woldu, A. R., Huang, Z., Zhao, P., Hu, L. & Astruc, D. Electrochemical CO2 reduction (CO2RR) to multi-carbon products over copper-based catalysts. *Coordination Chemistry Reviews* **454** http://dx.doi.org/10.1016/j.ccr.2021.214340 (2022).

130 Lai, Y., Jones, R. J. R., Wang, Y., Zhou, L. & Gregoire, J. M. Scanning Electrochemical Flow Cell with Online Mass Spectroscopy for Accelerated Screening of Carbon Dioxide Reduction Electrocatalysts. *ACS Comb Sci* **21**, 692-704, http://dx.doi.org/10.1021/acscombsci.9b00130 (2019).

131 Velasco-Velez, J. J. *et al.* Revealing the Active Phase of Copper during the Electroreduction of CO(2) in Aqueous Electrolyte by Correlating In Situ X-ray Spectroscopy and In Situ Electron Microscopy. *ACS Energy Lett* **5**, 2106-2111, http://dx.doi.org/10.1021/acsenergylett.0c00802 (2020).

132 Velasco-Velez, J. J. *et al.* On the Activity/Selectivity and Phase Stability of Thermally Grown Copper Oxides during the Electrocatalytic Reduction of CO(2). *ACS Catal* **10**, 11510-11518, http://dx.doi.org/10.1021/acscatal.0c03484 (2020).

133 Moradzaman, M. & Mul, G. In Situ Raman Study of Potential-Dependent Surface Adsorbed Carbonate, CO, OH, and C Species on Cu Electrodes During Electrochemical Reduction of CO2. *ChemElectroChem* **8**, 1478-1485, http://dx.doi.org/10.1002/celc.202001598 (2021).

134 Scherzer, M. *et al.* Electrochemical Surface Oxidation of Copper Studied by in Situ Grazing Incidence X-ray Diffraction. *The Journal of Physical Chemistry C* **123**, 13253-13262, http://dx.doi.org/10.1021/acs.jpcc.9b00282 (2019).

135 Wen, Y. & Xia, D. A thermodynamics model for morphology prediction of aluminum nano crystals fabricated by the inert gas condensation method. *Nanotechnology* **29**, 125301, http://dx.doi.org/10.1088/1361-6528/aaa84d (2018).

136 Whitehead, C. B. & Finke, R. G. Particle formation mechanisms supported by in situ synchrotron XAFS and SAXS studies: a review of metal, metal-oxide, semiconductor and selected other nanoparticle formation reactions. *Materials Advances* **2**, 6532-6568, http://dx.doi.org/10.1039/d1ma00222h (2021).

137 Akpomie, K. G., Ghosh, S., Gryzenhout, M. & Conradie, J. One-pot synthesis of zinc oxide nanoparticles via chemical precipitation for bromophenol blue adsorption and the antifungal activity against filamentous fungi. *Sci Rep* **11**, 8305, http://dx.doi.org/10.1038/s41598-021-87819-2 (2021).

138 Ghiyasiyan-Arani, M., Masjedi-Arani, M., Ghanbari, D., Bagheri, S. & Salavati-Niasari, M. Novel chemical synthesis and characterization of copper pyrovanadate nanoparticles and its influence on the flame

retardancy of polymeric nanocomposites. *Sci Rep* **6**, 25231, http://dx.doi.org/10.1038/srep25231 (2016).

139 Harcourt, A. V. XLIV.—On the observation of the course of chemical change. *Journal of the Chemical Society* **20**, 460-492, (1867).

140 Petr, P., Tomáš, O. & František, Š. in *Introducing the Effective Mass of Activated Complex and the Discussion on the Wave Function of this Instanton* (eds Ptáček Petr, Opravil Tomáš, & Šoukal František) Ch. 1 (IntechOpen, 2018).

141 Ostwald, W. On the assumed isomerism of red and yellow mercury oxide and the surface-tension of solid bodies. *Zeitschrift Fur Physikalische Chemie--Stochiometrie Und Verwandtschaftslehre* **34**, 495-503, (1900).

142 Karthika, S., Radhakrishnan, T. K. & Kalaichelvi, P. A Review of Classical and Nonclassical Nucleation Theories. *Crystal Growth & Design* **16**, 6663-6681, http://dx.doi.org/10.1021/acs.cgd.6b00794 (2016).

143 Alcântara Pessôa Filho, P. A., Medeiros Hirata, G. A., Watanabe, É. O. & Miranda, É. A. in *Comprehensive Biotechnology* 651-663 (2011).

144 Whitehead, C. B., Özkar, S. & Finke, R. G. LaMer's 1950 model of particle formation: a review and critical analysis of its classical nucleation and fluctuation theory basis, of competing models and mechanisms for phase-changes and particle formation, and then of its application to silver halide, semiconductor, metal, and metal-oxide nanoparticles. *Materials Advances* **2**, 186-235, http://dx.doi.org/10.1039/d0ma00439a (2021).

145 Cölfen, H. Nonclassical Nucleation and Crystallization. *Crystals* **10** (2020).

146 Gebauer, D. & Cölfen, H. Prenucleation clusters and non-classical nucleation. *Nano Today* **6**, 564-584, http://dx.doi.org/10.1016/j.nantod.2011.10.005 (2011).

147 Houk, L. R., Challa, S. R., Grayson, B., Fanson, P. & Datye, A. K. The definition of "critical radius" for a collection of nanoparticles undergoing Ostwald ripening. *Langmuir* **25**, 11225-11227, http://dx.doi.org/10.1021/la902263s (2009).

148 Lee, J., Yang, J., Kwon, S. G. & Hyeon, T. Nonclassical nucleation and growth of inorganic nanoparticles. *Nature Reviews Materials* **1** http://dx.doi.org/10.1038/natrevmats.2016.34 (2016).

149 You, H. & Fang, J. Particle-mediated nucleation and growth of solution-synthesized metal nanocrystals: A new story beyond the LaMer curve. *Nano Today* **11**, 145-167, http://dx.doi.org/10.1016/j.nantod.2016.04.003 (2016).

150 Wojnicki, M., Fitzner, K. & Luty-Blocho, M. Kinetic studies of nucleation and growth of palladium nanoparticles. *J Colloid Interface Sci* **465**, 190-199, http://dx.doi.org/10.1016/j.jcis.2015.11.066 (2016).

151 Watzky, M. A. & Finke, R. G. Transition Metal Nanocluster Formation Kinetic and Mechanistic Studies. A New Mechanism When Hydrogen Is the Reductant: Slow, Continuous Nucleation and Fast Autocatalytic Surface Growth. *Journal of the American Chemical Society* **119**, 10382-10400, http://dx.doi.org/10.1021/ja9705102 (1997).

152 Perala, S. R. & Kumar, S. On the two-step mechanism for synthesis of transition-metal nanoparticles. *Langmuir* **30**, 12703-12711, http://dx.doi.org/10.1021/la503199m (2014).

153 Amirjani, A. & Haghshenas, D. F. Modified Finke-Watzky mechanisms for the two-step nucleation and growth of silver nanoparticles. *Nanotechnology* **29**, 505602, http://dx.doi.org/10.1088/1361-6528/aae3dd (2018).

154 Bentea, L., Watzky, M. A. & Finke, R. G. Sigmoidal Nucleation and Growth Curves Across Nature Fit by the Finke–Watzky Model of Slow Continuous Nucleation and Autocatalytic Growth: Explicit Formulas for the Lag and Growth Times Plus Other Key Insights. *The Journal of Physical Chemistry C* **121**, 5302-5312, http://dx.doi.org/10.1021/acs.jpcc.6b12021 (2017).

155 Watzky, M. A. & Finke, R. G. Gold Nanoparticle Formation Kinetics and Mechanism: A Critical Analysis of the "Redox Crystallization" Mechanism. *ACS Omega* **3**, 1555-1563, http://dx.doi.org/10.1021/acsomega.7b01772 (2018).

156 Sandoe, H. E., Watzky, M. A. & Diaz, S. A. Experimental probes of silver metal nanoparticle formation kinetics: Comparing indirect versus more direct methods. *International Journal of Chemical Kinetics* **51**, 861-871, http://dx.doi.org/10.1002/kin.21315 (2019).

157 Iflah, Y. *et al.* Growth Behavior of Copper and Platinum Nanoparticles in an Imidazolium Based Ionic Liquid. *Journal of The Electrochemical Society* **164**, H5026-H5030, http://dx.doi.org/10.1149/2.0031708jes (2017).

158 Watzky, M. A., Finney, E. E. & Finke, R. G. Transition-Metal Nanocluster Size vs Formation Time and the Catalytically Effective Nucleus Number: A Mechanism-Based Treatment. *Journal of the American Chemical Society* **130**, 11959-11969, http://dx.doi.org/10.1021/ja8017412 (2008).

159 Handwerk, D. R., Shipman, P. D., Whitehead, C. B., Ozkar, S. & Finke, R. G. Mechanism-Enabled Population Balance Modeling of Particle Formation en Route to Particle Average Size and Size Distribution Understanding and Control. *J Am Chem Soc* **141**, 15827-15839, http://dx.doi.org/10.1021/jacs.9b06364 (2019).

160 Kent, P. D., Mondloch, J. E. & Finke, R. G. A four-step mechanism for the formation of supported-nanoparticle heterogenous catalysts in contact with solution: the conversion of Ir(1,5-COD)Cl/gamma-Al2O3 to Ir(0)(approximately 170)/gamma-Al2O3. *J Am Chem Soc* **136**, 1930-1941, http://dx.doi.org/10.1021/ja410194r (2014).

161 Liebig, F., Thunemann, A. F. & Koetz, J. Ostwald Ripening Growth Mechanism of Gold Nanotriangles in Vesicular Template Phases. *Langmuir* **32**, 10928-10935, http://dx.doi.org/10.1021/acs.langmuir.6b02662 (2016).

162 Voorhees, P. W. The theory of Ostwald ripening. *Journal of Statistical Physics* **38**, 231-252, http://dx.doi.org/10.1007/BF01017860 (1985).

163 Kregar, A., Kravos, A. & Katrašnik, T. Methodology for Evaluation of Contributions of Ostwald Ripening and Particle Agglomeration to Growth of Catalyst Particles in PEM Fuel Cells. *Fuel Cells* **20**, 487-498, http://dx.doi.org/10.1002/fuce.201900208 (2020).

164 Simonsen, S. B. *et al.* Ostwald ripening in a Pt/SiO2 model catalyst studied by in situ TEM. *Journal of Catalysis* **281**, 147-155, http://dx.doi.org/10.1016/j.jcat.2011.04.011 (2011).

165 Zhu, C. *et al.* In-situ liquid cell transmission electron microscopy investigation on oriented attachment of gold nanoparticles. *Nat Commun* **9**, 421, http://dx.doi.org/10.1038/s41467-018-02925-6 (2018).

166 Zhang, S. *et al.* Digestive ripening in the formation of monodisperse silver nanospheres. *Materials Chemistry Frontiers* **2**, 1328-1333, http://dx.doi.org/10.1039/c8qm00077h (2018).

167 Sahu, P. & Prasad, B. L. V. Effect of digestive ripening agent on nanoparticle size in the digestive ripening process. *Chemical Physics Letters* **525-526**, 101-104, http://dx.doi.org/10.1016/j.cplett.2011.12.078 (2012).

168 Prasad, B. L. V., Stoeva, S. I., Sorensen, C. M. & Klabunde, K. J. Digestive Ripening of Thiolated Gold Nanoparticles: The Effect of Alkyl Chain Length. *Langmuir* **18**, 7515-7520, http://dx.doi.org/10.1021/la020181d (2002).

169 Jose, D. & Jagirdar, B. R. Au@Pd Core−Shell Nanoparticles through Digestive Ripening. *The Journal of Physical Chemistry C* **112**, 10089-10094, http://dx.doi.org/10.1021/jp802721s (2008).

170 Grammatikopoulos, P., Sowwan, M. & Kioseoglou, J. Computational Modeling of Nanoparticle Coalescence. *Advanced Theory and Simulations* **2** http://dx.doi.org/10.1002/adts.201900013 (2019).

171 Ingham, B. *et al.* How Nanoparticles Coalesce: An in Situ Study of Au Nanoparticle Aggregation and Grain Growth. *Chemistry of Materials* **23**, 3312-3317, http://dx.doi.org/10.1021/cm200354d (2011).

172 Yun, K., Lee, J. & Nam, H.-S. Effect of Temperature on Coalescence Behavior of Unsupported Gold Nanoparticles. *Electronic Materials Letters* **15**, 133-139, http://dx.doi.org/10.1007/s13391-018-0090-6 (2018).

173 Wang, F. *et al.* Porous single-crystalline palladium nanoparticles with high catalytic activities. *Angew Chem Int Ed Engl* **51**, 4872-4876, http://dx.doi.org/10.1002/anie.201107376 (2012).

174 Long, R., Zhou, S., Wiley, B. J. & Xiong, Y. Oxidative etching for controlled synthesis of metal nanocrystals: atomic addition and subtraction. *Chemical Society Reviews* **43**, 6288-6310, http://dx.doi.org/10.1039/C4CS00136B (2014).

175 Zheng, Y., Zeng, J., Ruditskiy, A., Liu, M. & Xia, Y. Oxidative Etching and Its Role in Manipulating the Nucleation and Growth of Noble-Metal Nanocrystals. *Chemistry of Materials* **26**, 22-33, http://dx.doi.org/10.1021/cm402023g (2013).

176 Xiong, Y. *et al.* Understanding the Role of Oxidative Etching in the Polyol Synthesis of Pd Nanoparticles with Uniform Shape and Size. *Journal of the American Chemical Society* **127**, 7332-7333, http://dx.doi.org/10.1021/ja0513741 (2005).

177 Khelfa, A., Nelayah, J., Wang, G., Ricolleau, C. & Alloyeau, D. Studying the Effects of Temperature on the Nucleation and Growth of Nanoparticles by Liquid-Cell Transmission Electron Microscopy. *J Vis Exp* http://dx.doi.org/10.3791/62225 (2021).

178 Zhang, L., Wang, L., Jiang, Z. & Xie, Z. Synthesis of size-controlled monodisperse Pd nanoparticles via a non-aqueous seed-mediated growth. *Nanoscale Research Letters* **7**, 312, http://dx.doi.org/10.1186/1556-276X-7-312 (2012).

179 Deng, D., Jin, Y., Cheng, Y., Qi, T. & Xiao, F. Copper nanoparticles: aqueous phase synthesis and conductive films fabrication at low sintering temperature. *ACS Appl Mater Interfaces* **5**, 3839-3846, http://dx.doi.org/10.1021/am400480k (2013).

180 Imamura, H., Kamikoriyama, Y., Muramatsu, A. & Kanie, K. A mild aqueous synthesis of ligand-free copper nanoparticles for low temperature sintering nanopastes with nickel salt assistance. *Sci Rep* **11**, 24268, http://dx.doi.org/10.1038/s41598-021-03707-9 (2021).

181 Kettemann, F. *et al.* Reliable palladium nanoparticle syntheses in aqueous solution: the importance of understanding precursor chemistry and growth mechanism. *CrystEngComm* **17**, 1865-1870, http://dx.doi.org/10.1039/c4ce01025f (2015).

182 Song, Y., Zhang, M., Fang, H. & Xia, H. Shape transformation of gold nanoparticles in aqueous CTAB/CTAC solution to generate high-index facets for electrocatalysis and SERS activity. *ChemPhysMater* http://dx.doi.org/10.1016/j.chphma.2022.04.006 (2022).

183 Gao, W. *et al.* Atomistic insights into the nucleation and growth of platinum on palladium nanocrystals. *Nat Commun* **12**, 3215, http://dx.doi.org/10.1038/s41467-021-23290-x (2021).

184 Liu, J., He, F., Gunn, T. M., Zhao, D. & Roberts, C. B. Precise Seed-Mediated Growth and Size-Controlled Synthesis of Palladium Nanoparticles Using a Green Chemistry Approach. *Langmuir* **25**, 7116-7128, http://dx.doi.org/10.1021/la900228d (2009).

185 Niu, W., Zhang, L. & Xu, G. Seed-mediated growth method for high-quality noble metal nanocrystals. *Science China Chemistry* **55**, 2311-2317, http://dx.doi.org/10.1007/s11426-012-4681-z (2012).

186 Niu, W. *et al.* Seed-Mediated Growth of Nearly Monodisperse Palladium Nanocubes with Controllable Sizes. *Crystal Growth & Design* **8**, 4440-4444, http://dx.doi.org/10.1021/cg8002433 (2008).

187 Sood, A., Arora, V., Shah, J., Kotnala, R. K. & Jain, T. K. Ascorbic acid-mediated synthesis and characterisation of iron oxide/gold core–shell nanoparticles. *Journal of Experimental Nanoscience* **11**, 370-382, http://dx.doi.org/10.1080/17458080.2015.1066514 (2015).

188 Deraedt, C. *et al.* Sodium borohydride stabilizes very active gold nanoparticle catalysts. *Chem Commun (Camb)* **50**, 14194-14196, http://dx.doi.org/10.1039/c4cc05946h (2014).

189 Yue, J., Du, Z. & Shao, M. The role of citric acid and ascorbic acid in morphology control of palladium nanocrystals: A molecular dynamics and density functional theory study. *Chemical Physics Letters* **659**, 159-163, http://dx.doi.org/10.1016/j.cplett.2016.07.019 (2016).

190 Mozaffari, S. *et al.* Colloidal nanoparticle size control: experimental and kinetic modeling investigation of the ligand-metal binding role in controlling the nucleation and growth kinetics. *Nanoscale* **9**, 13772-13785, http://dx.doi.org/10.1039/c7nr04101b (2017).

191 Jang, K. *et al.* Three-dimensional atomic mapping of ligands on palladium nanoparticles by atom probe tomography. *Nat Commun* **12**, 4301, http://dx.doi.org/10.1038/s41467-021-24620-9 (2021).

192 Alam, M. S., Siddiq, A. M., Narayanan, S. S., Samanta, D. & Das, S. K. Cationic Surfactant (CTAC) Assisted Synthesis of Silver Nanoparticles with Controlled Size: Optical, Morphological and Bactericidal Studies. *Journal of Nanoengineering and Nanomanufacturing* **5**, 124-131, http://dx.doi.org/10.1166/jnan.2015.1238 (2015).

193 Wen, X. *et al.* Synthesis of Palladium Nanodendrites Using a Mixture of Cationic and Anionic Surfactants. *Langmuir* **36**, 1745-1753, http://dx.doi.org/10.1021/acs.langmuir.9b03804 (2020).

194 Guzman, M. *et al.* Effect of the Concentration and the Type of Dispersant on the Synthesis of Copper Oxide Nanoparticles and Their Potential Antimicrobial Applications. *ACS Omega* **6**, 18576-18590, http://dx.doi.org/10.1021/acsomega.1c00818 (2021).

195 Mozaffari, S. *et al.* Ligand-Mediated Nucleation and Growth of Palladium Metal Nanoparticles. *J Vis Exp* http://dx.doi.org/10.3791/57667 (2018).

196 Mozaffari, S. *et al.* The role of nanoparticle size and ligand coverage in size focusing of colloidal metal nanoparticles. *Nanoscale Adv* **1**, 4052-4066, http://dx.doi.org/10.1039/c9na00348g (2019).

197 Sharada, S. *et al.* Synthesis of palladium nanoparticles using continuous flow microreactor. *Colloids and Surfaces A: Physicochemical and Engineering Aspects* **498**, 297-304, http://dx.doi.org/10.1016/j.colsurfa.2016.03.068 (2016).

198 Xie, X. *et al.* Large-scale synthesis of palladium concave nanocubes with high-index facets for sustainable enhanced catalytic performance. *Sci Rep* **5**, 8515, http://dx.doi.org/10.1038/srep08515 (2015).

199 Klinkova, A., Larin, E. M., Prince, E., Sargent, E. H. & Kumacheva, E. Large-Scale Synthesis of Metal Nanocrystals in Aqueous Suspensions. *Chemistry of Materials* **28**, 3196-3202, http://dx.doi.org/10.1021/acs.chemmater.6b00936 (2016).

200 Xu, L., Peng, J., Srinivasakannan, C., Chen, G. & Shen, A. Q. Synthesis of copper nanocolloids using a continuous flow based microreactor. *Applied Surface Science* **355**, 1-6, http://dx.doi.org/10.1016/j.apsusc.2015.07.070 (2015).

201 Wu, S. H. & Chen, D. H. Synthesis of high-concentration Cu nanoparticles in aqueous CTAB solutions. *J Colloid Interface Sci* **273**, 165-169, http://dx.doi.org/10.1016/j.jcis.2004.01.071 (2004).

202 Wang, Y., Du, M., Xu, J., Yang, P. & Du, Y. Size-Controlled Synthesis of Palladium Nanoparticles. *Journal of Dispersion Science and Technology* **29**, 891-894, http://dx.doi.org/10.1080/01932690701783499 (2008).

203 Kim, H. S. *et al.* Concentration Effect of Reducing Agents on Green Synthesis of Gold Nanoparticles: Size, Morphology, and Growth Mechanism. *Nanoscale Res Lett* **11**, 230, http://dx.doi.org/10.1186/s11671-016-1393-x (2016).

204 Bakshi, M. S. How Surfactants Control Crystal Growth of Nanomaterials. *Crystal Growth & Design* **16**, 1104-1133, http://dx.doi.org/10.1021/acs.cgd.5b01465 (2015).

205 Hao, J., He, M., Liu, B. & Yang, J. Solvent Effect on the Synthesis of Oleylamine Modified Au Nanoparticles and Their Self-Assembled Film for SERS Substrate. *Chemosensors* **10**, 373, (2022).

206 Davidson, C. T. & University of, A. *The thermodynamics of colloidal surfactant solutions*. (University of Aberdeen, 1983).

207 Manning-Benson, S. *The dynamics of surfactant adsorption*. (University of Oxford, 1998).

208 Langille, M. R., Personick, M. L., Zhang, J. & Mirkin, C. A. Defining rules for the shape evolution of gold nanoparticles. *J Am Chem Soc* **134**, 14542-14554, http://dx.doi.org/10.1021/ja305245g (2012).

209 Personick, M. L. & Mirkin, C. A. Making sense of the mayhem behind shape control in the synthesis of gold nanoparticles. *J Am Chem Soc* **135**, 18238-18247, http://dx.doi.org/10.1021/ja408645b (2013).

210 Pastoriza-Santos, I., Sánchez-Iglesias, A., Rodríguez-González, B. & Liz-Marzán, L. M. Aerobic Synthesis of Cu Nanoplates with Intense Plasmon Resonances. *Small* **5**, 440-443, http://dx.doi.org/10.1002/smll.200801088 (2009).

211 Liu, Q.-m., Yasunami, T., Kuruda, K. & Okido, M. Preparation of Cu nanoparticles with ascorbic acid by aqueous solution reduction method. *Transactions of Nonferrous Metals Society of China* **22**, 2198-2203, http://dx.doi.org/10.1016/s1003-6326(11)61449-0 (2012).

212 Dai, S. *et al.* In situ atomic-scale observation of oxygen-driven core-shell formation in Pt(3)Co nanoparticles. *Nat Commun* **8**, 204, http://dx.doi.org/10.1038/s41467-017-00161-y (2017).

213 Harada, M. & Ikegami, R. In Situ Quick X-ray Absorption Fine Structure and Small-Angle X-ray Scattering Study of Metal Nanoparticle Growth in Water-in-Oil Microemulsions during Photoreduction. *Crystal Growth & Design* **16**, 2860-2873, http://dx.doi.org/10.1021/acs.cgd.6b00173 (2016).

214 Yoshimune, W., Kuwaki, A., Kusano, T., Matsunaga, T. & Nakamura, H. In Situ Small-Angle X-ray Scattering Studies on the Growth Mechanism of Anisotropic Platinum Nanoparticles. *ACS Omega* **6**, 10866-10874, http://dx.doi.org/10.1021/acsomega.1c00608 (2021).

215 Wu, S., Li, M. & Sun, Y. In Situ Synchrotron X-ray Characterization Shining Light on the Nucleation and Growth Kinetics of Colloidal Nanoparticles. *Angew Chem Int Ed Engl* **58**, 8987-8995, http://dx.doi.org/10.1002/anie.201900690 (2019).

216 Koerner, H., MacCuspie, R. I., Park, K. & Vaia, R. A. In Situ UV/Vis, SAXS, and TEM Study of Single-Phase Gold Nanoparticle Growth. *Chemistry of Materials* **24**, 981-995, http://dx.doi.org/10.1021/cm202633v (2012).

217 Polte, J. *et al.* Nucleation and Growth of Gold Nanoparticles Studied via in situ Small Angle X-ray Scattering at Millisecond Time Resolution. *ACS Nano* **4**, 1076-1082, http://dx.doi.org/10.1021/nn901499c (2010).

218 Panariello, L., Radhakrishnan, A. N. P., Papakonstantinou, I., Parkin, I. P. & Gavriilidis, A. Particle Size Evolution during the Synthesis of Gold Nanoparticles Using In Situ Time-Resolved UV–Vis Spectroscopy: An Experimental and Theoretical Study Unravelling the Effect of Adsorbed Gold Precursor Species. *The Journal of Physical Chemistry C* **124**, 27662-27672, http://dx.doi.org/10.1021/acs.jpcc.0c07405 (2020).

219 Karim, A. M. *et al.* Synthesis of 1 nm Pd Nanoparticles in a Microfluidic Reactor: Insights from in Situ X-ray Absorption Fine Structure Spectroscopy and Small-Angle X-ray Scattering. *The Journal of Physical Chemistry C* **119**, 13257-13267, http://dx.doi.org/10.1021/acs.jpcc.5b01681 (2015).

220 Harada, M. & Inada, Y. In situ time-resolved XAFS studies of metal particle formation by photoreduction in polymer solutions. *Langmuir* **25**, 6049-6061, http://dx.doi.org/10.1021/la900550t (2009).

221 Saeki, M. *et al.* In Situ Time-Resolved XAFS Studies on Laser-Induced Particle Formation of Palladium Metal in an Aqueous/EtOH Solution. *The Journal of Physical Chemistry C* **123**, 817-824, http://dx.doi.org/10.1021/acs.jpcc.8b09532 (2018).

222 Yao, S. *et al.* Insights into the Formation Mechanism of Rhodium Nanocubes. *The Journal of Physical Chemistry C* **116**, 15076-15086, http://dx.doi.org/10.1021/jp302471p (2012).

223 Godfrey, I. J., Dent, A. J., Parkin, I. P., Maenosono, S. & Sankar, G. Following the Formation of Silver Nanoparticles Using In Situ X-ray Absorption Spectroscopy. *ACS Omega* **5**, 13664-13671, http://dx.doi.org/10.1021/acsomega.0c00697 (2020).

224 Patakfalvi, R., Papp, S. & Dékány, I. The kinetics of homogeneous nucleation of silver nanoparticles stabilized by polymers. *Journal of Nanoparticle Research* **9**, 353-364, http://dx.doi.org/10.1007/s11051-006-9139-9 (2006).

225 Mizutani, T. *et al.* In situ UV–vis investigation of growth of gold nanoparticles prepared by solution plasma sputtering in NaCl solution. *Applied Surface Science* **354**, 397-400, http://dx.doi.org/https://doi.org/10.1016/j.apsusc.2015.04.139 (2015).

226 Huang, H. *et al.* Continuous flow synthesis of ultrasmall gold nanoparticles in a microreactor using trisodium citrate and their SERS performance. *Chemical Engineering Science* **189**, 422-430, http://dx.doi.org/10.1016/j.ces.2018.06.050 (2018).

227 Olivo, G. *et al.* Following a Chemical Reaction on the Millisecond Time Scale by Simultaneous X-ray and UV/Vis Spectroscopy. *J Phys Chem Lett* **8**, 2958-2963, http://dx.doi.org/10.1021/acs.jpclett.7b01133 (2017).

228 Chen, X., Wang, J., Pan, R., Roth, S. & Förster, S. Insights into Growth Kinetics of Colloidal Gold Nanoparticles: In Situ SAXS and UV–Vis Evaluation. *The Journal of Physical Chemistry C* **125**, 1087-1095, http://dx.doi.org/10.1021/acs.jpcc.0c09680 (2020).

229 Polte, J. *et al.* New insights of the nucleation and growth process of gold nanoparticles via in situ coupling of SAXS and XANES. *Journal of Physics: Conference Series* **247** http://dx.doi.org/10.1088/1742-6596/247/1/012051 (2010).

230 Wang, Y. C. *et al.* In Situ Single Particle Reconstruction Reveals 3D Evolution of PtNi Nanocatalysts During Heating. *Small* **20**, e2302426, http://dx.doi.org/10.1002/smll.202302426 (2024).

231 Longo, E., Avansi, W., Jr., Bettini, J., Andres, J. & Gracia, L. In situ Transmission Electron Microscopy observation of Ag nanocrystal evolution by surfactant free electron-driven synthesis. *Sci Rep* **6**, 21498, http://dx.doi.org/10.1038/srep21498 (2016).

232 Evans, J. E., Jungjohann, K. L., Browning, N. D. & Arslan, I. Controlled growth of nanoparticles from solution with in situ liquid transmission electron microscopy. *Nano Lett* **11**, 2809-2813, http://dx.doi.org/10.1021/nl201166k (2011).

233 Cheong, S., Watt, J., Ingham, B., Toney, M. F. & Tilley, R. D. In Situ and Ex Situ Studies of Platinum Nanocrystals: Growth and Evolution in Solution. *Journal of the American Chemical Society* **131**, 14590-14595, http://dx.doi.org/10.1021/ja9065688 (2009).

234 Fridman, H., Volokh, M. & Mokari, T. Dynamics of the nanocrystal structure and composition in growth solutions monitored by in situ lab-scale X-ray diffraction. *Nanoscale* **13**, 19076-19084, http://dx.doi.org/10.1039/d1nr05371j (2021).

235 Yakushkin, S. S., Kirillov, V. L., Shalygin, A. S. & Martyanov, O. N. The In Situ Study of the Fe3O4/DMSO Ferrofluid Synthesis. *Applied Magnetic Resonance* **50**, 1183-1189, http://dx.doi.org/10.1007/s00723-019-01136-6 (2019).

236 Nayak, C. *et al.* Insight into growth of Au-Pt bimetallic nanoparticles: an in situ XAS study. *J Synchrotron Radiat* **24**, 825-835, http://dx.doi.org/10.1107/s1600577517006257 (2017).

237 Ramamoorthy, R. K. *et al.* The role of pre-nucleation clusters in the crystallization of gold nanoparticles. *Nanoscale* **12**, 16173-16188, http://dx.doi.org/10.1039/d0nr03486j (2020).

238 Nayak, C., Bhattacharyya, D., Jha, S. N. & Sahoo, N. K. In Situ XAS Study on Growth of PVP-Stabilized Cu Nanoparticles. *ChemistrySelect* **3**, 7370-7377, http://dx.doi.org/https://doi.org/10.1002/slct.201801358 (2018).

239 Nishimura, S., Takagaki, A., Maenosono, S. & Ebitani, K. In situ time-resolved XAFS study on the formation mechanism of Cu nanoparticles using poly(N-vinyl-2-pyrrolidone) as a capping agent. *Langmuir* **26**, 4473-4479, http://dx.doi.org/10.1021/la904248z (2010).

240 Chang, S. Y. *et al.* Energy dispersive-EXAFS of Pd nucleation at a liquid/liquid interface. *Journal of Physics: Conference Series* **712**, 012058, http://dx.doi.org/10.1088/1742-6596/712/1/012058 (2016).

241 Chen, C. *et al.* In-Situ High-Resolution Transmission Electron Microscopy Investigation of Overheating of Cu Nanoparticles. *Sci Rep* **6**, 19545, http://dx.doi.org/10.1038/srep19545 (2016).

242 Liu, H. *et al.* QXAFS system of the BL14W1 XAFS beamline at the Shanghai Synchrotron Radiation Facility. *J Synchrotron Radiat* **19**, 969-975, http://dx.doi.org/10.1107/S0909049512038873 (2012).

Chapter 2. Characterization Principles and Methodology

2.1 Introduction

This chapter will outline the theoretical principles and chemical information that can be obtained from the characterization tools used in this work. To provide context to the scientific method, brief descriptions of relevant experimental procedures are included.

Material characterization performed outside of the reaction conditions are termed '*ex situ'* while those carried out under the reaction conditions are *'in situ'*. For catalysis, the '*operando'* characterization can be distinguished from *in situ* characterization, as occurring when the catalyst material is measured simultaneous to a recording of the catalytic performance. Due to the focus of this work on X-ray techniques, characterization tools are broadly classified as either synchrotron-based or lab-based techniques. Although there is an overlap between the techniques available in labs and at synchrotrons, these have mainly been divided according to the experiments carried out in this report. A key theme in the experiments is the use of time-resolved X-ray absorption spectroscopy (XAS), often employed *in situ* and compared with other *in situ* techniques, such as small angle X-ray scattering (SAXS) or electron paramagnetic resonance (EPR). This combination of characterization tools can provide different facets of information for the same system. The instrumentation, data analysis methods and limitations in achieving high time-resolution during *in situ* measurements will be addressed for these systems.

2.2 Synchrotron-based Characterization

X-rays are a form of electromagnetic radiation, often defined with wavelengths between 0.01 and 10 nm, corresponding to an energy range of 100 eV to 100 keV.[1] Practically, X-rays originate from excited electrons. Electromagnetic radiation within the X-ray energy range may interact with matter by being either transmitted, scattered, or absorbed (Figure 2.1 a). X-ray characterization techniques give chemical and physical information by recording these interactions or their consequences.

Transmitted X-rays pass through the sample, without being absorbed or scattered. They are generally measured for their inverse, to deduce the X-ray absorption of a sample. Transmitted X-rays are detected in X-ray absorption spectroscopy and in imaging where the density and morphology of a sample are mapped.

Scattered X-rays can give information about both the atomic structure and wider ordering in the sample, bridging the molecular and macro scales. Scattering may be classified under either elastic, where no energy is lost, or inelastic where an energy transfer has occurred so that the scattered X-ray has a different wavelength than the incident. These interactions give rise to various characterization techniques, which can be used to provide a range of material information.[2]

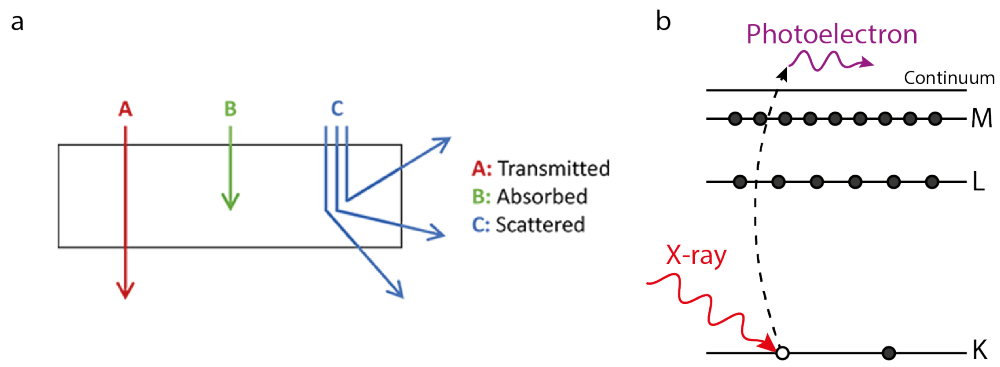

Figure 2.1 ***X-ray Interactions with Matter.*** *(a) Simplified representation of the three possible interactions between X-rays and matter; transmission (red), absorption (green) and scattering (blue). (b) Energy level schematic of the 'photoelectric effect' in which an X-ray (red) is absorbed by a core electron, exciting it to the continuum (purple) and leaving the atom in an excited state. Redrawn based on Miyanaga et al., 2016*[3] *and Newville, 2014.*[2]

Absorbed X-rays interact with a sample by virtue of the photoelectric effect. This phenomenon is observed as the release of charged particles, such as electrons, when a material is exposed to, and absorbs, electromagnetic radiation. The electrons released during this process are called 'photoelectrons'. The photon energy of the X-ray is transferred to a core electron, giving it enough energy to be excited to the continuum, leaving behind a core hole (Figure 2.1 b). The measured absorption at a given X-ray energy shows the probability of the excitation of electrons, which is only possible in cases where the binding energy of the electron is less than the energy of the X-ray. The absorption of the X-ray due to photoelectric effect gives rise to X-ray absorption spectroscopy (XAS), and the consequences of photoelectron release can be exploited to gain a range of information about the sample.

A synchrotron is a circular accelerator for charged particles, such as electrons. The acceleration of these particles and control of their circular orbit using

magnets, produces an intense bright light, mainly in the X-ray range, which can be applied to study the properties of matter at an atomic or molecular scale. The range of characterization tools available at synchrotrons provides valuable information for a wide variety of disciplines, from chemistry, physics and biology to history and geology.

A schematic of a typical synchrotron is given in Figure 2.2, to explain the working principle. To produce synchrotron light, electrons are first produced by an electron gun (1) *via* thermionic emission. These electrons are accelerated to close to the speed of light in a booster ring (2) using bending magnets and high voltage radio frequency, and later injected into the larger ring (3). An applied magnetic field forces the electrons, maintained under vacuum, to travel along a curved path, emitting high intensity synchrotron radiation as they change direction.

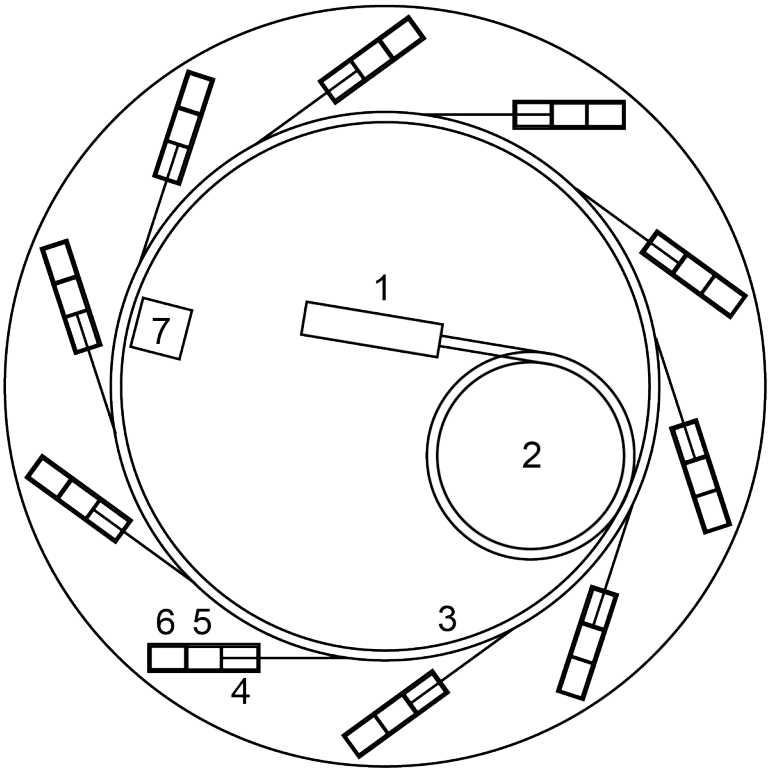

Figure 2.2 ***The Diamond Light Source Synchrotron.*** *Diamond Light Source, a 3rd generation synchrotron in Harwell, UK is shown as a representation of typical synchrotron facility used in this work. Layout of a synchrotron is shown, numbered by the progression of an X-ray through the facility. Not drawn to scale and based on Diamond Light Source.*[4]

The synchrotron radiation has a high flux and can be directed into beamlines, passing through a front end (4), optics hutch (5) and finally to the experimental hutch (6) where the desired energy range can be applied to a sample. Measurements are managed from the control room to protect users from the dangerous radiation. A radiofrequency cavity (7) is also necessary to provide a 'top-up' energy boost and maintain the orbit of electrons around the ring.[4]

The synchrotron radiation can be tuned to a wide range of wavelengths, making synchrotrons versatile and powerful characterization tools. For this research, the

experiments focus on the use of synchrotrons as a high flux X-ray radiation source.

2.2.1 XAS

X-ray Absorption Spectroscopy or XAS is a versatile characterization technique based on the principle that X-rays with energies near and above the core binding energy of its atoms are absorbed by a material.[5] Through this 'photoelectric effect', when a sample is exposed to X-ray energies high enough to excite an electron to an available state, the energy of the absorbed electromagnetic radiation causes the ejection of a photoelectron. XAS measures electron transitions from core states to either excited states (near-edge), or to the continuum (extended).

The probability of absorption at different energies varies depending on the physical and chemical properties of the absorbing atom and its neighbours. This information is recorded in the XAS spectrum which can be analysed to learn about the oxidation state of the excited atom, coordination environment (e.g., octahedral versus tetrahedral) and local coordination information such as coordination number, interatomic distances, and neighbouring species.

Beer's Law gives the absorption coefficient, μ, which is the probability that X-rays will be absorbed by a sample.

$$I_t = I_o e^{-\mu t} \qquad \textit{Equation 2.1}$$

where I_o is the incident X-ray intensity, I_t is the transmitted X-ray intensity, and t is the sample thickness. The absorption coefficient depends on the sample density (ρ), atomic number (Z), atomic mass (A) and X-ray energy (E), as

$$\mu \approx \frac{\rho Z^4}{AE^3} \qquad \textit{Equation 2.2}$$

A sudden increase in absorption is observed at energies just above the core electron binding energy, known as the ‘edge’. XAS records the modulation of the X-ray absorption probability by mapping the total intensity of absorption across an energy range. The data obtained holds information about the physical and chemical properties of the absorbing atom.

After the absorption, the atom is in an ‘excited state’, since a photoelectron has been ejected and a core hole remains in the sample (Figure 2.3 a). This state usually decays within femtoseconds, when the core hole is filled by an electron from a higher energy electron shell. The energy released during this decay can cause either the emission of a fluorescent X-ray of a well-defined characteristic energy (Figure 2.3 b), or the ejection of a secondary Auger electron into the continuum. In the first case, the fluorescent X-ray has a well-defined energy based on the energy difference between the initial and final states of the electron. Thus, it can be used to identify and quantify the atomic constituents of the sample.

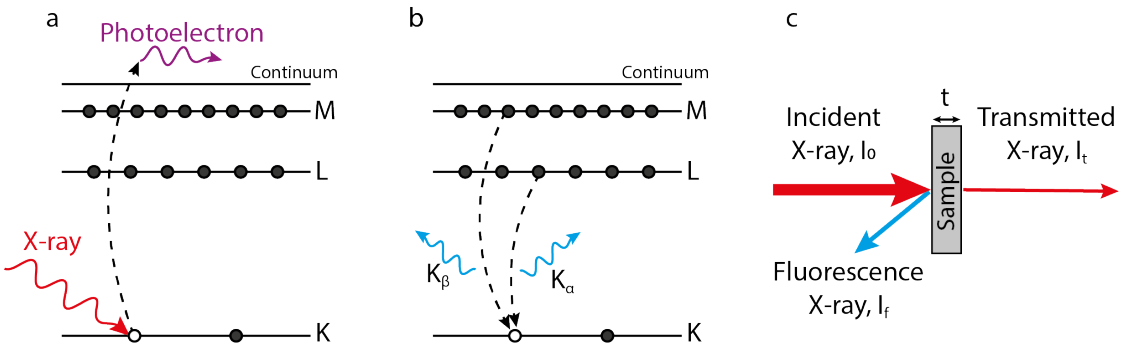

Figure 2.3 ***Transmission and Fluorescence Mode XAS.*** *Energy level diagrams show (a) the excitation of a core electron to the continuum by X-ray absorption (red) and (b) the release of X-ray fluorescence (blue) after relaxation of electrons in higher shells. Reproduced from Hummer and Rompel, 2013.*[6] *(c) Transmission (thin red) are detected directly across from the incident beam and fluorescence X-rays (blue) at an angle of 45° from the incident beam (thick red). Redrawn from Miyanaga et al., 2016.*[3]

The two most common modes of gathering XAS data are by measuring either the fluorescence signal or the transmitted signal (Figure 2.4). In transmission mode, the X-ray is detected before and after passing through the sample, and the difference between them is the energy absorbed by the sample. The XAS spectrum of absorption versus energy is plotted according to the Beer-Lambert Law where the relationship between the incident (I_o) and transmitted X-ray (I_t) is given by absorption,

$$A = ln\left(\frac{I_o}{I_t}\right) = \mu t \qquad \textit{Equation 2.3}$$

The absorption cross-section (A), a measure of the photon absorption of a molecule (cm^2 per molecule) is given by μ and the thickness (t) of the sample through which the X-ray is passing.

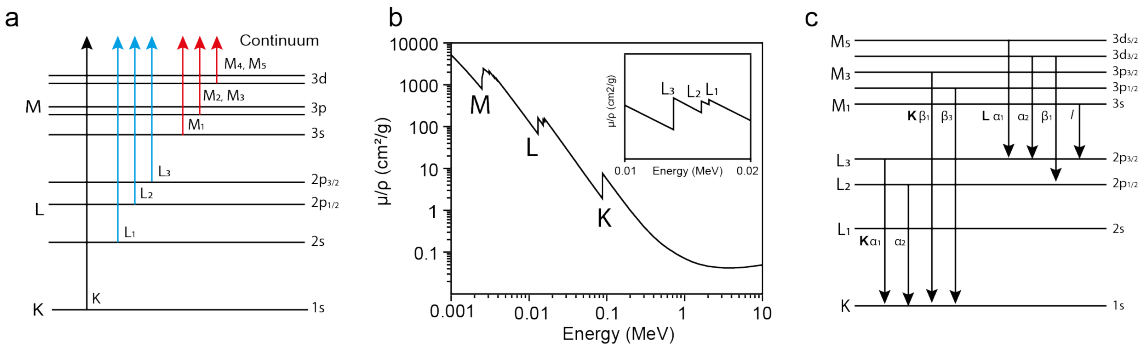

Figure 2.4 ***Transmission and Fluorescence Mode XAS.*** *(a) Energy level diagram showing the possible XAS core-electron excitations to the continuum, named after the principal quantum number as K (black), L (blue) and M (red). (b) These give rise to absorption edges at corresponding energies as shown in the Pb absorption spectrum. Redrawn based on Newville, 2014.*[2,7] *(c) Fluorescent decays are named by the core-hole filled and the initial electron level.*

The edge jump (Figure 2.4 b), or the difference in absorption before and after the edge energy, should ideally be greater than 0.1 to obtain useable data. This is difficult or impossible to achieve in samples with extremely low or high concentration of the absorbing element, where there is either poor attenuation or transmission. In these cases, the absorption can be gathered from the fluorescent X-rays. Absorption is calculated from fluorescent X-rays detected (I_f) by

$$A = \left(\frac{I_f}{I_o}\right) \qquad \textit{Equation 2.4}$$

The different signals may be collected by multiple (sometimes 36) detectors of different elements.

The XAS Spectrum

While X-rays within a certain energy range are shone on a sample, the intensity of the resulting transmitted or fluorescence X-rays are detected for each energy

point, giving a spectrum. This spectrum, obtained by plotting the X-ray intensity against the X-ray energy, is typically wide enough to include a single sharp edge, followed by an oscillating absorption region.

The X-ray absorption near-edge spectroscopy (XANES) region, 30 to 50 eV around the edge, gives information about the coordination geometry and the oxidation state of the absorbing atoms.[5] The maximum peak in the XANES region is often referred to as the 'white line'. The sinusoidal region after the XANES, created by the interaction of the photoelectrons with neighbouring atoms, is defined as the extended X-ray absorption fine structure (EXAFS) region (Figure 2.5). This can be observed in the spectra from 50 eV or 100 eV above the edge until around 1000 eV. These oscillations can be resolved to estimate coordination number, closest neighbours, bond length or inter-atomic distance, based on the information known about the system.[5]

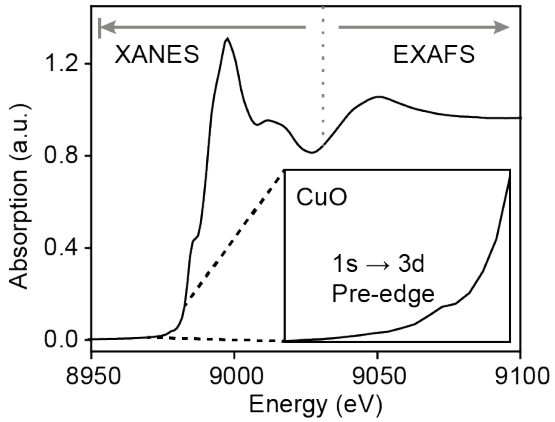

Figure 2.5 ***XANES and EXAFS Region.*** *On a typical Cu K-edge CuO XAS spectrum, the XANES region occurs immediately around the absorption edge, including the pre-edge (inset), while the EXAFS region encompasses the oscillations 50 eV above the edge onwards.*

XANES

The XANES region of the curve is dominated by the transition of a core electron to the continuum at the edge, fingerprinting the chemical species and the oxidation states present. However, pre-edge features are also present, particularly for 3d transition metals. Although the 1s to 3d transition is forbidden, 3d and 4p shell mixing allows limited transitions, giving a smaller peak before the edge in these cases. To quantify the features observed in the XANES, a few analysis techniques have emerged.

Oxidation states are often quantified through a mathematical fitting with standard spectra of known composition, called a linear combination fitting (LCF). In the absence of reliable standards, a simulation based on the expected configuration can be fitted with LCF.[8] Failing this, a principal component analysis (PCA) also gives an indication of the number of major components in the sample and their ratios, without indicating the actual materials present.

For certain elements, such as Pt, the white line intensity directly indicates the changing oxidation states. By marking changes in intensity, changes in Pt oxidation state are monitored.[9] This analysis of the XANES region can be extended to $\Delta\mu$-XANES in which the difference between the measured spectrum and a known standard can isolate the changes and identify surface interactions, such as adsorption, with more accuracy. These have also been applied for Pt, where $\Delta\mu$-XANES can distinguish the configuration of Pt-O and Pt-OH species at the surface.[10]

EXAFS

The EXAFS region is the oscillatory part of the spectrum, from around 100 or 150 eV to 1000 eV above the edge energy. Simplistically, when a photoelectron is

released from the core shell, it spreads out like a wave and interacts with neighbouring atoms. This produces coherent and incoherent interferences which respectively correspond to the sinusoidal peaks and troughs of the EXAFS oscillations (Figure 2.6).

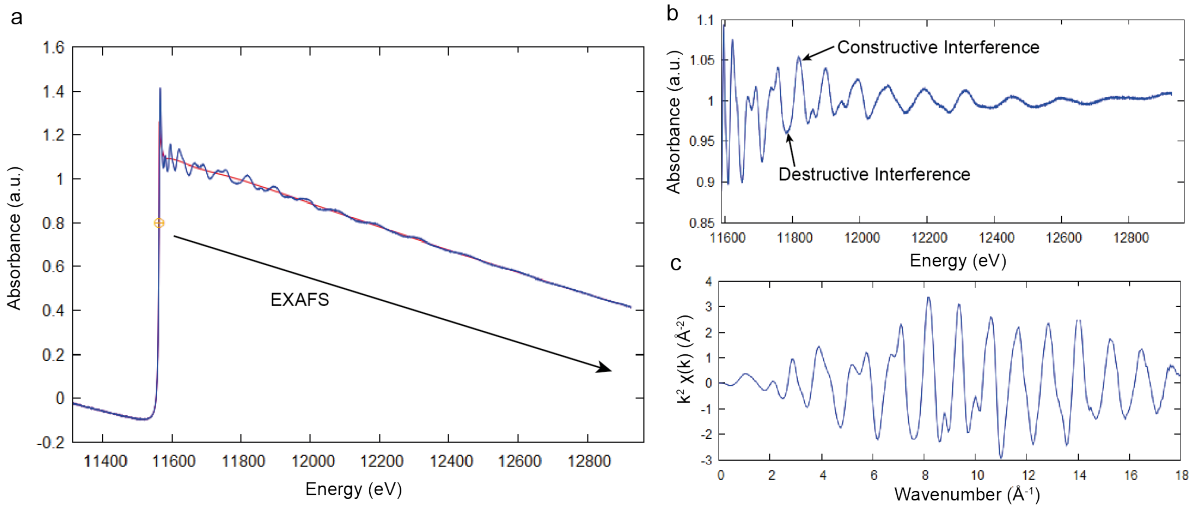

Figure 2.6 ***Background Subtraction for EXAFS.*** *(a) A typical XAS spectrum, measured for Pt foil at the Pt L_3-edge shows the background subtraction (red) applied to the EXAFS region (blue) to obtain the sinusoidal interference data. (b) A closer look at the constructive and destructive interference in EXAFS and (c) the corresponding k-space data, redrawn based on a diagram by Newville, 2014.*[2]

The EXAFS equation

To study the oscillations in the EXAFS region, the EXAFS equation was introduced in 1971 by Sayers, Stern and Lytle, and is generally considered to be the origin of modern EXAFS. This equation was derived by treating atoms as point scatterers in a spherical wave of the photoelectron, making the EXAFS similar to a photoelectric interference phenomenon.[11]

Since XAS is an effect caused by interference, it depends on the wavenumber of the photoelectron. The resulting energy-dependent oscillations can be expressed

in terms of photoelectron wavenumber (k). This can be calculated using Equation 2.5 to remove the 'bare atom' background and normalise the edge jump to 1.

$$\chi(E) = \frac{\mu(E) - \mu_o(E)}{\Delta\mu_o(E_o)} \qquad \textit{Equation 2.5}$$

Where $\mu(E)$ is the measured energy, $\mu_o(E)$ is the 'bare atom' background (Figure 2.7 a, red) and $\Delta\mu_o(E_o)$ is the edge step to give a normalised signal.

It is convenient to plot the EXAFS region using photoelectron wavenumber, k, rather than the original energy measured, such that

$$k = \sqrt{\frac{2m(E - E_o)}{h^2}} \qquad \textit{Equation 2.6}$$

Where E_0 is the absorption edge energy, m is the electron mass and h is Planck's constant. k can be weighted as k^2 or k^3 depending on the atomic mass of the atoms to amplify oscillations of interest (Figure 2.7 b-d). This plot of the k-weighting and the wavenumber is known throughout this work as the 'k-space'. A Fourier transform of the χ(k) gives 'R-space', which can allow us to select coordination shells of interest.

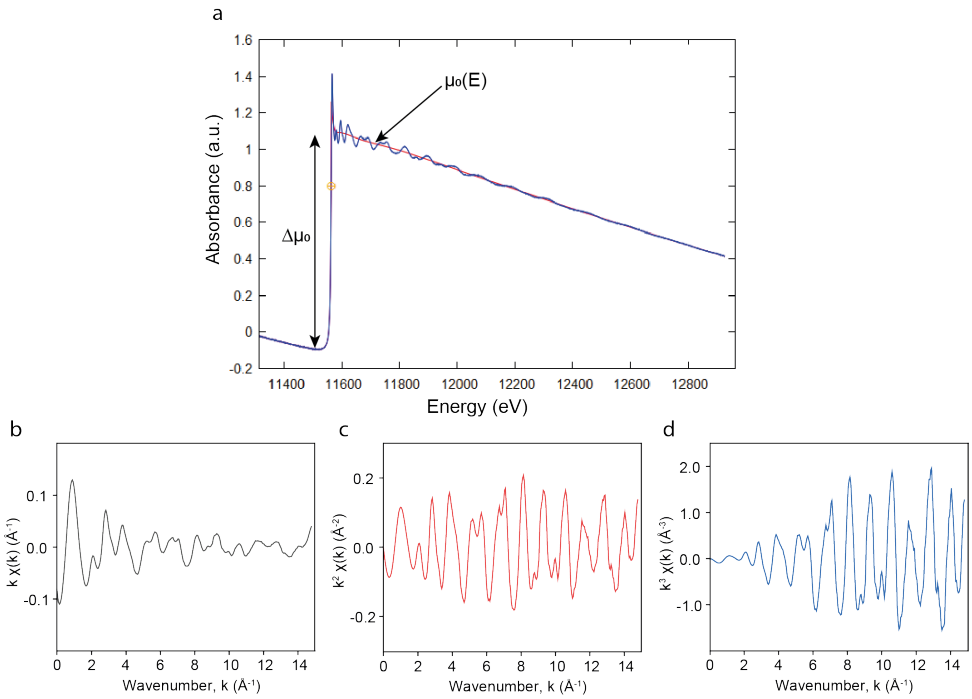

Figure 2.7. ***k-Weighting EXAFS Data.*** *The 'bare atom' signal ($\mu_o(E)$, red) and the edge step ($\Delta\mu_o(E_o)$), are removed from the spectrum to isolate EXAFS oscillations. (b) k (black), k^2 (red) and k^3 (blue) weighting of the same data can emphasise different wavenumbers in the oscillations. Redrawn with measured data based on Newville, 2014.*[2]

The 'R-space' provides an indication of the number of appropriate shells to fit and the approximate bond lengths with which they correspond (although a phase shift should be applied for a realistic value).

The original equation by Sayers, Stern and Lytle[12] was later refined to give the modern EXAFS equation, through improvements discussed in further detail in available resources.[11-15] The result was Equation 2.7, which could be solved to gain information about neighbouring atoms and inversely used to calculate the theoretical EXAFS for a known system.

$$\chi(k) = \sum_i \frac{(N_i S_0^2) F_i(k)}{kR_i^2} sin[2kR_i + \delta_i(k)] e^{-2\sigma_i^2 k^2} e^{-\frac{2R_i}{\lambda(k)}} \qquad \textit{Equation 2.7}$$

where $\chi(k)$ is the absorption as a function of energy, S_0^2 is the amplitude reduction factor, f(k) is the amplitude factor, R is the distance between atoms - half of the path length for a single scattering (termed R for radius), N is the degeneracy given by the coordination number, σ is a measure of disorder, λ(k) is the mean free path and δ(k) represents the phase shift.

Generally, the bond lengths (R), coordination numbers (N) and disorder in the system (σ) are obtained by solving the EXAFS equation. The other factors are either known values or, in the case of amplitude reduction factor, an experimentally variable term that can be calculated from standards. The possible combinations of these unknown variables are applied to the equation, within reasonable constraints, until the resulting k-space (now called q-space) has the optimal fit with the collected data. The more information is known about the system, the higher the chances of finding clever ways to optimise the system or limit the parameters to have a chemically and physically meaningful result.

The EXAFS equation is applied to find which discrete bonds contribute to each wave. If the fitting is good, we assume that the results have somewhat captured the observed system and we are able to extrapolate chemical information about the sample such as the bond lengths, number of neighbouring atoms and their species, geometry, and distortion in the system. Since the EXAFS waves are damped at higher energies, high data quality is required to form a clean EXAFS region capable of capturing information for one or more shells. When data quality is not sufficient, the EXAFS region can be improved through merging spectra, rebinning, or smoothing as it is susceptible to noise and data contamination. For poor EXAFS quality only the first shell is typically fitted, while with wider R-range, second and higher shells features can be fitted.

The setup of the XAS beamline and the X-ray flux have a direct impact on the energy ranges available, the time per spectrum, and the quality of data. The characterization techniques used in this work are introduced briefly.

General XAS

The most typical setup for XAS, shown in Figure 2.8, allows the beam to pass through a monochromator and an incident beam detector, before interacting with the sample. Generally, the transmission and fluorescence mode could be measured using the same general setup, by changing the location and type of detector used, since a transmission detector is aligned with the sample, but a fluorescence detector is placed at a 45º angle from the surface. A spectrum is obtained by scanning the monochromator through an energy range and recording the changes in the X-ray absorption by the sample at each energy step.

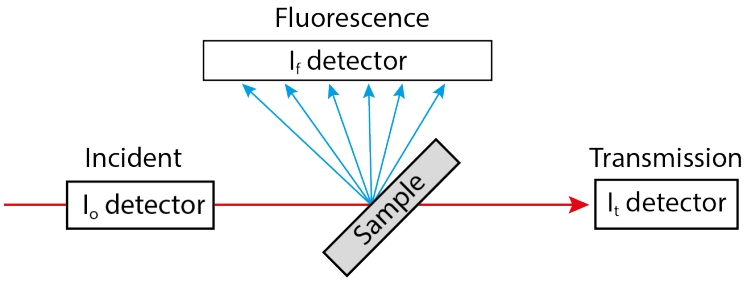

Figure 2.8 ***XAS Experimental Setup.*** *A simplified XAS setup shows the X-ray beam (red) passing through the incident detector before interacting with the sample. Transmitted (red) and fluorescent (blue) X-rays can be measured simultaneously. Redrawn based on Sun et al., 2013.*[16]

The energy range can be selected based on the known edge positions for each element and the information of interest in the sample. For example, if we are only interested in oxidation state changes in the material, we may choose a narrower energy range to capture only the XANES region, which could reduce the measurement time per spectrum. If more information is required, a full spectrum

can be collected, increasing in quality with measurement time. Since high quality data and fast measurements are both desirable, alternative techniques have been developed to increase the time-resolution of XAS measurements. XAS is particularly useful for the *in situ* monitoring of chemical and physical changes in a system since it is a versatile and non-destructive technique.

QXAFS

Quick X-ray absorption fine structure (QXAFS) spectroscopy is a technique used to obtain high time-resolution XAS data. It follows the same principle as XAS, with a monochromatic beam scanning through a range of beam energies. Previously, the limitation of data quality was not the acquisition time, but the delay caused when allowing vibrational settling at each energy data point.[17] However, a microsecond time-resolution can be achieved by sweeping, rather than stopping, at each energy point. With such a configuration, the limitations are the monochromator scan rate, rate of detection, rate of data acquisition and storage, and incident beam flux.[18,19] As of recent literature, a full EXAFS spectrum could be recorded under favourable experimental conditions with a time-resolution generally around 20 ms, although this could theoretically be reduced to less than 1 ms with the correct setup.[17]

Energy Dispersive XAS

Energy dispersive EXAFS (EDE) spectroscopy is a high time-resolution XAS technique which uses a polychromator (in place of a monochromator) to capture a full XAS spectrum instantaneously. As shown in Figure 2.9, the sample is placed at the focal point of the beam created by the curved polychromator. The desired range of X-ray energies are focussed onto the sample by the polychromator, before the transmitted signal diverges to the detector. Since all

energies are detected simultaneously, the angle of the divergent X-ray after passing through the sample can be translated to X-ray energy using a simple calibration. At the time of writing, a full spectrum could be recorded within micro- to nanoseconds, but often multiple measurements are required for merging before the signal quality is improved leading to millisecond time-resolution.

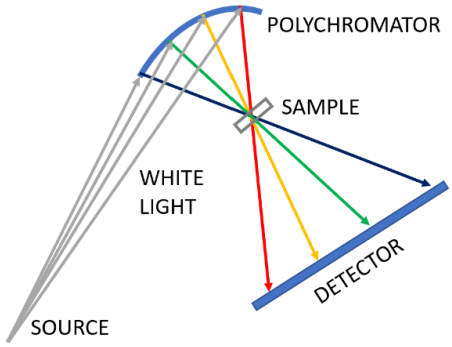

Figure 2.9 ***Energy Dispersive EXAFS Setup.*** *The incident beam (grey) is distributed as light of various wavelengths (blue, green, yellow, red lines) by the polychromator (blue curve). Placing the sample at the focal point, the detector (blue line) simultaneously measures absorption and the dispersion angle which is later converted to energy to give a XAS spectrum. Redrawn ased on a diagram by Ishiguro and Tada, 2018.*[20]

The EDE is a transmission mode measurement and is therefore capable of measuring most transmission samples, whether solid or liquid. This method leads to high time-resolution but can be especially challenging in cases where homogeneity is limited, beam damage is prominent or where nanoscale particles cause small angle scattering.[21] While the amplitude reduction factor generally falls within a narrow range for most XAS beamlines, damping effects in EDE are more significant.[22]

Applications of XAS

The use of XAS is versatile, and experiments lend themselves to design based on the chemical system of interest. XAS can be performed on solids and liquids and is generally non-destructive, barring beam-damage which can be mitigated in many cases.

Ex situ XAS is most often used to record the physical properties of a material. These measurements have been successfully used in the literature to estimate the size of nanoparticles, the degree of alloying of metals and the composition and structure of nanomaterials.[23-25] The limitations of *ex situ* XAS are sample damage and changes to the sample outside of reaction conditions. However, in many cases *ex situ* XAS are sufficient to gain considerable chemical information about a sample.

In situ XAS is applied in cases where the transient species or the reaction pathways are of interest. It has been used for a wide range of reaction conditions, from gaseous catalytic reactions, to electrochemical cells and liquid samples. *In situ* XAS has been instrumental in capturing intermediate species formed during a reaction and calculating their structures, as these materials often cannot be isolated.

As mentioned in the literature review, the use of XAS for the study of nanoparticle growth has also widely been practiced *in situ,* to catch the intermediates formed. During the oxygen reduction reaction and CO_2 reduction reaction, XAS can monitor the oxidation state information alongside electrochemical changes. As an undoubtedly powerful tool in forming an understanding of the chemistry of the system, XAS is one of the major focal points of this thesis.

Damping and Beam Damage

It is good practice to measure a foil standard for each day of XAS experiments, if not more often. This allows the accurate determination of the correction factor to allow for the lowered amplitude of recorded data, which in an ideal system would have a value equal to 1. The damping is shown in Figure 2.10.

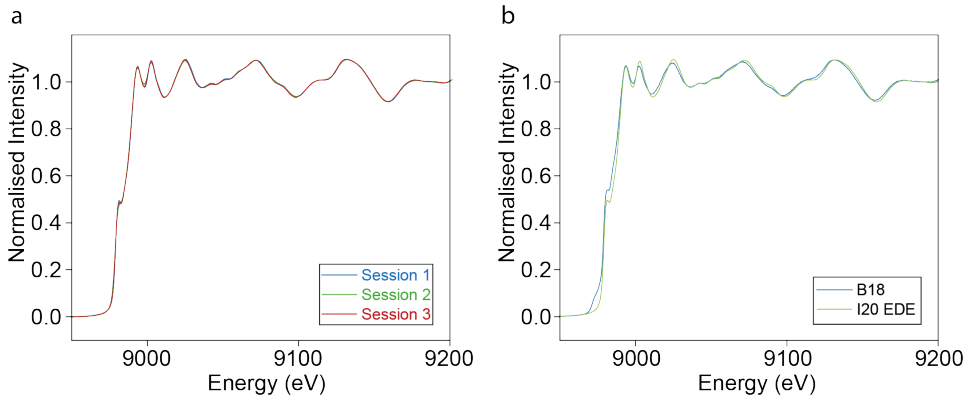

Figure 2.10 ***Damping and Reproducibility in XAS Standards.*** *(a) Standard Cu-K edge foil spectra measured on three separate occasions at I20-EDE show slight variations due to damping, and (b) Cu-K edge foil spectra measured at beamline B18*[26] *(blue) compared with I20-EDE (green) exhibit different degrees of damping (corrected by amplitude reduction factor) due to the measurement setup.*

One of the major issues with time-resolved XAS and transmission electron microscopy (TEM) is the acceleration or the effect of observation on the reaction mechanism being recorded. The main methods used to mitigate beam damage are the adjustment of beam intensity, reduction of exposure time and the comparison of beam exposed sample with a dark sample to quantify damage. The beam damage for each reaction is different and therefore before each experiment it is imperative to record beam damage and find the flux with least damage (Figure 2.11). The decrease in beam flux can be implemented by adjusting the slits, or adding layers of attenuating foils such as Pb and Al.

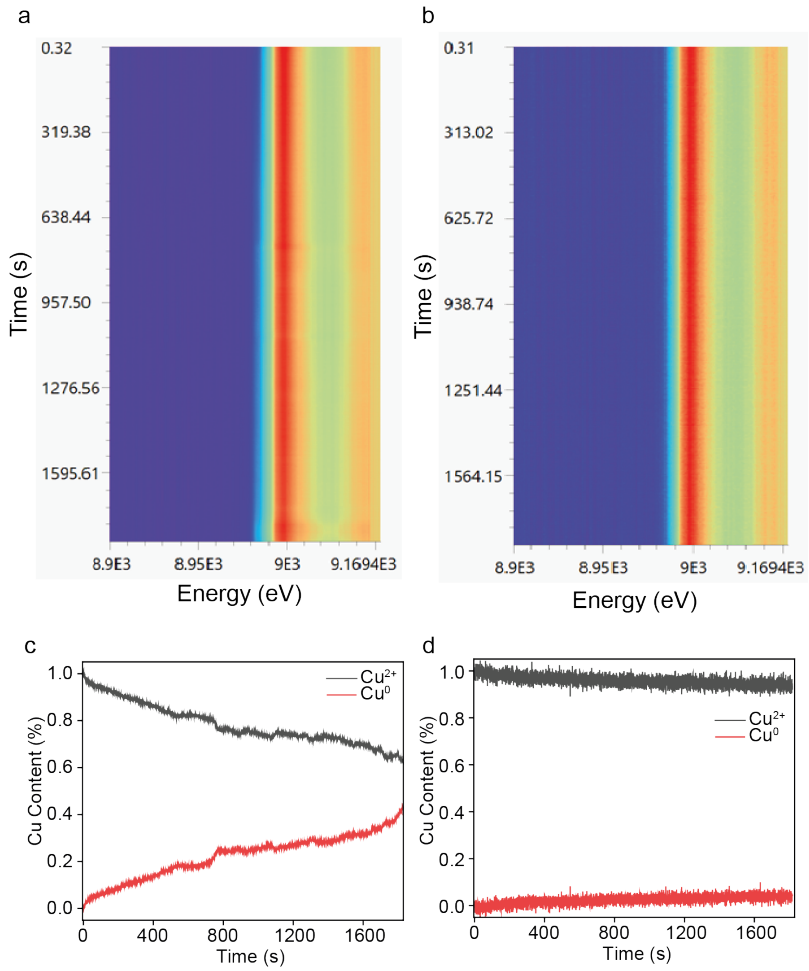

Figure 2.11 **XAS Beam Damage in Cu Solution.** *(a, c) Visual changes in Cu-K edge heat map of intensity for time-resolved spectra and corresponding LCF results (fitting Cu foil – red and $Cu(OAc)_2$ in H_2O - grey) show beam-induced reduction during 1800 seconds of exposure. (b, d) Beam damage measured at Cu K-edge can be mitigated with increased attenuation, showing less than 3% Cu reduction for the same irradiation time in LCF.*

Beam damage has been measured for all cases and is mentioned in the context of literature.

EXAFS and single sites

There is some debate about whether EXAFS results can be used to confirm the presence of single sites in a material.[27] Numerous papers have cited the use of EXAFS, in combination with other characterization tools, to prove the presence

of single sites.[28-32] However, these may be inconclusive in proving the unique presence of single sites, without some larger clusters present, since additional characterisation tools such as TEM are localised and unable to probe the entire material surface.

For this reason, while studying low-coordination materials in this work, no claim is made about the presence of single sites or even a single species, instead opting to refer to these states as 'dominated' by a species. The arguments against the identification of single sites mainly refers to the accuracy of observing a single metal atom, which is undercoordinated on a supporting material, such as carbon, and therefore has no crystalline environment.[27] These arguments cast doubt on the existing results, including those published in the literature. However, this inaccuracy may be reduced in results for alloyed species since both metal edges can be measured to calculate the coordination and there are fewer under-coordinated atoms. It should be noted that the identification of low-coordination sites remains controversial, and proper reasoning is required when presenting such results to assess viability for a given system.

2.2.2 High Resolution XANES

As mentioned previously, to form a typical XANES spectrum the monochromator is scanned through a range of energies and the resulting X-rays are detected. Due to the finite lifetime of the core hole, the spectra are broadened, and details may not be resolved. However, by monitoring a single fluorescence line using a fixed analyser crystal while sweeping the monochromator, a higher resolution than the core-hole lifetime can be achieved.[33] For high resolution XANES (HR-XANES), also called high energy resolution fluorescence detected XANES (HERFD-XANES) measurements, the monochromator energy is swept, while the

analyser crystal is fixed in a limited energy range (Figure 2.12 a, b). Using HR-XANES, features in the XANES region are recorded with improved energy resolution.

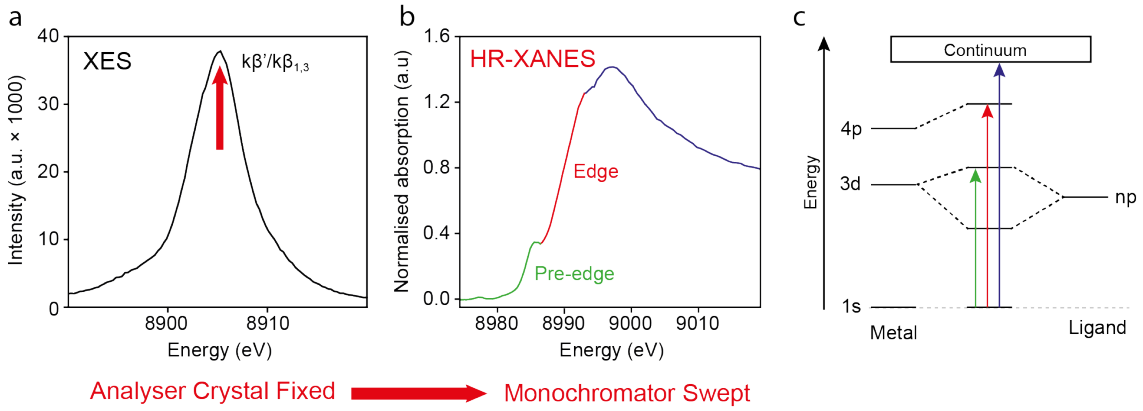

Figure 2.12 ***HR-XANES Measurement Setup.*** *(a) The analyser crystal is fixed at the peak XES position (red arrow) while (b, c) monochromator is swept to obtain a XANES spectrum, here shown for Cu K-edge. Pre-edge (green), edge (red) and EXAFS (blue) regions are shown alongside their corresponding electron transitions. Drawn with collected data based on Bauer, 2014 and Zimmermann et al., 2020.* [34,35]

In this study, the higher energy resolution, particularly in the pre-edge, is used to clearly distinguish the oxidation states of metals and transitions to ligand-bonding unoccupied electronic states like Cu 4*p* and 3*d* (Figure 2.12 c).[36]

2.2.3 Valence-to-Core XES

Valence-to-Core X-ray emission spectroscopy (VtC XES) is measured on the same system where, contrary to the HR-XANES, the monochromator is fixed, and the analyser crystal is swept (Figure 2.13 a, b). The monochromator energy is held above the binding energy of the core electrons (1*s*) while the analyser sweeps in the range of transitions from valence (3*d* → 1*s*). These relatively weak kβ" and $k\beta_{2,5}$ signals are isolated and observed for valence information, rather

than the more intense kα (2*p* → 1*s*) and kβ and kβ' lines (3*p* → 1*s*) (Figure 2.13 c). Thus, the VtC XES is sensitive to the ligands affecting the energy of valence shells, and has been used to distinguish even light ligands with similar mass, like N, C and O. Usually the $K\beta_{2,5}$ emission comes from valence orbitals with p character from ligand and p character from the metal.[37]

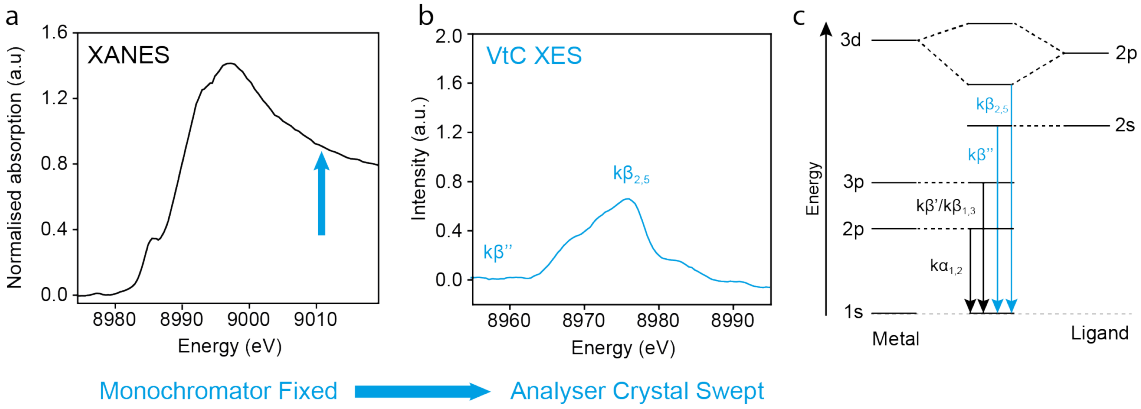

Figure 2.13 ***VtC XES Measurement Setup.*** *(a) The monochromatic incident beam is fixed above the edge position in XANES (blue arrow) to ensure fluorescence while (b) the analyser is swept to obtain a VtC XES spectrum, here shown for Cu kβ" and* $k\beta_{2,5}$ *peaks. (c) Corresponding energy transitions for Cu* $k\alpha_{1,2}$*, kβ' and* $k\beta_{1,3}$ *(black) and kβ" and* $k\beta_{2,5}$ *(blue) are shown alongside. Drawn with collected data based on Bauer, 2014 and Zimmermann et al., 2020.* [34,35]

For ordinary kβ and kβ' XES measurements, weak field ligands (like halides, OH^- and H_2O) with filled orbitals that can π bond with metal *d*-orbitals, produce low splitting between the *d*-orbitals and may not be inter-distinguishable. In such cases, VtC XES measuring kβ" and $k\beta_{2,5}$ can be used to determine weak field ligand coordination. This has been shown for Cu VtC XES measurements by Zhang et al., where Cu-O and Cu-N ligand coordination in zeolites showed different peak positions for both kβ" and $k\beta_{2,5}$.[38,39]

2.2.4 SAXS

Small angle X-ray scattering (SAXS) is a technique used to record nanoscale structure. A monochromatic beam is passed through a sample and the X-ray scattering caused by interaction with the sample is recorded by a 2D detector to make a scattering pattern. As the intensity of the scattered beam is orders of magnitude lower than the transmitted beam, this is generally blocked, to prevent detector overload, giving the distinct pattern of SAXS data (Figure 2.14). The SAXS system is particularly good for nanoparticles in colloidal solutions, where the size and structure of nanoparticles can be recorded non-destructively.

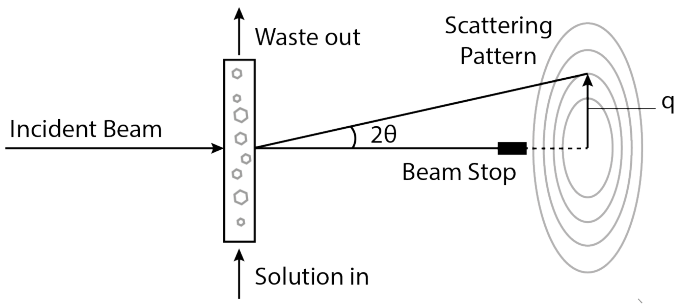

Figure 2.14 ***SAXS Measurement Setup and Spectrum.*** *(a) During SAXS, the X-ray scattering pattern of an incident beam after passing through a sample is captured. Using the angle of scattering (2θ), the pattern can be described by q-value (x-axis), plotted against signal intensity (y-axis). Redrawn for current experimental setup based on from Kikhney and Svergun, 2015.*[40]

SAXS data is often outputted as a graph of intensity I(q) (y-axis) vs. scattering vector q (x-axis), where q-value is obtained using the scattering angle (2θ) and wavelength (λ), with units of nm^{-1}.

$$q = \frac{4\pi \sin\theta}{\lambda} \qquad \textit{Equation 2.8}$$

This plot is fitted with the known parameters in the system to obtain information such as polydispersity, nanoparticle size, nanoparticle shape, and nanoparticle numbers. Wide angle X-ray scattering (WAXS) can be measured within the same setup.

2.2.5 Summary

When X-ray radiation is focused on a material, due to the events occurring with the photoelectric effect, a range of valuable chemical information can be obtained by measuring the resulting phenomena. These techniques, often measured at synchrotron facilities, can broadly be classified as XAS (recording the absorption of the incident X-ray), X-ray photoelectron spectroscopy or XPS (measuring the ejected photoelectrons), XES (capturing the energy of fluorescent X-rays emitted by the recombining electrons), and Auger emission spectroscopy or AES (counting the Auger electrons emitted) techniques.

Aside from the photoelectric effect, the scattering of X-rays may also give sample-specific information. Elastic X-ray scattering is measured more commonly in techniques such as XRD, SAXS and WAXS. However, inelastic scattering measurements like Raman scattering and RIXS, are showing increasing popularity in recent years.

Clearly, synchrotron radiation can be applied in a wide range of applications to obtain valuable chemical and physical information about a sample. The characterization tools applied in this thesis are summarised (Table 2.1), along with the associated with X-ray interaction, and the relevant chemical information obtained.

Table 2.1 ***Summary of X-ray Characterization Techniques.*** *A list of seven X-ray techniques applied in this thesis and the chemical or physical information obtained. *X-ray diffraction and **energy dispersive X-ray spectroscopy.*

	Incoming radiation	Recorded output	Transition recorded	Information obtained in this thesis
XAS	X-ray	Transmitted X-ray	K: 1*s* → continuum L_1:2*s* → continuum $L_{2,3}$:2*p*→ continuum M_1:3*s* → continuum $M_{2,3}$:3*p*→ continuum $M_{4,5}$:3*d*→ continuum	Oxidation state, coordination number, coordinating species, bond length
SAXS	X-ray	Elastic Scattered X-ray	Coherence of scattered X-rays	Shape, size and polydispersity
XPS	X-ray	Photoelectron released	Bound electrons to continuum	Elemental analysis and surface bonding
XRD*	X-ray	Diffraction pattern	Coherence of scattered X-rays	Crystal structure, degree of crystallinity
EDX**	Electron beam	Fluorescent X-ray	Electrons relaxing back to core levels	Elemental composition
VtC XES	X-ray	Emitted X-ray	4*p* → 1*s* Valence electrons relaxing back to core level	Ligand coordination
HR-XANES	X-ray	Transmitted X-ray	Core electron emission, 1*s* → 3*d* (edge) and 1*s* → continuum	Oxidation states

2.3 Lab-based Characterization

Lab-based characterization tools which make use of X-rays will first be explored in this section, followed by other lab-based techniques and their basic working principles. Formulas and procedures relevant to this work are outlined.

2.3.1 XPS

X-ray Photoemission Spectroscopy (XPS) can identify elements and chemical states at the surface of a material. X-rays are directed at a sample until photoelectrons are ejected. The kinetic energies (E_k) of emitted photoelectrons are recorded and plotted against number of electrons produced, as a relative count (Figure 2.15). Thus, knowing both the incident photon energy ($E_i = hv$) and the work function of the spectrometer (φ), the binding energy of electrons in the sample (E_b) can be calculated from the relationship:

$$E_i = E_b + (E_k + \phi) \qquad \textit{Equation 2.9}$$

Peaks of varying intensities are observed for the different orbitals of the elements present in the sample, giving an indication of the elements present, composition ratios in the sample and electronic states of the atoms.

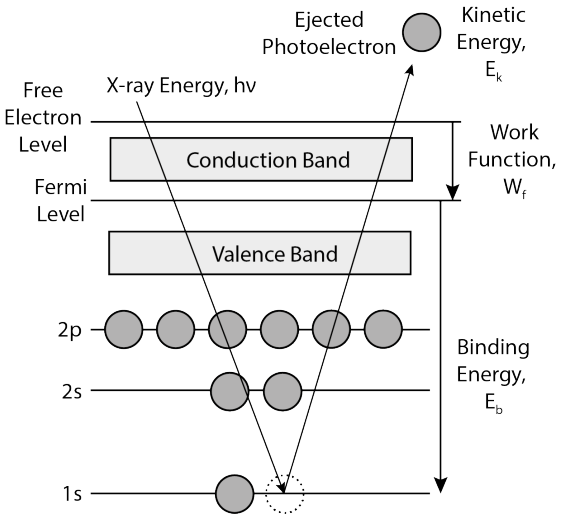

Figure 2.15 ***XPS Working Diagram.*** *Incident X-ray energy (E_i = hv) causes the ejection of a core-shell electron, which escapes from the material surface and is recorded by the detector. Values of incident beam energy (E_i), kinetic energy (E_k) and work function (W_f) are used to calculate the binding energy (E_b). Redrawn based on Mane and Patil, 2016.*[41]

XPS is surface sensitive because of the attenuation and interaction of the photoelectrons unable to escape from deeper within the material, preventing them from reaching the detector. This can be advantageous in catalysis, where the surface is the area of activity, and can be recorded without interference from the bulk.

2.3.2 XRD

For X-ray Diffraction (XRD), the pattern created when X-rays are diffracted by crystalline materials is used to identify the crystal lattice present, the lattice spacing and the degree of crystallinity of a sample. This X-ray diffraction pattern is formed when the in-phase diffracted X-rays are reinforced. Generally, the incident angle of the X-ray on the sample is varied across a range and plotted against the detected intensity. Based on the incident X-ray wavelength (λ) and its

angle to the lattice plane (θ) during constructive interference, the planar lattice spacing (d) can be calculated according to Bragg's law, nλ = 2d sinθ, where n is a whole number multiple of the wavelength (Figure 2.16).

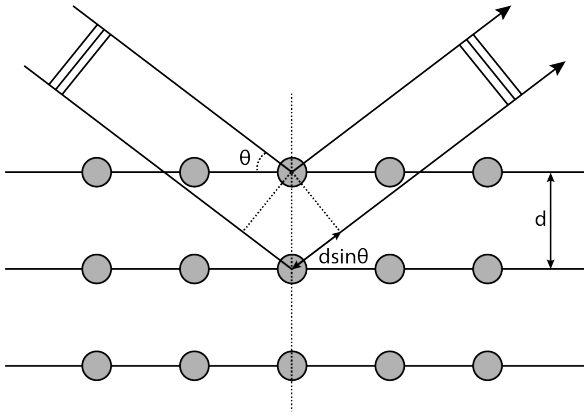

Figure 2.16 ***Bragg's Law Values from XRD.*** *The calculation of the lattice spacing (d) from XRD data using Bragg's Law requires the measurement of incident X-ray wavelength (λ) and the incident angle (θ) at a position where constructive interference is observed. Redrawn based on Gedde et al., 2021.*[42]

This lattice spacing can give the unit cell dimensions and the incident angle at which the intensity peaks can indicate the crystal facets present in the sample. This can be calculated from an ideal structure or compared with a standard pattern.

The calculation of the unit cell length (*a*) for cubic structures in this work, where *d* is the lattice spacing and *h*, *k* and *l* are the Miller indices, is given by:

$$\frac{1}{d^2} = \frac{h^2 + k^2 + l^2}{a^2}$$

These calculations are performed based on the Miller indices and XRD spacing results, to give the unit cell length, which can be compared with literature values for similar materials.

2.3.3 Electron Microscopy

Electron microscopy functions similarly to optical microscopy, except that high spatial resolution to the nanoscale can be achieved using a focused electron beam to visualise the sample. These are broadly classified under scanning electron microscopes (SEM) in which the reflected electrons are measured, and transmission electron microscopes (TEM) in which the transmitted electrons are measured.

Transmission Electron Microscopy

Transmission electron microscopy maps a sample, using the transmitted part of the electron beam. Generally, the morphology of a thin or finely loaded sample can be observed, in a 2D visualisation captured by scanning the electron beam across a fixed range of the sample surface. Since heavier elements absorb more of the transmitted electron beam, they generally appear with more contrast. Thus, in some cases the light and heavy elements present within a sample can be distinguished qualitatively, based on the intensity of the signal.

Crystal lattice fringes can also be observed directly using TEM, in cases where ordered crystals are present. These appear as parallel lines as described by Bragg's law, with the distance between them equivalent to the lattice spacing. These are used to confirm local information about the crystal domains present in the sample. In some cases, single atoms can be resolved. [29,32]

For this work, TEM is often used to confirm the shape, size and crystal domains of nanoparticles grown in the laboratory under different conditions. High Resolution TEM (HR-TEM) is also employed for improved resolution. This technique is effectively TEM with increased signal from increased beam intensity, leading to higher spatial resolution. HR-TEM is used in both the bright field and dark field mode, for optimised visualisation.

The calculations of shape and size of average nanoparticle from TEM images was performed using the ImageJ program. To limit the errors, it was necessary to have a convention for the measurement. For approximately spherical particles, a circle was fitted over the image, and the diameter of the circle was used to describe the nanoparticle diameter. For ellipsoidal particles, an ellipse was fitted for which the average of the long and short side diameters was used as nanoparticle diameter. For other geometries, it was necessary to fit a circle which enclosed the shape, even for triangular or square particles. This method is biased towards an underestimation of the metal volume in nanoparticles and overestimation of the average diameter.

2.3.4 Energy Dispersive Spectroscopy

Energy dispersive X-ray spectroscopy (EDX or EDS) is commonly used in combination with TEM, by inserting a fluorescence detector in the TEM setup. The electron beam from the electron microscope excites electrons in the sample, ejecting them and leaving holes in inner shells. These holes are filled by electrons from higher-energy orbitals, losing their remaining energy as a fluorescence signal. Since each element has a distinct fluorescence signal based on its electron configuration, EDS gives elemental composition information for the sample. The EDS spectrum is also, in some cases, used to approximate the ratios between elements, although the relationship between signal intensity and atomic ratios requires careful determination.[43] In this work, EDS was used to detect and map elemental distribution in an alloyed nanoparticle.

2.3.5 Electron Paramagnetic Resonance

Electron paramagnetic resonance (EPR), also known as electron spin resonance (ESR), is a non-destructive laboratory characterization technique used detect and quantify the presence of paramagnetic species within a sample.

The working principle of EPR is a result of the Zeeman effect, by which introducing a magnetic field to an unpaired electron changes the energy difference between the two possible spin states of the electron. The spin of the unpaired electron has an associated magnetic moment, and when it is aligned with the applied magnetic field, a low energy state occurs. A contrary high energy state is caused when the magnetic moment of the electron is aligned opposite to this applied magnetic field. The energy gap between these two states can therefore be modulated by the control of the intensity of the applied magnetic field. These states can be described by Equation 2.10.

$$E = g\mu_B B_0 m_s = \pm\frac{1}{2} g\mu_B B_0 \qquad \textit{Equation 2.10}$$

where g is the proportionality factor (or g-factor), μ_B is the Bohr magneton, B_0 is the magnetic field, and m_s is the electron spin quantum number. This equation shows that with no applied magnetic field ($B_0 = 0$), the energy gap between the spin states is zero ($\Delta E = 0$). It also means that with increasing intensity of magnetic field, the energy difference increases (Figure 2.17).

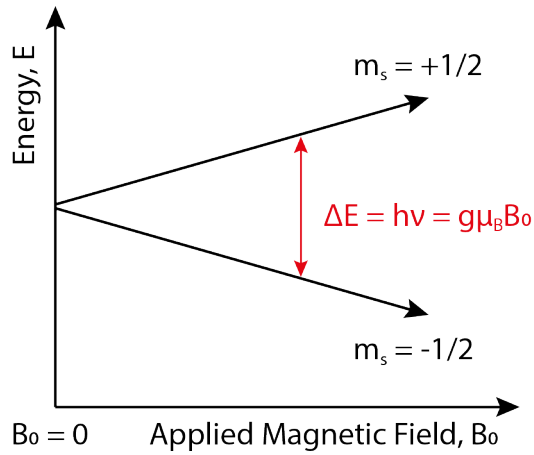

Figure 2.17 ***Spin Orbital Splitting Enables EPR Measurement.*** *Spin orbital splitting by an applied magnetic field make EPR measurements possible. The energy gap (∆E) between the high spin (m_s = +1/2) and low spin (m_s = -1/2) states, can be measured while varying the magnetic field intensity, B_0. Redrawn based on He et al., 2014.*[44]

Generally, spectroscopy directly measures the energy difference between molecular or atomic states by scanning a range of frequencies and recording the absorption. This is effective since electromagnetic radiation is absorbed when its frequency matches with the energy difference, as summarised by Planck's law in which ∆E = hv where the ∆E is the energy difference, h is Planck's constant and v is the frequency of the radiation. However, during EPR the frequency of the radiation is held constant while a magnetic field, or the energy difference is varied. In practice, a magnetic field of varying intensity is applied across a sample while measuring the absorption of a single applied microwave frequency. The magnetic field causes a variation in the energy gap between spin states and when this gap corresponds with the applied microwave frequency, an electron can be promoted to the high energy spin state. This is recorded by the absorption of the microwave (Figure 2.18). Thus, the energy gap (∆E) is measured by the absorption of a microwave at fixed energy while the magnetic field energy is swept.

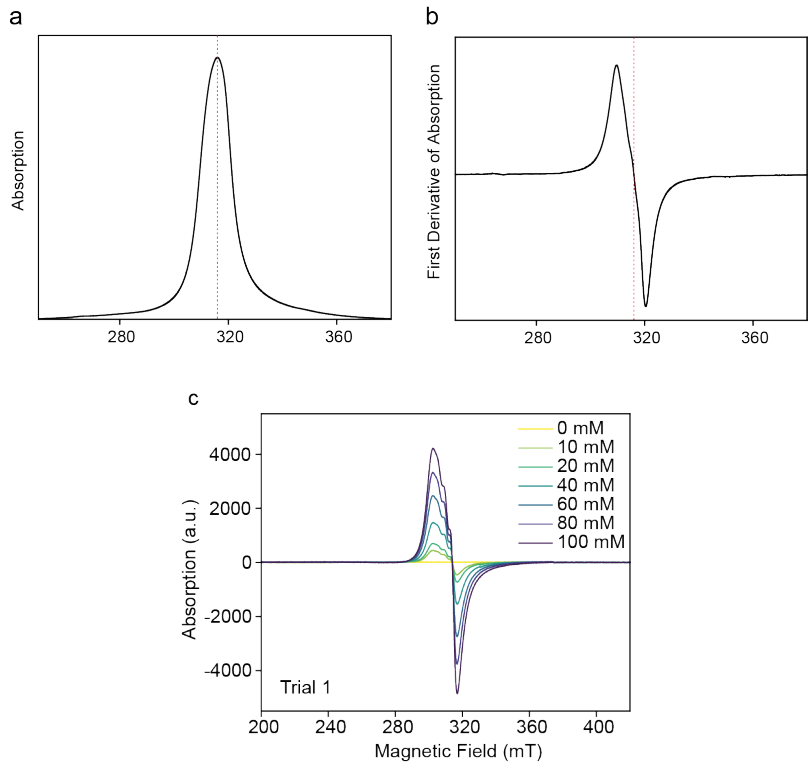

Figure 2.18 ***EPR Spectrum, First Derivative and Concentration Effects.*** *A typical EPR result can be plotted for (a) the absorption with different strength of magnetic field and (b) the first derivative of absorption versus magnetic field from which proportionality factor (g value) measurement is taken where the derivative crosses 0 (red dashed line). (c) EPR is concentration sensitive as shown with increasing absorption when $Cu(NO_3)_2$ concentration in DMF was increased from 0 mM to 100 mM.*

EPR is sensitive to the metal species, configuration and coordination environment. The proportionality factor (g) is defined as the point of maximum absorption where the first derivative of absorption passes through zero. This can be used to identify the material composition, with transition metals often showing values around 2, depending on the spin-orbit coupling and the zero-field splitting.[45]

In this work, EPR is measured for Cu salts with high concentrations (between 0 and 100 mM) where hyperfine interactions cannot be observed and are therefore

not discussed (Figure 2.18 c). The g-values for Cu salts reported in the literature generally range between 2 and 2.5 and are recorded as a metric for the changes in Cu coordination during EPR measurements.[45,46] In addition, the area beneath the EPR peaks is used to estimate the Cu concentration of EPR active species, calibrated against a similar solution of known concentrations, in this case $Cu(NO_3)_2$ dissolved in DMF.

2.3.6 UV-vis

Ultraviolet-visible spectroscopy (UV-vis) works by shining a range of wavelengths of light (typically between 190 and 900 nm) through a sample and detecting the wavelengths absorbed, transmitted and reflected. A spectrophotometer measures the intensity of light before and after passing through the sample. This can be used to determine a change in concentration of species within the sample, using the Beer-Lambert Law.

The Beer-Lambert law states that the absorbance (A) is directly related to the pathlength (b) and concentration (c) of the absorbing species, and the transmittance (T)

$$T = \frac{I}{I_0} \qquad \textit{Equation 2.11}$$

$$A = \varepsilon bc = log_{10}\left(\frac{I_0}{I}\right) = -log_{10}(T) \qquad \textit{Equation 2.12}$$

where ε is a constant called 'absorbtivity', I_o is the incident light intensity, and I is the transmitted light intensity. Since there are various factors which may affect the absorption of a certain materials, this Beer-Lambert relationship can be used more reliably in cases where the measured absorption can be compared to a calibration line of the same or similar material, prepared carefully with known

concentrations. Measurement effects introduced by the sample matrix may be removed using a background solution with a similar composition, measured before the sample (*Figure 2.19*).

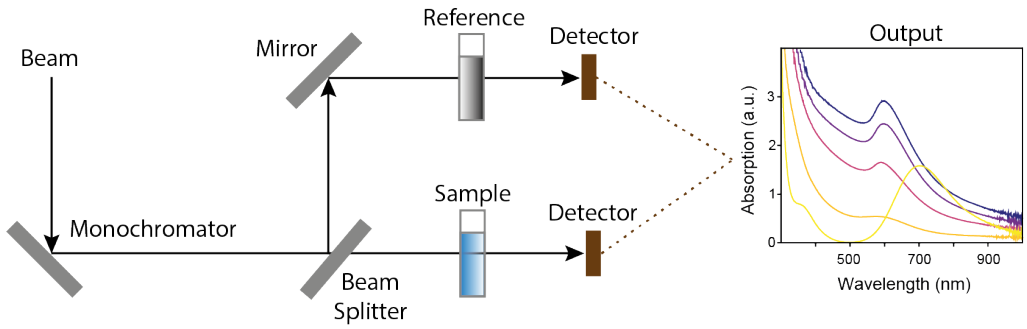

Figure 2.19 ***UV-vis Working Diagram****. UV-vis measurement setup consists of a monochromatic light, split with mirrors, and shone through both a sample and a reference, simultaneously, to detect the wavelengths of light absorbed. UV-vis results ("output") are plotted as a spectrum of wavelength (x-axis) versus absorption (y-axis). Redrawn with measured data based on schematic by Rocha et al.*[47]

For the transition metal salts studied in this work, there is a visible change in the colour of the solutions during reduction, which is indicative of changes in the *d*-band of the metal. When light is shone on the sample, a *d*-electron may gain energy and reach an excited state. Changes in complexation and oxidation state impact the *d*-band energy gap and can therefore be observed by UV-vis.[48]

2.3.7 Nitrogen Sorption Isotherms (with BET)

The controlled adsorption of nitrogen at 77 K across a material surface, followed by the desorption under different pressures provides a profile which can indicate the surface area and size of the pores in the material. The measured isotherms

are compared against sample masses, carefully measured before and after heating at 70ºC overnight in an Ar environment (to remove water vapour).

The Brunauer-Emmett-Teller (BET) theory is the most widely used for the estimation of surface area, although limited by the assumption that the monolayer formed is in a close-packed 'liquid' state.[49] For the effective pore size, the Barrett, Joyner and Halenda (BJH) calculation is popularly cited.[50] While these methods have limitations, both are often cited for the estimation of surface area and pore volume and are therefore adopted in this work.

2.3.8 MP-AES

Microwave plasma – atomic emission spectroscopy (MP-AES) is a destructive technique used for the simultaneous detection and quantification of trace elements within a sample. A solution containing the elements of interest is nebulised and passed through a microwave-induced N_2 plasma (around 5,000 K). The heat from the plasma causes the excitation of the atoms present, which give off a characteristic emission during relaxation back to the ground state. The wavelength and intensity of emitted light is measured with a monochromator selecting wavelengths reaching the charge coupled device (CCD) detector (Figure 2.20). The concentration of an element in a sample can be quantified by comparison with a calibration curve with known concentrations of the same element, to find the relationship between the concentration and emission intensity.

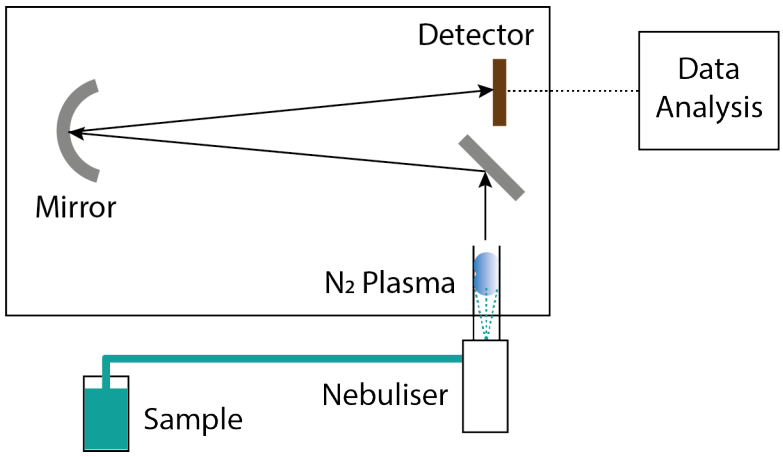

Figure 2.20 ***MP-AES Working Diagram.*** *To measure MP-AES, a nebulised sample solution is heated in a nitrogen (N_2) plasma, causing the excitation of ions present. The resulting characteristic emission is reflected to a detector where wavelength and intensity are measured and analysed to give information about the elemental composition and concentration of the sample. Based on diagram by Balaram, 2020.*[51]

In this work, MP-AES is primarily used to find the metal loading and ratio between metals of a system. It is ideal for nanoparticle systems as analysis only requires ppm loading of metal and 5 mL of solution. MP-AES samples are prepared by dissolving the metal of interest in a strong acid so that it remains in solution, as a highly uniform distribution of the metal is desirable. Generally, at lower concentrations of the element of interest, below 20 ppm to 40 ppm, the intensity calibration is approximately linear, giving optimal precision. Thus, the estimated metal concentration is diluted to within this range.

The total loading of each element, in this case metal loading, is calculated through precise measurement of the initial mass of sample dissolved and the final volume of the solution before measurement (Equation 2.12).

$$\textit{Metal Loading} = \frac{metal\ content\ (ppm) \times solution\ volume\ (l)}{mass\ of\ dissolved\ catalyst\ (mg)} \times 100\ \%$$ *Equation 2.13*

The metal loadings are compared with ideal values to estimate the metal loss during synthesis.

2.4 Chemical Precipitation Growth Rate Measurements

A primary focus of this work is on the rate of growth *via* chemical precipitation, where shape and size-controlled nanoparticles are formed in solution by reducing soluble metal salts. The chemical precipitation processes selected for study and the rationale behind their selection are briefly introduced here. The factors of significance in their growth, and synthesis procedures are defined and monitored to reproduce results. The methodology for the control and measurement of these factors are outlined and sources of error defined.

2.4.1 Adapting Synthesis Procedures

Nanoparticle synthesis procedures generally need to be adapted for *in situ* measurement, due to the increased concentrations required. The methodology applied towards the *in situ* characterization of a synthesis procedure involve the selection of an existing method from literature and laboratory replication, the adaptation and optimisation of parameters for characterization, and lastly reproducibility testing to ensure that the reaction conditions are adequately controlled.

Palladium Nanoparticle Growth

Pd nanoparticles formed were selected to have a high surface area and to remain below 100 nm in size in Chapters 3 to 5. The porous Pd nanoparticle synthesis

method was adapted from the procedure described by Wang et al.[52] The described Pd concentration of 0.01 M was below the detection limit for a XAS transmission edge jump above 0.1 (considered the minimum for reasonable data collection). An increase in concentration was necessary, having the additional effect of increasing the final particle size. The concentrations of the Pd precursor solution, the surfactant and the reducing agent were adapted so that the average nanoparticle size formed was maintained below 200 nm. These conditions were selected for Chapters 3 and 5, allowing the *in situ* study of nanoparticle growth with two different surfactants, cetyltrimethylammonium chloride (CTAC) and cetyltrimethylammonium bromide (CTAB).

Copper Nanoparticle Growth

In Chapter 6, studying Cu nanoparticle growth from copper acetate ($Cu(OAc)_2$), the aim of the synthesis was to compare the early growth stages in the reduction of faceted and spherical Cu nanoparticles. Since only the initial stages of growth were of interest, and initially formed nanoparticles were smaller than 100 nm, the final nanoparticle size was not set as a constraint on the growth parameters.

The procedure selected for faceted Cu nanoparticle growth was adapted from Pastoriza-Santos et al.[53], but the concentration of the $Cu(OAc)_2$ had to be increased to 7.5 times the reported value. The capping agent (polyvinylpyrrolidone or PVP) and reductant (hydrazine hydrate) concentrations were similarly increased, until a similar faceted platelet morphology was achieved.

To synthesise spherical Cu nanoparticles, the ascorbic acid reduction of $Cu(OAc)_2$ was designed within the lab, based on a broad literature search of similar reactions. The same $Cu(OAc)_2$ concentration in the reaction mixture was

selected for a direct comparison with faceted growth. The selected Cu concentration of 75 mM was comparable to literature values, such as the metallic Cu nanoparticle synthesis with ascorbic acid reduction described by Khan et al. for 100 mM aqueous $CuSO_4$. Liu et al. for 200 mM $CuSO_4$ and Lu et al. for 370 mM $CuCl_2$ also reported increased Cu concentration for increased nanoparticle yield, although avoiding agglomeration is challenging in such concentrated systems.[54-56] Similar results after high concentration growth were also yielded for Cu salts with acetate groups, showing 25 nm diameter Cu nanoparticles formed with 20 mM $Cu(acac)_2$,[57] and 135 nm CuO nanoparticles with 15 mM $Cu(OAc)_2$.[58] While these systems with increased concentration are not directly the same as the lab-based synthesis procedures described, they provide valuable insights into the nanoparticle growth at high concentrations.

2.4.2 Time-Resolved *Ex situ* Measurements

Since it is not always possible to monitor the growth of nanoparticles *in situ,* some time-resolved measurements have been measured *ex situ* using a separate sample for each time-point. This generally requires the pausing of a reaction at different run-times, to characterize the changes occurring at each stage. Since stopping a reaction is often challenging and may be imprecise, these methods do not have such a reliable time-resolution as *in situ* measurements, with temporal error generally varying from 10 s to 1 minute. Based on the samples required for measurement, the procedures for preparation vary, with the aim of minimising continued reaction time.

TEM and MP-AES

Ex situ TEM and MP-AES observations of growth both require the separation of the solid nanoparticles formed from the residual solution. For temperature-controlled reactions, this was achieved by a stationary reaction of the pre-heated solutions directly inside a temperature-controlled centrifuge, followed by timed initialisation of the centrifuge rotation. For TEM measurements, the residual precursor solution was removed and the nanoparticles were washed and resuspended in ethanol. For MP-AES measurements, the concentration of both the residual precursor solution and the solid nanoparticles was of interest, so the solution was carefully removed with a pipette and the nanoparticles dissolved for MP-AES measurement.

SAXS, VtC XES and HR-XANES

The data collected for SAXS, VtC XES and HR-XANES was also time-sensitive. Rather than physically removing the reactants, it was necessary to stop the reaction by quenching the system. Ice-bath quenching and refrigeration was effective to stabilise nanoparticles in solution within the capillary tube for *ex situ* SAXS measurement.

In the case of VtC XES and HR-XANES, samples were measured over long time-periods so the solid state at low temperatures was chosen to reduce beam damage. Samples were prepared by quenching the growth solution already in the measurement vial with liquid nitrogen. Once the solution was frozen, the reaction did not progress, as corroborated with EPR measurements before and after freezing. However, the samples were held for a longer time-period and measured remotely, so dry ice was used to transport samples and maintain their frozen state

until the time of measurement. A cryojet was applied to keep the sample frozen throughout the measurements (Figure 2.21).

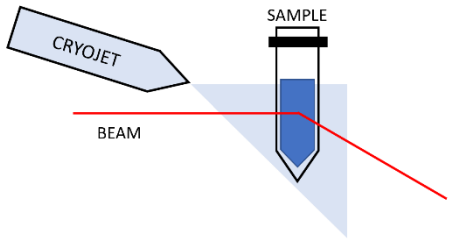

Figure 2.21 ***Cryojet Setup for VtC and HR-XANES Measurements.*** *VtC and HR-XANES measurements were performed at I20-Scanning (DLS), directly reacting the solution in the measurement vials and then freezing at various reaction times.*

2.4.3 *In situ* EPR Setup

In situ EPR measurements were run with the same setup as *ex situ* measurements. To measure growth *via* chemical precipitation, precursor solution and reducing agent were either directly mixed in an EPR tube or mixed and injected into the tube. Thus the measurement of reduction is effectively comparable to a stop-flow batch reaction. The EPR tube was filled with solutions above half-way to ensure a uniform measurement and the top of the tube was closed with a layer or parafilm to reduce oxidation of the liquid at the top of the tube. A blank solution containing the solvent and surfactant was measured before each growth experiment, for background subtraction.

Temperature-controlled reactions were held at the desired temperature directly within the EPR apparatus, using an integrated hot air flow system, reaching above 60ºC and monitored by a thermocouple close to the cell position. The

solutions were heated to temperature prior to mixing and insertion into the EPR tube. Measurements were run for over 5 hours.

2.4.4 *In situ* XAS and SAXS Flow-Cell Design (SFM-4000)

Specialised cells are often produced for *in situ* XAS, optimised for the system requirements and the mode of measurement. A brief description is given of the SFM-4000 flow-cell used for *in situ* XAS developed by Biokine and the experimental setup used for liquid measurements. It is a reliable tool for the heating and mixture of solutions. The typical setup used in this research is shown in Figure 2.22. The cell through which the X-ray beam is shone is made of quartz and is either 10 mm or 5 mm in transmission length, used either in the configuration of cell 1 or cell 2, depending on the required path length. Cell 2 was fitted with a replaceable capillary tube in the centre, allowing for better cleaning of the cell between measurements.

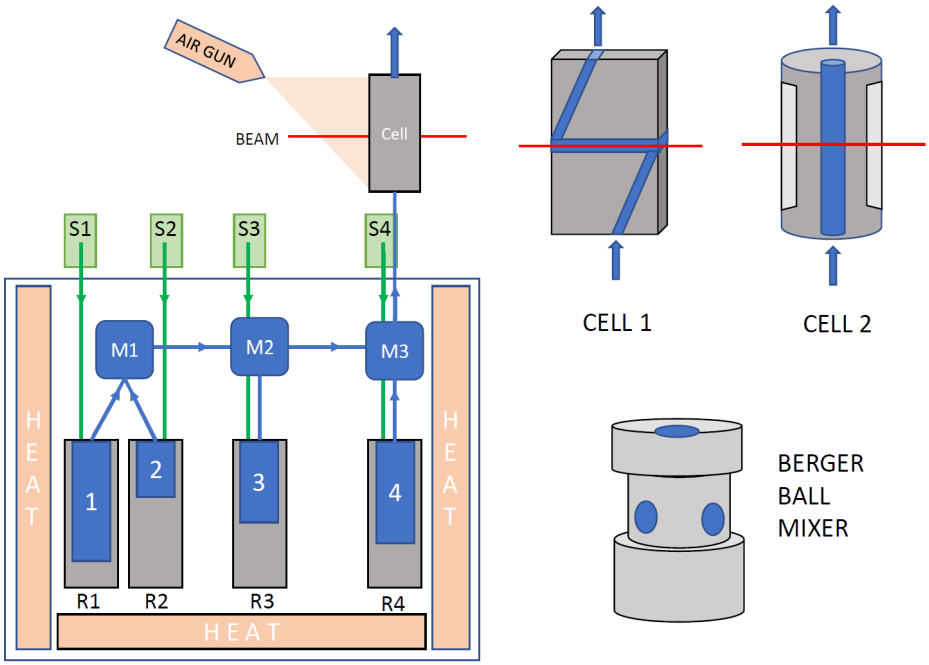

Figure 2.22 ***SFM-4000 Stop-Flow Cell Working Diagram.*** *Temperature-controlled reservoirs are filled with solution (R1-4, grey) using syringes (S1-4, green) to enable precise (± 0.5 µL) injection. A choice of two cells (top right) with lateral (Cell 1) and vertical (Cell 2) flow configurations could be applied, with the pathlengths measured. Berger ball mixers (bottom right) placed at M1-3 (blue) ensure a complete mixing of solutions prior to cell entry. Additional temperature control during measurements was ensured with a heat gun.*

To set up the stop-flow cell for measurements, four syringes (Figure 2.22 S1-S4) were filled with solutions prepared in the laboratory and fitted above the reservoirs. The contents were then passed into the 10 mL temperature-controlled reservoirs below (Figure 2.22 R1-R4), heated by a Lauda water bath. Unless otherwise specified, reservoirs 1 to 4 were generally filled with (1) deionised water to wash, (2) dilute acid (HNO_3 or HCl) to wash, (3) a solution containing the reducing agent, surfactant (and seeds when necessary) and (4) the metal salt precursor solution. Upon refilling the reservoirs, a period of 15 minutes was given to allow solutions to reach a steady temperature. A Berger Ball mixer (Figure 2.22

M1-M3) between channels ensured thorough mixing of solutions before entering the cell. The dead times and dead volumes of each component were precisely measured to ensure the correct volumes and time-scales for measurements (Table 2.2).

Table 2.2 ***SFM-4000 Stop-Flow Cell Dead Times and Volumes.*** *(*) The dead time was calculated with the maximum flow rate of 15 mL.s^{-1}. (**) The dead volume will be 5 µL less in cases when the channel is pre-washed with reservoir solution, and dead time for the updated dead volume is also given. (***) Dead volume for the cell was measured from the previous mixer to the central observation point. Cell 2 was made in-house, so precise values are not given.*

Description	Dead Volume (µL)	Dead Time* (ms)	Description	Dead Volume (µL)	Dead Time* (ms)
S1 ↔ R1	47 (-5**)	3.1 (2.8**)	R1 ↔ M1	79	5.3
S2 ↔ R2	47 (-5**)	3.1 (2.8**)	R2 ↔ M1	81	5.4
S3 ↔ R3	47 (-5**)	3.1 (2.8**)	R3 ↔ M2	89	5.9
S4 ↔ R4	47 (-5**)	3.1 (2.8**)	R4 ↔ M3	104	6.9
M1 ↔ M2	16	1.1	Cell 1***	30.2	2.0
M2 ↔ M3	20	1.3	Cell 2***	<30.2	<2.0

The profile of the injection is also important as with high time-resolution spectroscopy the mixing and injection times will impact the measurement. The duration of the injection phases will vary with the flow rate. During the injection, two phases can generally be seen, named the wash phase (1) and flow phase (2) in Figure 2.23. After the injection has stopped, the cell is in the “stopped-flow phase” (3) and the reaction is measured.

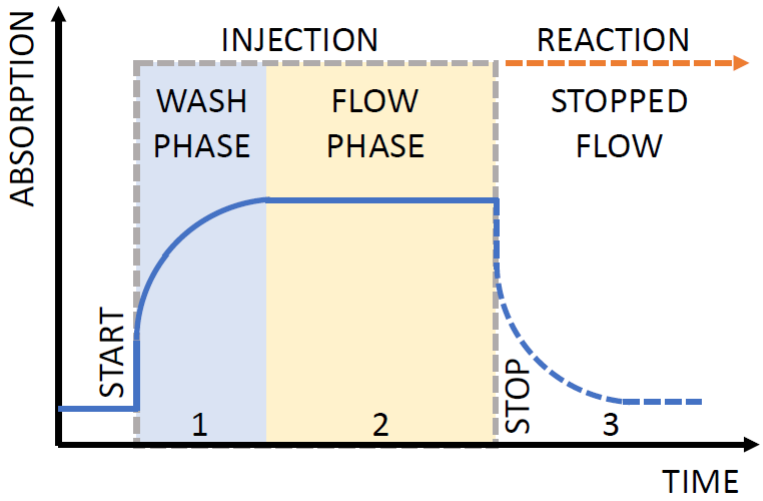

Figure 2.23 ***Concentration Profile of Reactants During Injection.***

Schematic of the X-ray absorption expected during the initial injection stages of the experiment, due to the solution flow mechanisms. When the injection in initiated by a programme, the solution concentration increases during the wash phase (1, blue), and stabilises in the flow phase (2, yellow). Once the flow is stopped, the concentration follows the trend of the reaction for the stopped flow phase (3, dashed line). Based on information available in the Biokine Manual.

The selection of the synthesis procedure follows three major stages: 1. procedure selection and replication, 2. adaptation and optimisation, and 3. reproducibility of the procedure. Synthetic conditions were selected and adapted based on the experimental requirements. The final synthetic procedures of growth will be described in more detail in their respective chapters.

2.5 Electrochemical Setup

Electrochemistry studies the changes between chemical states in a reaction by measuring the transfer of electrons. Based on Ohm's Law, the current (I) and voltage (V) have a relationship with the electrical resistance in the system (R), V

= I x R. The current or voltage can be varied to see the response of the other. Voltammetry measures the change of current in a system when a known voltage is applied.

Using the control of voltage and current, experiments can be set up to study the properties of a chemical system including the overpotential at which a reduction or oxidation occurs, number of electrons transferred, the reaction pathway followed, and intermediates formed.[59] However, the reaction parameters such as electrolyte concentration, scan rate, O_2 saturation, rotation rate and potential range affect the electrochemical results so standardised procedures are described in the literature.[60,61] In the case of ORR, this is a widely studied system where the activity between different catalysts needs to be compared. The CO_2 reduction reaction (CO_2RR) represents a more experimental system, in which Cu is the most active material known for the formation of C_{2+} products.[62,63] In this case, an understanding of the chemical changes which accompany electrochemical cycling is required.[64]

2.5.1 Three-electrode cell setup

The electrochemical testing for Oxygen Reduction Reaction (ORR) and CO_2RR are performed in a three-electrode cell setup (Figure 2.24) connected to a potentiostat.

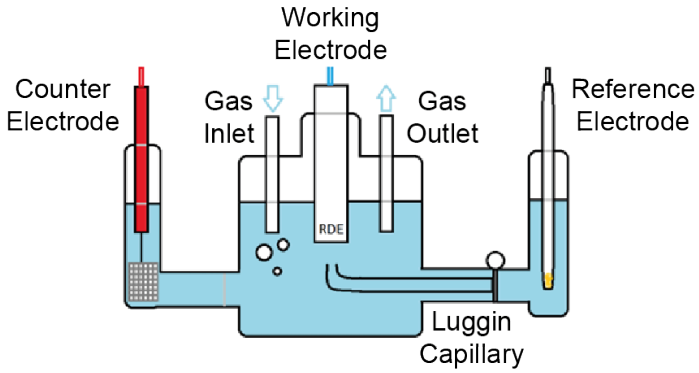

Figure 2.24 ***Three-Electrode Electrochemical Cell.*** *The typical three-electrode cell setup contains a counter electrode (left, shown here as Pt mesh), rotating disk electrode (centre, RDE) as a working electrode and a reference electrode (right) connected by a Luggin capillary to the main cell body. To measure catalytic activity, all electrodes are connected to a potentiostat, the catalyst material is loaded on the RDE and the electrolyte (blue) is saturated with relevant gases through the gas inlet and outlet.*

A glass cell is fitted with a Luggin capillary to protect the reference electrode. The cell is rinsed with acid prior to use and is washed with acid and distilled water for storage. The counter electrode is generally either a platinum mesh or a graphite rod. The reference electrodes used in this work are Ag/AgCl or a reversible hydrogen electrode (RHE), with the reported data calibrated accordingly. The same reference and counter electrodes were used for each test to ensure consistency across samples. Reference electrodes were calibrated variously with hydrogen or with a stable calomel electrode.

The working electrode is a polytetrafluoroethylene (PTFE) rotating disk electrode (RDE), with a glassy carbon centre on which the catalyst is loaded.

ORR Setup

0.1 M $HClO_4$ solution is used as the electrolyte in all oxygen reduction reaction (ORR) testing carried out in this work. Calibrated Ag/AgCl or RHE reference

electrodes were used, and the resulting data corrected accordingly. Graphite was used as a counter electrode to ensure that no Pt contamination occurred within the solution or at the working electrode. The catalyst of interest was applied at the working electrode.

A porous carbon material is used to support the metal nanoparticle catalyst to enable electrochemical testing. Pt-Pd/C Alloy nanoparticles, described in this work were synthesised based on a reaction described by Wang et al.[52] for highly porous Pd nanoparticles, directly on a porous carbon support (Ketjenblack). The support material is multifunctional, reducing the agglomeration of nanoparticles and acting as a conductive layer for electrochemical testing of nanoparticles.

2 mg of catalyst is dissolved in 1 mL Nafion solution (Nafion 0.11 wt% with Ethanol) to create an ink. The standard procedure followed is the weighing of the sample on a scale into a glass vial, pipetting of 1 mL of prepared Nafion solution and sonication for 30 minutes in an ice-bath to reduce loss of volatile components. 10 µL of ink is pipetted onto the glassy carbon surface of the rotating disk electrode. The sample is left to spin-dry for 5 minutes to ensure that the surface is completely dried.

A drop of the electrolyte is placed on the catalyst surface prior to loading the sample on the rotation device to ensure even wetting without air bubbles. Once loaded on the rotating electrode, bubbles were again removed by spinning at high speeds. N_2 gas is bubbled through the electrolyte for 20 minutes before the cyclic voltammetry test to remove oxygen dissolved in the water.

CO_2RR Setup

For CO_2RR testing, an electrolyte of 0.5 M KOH or $KHCO_3$ is selected based on literature values.[65] A platinum counter electrode was used, alongside an RHE reference. For the working electrode, a Cu foil was used, attached with an Au

wire. A fixed working electrode attachment with a clip holds the Cu foil steady, without rotation. The electrolyte solution was purged with N_2 or Ar gas for 20 minutes before cyclic voltammetry measurements.

2.5.2 ORR Catalytic Evaluation

The standard methodology for ORR testing described in the literature was applied for comparison of all catalyst materials.[60,61]

To begin, the electrolyte is N_2 purged. Open circuit potential (OCV) is measured beforehand to check the connections and current range. Cyclic voltammetry (CV) is performed within the scanning range, first at a sweep rate of 50 $mV.s^{-1}$ for 50 cycles to activate and wet the surface of the sample. [61,66] A slow CV scan is then run at 20 $mV.s^{-1}$ with and without rotation at 1600 rpm, to give a background subtraction curve for the data. Electrochemical impedance spectroscopy (EIS) is analysed to give the resistance in the setup.

Next, the electrolyte is O_2 purged. Linear sweep voltammetry (LSV) is performed for the anodic scan, with a scan rate of 20 $mV.s^{-1}$. EIS is run again to check the resistance under the adjusted conditions. N_2 background correction is performed during analysis and iR correction to reduce the effect of the experimental setup on the results.

To test the methanol tolerance, the electrolyte is changed, and the same procedure repeated. The methanol oxidation reaction is run for the same sample. The analysis of the resulting data is further discussed in the following sections.

Cyclic Voltammetry

Cyclic voltammetry (CV) is widely used to observe reversible changes in a redox reaction.[59] The integration of the area under the CV peaks can give an indication

of the electrochemical surface area of the catalyst, by comparing the charge density to oxidise a monolayer of hydrogen adsorbed on Pt. In the case of ORR, this is quantified by the area enclosed by the hydrogen adsorption or desorption peak in the low voltage range of a cyclic voltammogram.[66]

The equation for electrochemical surface area for ORR is given by,[60,67]

$$ECSA_{Cat}(m^2.g_{cat}^{-1}) = \frac{Q_{H-adsorption}\ (C)}{Q_{H-ideal}\ (\mu C.cm_{cat}^{-2})\ L_{cat}(mg.cm^{-3})\ A_g(cm^2)}$$

Where the charge of measured hydrogen adsorption of the sample ($Q_{H\text{-}adsorption}$) is compared to the charge of full coverage hydrogen adsorption on 1 cm^2 of metal ($Q_{H\text{-}ideal}$) is 210 $\mu C.cm^{-2}$ for Pt and 420 $\mu C.cm^{-2}$ for Pd.[60] L_{cat} is the catalyst loading and A_g is the surface area of the glassy carbon (0.1963 cm^2 in case of the rotating disk electrode used).

Linear Sweep Voltammetry

To test catalytic activity, linear sweep voltammetry (LSV) is generally used to compare the potential at which the reduction of oxygen occurs.[61] During the linear sweep voltammetry, the sample is rotated at 1600 rpm to reduce the mass transfer limitation at the catalyst surface.

Direct comparison of the activity can be performed using the half-wave potentials (Figure 2.25). However, since results with different sample loadings also need to be compared, the mass activity normalises experiments with different masses of active materials, to give an idea of the material performance.

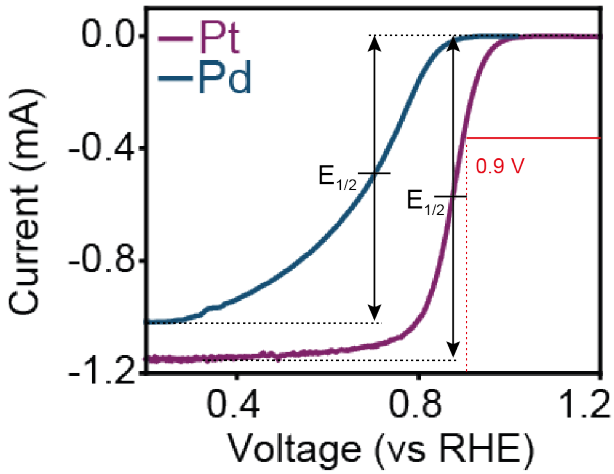

Figure 2.25 ***Typical ORR Sigmoidal LSV Result.*** *Standard ORR curves for Pt (purple) and Pd (blue) nanoparticles loaded on a carbon support, show catalytic activity in the anodic LSV scan, which can be compared using half-wave potentials ($E_{1/2}$) and 0.9 V current (red).*

Using the kinetic current (Figure 2.25), the mass activity of the sample can be calculated by:

$$mass\ activity = \frac{kinetic\ current\ at\ 0.9\ V}{working\ electrode\ Pt\ or\ total\ metal\ loading} \qquad \text{Equation 2.14}$$

Where the kinetic current corresponds to 0.9 V and the diffusion limiting current is generally taken as the minimum at a rotation speed of 1600 rpm.[60]

Tafel Equation

The Tafel equation relates the rate of an electrochemical reaction with the overpotential of the reaction. The slope of a curve plotted between overpotential, and log of current gives the Tafel slope. Assumptions made for the Tafel equation are 1) that the rate of the reaction is limited by the chemical reaction, 2) the mass-transfer rate is relatively small in comparison and 3) that the reverse reaction is negligible compared to the forward reaction at the electrode.

A Tafel plot is performed to see the rate of the reaction and understand the reaction pathways followed. For catalysis, Tafel slopes have been compared to understand the reaction pathways followed at the catalyst surface. Variations in the Tafel slope may indicate a changing mechanism. For example, during ORR on a Pt surface, a Tafel slope of 60 mV.dec^{-1} at a low overpotential and 120 mV.dec^{-1} at higher overpotentials is expected.[68-70]

iR Correction

Resistance from the electrolyte and experimental setup may affect the electrochemical result. Instead of recording resistance, which is simplified, the impedance can be measured. This is similar to voltammetry in that a voltage is applied and the current response is recorded on an electrochemical cell, except that an AC potential is introduced, and an AC current is measured. In a linear or pseudo-linear system, the sinusoidal current response has a phase shift (φ) compared with the voltage applied.

The excitation signal is given by:

$$E_t = E_0 sin(\omega t) \qquad \textit{Equation 2.15}$$

This is divided by the response signal,

$$I_t = I_0 sin(\omega t + \phi) \qquad \textit{Equation 2.16}$$

For impedance (Z):

$$Z = \frac{E_t}{I_t} = \frac{E_0 \, sin(\omega t)}{I_0 \, sin(\omega t + \phi)} = Z_0 \frac{sin(\omega t)}{sin(\omega t + \phi)} \qquad \textit{Equation 2.17}$$

This can also be written in terms of imaginary numbers using Eulers relationship,

$$exp(j\phi) = cos\phi + jsin\phi \qquad \textit{Equation 2.18}$$

To give the formula

$$Z(\omega) = \frac{E}{I} = Z_0\, exp(j\phi) = Z_0(cos\phi + jsin\phi) \qquad \textit{Equation 2.19}$$

A Nyquist plot is obtained by plotting the real part on the x-axis and the imaginary part on the y-axis. The resistance for the resistance (iR) correction of LSV data is taken from the Nyquist plot as the value of the real part of the impedance, where the imaginary part is zero or minimum.[71]

2.5.3 Cu Oxidation Evaluation

A cyclic voltammogram is measured for Cu foil with an inert environment, to capture the oxidation and reduction peaks. In addition, a carbon paper spray loaded with copper nanoparticles was also measured. For spray coating, 40 nm Cu nanoparticles were suspended in a mixture of H_2O and isopropyl alcohol (IPA), after sonicating for 30 minutes. This solution was hand-sprayed onto a carbon paper, with a 1 cm^2 mask. The mass of Cu loaded was recorded by weighing the change in total mass of the carbon paper. These are compared with the literature values measured for Cu.

The formation of $Cu(OH)_2$, Cu_2O, CuO and Cu at various reaction times can be identified by comparison with the standard curve published in the literature.[64] It should be noted that some debate remains about the reaction mechanisms and electron transfer between each step of the reaction, which are still under investigation.[64,72] CO_2RR conditions for setup selected were Ar-purged 0.5 M KOH electrolyte, with an RHE reference electrode, and a Pt counter electrode.

2.5.4 *In situ* Cell Design and Setup

Generally for *in situ* measurements, there is no glassy carbon surface available for nanoparticle loading, so an alternative conductive support is required. To this end, nanoparticles are dispersed in alcohol and spray-coated on a conductive, diffusion carbon paper, which behaves as a stand-alone support.

To run *in situ* electrochemical measurements, a specialised cell is developed. The criteria for the cell use was that the sample should be exposed to catalytic conditions while a XAS signal could be recorded simultaneously. The first cell used in this work was developed by Rosa Arrigo and Ruoyu Xu, building on experience from *in situ* cells published previously.[73] Shown in Figure 2.26, the cell could be used in both fluorescence and transmission modes, although transmission mode would face strong attenuation from the aqueous electrolyte. For this reason, transmission mode measurements were recorded at a sharp angle to the catalyst surface, to reduce the pathlength through electrolyte. The cell was made up of inert materials, such as PTFE, so as not to influence the reaction conditions or the XAS measurements. A graphite working electrode was also developed to prevent signal mixing from the stainless steel during fluorescence mode measurement.

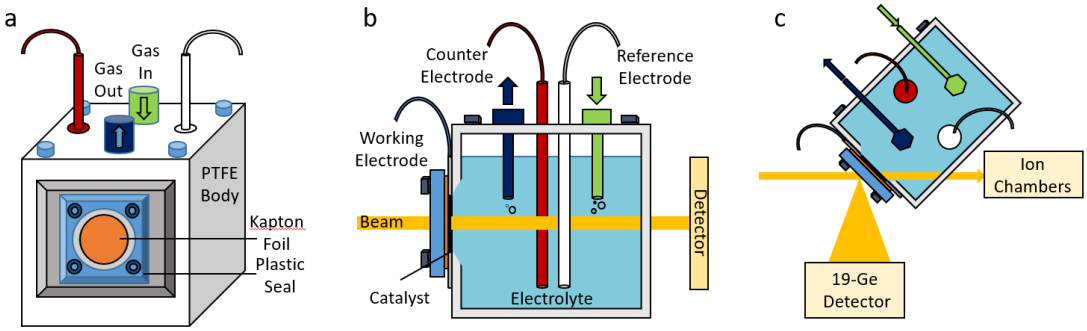

Figure 2.26 ***Three-Electrode in situ Fluorescence-XAS Cell.*** *In situ three-electrode electrochemical cell, showing Kapton window and working electrode (orange), counter electrode (red), reference electrode (white), gas inlet and outlet (green, blue) and the beam path (yellow). Cell visualised for (a) exterior view, (b) lateral cross-section and (c) horizontal cross-section from above, designed by Rosa Arrigo and Ruoyu Xu with working contact modifications by this author, for use in fluorescence mode at B18[26] and BL01B1[74] (SPring-8).*

For electrochemical flow experiments and improved transmission mode XAS, another *in situ* cell design was used, made by Yue Wen, Electrochemical Innovation Lab, UCL Chemical Engineering. A schematic of the electrode positions and setup are shown in Figure 2.27. Liquid electrolyte can continuously be pumped through the cell and refreshed, ensuring that purging of the electrolyte is more effective. The working electrode is connected by a conductive gold wire, with a Pt wire counter electrode. The reference electrode has electrolyte contact in a separate tube chamber, where a reversible hydrogen electrode or an Ag/AgCl electrode may be inserted.

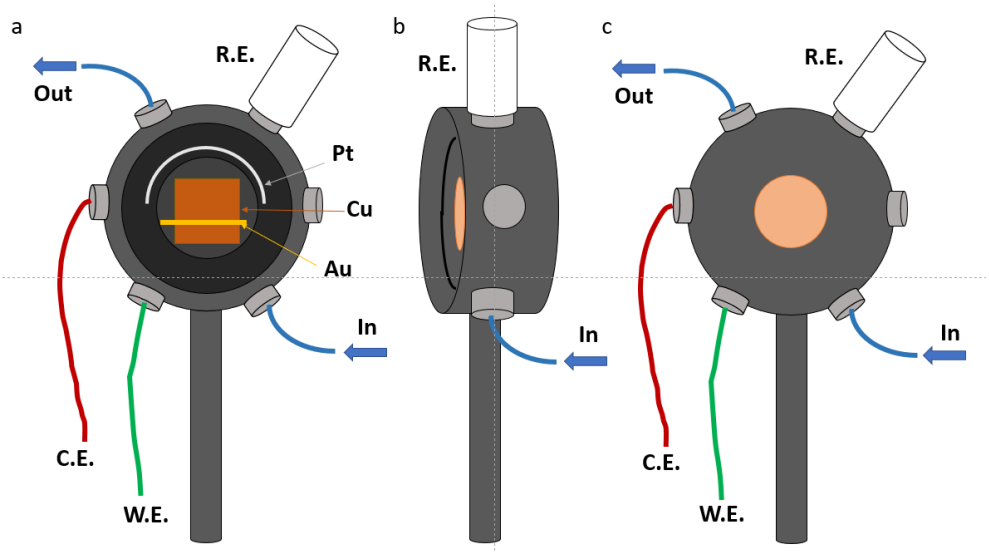

Figure 2.27 ***Three-Electrode in situ Transmission-XAS Liquid Flow Cell.*** *Three-electrode flow cell with working electrode connection (green) to Au contact and catalyst (orange), counter electrode connection (red) to Pt wire (grey), reference electrode insert (white) and electrolyte flow inlet and outlet (blue). Cell designed at Electrochemical Innovation Lab, UCL by Yue Wen is shown from (a) lateral cross-section, (b) side view and (c) frontal view, can be used in both transmission and fluorescence mode. Adjustments were made by this author to prevent pressure build-up, electrical disconnects and gas leakage.*

The cell was tested with standards of Pt mesh and Cu foil to check electrical connections and remove oxygen leaks, using electrolytes of 0.1 M $HClO_4$ and 0.5 M KOH, respectively.

2.6 Chemical Rate Determination

The rate of a reaction can be obtained experimentally by monitoring the concentration of the reactants over time. This is limited by the rate-determining step and is dependent on the concentrations of the reactants involved. This dependence given by the order of the reaction and most common reactions are

zero, first or second order. In a zero-order reaction, the rate is independent of the concentration of reactants. In comparison, a first-order reaction depends on the concentration of one reactant and a second-order reaction depends on the concentration of two reactants or the square of one reactant (Figure 2.28).

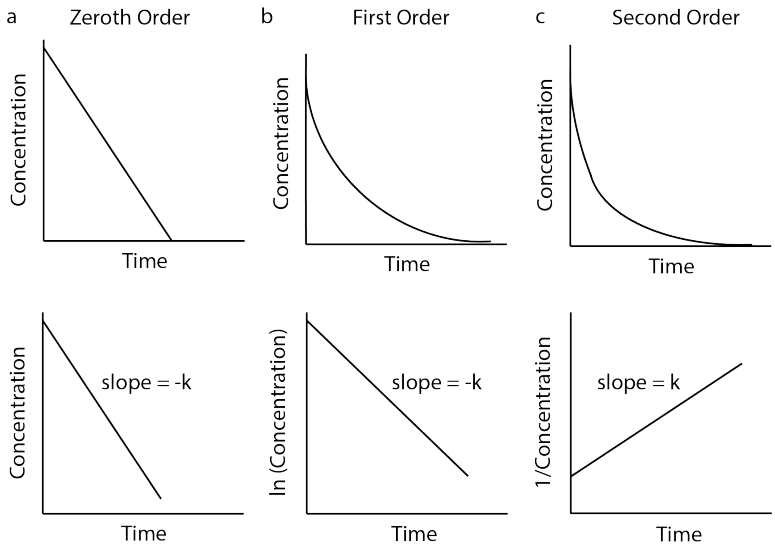

Figure 2.28 ***Determining Rate and Order of a Reaction.*** *A comparison of zero, first and second order reactions with (a-c) concentration-time curves and (b) rate constant calculation from slope.*

The order of the reaction and the determination of chemical equations has been a useful tool in all fields of chemistry, allowing the optimisation of reactant use and the increase of reaction rates, which are commercially valuable.

2.6.1 Rate of Reduction and Formation of Intermediate Species

The rate of reduction is often measured directly from the change in concentration of the precursor species. In this work, the rate of change of reactants, intermediates and products are measured at the linear region of the concentration-time plot. The formation of intermediate species are usually difficult to capture experimentally as they are transient and often similar to other reaction

materials. Using advanced characterisation, this work aims to isolate and track intermediate species, as explained in the discussion about *in situ* and *ex situ* characterisation tools. We explore the formation of intermediate species as interpreted from a combination of *in situ* results and the identification of intermediate species which have not been observed previously.

The reaction rates are measured under a variety of temperature, seeded growth, reducing agent concentration, solvent and reducing species conditions to learn more about the chemical responses of the systems being studied.

2.6.2 Activation Energy and Arrhenius Equation

Activation energy is required in chemical reactions which are thermodynamically favourable but kinetically unfavourable. In such reactions, although the products have a lower free energy than the reactants, the reaction does not come to pass unless an additional energy (activation energy) is added (Figure 2.29). Due to the intermediate process of bond breaking, restructuring or formation of intermediate reactants, the reaction rate depends on the activation energy being supplied to the reaction.

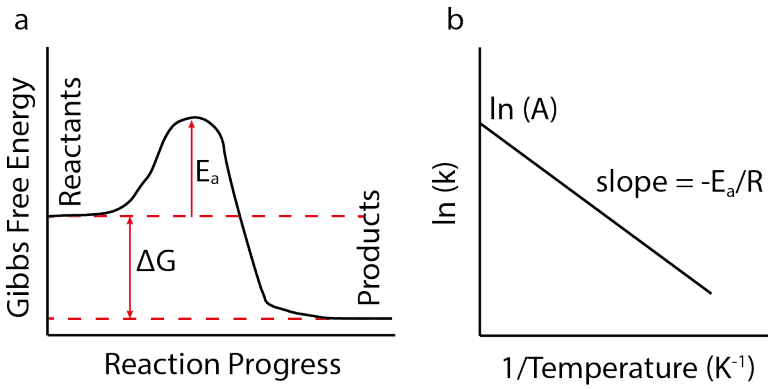

Figure 2.29 ***Free Energy Diagram and Arrhenius Plot.*** *(a) A plot of Gibb's free energy over time shows the thermodynamic energy difference between the reactants and products (∆G), where activation energy (E_a) is the additional energy required for the reaction to occur. (b) The slope of the Arrhenius plot, with log of rate constant against inverse temperature, provides the value of activation energy.*

Once the reaction rates have successfully been recorded for a temperature series, the activation energy of the reaction can be calculated. This could later be used to predict how many moles of a reactant would react at a certain temperature.

The Arrhenius equation describes the dependence of reaction rates on temperature.[75] The equation relates the rate constant (k), a pre-exponential factor (A), the activation energy of the reaction (E_a), temperature in Kelvin (T), and, depending on the units, either the gas constant (R = 8.314 $J.K^{-1}.mol^{-1}$) or the Boltzmann constant (k_B = 1.381 x 10^{-23} $J.K^{-1}$).[75]

$$k = Ae^{\frac{-E_a}{RT}} \; or \; k = Ae^{\frac{-E_a}{k_B T}} \qquad \textit{Equation 2.20}$$

To find the activation energy of the reaction using the Arrhenius equation, the natural logarithm of rate constants (y-axis) are plotted against the inverse of temperature (x-axis), to measure the resulting slope.

$$slope = -\frac{E_a}{R} \; or \; slope = -\frac{E_a}{k_B}$$ *Equation 2.21*

The activation energy and rates of a reaction make it possible to compare different systems, and to predict how readily a reaction will occur.

2.6.3 Rate of Electrochemical Oxidation

The rate of oxidation during electrochemical cycling is measured from *in situ* XAS observations, where the content of various oxidation states are calculated. In this thesis, the concentration of oxide species is calculated from LCF oxidation state calculations over time. Once oxidation state information is obtained *in situ* during a reaction, the slope of the concentration-time graph provides of the rate of oxidation at the surface. In catalytic applications the change in oxidation state may give an indication of the effectiveness of a catalyst.

The partial oxidation of metal surfaces during catalytic reactions is highly relevant as these processes may have a positive or negative impact on catalytic activity, in some cases passivating the catalyst surface over time. The rate of oxidation is therefore meaningful for the control of surface oxidation and the understanding of the rate of potential passivation under particular reaction conditions.

2.7 Sources of Error

The final area of methodology applied to all systems is a measurement of the degree of certainty and reproducibility for each result. This can be confirmed with reproducibility and reported with errors. Depending on the systems, the

methodology for these measurements vary. In general, a result is considered reproducible in this work, if it can be repeated three or more times, within an error limit.

2.7.1 Experimental Measurements

The errors for the various characterization tools used in this work are given alongside the results. A brief description of the major sources of error included and the system for description of errors is given below, in terms of experimental setup used for their measurement.

Mass and Volume

Mass of salts and solids was weighed with a 0.001 mg tolerance, while the liquids were measured by volume using a volumetric flask (+- 0.5 mL) or a graduated cylinder (0.05 mL). Some liquids were measured by mass, using the known density (mass = density × volume). Salt solutions were made up so that the final volume was correct, due to water of crystallization. Fresh solutions were prepared within each month, to prevent contamination, oxidation or evaporation of solutions which could impact concentrations.

Temperature Control

Temperature of reaction was controlled by a hot plate (0.5ºC control) with a stirred water or oil bath. Solution vials were immersed, and heated separately prior to mixing, often with a lid to prevent evaporation or oxidation on exposure to air and moisture. A thermocouple was held close to the location of the reaction, allowing more precise control and measurement.

Stirring And Mixing Control

The rate and location of addition of the reducing agent during nanoparticle growth may impact the final particles formed. Thus, the injection of the reducing agent was performed in a controlled dropwise manner, while the solution was vigorously stirred. During the *in situ* experiments, it was possible to mix the samples thoroughly prior to loading them in the cell. However, with the EPR measurements recorded directly in an EPR tube, there were some issues with the mixing, as samples were stirred by hand during and after the addition of the reductant. These were overcome by premixing samples, and injecting reactants into the EPR tube.

Purity and Aging of Chemicals

Samples were purchased from reliable sources, with high purity to avoid the presence of contaminants. These were handled with acid washed glassware and sterile plasticware. Solutions older than 1 month were replaced and where possible samples were prepared fresh before use. Stored solutions were sealed and kept in the fridge, as necessary, to prevent evaporation and metal reduction.

2.7.2 Reproducibility

During the *in situ* growth, there are variations in the rates and growth conditions so a single reaction is not sufficient to give a reliable dataset. Other factors include the cleanness of the cell, will also affect the rate of nucleation and the growth of small particles.

Generally, experiments are carried out three to four times to test reproducibility. In the case of nanoparticle growth, this is tested mainly through TEM imaging to gain an approximate understanding of the shape and size of particles formed.

For particles used in catalysis, the precise characterization and activity of the product was shape- and size-dependent. These particles were synthesised more than five times each and tested catalytically.

For particles synthesised *in situ* under different growth conditions, the shape and size of particles formed could not be captured directly within the experimental setup. For imaging, nanoparticles were grown *ex situ* and anticipated to produce a similar result.

The reproducibility of the *in situ* growth measurement when repeated within the same setup was clear from the trend of chemical changes observed. In some cases, it was only possible to repeat the growth experiments twice, due to lack of allocated experimental time. Error bars are given to reflect expected variations in the growth patterns, based on samples measured.

2.7.3 Data Analysis

Error can be introduced through the data analysis, when reducing and merging data, rebinning, smoothing, fitting and in selecting datasets for use. Thus, calculated values are printed with corresponding errors calculated to show certainty of the result. Where possible, inconsistencies have been avoided to reduce errors introduced during analysis.

When merging data, faulty datasets were defined as those containing errors of the measurement technique, such as lack of X-ray information when bubbles passed through the beam path. Such measurements, known to contain artefacts which did not reflect the chemical changes of interest were removed prior to analysis and glitches were removed when necessary. Merging data was necessary for the improvement of data quality, especially in XAS experiments.

However, at each stage of merging, the result was compared with the original data to ensure that additional errors were not introduced. Merging was only applied in reproducible systems, within 10% variation.

Rebinning, or the reduced number of datapoints for improved quality, was applied to noisy datasets where ample datapoints were collected. The removal of intermediate datapoints was replaced with an average value measured from neighbouring values. In the case of XAS data analysis, rebinning was applied more heavily to the EXAFS region, since small changes are not as significant to the results. On the contrary, the XANES region was minimally rebinned to allow any features to remain.

The Savitzky-Golay filter[76] was applied in this work for data smoothing, unless otherwise mentioned. Although it has limitations, particularly while fitting the end points of datasets, the filter was able to show datasets more clearly in cases where a consistent noise was present.[77] The number of points selected for the smoothing were adjusted according to the dataset analysed. In the case of XAS data, boxcar smoothing was also available to remove outlying datapoints but was avoided unless necessary.

While fitting data, the closeness of fit was used as a metric, shown alongside the data, in the errors calculated. Generally, R^2 (R-squared) values were provided which measure how close the data is to the fitted regression line. In the case of EXAFS fitting, the χ^2 (chi-squared) values are also given, which give closeness to the statistical distribution as a value for goodness-of-fit. Where possible, the data and fit are shown graphically together to directly observe the fitting.

Lastly, as expressed under reproducibility, certain datasets were selected to be representative of a larger set. Ideally, datasets were only selected when three repeats of the same result could be obtained. Where this was not possible, such

as in XAS experiments with limited measurement-time, the experiments were initially measured for two trials and only repeated again in cases of extreme variation or failure. The errors introduced during data analysis are more difficult to quantify, so when comparing datasets, a reproducible data processing method was applied equally to all datasets.

2.8 References

1 MacDonald, C. A. in *An Introduction to X-Ray Physics, Optics, and Applications* 3-9 (Princeton University Press, 2017).

2 Newville, M. Fundamentals of XAFS. *Reviews in Mineralogy and Geochemistry* **78**, 33-74, http://dx.doi.org/10.2138/rmg.2014.78.2 (2014).

3 Miyanaga, T., Suzuki, Y. & Narita, S. in *Zeolites - Useful Minerals* Ch. Chapter 8, (2016).

4 Materlik, G., Rayment, T. & Stuart, D. I. Diamond Light Source: status and perspectives. *Philos Trans A Math Phys Eng Sci* **373** http://dx.doi.org/10.1098/rsta.2013.0161 (2015).

5 Newville, M. *Fundamentals of XAFS*. (Consortium for Advanced Radiation Sources, 2004).

6 Hummer, A. A. & Rompel, A. X-ray absorption spectroscopy: a tool to investigate the local structure of metal-based anticancer compounds in vivo. *Adv Protein Chem Struct Biol* **93**, 257-305, http://dx.doi.org/10.1016/B978-0-12-416596-0.00008-7 (2013).

7 Housecroft, C. E. *Inorganic chemistry : Catherine E. Housecroft & Alan G. Sharpe*. (Pearson, 2018).

8 Rojsatien, S. *et al.* Quantitative analysis of Cu XANES spectra using linear combination fitting of binary mixtures simulated by FEFF9. *Radiation Physics and Chemistry* **202** http://dx.doi.org/10.1016/j.radphyschem.2022.110548 (2023).

9 Morris, D. J. & Zhang, P. In situ X-ray Absorption Spectroscopy of Platinum Electrocatalysts. *Chemistry–Methods* **1**, 162-172, http://dx.doi.org/https://doi.org/10.1002/cmtd.202000069 (2021).

10 Ramaker, D. E. & Koningsberger, D. C. The atomic AXAFS and Δμ XANES techniques as applied to heterogeneous catalysis and electrocatalysis. *Physical Chemistry Chemical Physics* **12**, 5514-5534, http://dx.doi.org/10.1039/B927120C (2010).

11 Stern, E. A., Sayers, D. E. & Lytle, F. W. Extended x-ray-absorption fine-structure technique. III. Determination of physical parameters. *Physical Review B* **11**, 4836-4846, http://dx.doi.org/10.1103/PhysRevB.11.4836 (1975).

12 Sayers, D. E., Stern, E. A. & Lytle, F. W. New Technique for Investigating Noncrystalline Structures: Fourier Analysis of the Extended X-Ray---Absorption Fine Structure. *Physical Review Letters* **27**, 1204-1207, http://dx.doi.org/10.1103/PhysRevLett.27.1204 (1971).

13 Rehr, J. J. & Albers, R. C. Theoretical approaches to x-ray absorption fine structure. *Reviews of Modern Physics* **72**, 621-654, http://dx.doi.org/10.1103/RevModPhys.72.621 (2000).

14 Mottana, A. & Marcelli, A. in *A Bridge between Conceptual Frameworks: Sciences, Society and Technology Studies* (ed Raffaele Pisano) 275-301 (Springer Netherlands, 2015).

15 Lee, P. A. & Pendry, J. B. Theory of the extended x-ray absorption fine structure. *Physical Review B* **11**, 2795-2811, http://dx.doi.org/10.1103/PhysRevB.11.2795 (1975).

16 Sun, Z. *et al.* XAFS in dilute magnetic semiconductors. *Dalton Transactions* **42**, 13779-13801, http://dx.doi.org/10.1039/C3DT50888A (2013).

17 Nachtegaal, M., Müller, O., König, C. & Frahm, R. in *X-Ray Absorption and X-Ray Emission Spectroscopy* 155-183 (2016).

18 Liu, H. *et al.* QXAFS system of the BL14W1 XAFS beamline at the Shanghai Synchrotron Radiation Facility. *J Synchrotron Radiat* **19**, 969-975, http://dx.doi.org/10.1107/S0909049512038873 (2012).

19 Zhang, G. *et al.* An integrated and versatile QXAFS system for general XAFS beamlines. *Nuclear Instruments and Methods in Physics Research Section A: Accelerators, Spectrometers, Detectors and Associated Equipment* **1042** http://dx.doi.org/10.1016/j.nima.2022.167428 (2022).

20 Ishiguro, N. & Tada, M. Structural Kinetics of Cathode Events on Polymer Electrolyte Fuel Cell Catalysts Studied by Operando Time-Resolved XAFS. *Catalysis Letters* **148**, 1597-1609, http://dx.doi.org/10.1007/s10562-018-2383-7 (2018).

21 Newton, M. A. & Dent, A. J. in *In-situ Characterization of Heterogeneous Catalysts* 75-119 (2013).

22 Kelly, S. D. *et al.* Comparison of EXAFS foil spectra from around the world. *Journal of Physics: Conference Series* **190** http://dx.doi.org/10.1088/1742-6596/190/1/012032 (2009).

23 Hwang, B.-J. *et al.* Structural Models and Atomic Distribution of Bimetallic Nanoparticles as Investigated by X-ray Absorption Spectroscopy. *Journal of the American Chemical Society* **127**, 11140-11145, http://dx.doi.org/10.1021/ja0526618 (2005).

24 Price, S. W. T. *et al.* Fitting EXAFS data using molecular dynamics outputs and a histogram approach. *Physical Review B* **85** http://dx.doi.org/10.1103/PhysRevB.85.075439 (2012).

25 Marinkovic, N. S., Sasaki, K. & Adzic, R. R. Determination of Single- and Multi-Component Nanoparticle Sizes by X-ray Absorption Spectroscopy. *Journal of The Electrochemical Society* **165**, J3222, http://dx.doi.org/10.1149/2.0281815jes (2018).

26 Dent, A. J. *et al.* B18: A core XAS spectroscopy beamline for Diamond. *Journal of Physics: Conference Series* **190** http://dx.doi.org/10.1088/1742-6596/190/1/012039 (2009).

27 Feng, K. *et al.* Single atoms or not? The limitation of EXAFS. *Applied Physics Letters* **116** http://dx.doi.org/10.1063/5.0008748 (2020).

28 Yang, S., Tak, Y. J., Kim, J., Soon, A. & Lee, H. Support Effects in Single-Atom Platinum Catalysts for Electrochemical Oxygen Reduction. *ACS Catalysis* **7**, 1301-1307, http://dx.doi.org/10.1021/acscatal.6b02899 (2017).

29 Shen, R. *et al.* High-Concentration Single Atomic Pt Sites on Hollow CuSx for Selective O2 Reduction to H2O2 in Acid Solution. *Chem* **5**, 2099-2110, http://dx.doi.org/10.1016/j.chempr.2019.04.024 (2019).

30 Kim, H. E. *et al.* Palladium Single-Atom Catalysts Supported on C@C3N4 for Electrochemical Reactions. *ChemElectroChem* **6**, 4757-4764, http://dx.doi.org/10.1002/celc.201900772 (2019).

31 Zhou, K. L. *et al.* Platinum single-atom catalyst coupled with transition metal/metal oxide heterostructure for accelerating alkaline hydrogen

evolution reaction. *Nat Commun* **12**, 3783, http://dx.doi.org/10.1038/s41467-021-24079-8 (2021).

32 Zhang, L. *et al.* Pt/Pd single-atom alloys as highly active electrochemical catalysts and the origin of enhanced activity. *ACS Catalysis* **9**, 9350-9358, http://dx.doi.org/10.1021/acscatal.9b01677 (2019).

33 Hamalainen, K., Siddons, D. P., Hastings, J. B. & Berman, L. E. Elimination of the inner-shell lifetime broadening in x-ray-absorption spectroscopy. *Phys Rev Lett* **67**, 2850-2853, http://dx.doi.org/10.1103/PhysRevLett.67.2850 (1991).

34 Bauer, M. HERFD-XAS and valence-to-core-XES: new tools to push the limits in research with hard X-rays? *Phys Chem Chem Phys* **16**, 13827-13837, http://dx.doi.org/10.1039/c4cp00904e (2014).

35 Zimmermann, P. *et al.* Modern X-ray spectroscopy: XAS and XES in the laboratory. *Coordination Chemistry Reviews* **423** http://dx.doi.org/10.1016/j.ccr.2020.213466 (2020).

36 Rudolph, J. & Jacob, C. R. Revisiting the Dependence of Cu K-Edge X-ray Absorption Spectra on Oxidation State and Coordination Environment. *Inorg Chem* **57**, 10591-10607, http://dx.doi.org/10.1021/acs.inorgchem.8b01219 (2018).

37 Miaja-Avila, L. *et al.* Valence-to-core X-ray emission spectroscopy of titanium compounds using energy dispersive detectors. *X-Ray Spectrometry* **50**, 9-20, http://dx.doi.org/10.1002/xrs.3183 (2020).

38 Zhang, R., Li, H. & McEwen, J.-S. Chemical Sensitivity of Valence-to-Core X-ray Emission Spectroscopy Due to the Ligand and the Oxidation State: A Computational Study on Cu-SSZ-13 with Multiple H2O and NH3 Adsorption. *The Journal of Physical Chemistry C* **121**, 25759-25767, http://dx.doi.org/10.1021/acs.jpcc.7b04309 (2017).

39 Gallo, E. & Glatzel, P. Valence to core X-ray emission spectroscopy. *Adv Mater* **26**, 7730-7746, http://dx.doi.org/10.1002/adma.201304994 (2014).

40 Kikhney, A. G. & Svergun, D. I. A practical guide to small angle X-ray scattering (SAXS) of flexible and intrinsically disordered proteins. *FEBS Lett* **589**, 2570-2577, http://dx.doi.org/10.1016/j.febslet.2015.08.027 (2015).

41 Mane, A. T. & Patil, V. B. in *Spectroscopy of Polymer Nanocomposites* (eds Sabu Thomas, Didier Rouxel, & Deepalekshmi Ponnamma) 452-467 (William Andrew Publishing, 2016).

42 Gedde, U. W., Hedenqvist, M. S., Hakkarainen, M., Nilsson, F. & Das, O. in *Applied Polymer Science* (eds Ulf W. Gedde *et al.*) 105-169 (Springer International Publishing, 2021).

43 Nachlas, W. O. *et al.* Evaluating Consensus in Experimental K-ratios from over 40 WDS and EDS Measurement Systems. *Microsc Microanal* **29**, 225-226, http://dx.doi.org/10.1093/micmic/ozad067.100 (2023).

44 He, W., Liu, Y., Wamer, W. G. & Yin, J.-J. Electron spin resonance spectroscopy for the study of nanomaterial-mediated generation of reactive oxygen species. *Journal of Food and Drug Analysis* **22**, 49-63, http://dx.doi.org/https://doi.org/10.1016/j.jfda.2014.01.004 (2014).

45 Husáriková, L. *et al.* Unusual EPR Spectra with Inverse Axial g values of Chlorosalicylate–Cu(II)–2,6-Pyridinedimethanol Complex in Frozen

Water–Methanol Solution. *Applied Magnetic Resonance* **44**, 571-582, http://dx.doi.org/10.1007/s00723-012-0431-9 (2013).

46 De, D. K., Sthanapati, J., Ghoshal, A. K. & Pal, A. K. Electron Paramagnetic Resonance Study of Copper(II) Fluosilicate Hexahydrate. *Journal of Magnetic Resonance*, 181-186, (1982).

47 Rocha, F. S., Gomes, A. J., Lunardi, C. N., Kaliaguine, S. & Patience, G. S. Experimental methods in chemical engineering: Ultraviolet visible spectroscopy—UV-Vis. *The Canadian Journal of Chemical Engineering* **96**, 2512-2517, http://dx.doi.org/10.1002/cjce.23344 (2018).

48 Edwards, A. A. & Alexander, B. D. in *Encyclopedia of Spectroscopy and Spectrometry (Second Edition)* (ed John C. Lindon) 2030-2039 (Academic Press, 2010).

49 Seri-Levy, A. & Avnir, D. The Brunauer-Emmett-Teller equation and the effects of lateral interactions. A simulation study. *Langmuir* **9**, 2523-2529, http://dx.doi.org/10.1021/la00034a009 (1993).

50 Wang, G. & Ju, Y. Organic shale micropore and mesopore structure characterization by ultra-low pressure N 2 physisorption: Experimental procedure and interpretation model. *Journal of Natural Gas Science and Engineering* **27**, 452-465, http://dx.doi.org/10.1016/j.jngse.2015.08.003 (2015).

51 Balaram, V. Microwave plasma atomic emission spectrometry (MP-AES) and its applications – A critical review. *Microchemical Journal* **159** http://dx.doi.org/10.1016/j.microc.2020.105483 (2020).

52 Wang, F. *et al.* Porous single-crystalline palladium nanoparticles with high catalytic activities. *Angew Chem Int Ed Engl* **51**, 4872-4876, http://dx.doi.org/10.1002/anie.201107376 (2012).

53 Pastoriza-Santos, I., Sánchez-Iglesias, A., Rodríguez-González, B. & Liz-Marzán, L. M. Aerobic Synthesis of Cu Nanoplates with Intense Plasmon Resonances. *Small* **5**, 440-443, http://dx.doi.org/10.1002/smll.200801088 (2009).

54 Khan, A., Rashid, A., Younas, R. & Chong, R. A chemical reduction approach to the synthesis of copper nanoparticles. *International Nano Letters* **6**, 21-26, http://dx.doi.org/10.1007/s40089-015-0163-6 (2015).

55 Liu, Q.-m., Yasunami, T., Kuruda, K. & Okido, M. Preparation of Cu nanoparticles with ascorbic acid by aqueous solution reduction method. *Transactions of Nonferrous Metals Society of China* **22**, 2198-2203, http://dx.doi.org/10.1016/s1003-6326(11)61449-0 (2012).

56 Lu, R. *et al.* A simple method for the synthesis of copper nanoparticles from metastable intermediates. *RSC Adv* **13**, 14361-14369, http://dx.doi.org/10.1039/d3ra01082a (2023).

57 Guillot, S., Chemelli, A., Bhattacharyya, S., Warmont, F. & Glatter, O. Ordered Structures in Carboxymethylcellulose−Cationic Surfactants−Copper Ions Precipitated Phases: in Situ Formation of Copper Nanoparticles. *The Journal of Physical Chemistry B* **113**, 15-23, http://dx.doi.org/10.1021/jp805613n (2009).

58 Dorner, L. *et al.* Cost-effective sol-gel synthesis of porous CuO nanoparticle aggregates with tunable specific surface area. *Sci Rep* **9**, 11758, http://dx.doi.org/10.1038/s41598-019-48020-8 (2019).

59 Elgrishi, N. *et al.* A Practical Beginner's Guide to Cyclic Voltammetry. *Journal of Chemical Education* **95**, 197-206, http://dx.doi.org/10.1021/acs.jchemed.7b00361 (2017).

60 Garsany, Y., Baturina, O. A., Swider-Lyons, K. E. & Kocha, S. S. Experimental Methods for Quantifying the Activity of Platinum Electrocatalysts for the Oxygen Reduction Reaction. *Analytical Chemistry* **82**, 6321-6328, http://dx.doi.org/10.1021/ac100306c (2010).

61 Kocha, S. S. *et al.* Best Practices and Testing Protocols for Benchmarking ORR Activities of Fuel Cell Electrocatalysts Using Rotating Disk Electrode. *Electrocatalysis* **8**, 366-374, http://dx.doi.org/10.1007/s12678-017-0378-6 (2017).

62 Wang, X. *et al.* Morphology and mechanism of highly selective Cu(II) oxide nanosheet catalysts for carbon dioxide electroreduction. *Nat Commun* **12**, 794, http://dx.doi.org/10.1038/s41467-021-20961-7 (2021).

63 Woldu, A. R., Huang, Z., Zhao, P., Hu, L. & Astruc, D. Electrochemical CO2 reduction (CO2RR) to multi-carbon products over copper-based catalysts. *Coordination Chemistry Reviews* **454** http://dx.doi.org/10.1016/j.ccr.2021.214340 (2022).

64 Giri, S. D. & Sarkar, A. Electrochemical Study of Bulk and Monolayer Copper in Alkaline Solution. *Journal of The Electrochemical Society* **163**, H252-H259, http://dx.doi.org/10.1149/2.0071605jes (2016).

65 Zou, J., Lee, C.-Y. & Wallace, G. G. Boosting Formate Production from CO2 at High Current Densities Over a Wide Electrochemical Potential Window on a SnS Catalyst. *Advanced Science* **8**, 2004521, http://dx.doi.org/https://doi.org/10.1002/advs.202004521 (2021).

66 Garsany, Y., Baturina, O. A., Swider-Lyons, K. E. & Kocha, S. S. Experimental methods for quantifying the activity of platinum electrocatalysts for the oxygen reduction reaction. *Analytical Chemistry* **82**, 6321–6328, http://dx.doi.org/10.1021/ac100306c (2010).

67 Chandran, P., Ghosh, A. & Ramaprabhu, S. High-performance platinum-free oxygen reduction reaction and hydrogen oxidation reaction catalyst in polymer electrolyte membrane fuel cell. *Scientific Reports* **8**, 3591, http://dx.doi.org/10.1038/s41598-018-22001-9 (2018).

68 Damjanovic, A. & Brusic, V. Electrode kinetics of oxygen reduction on oxide-free platinum electrodes. *Electrochimica Acta* **12**, 615-628, http://dx.doi.org/https://doi.org/10.1016/0013-4686(67)85030-8 (1967).

69 van der Vliet, D. F. *et al.* Mesostructured thin films as electrocatalysts with tunable composition and surface morphology. *Nat Mater* **11**, 1051-1058, http://dx.doi.org/10.1038/nmat3457 (2012).

70 Holewinski, A. & Linic, S. Elementary Mechanisms in Electrocatalysis: Revisiting the ORR Tafel Slope. *Journal of The Electrochemical Society* **159**, H864-H870, http://dx.doi.org/10.1149/2.022211jes (2012).

71 Shinozaki, K., Zack, J. W., Richards, R. M., Pivovar, B. S. & Kocha, S. S. Oxygen Reduction Reaction Measurements on Platinum Electrocatalysts Utilizing Rotating Disk Electrode Technique. *Journal of The Electrochemical Society* **162**, F1144-F1158, http://dx.doi.org/10.1149/2.1071509jes (2015).

72 Ambrose, J., Barradas, R. G. & Shoesmith, D. W. Investigations of copper in aqueous alkaline solutions by cyclic voltammetry. *Journal of*

Electroanalytical Chemistry and Interfacial Electrochemistry **47**, 47-64, http://dx.doi.org/https://doi.org/10.1016/S0022-0728(73)80344-4 (1973).

73 Timoshenko, J. & Roldan Cuenya, B. In Situ/Operando Electrocatalyst Characterization by X-ray Absorption Spectroscopy. *Chem Rev* **121**, 882-961, http://dx.doi.org/10.1021/acs.chemrev.0c00396 (2021).

74 Uruga, T. *et al.* Improvement in XAFS beamline BL01B1 at SPring-8. *Journal of Physics: Conference Series* **190** http://dx.doi.org/10.1088/1742-6596/190/1/012041 (2009).

75 Arrhenius, S. Über die Reaktionsgeschwindigkeit bei der Inversion von Rohrzucker durch Säuren. *Zeitschrift für Physikalische Chemie* **4U**, 226-248, http://dx.doi.org/doi:10.1515/zpch-1889-0416 (1889).

76 Savitzky, A. & Golay, M. J. E. Smoothing and Differentiation of Data by Simplified Least Squares Procedures. *Analytical Chemistry* **36**, 1627-1639, http://dx.doi.org/10.1021/ac60214a047 (1964).

77 Schmid, M., Rath, D. & Diebold, U. Why and How Savitzky-Golay Filters Should Be Replaced. *ACS Meas Sci Au* **2**, 185-196, http://dx.doi.org/10.1021/acsmeasuresciau.1c00054 (2022).

Chapter 3. Millisecond-Resolved *in situ* XAS and SAXS Study of CTAC-Capped Pd Nanoparticle Growth

A mechanistic understanding of morphology-controlled nanoparticle growth is crucial in the design of high performance catalytic materials. Alongside the extensive theoretical literature, detailed experimental evidence is required for verification and further observation of nucleation and growth processes. In particular, the formation of a transient growth species is often suggested but is rarely experimentally measured.

A 500 ms-resolved *in situ* X-ray absorption spectroscopy (XAS) study of the ascorbic acid (AA) reduction cetyltrimethylammonium chloride (CTAC)-capped K_2PdCl_4 for Pd nanoparticle growth, combined with *in situ* small angle X-ray scattering (SAXS) and time-resolved transmission electron microscope (TEM) images, allows the study of reaction rates under a range of temperature and seeded growth conditions. The measurement of reaction rates allows the calculation of activation energy and the duration of reaction stages, to better understand control of growth parameters. Such a combination of *in situ* XAS and SAXS results with TEM images, can be instrumental in capturing the growth kinetics of reactants and transient species to aid in modelling growth, as a step towards rational nanoparticle design.

Notable Contributions

Contributions were made by Hao Gu in preliminary XAS analysis and data collection, Liqun Kang batch XAS data fitting for both XANES and EXAFS and Ryan Wang in experimental design and ideas. SAXS fittings were performed by Alberto Alvarez Fernandez and time-resolved TEM was performed by Han Zhang.

3.1 Introduction

Palladium nanoparticles are widely applied in catalysis, including in industrial hydrogenation reactions and exhaust emission control (an estimated 84% of Pd produced worldwide).[1-3] However, Pd is both expensive and rare, making it undesirable commercially and for sustainability.[4,5] Nanoparticles represent a strategy for increased material efficiency for Pd in catalysis.[6] For improved catalytic behaviour, the shape and size control of nanoparticles is necessary. This can be achieved through the growth of Pd nanoparticles *via* chemical precipitation, where reaction conditions can control nanoparticle morphology.[7-11] Substantial empirical research has pinpointed key synthesis parameters which determine nanoparticle morphology during growth in solution.[8,10,12-17] Controls such as temperature,[12,16] concentration,[18] chemical surface control agents (surfactants)[8,14,19] and seed solutions[20,21] are often adjusted by trial-and-error to fine-tune morphology and, thereby, catalytic properties.[8,11,22-29] Yet a deeper fundamental understanding of the effect of these synthetic parameters on the growth mechanism is required to eventually reach the goal of rational nanoparticle design. Towards this goal, in recent years experimental *in situ* characterization techniques including SAXS, XAS, TEM and ultraviolet-visible spectroscopy (UV-vis), have been successfully combined to observe growth kinetics.[30,31]

The reduction of aqueous CTAC-capped K_2PdCl_4 with AA is recorded under controlled parameters of temperature and seeded growth to determine their effects on the resulting nanoparticle morphology.

Pd nanoparticle reduction with ascorbic acid has been cited to follow the Watzky-Finke (WF) two-step 'auto-catalytic' growth[29,30,32,33] with a proposed reaction mechanism of:

$$K_2PdCl_4 + C_6H_8O_6 \rightarrow Pd^0 + C_6H_6O_6 + 2KCl + 2HCl \qquad \textit{Equation 3.1}$$

However, there remains some debate about the intermediate growth precursors, and their effect on morphology. Theoretical investigations of a range of Pd nanoparticle growth systems have variously suggested Pd^{1+} coordinated intermediates,[34] zero-valent Pd^0 monomers and ligand-mediated Pd^0 as primary building blocks for nanoparticle nucleation and growth.[30,35,36] The formation of a ligand-coordinated M^0 growth species is considered most likely, since the presence of isolated atoms is energetically unfavourable.[37]

Capturing time-resolved intermediate growth species is experimentally challenging due to their transient nature and shared properties with either precursor or reaction products. A study of 1 nm Pd nanoparticle growth with a combination of SAXS and XAS by Karim et al. predicts the formation of ligand coordinated Pd^0 as a growth species within the solution, although this is not directly measured and gives valuable insight into the role of the surfactant for self-limiting size.[30] Alternatively, the formation of $M_{4\text{-}6}$ growth units is possible, as observed in Rh nanocube synthesis where $Rh_{4\text{-}6}$ growth species are chlorine coordinated.[31] The concentration of intermediate reduced species can also confirm the 'solution reduction' previously reported by Yang et al. with $PdCl_4^{2-}$ precursor, as opposed to 'surface reduction' observed for $PdBr_4^{2-}$.[38]

Here we present a 500 millisecond resolved *in situ* XAS and SAXS study of the AA reduction of K_2PdCl_4 under a range of temperatures and seed concentrations. CTAC was selected as the surfactant to form single-crystal porous nanoparticles, observe ligand-mediated reaction kinetics and detect growth species.[11] Previous

observations of CTAC-capped Pd nanoparticle growth have shown stages of nucleation and autocatalytic growth, fitting the WF two-step mechanism.[29,30,35] Applied to this system, the reaction is believed to have four principal stages.

Reduction:	$Pd^{2+} + 2e^- \rightarrow Pd^0$	Equation 1
Nucleation:	$nPd^0 \rightarrow (Pd^0)_n$	Equation 2
Growth:	$Pd^0 + (Pd^0)_n \rightarrow (Pd^0)_{n+1}$	Equation 3
Reoxidation:	$Pd^0 - 2e^- \rightarrow Pd^{2+}$ (solution)	Equation 4

First, the reduction of Pd^{2+} to Pd^0 (Equation 1), occurs by definition before the formation of Pd-Pd bonds or solid particles. Nucleation (Equation 2) follows with the first appearance Pd-Pd bonds, when growth species aggregate and reach a critical size to form 'nuclei'. The WF two-step theory combines reduction and nucleation in the first pseudo-elementary step since unbonded Pd^0 does not have an equilibrium.[35,36] During rapid growth (Equation 3) Pd growth species are incorporated onto an existing solid surface either from solution or *via* direct reduction at the surface. The decrease in Pd^0 concentration at long reaction times is attributed to reoxidative dissolution (Equation 4), reshaping or etching, which are known to occur in systems containing halide ligands, particularly in the synthesis of Cl^- capped palladium nanoparticles with Cl^-/O_2 pair.[11,39]

To observe growth *in situ,* the reaction setup (Figure 3.1 a) allows continuous spectroscopic measurements (Figure 3.1 b) and uniform automated solution injection. Five key parameters are experimentally measured during nanoparticle growth to distinguish the reaction stages and mechanism, namely Pd^{2+} concentration, Pd^0 concentration, Pd-Cl coordination, Pd-Pd coordination, and nanoparticle radius. SAXS records the growing radius of the nanoparticle, while

energy dispersive (EDE) XAS results capture temporal changes in oxidation states of palladium (Pd^0 and Pd^{2+}), and Pd coordination (Pd-Pd and Pd-Cl/O).

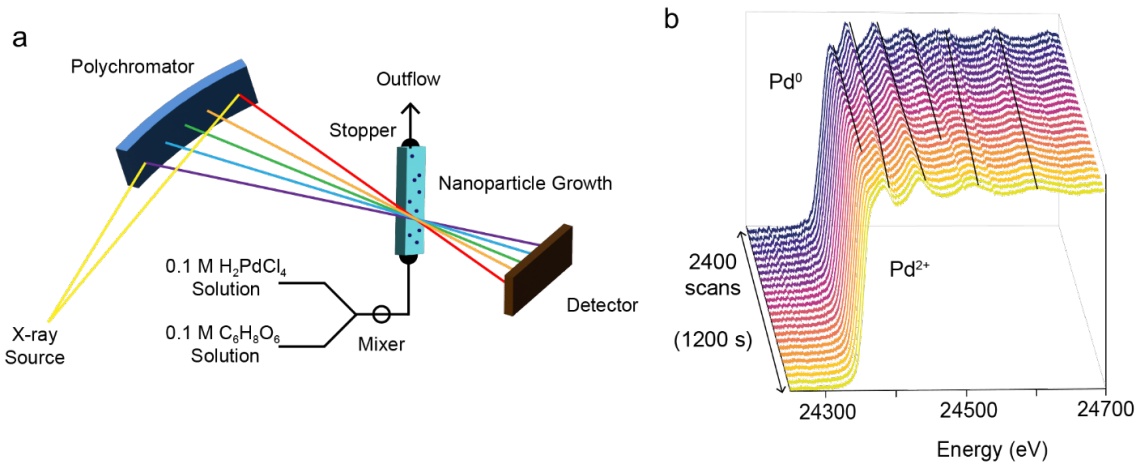

Figure 3.1 ***EDE Setup for Time-Resolved Spectra.*** *(a) The experimental setup at the I-20 EDE beamline (Diamond Light Source), showing the X-ray path through a capillary tube containing the reaction solutions. (b) A sample of the 2400 Pd K-edge XAS spectra collected over 1200 seconds of Pd reduction where changes in the XANES and EXAFS regions are indicated by black lines following peaks.*

By comparing the linear combination fit (LCF) results from X-ray absorption near edge structure (XANES) and the refinement of extended X-absorption fine structure (EXAFS) data, the concentration of a ligand coordinated Pd^0 species in solution could theoretically be calculated (described in detail in Section 4.4.5).

This calculation leads to the conclusion that by measuring the change in Pd^{2+} concentration (shown as (Pd^{2+})) from XANES between initial time (i) and a given time (t), the discrepancy in the corresponding change in Pd-Cl C.N. (shown as [Pd-Cl]) for the same time period gives a measurement of the total content of Pd^0-Cl. The contribution of fully coordinated Pd-Cl bonds ($[Pd\text{-}Cl]^i$) in unreduced Pd^{2+}

precursor ($(Pd^{2+})^t/(Pd^{2+})^i$) can be subtracted from the measured Pd-Cl coordination number ($Pd\text{-}Cl^{time}$), to give Pd^0-Cl coordination.

At a time t,

$$[Pd^0 - Cl]^t = [Pd - Cl]^t - \left([Pd - Cl]^i \times \frac{(Pd^{2+})^t}{(Pd^{2+})^i}\right) \qquad \textit{Equation 3.2}$$

The experimental calculation of Pd^0–Cl concentration from *in situ* XAS is performed for the first time, to our knowledge, during the AA reduction of CTAC-capped K_2PdCl_4. Thus, the combination of *in situ* characterization tools successfully records both growth kinetics and M^0-Cl species and could be applied to study a wide range of nanoparticle growth systems, as a step towards the rational design of nanocatalyst morphology.

3.2 Results and Discussion

3.2.1 Observing Nanoparticle Growth

The shape and size of nanoparticles are observed for a range of temperatures (Supplementary Figure 3.10, Supplementary Figure 3.11, Supplementary Table 3.1). Porous spherical Pd nanoparticles with an average radius of 76.97 ± 19.63 nm were achieved at the baseline condition of unseeded 60ºC growth measured for 1200 seconds. The structures of individual nanoparticles are flower-like, with a solid core from which nano-dendritic arms extend.

Time-resolved ex-situ TEM images of a 50ºC reduction show the key morphological changes in the nanoparticles during growth (Figure 3.2 a-j). First, the formation of spherical particles with an average diameter of 5.75 ± 1.30 nm, is observed at 60 s reaction time (Figure 3.2 a, Supplementary Table 3.2). After 120 s, increased anisotropy and aggregation occur, leading to the first structured

nanoparticles (Figure 3.2 b). The nanoparticles continue to grow from 360 until 480 s, where fully sized particles are formed (Figure 3.2 c, d). The shape, size and crystal structures of nanoparticles continue to adjust as the reaction time continues to 1200 s, likely driven by halide etching and reoxidation (Figure 3.2 e).

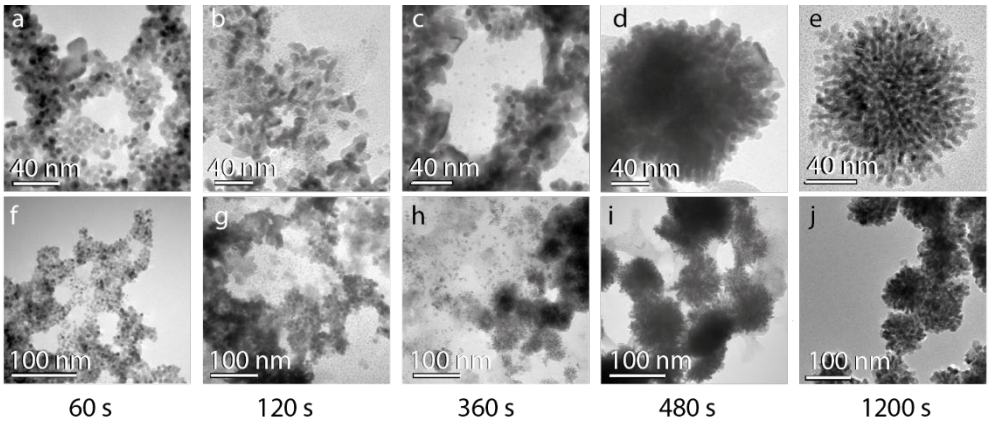

Figure 3.2 ***Time-Resolved Nanoparticle Morphology.*** *Representative bright-field TEM images of Pd nanoparticles formed at 50°C with approximate reaction times of (a, f) 60 s, (b, g) 120 s, (c, h) 360 s, (d, i) 480 s and (e, j) 1200 s with scalebars of 40 nm (a-e) and 100 nm (f-j).*

X-ray diffraction (XRD) results show that nanoparticles formed are highly crystalline, with a preferential (111) lattice (Supplementary Figure 3.12). A face-centred cubic crystal structure is present with lattice constant calculated as 3.96 ± 0.006 Å. All peaks were detected within the sample, with sharp (111) peak. This is confirmed by Pd(111) and Pd(100) crystal lattices observed in transmission electron microscopy (TEM) imaging (Supplementary Figure 3.13). The nanoparticle morphology formed has a high surface area, where dendritic structure and size are controlled by CTAC.

The molar ratio of reactants was modified from a previously described ascorbic acid reduction of CTAC-capped K_2PdCl_4 to enable *in situ* XAS characterization.[11] The combined visualisation of *in situ* XANES, EXAFS and SAXS results during a

60ºC reduction provides a typical experimental growth profile to reveal reaction stages of reduction, nucleation, growth and reoxidation (Figure 3.3 a).

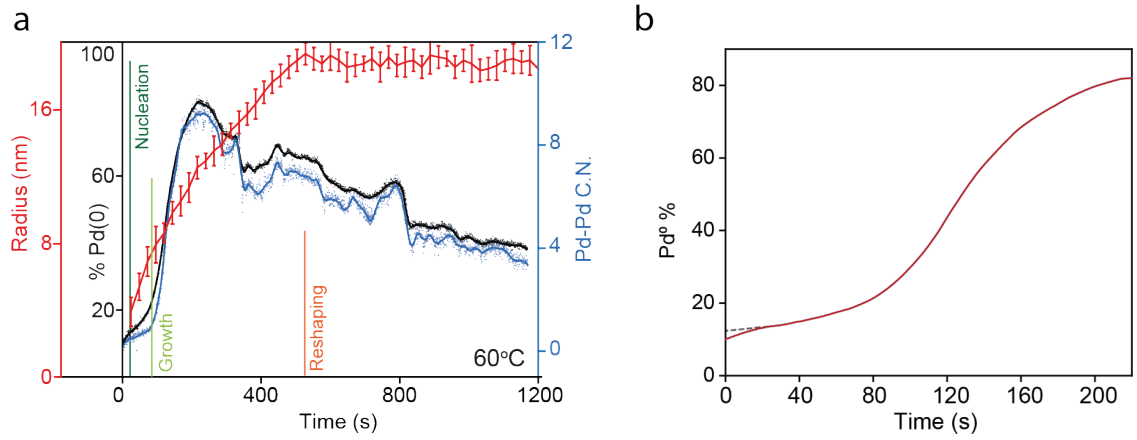

Figure 3.3 ***Nanoparticle Growth Stages and Early Reduction.*** *(a) Experimental reaction profile of Pd reduction under 60ºC measured with Pd K-edge XAS and SAXS compares the changing Pd^0 concentration (black), Pd-Pd coordination number (blue) and nanoparticle radius (red) over time to identify stages of nucleation, growth and reshaping (labelled). (b) From a closer view of the first 220 s of the reaction Pd^0% content calculated with LCF; the reduction stage shows a deviation in the curve from 0 to 20 s (black, dashed line) before the typical sigmoidal curve.*

The initial reduction stage is indicated as a sudden increase in Pd^0 content and the average Pd-Pd coordination number. Nucleation is continuous, but the reaction is growth-dominated once a critical radius is achieved. Reoxidation follows growth and dominates at the later stages of reaction where Pd^{2+} concentration is low. The rate and duration of nucleation depends on reaction conditions such as concentration and temperature, as well as the existence of pre-existing solid species within the solution.

SAXS monitoring of nanoparticle radius shows a steady increase before plateauing, likely caused by surfactant induced size limitation. In contrast, LCF

results from the XANES initially show a sigmoidal shape during the chemical reduction of Pd^{2+} to Pd^0 (%Pd(0), Figure 3.3 a). The deviation from sigmoid within the first seconds of reaction is attributed to rapid chemical reduction prior to nucleation (Figure 3.3 b). EXAFS fitting of Pd coordination number (Pd-Pd C.N.) shows a similar trend to oxidation state change, although the initial rates differ during reduction and nucleation stages. The negative reaction rate observed after sigmoidal growth profile is caused by reoxidation of nanoparticles formed.

Alongside the XAS, the microwave plasma-atomic emission spectroscopy (MP-AES) was used to track the Pd concentration in the residue and remaining in solution (Supplementary Figure 3.14) by sampling different reaction times. Although not strictly time-resolved or *in situ,* these results show the expected trend and contribute to confirming the rate of formation of solid species in the system.

3.2.2 Pd^0-Cl in Temperature-Controlled Growth

Every reaction stage is accelerated by increased temperature (Supplementary Figure 3.15), according to the experimental observation of a temperature series. Extended nucleation and slow growth are observed at 30ºC and 40ºC. Increasing reaction temperature shortens nucleation stages to 800 s and <100 s at 50ºC and 60ºC, respectively. The results are more reproducible at lower temperatures (Supplementary Figure 3.16), attributed to the rapid growth at increased temperatures causing a higher degree of irregularity in the system. The collected Pd^0 concentration and average Pd coordination at each temperature show a similar trend (Supplementary Figure 3.17, Supplementary Figure 3.18, Supplementary Table 3.3, Supplementary Table 3.4, Supplementary Table 3.5).

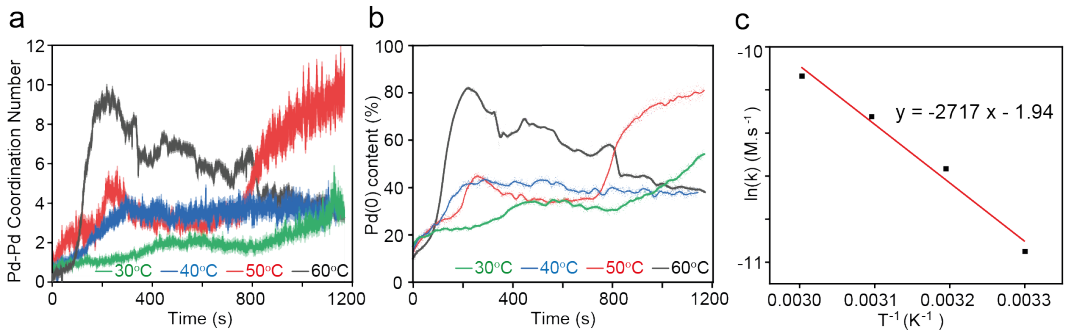

Figure 3.4 ***Temperature-Controlled LCF and EXAFS Fit Results.*** *Pd K-edge XAS results of the temperature effect on Pd reduction rates at 30ºC (green), 40ºC (blue), 50ºC (red) and 60ºC (grey), are compared for (a) EXAFS refinement results of Pd-Pd coordination number and (b) XANES LCF Pd(0) content using Pd foil and K_2PdCl_4 as standards. (c) an Arrhenius plot of nucleation rates versus temperature, where slope values were measured at -2717 K.*

Nucleation rates of -16.22 ± 0.38, -20.66 ± 0.45, -26.65 ± 0.39 and -38.50 ± 0.89 $\mu mol.L^{-1}.s^{-1}$ are measured at 30ºC, 40ºC, 50ºC and 60ºC, respectively (Supplementary Figure 3.19). This agrees with literature values where increased temperatures led to faster reaction rates and smaller Pd nanoparticles.[16,40,41] The steady increase in rate with temperature gives an Arrhenius plot with activation energy of 22.59 $kJ.mol^{-1}$ (gas constant = 8.314 $J.mol^{-1}.K^{-1}$, Supplementary Table 3.6). This value is influenced by the interaction of CTAC with Pd at the metal surface and is lower than, but within a reasonable range of previous literature values. The activation energy was calculated to be 37 kJ mol^{-1} for $Pd(OAc)_2$ with trioctylphosphine ligand with hexanol,[42] and 43.4 $kJ.mol^{-1}$ for the ascorbic acid reduction of Pd nanoparticles on seeds in the presence of CTAB.[38]

Further evidence of the role of CTAC in determining the shape and size of nanoparticles is the uniformity of average radius measured from SAXS (Supplementary Figure 3.20, Supplementary Table 3.7) and electron microscope data under different temperature conditions. Average particle diameters of 105.35

± 25.96 nm, 82.50 ± 21.01 nm, and 76.97 ± 19.63 nm are measured from TEM images.

Diameters from SAXS refinement at the plateaued region show increasing anisotropy with contributions from reoxidative etching, in which nanoparticle shape changes (Supplementary Figure 3.21). The trend of the SAXS curve appears to fit closely with the WF two-step mechanism nanoparticle size simulation by Mozaffari et al.[29] Yet the concentration of Pd converted to Pd^0 is only 55.6% (17.57 mM) at 30ºC and 38.5% (12.08 mM) at 40ºC at 1200 s. This can be understood as a lower volume of nanoparticles forming at low temperature reactions.

Experimental soluble Pd^0 values show a strong resemblance with expected results. The fit of the growth stages quantifies the dependence of each stage of the reaction on temperature (Figure 3.5 a-h), and the corresponding formation of soluble Pd^0 species. These processes compete, allowing the consecutive domination of reduction, nucleation, growth and reoxidation stages.

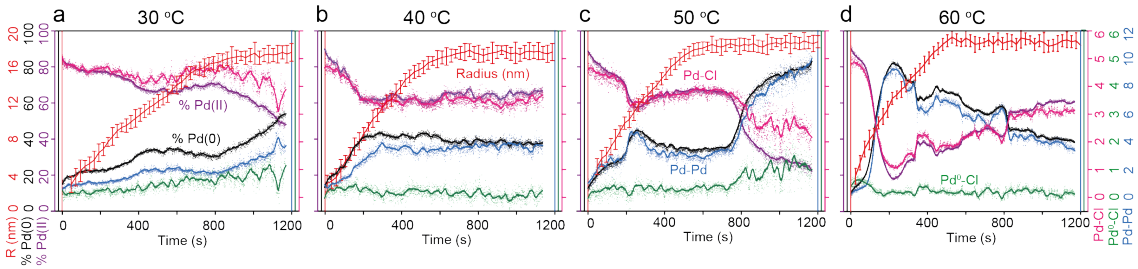

Figure 3.5 ***Characterization Results for a Temperature Range.*** *Pd K-edge XAS and SAXS results are compared for a temperature series of (a) 30ºC, (b) 40ºC, (c) 50ºC and (d) 60ºC, plotting P(r) nanoparticle radius (red, error bars), LCF Pd^0% concentration (black) and Pd^{2+}% concentration (purple), EXAFS-refined Pd-Cl (pink) C.N. and Pd-Pd C.N. (blue), and the calculated Pd^0-Cl C.N. (green).*

The calculated average Pd^0–Cl coordination for each temperature is given (Figure 3.6, Supplementary Table 3.8). The supersaturation of this species seems to occur prior to the rapid growth stage of the reaction which is consistent with the idea of their consumption during growth. The maximum concentration calculated for Pd^0-Cl species is 6.45 mM at 30ºC, 3.77 mM at 40ºC, 10.31 mM at 50ºC and 6.72 mM at 60ºC.

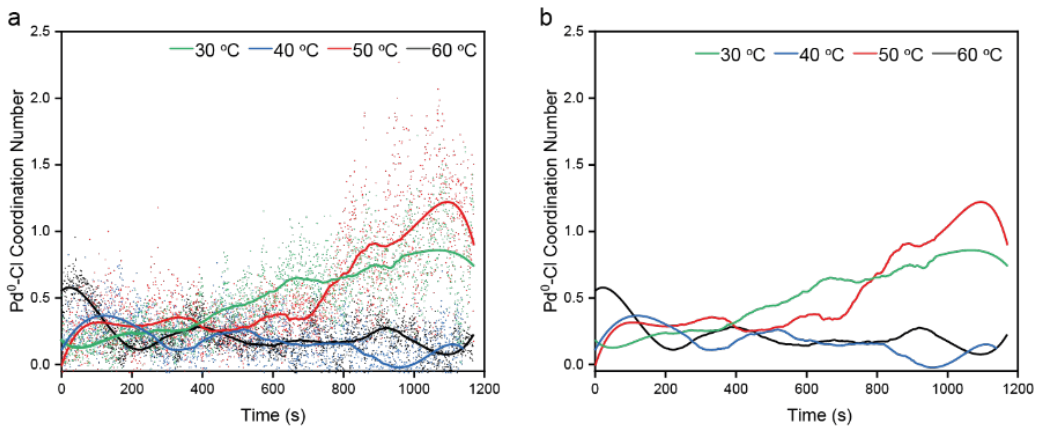

Figure 3.6 ***Calculated Pd^0-Cl Coordination for a Temperature Range.*** *Time-resolved estimated Pd^0-Cl coordination numbers at 30ºC (green), 40ºC (blue), 50ºC (red) and 60ºC (grey), with (a) full data (scatter) and best fit (line) and (b) only best fit lines for improved visualisation.*

It appears that the concentration of Pd^0-Cl is highest in cases where nucleation is rapid, so we study a case where the nucleation stage is replaced by the introduction of pre-existing seed surfaces.

3.2.3 Bypassing Nucleation with Seeded Growth

The addition of seeds to nanoparticle solutions increases monodispersity, based on SAXS measurements, providing a shape template for nanoparticle growth.[9] Pd seed morphology was characterised prior to growth, to understand its effect on the resulting particles. The size of seeds was found to be uniform as limited

by CTAC, and stable after completion. Due to the predicted small size of seeds, a combination of EXAFS (Supplementary Table 3.9) and SAXS fitting (Supplementary Figure 3.22) was used to measure spheres with an average diameter of 3.78 nm. This fits with previous reports of 3.4 nm,[43] 5 nm[28] and 3-4 nm[44] seeds and is comparable with the initial nucleated particles observed during unseeded growth (measured at 5.75 nm).

SAXS observations show that the shape of the nanoparticles do not change significantly with the introduction of pre-formed seeds, but the average size and monodispersity increase. The average diameter of nanoparticles obtained from SAXS fitting with seeded growth is 67.05 nm, compared with 54.1 nm in non-seeded growth (Supplementary Figure 3.22). The increase in size and monodispersity can be ascribed to the larger number of nucleation sites in the presence of seeds allowing even distribution of growth species. In cases where seeds are absent, the continuous nucleation is necessary for continued growth once nanoparticles have reached CTAC-limited size.[36]

The introduction of seeds shows a reaction profile, during controlled heterogeneous nucleation at 50ºC within our system, which bypasses the nucleation stage and immediately follows growth (Figure 3.7). Reproducibility of seeded growth results was most consistent in high concentration samples, which may be due to reduced accuracy in small volume measurements (Supplementary Figure 3.23). According to the literature, adding Pd seeds provides sites for nanoparticle growth and should increase the uniformity of size distribution and nanoparticle morphology.[13,22,45]

XAS results show the reaction rates at 50ºC for cases where 0 µL, 1 µL, 10 µL and 100 µL of seed solution were added to the reaction mixture (Figure 3.7, Supplementary Figure 3.24). Although the Pd growth rate is expected to be higher

when larger number of seeds are introduced, this is contrary to recorded data, indicating that the seed volumes experimentally added were always in excess of a 'high concentration' value. In cases where the size of the nuclei are constant and the growth is diffusion controlled, the growth rate should not change significantly, as experimentally observed.

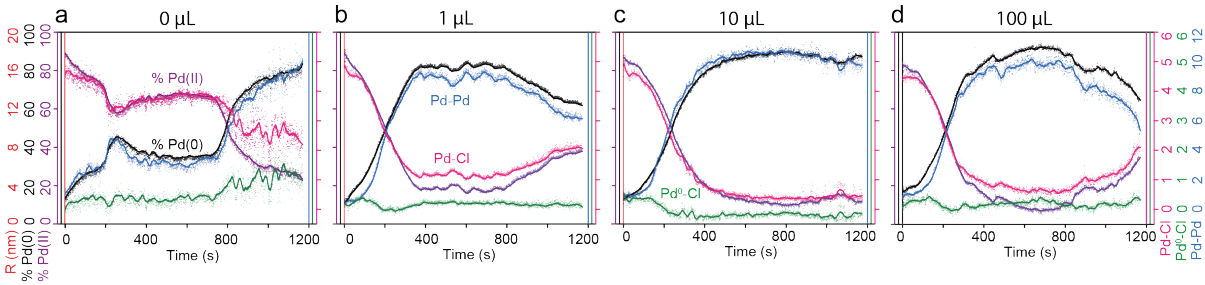

Figure 3.7 ***Combined Characterization Results for Seeded Growth.*** *Combined Pd K-edge XAS characterization results of a seeded growth series, showing LCF Pd^0% concentration (black) and Pd^{2+}% concentration (purple), EXAFS-refined coordination numbers of Pd-Cl (pink) and Pd-Pd (blue), and the calculated Pd^0-Cl coordination (green) at seed concentrations of (a) 0 µL, (b) 1 µL, (c) 10 µL and (d) 100 µL.*

A comparison of all seeded growth conditions for Pd-Pd coordination and Pd^0 conversion show that the rates of rapid growth are consistent throughout the series (Figure 3.8, Supplementary Figure 3.25, Supplementary Figure 3.26).

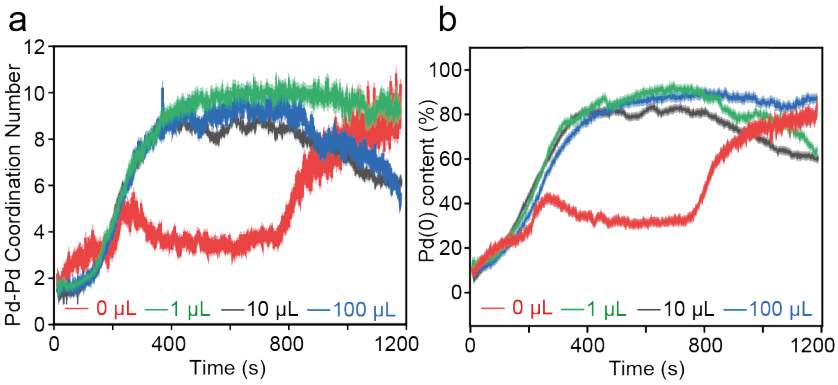

Figure 3.8 ***EXAFS and LCF Fit Results for Seeded Growth.*** *Pd K-edge XAS results of the seeded-growth effect at 50°C on Pd reduction rates with 0 µL (red), 1 µL (green), 10 µL (grey) and 100 µL (blue) of seed solutions added, shown for (a) EXAFS refinement results of Pd-Pd coordination number and (b) XANES LCF Pd(0) content using Pd foil and K_2PdCl_4 as standards.*

This suggests that the growth rate may be diffusion-limited instead of determined by available growth surfaces, and that reduction in solution is occurring simultaneously with the surface reduction. The calculated values of Pd^0-Cl show a similar trend in all seeded growth conditions, peaking before rapid growth (Figure 3.9, Supplementary Table 3.10Table 3.10). The supersaturation of this Pd^0-Cl species has maximum values of 4.83 mM with 1 µL seeds, 5.73 mM at 10 µL seeds and 4.05 mM at 100 µL seeds. The formation of Pd^0-Cl species within the solution is rapidly decreased as the growth species are used for nanoparticle formation directly on the seed templates.

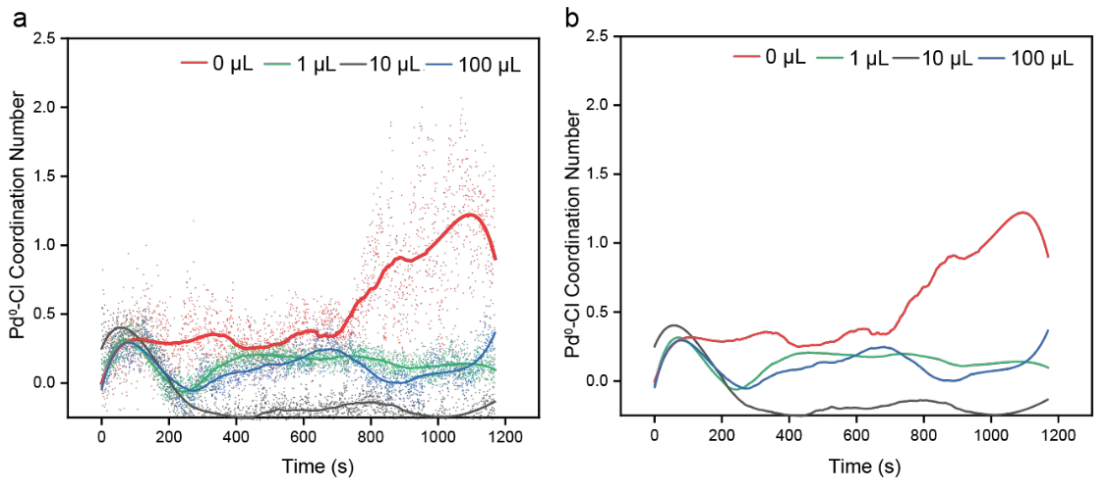

Figure 3.9 ***Pd^0-Cl Coordination for Seed Concentration Range.*** *Time-resolved estimated Pd^0-Cl coordination numbers with 0 µL (green), 1 µL (blue), 10 µL (red) and 100 µL (grey) of seed solution added, shown for (a) full data (scatter) and best fit (line) and (b) only best fit lines for improved visualisation.*

3.2.4 Discussion

The difference in rates of chemical reduction and bond formation indicate the formation of a Pd^0-Cl intermediate during Pd nanoparticle growth, as seen in Figure 3.6 and Figure 3.9. This ligand-capped growth species aligns with the literature which predicts the formation of Pd^0-Cl species in solution.[30] Supersaturation of this species is highest during the nucleation phase, which is consistent with the idea that Pd^0-Cl species are a driving force for continuous nucleation, aggregating to form nuclei. During growth, reduction in solution may occur simultaneously with direct reduction at the bonding surface based on the presence of such a species and it appears that a combination of monomer addition from solution, surface reduction and agglomeration of existing particles contribute to the rapid growth of nanoparticles. The concentration of Pd^0-Cl during nucleation peaks increased at higher temperatures as the reaction was

accelerated. The morphology of the nanoparticles formed is also consistent with a diffusion-dominated growth.

It can be noted that, despite the different chemical and physical processes involved, the rate of reduction, nucleation, rapid growth, and reoxidation, all scale with an increase in temperature. This is contrary to seeded growth, where the rapid growth rate was constant across all concentrations of seed solutions. The effect of seed solutions in obviating the nucleation stage is clearly shown. Yet the presence of Pd^0-Cl peaks with comparable concentrations suggest that solution reduction may dominate in the early stages. This would result in a rapid growth rate independent of available reduction surfaces, which are increased with higher seed concentrations.

In this case of porous Pd nanoparticles, it appears that the growth of initial spherical particles is largely contributed by solution reduced species, while the agglomeration and surface growth lead to dendritic growth. These findings show that Pd^0-Cl species may influence the morphology of particles formed and elucidate the mechanisms of CTAC-capped Pd growth.

3.3 Outcomes

Through a combination of characterization tools, a ligand coordinated reduced Pd species (Pd^0-Cl) concentration profile is monitored during Pd nanoparticle growth for the first time. This finding confirms the presence of solution reduction, particularly in the nucleation phase. Seeded growth results show that the nucleation stage is removed and that the rate of rapid growth is independent of seed concentration. Observations from a temperature series conclude that higher temperatures lead to increased supersaturation of Pd^0-Cl and smaller average

nanoparticle size. An activation energy of 22.59 kJ.mol^{-1} is calculated for the growth of Pd nanoparticles. Such calculations, directly gathered from the chemical reduction, are deemed accurate enough to be used for modelling and predictions of growth.

The presented work serves three purposes in furthering the literature of nanoparticle growth. First, experimental evidence corroborates the formation of a soluble Pd^0-Cl intermediate, suggesting reduction in solution rather than directly at a growth surface, which may be applied to a range of transition metal growth systems. Second, such high time-resolution fitting of XANES and EXAFS data during nanoparticle growth has not previously been published and is versatile in applicability to different materials. The improvement of time-resolution in growth characterization allows more detailed and complete observation of growth kinetics to verify and inform theoretical understanding. Lastly, the chemical understanding of the rate and activation energy in this reaction will contribute to the future rational design of Pd nanoparticles, once a large enough dataset is gathered. Rational design, to predict the properties of nanoparticles formed in solution, could be invaluable for the future application and development of Pd catalysts.

3.4 Experimental Details

3.4.1 Porous Pd Nanoparticle Synthesis

Aqueous 0.1 M K_2PdCl_4 (Solution A) was reacted with Solution B (surfactant, ascorbic acid) in a 1:2 ratio for 20 minutes under set reaction conditions of temperature, concentration, capping agent and presence of seeds. Standard reaction conditions were 333.15 K with 80 mM ascorbic acid and 0.1 M CTAC

(CTAC, MW = 320 g.mol^{-1}, 25 wt% solution in water) and no seed solution. To vary temperatures around the standard 303.15 K, 313.15 K, 323.15 K and 333.15 K with 80 mM ascorbic acid (AA, MW = 176.12 g.mol^{-1}, purity = 99%) were selected. The effect of seeds at a range of concentrations was tested with 1 µL, 10 µL, 100 µL and 1000 µL, of a Pd seed solution directly mixed into solution B.

The system was adapted to an increased concentration, from the method described by Wang et al.[11]

Seed solution was prepared by mixing 250 µL of 0.01 M H_2PdCl_4 solution with 9.5 mL of 0.1 M CTAC and lastly 600 µL of cold 0.01 M $NaBH_4$ solution. The mixture was shaken and left for 2 to 4 hours before use. 0 µL, 1 µL, 10 µL, 100 µL and 1000 µL of seed solution were added to 15 mL of Solution B and reacted at 323.15 K with 80 mM AA.

3.4.2 Lab-Based Characterization

TEM imaging

After reacting the two nanoparticle solutions (A and B), at temperature, the reaction could be stopped at different times and nanoparticles removed, to view the reaction progress. To allow separation without agglomeration, formed nanoparticles were centrifuged for 3 minutes at 11,000 rpm (Fisher Scientific). Solid residue was washed with ethanol thrice before redispersion for loading on a TEM grid. The JEOL 2100 TEM 200 kV at UCL was utilised.

***Ex situ* SAXS** was performed on the SAXS/WAXS (wide angle X-ray scattering) Ganesha 300XL, SAXSLAB at UCL Chemical Engineering, by loading prepared particles in capillary tubes. Samples of seed solution, nanoparticles grown with seeds and nanoparticles grown without seeds were measured. These were

freshly prepared prior to measurement and refrigerated to prevent further reduction. Each measurement was run for 1 hour.

MP-AES readings were recorded on the Agilent 4200 MP-AES (Agilent Technologies, U.S.). Reaction times every two minutes were selected, at 323.15 K with 80 mM AA. Nanoparticle solution was centrifuged at 30,000 rpm for 3 minutes to ensure total separation. Remaining liquid was pipetted out and both solid residue and liquid were dissolved with 70% HNO_3 for final volume of 1 mL. Solutions were diluted to estimated ~10 ppm of Pd, with HNO_3 blank, and the calibration standards were diluted from 1000 ppm Pd standard (Sigma Aldrich, 1 $g.L^{-1}$ Pd, 5% HCl), with DI water. Calibration was linear fitted within an error of 7%. The recorded total dissolved solids were below 2%.

3.4.3 Synchrotron Characterization

XAS measurement

***Ex situ* XAS** of Pd seeds and nanoparticles were performed at B18, BAG beamtime, with an Si(311) monochromator and a Pt mirror coating. The beamline operated at a ring energy of 3 GeV, with current of 298.0 mA. XAS was measured for an energy range of 24,150 eV to 25,200 eV (k range to 14 $Å^{-1}$) for 2104 data points using fluorescence mode Quick EXAFS, detected with a 36-element detector. Artemis fitting was performed for a k-range of 3 to 12.7 $Å^{-1}$. Nanoparticles were loaded on high surface area carbon powder (Ketjenblack) from solution *via* ultrasonication. Samples were loaded in plastic sachets and measured in fluorescence mode due to low Pd loading.

***In situ* XAS**

EDE measurements were collected at I20-EDE, Diamond Light Source, using a Freelon detector and a Si(311) polychromator crystal. Beamline was operating at 3 GeV, with current of 299.4 mA. Spectra were measured at the Pd K-edge (24350 eV) within a range of 24050 eV to 25500 eV (k range to 12 $Å^{-1}$), with 1024 pixels collected per spectrum. The data energy was calibrated with Pd foil and calculated by pixel. 2400 spectra were collected during each reaction, for a total measurement time of 1200 s. An I_0 H_2O background was measured and averaged I_0 used for data correction. 200 µm of Al foil was inserted into the beam-path to attenuate the beam for longer experiments. For a 1200 s measurement, 25 scans of 20 ms were merged to give a frame time of 0.5134 s.

The SFM-4000 stop-flow cell was set up for *in situ* measurement. Cell reservoirs were filled with reaction solutions A and B, as well as water and HCl for washing. The dead volume of the cell was approximately 40 µL, so 400 µL of reactants were injected per trial. Acid and water wash were carried out after each trial. Temperature of the cell and reservoirs were maintained with a Lauda hot water flow, and sample temperature was calibrated before the experiment with a thermocouple at the XAS measurement position.

DAWN software allows the mass processing of large data sets.[46] Larch relative normalisation was performed with pre-edge before E_0-20 eV and post-edge after E_0+100 eV, with a polynomial order of 2, “flattened”. Post-edge background subtraction for k-space was calculated for k-weight of 2, rbkg of 1.0 and Hanning window. Forward Fourier transform for R-space data was calculated with a k-weight of 2 and k range of 3 to 10 $Å^{-1}$. Principal Component Analysis was run to see the changes in the oxidation state in the XANES region of the curve. Selected points were then processed further using Athena and Artemis (Demeter Suite Software) for XANES LCF and EXAFS fitting within a range of k-range of 3 to 10

Å to resolve the bonds present in the sample and estimate the Pd-Pd coordination at different reaction times.[47]

The presence of chloride and oxide bonds is observed but cannot be reliably resolved as the bond lengths are similar. One way to test between the two is to look at changes to the k-space after different weightings.

SAXS measurement

In situ SAXS was performed at the I-22 beamline, Diamond Light Source. Solutions of matrix materials, nanoparticle seeds and known concentrations of nanoparticles were used for SAXS calibration. For *in situ* measurements, solutions were injected into a temperature controlled capillary tube using the SFM-4000 stop-flow cell used for XAS measurements. The use of the same flow cell favours comparable reaction results between both experiments. Solution temperature was maintained during measurements by a heat gun aimed at the measurement position.

3.4.4 Large Dataset Analysis

XAS Batch Analysis

The Energy Dispersive EXAFS (EDE) data were processed using in-house developed python scripts. The raw XAS data as well as the metadata obtained from I20-EDE beamline at Diamond Light Source (UK) were saved in nexus format and were first imported using the h5py package.[48] To analyse the imported XAS spectra, the XANES region before 24,015 eV and the EXAFS region after 25,563 eV were truncated, and then each individual XAS spectra was smoothed by the Savitzky-Golay filter using the .scipy package. The further data processing including pre-edge subtraction, post-edge normalisation, background

determination and Fourier Transform were performed using xraylarch (version 0.9.58).[49]

The normalisation was performed using E_0 value of 24,357 eV, with background subtraction between -200 eV and -75 eV (relative to the edge), normalisation range of 150 to 1,000 eV (relative to edge) and normalisation order of 2. R-space background removal (rbkg) was set to 1 Å. For the k-space transformation, a weighting of 2 was selected along with a Hanning window between 3.0 and 12.5 $Å^{-1}$.

In addition to the *in situ* experiment, XAS of $PdCl_2$ solution and Pd metal foil were measured as reference spectra and were used for the Linear Combination Fitting (LCF). The linear combination fitting was performed using the non-linear least-square fitting method built in the .lmfit package.[50] The LCF energy range was set to 24,300 eV to 24,420 eV (160 data points in total) for all XANES spectra, and the sum of two components ($PdCl_2$ (aq) and Pd metal) were fixed to be 100%.

FEFF Files Selection

FEFF files have been selected in this work based on similarity to the studied system and reaction conditions, as well as their relevance and perceived accuracy. The FEFF files selected in this work are:

Pd-Pd: 9008478, Wyckoff, R.W.G., Fm-3m, ccp

Pd-O: 4124668, Moore, W.J. and Pauling, L., P 42/m m c, tetragonal

Pd-Cl: 1010447, Wells, A.F., 1938, P n m n

To fit the R-space EXAFS spectra, two single scattering paths: Pd-Cl from $PdCl_2$ structure and Pd-Pd from Pd metal were first generated using the FEFF8L package.[51] The two scattering paths were imported as the fitting model. The

EXAFS spectra (1.0 < k < 12.0, 1.0 < R < 3.0) were then fitted using the non-linear least-square fitting method built in the lmfit package.[50]

To accelerate the processing of the large amount of XAS results produced from the beamline in EDE mode (1 second per spectra, in total more than 200,000 spectra), the LCF and EXAFS fitting were parallelly processed by the joblib tool using 16 CPU cores (32 threads).

Additional LCF and EXAFS fitting results from batch processing are too numerous to show in the Supplementary Information, but spectra and fitting parameters are available upon request. A MATLAB script published by Munoz et al.[52] was adapted to calculate continuous-cauchy wavelet transform figures.

SAXS Multi-point Fitting

SAXS data analysis was performed using SAXSGUI (v5.05) using Indirect Fourier transformation (IFT) analysis. SAXS spectra obtained during this work were fitted following this model in the q-range between 0.01 to 0.18 nm^{-1}. IFT of the scattering data allowed the pair distance distribution *P(r)* calculation. The scattering intensity *I(q)* is related to *P(r)* following Equation (1).

$$I\,(q) = 4\pi \int_0^\infty P(r)\,\frac{sinqr}{qr}\,dr \qquad (1)$$

Where q is the absolute value of the scattering vector. This methodology allows the calculation of basic structural parameters of the system such as nanoparticle shape or size following a model-free approach. Thus, P(r) function provides accurate structural information about the maximum dimension (D_{max}) and the radius of gyration (R_g) of the nanoparticle. Moreover, the shape of the P(r) function can also be directly related to the overall shape of the nanoparticles,

such as spherical vs. elongated particles or whether the nanoparticle contains multiple domains.

3.4.5 Calculating Pd^0-Cl Content

Provided here is the methodology and assumptions made for the calculation of soluble Pd^0-Cl content using *in situ* XAS results obtained during Pd nanoparticle growth.

From previous literature, it is considered most likely that Pd^0 is Cl-coordinated, due to the presence of ions from CTAC.[42,53] Based on this proposed synthesis, we deduce that the Pd^0 (aqueous) could be "observed" by a combination of XANES and EXAFS data analysis, mindful of the error limits of these techniques. The XANES region records the reduction of the metal while the EXAFS observes the formation of metal-metal (M-M) bonds. In addition to this direct calculation, each of the three assumptions made can be verified or partially corrected by the data provided by the XAS.

First, the assumption is made that the total number of Pd atoms in the measured system is a constant, as this is a closed system. This has potential errors as we only see the Pd atoms in the beam path, but we do not observe a trend of change in Pd concentration, as particle movement seems to be random. To bring this value closer to reality, we use the edge jump as a measure of the trend of changes of Pd concentration in the system, as low Pd concentration leads to less absorption and a smaller edge jump. A trend of decreasing edge jump during the reaction could be attributed to the precipitation and migration of larger Pd nanoparticles in the solution, away from the beam path.

At any given time, the total number of Pd atoms (NPd) is the sum of Pd^{2+} (NPd^{2+}-Cl) and Pd^0 (NPd^0-Cl, NPd^0-Pd) atoms.

$$NPd = NPd^{2+}\text{-}Cl + NPd^{0}\text{-}Cl + NPd^{0}\text{-}Pd \qquad \textit{Equation 3.3}$$

Similarly, the fraction of Pd^0 and Pd^{2+} at any time is given by χ,

$$\chi Pd^{2+} = \frac{NPd^{2+}\text{-}Cl}{N} \qquad \textit{Equation 3.4}$$

And

$$\chi Pd^{0} = \frac{(NPd^{0}\text{-}Cl + NPd^{0}\text{-}Pd)}{N} \qquad \textit{Equation 3.5}$$

Therefore

$$\chi Pd^{2+} + \chi Pd^{0} = 1 \qquad \textit{Equation 3.6}$$

The second assumption is that Pd dissolved in solution is always coordinated to neighbouring atoms, with full Pd-Cl/O coordination. This assumption is made so that the possible Pd^0 concentration is underestimated rather than overestimated. Pd atoms may be bonded or interact with close-neighbour atoms, whether another Pd atom, Cl or O from aqueous solution. This cannot be experimentally verified with the methods used here, except by observing under-coordination. We do not assume that Pd is always (or ever) fully coordinated, but that 'aqueous Pd^0' may still have Pd-Cl or Pd-O interactions measured by the EXAFS. Since Cl^- ligand species were previously bonded to the Pd in the salt, these are considered the most likely coordination. However, if the Pd^0 is instead coordinated with O or N in the solution, they are included in the Pd-Cl bond fitting, within the fitting error for bond length.

For this calculation, coordination number (C.N.) for a bond is shown with square brackets, so C.N. of Pd-Pd bond is [Pd-Pd]. The fraction of coordination (φ) to each element from Pd is given by:

$$Total\ C.N. = (2 \times [Pd\text{-}Cl]) + [Pd\text{-}Pd] \qquad \textit{Equation 3.7}$$

$$\varphi_{Pd\text{-}Cl} = \frac{[Pd\text{-}Cl]}{[Pd\text{-}Cl]_{initial}} \qquad \textit{Equation 3.8}$$

$$\varphi_{Pd\text{-}Pd} = \frac{[Pd\text{-}Pd]}{[Pd\text{-}Pd]_{final}} \qquad \textit{Equation 3.9}$$

$$\varphi_{Pd\text{-}Cl} + \varphi_{Pd\text{-}Pd} = 1 \qquad \textit{Equation 3.10}$$

The third assumption is that the breaking and formation of chemical bonds is faster than the recorded (millisecond) time-scale. We do not observe intermediate states of bond formation. This has been shown to be on the femtosecond time-scale for photoinduced formation of Au bonds from $([Au(CN)^{2-}]_3$.[54]

At the initial stage of the reaction, when no nanoparticles are present, Pd^0 = 0%, the XANES LCF normalised average content of Pd^{2+} is theoretically 100%, so $\chi Pd^{2+}{}_{initial} = 1$, and $\chi Pd^{0}{}_{initial} = 0$.

The initial total coordination fractions are given by $\varphi_{Pd\text{-}Cl} = 1$ and $\varphi_{Pd\text{-}Pd} = 0$.

In the reduction stage, these values are equivalent to

$$\varphi_{Pd-Cl} = \frac{[Pd\text{-}Cl]}{[Pd\text{-}Cl]_{initial}} \qquad \textit{Equation 3.11}$$

$$\varphi_{Pd-Pd} = \frac{[Pd\text{-}Pd]}{[Pd\text{-}Pd]_{final}} \qquad \textit{Equation 3.12}$$

And $$\varphi_{Pd^0-Cl} = \frac{[Pd^0\text{-}Cl]}{[Pd\text{-}Cl]_{initial}} \qquad \textit{Equation 3.13}$$

To calculate the fraction of Pd^0-Cl,

$$\varphi_{Pd^0\text{-}Cl} = \varphi_{Pd\text{-}Cl} - \chi Pd^{2+} \qquad \textit{Equation 3.14}$$

Substituting Equations 4.11 and 4.13,

$$[Pd^0\text{-}Cl] = [Pd\text{-}Cl] - \chi Pd^{2+}[Pd\text{-}Cl]_{initial} \qquad \textit{Equation 3.15}$$

Or

$$[Pd^0\text{-}Cl] = [Pd\text{-}Cl] - \frac{(Pd^{2+})}{(Pd^{2+})^{initial}}[Pd\text{-}Cl]_{initial}$$ *Equation 3.16*

This equation was used to calculate the C.N. of Pd^0-Cl.

Assuming that the Pd-Cl C.N. remained full with the Pd^0 in solution, the resulting concentration could be calculated from the fraction of the Pd^0-Cl C.N. obtained by the initial Pd-Cl C.N. (around 6).

In an ideal case, the initial Pd^{2+} would make up 100% of the solution, but as this was not found to be the case in our system, which likely misses the first moments of the reaction, there is a correction factor based on the first measured amount. In addition, the idealised Pd-Cl coordination is not used, but the initial fitting value, which is an average of the system. The supersaturation of these species has been hypothesised by the classical nucleation theory but to our knowledge has not been previously observed experimentally.

Since EXAFS cannot reliably distinguish the ligand species, Pd^0 coordinated with O or Cl are both counted under Pd^0-Cl coordination. The observations of such a reduced species and its kinetic profile reveal the reaction stages where growth processes dominate over agglomeration and Pd^0-Cl supersaturation drives the formation of new nuclei.

3.5 Supplementary Information

3.5.1 TEM Images and *ex situ* Characterization

Table 3.1 ***Temperature Settings for Pd Nanoparticle Growth with XAS.***

Set temperature (ºC)	Reservoir temperature (ºC)	Cell temperature (ºC)
23	23	23.0
30	30	29.5
40	40	38.0
50	50	49.2
60	60	59.1
70	70	69.5

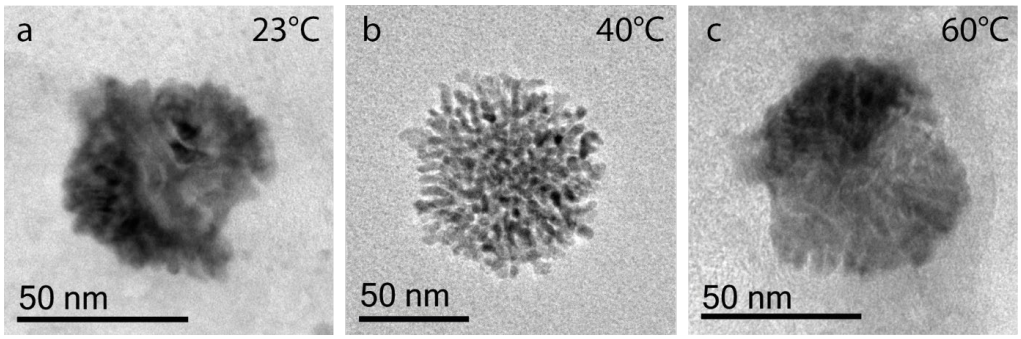

Figure 3.10 ***Nanoparticles formed at different temperatures.*** *TEM bright-field imaging shows 50 nm-scale morphology of CTAC-capped Pd nanoparticles reduced under reaction temperatures of (a) 23ºC, (b) 40ºC and (c) 60ºC.*

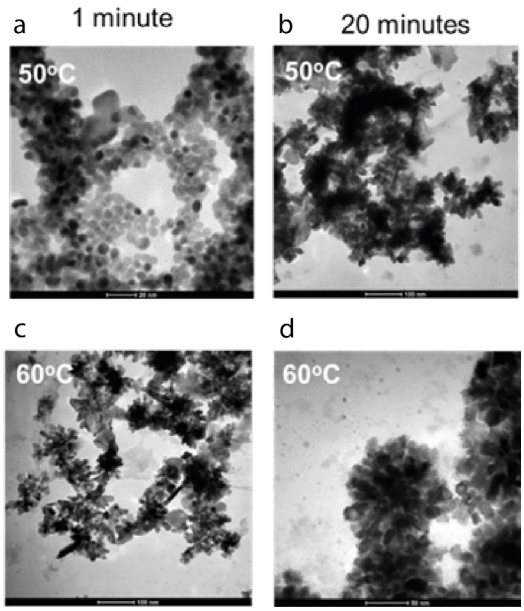

Figure 3.11 ***Initial and Final Nanoparticle Morphology****. TEM bright-field imaging shows the morphology of nanoparticles formed at 50ºC after reaction time of (a) 1 min and (b) 20 min, in comparison to 60ºC after (c) 1 and (d) 20 minutes of reaction.*

Table 3.2 ***Average Nanoparticles Sizes.*** *Measured from TEM images using ImageJ, for at least 140 particles, with diameter and radius provided in nanometres (nm).*

Condition	Particles Measured	Diameter (nm)	Error (nm)	Radius (nm)	Error (nm)
50°C, 1 min	2215	5.747	1.299	2.874	0.650
20°C, 20 min	144	105.353	25.957	52.677	12.979
40°C, 20 min	553	82.505	21.019	41.252	10.509
60°C, 20min	444	76.970	19.627	38.485	9.814

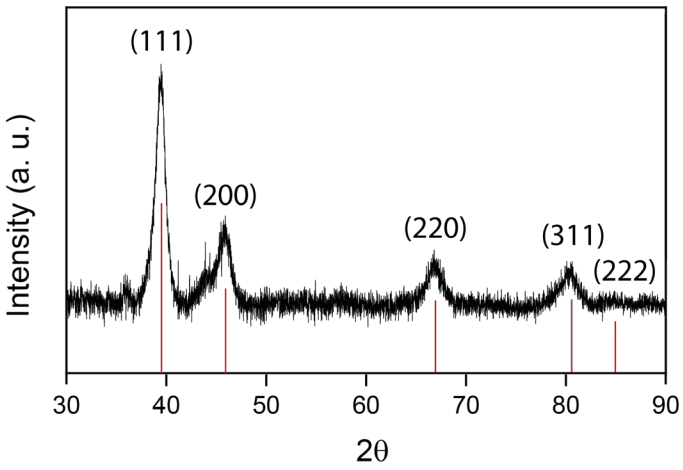

Figure 3.12 ***XRD Results.*** *XRD results for CTAC-capped Pd nanoparticles formed after 20 min reaction time at 60ºC. Literature 2θ values for Pd (red lines) are shown for Miller indices of (111), (200), (220), (311) and (222).*

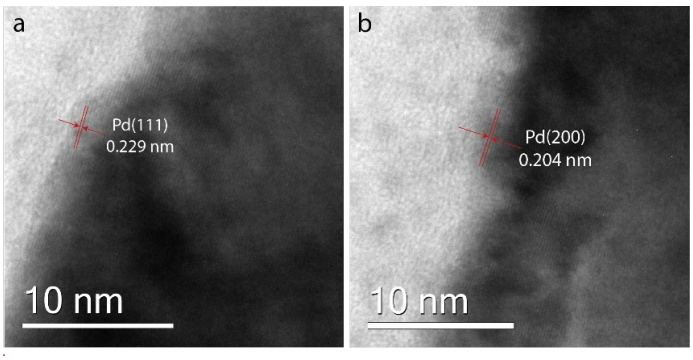

Figure 3.13 ***Lattice spacing in crystalline Pd nanoparticles.*** *10 nm-scale visualisations of Pd nanoparticle shows spacing of (a) 0.229 nm corresponding to Pd(111) and (b) 0.204 nm corresponding to Pd(200) facets at 60ºC.*

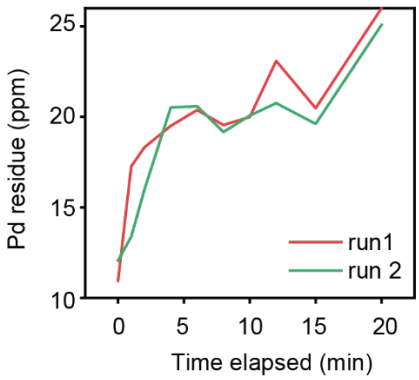

Figure 3.14. ***Time-Resolved MP-AES Results.*** *MP-AES results show trend of the metallic Pd content (ppm) at different reaction times for a 60°C. Results were replicated shown as red and green. The time-resolution of measurements was 2 to 4 minutes.*

3.5.2 Temperature-Controlled XAS and SAXS Results

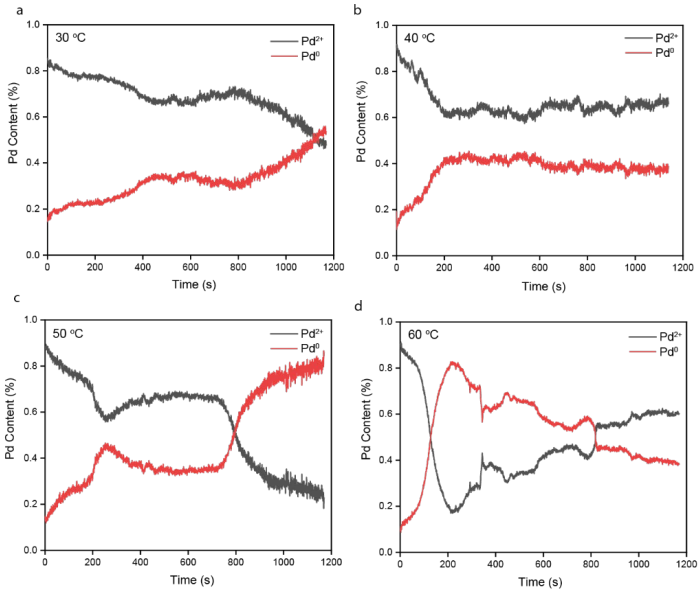

Figure 3.15 ***LCF Results for a Temperature Range.*** *Pd K-edge XANES LCF results for Pd reduction, showing Pd^{2+} (black) and Pd^{0} (red) at temperatures of (a) 30°C, (b) 40°C, (c) 50°C and (d) 60°C. Aqueous H_2PdCl_4 solution (Pd^{2+}) and Pd foil (Pd^{0}) were used as LCF standards.*

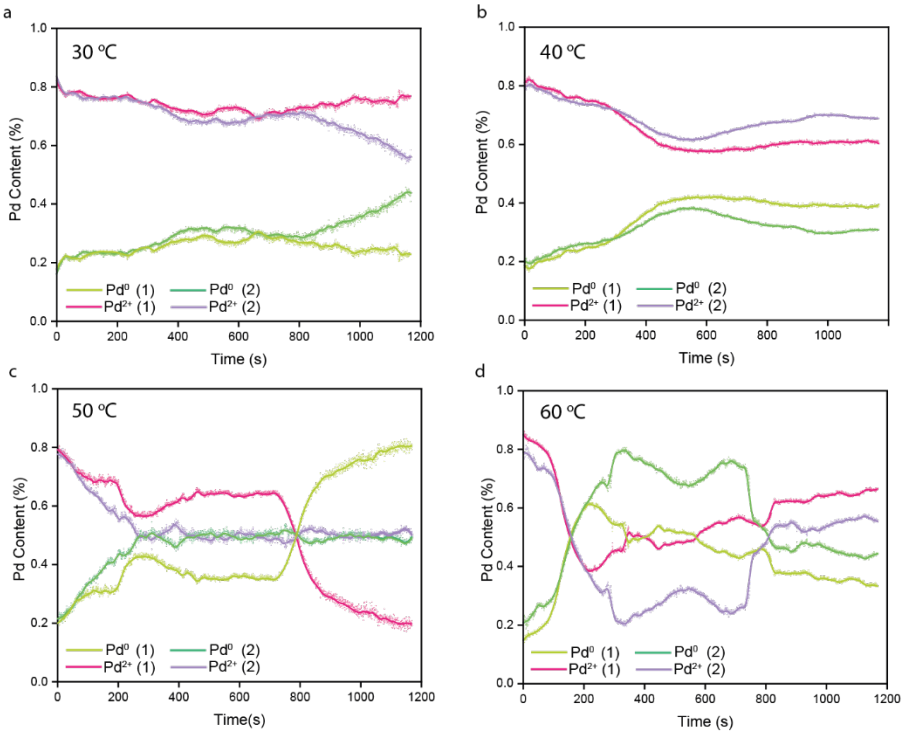

Figure 3.16 ***Reproducibility of LCF Results for a Temperature Range.*** *Reproducibility of Pd K-edge XANES LCF results for Pd^{2+} (pink and purple) and Pd^{0} (light and dark green) for two trials at temperatures of (a) 30°C, (b) 40°C, (c) 50°C and (d) 60°C. Aqueous H_2PdCl_4 solution (Pd^{2+}) and Pd foil (Pd^{0}) were used as LCF standards.*

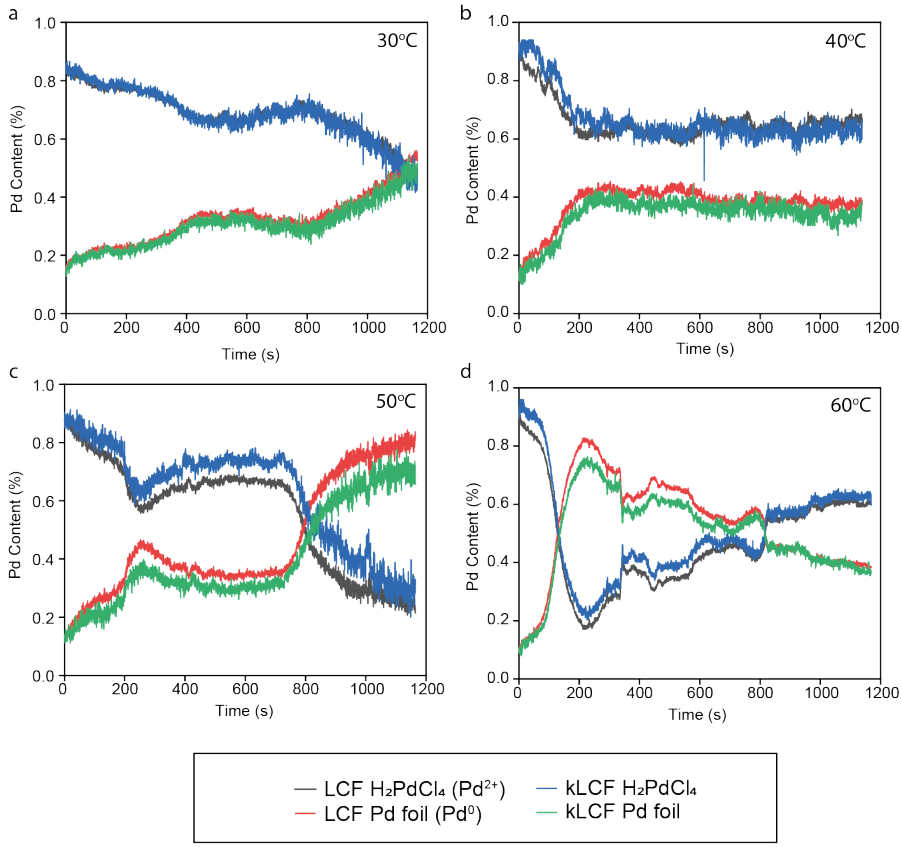

Figure 3.17 ***LCF and kLCF for a Temperature Range.*** Pd K-edge XANES LCF results showing content of Pd^{2+} (grey) and Pd^{0} (red) versus k-space LCF (range 0 to 10 $Å^{-1}$) content of Pd^{2+} (blue) and Pd^{0} (green) at temperatures of (a) 30ºC, (b) 40ºC, (c) 50ºC and (d) 60ºC.

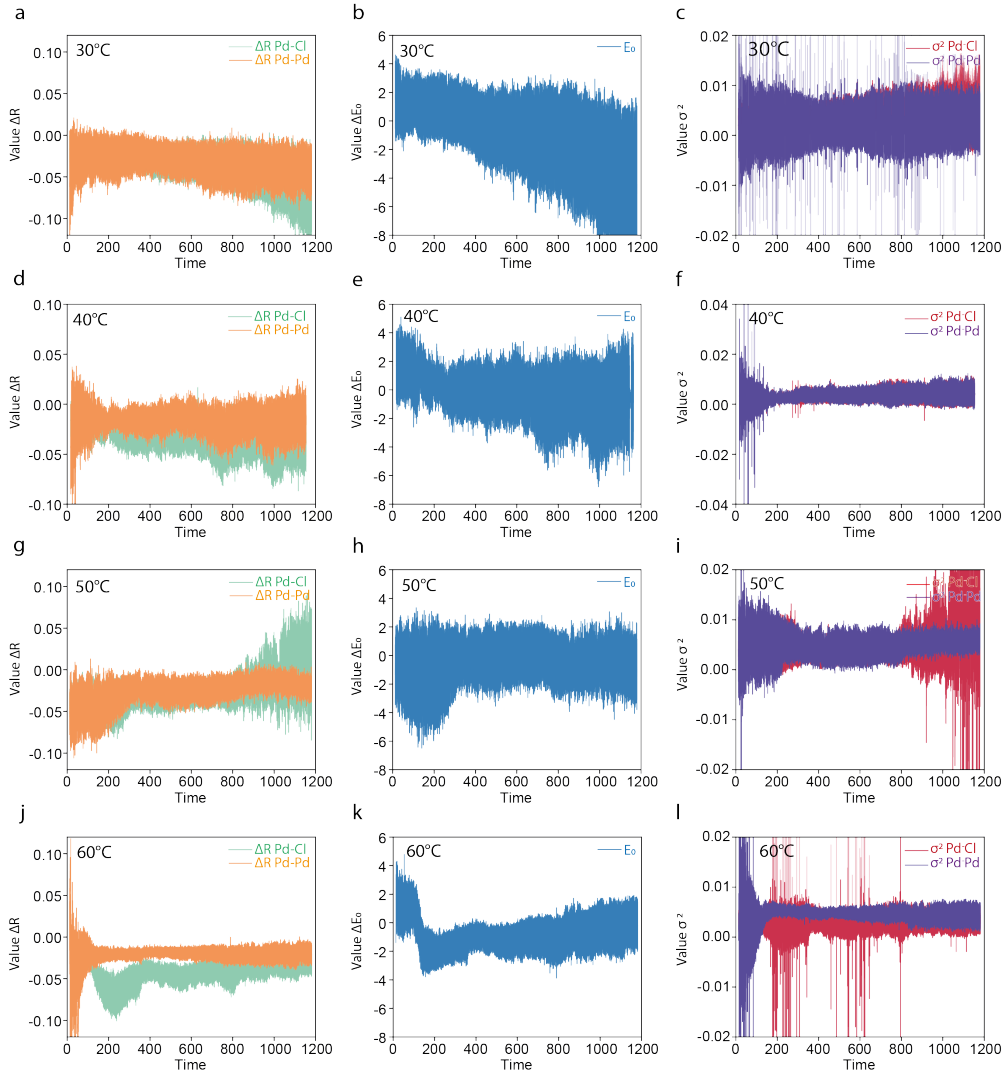

Figure 3.18 ***Time-Resolved EXAFS Fit Parameters for Pd NP Growth.*** *Fitting results for 2400 time-resolved XAS spectra for ΔR Pd-Cl (turquoise), ΔR Pd-Pd (orange), ΔE_0 (blue), σ^2 Pd-Cl (red) and σ^2 Pd-Pd (purple) at temperatures of (a-c) 30°C, (d-f) 40°C, (g-i) 50°C and (j-l) 60°C.*

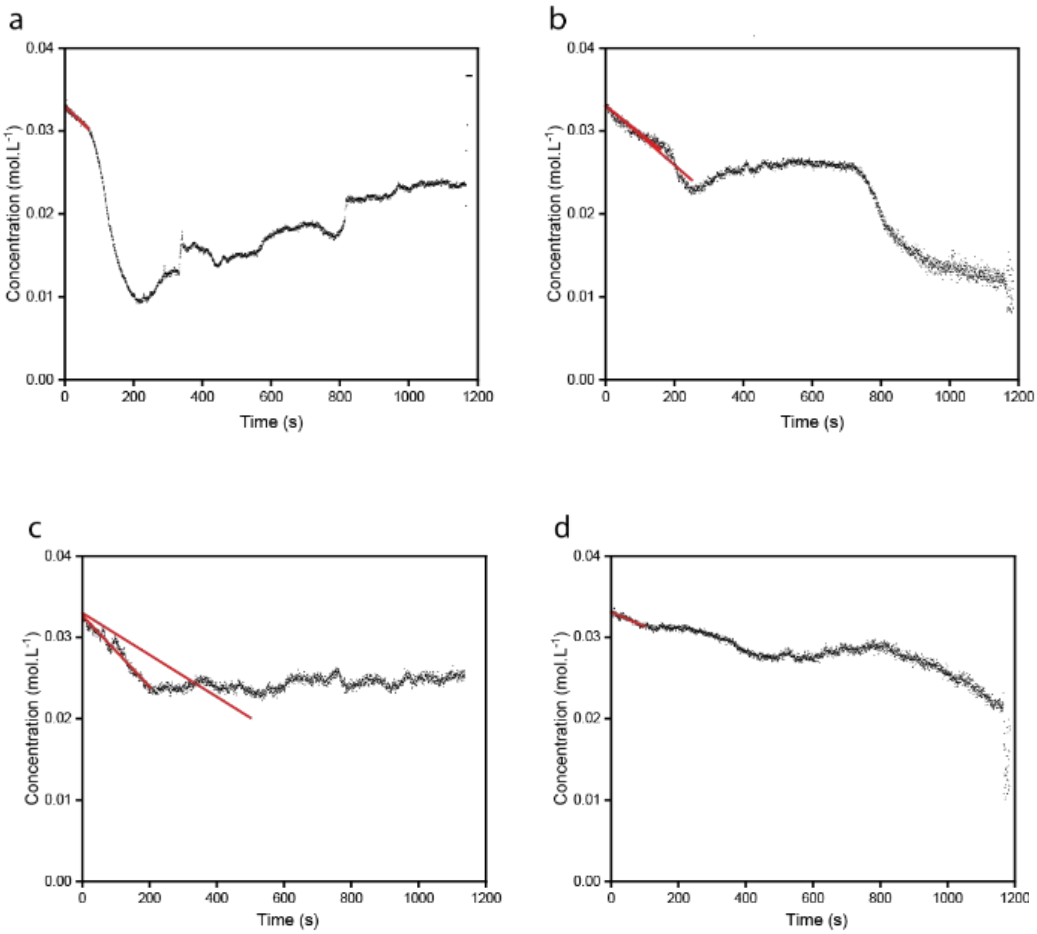

Figure 3.19 ***Reduction Rates and Arrhenius Plot.*** *Pd^{2+} reduction rate measured at the initial region (red) of Pd K-edge LCF at temperatures of (a) 60ºC, (b) 50ºC, (c) 40ºC and (d) 30ºC.*

Table 3.3 ***LCF Results for Temperature-Controlled Pd Growth.*** *Pd K-edge LCF performed in Athena, using H_2PdCl_4 solution as Pd^{2+} standard and Pd foil as Pd^0 standard for temperature conditions, fitting E_0-20 eV to E_0+30 eV.*

Temperature Condition (ºC)	Reaction Time (s)	R-factor	Weight Pd^{2+} (×100 %)	Pd^{2+} Error (×100 %)	Weight Pd^0 (×100 %)	Pd^0 Error (×100 %)
30	5	0.0014	0.734	0.020	0.265	0.020
	100	0.0020	0.670	0.024	0.329	0.024
	600	0.0009	0.614	0.016	0.385	0.016
	1100	0.0005	0.559	0.012	0.440	0.013
40	0	0.0110	0.746	0.059	0.254	0.059
	100	0.0138	0.689	0.066	0.311	0.066
	600	0.0134	0.595	0.064	0.405	0.064
	1100	0.0169	0.677	0.073	0.323	0.073
50	0	0.0040	0.737	0.034	0.262	0.049
	135	0.0117	0.666	0.060	0.333	0.070
	455	0.0045	0.612	0.036	0.387	0.051
	725	0.0042	0.603	0.035	0.396	0.050
	755	0.0050	0.541	0.038	0.458	0.052
	795	0.0083	0.421	0.048	0.578	0.060
	870	0.0124	0.266	0.058	0.733	0.068
	920	0.0117	0.241	0.056	0.758	0.066
60	5	0.0023	0.255	0.026	0.744	0.026
	55	0.0015	0.278	0.021	0.721	0.021
	95	0.0006	0.323	0.014	0.676	0.014
	145	0.0017	0.475	0.021	0.524	0.021
	185	0.0020	0.571	0.022	0.428	0.022
	230	0.0022	0.601	0.023	0.398	0.023
	400	0.0011	0.533	0.017	0.466	0.017
	700	0.0004	0.472	0.011	0.527	0.012
	1100	0.0010	0.391	0.018	0.608	0.017

Table 3.4 ***EXAFS Results for Temperature-Controlled Pd Growth (1).*** *Results of Pd K-edge Artemis EXAFS fitting, where amplitude reduction factor is set at 0.667. Bond lengths of 2.75 Å (Pd-Pd), 2.30 Å (Pd-Cl) and 2.05 Å (Pd-O) were selected. Common values of σ^2 were calculated as σ^2(Cl) 0.002, σ^2(Pd) 0.0037 and σ^2(O) 0.002.*

ºC	Time (s)	ΔE_0	Pd-Pd C.N.	Pd-Cl C.N.	Pd-O C.N.	ΔR Pd-Pd	ΔR Pd-Cl	ΔR Pd-O
30ºC	5	4.47	0.62	4.01	1.39	-0.013	0.003	0.012
	Error	2.74	0.57	0.69	1.20	-	0.020	-
	100	3.68	0.99	3.88	1.18	-0.013	-0.001	0.013
	Error	2.07	0.38	0.51	0.92	-	0.015	-
	600	0.77	2.07	3.17	0.76	-0.013	-0.014	-0.049
	Error	1.31	0.39	0.35	0.63	-	0.021	-
	1100	0.49	3.84	2.39	1.10	-0.008	-0.008	-0.061
	Error	0.65	0.40	0.30	0.42	-	0.008	-
40ºC	0	0.47	0.83	3.26	2.40	-0.04	0.02	0.04
	Error	1.76	0.41	0.44	0.79	0.04	0.01	0.04
	100	-2.11	1.25	3.19	1.88	-0.01	100	-2.11
	Error	1.78	0.33	0.45	0.84	-	0.01	-
	600	1.96	3.46	2.92	0.83	0.003	-0.02	-0.02
	Error	0.82	0.34	0.27	0.48	0.004	0.007	-
	1100	1.96	3.32	2.70	1.27	-0.001	-0.02	-0.007
	Error	1.41	0.52	0.45	0.83	-	0.013	-

Table 3.5 ***EXAFS Results for Temperature-Controlled Pd Growth (2).*** *(above)*

ºC	Time (s)	ΔE_0	Pd-Pd C.N.	Pd-Cl C.N.	Pd-O C.N.	ΔR Pd-Pd	ΔR Pd-Cl	ΔR Pd-O
50ºC	0	5.16	1.25	2.76	2.18	-0.013	0.001	0.013
	Error	1.36	0.40	0.31	0.51	-	0.011	-
	135	4.10	1.97	3.16	1.80	-0.013	-0.023	0.013
	Error	2.13	0.45	0.53	0.90	-	0.016	-
	455	3.10	3.14	2.96	1.29	-0.013	-0.028	0.013
	Error	1.27	1.07	0.43	0.72	-	0.010	-
	725	1.87	3.16	2.98	0.85	-0.013	-0.033	0.013
	Error	0.99	0.89	0.31	0.52	-	0.008	-
	755	0.14	3.95	3.02	0.96	-0.013	-0.031	0.013
	Error	1.08	0.44	0.38	0.67	-	0.009	-
	795	2.18	5.54	2.23	1.49	-0.013	-0.036	0.013
	Error	1.4	2.06	0.67	1.06	-	0.018	-
	870	3.70	6.52	1.51	1.86	-0.013	-0.024	0.013
	Error	2.02	0.73	0.57	0.98	-	0.028	-
	920	2.54	7.10	1.45	1.81	-0.013	-0.025	0.013
	Error	1.97	0.84	0.61	1.04	-	0.031	-
60ºC	5	2.22	0.26	4.73	-	-0.043	-0.015	-
	Error	1.62	0.41	0.30	-	0.086	0.010	-
	55	1.61	0.78	4.54	-	-0.015	-0.017	-
	Error	1.39	0.37	0.26	-	0.027	0.009	-
	95	1.06	1.67	3.97	-	-0.014	-0.024	-
	Error	1.36	0.34	0.24	-	0.014	0.009	-
	145	-1.91	4.88	2.16	-	-0.019	-0.052	-
	Error	1.57	0.42	0.31	-	0.009	0.016	-
	185	-2.40	8.26	1.35	-	-0.019	-0.061	-
	Error	1.33	1.64	0.37	-	0.008	0.023	-
	230	-1.41	6.51	1.44	-	-0.019	-0.060	-
	Error	1.43	0.45	0.33	-	0.007	0.022	-

°C	Time (s)	ΔE_0	Pd-Pd C.N.	Pd-Cl C.N.	Pd-O C.N.	ΔR Pd-Pd	ΔR Pd-Cl	ΔR Pd-O
	700	-1.45	4.69	2.56	-	-0.015	-0.037	-
	Error	1.20	1.04	0.27	-	0.008	0.011	-
	1100	-0.35	3.41	3.28	-	-0.011	-0.029	-
	Error	1.33	1.06	0.28	-	0.009	0.010	-

Table 3.6 ***Activation Energy Calculation.*** *Values of inverse temperature and reaction rates for the Arrhenius plot are given alongside the error values measured.*

Temperature Condition (°C)	1/T (K^{-1})	Reaction Rate, k ($M^{-1}.s^{-1}$)	Error ($M^{-1}.s^{-1}$)
30	0.00330	-16.22	0.38
40	0.00319	-20.66	0.45
50	0.00310	-26.65	0.39
60	0.00300	-38.50	0.89

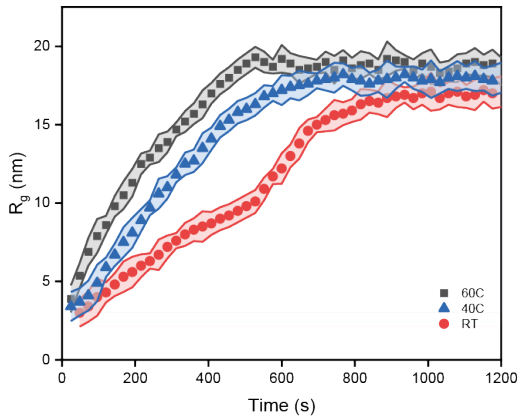

Figure 3.20 ***Time-Resolved SAXS for a Temperature Range.*** *Comparison of SAXS radius results calculated for 23°C/RT (red, circles), 40°C (blue, triangles) and 60°C (grey, squares) shows the physical growth rate of nanoparticles.*

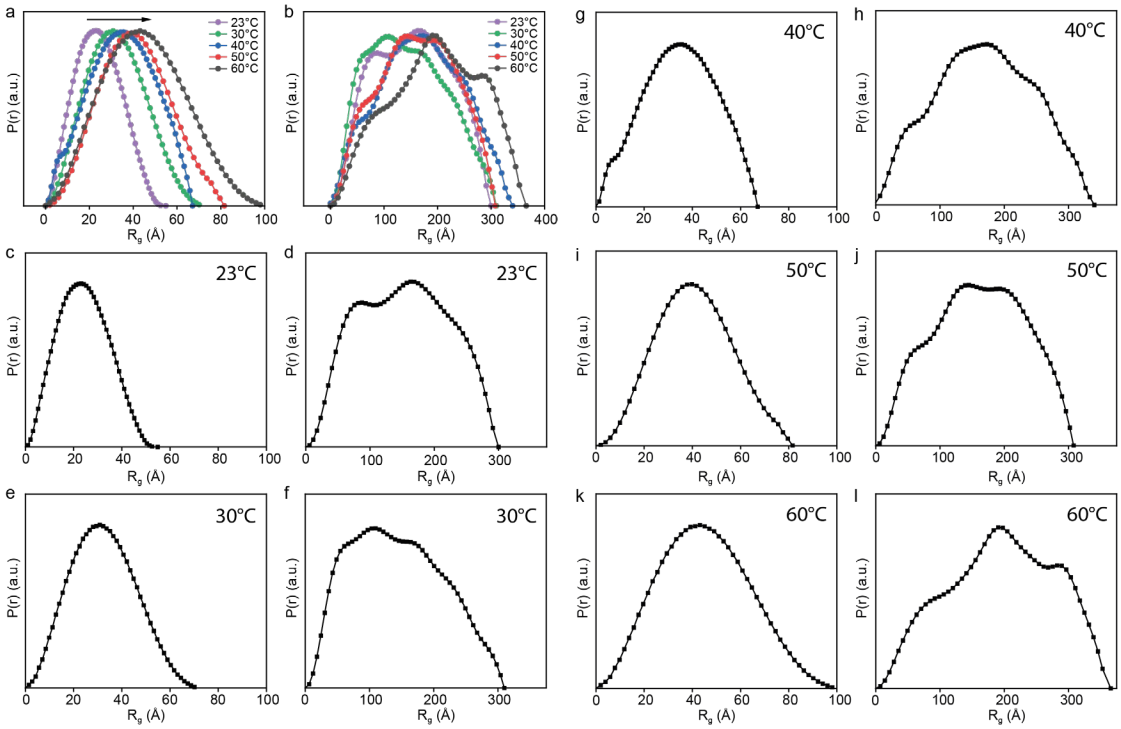

Figure 3.21 ***Temperature-Controlled Initial and Final SAXS Data.*** *P(r) results from SAXS show reduced symmetry with increased reaction time, as shown for a combined view of P(r) for a temperature series at (a) initial reaction time of 5 s and (b) final reaction time of 1100 s, followed by the separated results of (c, d) 23°C, (e, f) 30°C, (g, h) 40°C, (i, j) 50°C and (k, l) 60°C.*

Table 3.7 ***SAXS Results for Temperature-Controlled Pd Growth.*** *SAXS fitting calculated maximum radius and diameter of the plateaued region in Figure S12 under temperature conditions of 23°C, 40°C and 60°C.*

Reaction Condition, Time	Reaction Time (s)	Diameter (nm)	Standard Deviation (nm)	Radius (nm)	Standard Deviation (nm)
23°C, 20 min	840	34.4	1.462	17.2	0.731
40°C, 20 min	696	36.4	1.432	18.2	0.716
60°C, 20 min	480	38.6	1.328	19.3	0.664

Table 3.8 ***Temperature-Controlled Peak Pd^0-Cl Concentration.*** *Calculated Pd^0-Cl percentages and minimum concentration values in solution for temperature series and seed concentration series.*

Temperature (ºC)	Max. Pd^0-Cl (%)	Approximated Pd^0-Cl Concentration (mM)
60	21.39	6.72
50	32.84	10.31
40	12.00	3.768
30	20.54	6.45

3.5.3 Seed-Controlled XAS and SAXS Results

Table 3.9 ***EXAFS Fit Results of Pd Seeds on Carbon.*** *Pd K-edge Artemis fitting was performed using amplitude reduction factor of 0.667, as measured for a Pd foil standard. Low Pd-Pd (R = 2.75 Å) coordination number of 0.35 indicates that the small nanoparticle size is maintained, and the Pd-Cl (R = 2.30 Å) and Pd-O (R = 2.05 Å) coordination represent the surfaces exposed to Cl ligands and air.*

Parameter	Value	Error
ΔE_0	3.64	1.19
Pd-Pd	0.35	0.21
Pd-Cl	2.52	0.14
Pd-O	1.22	0.22
ΔR Pd-Pd	-0.014	0.034
ΔR Pd-Cl	-0.003	0.008
ΔR Pd-O	0.004	0.021
σ^2 Pd-Pd	0.005	
σ^2 Pd-Cl	0.002	
σ^2 Pd-O	0.002	

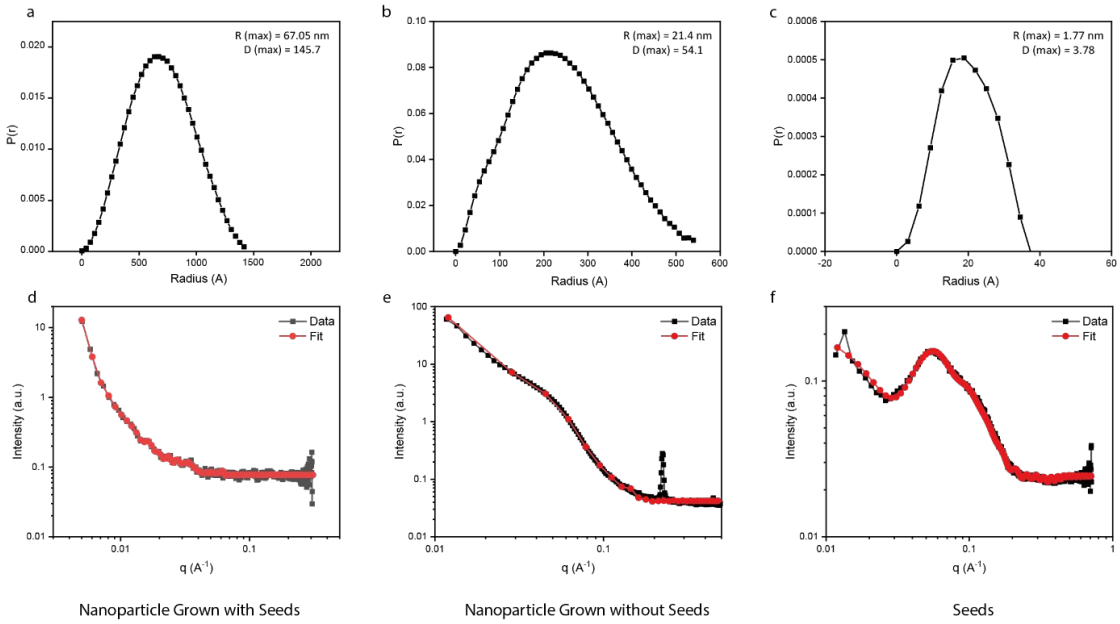

Figure 3.22 ***P(r) Results of Seeded Growth.*** *P(r) plot shows the distribution of diameters calculated for (a) seeded nanoparticle growth (145.7 nm) (b) non-seeded nanoparticle growth (54.1 nm) and (c) seed solution (3.78 nm) alongside (d-f) the respective data (black) and fit (red).*

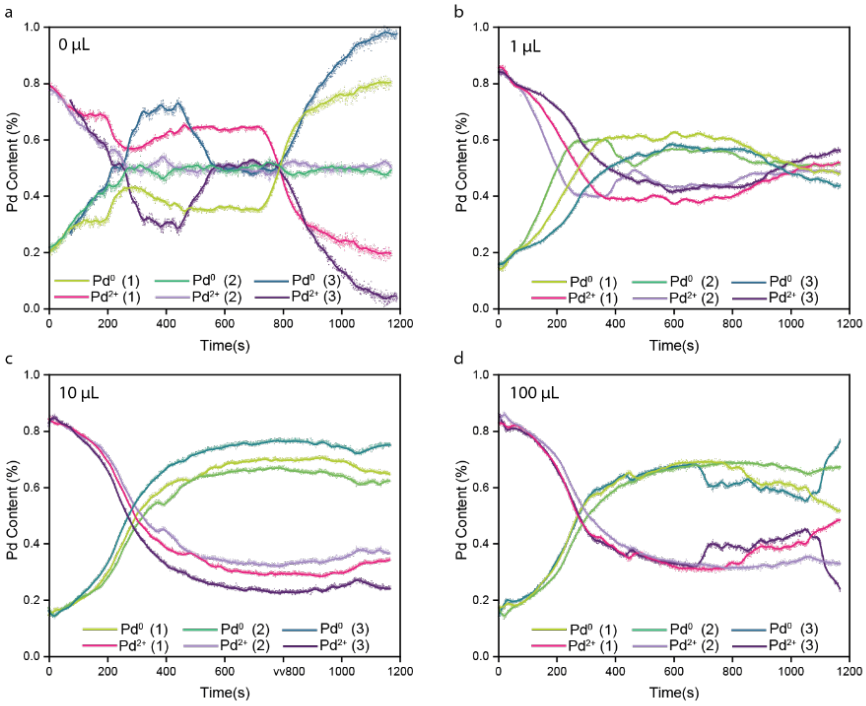

Figure 3.23 ***Reproducibility of LCF Results by Seed Concentrations.*** *Pd K-edge XANES LCF Pd^0 (shades of green) and Pd^{2+} (shades of purple) reproduced for three trials for solutions with seed concentrations of (a) 0 µL, (b) 1 µL, (c) 10 µL and (d) 100 µL at 50°C.*

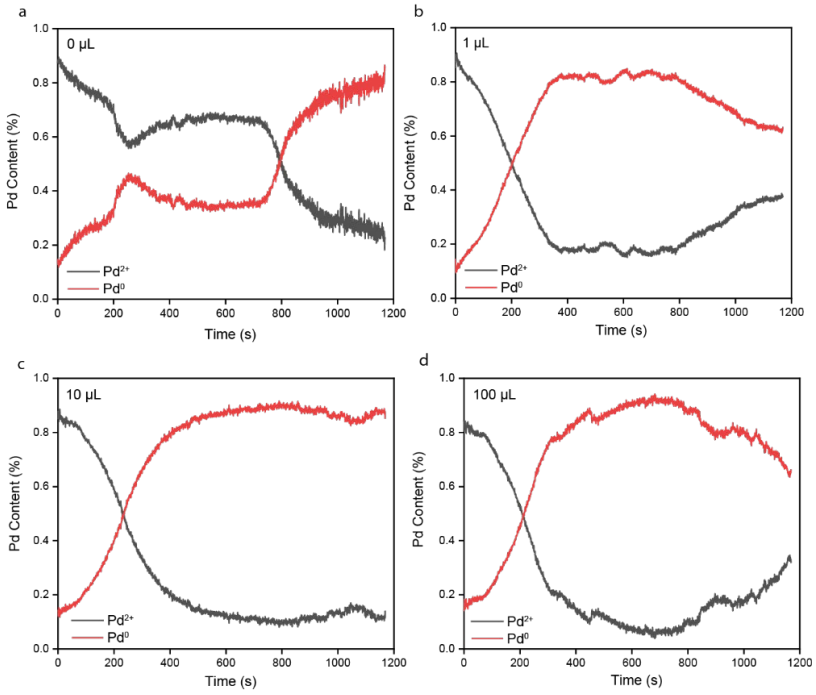

Figure 3.24 ***Selected LCF Results for Seed Concentration Range.*** *Pd K-edge XANES LCF show Pd^{2+} content (grey) and Pd^{0} content (red), for seeded solutions with seed concentrations of (a) 0 µL, (b) 1 µL, (c) 10 µL and (d) 100 µL at 50ºC. Aqueous H_2PdCl_4 solution (Pd^{2+}) and Pd foil (Pd^{0}) were used as standards.*

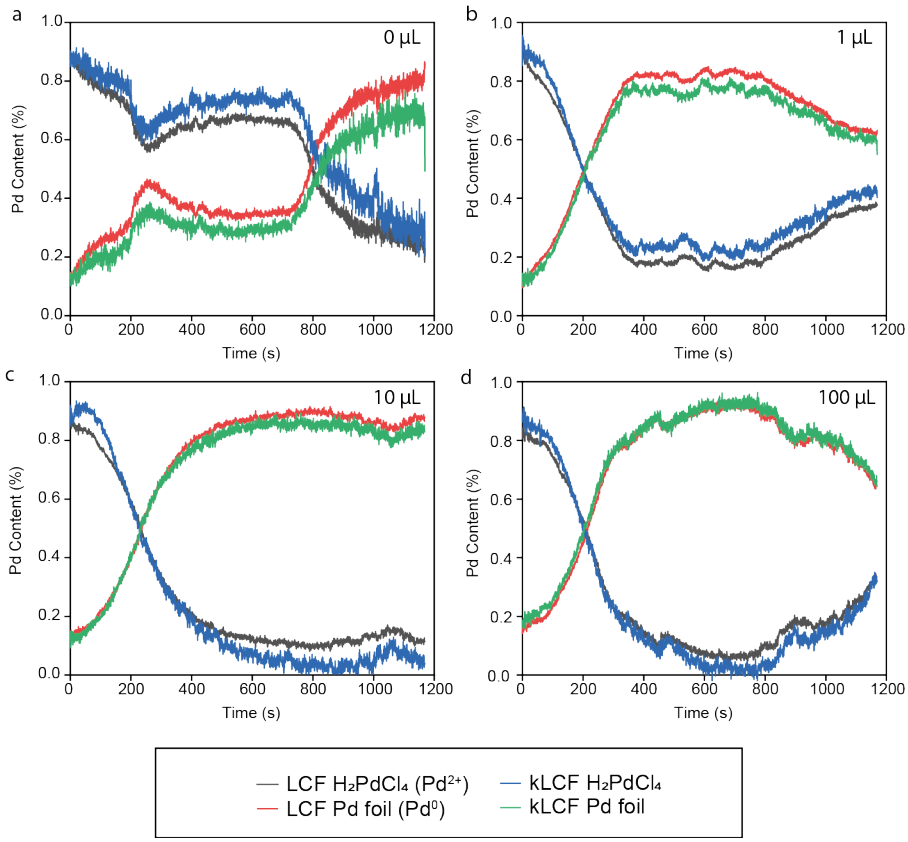

Figure 3.25 ***LCF and kLCF Results for Seed Concentration Range.*** *Pd K-edge XANES LCF Pd^0 (red) and Pd^{2+} (grey) versus k-space LCF between 0 to 10 $Å^{-1}$ (kLCF) Pd^0 (green) and Pd^{2+} (blue) for Pd growth with seed concentrations of (a) 0 µL, (b) 1 µL, (c) 10 µL and (d) 100 µL at 50°C.*

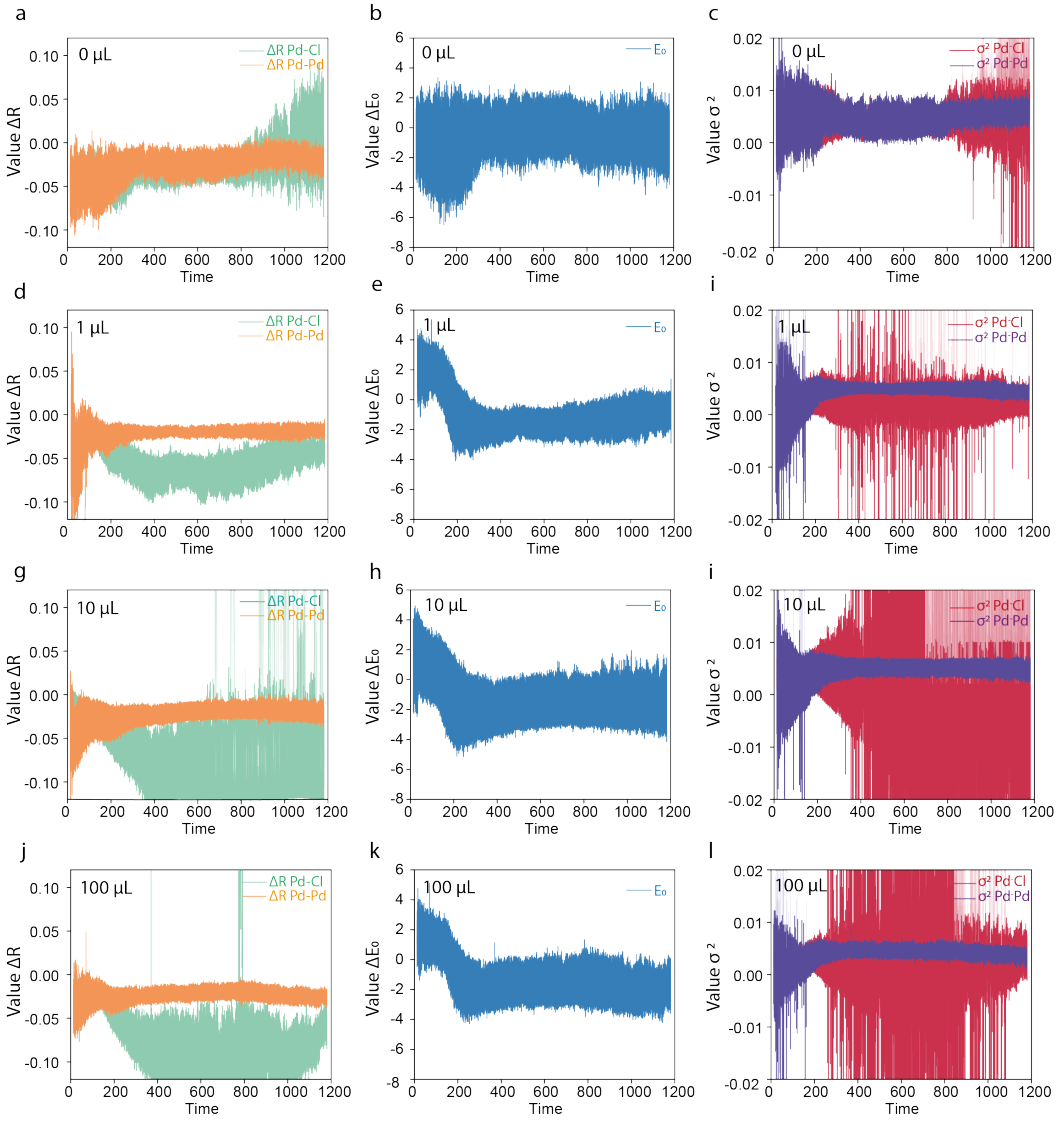

Figure 3.26 ***Time-Resolved EXAFS Parameters for Seeded Growth.*** *Fitting results for 2400 time-resolved XAS spectra for ΔR Pd-Cl (turquoise), ΔR Pd-Pd (orange), ΔE_0 (blue), σ^2 Pd-Cl (red) and σ^2 Pd-Pd (purple) with seed concentrations of (a-c) 0 µL, (d-f) 1 µL (g-i) 10 µL and (j-l) 100 µL.*

Table 3.10 ***Pd^0-Cl Peak Concentration for Seed-Controlled Growth.*** *The values of Pd^0-Cl % are calculated from the converted content and approximated as a concentration.*

Condition	Max. Pd^0-Cl (%)	Pd^0-Cl Concentration (mM)
50ºC	32.84	10.31
1 µL seeds	15.38	4.83
10 µL seeds	18.24	5.73
100 µL seeds	12.89	4.05

3.6 References

1 Brown, S. *et al.* PGM Market Report May 2023. *Johnson Matthey* (2023).

2 Favier, I., Pla, D. & Gomez, M. Palladium Nanoparticles in Polyols: Synthesis, Catalytic Couplings, and Hydrogenations. *Chem Rev* **120**, 1146-1183, http://dx.doi.org/10.1021/acs.chemrev.9b00204 (2020).

3 Datye, A. K. & Votsmeier, M. Opportunities and challenges in the development of advanced materials for emission control catalysts. *Nat Mater* **20**, 1049-1059, http://dx.doi.org/10.1038/s41563-020-00805-3 (2021).

4 Chen, M. Y., Li, Y., Wu, H. R., Lu, B. A. & Zhang, J. N. Highly Stable Pt-Based Oxygen Reduction Electrocatalysts toward Practical Fuel Cells: Progress and Perspectives. *Materials (Basel)* **16** http://dx.doi.org/10.3390/ma16072590 (2023).

5 Chen, A. & Ostrom, C. Palladium-Based Nanomaterials: Synthesis and Electrochemical Applications. *Chem Rev* **115**, 11999-12044, http://dx.doi.org/10.1021/acs.chemrev.5b00324 (2015).

6 Agostini, G. *et al.* Determination of the Particle Size, Available Surface Area, and Nature of Exposed Sites for Silica−Alumina-Supported Pd Nanoparticles: A Multitechnical Approach. *The Journal of Physical Chemistry C* **113**, 10485-10492, http://dx.doi.org/10.1021/jp9023712 (2009).

7 Garnier, E., Vidal-Iglesias, F. J., Feliu, J. M. & Solla-Gullon, J. Surface Structure Characterization of Shape and Size Controlled Pd Nanoparticles by Cu UPD: A Quantitative Approach. *Front Chem* **7**, 527, http://dx.doi.org/10.3389/fchem.2019.00527 (2019).

8 Wen, X. *et al.* Synthesis of Palladium Nanodendrites Using a Mixture of Cationic and Anionic Surfactants. *Langmuir* **36**, 1745-1753, http://dx.doi.org/10.1021/acs.langmuir.9b03804 (2020).

9 Kim, S.-W. *et al.* Synthesis of Monodisperse Palladium Nanoparticles. *Nano Letters* **3**, 1289-1291, http://dx.doi.org/10.1021/nl0343405 (2003).

10 Lee, S., Cho, H., Kim, H. J., Hong, J. W. & Lee, Y. W. Shape- and Size-Controlled Palladium Nanocrystals and Their Electrocatalytic Properties in the Oxidation of Ethanol. *Materials (Basel)* **14** http://dx.doi.org/10.3390/ma14112970 (2021).

11 Wang, F. *et al.* Porous single-crystalline palladium nanoparticles with high catalytic activities. *Angew Chem Int Ed Engl* **51**, 4872-4876, http://dx.doi.org/10.1002/anie.201107376 (2012).

12 Tran, M., DePenning, R., Turner, M. & Padalkar, S. Effect of citrate ratio and temperature on gold nanoparticle size and morphology. *Materials Research Express* **3** http://dx.doi.org/10.1088/2053-1591/3/10/105027 (2016).

13 Polavarapu, L., Mourdikoudis, S., Pastoriza-Santos, I. & Pérez-Juste, J. Nanocrystal engineering of noble metals and metal chalcogenides: controlling the morphology, composition and crystallinity. *CrystEngComm* **17**, 3727-3762, http://dx.doi.org/10.1039/c5ce00112a (2015).

14 Alam, M. S., Siddiq, A. M., Narayanan, S. S., Samanta, D. & Das, S. K. Cationic Surfactant (CTAC) Assisted Synthesis of Silver Nanoparticles

with Controlled Size: Optical, Morphological and Bactericidal Studies. *Journal of Nanoengineering and Nanomanufacturing* **5**, 124-131, http://dx.doi.org/10.1166/jnan.2015.1238 (2015).

15 Zhang, L., Lee, K. & Zhang, J. The effect of heat treatment on nanoparticle size and ORR activity for carbon-supported Pd–Co alloy electrocatalysts. *Electrochimica Acta* **52**, 3088-3094, http://dx.doi.org/10.1016/j.electacta.2006.09.051 (2007).

16 Abbas, G., Kumar, N., Kumar, D. & Pandey, G. Effect of Reaction Temperature on Shape Evolution of Palladium Nanoparticles and Their Cytotoxicity against A-549 Lung Cancer Cells. *ACS Omega* **4**, 21839-21847, http://dx.doi.org/10.1021/acsomega.9b02776 (2019).

17 An, K. & Somorjai, G. A. Size and Shape Control of Metal Nanoparticles for Reaction Selectivity in Catalysis. *ChemCatChem* **4**, 1512-1524, http://dx.doi.org/10.1002/cctc.201200229 (2012).

18 N, A., Ang, B. C., M.A, A. & Bong, C. W. Influence of Precursor Concentration and Temperature on the Formation of Nanosilver in Chemical Reduction Method. *Sains Malaysiana* **47**, 157-168, http://dx.doi.org/10.17576/jsm-2018-4701-19 (2018).

19 Song, Y., Zhang, M., Fang, H. & Xia, H. Shape transformation of gold nanoparticles in aqueous CTAB/CTAC solution to generate high-index facets for electrocatalysis and SERS activity. *ChemPhysMater* http://dx.doi.org/10.1016/j.chphma.2022.04.006 (2022).

20 Niu, W., Zhang, L. & Xu, G. Seed-mediated growth method for high-quality noble metal nanocrystals. *Science China Chemistry* **55**, 2311-2317, http://dx.doi.org/10.1007/s11426-012-4681-z (2012).

21 Hornberger, E. *et al.* Seed-Mediated Synthesis and Catalytic ORR Reactivity of Facet-Stable, Monodisperse Platinum Nano-Octahedra. *ACS Applied Energy Materials* **4**, 9542-9552, http://dx.doi.org/10.1021/acsaem.1c01696 (2021).

22 Gao, W. *et al.* Atomistic insights into the nucleation and growth of platinum on palladium nanocrystals. *Nat Commun* **12**, 3215, http://dx.doi.org/10.1038/s41467-021-23290-x (2021).

23 Duy Mai, H., Kim, S. & Yoo, H. Controllable growth of palladium on gold multipod nanoparticles and their enhanced electrochemical oxygen reduction reaction performances. *Journal of Catalysis* **388**, 20-29, http://dx.doi.org/10.1016/j.jcat.2020.04.024 (2020).

24 Bakshi, M. S. How Surfactants Control Crystal Growth of Nanomaterials. *Crystal Growth & Design* **16**, 1104-1133, http://dx.doi.org/10.1021/acs.cgd.5b01465 (2015).

25 Wu, S., Li, M. & Sun, Y. In Situ Synchrotron X-ray Characterization Shining Light on the Nucleation and Growth Kinetics of Colloidal Nanoparticles. *Angew Chem Int Ed Engl* **58**, 8987-8995, http://dx.doi.org/10.1002/anie.201900690 (2019).

26 Thanh, N. T., Maclean, N. & Mahiddine, S. Mechanisms of nucleation and growth of nanoparticles in solution. *Chem Rev* **114**, 7610-7630, http://dx.doi.org/10.1021/cr400544s (2014).

27 Wu, Z., Yang, S. & Wu, W. Shape control of inorganic nanoparticles from solution. *Nanoscale* **8**, 1237-1259, http://dx.doi.org/10.1039/c5nr07681a (2016).

28 Zhang, L., Wang, L., Jiang, Z. & Xie, Z. Synthesis of size-controlled monodisperse Pd nanoparticles via a non-aqueous seed-mediated growth. *Nanoscale Research Letters* **7**, 312, http://dx.doi.org/10.1186/1556-276X-7-312 (2012).

29 Mozaffari, S. *et al.* Colloidal nanoparticle size control: experimental and kinetic modeling investigation of the ligand-metal binding role in controlling the nucleation and growth kinetics. *Nanoscale* **9**, 13772-13785, http://dx.doi.org/10.1039/c7nr04101b (2017).

30 Karim, A. M. *et al.* Synthesis of 1 nm Pd Nanoparticles in a Microfluidic Reactor: Insights from in Situ X-ray Absorption Fine Structure Spectroscopy and Small-Angle X-ray Scattering. *The Journal of Physical Chemistry C* **119**, 13257-13267, http://dx.doi.org/10.1021/acs.jpcc.5b01681 (2015).

31 Yao, S. *et al.* Insights into the Formation Mechanism of Rhodium Nanocubes. *The Journal of Physical Chemistry C* **116**, 15076-15086, http://dx.doi.org/10.1021/jp302471p (2012).

32 Wojnicki, M., Fitzner, K. & Luty-Blocho, M. Kinetic studies of nucleation and growth of palladium nanoparticles. *J Colloid Interface Sci* **465**, 190-199, http://dx.doi.org/10.1016/j.jcis.2015.11.066 (2016).

33 Saeki, M. *et al.* In Situ Time-Resolved XAFS Studies on Laser-Induced Particle Formation of Palladium Metal in an Aqueous/EtOH Solution. *The Journal of Physical Chemistry C* **123**, 817-824, http://dx.doi.org/10.1021/acs.jpcc.8b09532 (2018).

34 Michaelis, M. & Henglein, A. Reduction of palladium (II) in aqueous solution: stabilization and reactions of an intermediate cluster and palladium colloid formation. *The Journal of Physical Chemistry* **96**, 4719-4724, http://dx.doi.org/10.1021/j100190a105 (1992).

35 Watzky, M. A. & Finke, R. G. Transition Metal Nanocluster Formation Kinetic and Mechanistic Studies. A New Mechanism When Hydrogen Is the Reductant: Slow, Continuous Nucleation and Fast Autocatalytic Surface Growth. *Journal of the American Chemical Society* **119**, 10382-10400, http://dx.doi.org/10.1021/ja9705102 (1997).

36 Mozaffari, S. *et al.* Ligand-Mediated Nucleation and Growth of Palladium Metal Nanoparticles. *J Vis Exp* http://dx.doi.org/10.3791/57667 (2018).

37 Finney, E. E. & Finke, R. G. Nanocluster nucleation and growth kinetic and mechanistic studies: a review emphasizing transition-metal nanoclusters. *J Colloid Interface Sci* **317**, 351-374, http://dx.doi.org/10.1016/j.jcis.2007.05.092 (2008).

38 Yang, T. H. *et al.* Toward a Quantitative Understanding of the Reduction Pathways of a Salt Precursor in the Synthesis of Metal Nanocrystals. *Nano Lett* **17**, 334-340, http://dx.doi.org/10.1021/acs.nanolett.6b04151 (2017).

39 Zheng, Y., Zeng, J., Ruditskiy, A., Liu, M. & Xia, Y. Oxidative Etching and Its Role in Manipulating the Nucleation and Growth of Noble-Metal Nanocrystals. *Chemistry of Materials* **26**, 22-33, http://dx.doi.org/10.1021/cm402023g (2013).

40 Khelfa, A., Nelayah, J., Wang, G., Ricolleau, C. & Alloyeau, D. Studying the Effects of Temperature on the Nucleation and Growth of Nanoparticles by Liquid-Cell Transmission Electron Microscopy. *J Vis Exp* http://dx.doi.org/10.3791/62225 (2021).

41 Jiang, X. C., Chen, W. M., Chen, C. Y., Xiong, S. X. & Yu, A. B. Role of Temperature in the Growth of Silver Nanoparticles Through a Synergetic Reduction Approach. *Nanoscale Res Lett* **6**, 32, http://dx.doi.org/10.1007/s11671-010-9780-1 (2010).

42 Mozaffari, S. *et al.* The role of nanoparticle size and ligand coverage in size focusing of colloidal metal nanoparticles. *Nanoscale Adv* **1**, 4052-4066, http://dx.doi.org/10.1039/c9na00348g (2019).

43 Liu, J., He, F., Gunn, T. M., Zhao, D. & Roberts, C. B. Precise Seed-Mediated Growth and Size-Controlled Synthesis of Palladium Nanoparticles Using a Green Chemistry Approach. *Langmuir* **25**, 7116-7128, http://dx.doi.org/10.1021/la900228d (2009).

44 Niu, W. *et al.* Seed-Mediated Growth of Nearly Monodisperse Palladium Nanocubes with Controllable Sizes. *Crystal Growth & Design* **8**, 4440-4444, http://dx.doi.org/10.1021/cg8002433 (2008).

45 Tsuji, M., Miyamae, N., Nishio, M., Hikino, S. & Ishigami, N. Shape Selective Oxidative Etching and Growth of Single-Twin Plate-Like and Multiple-Twin Decahedral and Icosahedral Gold Nanocrystals in the Presence of Au Seeds under Microwave Heating. *Bulletin of the Chemical Society of Japan* **80**, 2024-2038, http://dx.doi.org/10.1246/bcsj.80.2024 (2007).

46 Basham, M. *et al.* Data Analysis WorkbeNch (DAWN). *J Synchrotron Radiat* **22**, 853-858, http://dx.doi.org/10.1107/S1600577515002283 (2015).

47 Ravel, B. & Newville, M. ATHENA, ARTEMIS, HEPHAESTUS: data analysis for X-ray absorption spectroscopy using IFEFFIT. *J Synchrotron Radiat* **12**, 537-541, http://dx.doi.org/10.1107/S0909049505012719 (2005).

48 Collette, A. Python and HDF5. *O'Reilly* (2013).

49 Newville, M. Larch: An Analysis Package for XAFS and Related Spectroscopies. *Journal of Physics: Conference Series* **430**, 012007, http://dx.doi.org/10.1088/1742-6596/430/1/012007 (2013).

50 Newville, M., Stensitzki, T., Allen, D. B. & Ingargiola, A. *LMFIT: Non-Linear Least-Square Minimization and Curve-Fitting for Python*. (2014).

51 Ankudinov, A. L., Ravel, B., Rehr, J. J. & Conradson, S. D. Real-space multiple-scattering calculation and interpretation of x-ray-absorption near-edge structure. *Physical Review B* **58**, 7565-7576, http://dx.doi.org/10.1103/PhysRevB.58.7565 (1998).

52 Muñoz, M., Farges, F. & Argoul, P. Continuous Cauchy wavelet transform of XAFS spectra. *Physica Scripta* **2005**, 221, http://dx.doi.org/10.1238/Physica.Topical.115a00221 (2005).

53 Xie, M. *et al.* A Quantitative Analysis of the Reduction Kinetics Involved in the Synthesis of Au@Pd Concave Nanocubes. *Chemistry* **25**, 16397-16404, http://dx.doi.org/10.1002/chem.201904074 (2019).

54 Kuramochi, H., Takeuchi, S., Iwamura, M., Nozaki, K. & Tahara, T. Tracking Photoinduced Au-Au Bond Formation through Transient Terahertz Vibrations Observed by Femtosecond Time-Domain Raman Spectroscopy. *J Am Chem Soc* **141**, 19296-19303, http://dx.doi.org/10.1021/jacs.9b06950 (2019).

Chapter 4. Engineering the Pt-Pt Coordination Environment to Study Activity for Oxygen Reduction Reaction

The oxygen reduction reaction (ORR) in proton exchange membrane fuel cells plays an important role in the H_2 economy. Pt based alloy catalysts with tuned *d*-band centres are widely regarded as the most efficient catalysts. In this chapter, the average size of Pt sites in a Pt-Pd alloy, described as the Pt-Pt coordination number (C.N.), is shown to be a key geometric descriptor for the ORR activity. The decrease of Pt-Pt C.N. from 10.8 in commercial Pt nanoparticles[1] to 1.33 in Pt_1Pd_{493} alloy, with a similar morphology, allows the comparison of different Pt cluster sizes in ORR. Density functional theory (DFT) calculations and *in situ* X-ray absorption spectroscopy (XAS) measurements during ORR provide further insight into the reaction mechanism. *In situ* XAS is further able to monitor the surface oxidation and track C.N. changes in the catalyst. The precise engineering of Pt-Pt C.N. in an alloy is critical for optimising metal use in the activation of chemically stable compounds, particularly in the context of catalysis for renewable energy.

Notable Contributions

Contributions were made by Ruoyu Xu in electrochemical data measurements, Liqun Kang in TEM and XAS data collection and Ryan Wang in experimental design. All DFT calculations were carried out by Matthew T. Darby. Preprint available with DOI: 10.26434/chemrxiv-2023-hbk8d.

4.1 Introduction: A model catalyst to test the O-O dissociation

As explored in Chapter 1, there is substantial motivation to either find cheaper, more abundant alternatives to Pt, or reduce the amount of Pt required in proton exchange membrane (PEM) fuel cells by improving Pt efficiency for ORR activity. Common strategies for reducing Pt usage in ORR electrocatalysts are the modification of size and shape of Pt nanoparticles[2-4], utilisation of Pt alternatives[5,6] and alloying with secondary metals.[7-9] Alloying has been proven to be highly effective, for example, in top performing catalysts Pt_3Ni[7,10-12] and Pt_3Co.[13,14] Pt and Pd have also been successfully alloyed to give a similarly high ORR activity,[8,15-18] up to 1.09 $A.mg_{Pt}^{-1}$ with an octahedral single atom alloy.[19] By nature, alloying reduces the loading of Pt and in some cases, such as Pt_3Ni, leads to significant improvements in ORR activity. However, it remains unclear how much the loading of Pt can be reduced before the activity is diminished. Recent theoretical and experimental reports have suggested that single atom alloys with Pt as the minority metal exhibit high mass activity,[19,20] yet the question remains how Pt dimers and trimers behave as a function of size.[21-23]

'Domain' is used to describe Pt atom sites inserted within the Pd matrix from monomers to dimers and larger clusters. A key descriptor for the size of Pt domains within an alloy is the Pt-Pt coordination number (C.N.).[24] Its identification plays an important role in determining the specific ORR reaction pathways on novel low Pt loading materials. The four-electron ORR pathway on pure Pt is generally accepted to follow the adsorption of O_2 and either dissociation to O* before reduction to OH* and H_2O, or direct reduction from O_2* to OOH* and subsequent reduction therefrom. These pathways are referred to as the dissociative and associative mechanisms, respectively.[25-27] Common to both pathways is the adsorption of molecular oxygen on Pt which has three primary

modes, *via* bridging a pair of neighbouring Pt atoms (Pt-O-O-Pt, Yeager model), flat on top of a single Pt atom (Pt-η^2-O_2, Griffiths model), or end-on adsorption on a single Pt atom (Pt-η^1-O_2 Pauling model).[28] Of these, the Yeager model[29] undergoes fast O-O dissociation followed by a reaction with two protons (eq. 1-3),[30] and avoids the formation of H_2O_2 *via* two-electron reduction.

Dissociative: $Pt\text{-}O\text{-}O\text{-}Pt \rightarrow 2\ Pt\text{-}O^*$ Equation 1

$2\ Pt\text{-}O^* + 2\ H^+ + 2\ e^- \rightarrow 2\ Pt\text{-}OH$ Equation 2

Associative: $Pt\text{-}O\text{-}O\text{-}H + H^+ + e^- \rightarrow Pt\text{-}O^* + H_2O$ Equation 3

The Yeager model requires a minimum of two contingent Pt atoms for which the lowest Pt-Pt C.N. is 1, whereas other adsorption modes are possible for a single Pt atom with a Pt-Pt C.N. of zero.[20] *Li et al.* (2021) showed with DFT calculations that a pair of Pt atoms in a "dimer" configuration, as well as Pt sites with low Pt-Pt C.N. (i.e. above the single atom limit) in Co-Pd core-shell alloys can adsorb O_2 in all of the aforementioned modes. Behaving similarly to pure Pt surfaces, with reduced Pt loading, this results in higher atomic efficiency.[21] In addition, Li *et al.* showed that the O-O dissociation reaction barrier of 0.44 eV on Pt-dimers decorated on a Co-Pd core-shell system is notably lower than on the Pd(111) (0.62 eV) and Pt(111) surfaces (1.04 eV).[21] The activity over species with very low Pt-Pt C.N. is rarely discussed from an experimental standpoint, although recently Jia *et al.* showed that for Pt-Co core-shell catalysts, as the Pt-Pt C.N. is reduced the mass activity increases, which is attributed to a concurrent increase in strain effects.[1,31-33] This Pt-Pt C.N. versus activity relation motivates us to experimentally study the ORR behaviour over extreme cases, such as Pt-dimers and other surface domains with low Pt-Pt C.N., extending the understanding of surface alloy structures in catalytic reactions.

To design a catalyst in which the Pt-Pt C.N. can be controlled and monitored without particle size or strain effects, a host with a similar lattice constant and crystal structure is desirable. Pt should be anchored on a metal support which can not only firmly bind with the metal and prevent agglomeration of Pt sites, but also exhibit efficient electron supply and promote the reduction of ORR intermediates with four proton-electron pairs. Pd is a top candidate as it satisfies all these criteria and does not exhibit high ORR activity. The metal-supported Pt sites can be considered as replacing certain Pd atoms with Pt, for which the strong electronic interaction between Pt and the supporting Pd offers control of the metal *d*-states that are well correlated to catalytic activity.[34]

Thus, we synthesize Pt-Pd alloys with different Pt-Pt C.N. by dispersing Pt atoms within the Pd lattice and study their ORR performance and the influence of the Pt-Pt C.N. on the reaction pathway. Pt is dispersed within the Pd host matrix by virtue of its face-centred-cubic crystal structure and similar lattice constant (Pd 0.389 nm, Pt 0.392 nm[35]). When the Pt loading in Pd is reduced from 58 wt% to 0.38 wt%, the Pt-Pt C.N. decreases from 6.15 ± 0.57 to 1.33 ± 0.63. Such low Pt-Pt C.N. systems are of scientific interest and serve as a proof-of-concept for the design of controlled surface Pt species for O_2 reduction.

4.2 Results and Discussion

4.2.1 Structure and Identification of Pt dimers in the Pd matrix

Pt-Pd alloy particles were synthesised directly over carbon *via* a Pd seed mediated method.[36] To achieve a range of Pt cluster sizes within the nanoparticles, various Pt:Pd ratios were synthesised and characterised. Pt:Pd atomic ratios of 1:2.4, 1:22, 1:142 and 1:493 were achieved, as confirmed by MP-

AES measurements (Table 4.1). The corresponding particle formulations are denoted as $Pt_1Pd_{2.4}$, Pt_1Pd_{22}, Pt_1Pd_{142} and Pt_1Pd_{493}, respectively.

Table 4.1 ***MP-AES Results.*** *Detected Pt and Pd parts per million (ppm), alongside calculated Pt loading and total metal loading.*

Sample	Detected Pt (ppm)	Detected Pd (ppm)	Pt loading (wt%)	Metal loading (wt%)
$Pt_1Pd_{2.4}$	**3.93 ± 0.05**	**4.96 ± 0.06**	**16.17**	**30**
Pt_1Pd_{22}	**1.10 ± 0.06**	**13.14 ± 0.13**	**0.43 ± 0.024**	**5.59 ± 0.06**
Pt_1Pd_{142}	**0.16 ± 0.04**	**12.56 ± 0.08**	**0.06 ± 0.002**	**4.89 ± 0.03**
Pt_1Pd_{493}	**0.076 ± 0.03**	**20.53 ± 0.27**	**0.026 ± 0.009**	**6.86 ± 0.09**
Pd Pure	**0.006 ± 0.01**	**17.15 ± 0.13**	**0.002 ± 0.004**	**5.76 ± 0.04**

The average sizes of nanoparticles were measured from a minimum of 250 nanoparticles, at different regions of the sample. Average particle diameters of 45.3 ± 13.1 nm, 46.3 ± 13.3 nm, 46.2 ± 16.6 nm and 58.3 ± 22.4 nm are calculated for $Pt_1Pd_{2.4}$, Pt_1Pd_{22}, Pt_1Pd_{142} and Pt_1Pd_{493}, respectively (Figure 4.1, Supplementary Table 4.7).

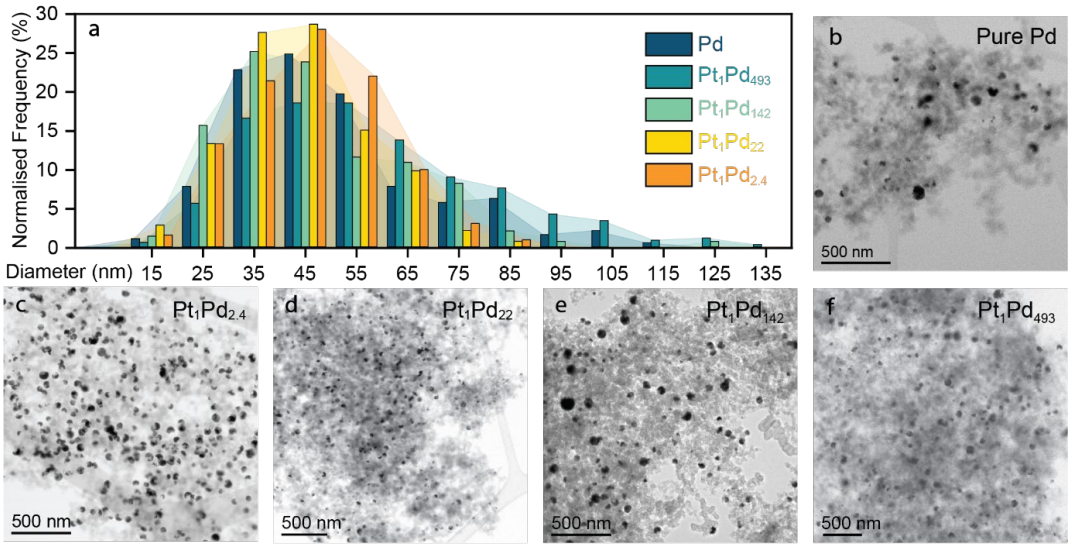

Figure 4.1 ***Average Nanoparticle Diameter.*** *(a) Distribution of nanoparticle sizes by measured diameters and corresponding example of TEM images with a scale bar of 500 nm for (b) pure Pd, (c) $Pt_1Pd_{2.4}$, (d) Pt_1Pd_{22}, (e) Pt_1Pd_{142} and (f) Pt_1Pd_{493}. Note that scalebar lengths may vary.*

A rounded porous nanoparticle morphology, with dendrites growing from a central point, is observed at all Pt loadings (Figure 4.2, Supplementary Figure 4.12). Individual intensities of Pt and Pd cannot be distinguished from the high-angle annular dark field (HAADF) STEM images (Figure 4.2 b, g, l, q). Energy-dispersive X-ray spectroscopy (EDS) maps show a preferential peripheral enrichment in $Pt_1Pd_{2.4}$, whereas for Pt_1Pd_{22}, Pt_1Pd_{142} and Pt_1Pd_{493}, Pt is evenly distributed throughout the particle (Figure 4.2 e, j, o, t). Each particle comprises of the dendritic assembly of small clusters with average radii of 1.99 ± 0.08 nm, 2.49 ± 0.32 nm, 2.88 ± 0.51 nm, 3.00 ± 0.40 nm, respectively (Supplementary Table 4.7). Varying the Pt loading from $Pt_1Pd_{2.4}$ to Pt_1Pd_{493} has little effect on the morphology and size of the particles. Pure Pd particles show the same morphology with a size of 50.5 ± 18.6 nm and average cluster radius of 2.48 ± 0.20 nm (Supplementary Figure 4.13).

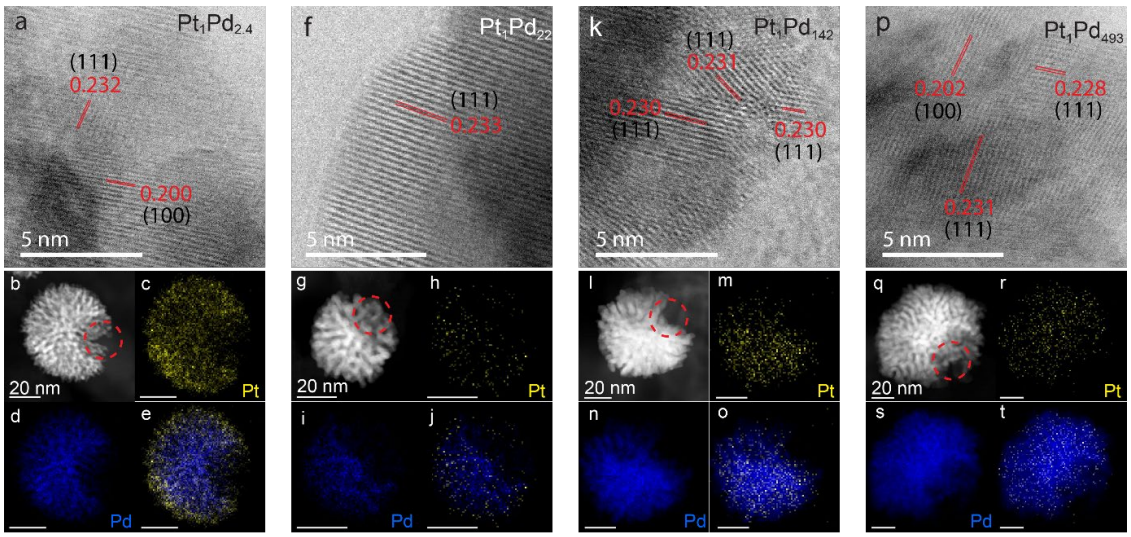

Figure 4.2 ***Morphology of Pt-Pd particles over carbon.*** *(a-e) $Pt_1Pd_{2.4}$, (f-j) Pt_1Pd_{22}, (k-o) Pt_1Pd_{142} and (p-t) Pt_1Pd_{493} imaging of 5 nm-scale BF-STEM lattice images of Pt-Pd samples above 20 nm-scale dark field STEM images with corresponding EDS element mapping of Pt (yellow) and Pd (blue).*

The particles' outer shape is not perfectly spherical as the surface curvature of the carbon is assumed during growth around an anchoring point (red circle in Figure 4.2). The surface area of the nanoparticles was found to decrease when loaded with nanoparticles (Supplementary Figure 4.14), due to the nanoparticles anchoring on the surface. The carbon support, Ketjenblack EC-300J had a high Brunauer-Emmet-Teller (BET) surface area of 837 $m^2.g^{-1}$, which decreases to 380.654 $m^2.g^{-1}$ with nanoparticles attached on the surface (Supplementary Figure 4.14).

Pd(111) and Pd(100) crystal lattices were observed in bright field scanning transmission electron microscopy (BF-STEM) images for all four types of particles (Figure 4.2). This was confirmed with an X-ray diffraction (XRD) measurement of each ratio (Figure 4.3), showing a slight shift in the peaks, with highest peaks in Pt/Pd (111) and Pt/Pd (200). Due to the similar lattice structure of both metals, and broadening of peaks, it is not possible to distinguish Pt from Pd peaks based

on the XRD results. However, it is expected that Pt atoms have been inserted into the Pd lattice. Face-centred cubic (FCC) crystal structure is present with lattice constants calculated as 3.934 ± 0.004 Å, 3.941 ± 0.003 Å and 3.962 ± 0.006 Å, respectively for Pt_1Pd_{22}, Pt_1Pd_{142} and Pt_1Pd_{493}. The Pt and Pd (111), (200), (220), (311) and (222) peaks were detected.

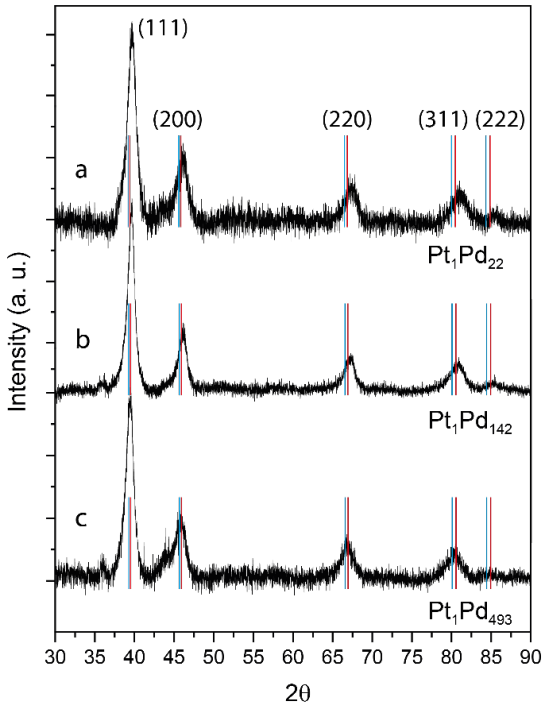

Figure 4.3 ***XRD Results.*** *XRD peaks for Pt_1Pd_{22} (a), Pt_1Pd_{142} (b) and Pt_1Pd_{493} (c). Literature 2θ values for Pt (blue lines) and Pd (red lines) are shown for Miller indices of (111), (200), (220), (311) and (222).*

The relatively similar particle shape, dendrite thickness and individual cluster size minimize the morphological influence on the ORR activity between different samples. This enables us to study the influence of the Pt:Pd ratio (and therefore, Pt-Pt C.N.) in isolation. The distribution of Pt within the Pd lattice is more precisely resolved with X-ray absorption fine structure (XAFS) measured at the Pt-L_3 edge, based on the positive relationship between the average Pt domain size in the alloy and the Pt-Pt C.N.[37,38] The bulk Pt-Pt C.N. is determined from the extended

XAFS (EXAFS) fitting in Pt foil to be 12. This decreases to 6.15 ± 0.57, 3.27 ± 0.882, 2.24 ± 0.87 and 1.33 ± 0.63 for $Pt_1Pd_{2.4}$, Pt_1Pd_{22}, Pt_1Pd_{142} and Pt_1Pd_{493}, respectively (Figure 4.4, Table 4.2). This is because as the Pt loading is decreased, the first coordination shell contains more Pd atoms than Pt.

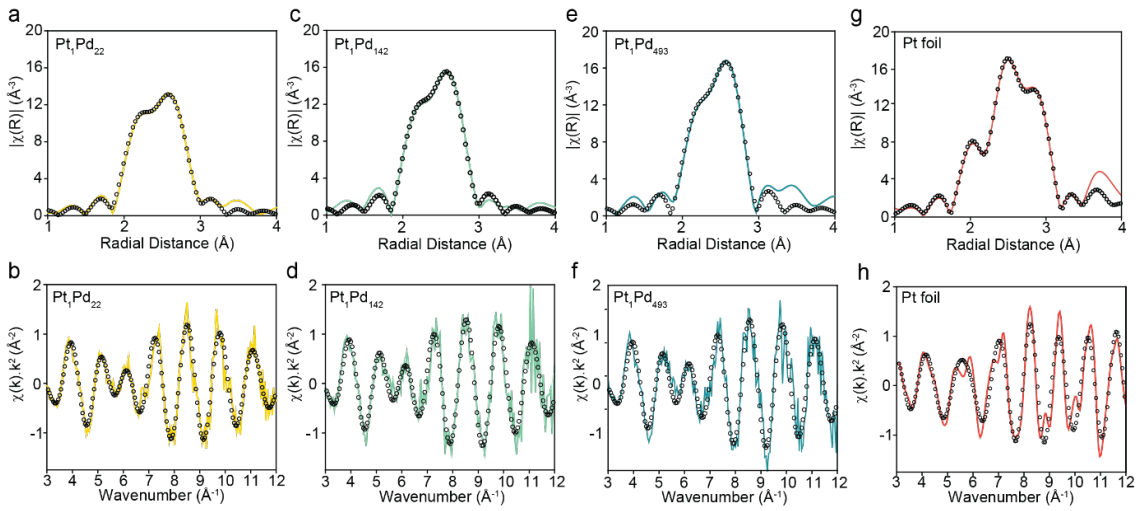

Figure 4.4 ***Ex situ EXAFS Fit Results.*** *k^2-weighted R-space and k-space data for (a, b) Pt_1Pd_{22}, (c, d) Pt_1Pd_{142} and (e, f) Pt_1Pd_{493} with (g, h) Pt foil measured at the Pt L_3-edge. Fitting is shown as black circles and data as coloured line.*

Table 4.2 ***Ex situ EXAFS Fit Results.*** *Artemis fit results for Pt-Pt C.N. from Pt L_3-edge recorded EXAFS. The amplitude reduction factor for all samples was set at 0.7944 from reference Pt foil. Reduced chi-squared 8.142 and R-factor 0.012.*

Sample	Path	C.N.	Bond length (Å)	Debye Waller factor, σ^2	Total Pt C.N.	ΔE_0 (eV)
Pt foil	Pt-Pt	12	2.77 ± 0.002	0.0044 ± 0.0002	12	8.12 ± 0.35
Pt_1Pd_{22}	Pt-Pt	3.27 ± 0.88	2.77 ± 0.010	0.0031 ± 0.0019	9.93 ± 1.55	5.52 ± 0.57
	Pt-Pd	6.66 ± 0.66	2.73 ± 0.005	0.0044 ± 0.0008		
Pt_1Pd_{142}	Pt-Pt	2.24	2.77	0.0025	10.26	5.46

Sample	Path	C.N.	Bond length (Å)	Debye Waller factor, σ^2	Total Pt C.N.	ΔE_0 (eV)
		± 0.87	± 0.020	± 0.0019	± 2.10	± 0.77
	Pt-Pd	8.02 ± 1.23	2.73 ± 0.005	0.0048 ± 0.0011		
Pt_1Pd_{493}	Pt-Pt	1.33 ± 0.63	2.77 ± 0.023	0.0020 ± 0.0019	9.47 ± 1.58	6.18 ± 0.65
	Pt-Pd	8.14 ± 0.95	2.73 ± 0.005	0.0049 ± 0.0008		

The calculation of J-value from the extended X-ray absorption fine structure (EXAFS) results is based on the work by Hwang et al., to find the distribution of metals within the nanoparticles.[39] Based on the results, it appears that all samples have an even distribution of Pt within the Pd matrix, with a slight surface enrichment of Pt, leading to undercoordination of Pt sites (Table 4.3, Supplementary Table 4.8, Supplementary Figure 4.16). However, the Pt site coordination is not as low as would be expected for an isolated site, indicating that the Pt has been incorporated into the Pd matrix.

Table 4.3 ***J-value Calculations.*** *Based on the Pt and Pd bonds resolved from Pt L_3-edge and Pd K-edge EXAFS.*

Sample	J_{Pt}	J_{Pd}	J_{Pt} Conclusion	J_{Pd} Conclusion	Total C.N. Pt	Total C.N. Pd
Pt_1Pd_{142}	351.23	0.15	Pt dispersed, surface-enriched	Pd clusters, core enriched	10.38	11.42
Pt_1Pd_{493}	106.34	0.27	Pt dispersed, surface-enriched	Pd clusters, core enriched	10.61	12.86
Pt_1Pd_1[40]	0.812	0.72	Pt clusters, evenly distributed	Pd clusters, evenly distributed	10.1	10.5

Pt-Pd C.N. increases from 3.70 ± 0.23 to 6.66 ± 0.66, 8.02 ± 1.23 and 8.14 ± 0.95, when the Pt content is reduced (Figure 4.5 a). On the other hand, the total Pt-metal coordination of both Pt-Pt and Pt-Pd, remain between 9 and 10.5, which is similar to that of commercial Pt/C (10.8).[1] The exposed Pt atoms are inserted into the Pd matrix, rather than sitting above the surface where they would be highly under-coordinated. Avoiding such under-coordinated sites is desirable, as according to literature, those under-coordinated Pt atoms strongly adsorb O_2, thereby limiting formation and desorption of intermediates and slowing the ORR.[41]

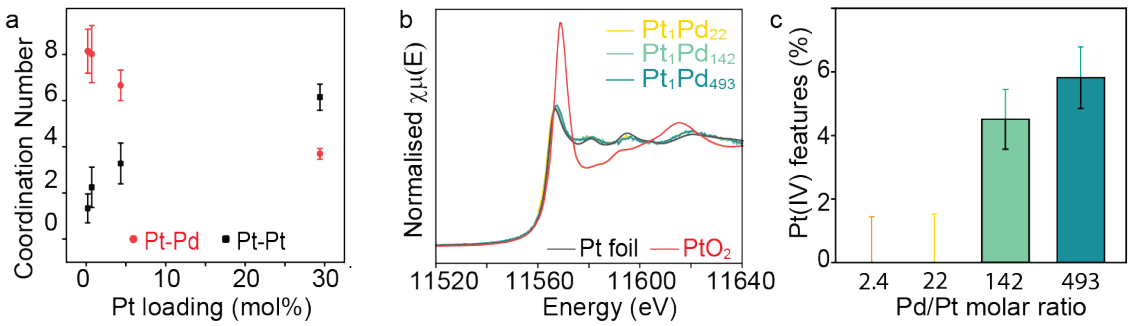

Figure 4.5 ***Pt coordination and PtO_2 content resolved with XAS.*** *(a) Average coordination of Pt-Pt (black) and Pt-Pd (red) with increasing Pt loading are obtained by refining EXAFS data measured at the Pt L_3-edge. Error bars are given in standard error (S.E.) (b) Pt L_3-edge normalised XANES of Pt_1Pd_{22} (yellow), Pt_1Pd_{142} (turquoise) and Pt_1Pd_{493} (blue) compared with Pt foil (black) and PtO_2 (red) as references. (c) Pt(IV) content against Pd/Pt molar ratio, determined by LCF analysis.*

The next feature of interest for catalytic particles is the oxidation state of the metals. This is achieved through the fitting of X-ray absorption near-edge structure (XANES) data. Pt-L_3 XANES spectra of the alloys show similar absorption features to those of Pt foil (Figure 4.5 b). An increase in Pt white line peak intensity (11,564 eV) corresponds to increasing Pt(IV) content. Linear combination fitting (LCF) of the XANES spectra reveals 4.5% and 5.8% Pt(IV) features in Pt_1Pd_{142} and Pt_1Pd_{493}, whereas other alloys show no obvious Pt(IV) features within the fitting error of <2% (Figure 4.5 c and Supplementary Table 4.9). Such Pt(IV) features stem from surface Pt atoms susceptible to oxidation.[42]

In addition to interest in the Pt oxidation state measured by XAS, the Pd oxidation state may influence the catalytic activity. Since the surface is most catalytically active, the presence of oxides is measured further with X-ray photoelectron spectroscopy (XPS), which is surface sensitive. The surface Pd is a mixture of Pd(0) and Pd(II) oxidation states, as shown from the area ratio between Pd(0)

and Pd (II) peaks in XPS (Figure 4.6 a-h).[43] Due to the low Pt loading, only the Pt_1Pd_{22} sample has a Pt 4*f* XPS signal, dominated by Pt(0) (Figure 4.6 i-k), with a weak Pt(0) signal observed in Pt_1Pd_{142}. The oxidation of Pd is likely caused by the high surface area of nanoparticles exposed to air.

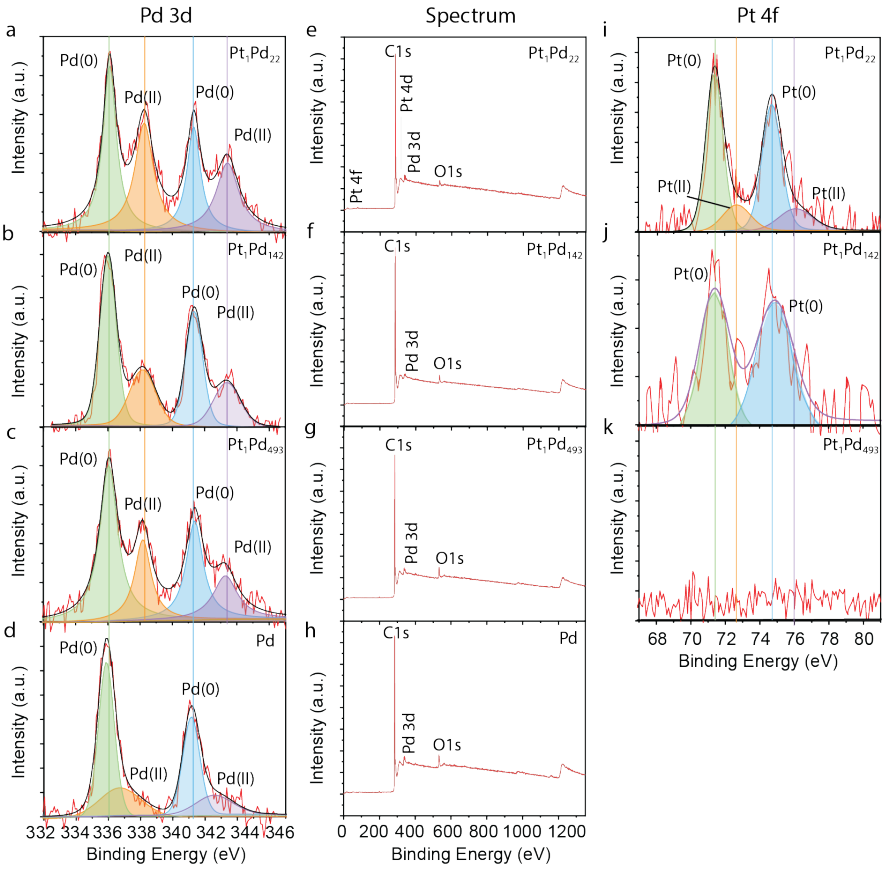

Figure 4.6 ***XPS Fit Results.*** *A comparison of Pt_1Pd_{22}, Pt_1Pd_{142} and Pt_1Pd_{493} binding energy peaks for (a-c) Pd 3d, (e-g) survey spectrum and (i-k) Pt 4f, as labelled. Survey spectra peaks are labelled C 1s, Pd 3d, Pt 4d, Pt 4f and O 1s.*

The Pt-Pt C.N. is used to estimate the average number of Pt atoms per domain assuming a uniform alloy. As Pt_1Pd_{493} showed an average coordination of 1.33 ± 0.63, it is likely composed predominantly of dimers, with a small number of single atoms and domains with 3 or more Pt atoms. On increasing Pt loading to Pt_1Pd_{142} and Pt_1Pd_{22}, an increase in the number of Pt atoms per domain is expected. The influence of the Pt-Pt C.N. on ORR activity can then be studied.

4.2.2 Electrochemical Behaviour of Pt Dimers and Clusters

Considering the cyclic voltammetry (CV) curves, pure Pd nanoparticles have no oxidation peak in the anodic scan, and a small oxygen reduction peak at 0.755 V vs Reversible Hydrogen Electrode (RHE) in the cathodic scan (Figure 4.7 a, Supplementary Figure 4.15). Alloying with just 0.2% and 0.7% Pt changes the CV profiles. An oxidation shoulder appears between 0.81 and 0.93 V vs RHE, and a sharp reduction peak is observed at 0.780 and 0.752 V vs RHE for Pt_1Pd_{493} and Pt_1Pd_{142}, respectively. The anodic peak indicates the surface O oxidation, with formation of Pt-OH and Pt-O_2, while the cathodic peak shows their reduction. The anodic and cathodic peaks between 0 and 0.2 V vs RHE are due to the surface H adsorption and desorption.

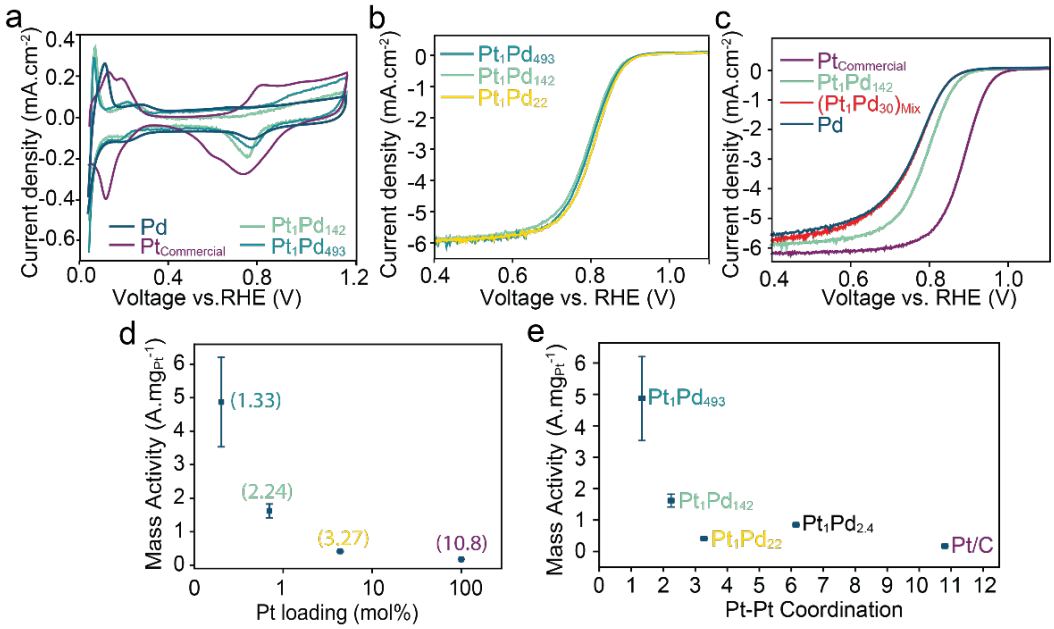

Figure 4.7 ***ORR Performance.*** *(a) CV results of commercial Pt/C, Pd/C, Pt_1Pd_{142} and Pt_1Pd_{493} are measured at 50 mV.s-1 in N_2-saturated 0.1 M $HClO_4$. O_2-saturated LSV curves without iR-correction measured with scan rate of 20 mV.s^{-1} are compared for (b) Pt_1Pd_{22}, Pt_1Pd_{142} and Pt_1Pd_{493} and (c) Pt_1Pd_{142}, physical mixture of Pt_1Pd_{30}, Pt/C and Pd/C standards. Mass activity is plotted against (d) Pt loading (mol%) and (e) Pt-Pt C.N with error bars from Pt content analysis.*

The kinetic current at 0.9 V vs RHE for the pure Pd catalyst, as calculated from the linear sweep voltammetry (LSV) curve in Figure 4.7 (b) is 0.001 mA. Adding just 0.2 wt% of Pt to Pd (Pt_1Pd_{493}) increases the kinetic current to 0.025 mA (Figure 4.7 c). For Pt_1Pd_{22} and Pt_1Pd_{142}, the kinetic currents are 0.033 mA and 0.020 mA, respectively. As seen in Figure 4.7 (c) and Table 4.4 the LSV curves for ORR are similar regardless of the Pt content in the alloy. The half-wave potentials of Pt_1Pd_{22}, Pt_1Pd_{142} and Pt_1Pd_{493} are 0.804 V, 0.796 V and 0.803 V, respectively. This indicates that though the content of Pt decreases significantly from Pt_1Pd_{22} to Pt_1Pd_{493}, the current density remains at the same level in the ORR potential range. To understand the role of alloying in increasing ORR activity, a physical mixture of commercial Pt/C and Pd nanoparticles in a molar ratio of 1:30

is compared with alloys (Figure 4.7 c). This mixture has a higher Pt content in the form of separate Pt nanoparticles than the alloyed Pt domains in Pt_1Pd_{142} and Pt_1Pd_{493}. However, the LSV curve of the physical mixture is very similar to that of pure Pd catalysts, with Pt mass activity of only 0.07 $A.mg_{Pt}^{-1}$.[44,45]

Table 4.4 ***Electrochemical ORR Performance****. I_k, kinetic current at 0.9 V (mA), M.A. or mass activity for Pt loading and total metal loading ($A \cdot mg_{Pt}^{-1}$), ECSA or electrochemical surface area ($cm^2.g^{-1}$) and $E_{1/2}$ or halfwave potential (V) collected for all samples.*

Sample Name	I_k (mA)	M.A.(Pt) ($A \cdot mg_{Pt}^{-1}$)	M.A.(Metal) ($A \cdot mg_{Metal}^{-1}$)	ECSA ($cm^2.g^{-1}$)	$E_{1/2}$ (V)
Pt/C	0.69	0.17 ± 0.001	0.17 ± 0.0006	44.11 ± 0.46	0.89
$Pt_1Pd_{2.4}$	2.55	0.85	0.57	7.44 ± 0.08	0.96
Pt_1Pd_{22}	0.03	0.38 ± 0.02	0.03 ± 0.002	15.09 ± 0.66	0.80
Pt_1Pd_{142}	0.02	1.62 ± 0.20	0.02 ± 0.003	61.11 ± 8.09	0.80
Pt_1Pd_{493}	0.03	4.87 ± 1.34	0.018 ± 0.006	60.82 ± 17.29	0.80
Pd	0.001	0.00 ± 0.002	0.00067 ± 0.039	52.25 ± 2.04	0.77

The calculated Pt mass activities are 0.82, 0.38, 1.62 and 4.86 $A.mg_{Pt}^{-1}$ for $Pt_1Pd_{2.4}$, Pt_1Pd_{22}, Pt_1Pd_{142} and Pt_1Pd_{493}, respectively, whereas the mass activity of the commercial Pt/C is 0.18 $A.mg_{Pt}^{-1}$ (Figure 4.7 d). Pd has a contribution towards ORR, but with a low kinetic current of 0.001 mA at 0.9 V. We further calculate the mass activity for total metal loading of Pt and Pd (Table 4.4), showing 27 times increase from 0.00067 in pure Pd to 0.018 $A.mg_{metal}^{-1}$ in Pt_1Pd_{493} when only 0.005 µg of Pt is introduced to ~1 µg of Pd. This result suggests that in Pt_1Pd_{493}, majority of the current is generated as a result of alloyed Pt species.

The same nanoparticles are run through accelerated durability test (ADT) cycling but the effect of the alloy ratio on the stability is not significant (Figure 4.8).

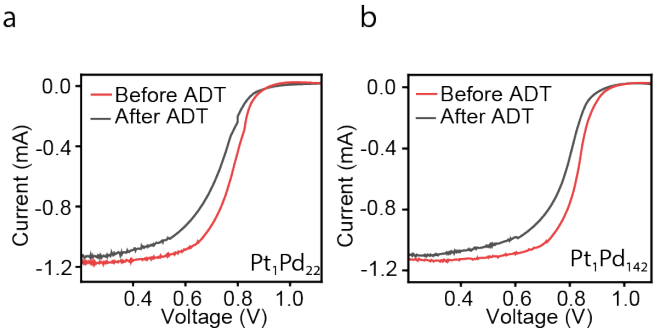

Figure 4.8 ***Durability Testing.*** *ADT results before (red) and after (black) in 0.1 M $HClO_4$ for (d) Pt_1Pd_{22} and (e) Pt_1Pd_{142}.*

The relative increase in mass activity with the addition of a small amount of Pt compared to the higher loading leads us to conclude that low Pt-Pt C.N. domains within the alloy are highly active compared to those with high Pt-Pt C.N. as well as Pt nanoparticles. A substantial increase in mass activity is observed when Pt-Pt C.N. is decreased from 10.8 to 1.33. The Pt_1Pd_{493} is the most active material per Pt atom, with a Pt mass activity that is 3, 13 and 29 times that of Pt_1Pd_{142}, Pt_1Pd_{22} and commercial Pt/C, respectively. With an average of Pt-Pt C.N. of only 1.33, it is likely that such activity originates from Pt dimers, as shown in the DFT calculation below.

4.2.3 Structure-Activity Relationship and Reaction Pathways of Pt Oligomers and Clusters

DFT calculations were performed to discern the free energy of reaction for each elementary step during the four-electron ORR process on Pt(111), Pd(111), Pt_2Pd(111) and Pt_1Pd(111), covered by an ice-like water bilayer. The former two are pure metal surfaces, whereas the latter two represent the surface Pt dimer

and single atom alloy. We analysed Gibbs free energy profiles for four-electron ORR for each model catalyst in the calculation (Figure 4.9).

The different stages in the associative and dissociative pathways and the corresponding chemical changes are visually shown in Figure 4.9 (a). Below, the calculation results for each stage are given, as performed on the four cases outlined. It should be noted that these are idealised systems, where the monomer or dimer has full surface exposure and the surface is a perfect (111) facet. The cases where dimers are partly submerged may show behaviour more similar to the single site, since only one Pt atom is exposed, although modification of the *d*-states may alter the energy barrier slightly. For this work, fully submerged Pt sites are not calculated since only the activity at the Pt surface is being studied and the Pd would be the active site in case of submersion. The presence of Pt at the reaction surface has been previously confirmed by XAS and XPS.

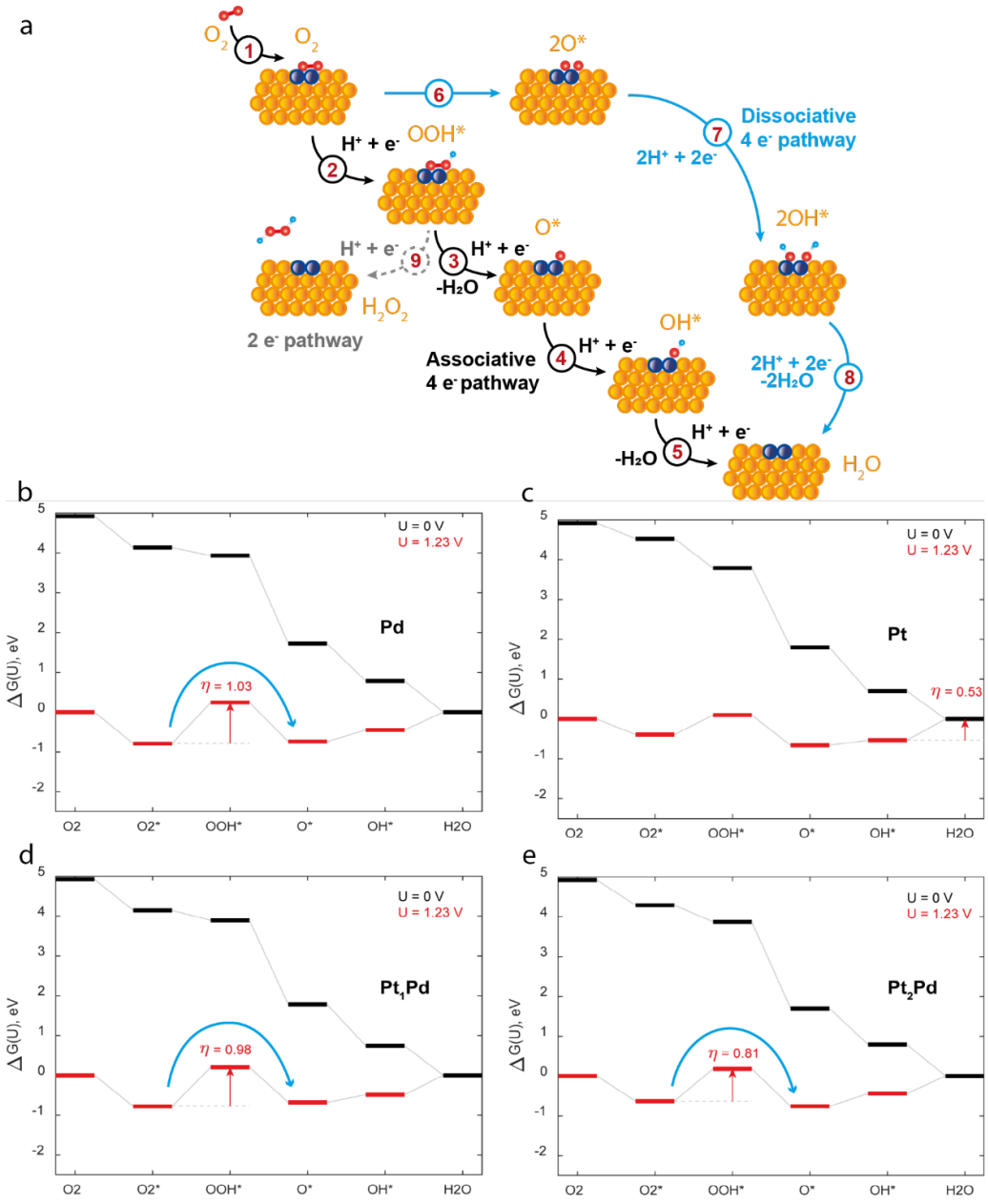

Figure 4.9 ***DFT Free Energy Calculation.*** *(a) Associative (black) and dissociative (blue) mechanisms of oxygen reduction over a Pt dimer. (b-e) Free energy of oxygen reduction reaction intermediates at 0 V (black) and 1.23 V (red) over Pd(111) (b), Pt(111) (c), Pt single site Pt_1Pd (e) and Pt dimer Pt_2Pd (f) in Pd(111) slabs, calculated using DFT. The dissociative oxygen reduction pathway is shown with blue arrows.*

Considering the associative pathway, we determine the theoretical overpotential, which is the potential difference below the equilibrium ORR potential (1.23 V) for

which all steps in the reduction are thermodynamically downhill. In other words, the theoretical overpotential is the difference between the limiting potential and the equilibrium potential and is a descriptor for catalytic activity, whereby lower values of η indicate better performance.[27] We calculate η for Pt(111) to be 0.53 eV, which compares well with reported experimental overpotentials of 0.4-0.5 eV[21,46,47] for pure Pt ORR catalysts. For Pd(111), Pt monomer ($Pt_1Pd(111)$) and Pt dimer in Pd lattice ($Pt_2Pd(111)$), we calculate notably higher overpotential values of 1.03 eV, 0.98 eV and 0.81 eV, respectively (Figure 4.9 b-d), indicating significantly less favourable thermodynamics for the associative four-electron ORR on these model catalysts. In all cases, the thermodynamically limiting step is the reduction of O_2* to OOH*.

Considering the dissociative pathway, reduction to OOH* is avoided *via* the dissociation of the O_2 dimer to O* (Figure 4.9 b, d, e). In this case, the η for the dissociative reduction on Pt(111) remains unchanged, but on Pd(111), $Pt_1Pd(111)$ and $Pt_2Pd(111)$ it is reduced to 0.45, 0.49 and 0.44 eV, respectively (Table 4.5).

Table 4.5 ***Free Energies of Adsorption.*** *Computed at U = 0 V from DFT for ORR intermediates O_2*, OOH*, O* and OH* on Pd(111), Pt(111), $Pt_1Pd(111)$ and $Pt_2Pd(111)$ covered in a bilayer of ice-like water. Energies are given in units of eV.*

	ΔG_{ads} at U = 0 V (eV)			
Slab	O_2*	OOH*	O*	OH*
Pd(111)	4.13	3.93	1.72	0.78
Pt(111)	4.53	3.79	1.80	0.70
$Pt_1Pd(111)$	4.14	3.89	1.78	0.74
$Pt_2Pd(111)$	4.29	3.87	1.70	0.79

The values of η suggest that if O_2 dissociation is facile, these surfaces will catalyse the ORR better than Pt(111). For Pd(111) the O_2 dissociation barrier is 0.47 eV and is assumed to be independent of the applied potential. On the other hand, Pt monomers and dimers in Pd(111) significantly enhance the O_2 dissociation efficacy, exhibiting activation barriers of 0.18 eV and 0.20 eV, respectively.

These DFT calculations suggest that Pt dimers with low Pt-Pt C.N. perform ORR *via* the dissociative pathway, whereas pure Pt surface or alloys with high Pt-Pt C.N. prefer the associative pathway. The O-O dissociation in the former is a non-electrochemical process and therefore is assumed to be independent of the applied potential.

4.2.4 *In situ* XAS results

To validate our calculations, the oxidation and reduction behaviour of Pt is studied *via in situ* XAS for low (Pt_1Pd_{142}) and high ($Pt_1Pd_{2.4}$) Pt-Pt C.N. catalysts (Figure 4.10). The oxidation state of Pt is often used as an indicator of catalytic activity during ORR[1,48,49] as the formation of oxides during the reaction passivates the surface.[1] Performing LCF analysis of the *in situ* XAS spectra shows that the Pt clusters in $Pt_1Pd_{2.4}$ initially contain 100% Pt(0) and are steadily oxidised to 12.4% Pt(IV) between 1.2 V (anodic) and 0.8 V (cathodic) vs. RHE (Figure 4.10 e, h, Supplementary Table 4.10).

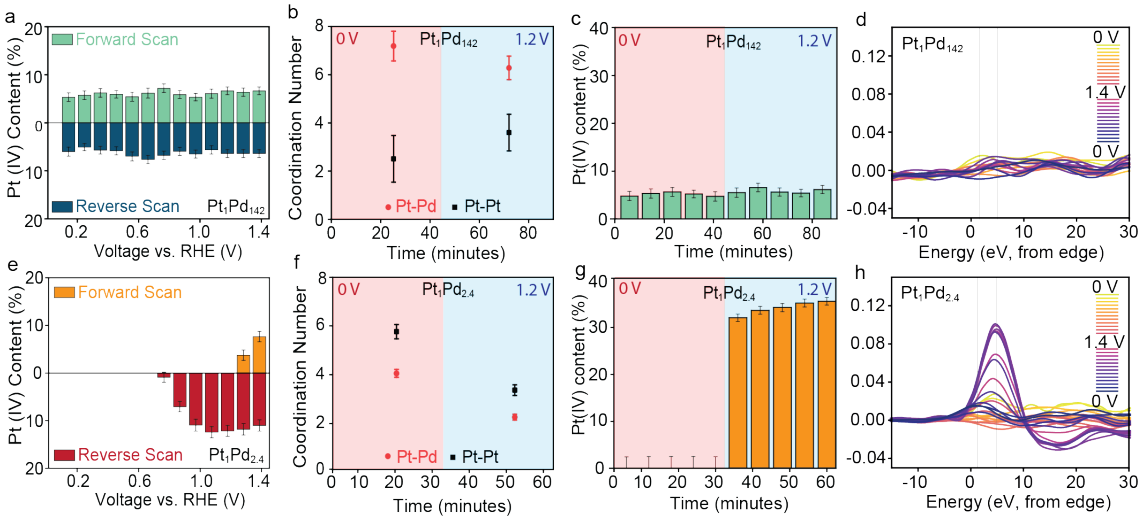

Figure 4.10 ***In situ XAS during CV.*** *LCF results at the Pt L_3-edge show the Pt(IV) content during a single in situ CV cycle of (a) Pt_1Pd_{142} and (e) $Pt_1Pd_{2.4}$. The corresponding change in C.N. and the Pt(IV) content at held potentials of 0 V and 1.2 V for 30 minutes are respectively compared for (b, c) Pt_1Pd_{142} and (f, g) $Pt_1Pd_{2.4}$. Δμ XANES difference of in situ CV results are calculated for (d) Pt_1Pd_{142} (h) and $Pt_1Pd_{2.4}$, shown with yellow to red gradient during forward scan (0 V to 1.4 V) and red to blue during reverse scan (1.4 V to 0 V).*

The complete reduction to metallic Pt occurs at 0.7 V (cathodic) vs. RHE, corresponding well with the reduction peaks during CV. A previous study on commercial Pt/C shows a similar trend but with 30% Pt(IV) at 1.3 V (cathodic).[50] In comparison, the Pt in Pt_1Pd_{142} maintains a low Pt(IV) content in the range of 5% to 7% throughout the cycling (Figure 4.10 a, d, Supplementary Table 4.11). The oxidation of Pt is not obvious even at high potentials (Figure 4.10 b, c). This fits well with the dissociative pathway for which the O-O bond breaking does not change with potentials. We are not able to study Pt_1Pd_{493} *in situ* because the ultralow Pt loading results in weak XAS signals that preclude reliable interpretation.

Pt_1Pd_{142} (Figure 4.10 b, c) and $Pt_1Pd_{2.4}$ (Figure 4.10 f, g) were held at 1.2 V to study the change of both Pt oxidation states and coordination structure. Before and after applying voltage to Pt_1Pd_{142} the Pt(IV) content remains the same, suggesting that Pt domains in the alloy remain in the metallic state (Supplementary Table 4.12). However, the Pt-Pt C.N. increases from 2.5 ± 0.97 to 3.60 ± 0.76, indicating an increase in the average number of Pt atoms in each domain (Figure 4.11, Table 4.6). This is ascribed to the surface oxidation and reduction process, in which Pt atoms first oxidise into solution, then reduce and deposit on surface to form a larger Pt domain with increased Pt-Pt C.N. The Pt-Pd C.N. thus decreases from 7.19 ± 0.62 to 6.28 ± 0.49 (Figure 4.10 b).

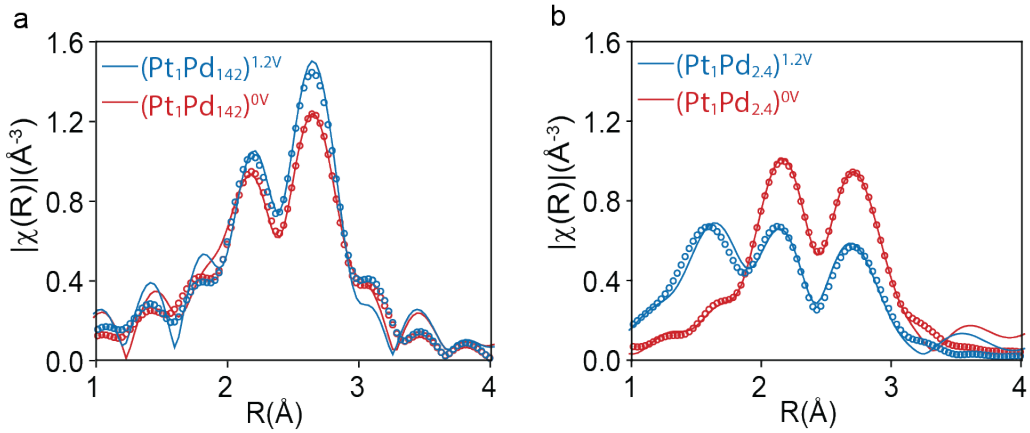

Figure 4.11 ***R-Space Fit Results.*** *Pt L_3-edge EXAFS fit results compared for (a) Pt_1Pd_{142} and (b) $Pt_1Pd_{2.4}$ after being held at potentials of 0 V (red) and 1.2 V (blue) for 30 minutes. The data is shown as a solid line and the fit as circles.*

Table 4.6 ***Held-Potentials EXAFS Fitting.*** *Artemis fitting of Pt L_3-edge EXAFS of Pt_1Pd_{142} and $Pt_1Pd_{2.4}$ at held potentials of 0 V and 1.2 V. The amplitude reduction factor for Pt was set at 0.7944, as measured for reference Pt foil. R values for Pt-Pt, Pt-Pd and Pt-O were set to 2.77 Å, 2.73 Å and 2.05 Å, respectively. Reduced chi-squared 13.247 and R-factor of 0.0182.*

Sample	Path	C.N.	∆R (Å)	Debye Waller factor, σ^2	Total Pt C.N.	ΔE_0 (eV)
0 V Pt_1Pd_{142}	Pt-Pt	2.50 ± 0.53	-0.042	0.0054 ± 0.00051	11.45 ± 0.61	5.078 ± 0.79
	Pt-Pd	7.23 ± 0.61	0.054	0.0064 ± 0.00051		
	Pt-O	0.86 ± 0.55	-0.166	0.0069 ± 0.00051		
1.2 V Pt_1Pd_{142}	Pt-Pt	3.53 ± 0.46	-0.042	0.0054 ± 0.00051	11.21 ± 0.52	5.078 ± 0.79
	Pt-Pd	6.39 ± 0.52	0.054	0.0064 ± 0.00051		
	Pt-O	0.65 ± 0.40	-0.166	0.0069 ± 0.00051		
0 V $Pt_1Pd_{2.4}$	Pt-Pt	5.79 ± 0.29	-0.06	0.0045 ± 0.0003	10.74 ± 0.29	4.883 ± 0.29
	Pt-Pd	4.09 ± 0.16	-0.05	0.0038 ± 0.0002		
	Pt-O	0.43 ± 0.20	-0.05	0.0102 ± 0.004		
1.2 V $Pt_1Pd_{2.4}$	Pt-Pt	3.41 ± 0.22	-0.06	0.0044 ± 0.0003	12.00 ± 0.30	5.802 ± 0.35
	Pt-Pd	2.31 ± 0.12	-0.05	0.0038 ± 0.0002		
	Pt-O	3.14 ± 0.30	-0.05	0.0078 ± 0.0013		

This behaviour is not observed in $Pt_1Pd_{2.4}$ where the Pt(IV) content sharply increases to 30% under 1.2 V (Supplementary Table 4.13) and both Pt-Pt and Pd-Pd coordination decrease as the result of leaching (Figure 4.10 f, Figure 4.11 and Table 4.6). This may be due to the stabilising effect of the host Pd on neighbouring Pt atoms,[16,44,51] which are more abundant in low Pt-Pt C.N. catalysts, or due to the weakened oxygen adsorption on Pt-Pd/C.[44,52]

4.3 Outcomes

The number of atoms in the active centre, here monitored by the Pt-Pt C.N., is a key descriptor for ORR performance. Decreasing the Pt-Pt C.N. in the Pt-Pd alloy is believed to cause the transition from associative to dissociative reaction

pathway. Enabling ORR to proceed *via* the dissociative pathway, together with the high Pt atom utilisation efficiency of the Pt-Pt C.N. catalyst (Pt_1Pd_{493}, Pt_1Pd_{142}), leads to the exponential increase of ORR Pt mass activity at low Pt-Pt C.N. It is significant that the slight addition of Pt into the pure Pd lattice achieves a 27-fold increase in mass activity. The importance of alloying is supported by the ORR activity of the physical mixture of Pt and Pd, which is almost the same as that of pure Pd. The Pt efficiency is the highest in nanoparticles with majority of dimeric Pt sites, which exhibit an exceptionally high mass activity of 4.87 $A \cdot mg_{Pt}^{-1}$. At the same amount of total metal loading, the Pt dimers achieve 10% of the kinetic current with only 0.4% of Pt.

Our studies have focused on an ideal Pt-Pd catalyst system, which has two limitations: 1) the low number of Pt sites in our dilute system needs to be increased for practical applications; and 2) the Pt domain structure within the Pd matrix may contain monomers and trimers, as well as dimers, which are difficult to differentiate with current characterization techniques. Nevertheless, it is scientifically important to find out that Pt dimers can dissociate O-O directly without an electrochemical potential. A system with higher loading of such Pt dimers on earth-abundant metal frameworks, such as Ni and Co will eventually develop into a practical catalyst with high atom utilization efficiency, not only for ORR in PEM fuel cells but other oxidation chemistries in heterogeneous catalysis.

4.4 Experimental Methods

4.4.1 Nanoparticle Synthesis

Pt-Pd nanoparticles were synthesised *via* seed-mediated colloidal growth. Pd seeds were grown from 10 mM H_2PdCl_4 solution by ripening for four hours with

10 mM $NaBH_4$ (Sigma Aldrich, 99%) and cetyltrimethylammonium chloride (CTAC, Sigma Aldrich, 25 wt% in H_2O), as previously described by Wang et al. in 2012.[53] H_2PdCl_4 solution is prepared by mixing $PdCl_2$ (Sigma Aldrich, 99%) and HCl (ACS reagent, 37%) with deionised water at 333 K.

100 mL of seed solution is sonicated with DI water and 40 mg commercially available carbon black, Ketjenblack EC-300J (Fuel Cell Store). To the carbon/seed solution, a mixture of 10 mM H_2PdCl_4 and 10 mM H_2PtCl_6 (ACS reagent, ≥ 37.5% Pt basis), CTAC and L-Ascorbic acid (AA, Sigma Aldrich, 99%) were added in a volume ratio of 97.1(seeds):1.6(metal salts):0.5(CTAC):0.8(AA). This is reduced for 12 hours at 333 K, followed by water (Millipore) and ethanol (Fisher Scientific, 99%+) wash. Five samples were synthesised with Pt:Pd molar ratios of 1:0, 1:2.4, 1:22, 1:142 and 1:493.

4.4.2 Lab-Based Characterization

A Micromeritics 3Flex surface characterization analyser measured **nitrogen adsorption-desorption isotherms**. Samples were held at 373 K overnight to strip surface impurities before running nitrogen sorption at 77 K. Surface area is obtained with Brunauer-Emmett-Teller (BET) analysis.

MP-AES is measured with Agilent 4200 MP-AES (Agilent Technologies, U.S.). 5 to 10 mg of sample is dissolved in 1 to 4 mL of 50% conc. aqua regia (1:3 HNO_3:HCl), with higher loading used for samples with low Pt content. A PTFE filter (Fisher Scientific) is used to remove residual carbon. Samples were measured for Pt at wavelengths of 265.945, 292.979, 299.796 and 306.471 nm, and for Pd at wavelengths of 324.270, 340.458, 360.955, 363.470 nm. Calibration is performed with 1000 $mg.L^{-1}$ Pt and Pd standard solutions (Sigma Aldrich, in hydrochloric acid) diluted to 1 ppm, 2 ppm, 5 ppm, 10 ppm, 20 ppm and 50 ppm.

Calibration errors were set within 10% for a linear fit. Metal loadings, and individual Pt and Pd loading, were calculated from the detected concentration, mass of dissolved metal and final solution volume, as described in Section 2.3.8. The molar Pt:Pd ratios were obtained using the standard atomic weights of 195.08 u (Pt) and 106.42 u (Pd).

HAADF-STEM and TEM samples were prepared by dry loading on a carbon supported copper grid. Images were acquired on a JEOL-2100 (JEOL, Japan) with an acceleration range of 200 keV. Average diameter was calculated with ImageJ. For HAADF-STEM, samples were dry loaded on a copper grid. A probe and image corrected JEOL ARM 300CF (JEOL, Japan) at E02, Diamond Light Source is operated at 200 keV and lattice spacing is measured using Gatan Digital Micrography software. **EDS data** was obtained on the probe-corrected JEM ARM 200CF (JEOL, Japan) fitted with a detector, at E01, Diamond Light Source, for element mapping. EDS signal is obtained in STEM imaging mode for Pt, Pd, C, Si and O.

XRD patterns were measured for Pt_1Pd_{22}, Pt_1Pd_{142} and Pt_1Pd_{493} at UCL on the Rigaku SmartLab XRD with a Cu-α X-ray source with 2θ value range of 30 to 90° and fitted to elemental standards. **XPS** is measured between 0 and 1400 eV binding energy (B.E.) on a ThermoFisher Scientific NEXSA spectrometer. Adventitious C 1*s* peak at 284.8 eV is used for calibration. Pd 3*d* peaks were fitted to values of Pd(0) and Pd(II). Data analysis is performed with CasaXPS software (version: 2.3.18PR1.0) and Origin(Pro)[54].

4.4.3 Electrochemical Testing

Oxygen reduction reaction testing: For electrochemical testing, a Gamry potentiostat is used to control the potential and record current across a three-

electrode cell. 2 mg of catalyst is dispersed in 1 mL 0.11 wt% Nafion in ethanol/water (from Alfa Aesar Nafion D-521 5% in water and ethanol). At the working electrode, 10 µl of catalyst ink is loaded on a glassy carbon rotating disk electrode (RDE) and spin-dried to form a uniform coating. 0.1 M $HClO_4$ electrolyte is used with platinum mesh as a counter electrode and calibrated Ag/AgCl (RHE +0.265 V) as a reference electrode. N_2 and O_2 were purged for at least 20 minutes prior to testing. After activation in N_2, cyclic voltammetry is measured with a standard range of 0.04 V to 1.2 V vs reference hydrogen electrode[55] at a rate of 50 $mV \cdot s^{-1}$. Linear sweep voltammetry measurements were recorded in O_2 environment, scanning 20 $mV \cdot s^{-1}$ at rotation speeds of 800, 1200, 1600 and 2000 rpm. Readings at 1600 rpm have been reported throughout.

Original LSV data is recorded, without iR correction or N_2 background correction as a direct comparison between samples within the same system. Kinetic current was calculated at 0.9 V and divided by Pt loading or total metal loading measured with MP-AES to obtain the mass activity of each sample.

Electrochemical surface area was measured between 0.04 V and 0.35 V, and calculated with the hydrogen adsorption and desorption areas using the hydrogen charge transfer for either Pd (420 $\mu C \cdot m^{-2}$) or Pt (210 $\mu C \cdot m^{-2}$), as appropriate.[5] Background subtraction data was gathered in N_2 environment with a rotating and stationary electrode. iR correction was run using resistance obtained from EIS results with a Nyquist Plot.

4.4.4 Modelling: DFT Calculation Setup and Parameters

Periodic DFT calculations were performed using the Vienna Ab initio Simulation Package (VASP)[56-59] version 5.4.1. The projector augmented wave (PAW) method is used to model the core ionic potentials.[60,61] The revised generalised

gradient of Perdew, Burke and Ernzerhof (RPBE) is used throughout.[62] The empirical correction scheme of Grimme et al. is employed to model the effects of dispersion.[63] For all systems, a 3 × 3 × 5 slab unit cell is used for which the bottom three layers are fixed at the RPBE bulk FCC lattice constant of the corresponding metal (4.01 Å and 4.00 Å for Pt and Pd, respectively) and for dilute surface alloys, the host material lattice parameter is used. For calculations on surface alloys, n surface host atoms were replaced by n dopant atoms giving a surface loading of n/9. An approximate vacuum region of 20 Å above the surface is used to minimise periodic interactions in the z-direction. A hexagonal ice-like water layer is added above the surface at a coverage of 2/3 ML. A dipole correction accounted for the net dipole moment caused by slab asymmetry along z. 3 × 3 × 1 and 7 × 7 × 1. Monkhorst-Pack k-point meshes were used for geometry optimisation and density of states calculations, respectively. The plane-wave kinetic energy cut-off is set to 400 eV. To aid with convergence, we employed Methfessel-Paxton smearing with a width of k_BT = 0.1 eV; the final electronic energy is extrapolated to k_BT = 0 eV. Electronic self-consistency is ensured up to a tolerance of 10^{-7} eV. To locate stable configurations in the potential energy surface, conjugate gradient minimisation of the Hellmann-Feynman forces is performed on all atoms to within a tolerance of 10^{-2} eV·Å^{-1}. Transition state searches were conducted with the dimer formalism of Jónsson and Henkelman.[64] The transition states for O_2 dissociation were computed in the absence of solvent to prevent over-confinement of the reaction pathway caused by the structural rigidity of the ice-like water. Notably only a minor stabilisation is computed for O_2 and O in the presence of water, which is deemed sufficiently small to neglect in favour of the greater configurational freedom of the dissociation in vacuum. To validate that states found correspond to first order saddle points, vibrational frequency

analysis is performed. Vibrational frequencies were calculated using a harmonic approximation with finite displacements of 0.02 Å and the presence of only one imaginary frequency is verified.

Notes and figures describing the Definition of Free Energy, the Re-aligning of Free energy to RHE, Definition of the Theoretical Overpotential and Model Surface and Double Layer Structure are provided in the Supplementary Information.

4.4.5 Beamline Setup and Data Analysis

***Ex-situ* XAS collection:** XANES and EXAFS of the Pt L_3-edge (11.5637 keV) were measured for all samples at beamline B18, Diamond Light Source (UK) with a ring energy of 3.0 GeV and a beam current of 300 mA.[65] Quick EXAFS (QEXAFS) is set up with a Si(111) double crystal monochromator and a Cr-coated collimating mirror which are also active in harmonic rejection for the intermediate energy range. The XAS spectra were measured in an energy range of 11.364 to 13.262 keV. The beam size is 200 μm × 250 μm with a time-resolution of 2.5 min per spectrum (k_{max}=14.5, step size of 0.43 eV). Due to low Pt loading, all samples were measured in fluorescence mode with a 36-element Ge detector, using Pt foil for energy calibration. Sample powder is placed in a plastic sachet with uniform thickness during measurements.

Linear combination fit (LCF), a mathematical fitting of standard XAS spectra of known materials to a spectrum of a sample was used, in this case, to estimate the degree of oxidation of Pt in the nanoparticles. Pt foil and PtO_2 were used as standards of oxidation states for Pt(0) and Pt(IV). LCF was run for XANES region of *ex situ* samples between -20 and 30 eV from E_0. This LCF serves as a comparison of oxidation between samples and absolute values may only be

accurate to within 10%. The change in oxidation at the Pt edge can alternatively be observed as a change in the white line intensity. LCF values are reported as % with errors given according to the goodness of fit.

Ex situ samples were measured at Pt L_3-edge (11.5637 keV) and Pd K-edge at beamline BL01B1, SPring-8 (Japan). *In situ* samples were measured only for Pt L_3-edge (11.5637 keV) with electrochemical *in situ* cell. The fluorescence spectra of samples were measured 6 to 10 times with 15 to 30 minute acquisition time and later merged to improve signal-to-noise ratio.

***In situ* XAS and Electrochemistry measurement:** *In situ* XANES and EXAFS were measured using a specially designed three-electrode cell with a Kapton window and vertical configuration of working electrode. The catalyst is uniformly distributed on carbon paper using the automated Exactacoat spray machine. Sample loading is measured by mass, aiming to achieve 1 $mg \cdot cm^{-2}$ sprayed over a 5 cm^2 area. A 1 cm^2 square uniform piece is wetted and activated before loading into the cell. O_2 and N_2 gas lines were fitted to the cell and operations were run at room temperature. The 100 mM $HClO_4$ electrolyte, reference and working electrodes were kept the same as that of electrochemical testing. The *in situ* cell is used at B18,[65] with the same beamline configuration and data acquisition settings for samples held at 0 V and 1.2 V over a period of 45 minutes.

While running cyclic voltammetry (CV) *in situ* XANES and EXAFS spectra were collected at the Pt L_3-edge in fluorescence mode at beamline BL01B, SPring-8 (Japan) with ring energy of 8 GeV and ring current of 99.5 mA. The collimating and focusing mirrors were Rh-coated and a double crystal Si (111) monochromator is used. The spectra were collected with a 19-element Ge detector with a scanning range of 11.37 to 12.20 keV (k_{max} = 13.1, step size of 0.36 eV). *In situ* samples were measured with a time-resolution of 10 min per

spectrum and CV scan rate is adjusted accordingly, allowing 15-20 spectra during a cycle.

Data Analysis: Demeter (Athena and Artemis, version 0.9.26) is used to analyse XAS data.[66] Athena software is used for data extraction and XANES analysis while Artemis software is used to analyse the EXAFS region. LCF is run for XANES with measured Pt foil and PtO_2 as standards, between -20 and 30 eV from E_o. The k^2-weighted EXAFS data is fitted in real space with 3.1 $Å^{-1}$ < *k* < 12.4 $Å^{-1}$ and 1.25 Å < R < 3.3 Å. The amplitude reduction factor (S_0^2) is set at 0.7944 during EXAFS fitting, as calculated for Pt foil and 0.866 for Pd foil. Pt, Pd and Pt-Pd path lengths were selected from crystallographic data.[35] The Debye-Waller factor (σ^2) is calculated to be similar for all Pt-Pd paths, as *ex situ* testing conditions were constant. This value is later set as a defined parameter to improve fitting.

4.5 Supporting Information

The first experiment, in Chapter 4, investigates the formation of Pt-Pd alloy nanoparticles with a growth *via* chemical precipitation method and correlates the electrochemical activity and mechanisms with the alloy composition. TEM, XPS, XRD, XAS and DFT results were used to support the conclusions drawn, using the methods previously described. Reproducibility of TEM imaging for nanoparticles, a further description of the electrochemical method and results, beamlines descriptions of the two beamlines used to collect data for this experiment and some notes on the DFT calculation definitions are provided for further clarity on experiments.

4.5.1 TEM Additional Images

Additional TEM images are obtained for each nanoparticle composition (Figure 4.12) of Pt_1Pd_{22} (a), Pt_1Pd_{142} (b), Pt_1Pd_{493} (c), Pd (d) and Pt (e). These alloyed Pt and Pd nanoparticles are loaded on a porous carbon surface.

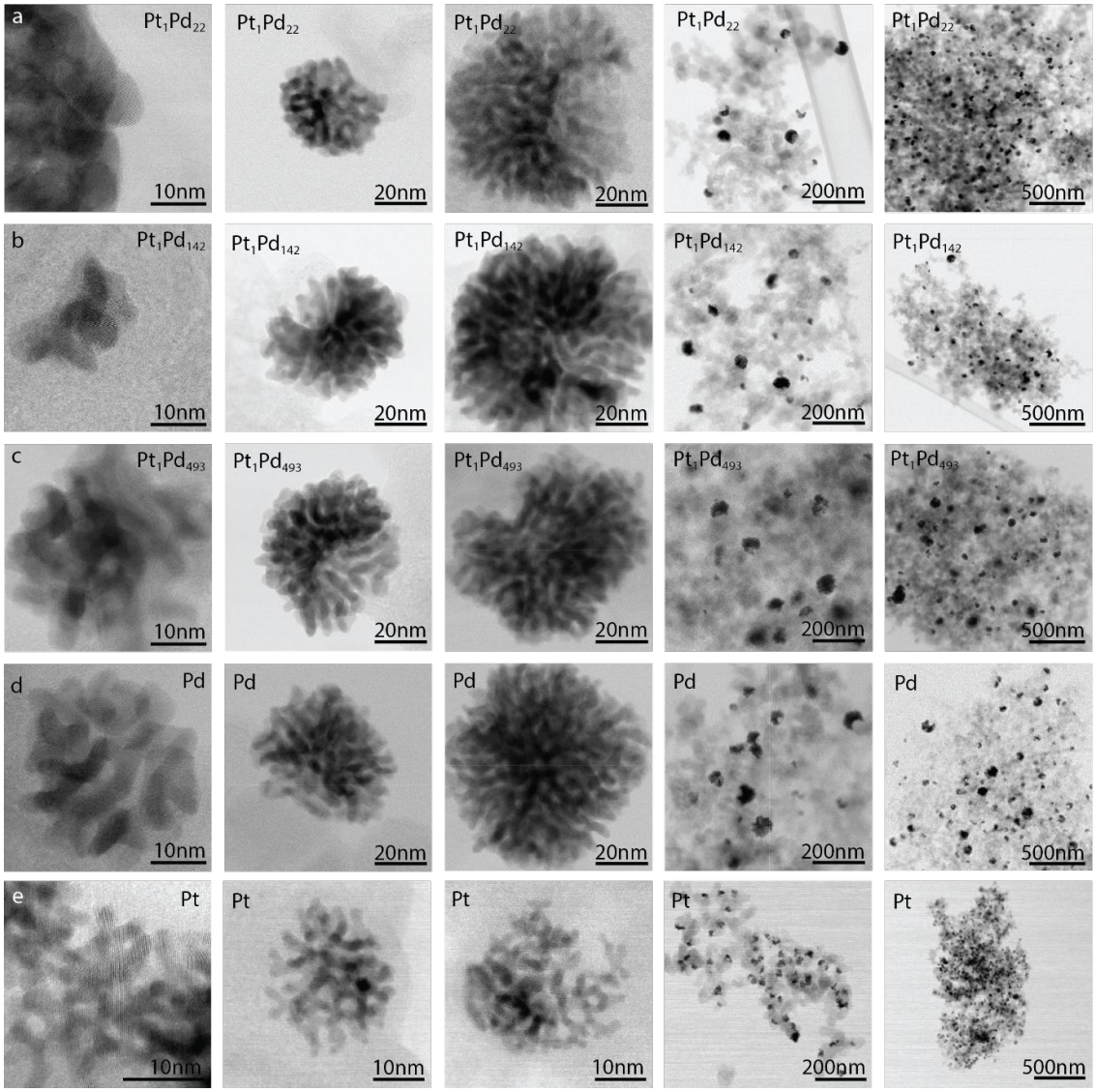

Figure 4.12 ***Additional TEM Images of Pt_xPd_y/C Nanoparticles.*** *BF-STEM visualisation of carbon-supported Pt_xPd_y nanoparticles at 10 nm to 500 nm-scale for rows (a) Pt_1Pd_{22}, (b) Pt_1Pd_{142}, (c) Pt_1Pd_{493}, (d) Pd and (e) Pt.*

Table 4.7 ***Average Nanoparticle Size Results.*** *Measured from TEM images on ImageJ.*

Sample Name	Number of particles	Average diameter (nm ± S.D.)	Number of clusters	Cluster Radius (nm ± S.D.)
$Pt_1Pd_{2.4}$	332	45.33 ± 13.05	99	1.99 ± 0.08
Pt_1Pd_{22}	370	44.23 ± 13.30	220	2.49 ± 0.32
Pt_1Pd_{142}	247	50.66 ± 26.95	174	2.88 ± 0.51
Pt_1Pd_{493}	430	58.24 ± 23.30	361	3.00 ± 0.41
Pd	282	48.72 ± 18.55	136	2.48 ± 0.20

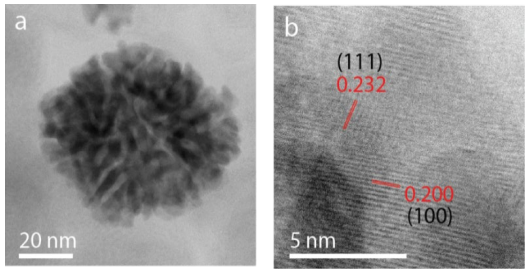

Figure 4.13 ***Lattice Spacing in Pd/C nanoparticles.*** *Bright Field HAADF-STEM imaging of Pd/C nanoparticle at (a) 20 nm-scale to observe morphology and (b) 5 nm-scale where lattice fringes with spacing of 0.232 nm and 0.200 nm indicate presence of Pd(111) and Pd(100) facets, respectively.*

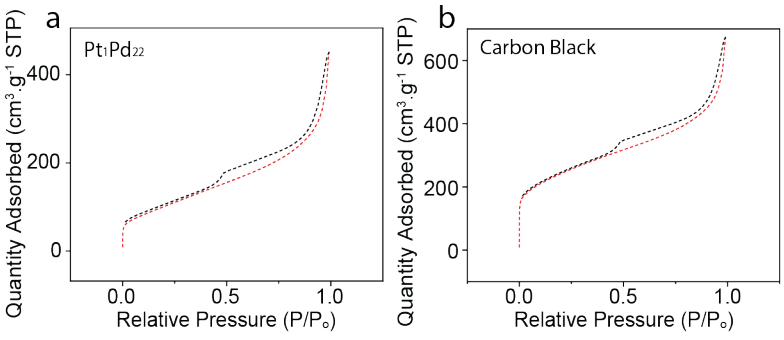

Figure 4.14 ***Nitrogen Sorption Isotherms of NP Loaded Carbon Black.*** *BET analysis of nitrogen sorption isotherms show a decrease in surface area after nanoparticle loading, where surface area of (a) Pt_1Pd_{22} is 380.654 $m^2.g^{-1}$ and (b) Carbon black (Ketjenblack EC-300J) is 836.767 $m^2.g^{-1}$.*

4.5.2 Electrochemical Method and Results

Electrochemical results for samples not included in Chapter 4, are given in Figure 4.15. These were recorded with a graphite counter electrode to ensure that Pt contamination does not occur during the electrochemical measurements. The LSV results of samples produced are obtained for at least three datasets to ensure reproducibility, and to select the average or intermediate result.

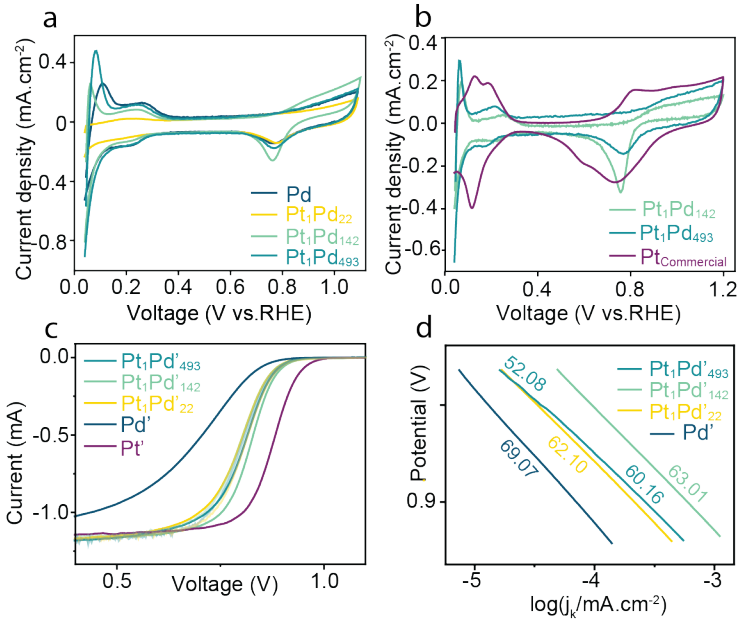

Figure 4.15 ***CV, LSV and Tafel Results of Pt_xPd_y/C Nanoparticles.*** *CV results collected at a rate of 5 mV.s^{-1} ranging from 0.04 V to 1.2 V in 0.1 M $HClO_4$ are compared for (a) Pt_1Pd_{22} (yellow), Pt_1Pd_{142} (turquoise), Pt_1Pd_{493} (blue) and Pd (dark blue) nanoparticles and (b) Pt_1Pd_{142} (turquoise), Pt_1Pd_{493} (blue) and commercial Pt/C (purple) nanoparticles. The same materials are measured under (c) LSV with a graphite counter electrode, showing the same results as Pt counter electrode and (d) corresponding Tafel plots are calculated with slope measurements indicated.*

4.5.3 Beamlines B18 (DLS) and BL01B1 (SPring-8)

B18[65] is a hard X-ray beamline at Diamond Light Source, UK, which uses a bending magnet to provide a high flux and energy range of 2.05 to 35 keV. Thus, B18 is the ideal beamline for Pd K edge (24.4 keV) and Pt L_3 edge (11.5 keV) measurements. In the case of Pt-Pd extreme ratio alloys, both transmission and fluorescence mode were applied, for high concentration of Pd and weak Pt signal, respectively. As it was not possible to create pellets from carbon-loaded nanoparticles due to the lack of integrity of carbon pellets, the samples were measured as powders tightly packed into a plastic sachet for *ex situ* measurements. No dilution was applied due to the low metal loading and low Pt concentration.

In situ experiments were performed with a specially designed electrochemical cell as described earlier. Cell design was adjusted to substitute a steel working electrode connection with a graphite plate to reduce interference of metals near the fluorescent beam while measuring the low Pt concentration.

Additional *in situ* measurements were performed at SPring-8 beamline BL01B1,[67] a hard X-ray beamline with an energy range of 3.8 to 113 keV. The same *in situ* electrochemical cell and reaction setup were used, except that the carbon paper loaded catalyst was activation cycled in a separate chamber prior to introduction into the cell. A second run of activation was performed within the cell to ensure that no oxygen remained before the cyclic voltammetry measurement. Slow cycling was performed to allow time for fluorescence measurements at the Pt L_3 edge. Samples were measured *ex situ* in powder form and compared with the carbon paper loading, to investigate changes during catalyst use.

4.5.4 XAS Analysis and Fit Results

Degree of Alloying (J-value)

EXAFS refinement gives an indication of the average coordination of metals within an alloy. The work by Hwang et al.[39] devises a logical system to correlate the coordination numbers obtained from XAS to define the degree of alloying in a bimetallic system. The basic principle is that a well-distributed alloy will have a lower self-coordination and higher alloy coordination, compared with a segregated alloy. This can be simply calculated by applying the coordination numbers calculated for both metals to the J-value formula.

$$P_{observed} = \frac{N_{A-B}}{\sum N_{A-i}} \qquad \textit{Equation 4.1}$$

$$R_{observed} = \frac{N_{B-A}}{\sum N_{B-i}} \qquad \textit{Equation 4.2}$$

$$P_{random} = \frac{ideal\ ratio\ of\ N_{A-A}}{idea\ ratio\ of\ N_{A-B}} \qquad \textit{Equation 4.3}$$

$$R_{random} = \frac{ideal\ ratio\ of\ N_{B-B}}{idea\ ratio\ of\ N_{B-A}} \qquad \textit{Equation 4.4}$$

$$J_A = \frac{P_{observed}}{P_{random}} \times 100\% \qquad \textit{Equation 4.5}$$

$$J_B = \frac{R_{observed}}{R_{random}} \times 100\% \qquad \textit{Equation 4.6}$$

This methodology is applied for the case of Pt-Pd alloys to better understand, not only the degree of alloying within the samples but also to get a better understanding of the ratios between these metals as observed.

FEFF files Selection

FEFF files are crystallographic information files used to simulate the atomic configuration and bond lengths calculated for a given material. These are often made by scientists based on various research and stored on a centralised database known as the Crystallographic Open Database. FEFF files have been selected in this work based on similarity to the studied system and reaction conditions, as well as their relevance and perceived accuracy.

The FEFF files selected in this work for are:

Pt-Pt: 9008480, Wyckoff, R. W. G., Fm-3m, ccp

Pd-Pd: 9008478, Wyckoff, R.W.G., Fm-3m, ccp

Pd-O: 4124668, Moore, W.J. and Pauling, L., P 42/m m c, tetragonal

The estimated first shell fitting was carried out for bonds which did not have an existing reasonable fit .cif file. These were created in Artemis using the 'Quick First Shell Fitting' function, by inputting the bonded elements and the expected bond length, based on literature values.[66]

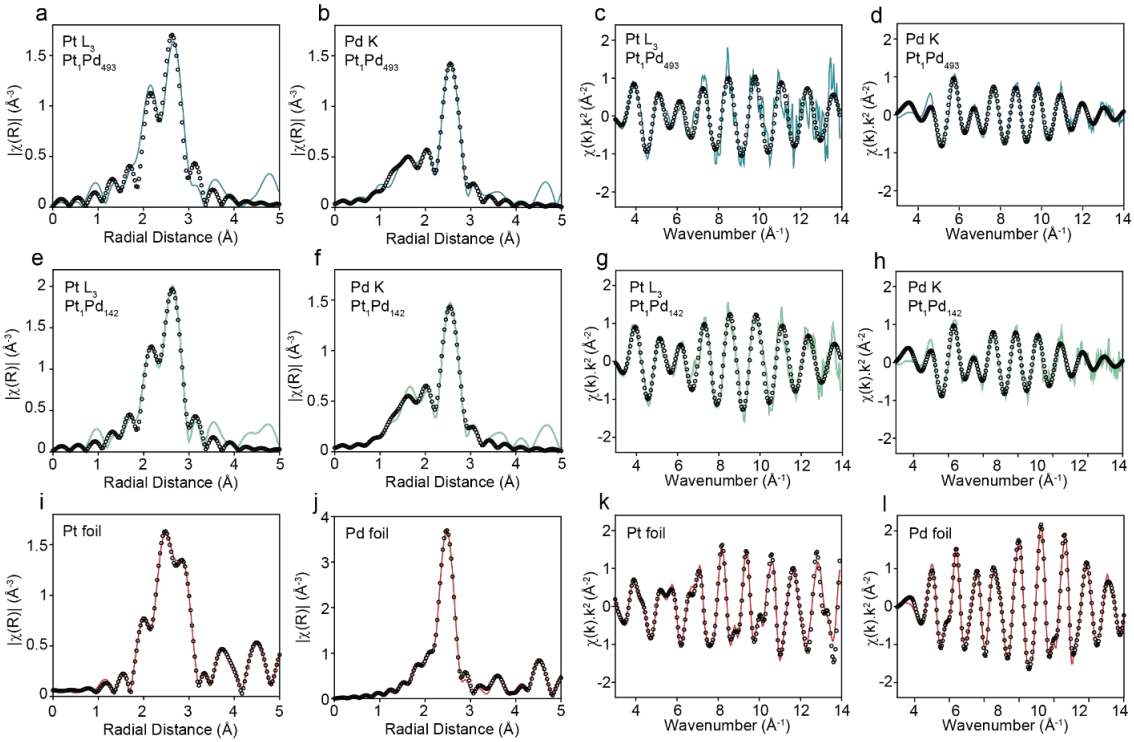

Figure 4.16 ***EXAFS Fitting of Pt/C, Pd/C and Pt_xPd_y/C Nanoparticles.*** *EXAFS k^2-weighted data and fit for (a-d) Pt_1Pd_{493}, (e-h) Pt_1Pd_{142}, (i, k) Pt foil and (j, l) Pd foil shown as (a, e, i) R-space of Pt L_3-edge data, (b, f, j) R-space of Pd K-edge data, (c, g, k) k-space of Pt L_3-edge data, and (d, h, l) k-space of Pd K-edge data. Data is shown as a solid line and fit as black circles, with fitting window of 1.25 to 3.3 Å in R-space and 3 to 12 $Å^{-1}$ in k-space.*

Table 4.8 ***EXAFS Fitting Results for Pt_xPd_y/C Nanoparticles.*** *Artemis fit results of the calculation of Pt C.N. from Pt L_3-edge and Pd K-edge EXAFS. The amplitude reduction factor for Pt was set at 0.7944, as measured for reference Pt foil, while that of Pd foil was set at 0.866 based on Pd foil standard. Bond lengths of 2.77 Å (Pt-Pt), 2.73 Å (Pt-Pd), 2.76 Å (Pd-Pd), 2.05 Å (Pd-O) and 2.05 Å (Pt-O) were selected. Reduced chi-squared 57.26 and R-factor 0.0175.*

Sample (edge)	Path	C.N.	ΔR (Å)	σ^2	M-M C.N.	ΔE_0 (eV)
Pt_1Pd_{142} (Pd K)	Pd-Pd	7.64 ± 0.67	0.005 ± 0.006	0.009	11.13 ± 0.65	-3.77
	Pd-Pt	3.49 ± 1.02	-0.068 ± 0.021			
	Pd-O	1.73 ± 0.50	-0.011 ± 0.028			
Pt_1Pd_{142} (Pt L_3)	Pt-Pt	1.56 ± 0.84	-0.065 ± 0.035	0.005	9.46 ± 0.84	5.89 ± 0.53
	Pt-Pd	7.89 ± 0.53	-0.030 ± 0.005			
	Pt-O	0.58 ± 0.30	-0.064 ± 0.046			
Pt_1Pd_{493} (Pd K)	Pd-Pd	7.98 ± 0.32	0.032 ± 0.003	0.009	9.64 ± 0.48	-3.77
	Pd-Pt	1.66 ± 0.48	-0.060 ± 0.023			
	Pd-O	1.78 ± 0.24	-0.003 ± 0.013			
Pt_1Pd_{493} (Pt L_3)	Pt-Pt	1.50 ± 1.60	0.032 ± 0.003	0.005	8.87 ± 1.60	5.89 ± 0.53
	Pt-Pd	7.38 ± 0.91	-0.013 ± 0.007			
	Pt-O	0.75 ± 0.84	-0.072 ± 0.102			

Table 4.9 ***LCF of Pt L_3-edge data.*** *Pt foil and PtO_2 standards were fitted in Athena with a XANES range of E_0-20 eV to E_0+30 eV.*

Data	R-factor	Pt(IV) weight (%)	Pt(IV) error (%)	Pt(0) weight (%)	Pt(0) error (%)
$Pt_1Pd_{2.4}$	0.0095	4.41×10^{-08}	1.45	100	1.45
Pt_1Pd_{22}	0.0087	4.2×10^{-07}	1.53	100	1.53
Pt_1Pd_{142}	0.0040	4.51	0.94	95.49	0.94
Pt_1Pd_{493}	0.0031	5.82	0.97	94.18	0.97

Table 4.10 ***LCF Results During $Pt_1Pd_{2.4}$/C CV****. LCF results of $Pt_1Pd_{2.4}$ in situ XANES during CV fitted between E_0-20 eV to E_0+30 eV in Athena with Pt foil and PtO_2 as standards measured at Pt L_3-edge.*

Scan Number	Voltage (V)	R-factor	Pt(0) weight (%)	Pt(IV) weight (%)	Error (%)
1	0.14	0.0049	100	0	0
2	0.25	0.0042	100	0	0
3	0.35	0.0041	100	0	0
4	0.45	0.0052	100	0	0
5	0.56	0.0050	100	0	0
6	0.66	0.0048	100	0	0
7	0.77	0.0044	100	0	0
8	0.87	0.0046	100	0	0
9	0.97	0.0052	100	0	0
10	1.08	0.0045	100	0	0
11	1.18	0.0043	100	0	0
12	1.28	0.0049	100	0	0
13	1.39	0.0058	100	0	0
14	1.28	0.0055	96.25	3.75	1.09
15	1.18	0.0055	92.34	7.66	1.10
16	1.08	0.0062	89.00	11.01	1.17
17	0.97	0.0063	88.12	11.81	1.19
18	0.87	0.0059	87.85	12.15	1.14
19	0.76	0.0062	87.59	12.41	1.18
20	0.66	0.0070	89.07	10.93	1.25
21	0.56	0.0054	92.93	7.07	1.08
22	0.45	0.0053	99.13	0.87	1.07
23	0.35	0.0054	100	0	0
24	0.25	0.0043	100	0	0
25	0.14	0.0055	100	0	0
26	0.04	0.0060	100	0	0

Table 4.11 ***LCF Results During Pt_1Pd_{142}/C CV****. LCF results of Pt L_3-edge Pt_1Pd_{142} in situ XANES during CV fitted between E_0-20 eV to E_0+30 eV in Athena with Pt foil and PtO_2 as standards. Generally, the Pt(IV) content does not change during CV.*

Scan Number	Voltage (V)	R-factor	Pt(IV) weight (%)	Pt(0) weight (%)	Error (%)
1	0.14	0.0040	5.34	94.66	0.89
2	0.25	0.0041	5.74	94.27	0.91
3	0.35	0.0041	6.23	93.77	0.91
4	0.45	0.0030	5.95	94.05	0.77
5	0.56	0.0044	5.44	94.56	0.94
6	0.66	0.0051	6.19	93.81	10.22
7	0.77	0.0040	7.20	92.80	0.90
8	0.87	0.0034	5.88	94.12	0.82
9	0.97	0.0029	5.35	94.65	0.77
10	1.08	0.0045	6.08	93.92	0.96
11	1.18	0.0033	6.66	93.34	0.81
12	1.28	0.0037	6.38	93.63	0.86
13	1.39	0.0037	6.38	93.63	0.86
14	1.28	0.0035	6.40	93.61	0.83
15	1.18	0.0037	5.63	94.37	0.86
16	1.08	0.0037	5.63	94.37	0.86
17	0.97	0.0035	6.50	93.50	0.83
18	0.87	0.0037	5.93	94.07	0.86
19	0.77	0.0037	6.77	93.23	0.86
20	0.66	0.0038	7.65	92.35	0.87
21	0.56	0.0044	6.98	93.02	0.94
22	0.45	0.0034	5.82	94.18	0.83
23	0.35	0.0032	5.69	94.31	0.80
24	0.25	0.0028	5.07	94.94	0.74
25	0.14	0.0045	6.00	94.00	0.94

Table 4.12 ***LCF Results During Pt_1Pd_{142}/C Held Potentials****. LCF results for Pt L_3-edge Pt_1Pd_{142} at 0 V and held at 1.2 V over a period of 45 minutes, fitted in Athena from E_0-20 eV to E_0+30 eV with Pt foil and PtO_2 as references.*

Time Elapsed (minutes)	Hold Potential (V)	R-factor	Pt(IV) weight (%)	Pt(0) weight (%)	Error (%)
10	0	0.0044	4.79	95.21	0.95
20	0	0.0045	5.33	94.68	0.97
30	0	0.0041	5.65	94.35	0.93
40	0	0.0030	5.21	94.79	0.78
50	0	0.0046	4.73	95.27	0.98
60	1.2	0.0045	5.50	94.50	0.98
70	1.2	0.0037	6.58	93.42	0.89
80	1.2	0.0034	5.62	94.38	0.85
90	1.2	0.0029	5.41	94.59	0.78
100	1.2	0.0035	6.15	93.85	0.86

Table 4.13 ***LCF Results During $Pt_1Pd_{2.4}$/C Held Potentials****. LCF results for Pt L_3-edge $Pt_1Pd_{2.4}$ at 0 V and held at 1.2 V over a period of 30 minutes, fitted in Athena from E_0-20 eV to E_0+30 eV with Pt foil and PtO_2 as references.*

Time Elapsed (minutes)	Hold Potential (V)	R-factor	Pt(IV) weight (%)	Pt(0) weight (%)	Error (%)
3	0	0.020	1.69E-06	100	2.31
6	0	0.021	3.22E-06	100	2.36
9	0	0.020	3.15E-06	100	2.28
12	0	0.020	6.85E-06	100	2.35
15	0	0.020	2.59E-06	100	2.31
18	0	0.021	5.48E-06	100	2.38
21	0	0.021	2.61E-06	100	2.30
24	0	0.021	2.55E-06	100	2.38
27	0	0.02	3.80E-06	100	2.34
30	0	0.02	3.06E-06	100	2.33
33	1.2	0.002	29.97	70.03	0.82
36	1.2	0.002	31.39	68.61	0.79
39	1.2	0.002	32.13	67.87	0.78
42	1.2	0.002	32.94	67.06	0.82
45	1.2	0.002	33.63	66.37	0.86
48	1.2	0.002	33.54	66.46	0.85
51	1.2	0.002	34.09	65.92	0.83
54	1.2	0.002	34.47	65.53	0.82
57	1.2	0.002	34.80	65.20	0.82
60	1.2	0.002	34.83	65.17	0.80

4.5.5 DFT Definitions and Figures

Definition of the Free Energy

We calculate the free energy of adsorption (ΔG_{ads}) for intermediates ($O_m H_n$) in the ORR pathway by using H_2(g) and H_2O(g) as reference species, such that:

$$\Delta G_{ads} = \Delta E_{tot} + \Delta E_{ZPE} - T\Delta S$$

where ΔE_{tot} is the change in DFT total energy between the adsorbed metal-intermediate system ($M - O_m H_n$) and the sum of total energies for the isolated metal (M), m gas phase H_2O and $\frac{n}{2} - m$ gas phase H_2, ΔE_{ZPE} is the change in zero point energy between these systems and ΔS is the corresponding change. The change in DFT total energy is given as:

$$\Delta E_{tot} = E_{tot}^{M-O_m H_n} - \left(E_{tot}^{M} + m \cdot E_{tot}^{H_2O} + \left(\frac{n}{2} - m\right) \cdot E_{tot}^{H_2}\right).$$

We assume that there is no change in the ZPE and entropic contribution of the metal upon adsorption, thereby approximating ΔE_{ZPE} and ΔS as the change in each between adsorbed $O_m H_n$ and m gaseous H_2O plus $\left(\frac{n}{2} - m\right)$ H_2 as computed from standard equations of statistical mechanics using vibrational frequencies and geometries computing using DFT. It is assumed that surface bound $O_m H_n$ has no translational or rotational component of the entropy and these contributions are instead engulfed into the vibrational entropy by taking the frustrated modes to be pure vibrations. ΔS and ΔG_{ads} are calculated at 298.15 K and 101,325 Pa. We note that values of ΔG_{ads} that are less than zero correspond to an exergonic adsorption process.

Re-aligning the Free Energy to the RHE

To model the effect of an applied potential to our computed values of ΔG_{ads}, we make use of the computational hydrogen electrode (CHE) model of Norskov and

co-workers. The CHE applies an *a priori* correction to the free energy, realigning it to the potential scale of the reversible hydrogen electrode (RHE). We reference zero voltage ($U = 0$) to the RHE such that, under standard conditions (298.15 K, 101,325 Pa) and all pH values, a proton and electron pair is in equilibrium with half a mole of gaseous hydrogen:

$$(\mathrm{H^+ + e^-}) \leftrightarrow \frac{1}{2}\mathrm{H_{2(g)}}$$

and the following relationship between these species' chemical potentials exists:

$$\mu_{\mathrm{H^+}} + \mu_{\mathrm{e^-}}^{U=0} = \frac{1}{2}\mu_{\mathrm{H_{2(g)}}}$$

The chemical potential of $\mathrm{e^-}$ is linearly related to electrical potential by $\mu_{\mathrm{e^-}} = \mu_{\mathrm{e^-}}^{U=0} - eU$, where e is the elementary positive charge and U is the potential with respect to the RHE. We calculate the total chemical potential of a proton-electron pair under an applied potential as:

$$\mu_{\mathrm{H^+}} + \mu_{\mathrm{e^-}} = \frac{1}{2}\mu_{\mathrm{H_{2(g)}}} - eU$$

Thus, we are able to compute the free energy of adsorption under an applied potential without explicit calculation of the free energy of $\mathrm{H^+}$ and $\mathrm{e^-}$ such that:

$$\Delta G_{ads} = \Delta E_{tot} + \Delta E_{ZPE} - T\Delta S - neU$$

Definition of the Theoretical Overpotential

For each step i in the ORR pathway the free energy of reaction ($i = 1,2,3,4$) is calculated as the difference in the free energy between the final and initial states:

$$\Delta G_{rxn} = \Delta G_{ads}^{Final} - \Delta G_{ads}^{Initial}$$

such that negative values of ΔG_{rxn} correspond to an exergonic process. Finally, the theoretical overpotential (η) is defined as the difference between the equilibrium potential and the potential required to ensure all steps in the forward

ORR process are thermodynamically downhill. Thus, the theoretical overpotential is expressed as:

$$\eta = \max_{i}(\Delta G_{rxn}^{i}) \text{ for } U = 1.23 \text{ V};\ i = 1,2,3,4.$$

The value of η is used as an indicator for catalytic performance, whereby lower values of η indicate more effective ORR catalysis.

Model Surface and Double Layer Structure

Each model surface consists of a 3 × 3 × 5 hexagonal slab unit cell, with n surface host atoms replaced by n dopant atoms giving a surface loading of n/9 for alloy structures. A bilayer of water is used as an approximation to the electrochemical double layer. The surface structure is commensurate with the hexagonal structure of ice. The bilayer consists of six water molecules oriented in the "H-down" ice structures for which every other H_2O molecule is flat to the surface with the next H_2O being oriented with the O-H bond vector anti-parallel the [1 1 1] surface normal (Figure 4.17).

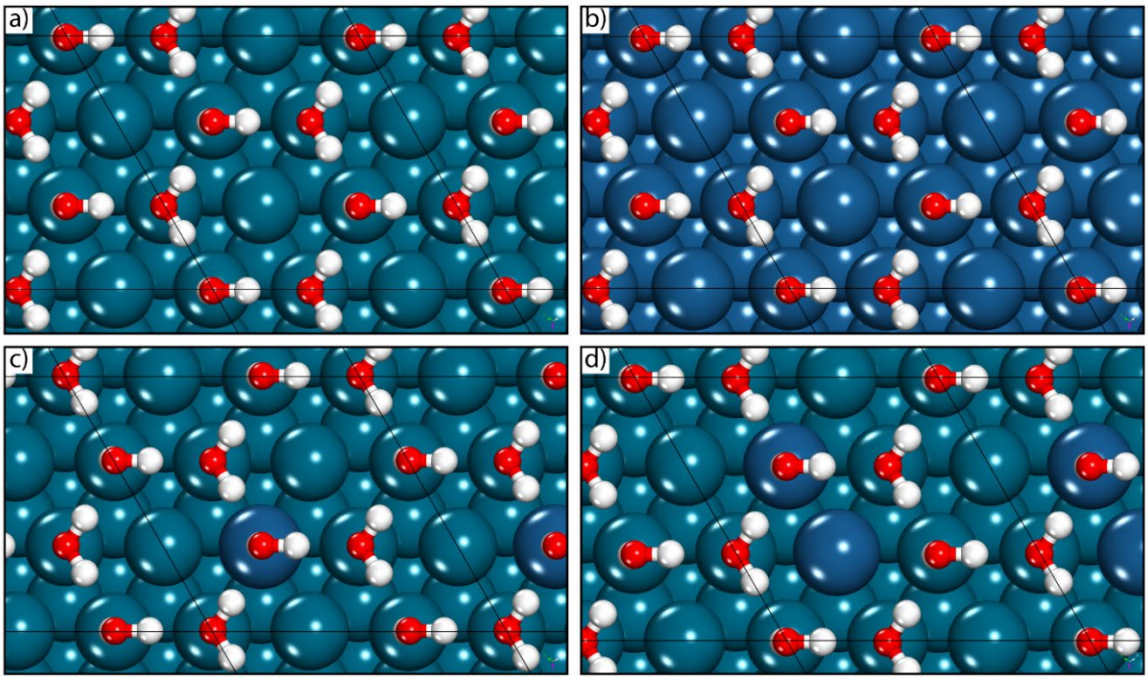

Figure 4.17 ***Water/Ice Bilayer Over Pt_xPd_y Slab Configurations.*** *Schematic showing the top down view along the [1 1 -1] vector of a) Pd(111); b) Pt(111); c) $Pt_1Pd(111)$; and d) $Pt_2Pd(111)$ slabs covered in a water/ice bilayer. The structures shown are the lowest energy structures of the adsorbed water bilayer after geometry optimisation. The 3 × 3 unit cell is drawn in black. Pd atoms are shown in teal, Pt are blue, O are red, and H are white.*

This structure of the ice bilayer is used as the reference state for the solvated slab. In the case of alloy structures, the surface symmetry is reduced. Consequently, for $Pt_1Pd(111)$, the single Pt surface atom may either be i) bare; ii) covered by flat H; or iii) covered by H-down water. We chose not to study i), for which the Pt dopant atom is bare, since the adsorption of ORR intermediates involves the direct substitution of a water molecule from the bilayer and therefore the intermediate would not be bound to the Pt ensemble of interest. For the remaining cases, we determined that structure iii) is the most stable, though ii) has an energy of formation that is only 10 meV more negative (i.e., more favourable) than structure iii). However, upon replacing the water molecule

located above the Pt atom with OH* or OOH*, there is greater disruption to the H-bonding network that renders the adsorption of these intermediates into structure ii) less favourable than into structure iii). Given the marginal difference in energy between structures ii) and iii), we use the latter (H-down water above the Pt atom (Figure 4.17 c) as a reference structure for $Pt_1Pd(111)$. In the case of $Pt_2Pd(111)$, the two contingent Pt atoms can be covered by either iv) one "H-down" plus one flat water; v) one flat water only; or vi) one "H-down" water only. Here we are forced to exclude bare Pt since the structure of hexagonal water dictates that at least one of the two sequential Pt atoms in the dimer is covered. Considering possible configurations iv-vi), we determine that structure vi), for which one surface Pt atom is covered by one "H-down" water molecule while the neighbouring Pt atom is bare, is the most stable and is therefore used as our reference for $Pt_2Pd(111)$ (Figure 4.17 d). ORR intermediate adsorption calculations use the bilayer covered slab models (Figure 4.17) as reference structures.

Using harmonic transition state theory,[20] we compute kinetic constants of 1.56×10^{10} s^{-1} and 4.39×10^{9} s^{-1} for O_2 bond cleavage on $Pt_1Pd(111)$ and $Pt_2Pd(111)$, compared to 3.23×10^{5} s^{-1} on Pd(111), which suggests facile dissociation at room temperature on the dilute alloys that proceeds 10^4 to 10^5 times faster than on pure Pd(111). Thus, from our calculations we conclude that the observed high mass activity of Pt_1Pd_{493} can be explained by the presence of Pt dimers (and possibly monomers) that facilitate dissociative ORR, with a low overpotential compared to Pt(111).

In this case, a H_2O molecule is removed from the bilayer and replaced by O_2* (Figure 4.18 a-d), OOH* (Figure 4.18 e-h), O* (Figure 4.18 i-l) and OH* (Figure 4.18 m-p), with the additional atoms removed/extra atoms required for the ORR

species from H_2O going to/coming from a gas phase reservoir of H_2 and H_2O (Figure 4.17).

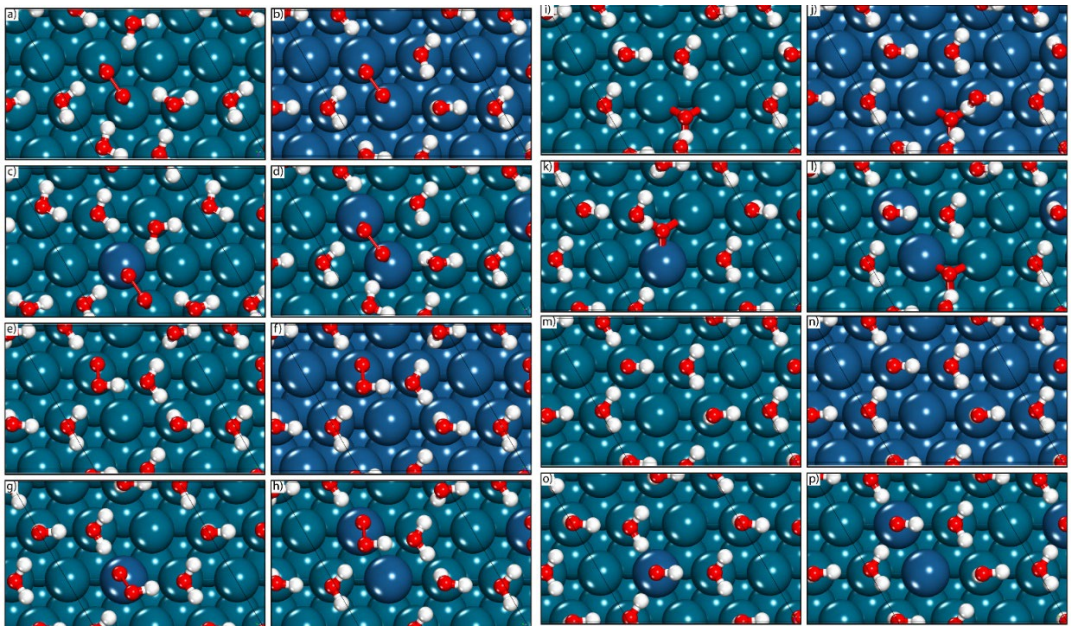

Figure 4.18 ***ORR Intermediates Top-Down View.*** *Schematic showing the top-down view along the [1 1 -1] vector of ORR intermediates O_2* (a-d), OOH* (e-h), O* (i-l) and OH* (m-p) on Pd(111), Pt(111), $Pt_1Pd(111)$, and $Pt_2Pd(111)$ slabs covered in a water/ice bilayer with one H_2O removed. The structures shown are the lowest energy structures after geometry optimisation. The 3 × 3 unit cell is drawn in black. Pd atoms are shown in teal, Pt are blue, O are red, and H are white.*

The most favourable water molecule to remove is in the “H-down” structure, rather than the flat mode in all cases. For alloy surfaces, this water molecule is removed from a Pt site rather than Pd. The resulting structures are shown in Figure 4.18 and free energies of adsorption at U = 0 V are given in Table 4.5. The reaction free energies calculated at the equilibrium ORR potential (U = 1.23 V) and corresponding overpotentials are given in Table 4.14.

Table 4.14 ***Free Energies of Reaction at U = 1.23 V.*** *Computed from DFT for the reduction of ORR intermediates O_2*, OOH*, O* and OH* in the four electron ORR pathway on Pd(111), Pt(111), Pt_1Pd(111) and Pt_2Pd(111) covered in a bilayer of ice-like water. Energies are given in units of eV. The theoretical overpotential μ is the maximum value of ΔG_{rxn} at 1.23 V computed along the full pathway and is also given in units of eV.*

	ΔG_{rxn} at U = 1.23 V (eV)					
Slab	$O_2 \rightarrow O_2$*	O_2* + ($H^+ + e^-$) → OOH*	OOH* + ($H^+ + e^-$) → O* + H_2O	O* + ($H^+ + e^-$) → OH*	OH* + ($H^+ + e^-$) → H_2O	μ (eV)
Pd(111)	-0.79	1.03	-0.98	0.29	0.45	1.03
Pt(111)	-0.39	0.50	-0.76	0.13	0.53	0.53
Pt_1Pd(111)	-0.78	0.97	-0.88	0.19	0.49	0.97
Pt_2Pd(111)	-0.63	0.82	-0.94	0.32	0.44	0.82

The dissociation of the O_2 dimer is computed in vacuum and the activation energies are given in Table 4.15 and the transition state structures are shown in Figure 4.19. The activation energy (E_a) is computed as the difference in DFT total energy between the O_2* adsorbed state ($E_{tot}^{M-O_2*}$) and the transition state (E_{tot}^{M-TS}) such that $E_a = E_{tot}^{M-TS} - E_{tot}^{M-O_2*}$.

Table 4.15 ***Activation Barriers of Dissociation.*** *Calculated for a pre-adsorbed O_2 dimer on Pd(111), Pt(111), $Pt_1Pd(111)$ and $Pt_2Pd(111)$ in vacuum.*

Slab	E_a (eV)
Pd(111)	0.47
Pt(111)	0.13
$Pt_1Pd(111)$	0.18
$Pt_2Pd(111)$	0.20

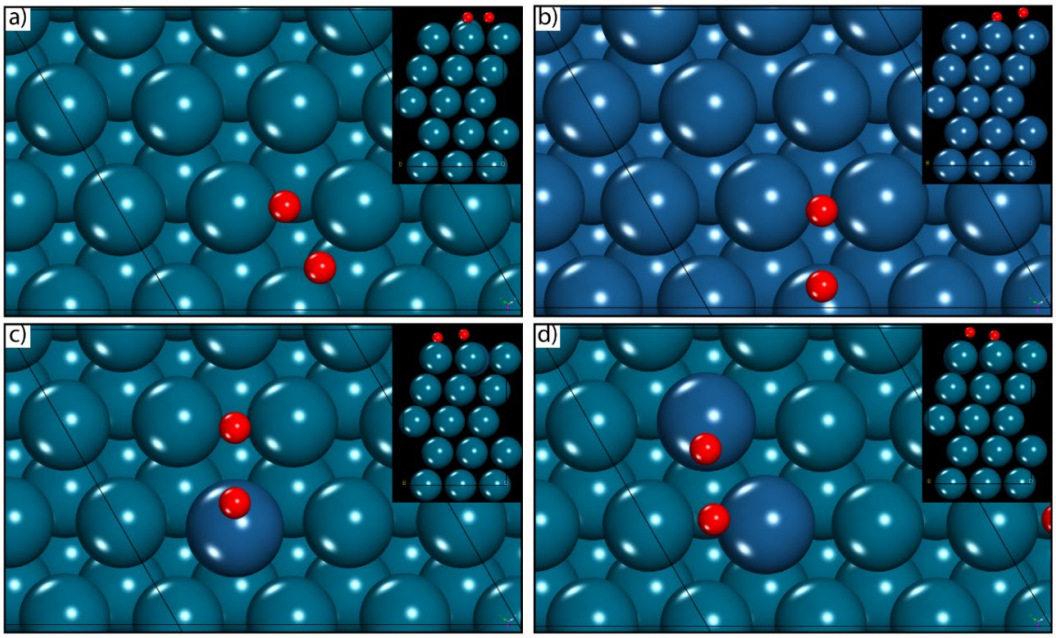

Figure 4.19 ***Optimised O_2 Dissociation Transition States.*** *Schematic showing the top-down view along the [1 1 -1] vector of DFT optimised geometries of the O_2 dimer dissociation transition state on (a) Pd(111); (b) Pt(111); (c) $Pt_1Pd(111)$; and (d) $Pt_2Pd(111)$ slabs in vacuum. The 3 × 3 unit cell is drawn in black. Pd atoms are shown in teal, Pt are blue, and O are red. Insets show the side-on view parallel to the surface.*

4.6 References

1 Nagasawa, K. *et al.* Performance and durability of Pt/C cathode catalysts with different kinds of carbons for polymer electrolyte fuel cells characterized by electrochemical and in situ XAFS techniques. *Physical Chemistry Chemical Physics* **16**, 10075-10087, http://dx.doi.org/10.1039/c3cp54457e (2014).

2 Shao, M. *et al.* Manipulating the oxygen reduction activity of platinum shells with shape-controlled palladium nanocrystal cores. *Chemical Communications* **49**, 9030-9032, http://dx.doi.org/10.1039/c3cc43276a (2013).

3 Yano, H. *et al.* Particle-size effect of nanoscale platinum catalysts in oxygen reduction reaction: an electrochemical and 195Pt EC-NMR study. *Phys Chem Chem Phys* **8**, 4932-4939, http://dx.doi.org/10.1039/b610573d (2006).

4 Zhang, J., Yang, H., Fang, J. & Zou, S. Synthesis and oxygen reduction activity of shape-controlled Pt_3Ni nanopolyhedra. *Nano Lett* **10**, 638-644, http://dx.doi.org/10.1021/nl903717z (2010).

5 Chandran, P., Ghosh, A. & Ramaprabhu, S. High-performance platinum-free oxygen reduction reaction and hydrogen oxidation reaction catalyst in polymer electrolyte membrane fuel cell. *Scientific Reports* **8**, 3591, http://dx.doi.org/10.1038/s41598-018-22001-9 (2018).

6 He, Y. & Wu, G. PGM-Free oxygen-reduction catalyst development for proton-exchange membrane fuel cells: challenges, solutions, and promises. *Accounts of Materials Research* **3**, 224-236, http://dx.doi.org/10.1021/accountsmr.1c00226 (2022).

7 Shen, X. *et al.* Deconvolution of octahedral Pt_3Ni nanoparticle growth pathway from in situ characterizations. *Nature Communications* **9**, 4485, http://dx.doi.org/10.1038/s41467-018-06900-z (2018).

8 Tseng, Y. C., Chen, H. S., Liub, C.-W., Yeh, T. H. & Wang, K. W. The effect of alloying on the oxygen reduction reaction activity of carbon-supported PtCu and PtPd nanorods. *Journal of Materials Chemistry A*, 1-3, http://dx.doi.org/10.1039/x0xx00000x (2014).

9 Zhang, L., Lee, K. & Zhang, J. The effect of heat treatment on nanoparticle size and ORR activity for carbon-supported Pd–Co alloy electrocatalysts. *Electrochimica Acta* **52**, 3088-3094, http://dx.doi.org/10.1016/j.electacta.2006.09.051 (2007).

10 Yang, Z., Wang, J. & Yu, X. The adsorption, diffusion and dissociation of O_2 on Pt-skin $Pt_3Ni(111)$: a density functional theory study. *Chemical Physics Letters* **499**, 83-88, http://dx.doi.org/10.1016/j.cplett.2010.09.021 (2010).

11 Stamenkovic, V. R. *et al.* Improved oxygen reduction activity on $Pt_3Ni(111)$ via increased surface site availability. *Science* **315**, 493-497, http://dx.doi.org/10.1126/science.1135941 (2007).

12 Sheng, H. *et al.* Carbon dioxide dimer radical anion as surface intermediate of photoinduced CO_2 reduction at aqueous Cu and CdSe nanoparticle catalysts by rapid-scan FT-IR spectroscopy. *Journal of the American Chemical Society* **140**, 4363-4371, http://dx.doi.org/10.1021/jacs.8b00271 (2018).

13 Huang, J., Ding, C., Yang, Y., Liu, G. & Cai, W.-B. An alternate aqueous phase synthesis of the Pt_3Co/C catalyst towards efficient oxygen reduction reaction. *Chinese Journal of Catalysis* **40**, 1895-1903, http://dx.doi.org/10.1016/s1872-2067(19)63338-3 (2019).

14 Xiong, Y., Xiao, L., Yang, Y., DiSalvo, F. J. & Abruña, H. D. High-loading intermetallic Pt_3Co/C core–shell nanoparticles as enhanced activity electrocatalysts toward the Oxygen Reduction Reaction (ORR). *Chemistry of Materials* **30**, 1532-1539, http://dx.doi.org/10.1021/acs.chemmater.7b04201 (2018).

15 Thanasilp, S. & Hunsom, M. Effect of Pt: Pd atomic ratio in Pt–Pd/C electrocatalyst-coated membrane on the electrocatalytic activity of ORR in PEM fuel cells. *Renewable Energy* **36**, 1795-1801, http://dx.doi.org/10.1016/j.renene.2010.10.024 (2011).

16 Carlos Calderón, J., Ndzuzo, L., Bladergroen, B. J. & Pasupathi, S. Catalytic activity of carbon supported-Pt-Pd nanoparticles toward the oxygen reduction reaction. *Materials Today: Proceedings* **5**, 10551-10560, http://dx.doi.org/10.1016/j.matpr.2017.12.387 (2018).

17 Duan, H. & Xu, C. Nanoporous PtPd alloy electrocatalysts with high activity and stability toward Oxygen Reduction Reaction. *Electrochimica Acta* **152**, 417-424, http://dx.doi.org/10.1016/j.electacta.2014.11.160 (2015).

18 Chen, H. S. *et al.* Graphene-supported Pt and PtPd nanorods with enhanced electrocatalytic performance for the oxygen reduction reaction. *Chemical Communications* **50**, 11165-11168, http://dx.doi.org/10.1039/c4cc04595e (2014).

19 Zhang, L. *et al.* Pt/Pd single-atom alloys as highly active electrochemical catalysts and the origin of enhanced activity. *ACS Catalysis* **9**, 9350-9358, http://dx.doi.org/10.1021/acscatal.9b01677 (2019).

20 Darby, M. T. & Stamatakis, M. Single-atom alloys for the electrochemical oxygen reduction reaction. *Chemphyschem* **22**, 499-508, http://dx.doi.org/10.1002/cphc.202000869 (2021).

21 Li, H. *et al.* Collaboration between a Pt-dimer and neighboring Co-Pd atoms triggers efficient pathways for oxygen reduction reaction. *Physical Chemistry Chemical Physics* **23**, 1822-1834, http://dx.doi.org/10.1039/d0cp05205a (2021).

22 Lu, B. *et al.* Oxygen reduction reaction catalyzed by carbon-supported platinum few-atom clusters: significant enhancement by doping of atomic cobalt. *Research* **2020**, 1-12, http://dx.doi.org/10.34133/2020/9167829 (2020).

23 Zhang, W. *et al.* Emerging dual-atomic-site catalysts for efficient energy catalysis. *Advanced Materials* **33**, 1-17, http://dx.doi.org/10.1002/adma.202102576 (2021).

24 Jia, Q. *et al.* Activity descriptor identification for oxygen reduction on platinum-based bimetallic nanoparticles: in situ observation of the linear composition strain activity relationship. *ACS Nano* **9**, 387-400, http://dx.doi.org/https://doi.org/10.1021/nn506721f (2015).

25 Keith, J. A. & Jacob, T. Theoretical studies of potential-dependent and competing mechanisms of the electrocatalytic oxygen reduction reaction on Pt(111). *Angewandte Chemie International Edition in English* **49**, 9521 –9525, http://dx.doi.org/10.1002/anie.201004794 (2010).

26 Lim, D.-H. & Wilcox, J. Mechanisms of the oxygen reduction reaction on defective graphene-supported Pt nanoparticles from first-principles. *The Journal of Physical Chemistry C* **116**, 3653-3660, http://dx.doi.org/10.1021/jp210796e (2012).

27 Nørskov, J. K. *et al.* Origin of the overpotential for oxygen reduction at a fuel-cell cathode. *Journal of Physical Chemistry B* **108**, 17886-17892, http://dx.doi.org/10.1021/jp047349j (2004).

28 Kinoshita, K. *Electrochemical oxygen technology*. (Wiley, 1992).

29 Yeager, E. Electrocatalysts for O_2 reduction. *Electrochimica Acta* **29**, 1527-1537, http://dx.doi.org/0013-4686/84 (1984).

30 Okamoto, Y. First-principles simulation identifying metal dimers suitable for catalyzing oxygen-reduction reactions. *The Journal of Physical Chemistry C* **112**, 5888-5891, http://dx.doi.org/10.1021/jp0769173 (2008).

31 Ishiguro, N. *et al.* Operando time-resolved X-ray absorption fine structure study for surface events on a Pt_3Co/C cathode catalyst in a polymer electrolyte fuel cell during voltage-operating processes. *ACS Catalysis* **2**, 1319-1330, http://dx.doi.org/10.1021/cs300228p (2012).

32 Nagamatsu, S.-i. *et al.* Potential-dependent restructuring and hysteresis in the structural and electronic transformations of Pt/C, Au(Core)-Pt(Shell)/C, and Pd(Core)-Pt(Shell)/C cathode catalysts in polymer electrolyte fuel cells characterized by in situ X-ray absorption fine structure. *The Journal of Physical Chemistry C* **117**, 13094-13107, http://dx.doi.org/10.1021/jp402438e (2013).

33 Nagamatsu, S.-i. *et al.* Structural and electronic transformations of Pt/C, Pd@Pt(1 ML)/C and Pd@Pt(2 ML)/C cathode catalysts in polymer electrolyte fuel cells during potential-step operating processes characterized by in-situ time-resolved XAFS. *Surface Science* **648**, 100-113, http://dx.doi.org/10.1016/j.susc.2015.10.053 (2016).

34 Norskov, H. a. Why gold is the noblest of all the metals. *Nature Letters* **376**, 238-240, http://dx.doi.org/https://doi.org/10.1038/376238a0 (1995).

35 Wyckoff, R. W. G. *Crystal Structures - Volume 1*. 2nd edn, (John Wiley and Sons, 1965).

36 Wang, F. *et al.* Porous single-crystalline palladium nanoparticles with high catalytic activities. *Angew Chem Int Ed Engl* **51**, 4872-4876, http://dx.doi.org/10.1002/anie.201107376 (2012).

37 Abdullah, N. *et al.* Pd local structure and size correlations to the activity of Pd/TiO_2 for photocatalytic reforming of methanol. *Physical Chemistry Chemical Physics* **21**, 16154-16160, http://dx.doi.org/10.1039/c9cp00826h (2019).

38 Beale, A. M. & Weckhuysen, B. M. EXAFS as a tool to interrogate the size and shape of mono and bimetallic catalyst nanoparticles. *Phys Chem Chem Phys* **12**, 5562-5574, http://dx.doi.org/DOI: 10.1039/b925206a (2010).

39 Hwang, B.-J. *et al.* Structural Models and Atomic Distribution of Bimetallic Nanoparticles as Investigated by X-ray Absorption Spectroscopy. *Journal of the American Chemical Society* **127**, 11140-11145, http://dx.doi.org/10.1021/ja0526618 (2005).

40 Xu, R. *et al.* Improving the ORR Performance by Enhancing the Pt Oxidation Resistance. *Journal of Catalysis* **416**, 311-321, http://dx.doi.org/https://doi.org/10.1016/j.jcat.2022.10.025 (2022).

41 Calle-Vallejo, F. *et al.* Why conclusions from platinum model surfaces do not necessarily lead to enhanced nanoparticle catalysts for the oxygen reduction reaction. *Chemical Science* **8**, 2283-2289, http://dx.doi.org/10.1039/c6sc04788b (2017).

42 Coleman, E. J. & Co, A. C. The complex inhibiting role of surface oxide in the oxygen reduction reaction. *ACS Catalysis* **5**, 7299-7311, http://dx.doi.org/10.1021/acscatal.5b02122 (2015).

43 Mathew, J. P. & Srinivasan, M. Photoelectron spectroscopy (XPS) studies on some palladium catalysts. *European Polymer Journal* **31**, 835-839, http://dx.doi.org/https://doi.org/10.1016/0014-3057(95)00027-5 (1995).

44 Wang, W., Wang, Z., Wang, J., Zhong, C. J. & Liu, C. J. Highly active and stable Pt-Pd alloy catalysts synthesized by room-temperature electron reduction for oxygen reduction reaction. *Advanced Science* **4**, 1-9, http://dx.doi.org/10.1002/advs.201600486 (2017).

45 Sasaki, K. *et al.* Recent advances in platinum monolayer electrocatalysts for oxygen reduction reaction: scale-up synthesis, structure and activity of Pt shells on Pd cores. *Electrochimica Acta* **55**, 2645-2652, http://dx.doi.org/10.1016/j.electacta.2009.11.106 (2010).

46 Li, Y. & Liu, Z. F. Solvated proton and the origin of the high onset overpotential in the oxygen reduction reaction on Pt(111). *Physical Chemistry Chemical Physics* **22**, 22226-22235, http://dx.doi.org/10.1039/d0cp04211k (2020).

47 Wang, J. X., Zhang, J. & Adzic, R. R. Double-trap kinetic equation for the oxygen reduction reaction on Pt(111) in acidic media. *Journal of Physical Chemistry A* **111**, 12702-12710, http://dx.doi.org/10.1021/jp076104e (2007).

48 Ohkubo, K., Takahashi, H., Watters, E. P. J. & Taguchi, M. In-situ analysis of CO_2 electroreduction on Pt and Pt oxide cathodes. *Electrochemistry* **88**, 210-217, http://dx.doi.org/10.5796/electrochemistry.19-00066 (2020).

49 Van Spronsen, M. A., Frenken, J. W. M. & Groot, I. M. N. Observing the oxidation of platinum. *Nature Communications* **8**, 1-7, http://dx.doi.org/10.1038/s41467-017-00643-z (2017).

50 Xu, R. *Structure-activity relationship of porous materials for energy conversion and storage* Doctor of Philosophy thesis, University College London, (2020).

51 Xie, S. *et al.* Atomic layer-by-layer deposition of Pt on Pd nanocubes for catalysts with enhanced activity and durability toward oxygen reduction. *Nano Letters* **14**, 3570-3576, http://dx.doi.org/10.1021/nl501205j (2014).

52 Shao, M. H. *et al.* Palladium monolayer and palladium alloy electrocatalysts for oxygen reduction. *Langmuir* **22**, 10409-10415, http://dx.doi.org/10.1021/la0610553 (2006).

53 Wang, F. *et al.* Porous single-crystalline palladium nanoparticles with high catalytic activities. *Angewandte Chemie International Edition in English* **51**, 4872-4876, http://dx.doi.org/10.1002/anie.201107376 (2012).

54 Origin(Pro). Version 2023. *OriginLab Corporation, Northampton, MA, USA*.

55 Garsany, Y., Baturina, O. A., Swider-Lyons, K. E. & Kocha, S. S. Experimental methods for quantifying the activity of platinum electrocatalysts for the oxygen reduction reaction. *Analytical Chemistry* **82**, 6321–6328, http://dx.doi.org/10.1021/ac100306c (2010).

56 Kresse, G. & Hafner, J. Ab initio molecular dynamics for liquid metals. *Physical Review B* **47**, 558-561, http://dx.doi.org/10.1103/physrevb.47.558 (1993).

57 Kresse, G. & Furthmuller, J. Efficiency of ab-initio total energy calculations for metals and semiconductors using a plane-wave basis set. *Computational Materials Science* **6**, 15-50, http://dx.doi.org/https://doi.org/10.1016/0927-0256(96)00008-0 (1996).

58 Kresse, G. & Furthmüller, J. Efficient iterative schemes for ab initio total-energy calculations using a plane-wave basis set. *Physical Review B* **54**, 11169-11186, http://dx.doi.org/https://doi.org/10.1103/PhysRevB.54.11169 (1996).

59 Dong, W., Kresse, G., Furthmüller, J. & Hafner, J. Chemisorption of H on Pd(111): An ab initio approach with ultrasoft pseudopotentials. *Physical Review B* **54**, 2157-2166, http://dx.doi.org/10.1103/PhysRevB.54.2157 (1996).

60 Kresse, G. & Joubert, D. From ultrasoft pseudopotentials to the projector augmented-wave method. *Physical Review B* **59**, 2157-2166, http://dx.doi.org/https://doi.org/10.1103/PhysRevB.59.1758 (1999).

61 Blochl, P. E. Projector augmented-wave method. *Phys Rev B Condens Matter* **50**, 17953-17979, http://dx.doi.org/10.1103/physrevb.50.17953 (1994).

62 Hammer, B., Hansen, L. B. & Nørskov, J. K. Improved adsorption energetics within density-functional theory using revised Perdew-Burke-Ernzerhof functionals. *Physical Review B* **59**, 7413, http://dx.doi.org/https://doi.org/10.1103/PhysRevB.59.7413 (1999).

63 Grimme, S., Antony, J., Ehrlich, S. & Krieg, H. A consistent and accurate ab initio parametrization of density functional dispersion correction (DFT-D) for the 94 elements H-Pu. *Journal of Chemical Physics* **132**, 154104, http://dx.doi.org/10.1063/1.3382344 (2010).

64 Henkelman, G. & Jónsson, H. Optimization methods for finding minimum energy paths. *Journal of Chemical Physics* **111**, 7010-7022, http://dx.doi.org/10.1063/1.480097 (1999).

65 Dent, A. J. *et al.* B18: A core XAS spectroscopy beamline for Diamond. *Journal of Physics: Conference Series* **190** http://dx.doi.org/10.1088/1742-6596/190/1/012039 (2009).

66 Ravel, B. & Newville, M. ATHENA, ARTEMIS, HEPHAESTUS: data analysis for X-ray absorption spectroscopy using IFEFFIT. *J Synchrotron Radiat* **12**, 537-541, http://dx.doi.org/10.1107/S0909049505012719 (2005).

67 Uruga, T. *et al.* Improvement in XAFS beamline BL01B1 at SPring-8. *Journal of Physics: Conference Series* **190** http://dx.doi.org/10.1088/1742-6596/190/1/012041 (2009).

Chapter 5. The Role of Surfactants in Pd Nanoparticle Growth: CTAB versus CTAC.

Surfactants are a key factor in controlling nanoparticle morphology during growth *via* chemical precipitation.[1-4] This work compares the roles of cetyltrimethylammonium bromide (CTAB) and cetyltrimethylammonium chloride (CTAC) surfactants in determining Pd nanoparticle morphology, since faceted nanoparticles are formed with CTAB contrary to the porous, dendritic nanoparticles grown with CTAC. *In situ* X-ray absorption spectroscopy (XAS), supported by transmission electron microscopy (TEM) images, measures the rate and mechanisms of the ascorbic acid (AA) reduction of aqueous CTAB-capped K_2PdBr_4 solution, forming solid Pd nanoparticles. A temperature and AA concentration series are measured to observe their effects on the rate of nanoparticle growth. Similar to Chapter 3, the formation of an intermediate Pd^0-Br species was studied, to ascertain whether growth occurs at the surface or in solution. The results obtained in this project speak to the effects caused by the surfactant, the AA concentration and the temperature in controlling reduction and growth rates, and further seeks to reveal the mechanism of Pd reduction in the presence of Br- ions. Such measurements could be applied in future for the prediction of nanoparticle growth and in the rational design of Pd nanoparticles.

Notable Contributions

Contributions were made by Hao Gu in preliminary XAS analysis and data collection, Jay Yan in batch XAS data fitting for EXAFS and Ryan Wang in experimental design.

5.1 Introduction

During the chemical precipitation synthesis of metal nanoparticles, surfactants decrease the surface tension of solution and interact with the metal surface, to control the resulting nanoparticle morphology.[5] It has been observed that surfactant addition has a significant impact on the kinetics of growth, the growth species formed and in determining the mechanisms of nucleation and growth.[6,7] Widely applied in growth for shape and size regulation, they are also instrumental in preventing agglomeration of nanoparticles and achieving monodispersity.[1,8]

Surfactants generally consist of a hydrophilic 'head' with a hydrocarbon chain 'tail'. Surfactant parameters which can be tuned to control nanoparticle morphology include the tail length,[3] the concentration[5] and the ligand species in the head group.[1] In this project we compare the effect on Pd nanoparticle growth kinetics of two quaternary ammonium cationic surfactants with the same 'tail' (Figure 5.1), differing only in halide cations of Br^- and Cl^-, namely cetyltrimethylammonium bromide (CTAB, $C_{19}H_{42}N.Br$) and cetyltrimethylammonium chloride (CTAC, $C_{19}H_{42}N.Cl$). Experimental evidence has indicated the interaction of surfactant ligands of different strengths binding to various facets of the nanoparticle to control the shape.[5,9,10]

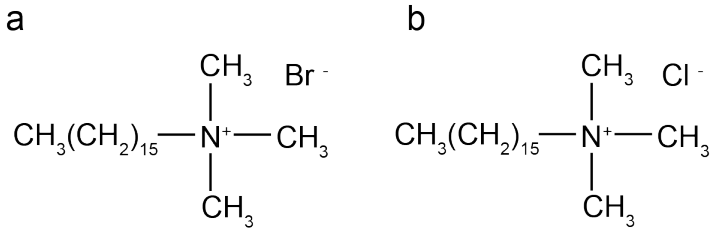

Figure 5.1 ***Chemical Structure of CTAB and CTAC.*** *(a) Cetyltrimethylammonium bromide and (b) cetyltrimethylammonium chloride have the chemical structure $C_{19}H_{42}N^+$ with Br^- and Cl^-, respectively.*

The literature shows that CTAC-capped growth leads to single-crystalline nanoporous spherical particles, while CTAB-capping gives rise to highly faceted polygonal particles.[1,7,11] Extensive research has studied the mechanistic differences in CTAC- and CTAB-capped growth, individually and combined, due to the divergence in nanoparticle shapes formed. Since the tail length and concentration are constant, the main difference between the two materials is the ligand species in the head group. *In situ* studies determine the effect of metal-ligand interaction strength on reaction rate and the growth surface. A study by Stolas et al. shows that during Pd growth with CTAB, Br^- ions lead to slow reaction kinetics compared to CTAC with Cl^- ions.[5] A study of the surfactant interaction at the metal surface during seeded growth anticipates a more densely packed surfactant with CTAB, leading to a higher control of surface faceted growth.[12] The weaker, dispersed CTAC interaction allows for increased oxidative dissolution growth on multiple facets, to give a porous structure.[11] However, the oxidative dissolution may not be the only factor in morphology determination, as works studying the formation of porous Pt and Pd nanoparticles, state that the primary reason for the dendritic shape is aligned-agglomeration or oriented attachment.[1,13-15]

Synthesis procedures including CTAB have also shown the formation of $[PdBr_4]^{2-}$ ions as growth species, which behaves differently to $[PdCl_4]^{2-}$. For example, one study showed that the $[PdBr_4]^{2-}$ was more likely to have surface reduction while $[PdCl_4]^{2-}$ reduced in solution and at the metal surface simultaneously, leading to the formation of new nuclei in addition to particle growth at existing sites.[7] However, the concentration of reduced species in solution has not been measured before, as outlined in Chapter 3. Here we explore the growth of Pd nanoparticles with both surfactants using a combination of high resolution X-ray

absorption near-edge structure (XANES) and extended X-ray absorption fine structure (EXAFS) data, following intermediate reduced species, and comparing chemical growth profiles for both reactions.

We present a 500 ms time-resolved *in situ* X-ray absorption spectroscopy (XAS) observation of rate of oxidation and bond formation, for CTAC- and CTAB-capped Pd nanoparticles, during ascorbic acid reduction of K_2PdCl_4 and K_2PdBr_4. A mechanism of growth and the growth species formed are determined based on experimental results. The distinct differences in particle shapes formed under each surfactant, one porous and the other solid, makes this a particularly interesting case to compare reaction profiles. As with the previous studies, the rate of reaction, activation energy and the growth profile, contribute to the understanding of the mechanism for shape determination in this case.

For such common systems of nanoparticle growth, rational design of nanoparticles depends heavily on *in situ* observations and comparison of growth parameters. This work provides a first look at such studies and suggests avenues for further studies to elucidate the growth mechanisms and controls which could one day be valuable in rational control of nanoparticle morphology. The techniques used here could be applied to a wide range of systems and surfactant materials to confirm the current suggestions in the literature about their crucial role in chemical precipitation induced growth.

5.2 Results and Discussion

Since the parameter of interest in this work is the ligand in the head groups, CTAC and CTAB with chain length of 19 units were used. The concentration of CTAC and CTAB solutions used during reduction was 0.1 M in both cases, leading to a

similar concentration of Cl^- or Br^- ions. K_2PdCl_4 was used as a precursor for CTAC-capped growth while K_2PdBr_4 was used with CTAB to reduce effects of ligand substitution. *In situ* XAS was measured within a single session using the same temperature controls and mixing chambers. The effect on nanoparticle morphology is observed from *ex situ* TEM imaging and changes during the reaction are monitored by *in situ* XAS, to gain a deeper understanding of the reaction kinetics.

5.2.1 Faceted Pd Nanoparticle Growth

Electron imaging shows the drastically different morphologies created by CTAC- versus CTAB-capped growth (Figure 5.2, Supplementary Figure 5.15). While CTAC-capping creates a spherical, porous, dendritic morphology (as explored in Chapter 3), CTAB-capping leads to solid, faceted nanoparticles.

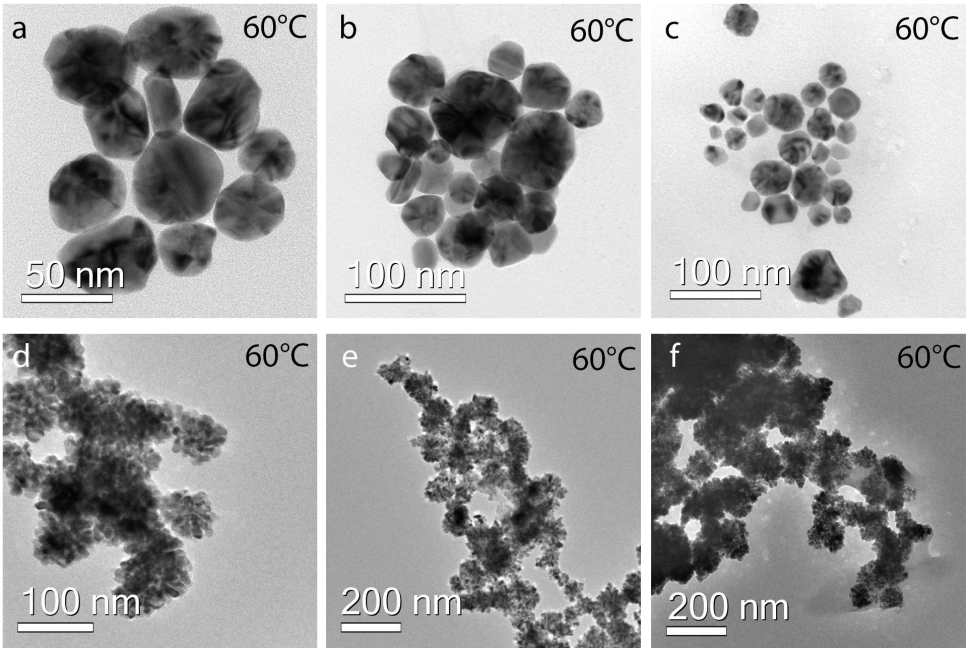

Figure 5.2 ***Morphology of CTAB- and CTAC-Capped Nanoparticles.*** *Bright-field TEM images of Pd nanoparticles formed at 60ºC during (a-c) CTAB-capped growth at 50 nm and 100 nm-scale and (d-f) CTAC-capped growth at 100 nm to 200 nm-scale.*

At a reaction temperature of 60ºC, the average nanoparticle size formed with CTAB is 50.535 nm and with CTAC is 76.97 nm after 20 minutes (Supplementary Table *5.1*). CTAC-capped Pd particles are expected to show a significantly higher surface area since they are porous in comparison with CTAB-capping. Although the final shape of CTAB-capped growth is faceted, there do appear to be a limited formation of dendritic species within the structure, making it appear that the nanoparticles may agglomerate during the course of the reaction. This is corroborated by the presence of smaller, non-faceted particles at high concentration reductions (Figure 5.3).

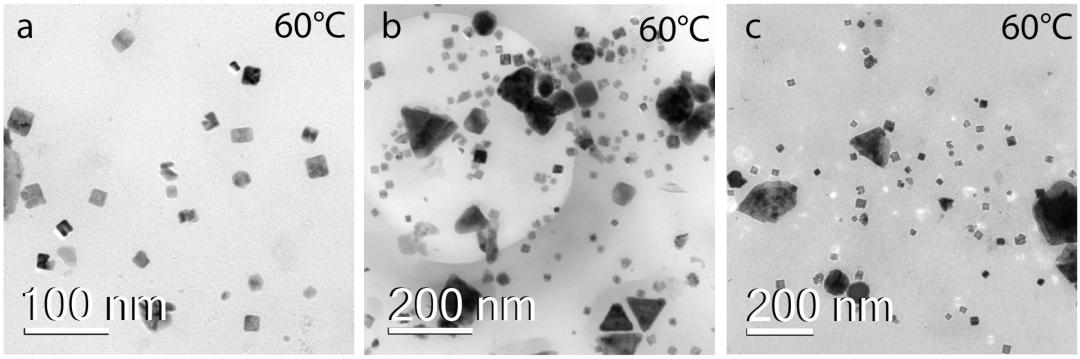

Figure 5.3 ***Aggregated Small CTAB-Capped Nanoparticles.*** *Bright-field TEM images of faceted Pd nanoparticles formed under CTAB-capped growth at 60°C after 1 minute, with a scale of (a) 100 nm and (b, c) 200 nm.*

The faceted growth of CTAB-capped Pd nanoparticles shows a Pd (100) lattice, which is described in the literature to be stabilised by Br^- with CTAB-capping (Figure 5.5).[10] In comparison, facets of Pd (111) and Pd (011) were previously measured in Pd nanoparticles grown with CTAC-capping (Section 4.2.1).

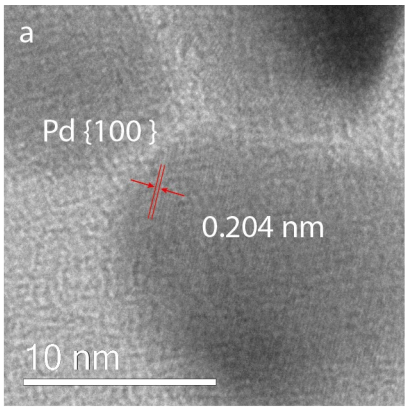

Figure 5.4 ***Lattice Spacing of Pd Nanoparticles with CTAB.*** *Value of 0.204 nm was measured for lattice spacing, which corresponds with Pd (100) facets.*[16]

Based on these observations, the morphological differences observed with CTAB begin early in the nanoparticle growth, even from the initial nucleation stages. The preferential growth on certain Pd facets (in this case (100)) leads to the growth of defined crystalline nanoparticles, forming nanocubes even in the early stages. Etching does not appear to be significant after long reaction times. In

contrast, CTAC-capped growth is observed to first form irregular spherical particles, which are etched and reshaped in later stages for the final porous morphology.[17]

5.2.2 Br^- Ligand-Mediated Growth Profile

In situ XAS measurements of the nanoparticle growth allow the comparison of mechanisms which determine nanoparticle morphology. The growth behaviour measured for CTAB-capped nanoparticles shows that the faceted growth has a different profile compared with that of a porous spherical growth as in the previous chapter with CTAC.

The CTAB-capped Pd growth profile, obtained from a linear combination fitting (LCF) of XANES data, shows a rapid initial reduction which plateaus as reactant concentration decreases (Figure 5.5). The nucleation stage cannot be observed here, starting directly with the rapid growth. The reaction stages observed are two-fold with nucleation and rapid growth, followed by slow growth, showing a slowed rate of reduction. However, it is notable that in this case, two rapid growth stages are observed under each condition.

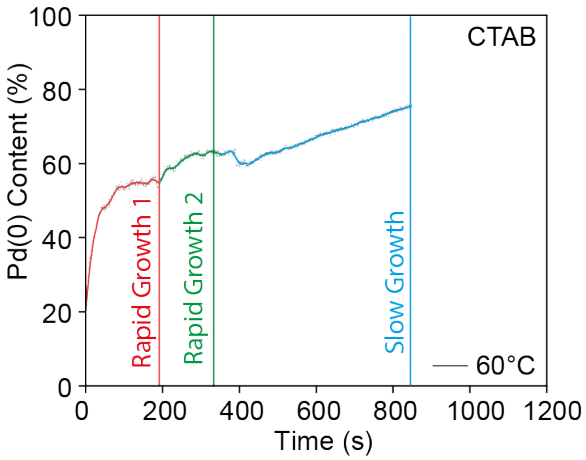

Figure 5.5 ***Reaction Profile of CTAB-Capped Growth.*** *Growth profile of Pd^0 content calculated with LCF for CTAB-capped K_2PdCl_4 reduction with ascorbic acid shows two stages of rapid growth (red, green), followed by slow growth (blue).*

It is expected that CTAB-capped Pd growth will follow the same reaction stages observed with CTAC-capping: reduction, nucleation, rapid growth and reoxidation. In comparison with CTAC as a surfactant, it is expected that CTAB leads to a decreased Pd^0-Br formation, except initially, and prefers direct reduction at the surface.

5.2.3 Rate of Temperature Controlled Reduction

The temperature series shows the changes in CTAB-capped growth at 30ºC, 40ºC, 50ºC and 60ºC (Figure 5.6, Supplementary Figure 5.16). It is interesting to note that the initial reaction rate does not vary significantly between different temperatures. From the LCF oxidation state results, the first seconds of the reaction are not visible, so it is impossible to observe reduction before nucleation and growth (Supplementary Table 5.2). However, the peak positions of the first and second rapid reduction curves show a trend, peaking sooner at high temperatures. At 30ºC, 40ºC, 50ºC and 60ºC the first peak maxima are observed

at 83 s, 58 s, 22 s and 14 s, respectively. This is followed by a second peak with increased intensity at 180 s, 150 s and 40 s under 30ºC, 40ºC and 50ºC, respectively. Thus, a decrease in temperature leads to extended duration of the identified growth stages (rapid reduction stages 1 and 2, and slow growth) and a lower total Pd^0 content at the end of the reaction time. Although it does not significantly affect the initial growth rate, an increase in temperature increases the rate of each reaction stage.

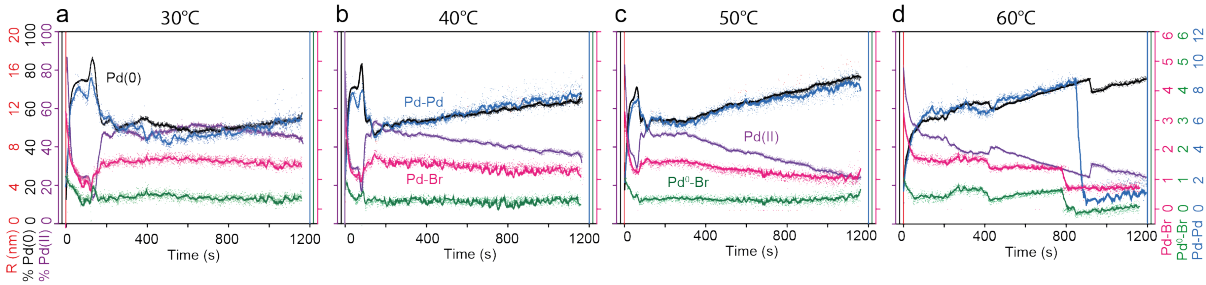

Figure 5.6 ***Temperature-Controlled CTAB-Capped XAS Results.*** *Pd K-edge XAS calculated for Pd^0 (black) and Pd^{2+} content (purple), coordination numbers of Pd-Br (pink), Pd-Pd (blue) and calculated Pd^0-Br coordination numbers (green) at temperatures of (a) 30°C, (b) 40°C, (c) 50°C and (d) 60°C.*

EXAFS values were calculated for each data point, for comparison against the XANES LCF results. Using the same calculation as in Chapter 3, the Pd^0-Br coordination ([Pd^0-Br]) is calculated from initial measurement (i) at reaction time (t) by

$$[\boldsymbol{Pd^0 - Br}]^t = [\boldsymbol{Pd - Br}]^t - \left([\boldsymbol{Pd - Br}]^i \times \frac{(\boldsymbol{Pd^{2+}})^t}{(\boldsymbol{Pd^{2+}})^i}\right) \qquad \text{Equation 5.1}$$

5.1 The results are shown (Figure 5.6, green) for Pd^0-Br coordination values to be almost constant, with a peak during the initial rapid growth phase. This low concentration measured can be attributed to the reduction of Pd directly at the metal surface, rather than forming Pd^0-Br within solution. Such a result

confirms the observation that CTAB-capping leads to a surface reduction mechanism, contrary to CTAC-capped growth.[12] In this case, it can be observed in the XAS results, as the formation of Pd-Pd bonds in EXAFS as soon as Pd^0 content increases (Supplementary

Table **5.3**). The comparison of all temperature-controlled growth LCF results are compared to track the trend of changes (Figure 5.7, Supplementary Figure 5.17, Supplementary Table 5.2).

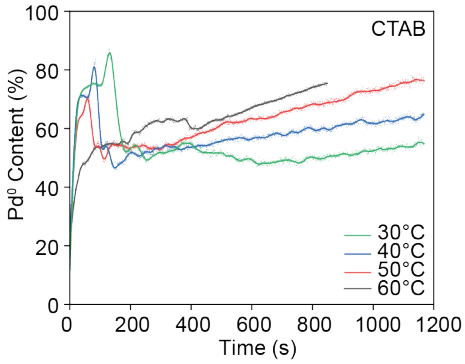

Figure 5.7 ***LCF for CTAB-Capped Temperature Range.*** *Pd K-edge XANES LCF results of Pd^0 content over time for CTAB-capped Pd nanoparticle growth at 50°C with a temperature series of 30°C (green), 40°C (blue), 50°C (red) and 60°C (grey). LCF standards of Pd foil (Pd^0) and K_2PdCl_4 (Pd^{2+}) were used.*

From the initial measured data (Figure 5.8 a, b), rate values of -0.00101, -0.00102, 0.00079 and 0.00061 are measured for Pd^{2+} at 30°C, 40°C, 50°C and 60°C, respectively. These values are within the error limits of the measurement, so the rapid reduction can be interpreted as temperature independent. However, assuming that the measured results are accurate, an Arrhenius plot (Figure 5.8 c) yields a negative activation energy (E_a).

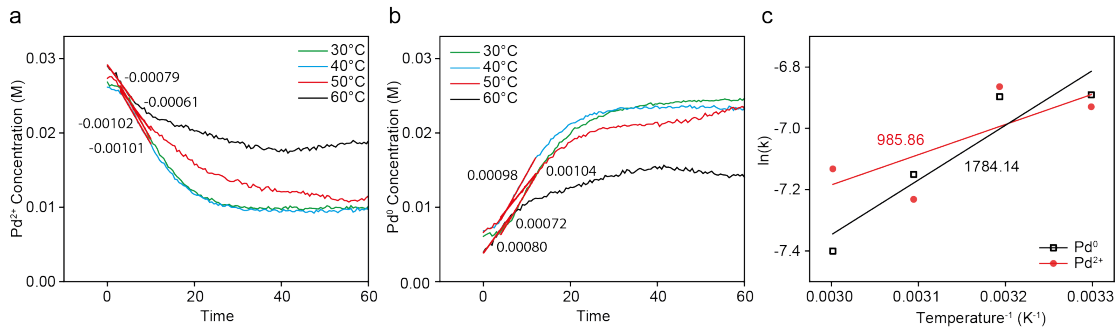

Figure 5.8 Rate Calculation and Arrhenius Plot. Measurement from LCF results of Pd K-edge XANES for initial rates (red) of (a) Pd^{2+} reduction and (b) Pd^{0} formation of 30°C, 40°C, 50°C and 60°C. (c) Arrhenius plot of the reaction rates for each temperature gives slope of 1784.14 K (Pd^{0}) and 985.86 K (Pd^{2+}).

Based on the Arrhenius slope, the calculated activation energy for Pd^{2+} reduction is -8.20 kJ.mol^{-1} and for Pd^{0} formation is -14.83 kJ.mol^{-1}. Since a negative activation energy is not possible, this result can be attributed to the rate-determining blocking-effect of Br^{-} ions at the Pd surface. This is an unusual phenomenon, which may occur when two consequences of increased temperature are in competition, such as heat energy available to overcome the activation barrier (increases with temperature) and adsorption for formation of reaction intermediates (decreases with temperature). This activation energy calculation is not comparable with the 43.4 kJ.mol^{-1} measured for the surface reduction of ascorbic acid reduction for Pd nanoparticles on seeds in the presence of CTAB, since the rapid growth rates are measured instead of nucleation rates.[18]

5.2.4 Role of AA Concentration in Growth Rate

The concentration of AA was varied to measure reaction rate changes. These reactions were not as cleanly reproducible as the temperature series but show a

clear trend when compared together (Supplementary Figure 5.18). The results are shown for AA concentrations of 50 mM, 80 mM and 100 mM (Figure 5.9 a-c).

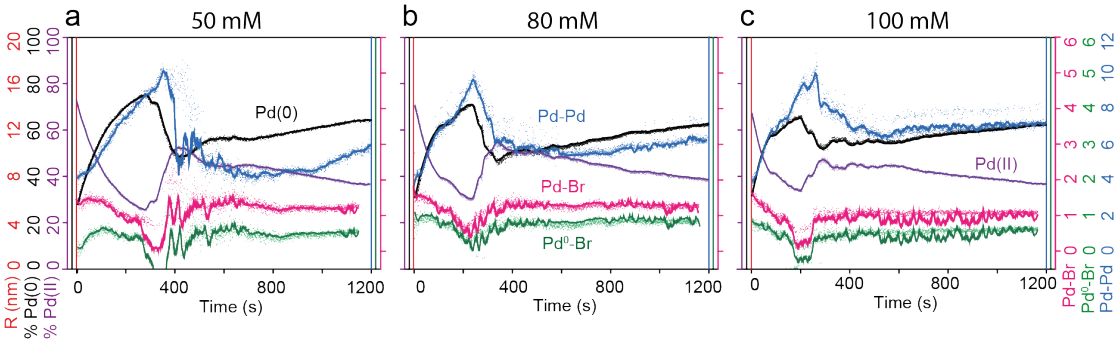

Figure 5.9 ***AA-Controlled CTAB-Capped XAS Results.*** *Pd K-edge XAS and calculated for Pd^0 (black) and Pd^{2+} content (purple), coordination numbers of Pd-Br (pink), Pd-Pd (blue) and calculated Pd^0-Br coordination numbers (green) with AA concentrations of (a) 50 mM, (b) 80 mM and (c) 100 mM at 50°C.*

EXAFS measurements show a similar trend to LCF oxidation state changes. A negative value for Pd^0-Br is calculated near the peak of the Pd(0) concentration (Figure 5.9, green). Once again, the overall Pd^0-Br coordination seems to be approximately constant except at the initial reaction stage, corroborating the surface reduction.

The combined LCF results of the AA concentration series show that although there is a different reaction profile for growth, the final concentration of Pd(0) in each condition is the same, with approximately 75% of Pd reduced to nanoparticles (Figure 5.10, Supplementary Figure 5.19, Supplementary Table 5.4).

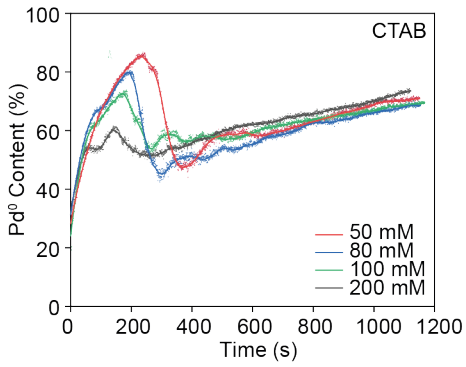

Figure 5.10 ***Full Series LCF for CTAB AA Concentration.*** *Pd K-edge XANES LCF results of Pd^0 content over time for CTAB-capped Pd nanoparticle growth at 50ºC with an AA concentration series of 50 mM (red), 80 mM (blue), 100 mM (green) and 200 mM (grey). LCF standards of Pd foil (Pd^0) and K_2PdCl_4 (Pd^{2+}) were used.*

As with increasing temperatures, it seems that increasing the AA concentration leads to a shorter reaction duration before reaching the "critical mass" and beginning the slow growth phase. The measured peak positions for rapid reduction are 260 s, 215 s, 180 s and 145 s of reaction, for AA concentrations of 50 mM, 80 mM, 100 mM and 200 mM. The growth rate dependence on the concentration of reducing agent can be observed from the rate of change of Pd^{2+} concentration at each condition (Figure 5.11).

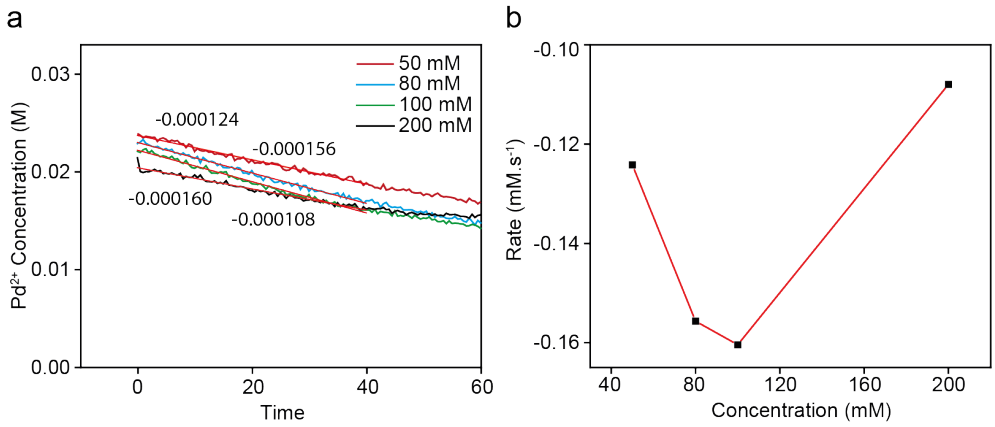

Figure 5.11 ***Growth Rate for AA Concentration Range.*** *(a) Measurement from LCF results of Pd K-edge XANES for initial rates (red) of Pd^{2+} reduction with AA concentrations of 50 mM, 80 mM, 100 mM and 200 mM. (b) Plot of the reaction rates measured versus the reaction concentration.*

The rate of growth with increasing ascorbic acid concentration does not show a continuous trend of increase. Above 100 mM, the rapid growth rate decreases, although the preliminary Pd^{2+} content is low, indicating partial reduction to Pd^{0} before the time of measurement. This concurs with the EXAFS fitting results which show the same trend for Pd-Pd bond formation (Supplementary Table 5.5). Since only one iteration of the 200 mM measurement was taken, this data is not as reliable as that collected for other conditions.

5.2.5 Surfactant Effect: CTAB versus CTAC

Lastly, we compare the results of the same temperature series for CTAC and CTAB- capped growth (Figure 5.12). The change of the growth conditions with a different surfactant is considerable.

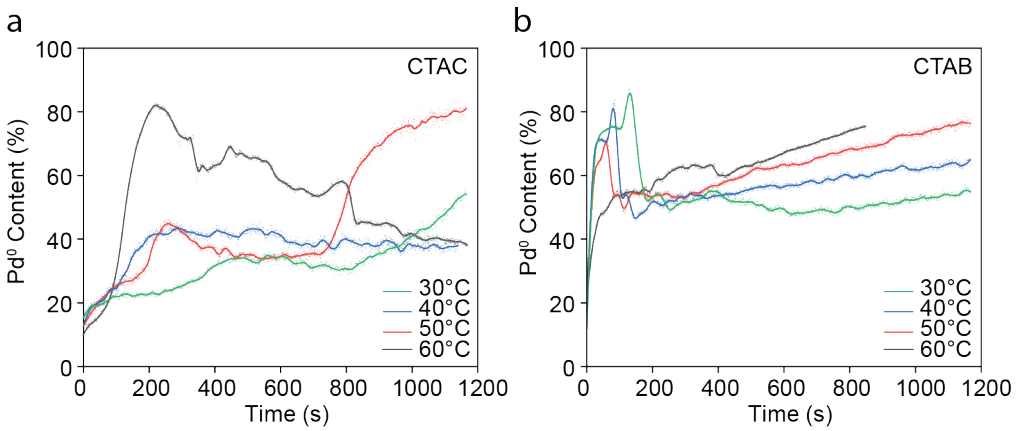

Figure 5.12 ***Temperature-Controlled Pd^0 Content with CTAC and CTAB.*** *A comparison Pd nanoparticle growth from Pd K-edge XANES LCF showing the rate of Pd(0) formation at temperatures of 30°C (green), 40°C (blue), 50°C (red) and 60°C (grey) capped with (a) CTAC and (b) CTAB.*

The difference in growth rates and growth profiles of CTAC and CTAB, under the same temperature conditions, gives an insight into the mechanisms of formation. During growth with CTAC, the initial nucleation and growth are relatively slow, which could lead to a more distributed range of nanoparticle sizes, and the agglomeration of clusters of smaller spheres. In the case of CTAB, the initial stage is rapid, which corresponds with the formation of numerous particles of a similar size in the solution. Once these particles reach a critical size, there appears to be a reoxidation and reshaping of nanoparticles.

The growth behaviour for CTAB nanoparticle shows that the faceted growth has a different profile compared with that of porous, spherical, CTAC-capped Pd nanoparticle growth. The formation of bonds within the solution can be further visualised with wavelet transforms of the EXAFS data collected at a range of reaction times (Figure 5.13).

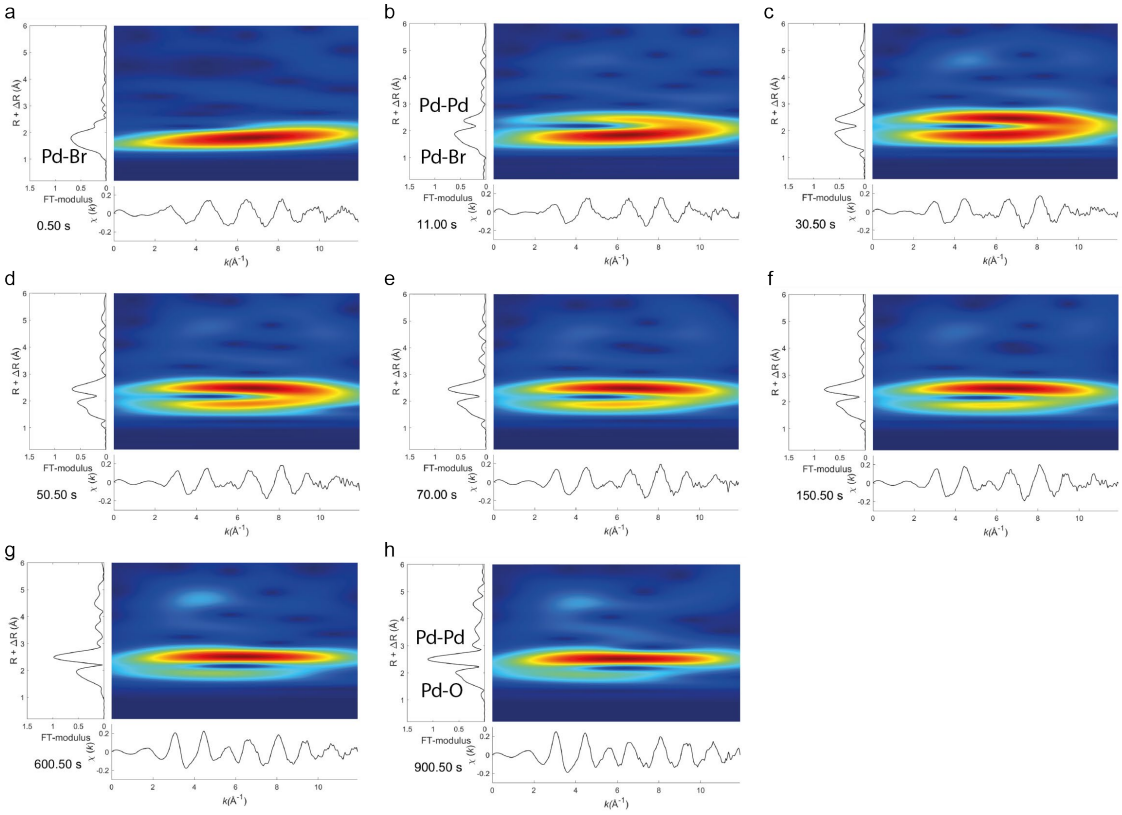

Figure 5.13 ***Wavelet Transform of CTAB-capped Pd NP growth.*** *Continuous Cauchy wavelet transforms combining the k-space (x-axis) and R-space (y-axis) Pd K-edge XAS data to form a heat map (red for high intensity and blue for low intensity) show the growth of CTAB-capped Pd nanoparticles at 60ºC, at reaction times of (a) 0 s, (b) 11 s, (c) 30 s, (d) 50 s, (e) 70 s, (f) 150 s, (g) 600 s and (h) 900 s.*

The wavelet transforms for CTAB-capped Pd growth (Figure 5.13) shows that the reduction of Pd-Br (low R-value and high k-value) to Pd-Pd (high R-value, high k-value) begins within the first seconds of the reaction. Pd-Br and Pd-O can be visually distinguished since Br has a higher atomic mass than O, and therefore Br appears more strongly at higher k-values than O.[19] The Pd reduction continues until a majority of Pd-Pd and Pd-O (low k-value and low R-value) remain at the end of the reaction (900 s, Figure 5.13 h).

In comparison the wavelet transform results for CTAC (Figure 5.14) show little distinction between Pd-Cl and Pd-O at a lower k-value than the Pd-Br observed previously. The reoxidation can be observed for longer reaction times (1150 s, Figure 5.14 h), showing lower final Pd content.

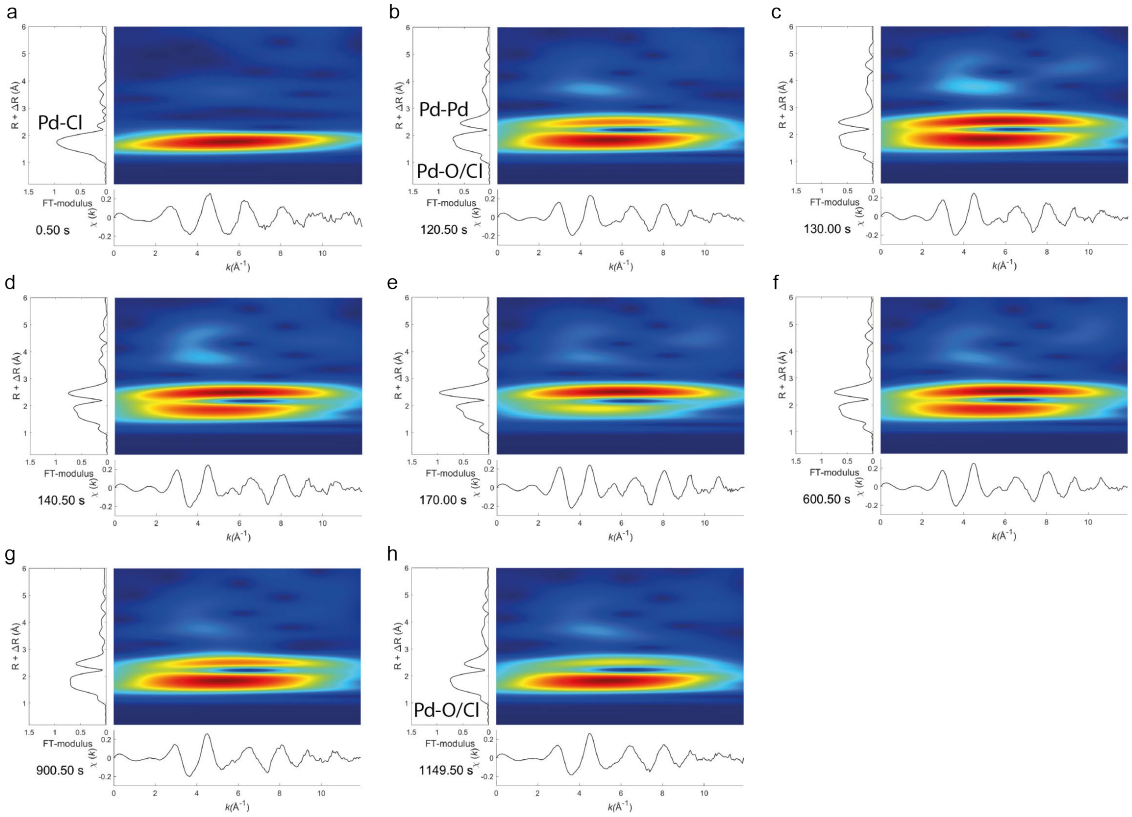

Figure 5.14 ***Wavelet Transforms of CTAC-capped Pd NP growth.*** *Continuous Cauchy wavelet transforms combining the k-space (x-axis) and R-space (y-axis) Pd K-edge XAS data to form a heat map (red for high intensity and blue for low intensity) show the growth of CTAC-capped Pd nanoparticles at 60ºC, at reaction times of (a) 0 s, (b) 120 s, (c) 130 s, (d) 140 s, (e) 170 s, (f) 600 s, (g) 900 s and (h) 1150 s.*

In CTAC-capped growth, the reaction ends with a combination of Pd-Pd, Pd-Cl and Pd-O bonds due to the reoxidation in solution, while in CTAB-capped growth a majority of Pd-Pd is observed with a weak Pd-O signal.

5.3 Outcomes

It is clear from the reaction profile that the reduction of CTAC- and CTAB-capped Pd nanoparticles take different routes, determining nanoparticle morphology. The variation in shape and size of nanoparticles formed may be due in incomplete interaction of the surfactant at the nanoparticle surface, controlling some surfaces more than others. The differences between CTAC- and CTAB-capped growth are attributed to the interactions of Br^- and Cl^- at the Pd surface. This leads to direct surface reduction in cases of CTAB-capped growth, rather than reduction within the solution. The surface reduction is shown from the low values for Pd^0-Br coordination calculated in this Chapter.

The shape of CTAB-capped Pd growth profile can be attributed to the Br^- blocking facets, leading to preferential formation of the Pd (100) facet and contributing to the morphology of the nanoparticles formed. Finally, after a critical mass of nanoparticles is reached, the reaction continues through the agglomeration and reshaping of existing nanoparticles during slow reduction. The Cl^- content in CTAC-capped growth appears to have a more severe etching effect, which may be the cause of higher degree of porosity in the nanoparticles formed. The size of the nanoparticles formed with CTAC is greater than the nanoparticles formed with CTAB.

These results show the significant contribution of rate-determination during a reaction to identify the mechanisms controlling the growth and to observe the reaction stages in which they are dominant. From the temperature growth series of CTAB-capped growth, it is also shown that the experimental results may be contrary to expectations, highlighting the importance of experimental observations to inform theoretical calculations.

5.4 Experimental Details

5.4.1 Faceted Pd Nanoparticle Synthesis

In the case of CTAC-capped growth, 0.1 M K_2PdCl_4 was reduced with solution of 0.1 M CTAC (MW = 320 $g.mol^{-1}$, 25 wt% solution in water) and 80 mM ascorbic acid (AA, MW = 176.12 $g.mol^{-1}$, purity = 99%) for 20 minutes. Reaction temperature and AA concentration were controlled for comparison. The temperatures selected were 303.15, 313.15, 323.15 and 333.15 K with 80 mM AA.

With CTAB as a surfactant, for ligand substitution KBr (ACS reagents, ≥99.0%) was added to 0.1 M K_2PdCl_4 before reduction with solution of 0.1 M CTAB (MW = 364.45 $g.mol^{-1}$, purity = ≥98%) and 80 mM AA for 20 minutes. To facilitate comparison with CTAC, temperatures of 303.15, 313.15, 323.15 and 333.15 K were measured. Ascorbic acid concentrations were also varied from 50 mM, 80 mM, 100 mM to 200 mM, at a temperature of 50ºC. AA, CTAC and CTAB were sourced from Sigma Aldrich. DI water used had resistivity of 18.2 MΩ.cm. $PdCl_2$ (Sigma Aldrich, ≥99.9%) and concentrated HCl (37%, Fisher Scientific) were purchased for the synthesis of K_2PdCl_4.

5.4.2 Nanoparticle Imaging

TEM imaging was performed on the JEOL-2100 (JEOL, Japan) with an acceleration range of 200 keV. Sample grids were prepared by centrifuging nanoparticle solutions at 11,500 rpm for three minutes and washing three times with water and ethanol. Nanoparticles were redispersed in 1 to 2 mL ethanol and sonicated for 15 minutes before drop casting on a lacey carbon Cu TEM grid.

Nanoparticle images were analysed with Gatan Digital Micrograph (GMS 3) to measure lattice spacing and ImageJ to estimate average nanoparticle size.

5.4.3 Synchrotron Characterization

EDE measurements were collected at I20-EDE, Diamond Light Source, using a Freelon detector and a Si(311) polychromator crystal. Beamline was operating at 3 GeV, with current of 299.4 mA. Spectra were measured at the Pd K-edge (24350 eV) within a range of 24050 eV to 25500 eV (k range to 12 $Å^{-1}$), with 1024 pixels collected per spectrum. The data energy was calibrated with Pd foil and calculated by pixel. 2400 spectra were collected during each reaction, for a total measurement time of 1200 s. An I_0 H_2O background was measured and averaged I_0 used for data correction. 200 µm of Al foil was inserted into the beam-path to attenuate the beam for longer experiments. For a 1200 s measurement, 25 scans of 20 ms were merged to give a frame time of 0.5134 s. Foils, pellet standards and standard solutions were measured for longer time-period before loading the *in situ* cell.

The SFM-4000 stop flow cell was used for *in situ* measurements. Four syringes containing the reactants (Solution A and Solution B) and wash solutions (H_2O and 10% HNO_3) were heated. Temperature was recorded at measurement position. Standards of Pd foil, Pd nanoparticles and 100 mM H_2PdCl_4 solution were recorded *ex situ* and 0.1 M CTAC in DI water was used as an Io for background subtraction.

DAWN software allows the mass processing of large data sets.[20] Larch relative normalisation was performed with pre-edge before E_0-20 eV and post-edge after E_0+100 eV, with a polynomial order of 2, “flattened”. Post-edge background subtraction for k-space was calculated for k-weight of 2, rbkg of 1.0 and Hanning window. Forward Fourier transform for R-space data was calculated with a k-

weight of 2 and k range of 3 to 10 $Å^{-1}$. Principal Component Analysis was run to see the changes in the oxidation state in the XANES region of the curve. Selected points were then processed further using Athena and Artemis (Demeter Suite Software) for XANES LCF and EXAFS fitting within a range of R of 1 to 3.2 Å to resolve the bonds present in the sample and estimate the Pd-Pd coordination at different reaction times.[21]

LCF was performed in DAWN, with a range of E_0-20 eV to E_0+40 eV and using Pd-foil and K_2PdBr_4 as standards. Large datasets were batch analysed using xraylarch program, as described below.

5.4.4 Data Analysis

The data reduction, rebinning, post-edge background subtraction and forward Fourier transform were performed with DAWN software, allowing the mass processing of large data sets.[20] Principal Component Analysis and Linear Combination Fitting were run for the XANES region of the curve to see the changes in the oxidation state. Selected points were then processed further using Artemis (Demeter Suite Software) to resolve the bonds present in the sample and estimate the Pd-Pd coordination at different reaction times.[21]

A python script was used to run xraylarch for batch EXAFS analysis using the least square mean fit model. The amplitude reduction factor was set a fixed value of 0.667 and the resulting values of C.N., bond length, σ^2 and ΔE_0 were calculated. The FEFF files selected in this work are:

Pd-Pd: 9008478, Wyckoff, R.W.G., Fm-3m, ccp

Pd-O: 4124668, Moore, W.J. and Pauling, L., P 42/m m c, tetragonal

Pd-Cl: 1010447, Wells, A.F., 1938, P n m n

Pd-Br: 1534319, Broderson, K. et al., 1966, P 1 21/c 1

Additional LCF and EXAFS fitting results from batch processing are too numerous to show in the Supplementary Information, but spectra and fitting parameters are available upon request.

The presence of Pd-O and Pd-Cl coordination is expected but cannot be reliably resolved from EXAFS refinement. The continuous Cauchy wavelet transform[22] provides a method of visually distinguishing between bonds of similar lengths for elements of higher and lower molecular weights. Although this processing method cannot quantify both bonds, it provides an indication of their presence within the sample. A MATLAB script published by Munoz et al.[22] was adapted to calculate continuous-cauchy wavelet transform figures.

5.5 Supplementary Information

5.5.1 TEM Images and Measurements

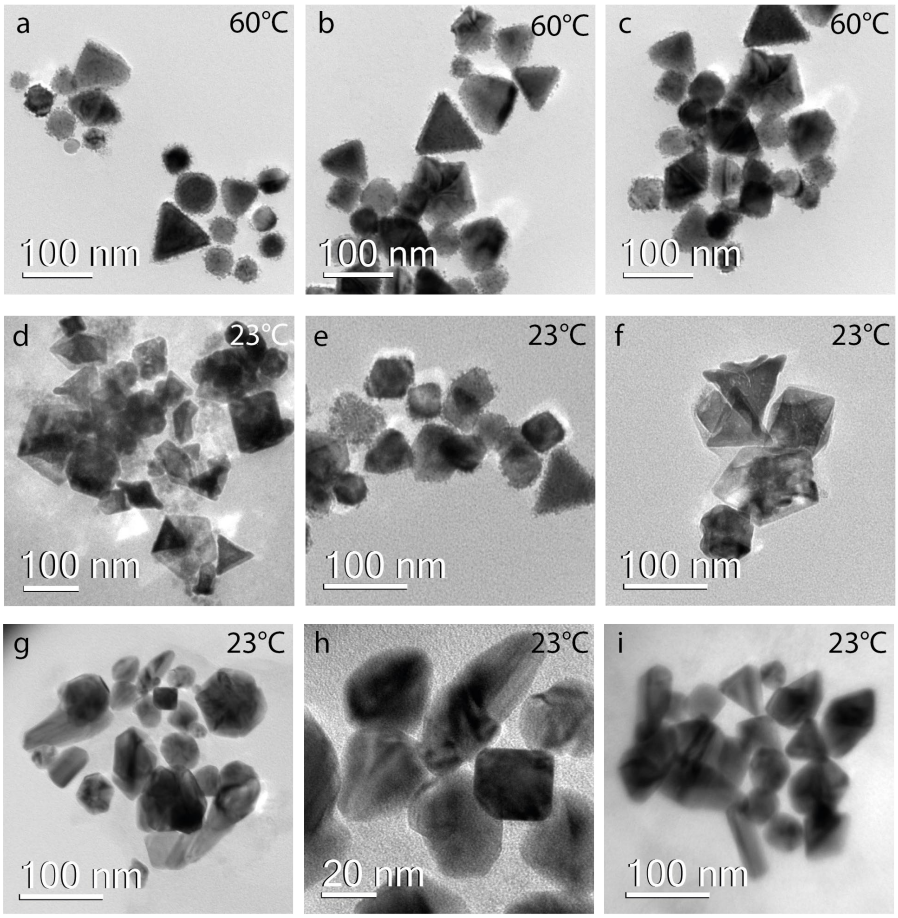

Figure 5.15 ***Morphology of CTAB-Capped Nanoparticles at 60ºC and 23ºC.*** *Bright-field TEM images of the morphology of Pd nanoparticles formed during CTAB-capped growth at temperatures of (a-c) 60ºC and (d-i) 23ºC.*

Table 5.1 ***Nanoparticle Size Measurements in CTAB-capped growth.*** *Measured nanoparticle diameter and radius of CTAB-capped Pd nanoparticles grown at temperatures of 23°C, 40°C and 60°C.*

Condition	Particles Measured	Diameter (nm)	Error (nm)	Radius (nm)	Error (nm)
23°C	88	54.670	22.034	27.335	11.017
40°C	348	53.850	24.257	26.925	12.128
60°C	277	50.535	17.097	25.267	8.548

5.5.2 XAS Analysis and Fit Results

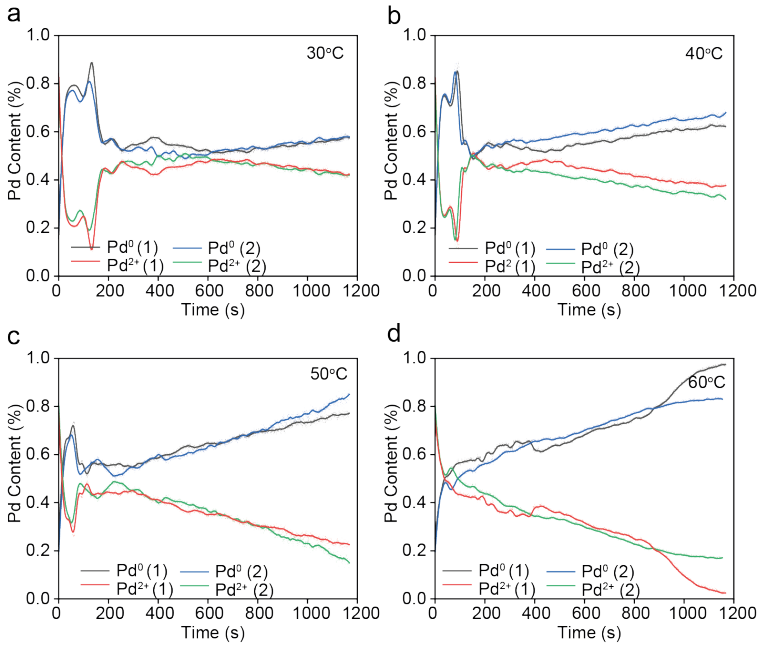

Figure 5.16 ***Reproducibility of LCF Results for a Temperature Range.*** *Reproducibility of Pd K-edge XANES LCF results for CTAB-capped nanoparticle growth forming Pd^{2+} (red and green) and Pd^{0} (black and blue) with two trials at temperatures of (a) 30°C, (b) 40°C, (c) 50°C and (d) 60°C. Aqueous H_2PdCl_4 solution (Pd^{2+}) and Pd foil (Pd^{0}) were used as LCF standards.*

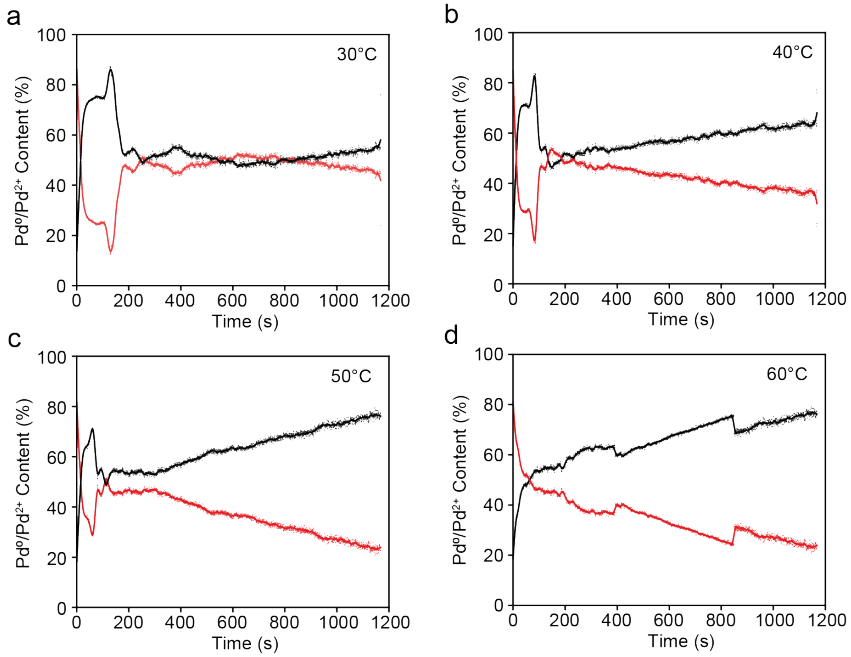

Figure 5.17 ***Temperature-Controlled CTAB-capped LCF.*** *Pd K-edge XANES LCF results for Pd reduction, showing Pd^{2+} (red) and Pd^{0} (black) at temperatures of (a) 30°C, (b) 40°C, (c) 50°C and (d) 60°C. Aqueous H_2PdCl_4 solution (Pd^{2+}) and Pd foil (Pd^{0}) were used as LCF standards.*

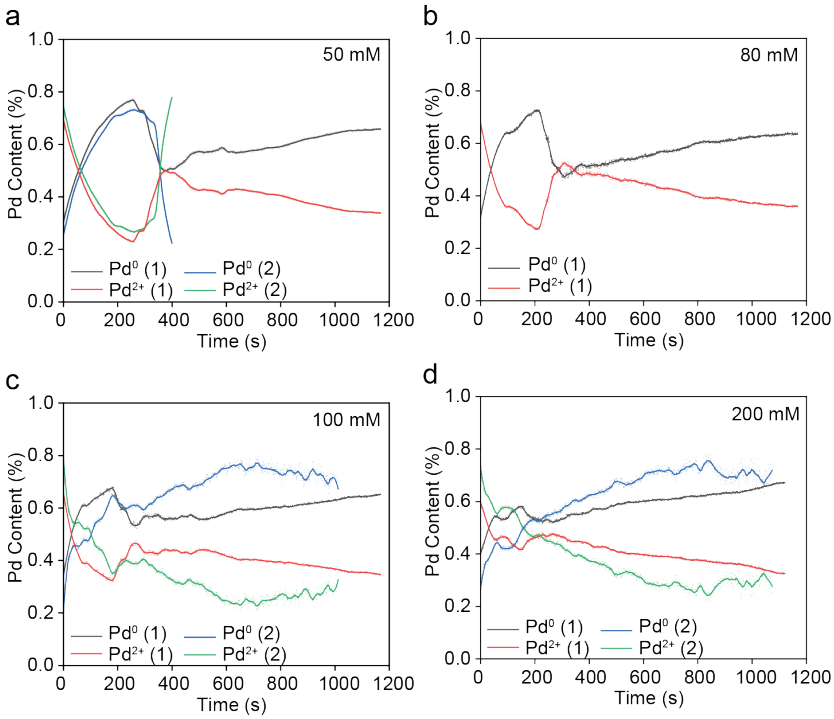

Figure 5.18 ***Reproducibility of LCF for an AA Concentration Range.*** *Reproducibility of Pd K-edge XANES LCF results for CTAB-capped nanoparticle growth forming Pd^{2+} (red and green) and Pd^{0} (black and blue) with two trials at concentrations of (a) 50 mM, (b) 80 mM, (c) 100 mM and (d) 200 mM. Aqueous H_2PdCl_4 solution (Pd^{2+}) and Pd foil (Pd^{0}) were used as LCF standards.*

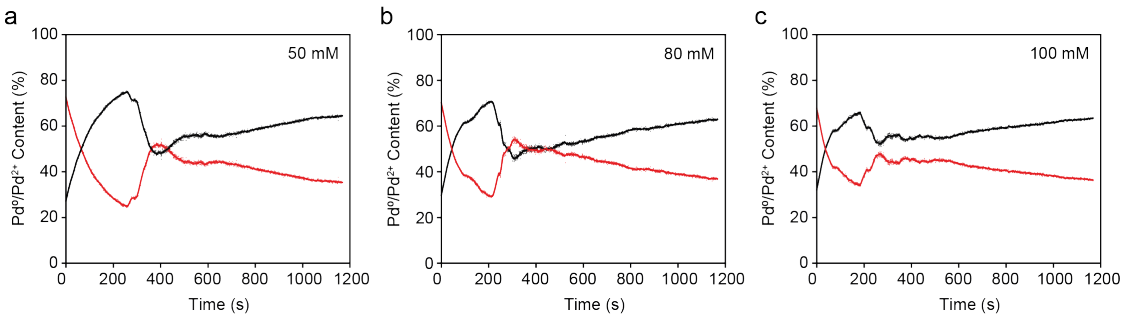

Figure 5.19 ***AA Concentration CTAB-capped LCF.*** *Pd K-edge XANES LCF results for Pd reduction, showing Pd^{2+} (red) and Pd^{0} (black) with AA concentrations of (a) 50 mM, (b) 80 mM and (c) 100 mM. Aqueous H_2PdCl_4 solution (Pd^{2+}) and Pd foil (Pd^{0}) were used as LCF standards.*

Table 5.2 ***Temperature Series LCF CTAB-Capped Pd Growth***. *Pd K-edge XANES LCF fitting was run with Athena between a range of E_0-20 eV and E_0+30 eV using K_2PdBr_2 and Pd foil as standards for Pd^{2+} and Pd^0, respectively. LCF fittings were performed for individual points, before batch fitting the full datasets.*

	Time	R-factor	Pd^{2+} Weight (× 100%)	Pd^{2+} Error (× 100%)	Pd^0 Weight (× 100%)	Pd^0 Error (× 100%)
30ºC	15	0.001	0.535	0.018	0.465	0.018
	50	0.007	0.737	0.042	0.263	0.042
	90	0.003	0.778	0.027	0.222	0.027
	115	0.004	0.841	0.031	0.159	0.031
	215	0.002	0.606	0.020	0.394	0.020
	825	0.003	0.575	0.024	0.425	0.024
	1155	0.002	0.653	0.021	0.347	0.021
40ºC	10	0.000	0.413	0.015	0.587	0.015
	35	0.004	0.609	0.045	0.391	0.045
	60	0.000	0.867	0.010	0.133	0.010
	94	0.000	1.000	0.000	0.000	0.000
	110	0.001	0.738	0.017	0.262	0.017
	450	0.001	0.570	0.023	0.430	0.023
	825	0.001	0.690	0.023	0.310	0.023
	1168	0.001	0.718	0.024	0.282	0.024
50ºC	45	0.004	0.522	0.030	0.478	0.030
	85	0.004	0.623	0.031	0.377	0.031
	120	0.003	0.674	0.026	0.326	0.026
	175	0.002	0.736	0.023	0.264	0.023
	300	0.006	0.624	0.036	0.376	0.036
	825	0.004	0.638	0.029	0.362	0.029

	Time	R-factor	Pd^{2+} Weight (× 100%)	Pd^{2+} Error (× 100%)	Pd^{0} Weight (× 100%)	Pd^{0} Error (× 100%)
	1168	0.005	0.731	0.031	0.269	0.031
60ºC	30	0.002	0.502	0.021	0.498	0.021
	100	0.002	0.387	0.020	0.613	0.020
	150	0.002	0.381	0.021	0.619	0.021
	250	0.002	0.287	0.018	0.713	0.018
	450	0.002	0.233	0.019	0.767	0.019
	825	0.002	0.067	0.020	0.933	0.020
	1168	0.006	0.000	0.034	1.000	0.034

Table 5.3 ***EXAFS Temperature Series CTAB-Capped Pd Growth****. Pd K-edge Artemis EXAFS refinement was performed with a set amplitude reduction value of 0.667, calculated from a Pd foil standard. The bond lengths selected (R) are 2.75 Å (Pd-Pd), 2.10 Å (Pd-O), 2.30 Å (Pd-Cl) and 2.35 Å (Pd-Br) The resulting* σ^2 *values were found to be in the range of 0.003 for* σ^2 *Pd-Pd and* σ^2 *Pd-Br/Cl/O.*

ºC	Time (s)	ΔE_0	Pd-Pd C.N.	ΔR Pd-Pd	Pd-O C.N.	ΔR Pd-O	Pd-Cl C.N.	ΔR Pd-Cl	Pd-Br C.N.	ΔR Pd-Br
40	0	0.486	0.488	-0.036	-0.004	0.039	2.812	-0.033	1.643	-0.040
	10	-1.662	2.718	-0.017	-0.419	0.039	2.184	-0.033	1.539	-0.040
	35	-2.189	5.977	-0.016	-0.552	0.039	1.255	-0.033	1.078	-0.040
	60	-2.328	6.827	-0.013	0.516	0.039	0.571	-0.033	0.402	-0.040
	94	-2.949	7.005	-0.014	-0.551	0.039	1.184	-0.033	0.148	-0.040
	100	-1.061	4.925	-0.008	0.781	0.039	0.524	-0.033	1.943	-0.040
	450	0.730	3.477	-0.011	0.162	0.039	0.978	-0.033	2.124	-0.040

ºC	Time (s)	ΔE_0	Pd-Pd C.N.	ΔR Pd-Pd	Pd-O C.N.	ΔR Pd-O	Pd-Cl C.N.	ΔR Pd-Cl	Pd-Br C.N.	ΔR Pd-Br
	825	-0.037	4.449	-0.011	0.374	0.039	0.756	-0.033	1.694	-0.040
	1168	-2.161	5.588	-0.024	0.409	-0.043	0.618	-0.033	1.545	-0.067
50	0	-1.587	1.770	-0.042	0.606	-0.044	0.351	-0.033	3.392	-0.037
	45	0.137	3.863	-0.022	0.310	0.046	0.480	-0.033	2.687	-0.049
	85	-1.706	4.604	-0.015	0.000	0.046	0.542	-0.033	2.418	-0.044
	120	-1.672	5.078	-0.019	0.115	0.046	0.419	-0.033	2.042	-0.047
	175	-0.315	5.846	-0.019	0.191	0.100	0.373	-0.033	1.717	-0.049
	300	2.055	4.626	-0.023	0.730	0.046	0.030	-0.033	2.342	-0.049
	450	0.454	4.092	-0.026	0.651	0.046	0.054	-0.033	2.730	-0.055
	825	-1.841	4.250	-0.030	0.247	-0.051	0.249	-0.033	2.310	-0.060
	1168	-0.841	4.578	-0.026	0.133	0.022	0.471	-0.033	2.060	-0.064
60	250	-1.817	5.605	-0.012	0.331	0.039	1.147	-0.033	1.272	-0.052
	450	-1.507	5.161	-0.017	0.330	-0.072	0.810	-0.033	1.395	-0.040
	825	-3.048	6.621	-0.014	0.145	0.039	1.046	-0.033	1.104	-0.088
	1168	-2.995	7.572	-0.019	-0.440	-0.030	0.860	-0.033	0.758	-0.100

Table 5.4 ***AA Concentration Series LCF CTAB-Capped Pd Growth***. *Pd K-edge XANES LCF fitting was run for individual points (Athena) between a range of E_0-20 eV and E_0+30 eV using K_2PdBr_2 (Pd^{2+}) and Pd foil (Pd^0) as standards.*

AA	Time (s)	R-factor	Pd^{2+} (×100%)	Error (×100%)	Pd^0 (×100%)	Error (×100%)
50 mM	0	0.002	0.374	0.037	0.626	0.037
	80	0.001	0.537	0.026	0.463	0.026
	190	0.002	0.703	0.029	0.297	0.029
	275	0.002	0.752	0.033	0.248	0.033
	325	0.003	0.707	0.042	0.293	0.042
	375	0.003	0.626	0.043	0.374	0.043
	480	0.003	0.585	0.042	0.415	0.042
100 mM	0	0.002	0.446	0.030	0.554	0.030
	30	0.001	0.504	0.023	0.496	0.023
	60	0.001	0.578	0.029	0.422	0.029
	100	0.001	0.638	0.028	0.362	0.028
	130	0.001	0.741	0.018	0.259	0.018
	240	0.004	0.787	0.048	0.213	0.048
	825	0.001	0.794	0.022	0.206	0.022
	1166	0.001	0.767	0.023	0.233	0.023
200 mM	0	0.001	0.385	0.027	0.385	0.027
	25	0.001	0.361	0.022	0.361	0.022
	50	0.001	0.324	0.017	0.324	0.017
	90	0.001	0.202	0.023	0.202	0.023
	115	0.001	0.219	0.017	0.219	0.017
	170	0.001	0.152	0.021	0.152	0.021
	300	0.001	0.326	0.021	0.326	0.021
	825	0.001	0.215	0.020	0.215	0.020

Table 5.5 ***EXAFS AA Concentration Series CTAB-Capped Pd Growth****. Pd K-edge Artemis EXAFS refinement was performed with a set amplitude reduction value of 0.667, calculated from a Pd foil standard, with resulting σ^2 values of 0.003 for σ^2 Pd-Pd and 0.0034 σ^2 for Pd-Br/Cl/O.*

	Time	ΔE_0	Pd-Pd C.N.	R Pd-Pd	Pd-Cl C.N.	R Pd-Cl	Pd-O C.N.	R Pd-O	Pd-Br C.N.	R Pd-Br
50 mM	0	-0.254	1.550	2.705	0.153	2.276	0.313	2.099	3.170	2.413
	80	-2.127	3.641	2.735	0.112	2.276	0.041	2.099	2.615	2.413
	190	-2.862	5.250	2.744	0.159	2.312	1.732	2.099	-0.033	2.413
	275	-1.461	5.702	3.071	0.054	2.312	1.636	1.960	-0.033	2.413
	325	0.708	4.982	2.734	0.292	2.276	0.099	2.099	2.112	2.413
	825	-0.251	3.861	2.738	0.263	2.276	0.398	2.099	2.515	2.413
	1168	0.112	4.217	2.739	0.098	2.276	0.496	2.099	2.114	2.413
100 mM	0	2.070	2.717	2.724	2.729	2.276	0.676	2.099	0.560	2.413
	30	1.476	4.093	2.727	0.405	2.276	0.428	2.099	2.413	2.413
	60	-1.119	4.893	2.732	0.460	2.276	0.315	2.099	2.053	2.413
	100	0.385	5.342	2.728	0.339	2.276	-0.089	2.099	1.662	2.413
	130	0.167	5.625	2.731	0.386	2.276	0.138	2.099	1.517	2.413
	240	1.232	5.632	3.431	-0.060	2.312	2.053	2.099	-0.033	2.413
	400	-0.787	4.861	2.731	0.171	2.276	0.729	2.099	1.979	2.413
	825	1.278	4.917	2.739	0.300	2.276	0.464	2.099	2.176	2.413
	1160	-0.480	5.117	2.739	0.325	2.276	0.513	2.099	2.034	2.413
200 mM	0	2.517	3.557	2.739	0.800	2.350	0.746	2.056	2.755	2.419
	50	-0.183	5.148	2.729	0.460	2.350	0.577	2.056	1.925	2.404

Time	ΔE_0	Pd-Pd C.N.	R Pd-Pd	Pd-Cl C.N.	R Pd-Cl	Pd-O C.N.	R Pd-O	Pd-Br C.N.	R Pd-Br
90	-0.060	5.356	2.728	0.520	2.350	0.641	2.056	1.909	2.399
115	0.115	5.739	2.733	0.701	2.350	0.585	2.056	1.972	2.400
170	0.034	6.175	2.731	0.631	2.350	0.650	2.056	1.965	2.398
300	-0.055	4.739	2.730	0.399	2.350	0.426	2.056	2.299	2.408
825	-1.308	5.269	2.734	0.733	2.350	0.041	2.056	2.221	2.395
1121	-0.291	5.559	2.731	0.678	2.350	0.136	1.980	1.959	2.389

5.6 References

1 Wen, X. *et al.* Synthesis of Palladium Nanodendrites Using a Mixture of Cationic and Anionic Surfactants. *Langmuir* **36**, 1745-1753, http://dx.doi.org/10.1021/acs.langmuir.9b03804 (2020).

2 Lee, S., Cho, H., Kim, H. J., Hong, J. W. & Lee, Y. W. Shape- and Size-Controlled Palladium Nanocrystals and Their Electrocatalytic Properties in the Oxidation of Ethanol. *Materials (Basel)* **14** http://dx.doi.org/10.3390/ma14112970 (2021).

3 Bakshi, M. S. How Surfactants Control Crystal Growth of Nanomaterials. *Crystal Growth & Design* **16**, 1104-1133, http://dx.doi.org/10.1021/acs.cgd.5b01465 (2015).

4 Alam, M. S., Siddiq, A. M., Narayanan, S. S., Samanta, D. & Das, S. K. Cationic Surfactant (CTAC) Assisted Synthesis of Silver Nanoparticles with Controlled Size: Optical, Morphological and Bactericidal Studies. *Journal of Nanoengineering and Nanomanufacturing* **5**, 124-131, http://dx.doi.org/10.1166/jnan.2015.1238 (2015).

5 Stolaś, A., Darmadi, I., Nugroho, F. A. A., Moth-Poulsen, K. & Langhammer, C. Impact of Surfactants and Stabilizers on Palladium Nanoparticle–Hydrogen Interaction Kinetics: Implications for Hydrogen Sensors. *ACS Applied Nano Materials* **3**, 2647-2653, http://dx.doi.org/10.1021/acsanm.0c00020 (2020).

6 Yoshimune, W., Kuwaki, A., Kusano, T., Matsunaga, T. & Nakamura, H. In Situ Small-Angle X-ray Scattering Studies on the Growth Mechanism of Anisotropic Platinum Nanoparticles. *ACS Omega* **6**, 10866-10874, http://dx.doi.org/10.1021/acsomega.1c00608 (2021).

7 Xie, M. *et al.* A Quantitative Analysis of the Reduction Kinetics Involved in the Synthesis of Au@Pd Concave Nanocubes. *Chemistry* **25**, 16397-16404, http://dx.doi.org/10.1002/chem.201904074 (2019).

8 Kim, S.-W. *et al.* Synthesis of Monodisperse Palladium Nanoparticles. *Nano Letters* **3**, 1289-1291, http://dx.doi.org/10.1021/nl0343405 (2003).

9 Karim, A. M. *et al.* Synthesis of 1 nm Pd Nanoparticles in a Microfluidic Reactor: Insights from in Situ X-ray Absorption Fine Structure Spectroscopy and Small-Angle X-ray Scattering. *The Journal of Physical Chemistry C* **119**, 13257-13267, http://dx.doi.org/10.1021/acs.jpcc.5b01681 (2015).

10 Peng, H. C., Xie, S., Park, J., Xia, X. & Xia, Y. Quantitative analysis of the coverage density of Br- ions on Pd100 facets and its role in controlling the shape of Pd nanocrystals. *J Am Chem Soc* **135**, 3780-3783, http://dx.doi.org/10.1021/ja400301k (2013).

11 Wang, F. *et al.* Porous single-crystalline palladium nanoparticles with high catalytic activities. *Angewandte Chemie International Edition in English* **51**, 4872-4876, http://dx.doi.org/10.1002/anie.201107376 (2012).

12 Jang, K. *et al.* Three-dimensional atomic mapping of ligands on palladium nanoparticles by atom probe tomography. *Nat Commun* **12**, 4301, http://dx.doi.org/10.1038/s41467-021-24620-9 (2021).

13 Guo, K., Xu, D., Xu, L., Li, Y. & Tang, Y. Noble metal nanodendrites: growth mechanisms, synthesis strategies and applications. *Mater Horiz* **10**, 1234-1263, http://dx.doi.org/10.1039/d2mh01408d (2023).

14 Lim, B., Jiang, M., Yu, T., Camargo, P. H. C. & Xia, Y. Nucleation and growth mechanisms for Pd-Pt bimetallic nanodendrites and their electrocatalytic properties. *Nano Research* **3**, 69-80, http://dx.doi.org/10.1007/s12274-010-1010-8 (2010).

15 Lim, B. *et al.* Pd-Pt Bimetallic Nanodendrites with High Activity for Oxygen Reduction. *Science* **324**, 1302-1305, http://dx.doi.org/doi:10.1126/science.1170377 (2009).

16 Fang, G. *et al.* Differential Pd-nanocrystal facets demonstrate distinct antibacterial activity against Gram-positive and Gram-negative bacteria. *Nat Commun* **9**, 129, http://dx.doi.org/10.1038/s41467-017-02502-3 (2018).

17 Wang, F. *et al.* Porous single-crystalline palladium nanoparticles with high catalytic activities. *Angew Chem Int Ed Engl* **51**, 4872-4876, http://dx.doi.org/10.1002/anie.201107376 (2012).

18 Yang, T. H. *et al.* Toward a Quantitative Understanding of the Reduction Pathways of a Salt Precursor in the Synthesis of Metal Nanocrystals. *Nano Lett* **17**, 334-340, http://dx.doi.org/10.1021/acs.nanolett.6b04151 (2017).

19 Newville, M. *Fundamentals of XAFS*. (Consortium for Advanced Radiation Sources, 2004).

20 Basham, M. *et al.* Data Analysis WorkbeNch (DAWN). *J Synchrotron Radiat* **22**, 853-858, http://dx.doi.org/10.1107/S1600577515002283 (2015).

21 Ravel, B. & Newville, M. ATHENA, ARTEMIS, HEPHAESTUS: data analysis for X-ray absorption spectroscopy using IFEFFIT. *J Synchrotron Radiat* **12**, 537-541, http://dx.doi.org/10.1107/S0909049505012719 (2005).

22 Muñoz, M., Farges, F. & Argoul, P. Continuous Cauchy wavelet transform of XAFS spectra. *Physica Scripta* **2005**, 221, http://dx.doi.org/10.1238/Physica.Topical.115a00221 (2005).

Chapter 6. The Role of Intermediates in Cu Nanoparticle Growth

The intermediate complexes and oxidation states formed during nanoparticle growth affect the reduction rate and determine nanoparticle morphologies. This is particularly clear for the reduction of Cu nanoparticles, where undesirable oxide formation in and on the surface of nanoparticles grown in solution is a common problem in their synthesis.

We present a study of Cu nanoparticle growth under three major reaction conditions to compare the effects of intermediates formed with different solvents and different reducing agents. The reduction of copper acetate ($Cu(OAc)_2$) dissolved in water ($Cu(OAc)_2/H_2O$) and dimethylformamide ($Cu(OAc)_2$/DMF) are studied under ascorbic acid (AA) reduction. $Cu(OAc)_2$/DMF reduction in AA is compared with hydrazine (N_2H_4) reduction under similar concentrations. A combination of *in situ* X-ray absorption spectroscopy (XAS), *in situ* electron paramagnetic resonance spectroscopy (EPR), Valence-to-Core X-ray emission spectroscopy (VtC XES), high resolution X-ray absorption near edge structure (HR-XANES) and transmission electron microscopy (TEM), gives a unique perspective on the growth mechanisms followed. This study shows the importance of complementary characterisation techniques and high resolution measurements to observe nanoparticle growth mechanisms.

Notable Contributions

Jay Yan contributed *in situ* TEM data analysis and co-developed the XAS batch-fitting programs and Ryan Wang contributed research ideas and experimental design.

6.1 Introduction

Copper nanoparticles have emerged as a cheaper alternative to platinum group metals and have shown catalytic activity for valuable reactions including the electrochemical carbon dioxide reduction reaction (CO_2RR),[1-3] organic coupling reactions[4,5] and the water-gas-shift reaction.[6,7] The catalytic behaviour of Cu nanoparticles generally depends on morphology-controlled surface area, exposed active sites and surface copper species, among other factors.[8] The formation of intermediate species is particularly interesting in the case of Cu nanoparticles, which are easily oxidised during synthesis.

In practice, aqueous solvents may to contribute to the formation of CuO or Cu_2O in nanoparticles, undesirable in catalytic applications.[9,10] This observation echoes the literature on aqueous Cu^{2+} reduction, in which Cu^{1+} is designated as the intermediate responsible for the integration of oxide species into the framework for CuO nanoparticles. Solvent substitution, such as with DMF was found to stabilise metallic copper nanoparticles, without the presence of a surfactant, a property attributed to the interaction of the DMF molecules with the Cu surface.[11] Thus, AA reduction was compared for H_2O ($Cu(OAc)_2/H_2O$/AA) and DMF ($Cu(OAc)_2$/DMF/AA), selected as two representative solvents for the *in situ* comparison of the solvent effect on Cu nanoparticle growth.

The reducing agent selection may also play various roles in the determination of nanoparticle morphology.[12,13] The most direct effect is on the reaction rate, where increased concentration or increased reducing agent strength will accelerate the reaction.[14,15] In addition reducing agents such as AA have been found to behave as a capping agent or to form intermediate species after interacting with the metal salt.[13,16,17] The formation of by-products, such as N_2 formed during N_2H_4 reduction can assist with anaerobic conditions, while the formation of intermediate

complexes can further determine reaction pathways.[18] In fact, Pastoriza-Santos et al. describe the formation of crystalline, metallic Cu nanoplatelets through N_2H_4 reduction of $Cu(OAc)_2$/DMF, capped with polyvinylpyrrolidone (PVP) and attribute the complete reduction of Cu to anaerobic growth and the intermediate reacting species.[18] Thus, a final condition $Cu(OAc)_2$/DMF reduction with N_2H_4 ($Cu(OAc)_2$/DMF/N_2H_4) allows a comparison with AA reduction in the same solvent. Thus, three synthesis conditions of $Cu(OAc)_2$/H_2O/AA, $Cu(OAc)_2$/DMF/AA and $Cu(OAc)_2$/DMF/N_2H_4 were selected for an *in situ* XAS study of the reduction rates, intermediate species, reaction stages and resulting nanoparticle morphology under a range of temperatures.

The increased time-resolution of *in situ* characterization is the key to understanding such growth behaviour.[19] *In situ* XAS measurements allow the simultaneous monitoring of oxidation states and bond formation during reactions, but most reported results are at the second to minute scale.[20-22] Quick XAS measurements during Ag and Pd nanoparticle growth have achieved resolutions of 13.8 s and 15 s, respectively[23,24] and energy dispersive extended X-ray absorption fine structure spectroscopy (EDE) has achieved higher resolutions still, with a notable 6.6 s resolution measured by Yao et al. in 2012, observing Rh nanoparticle growth.[22] Thus EDE measurements, as measured here, can achieve high time-resolutions and are particularly suited to liquid measurements, previously applied to the observation of copper acetate reduction with $NaBH_4$.[21,25,26]

To capture high time-resolution EDE data, including in the extended X-ray absorption fine structure (EXAFS) region, a method of batch merging was applied here. Where poor data was achieved due to fast measurements, the spectra quality was improved without losing time-resolution by merging results from 50

repetitions of each experiment (Figure 6.1). Using this technique, we present the time-resolved *in situ* capture and analysis of more than 14 million XAS spectra during Cu nanoparticle growth, along with a framework for batch analysis and data management of large datasets. The higher time-resolution provides dual benefits of capturing short-term processes (overlooked with slow measurements) and increasing the number of observation points (even for slow reactions) to improve the statistical accuracy of results.

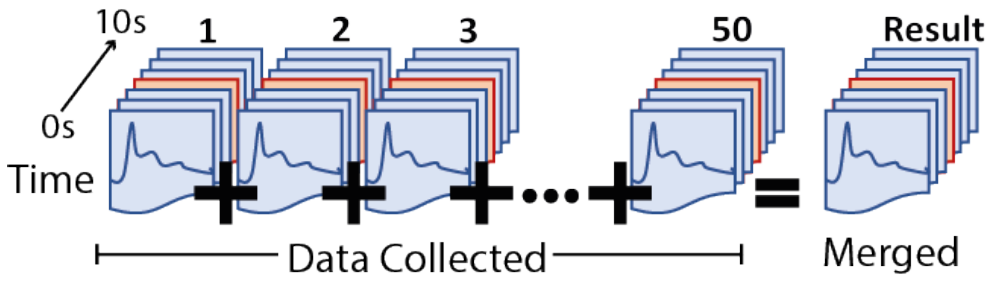

Figure 6.1 ***Merging Repeated XAS Data.*** *Reactions measured for 10 seconds may have poor data quality at individual timepoints, which can be improved by repeating the same reaction 50 times and merging to maintain the resolution. Datasets shown in red are measured at the same reaction time and can be merged for a resulting spectrum with improved data quality.*

Through a combination of highly time-resolved *in situ* XAS, *in situ* EPR, time resolved VtC XES and HR-XANES, and *ex situ* TEM observations, a detailed observation of the stages of Cu nanoparticle growth and the formation of morphology-determining intermediate species is obtained in this work. The reaction rates, chemical changes and intermediate species formed shed light on the diverse mechanisms of Cu nanoparticle formation. This methodology is versatile and could later be applied to other transition-metal nanoparticle growth

systems, as a framework for future large-scale time-resolved XAS refinement, and further *in situ* studies of growth in solution.

6.2 Results and Discussion

The results present the expected reaction mechanisms and complementary characterization techniques used to observe Cu nanoparticle growth and distinguish reaction stages. For the results, observations of standard solutions are shown first, to give a baseline for comparison and to ascertain the initial configuration of the Cu in solution. This is followed by a comparison of the solvent-effect on the reduction mechanism of $Cu(OAc)_2/H_2O$ and $Cu(OAc)_2$/DMF with AA. An *in situ* TEM observation of beam-induced reduction of $Cu(OAc)_2/H_2O$ is also shown to give an insight into the growth behaviour. Lastly, the role of the reducing agent is elucidated by comparing the $Cu(OAc)_2$/DMF/AA mechanism with $Cu(OAc)_2$/DMF/N_2H_4, to identify the key conditions for a faceted Cu nanoparticle structure.

6.2.1 Expected Reduction Mechanisms and Characterization

The growth mechanism of Cu nanoparticles will be described using major stages of reduction, nucleation and growth. These stages are anticipated because Cu nanoparticles have previously been experimentally observed to follow the Watzky Finke two-step growth mechanism, showing a distinctive sigmoidal reduction curve.[27-30]

The literature for ascorbic acid reduction supports a two-step dehydrogenation, observed in the reduction of aqueous $CuCl_2$ and $CuSO_4$ solutions to produce a

Cu^{1+} intermediate.[31,32] Lui et al. used time-resolved X-ray diffraction (XRD) measurements to measure the formation of $Cu(OH)_2$ or Cu_2O as intermediates, later converted to metallic Cu, during AA reduction of Cu salts.[32] Thus, Reaction Pathway 1 is provisionally used to describe $Cu(OAc)_2/H_2O$/AA and $Cu(OAc)_2$/DMF/AA. These steps are written simply, in terms of the corresponding changes in Cu oxidation state and Cu coordination, to be tested with *in situ* characterisation.

Reaction Pathway 1:

$$Cu^{2+}\text{-}O + 1e^- \rightarrow Cu^{1+}\text{-}O \quad \textit{(Reduction Stage 1)} \qquad \textit{Equation 6.1}$$

$$Cu^{1+}\text{-}O + 1e^- \rightarrow Cu^{0}\text{-}Cu \quad \textit{(Reduction Stage 2)} \qquad \textit{Equation 6.2}$$

$$n(Cu^{0}\text{-}Cu) \rightarrow Cu^{0}_{n} \quad \textit{(Growth Stage)} \qquad \textit{Equation 6.3}$$

$Cu(OAc)_2$/DMF/N_2H_4 reduction is believed not to follow the same mechanism, instead taking the direct reduction of Cu^{2+} to Cu^0. This has been hypothesised by Pastorizas-Santos et al., since Cu^{1+} formation was not observed during reduction.[18] A provisional mechanism for this reaction, showing the expected changes observable in XAS measurements, is therefore given in Reaction Pathway 2.

Reaction Pathway 2:

$$Cu^{2+}\text{-}O \rightarrow Cu^{2+}\text{-}N \quad \textit{(Coordination Stage)} \qquad \textit{Equation 6.4}$$

$$Cu^{2+}\text{-}N + 2e^- \rightarrow Cu^{0}\text{-}Cu \quad \textit{(Reduction Stage)} \qquad \textit{Equation 6.5}$$

$$n(Cu^{0}\text{-}Cu) \rightarrow Cu^{0}_{n} \quad \textit{(Growth Stage)} \qquad \textit{Equation 6.6}$$

A combination of time-resolved characterization tools are applied to capture the two different reaction mechanisms occurring, by directly monitoring physical and chemical changes in the system (Figure 6.2).

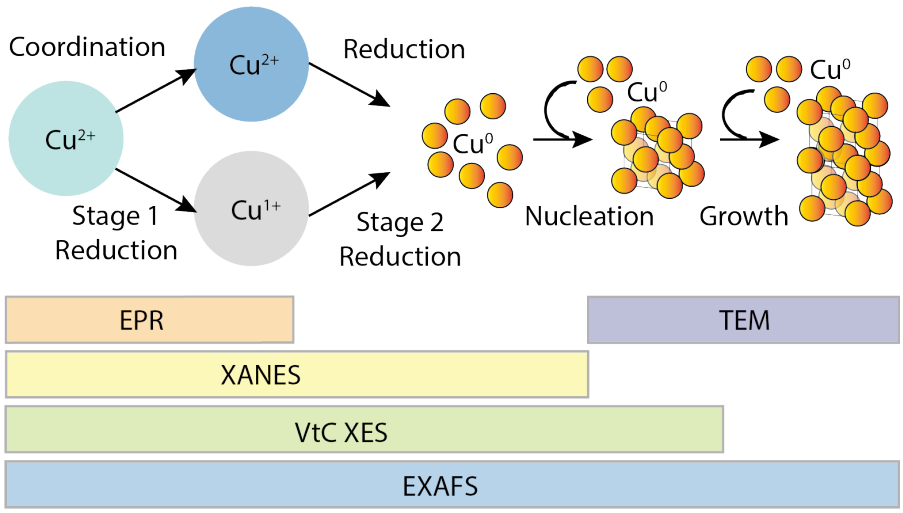

Figure 6.2 ***Cu Growth Stages and Characterization Methods.*** *Predicted routes of Cu^{2+} reduction to Cu^{0} nanoparticles, with a Cu^{2+} coordination intermediate (above) and a Cu^{1+} intermediate (below) and the corresponding characterization tools used for the observation of each step in this work; EPR (orange), TEM (purple), XANES (yellow), VtC XES (green) and EXAFS (blue).*

TEM gives a visual indication of the shapes of nanoparticles formed while *in situ* EPR measures the concentrations of Cu^{2+} species (and their ligand coordination). The Cu-ligand coordination can be further monitored by Valence-to-Core (VtC) XES, to distinguish between Cu-N, Cu-O, and Cu-Cu coordination. To differentiate Cu^{2+}, Cu^{1+} and Cu^{0}, HR-XANES and microsecond-resolved *in situ* X-ray absorption near-edge structure (XANES) provide detailed oxidation state information. The extended X-ray absorption fine structure (EXAFS) results monitor the corresponding coordination number (C.N.) changes.

6.2.2 Cu Standards and Solvents: H_2O versus DMF

It is apparent from the blue colour of $Cu(OAc)_2/H_2O$ versus the deep turquoise of $Cu(OAc)_2$/DMF, that there is some difference caused by the solvent in the Cu configuration. To observe the configuration of copper acetate in $Cu(OAc)_2/H_2O$

and $Cu(OAc)_2$/DMF, both solutions are studied with EPR. Cu^{2+} (d^9 configuration) has an unpaired electron making it notably active in EPR, which signal is lost when the electrons are paired such as in Cu^0 and Cu^{1+} (d^{10} configuration). EPR is also sensitive to the local coordination around Cu atoms, Cu^{2+} concentration and Cu clustering behaviour, making it possible to identify the differences between $Cu(OAc)_2$ interaction with each solvent.[33,34]

The EPR signal of $Cu(OAc)_2/H_2O$ shows symmetrical peaks between 300 mT and 320 mT, with g-value of 315 mT (Figure 6.3 a). This is a typical value for Cu coordinated salts, and likely corresponds with H_2O coordination around a central Cu atom in solution. This result is comparable to common Cu salts with known Cu-O coordination such as $CuSO_4$ and $Cu(NO_3)_2$ (Figure 6.3 b).

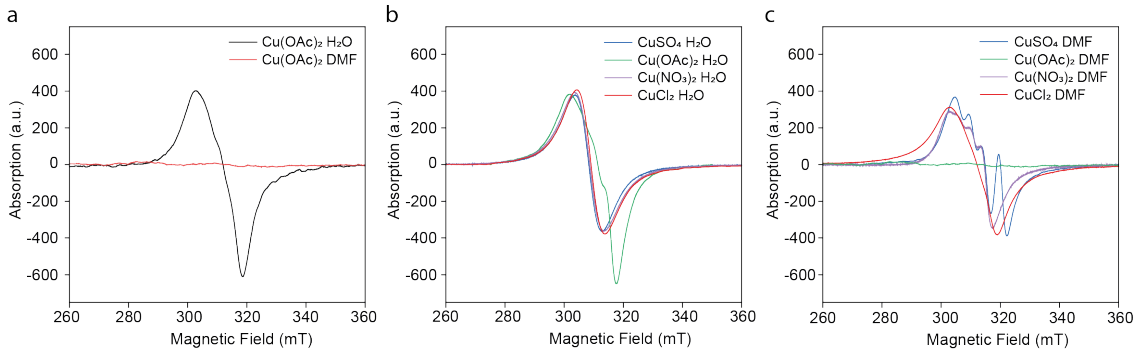

Figure 6.3 ***EPR Results of Cu Salts with H_2O and DMF.*** *EPR signals compared for (a) $Cu(OAc)_2$ dissolved in H_2O and DMF. (b) Superimposed EPR signal for solutions of $CuSO_4$, $Cu(OAc)_2$, $Cu(NO_3)_2$ and $CuCl_2$ in H_2O and (c) the same Cu salts dissolved in DMF.*

In contrast, $Cu(OAc)_2$/DMF is EPR silent (Figure 6.3 a). This is particularly the case for $Cu(OAc)_2$, since $CuSO_4$, $Cu(NO_3)_2$ and $CuCl_2$ continue to be EPR active when dissolved in DMF, although with a different EPR spectrum (Figure 6.3 c). The oxidation state of Cu in both $Cu(OAc)_2/H_2O$ and $Cu(OAc)_2$/DMF remains the same (Cu^{2+}), as confirmed by HR-XANES measurements which show the same

edge energy for both salts (Figure 6.4). This flat-line EPR result may indicate a dimeric structure or clustering of Cu atoms in $Cu(OAc)_2$/DMF, leaving no unpaired electrons for EPR excitation. $Cu(OAc)_2$ dissolved in organic solvents has been shown to cluster, making this a likely option in the case of DMF dissolution.[35,36]

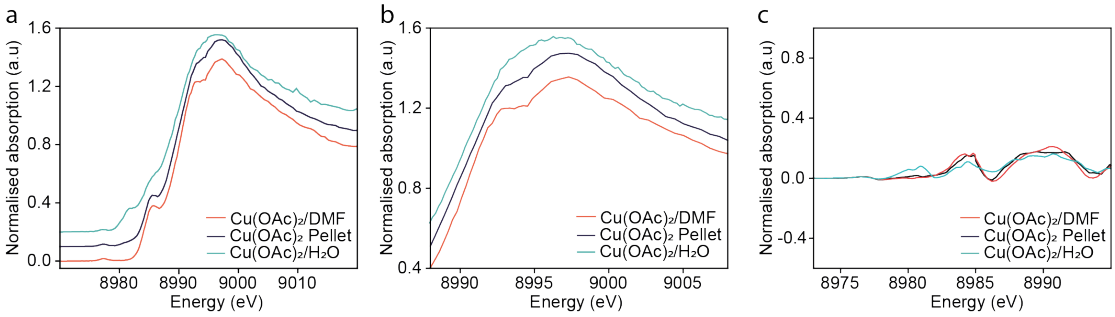

Figure 6.4 ***HR-XANES Spectra for $Cu(OAc)_2$ Standards.*** *Cu K-edge HR-XANES results for (a) $Cu(OAc)_2$ as a powder (black) and dissolved in H_2O (blue) and DMF (red), alongside (b) a closer view of the HR-XANES and (c) the derivative of these curves.*

HR-XANES of $Cu(OAc)_2/H_2O$ and $Cu(OAc)_2$/DMF, compared with the $Cu(OAc)_2$ salt pellet shows the same edge position measured at 8984 eV (Figure 6.4 a). The observed softening of the HR-XANES double peak (Figure 6.4 b) and the slight difference in edge features (Figure 6.4 c) for $Cu(OAc)_2/H_2O$ have been previously reported in the literature.[37,38]

A comparison of HR-XANES edge energies, measured for Cu-O and Cu-N coordinated standards with known oxidation states of Cu^{2+}, Cu^{1+} and Cu^0 (Figure 6.5 a, c), confirms that $Cu(OAc)_2$ has Cu^{2+}-O oxidation state. Edges are observed at 8981 eV (Cu^{1+}-O) and 8984 eV (Cu^{2+}-O) with copper oxide standards (Figure 6.5 a, b) shifting to 8982 eV (Cu^{1+}-N) and 8985 eV (Cu^{2+}-N) in copper-ammonia complex standards (Figure 6.5 c, d). Copper foil (Cu^0-Cu) is used as a calibration standard with an edge energy of 8979 eV.

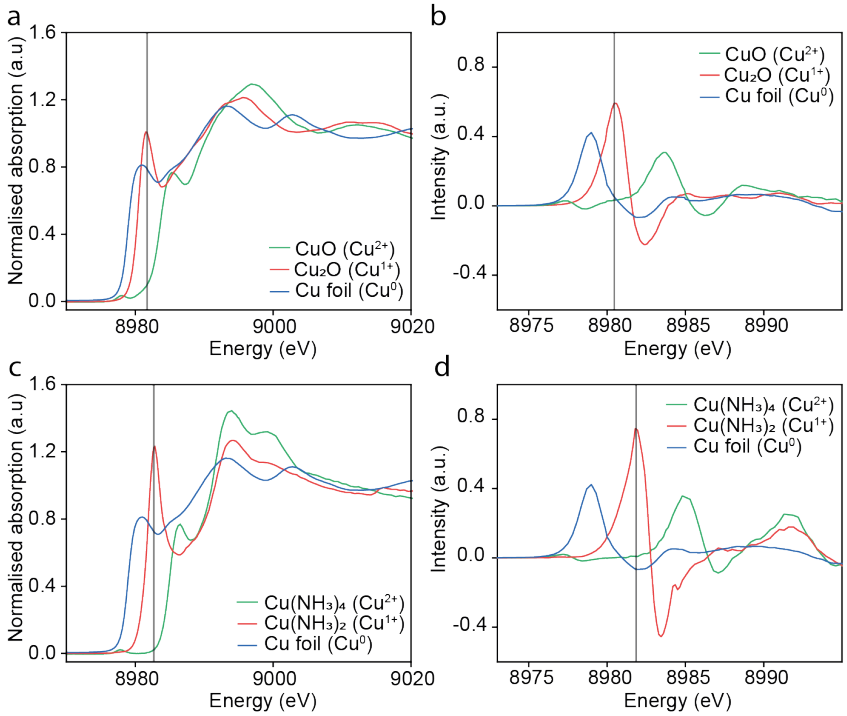

Figure 6.5 ***HR-XANES Comparison for Cu^0, Cu^{1+} and Cu^{2+} Standards.*** *Cu K-edge Normalised HR-XANES spectra of Cu^0 (blue), Cu^{1+} (red) and Cu^{2+} (green) measured for (a) Cu-O coordination in CuO, Cu_2O and Cu foil to show the shift in edge energy, alongside (b) the derivative. (c) A similar comparison of Cu-N coordination in $Cu(NH_3)_4$, $Cu(NH_3)_2$ and Cu foil, alongside (d) the derivative.*

Ligand-sensitive VtC XES spectra of a $Cu(OAc)_2$ pellet, $Cu(OAc)_2$/DMF and $Cu(OAc)_2/H_2O$ both show a Cu-O shoulder at 8969.5 eV with a peak at 8976 eV (Figure 6.6 a, b), comparable to the VtC XES spectrum observed for a CuO standard (Cu-O shoulder, peak at 8976 eV, Figure 6.6 b, d). VtC XES peak positions of Cu-N and Cu-Cu are observed at a similar energy around 8976 eV. In the case of Cu-N coordination, the Cu-O shoulder is shifted to 8970.5 eV, providing the only distinguishable feature between Cu-N and Cu-Cu, since their main peak (8973.5 eV) coincides (Figure 6.6 b, d).

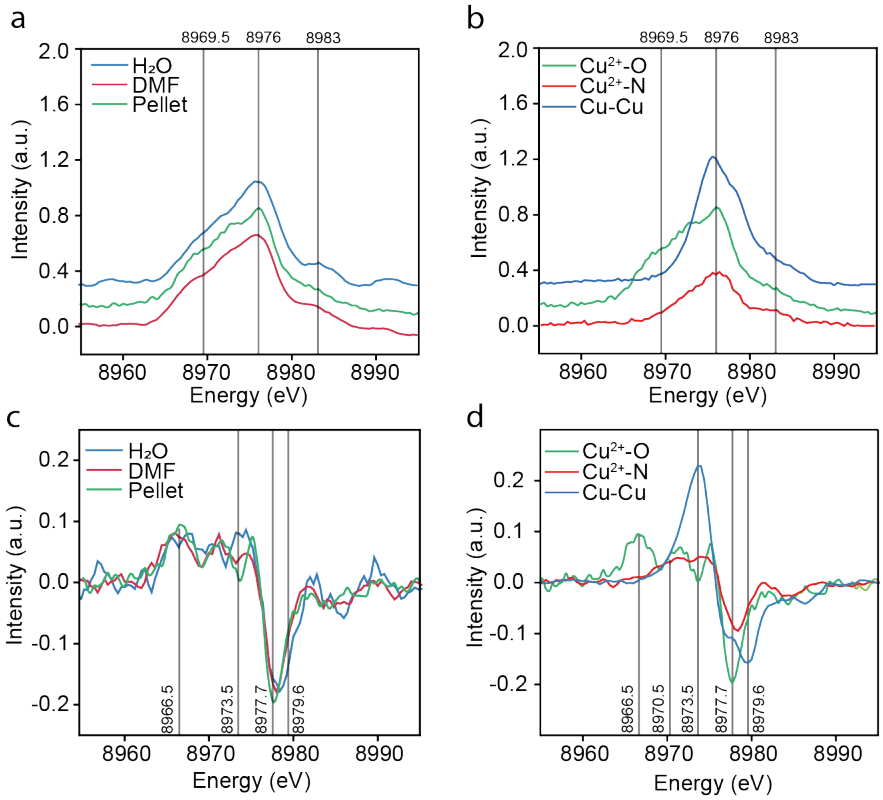

Figure 6.6 ***VtC XES Spectra of Cu(OAc)$_2$ and Cu^{2+} Standards.*** *Cu kβ^{2,5} VtC XES results measured for (a) Cu(OAc)$_2$ pellet (green), Cu(OAc)$_2$/H$_2$O (blue) and Cu(OAc)$_2$/DMF (red) and (c) the derivative. (b) Corresponding VtC XES results of Cu^{2+}-O, Cu^{2+}-N, Cu-Cu and (d) the derivative.*

These results confirm that Cu(OAc)$_2$/DMF has a limited interaction with the solvent and is still Cu-O coordinated, rather than Cu-N or Cu-Cu coordinated. EXAFS results fitted to give coordination numbers show the Cu coordination in both Cu(OAc)$_2$/H$_2$O and Cu(OAc)$_2$/DMF (Table 6.1). Cu(OAc)$_2$/H$_2$O was expected to show a six-oxygen coordination structure given in Figure 6.7(a), with a Cu atom surrounded by water and acetate groups. Literature values for the bond lengths in solution were reported as four bonds of equal length (~1.96 Å) in a square planar structure, with two elongated pyramidal bonds of varying length (>2.00 Å) in Cu(OAc)$_2$/H$_2$O.[39-41] Cu(OAc)$_2$/DMF may take on a similar configuration. In contrast, the copper acetate in the solid pellet is expected to

have a configuration of a dimer, due to the “paddle-wheel” structure widely cited (Figure 6.7 b).[42]

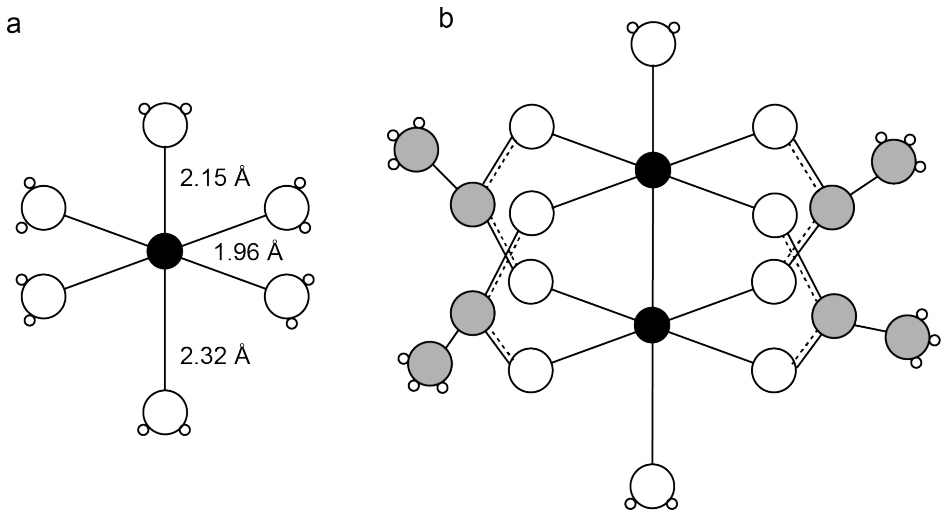

Figure 6.7 ***Chemical Structure of Cu(OAc)$_2$.*** *Ball-and-stick diagram of (a) Cu(OAc)$_2$/H$_2$O as a typical H$_2$O ligated Cu[39-41] versus (b) Cu(OAc)$_2$ structure give an indication of the structural differences in their configuration.*

First-shell EXAFS fitting (Table 6.1) of Cu(OAc)$_2$/DMF calculates an average Cu-O coordination number of 4.135 at a range of 1.95 Å. Thus, Cu(OAc)$_2$/DMF as observed under EPR, VtC XES and XAS is expected to have either a dimeric or clustered Cu configuration, with an average of four Cu-O bonds within the range of 1.95 Å.

The same fitting parameters for Cu(OAc)$_2$/H$_2$O yield five Cu-O coordinations at a range of 1.95 Å, possibly including a shortening of the vertical axis bond with an expected bond-length of 2.15 Å (Figure 6.7 a). Copper acetate powder is expected to exhibit a paired Cu structure from the paddle-wheel configuration (Figure 6.7 b), corroborated by EXAFS fitting which resolves five Cu-O bonds (Table 6.1, Supplementary Figure 6.33).

Table 6.1 ***EXAFS Refinement of $Cu(OAc)_2$ Standards.*** *Cu K-edge EXAFS data was refined with Artemis to yield parameters of E_0, C.N., ΔR and σ^2 for $Cu(OAc)_2/H_2O$, $Cu(OAc)_2$/DMF and $Cu(OAc)_2$ powder. Bond length (R) values were set as 2.00 Å (Cu-O) and 2.44 Å (Cu-Cu). Amp is shortened from amplitude reduction factor.*

Sample	ΔE_0	Error	Cu-O C.N.	Error	ΔR Cu-O	Error	σ^2 Cu-O	Error	amp
H_2O	-3.122	1.580	5.028	0.733	0.010	0.013	0.010	0.002	0.915
DMF	-5.679	2.572	4.135	0.967	-0.013	0.018	0.006	0.003	0.915
Powder	-2.438	5.152	5.031	2.411	0.021	0.041	0.008	0.007	0.850

These structures represent an average of the solution in which they are measured and are expected to be significantly altered upon addition of the reducing species, in this case either AA or N_2H_4.

6.2.3 Ascorbic Acid: Two Stage Reduction

The mechanism and rates of AA reduction are compared for $Cu(OAc)_2/H_2O$ and $Cu(OAc)_2$/DMF (Section 6.4.1). The nanoparticles formed in both conditions show a spherical shape at temperatures of 23ºC and 60ºC. This is in agreement with previous reports of $Cu(OAc)_2/H_2O$/AA reduction producing spherical nanoparticles, and may also be attributed to the use of polyvinyl pyrrolidone (PVP) as a surfactant.[43-45] Cu nanoparticles formed at 23ºC showed similar average diameters of 213.32 ± 61.06 in $Cu(OAc)_2/H_2O$ (Figure 6.8 a-c) and 209.12 ± 95.11 nm in $Cu(OAc)_2$/DMF (Figure 6.8 d-f). At 60ºC these increased significantly in $Cu(OAc)_2$/DMF to 408.47 ± 60.34 nm, but less so in $Cu(OAc)_2/H_2O$

giving 223.98 ± 111.67 nm (Supplementary Figure 6.34 a-f, Supplementary Table 6.5).

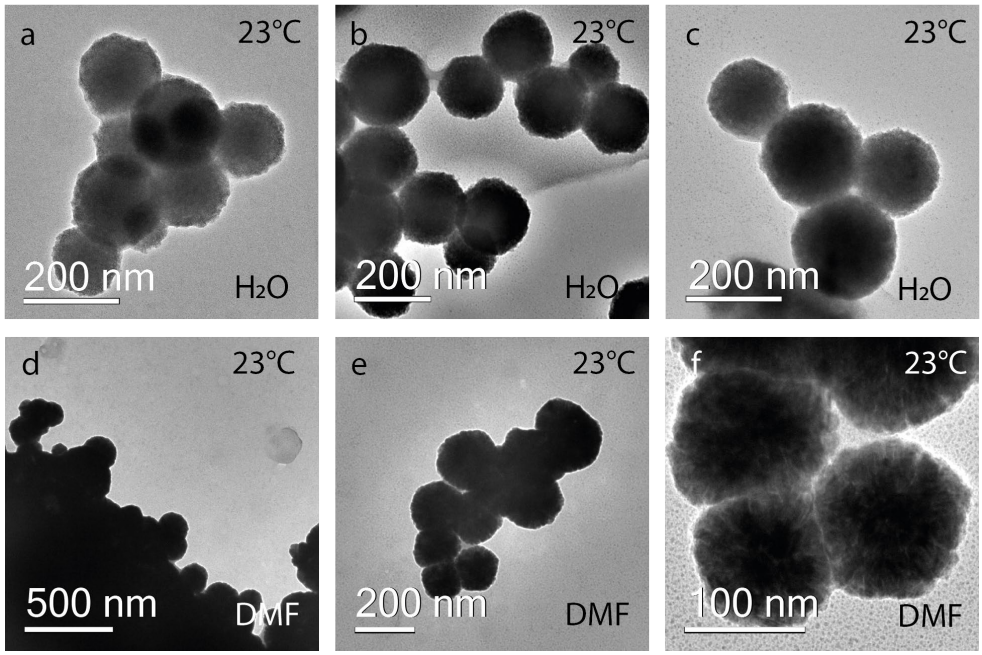

Figure 6.8 ***Morphology of AA-Reduced Copper Nanoparticles.*** *Bright-field TEM images of Cu nanoparticles formed during AA reduction of (a-c) $Cu(OAc)_2/H_2O$ at temperatures of 23ºC with scalebars of 200 nm, and (d-f) $Cu(OAc)_2$/DMF at temperatures of 23ºC with scalebars of (d) 500 nm, (e) 200 nm and (f) 100 nm.*

While the average size of nanoparticles formed at the end of the reaction time and measured *ex situ,* is above 200 nm, nanoparticle sizes achieved during *in situ* studies are likely maintained below the 50 nm range for early reaction times. The size limiting effect of PVP surfactant appears to be less effective with DMF as a solvent. Lattice spacings show a majority of crystalline Cu(111) features under $Cu(OAc)_2/H_2O$ (Supplementary Figure 6.35) and $Cu(OAc)_2$/DMF reduction (Supplementary Figure 6.36). However, particles are not single-crystalline, as indicated by the misalignment of crystalline regions within a single particle.

In situ EPR observation of reduction in $Cu(OAc)_2/H_2O$ and $Cu(OAc)_2$/DMF shows the change in concentration of Cu^{2+} species during a reaction (Figure 6.9). The EPR signal of $Cu(OAc)_2/H_2O$ decreases as Cu^{2+} is reduced to Cu^{1+} or Cu^0 (Figure 6.9b). Since no EPR signal is achieved during the reduction of $Cu(OAc)_2$/DMF, it can be concluded that the intermediate and final species are also EPR silent, and likely to be Cu^{1+} and Cu^0.

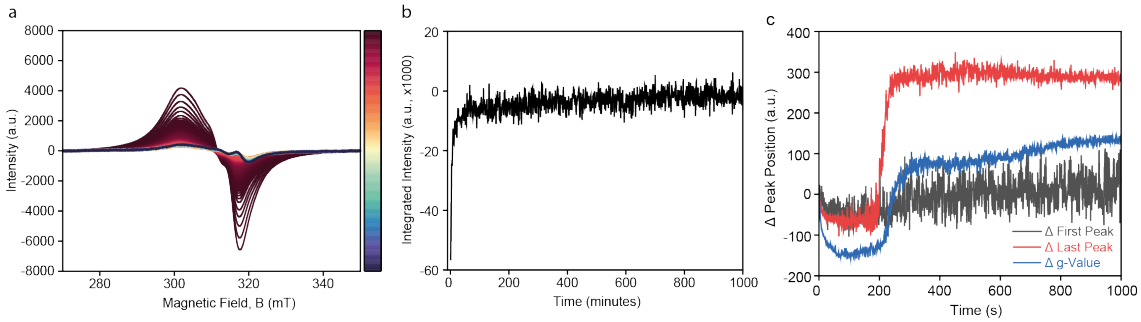

Figure 6.9 ***In situ EPR Results of $Cu(OAc)_2/H_2O$/AA Reduction.***

(a) EPR spectra obtained show the reduction of $Cu(OAc)_2$ as a loss of peak intensity over time (b) Time-resolved change in EPR-calibrated Cu concentration calculated from the integrated intensity of the negative peak in EPR spectra. (c) Change in positions for the first (grey) and last (red) peak and g-values (blue).

VtC XES of $Cu(OAc)_2/H_2O$/AA reduction at 60ºC in Figure 6.10 (a) shows the transition from Cu^{2+}-O (0 to 10 s) to Cu^{1+}-O (3 to 10 minutes) and finally Cu-Cu bonds (30+ minutes). These three phases correspond with the HR-XANES states of Cu^{2+}, Cu^{1+} and Cu^0 measured for the same solution (Figure 6.10 b, c). A lag is observed between HR-XANES and VtC XES changes, such as at a time of 10 seconds where a sharp Cu^{1+} peak is observed in HR-XANES, but the VtC XES spectrum remains in the original state. The intermediate phase could also be attributed to a Cu^{1+}-AA intermediate, previously described in the literature based

on an Fourier transform infrared spectroscopy measurement of Cu nanoparticle growth with AA.[17]

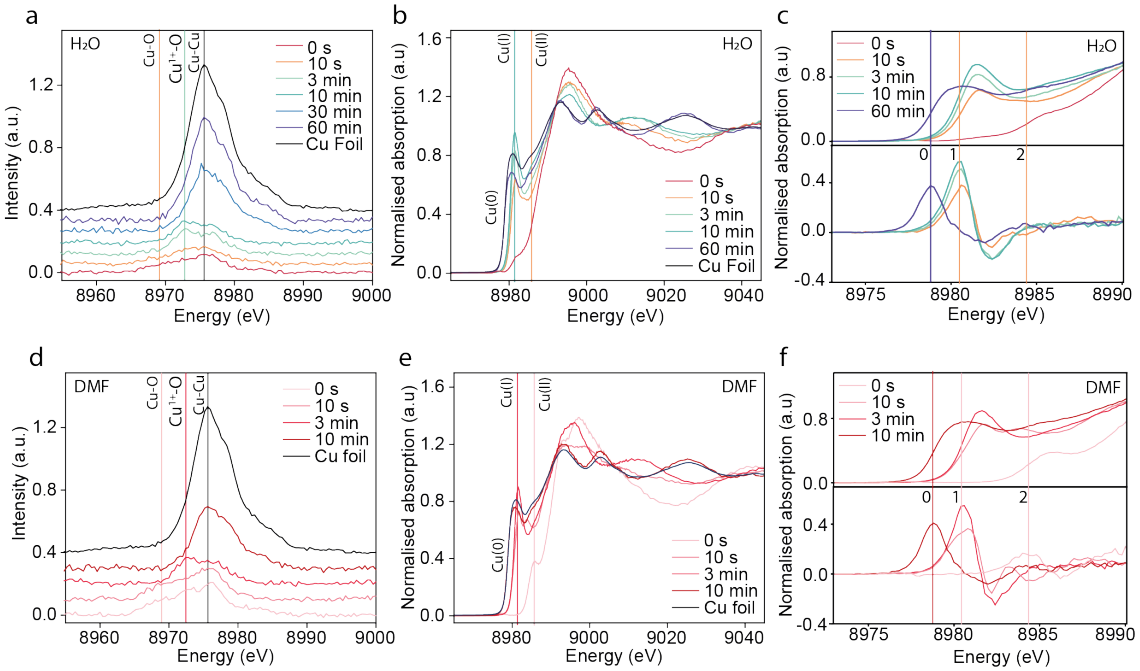

Figure 6.10 ***VtC XES and HR-XANES Results of AA-Reduction.*** *Time-resolved Cu kβ[2,5] VtC XES and Cu K-edge HR-XANES with derivative are measured at 60°C for (a-c) $Cu(OAc)_2/H_2O$/AA reduction (blue to red) and (d-f) $Cu(OAc)_2$/DMF/AA reduction (pink to red). Positions of Cu-O, Cu^{1+}-O and Cu-Cu coordination peaks are labelled on VtC XES curves, while for HR-XANES and derivative, edge position for oxidation states of Cu^0 (0), Cu^{1+} (1) and Cu^{2+} (2) are indicated.*

In $Cu(OAc)_2$/DMF, the same mechanism of Cu^{2+}-O to Cu^{1+}-O to Cu^0-Cu is observed but at a different rate (Figure 6.10 d). At 3 minutes a Cu^{1+}-O peak appears alongside HR-XANES Cu^{1+} formation (Figure 6.10 e, f), likely due to AA coordination during reduction. At 10 minutes, Cu-Cu dominant coordination is observed, where Cu^0 is formed.

Thus, the combination of HR-XANES and VtC XES shows that the AA reduction of $Cu(OAc)_2/H_2O$ and $Cu(OAc)_2$/DMF follow the same major reaction stages, but

at different rates. These are believed to result from AA coordination with the Cu during rapid reduction followed by increase in Cu-Cu peak intensity during the formation of increasingly large nanoparticles. Although the time-resolution of *in situ* VtC XES and HR-XANES measurements cannot directly capture reaction rates, they provide a valuable foundation for subsequent microsecond-resolved *in situ* XANES and EXAFS fitting. The linear combination fitting of HR-XANES gives an additional indication of the content of various copper oxidation states at a given reaction time (Supplementary Figure 6.37 and Supplementary Figure 6.38).

Standards measured for Cu^0, Cu^{1+} and Cu^{2+} oxidation states show distinct profile differences (Figure 6.11), used to quantify the content of each oxidation state with linear combination fitting (LCF) of the XANES region (Supplementary Figure 6.39, Supplementary Table 6.6) and used as standards to select amplitude reduction values and bond lengths when fitting the EXAFS region for Cu-Cu and Cu-O/N bonds (Supplementary Table 6.7).

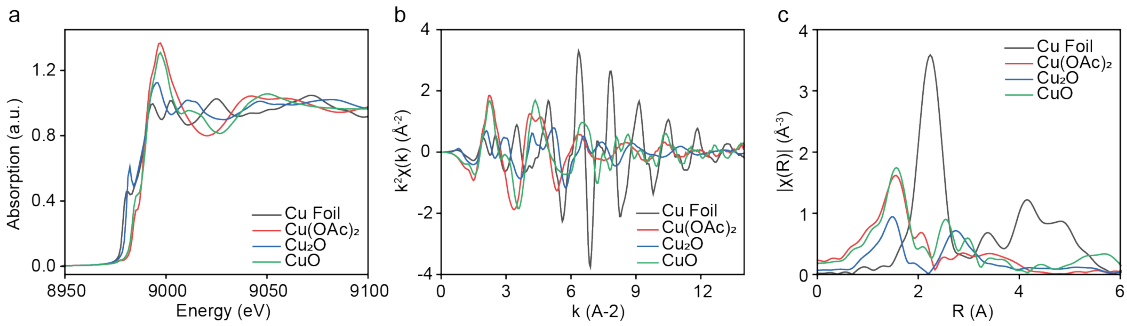

Figure 6.11 ***XAS of Standards of Cu^0, Cu^{1+} and Cu^{2+}.*** *XAS comparison of (a) XANES energy, (b) k-space and (c) R-space of $Cu(OAc)_2$ pellet (red) with Cu foil (black), Cu_2O (blue) and CuO (green).*

To further observe the mechanism of formation of nanoparticles in $Cu(OAc)_2/H_2O/AA$, the XAS results can first be visually assessed with a

Continuous Cauchy wavelet transform (CCWT) to enhance the distribution of bonds within the sample and their respective molecular masses (Figure 6.12). Non-phase-corrected R + ΔR values (y-axis) of 1.3 Å correspond with the Cu-O/N bonds of $Cu(OAc)_2/H_2O$. These are shown to reduce, first to a Cu^{1+}-O intermediate at around 2.8 Å after 5 s, and further to Cu-Cu at 2.1 Å after 9 s.

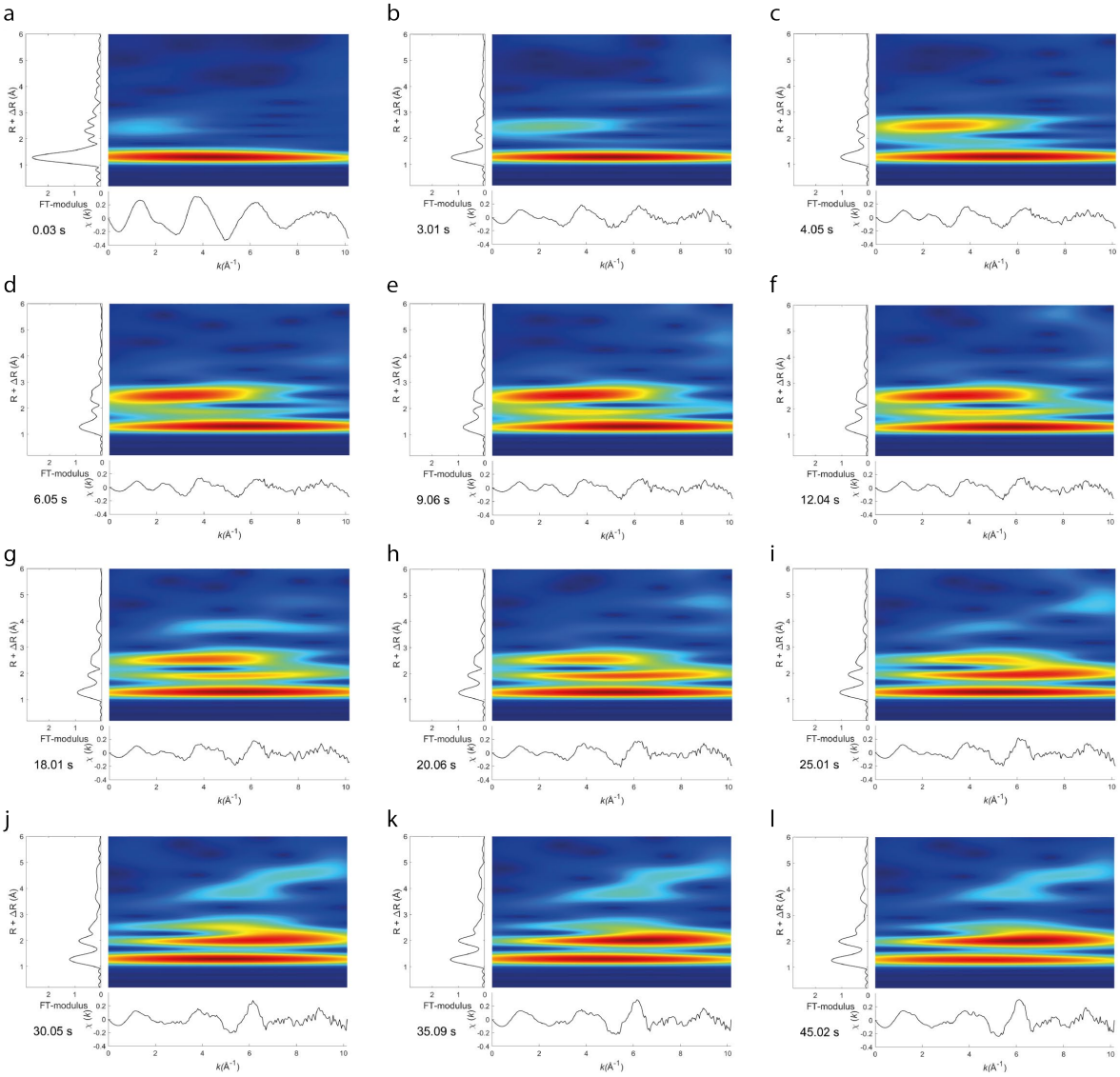

Figure 6.12 ***Time-Resolved Wavelet Transforms of $Cu(OAc)_2/H_2O$/AA Reduction.*** *Continuous Cauchy wavelet transforms combining the k-space (x-axis) and R-space (y-axis) Cu K-edge XAS data to form a heat map showing $Cu(OAc)_2/H_2O$/AA reduction at 60ºC, at reaction times of (a) 0 s, (b) 3 s, (c) 12 s, (d) 18 s, (e) 20 s, (f) 25 s, (g) 30 s, (h) 35 s and (i) 45 s.*

To further quantify the differences in chemical kinetics, *in situ* XAS is measured at a range of temperatures for both $Cu(OAc)_2/H_2O$ and $Cu(OAc)_2$/DMF, with a time-resolution of 1.27 ms. XANES analysis provides a profile of the change in copper oxidation state during the reaction, giving the concentrations of Cu^{2+}, Cu^{1+} and Cu^0.

First, LCF results were selected for $Cu(OAc)_2/H_2O$/AA reduction (Figure 6.13), based on an average of reproducible results (Supplementary Figure 6.40, Supplementary Figure 6.41, Supplementary Figure 6.42, Supplementary Table 6.8).

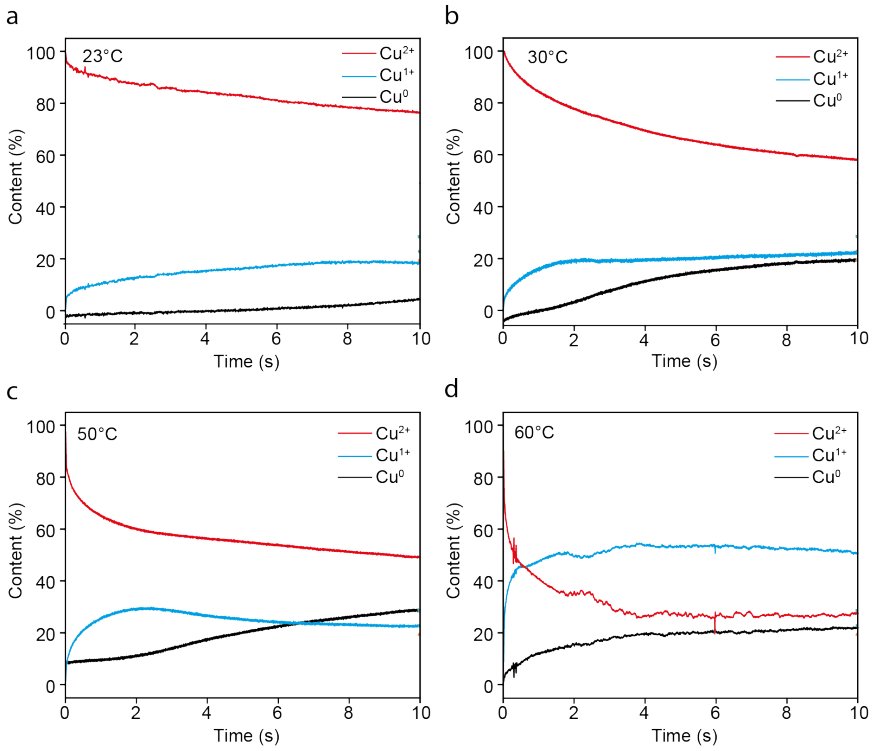

Figure 6.13 ***LCF Time-Series of $Cu(OAc)_2/H_2O$/AA.*** *Cu K-edge XANES LCF results for $Cu(OAc)_2/H_2O$/AA show the content of Cu^0 (black), Cu^{1+} (blue) and Cu^{2+} (red) at temperatures of (a) 23°C, (b) 30°C, (c) 50°C and (d) 60°C.*

The LCF results of the first ten seconds of the reaction show a predominance of Cu^{1+} species, which agrees with the HR-XANES observations at 10 s. However,

these results also indicate the further reduction of Cu^{1+} to Cu^{0} after around 2 s above 23ºC. These results can be compared to observe the trend of increasing rate at increased temperature (Figure 6.14 a-c). EXAFS fitting of the same data shows a similar trend to the LCF results but can only distinguish Cu-Cu and Cu-O bonds (Figure 6.14 d-f, Supplementary Table 6.9). Based on the combined EXAFS fitted results, it can be concluded that Cu^{1+} is oxygen coordinated and that the formation of Cu^{0} within solution is possible, where the Cu^{0} oxidation state is observed but Cu-Cu bonds have not emerged. This could equally be a case of a large number of nuclei forming with Cu-Cu coordination below the resolution of the EXAFS fitting, and therefore appearing as Cu-O bonds.

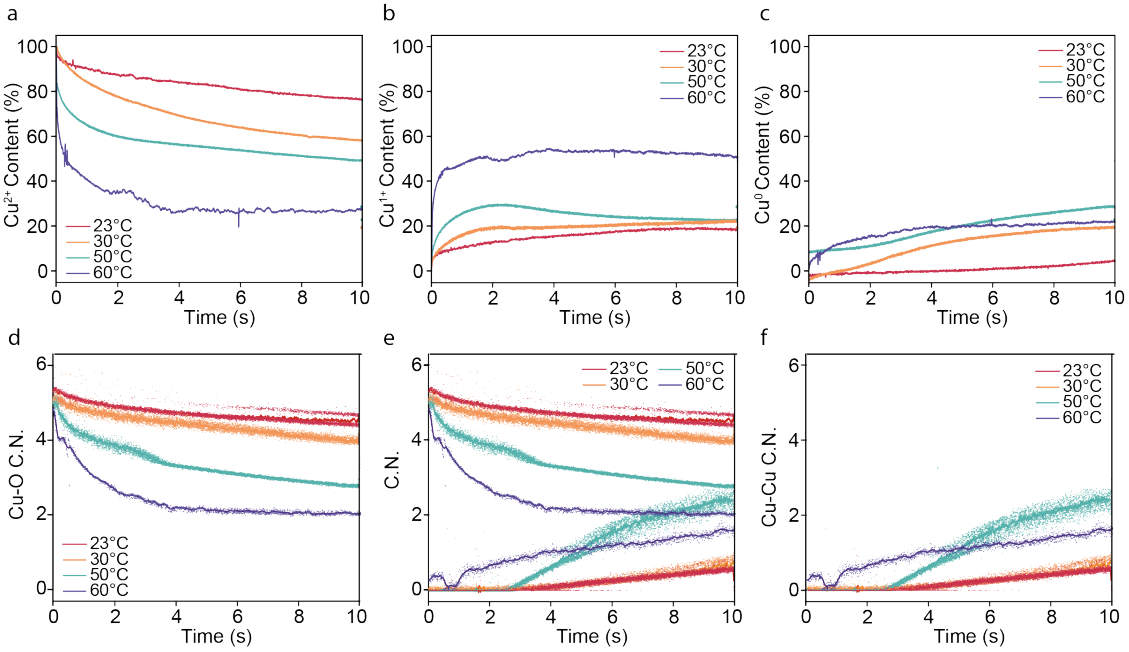

Figure 6.14 ***XAS results for Temperature-Series of Cu(OAc)₂/H₂O/AA.*** *XAS data measured during $Cu(OAc)_2/H_2O/AA$ at the Cu K-edge are used to calculate the rate of change of (a) Cu^{2+} content, (b) Cu^{1+} content and (c) Cu^{0} content, from XANES LCF and (d) Cu-O C.N., (e) combined C.N. results and (f) Cu-Cu C.N. from EXAFS refinement, at temperatures of 23ºC (red), 30ºC (orange), 50ºC (turquoise) and 60ºC (purple).*

The rate of the reaction for the Arrhenius plot can be measured within the initial range for each curve, to find the rate of Cu^{2+} reduction, and Cu^{1+} and Cu^{0} formation. The measured reaction rates were plotted against the temperatures to obtain an Arrhenius plot and measure activation energy (Figure 6.15). Based on the slope of the Arrhenius plot, the activation energy for the reduction of $Cu(OAc)_2/H_2O$ by ascorbic acid is 13.010 ± 3.231 $kJ.mol^{-1}$. The formation of Cu^{1+} and Cu^{0} have activation energies calculated to be 16.042 ± 3.235 $kJ.mol^{-1}$ and 16.129 ± 10.947 $kJ.mol^{-1}$, respectively. The significant error value in activation energy for Cu^{0} formation is introduced by the poor fit in the Arrhenius plot.

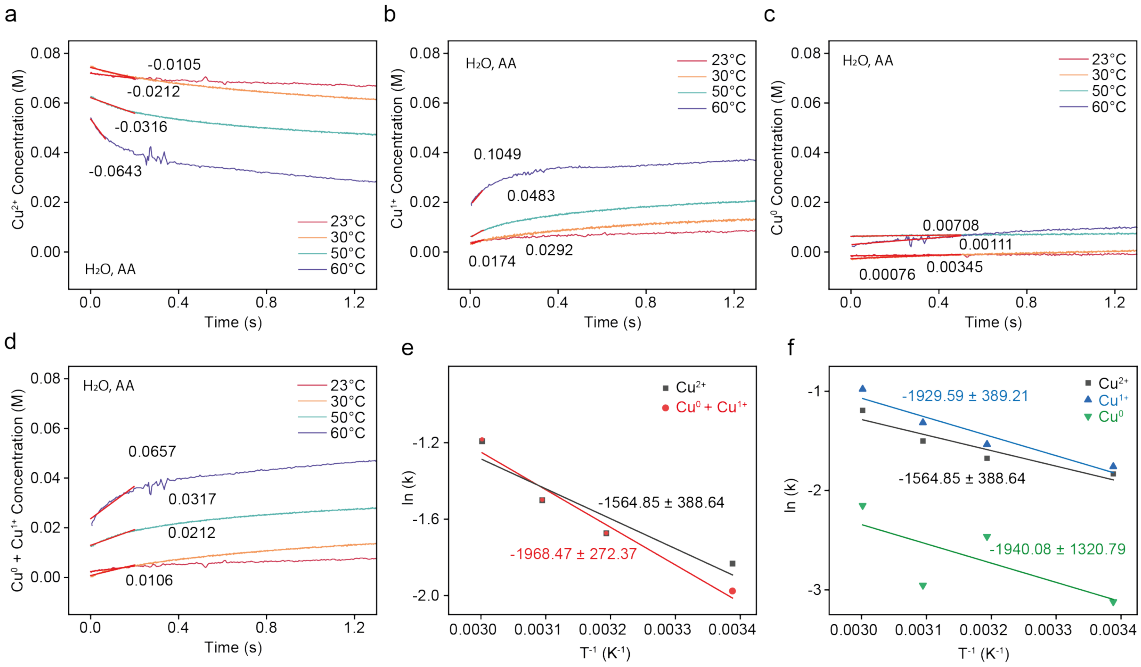

Figure 6.15 ***Arrhenius Plot from $Cu(OAc)_2/H_2O/AA$.*** *Reaction rates (red) measured during $Cu(OAc)_2/H_2O/AA$ with temperatures of 23°C (red), 30°C (orange), 50°C (turquoise) and 60°C (purple) at the Cu K-edge for XANES LCF of (a) Cu^{2+} content, (b) Cu^{1+} content and (c) Cu^{0} content and (d) Cu^{0}+Cu^{1+} content. (e) Arrhenius plot of with slopes of -1968.47 K for Cu^{0}+Cu^{1+} (red) and -1564.85 K for Cu^{2+} (black) and (f) Arrhenius plot of -1940.08 K for Cu^{0} (green), -1929.59 K for Cu^{1+} (blue) and -1564.85 K for Cu^{0} (black).*

Observing $Cu(OAc)_2$/AA reduction for a period of 180 seconds, it is found that the formation of Cu^{1+} continues, only partially converting to Cu^0, even at higher temperatures such as 60ºC. The Cu^{1+} appears to transition back to Cu^{2+} at longer reaction times (Supplementary Figure 6.43, Supplementary Figure 6.44). The Cu^{1+} is clearly formed as an intermediate, showing an initial peak which is later reduced for Cu^0 formation.

The same XAS analysis is performed with $Cu(OAc)_2$/DMF, to determine differences in the results. The CCWT (Figure 6.16) begins with the same non-phase-corrected R + ∆R value (y-axis) of 1.3 Å, with Cu-O/N bonding. This does not considerably change over time, although a weak 2.1 Å is observed before settling on 2.8 Å measured with $Cu(OAc)_2/H_2O$ after 120 s. This likely corresponds with the slight formation of Cu^0 and Cu^{1+}-O formation.

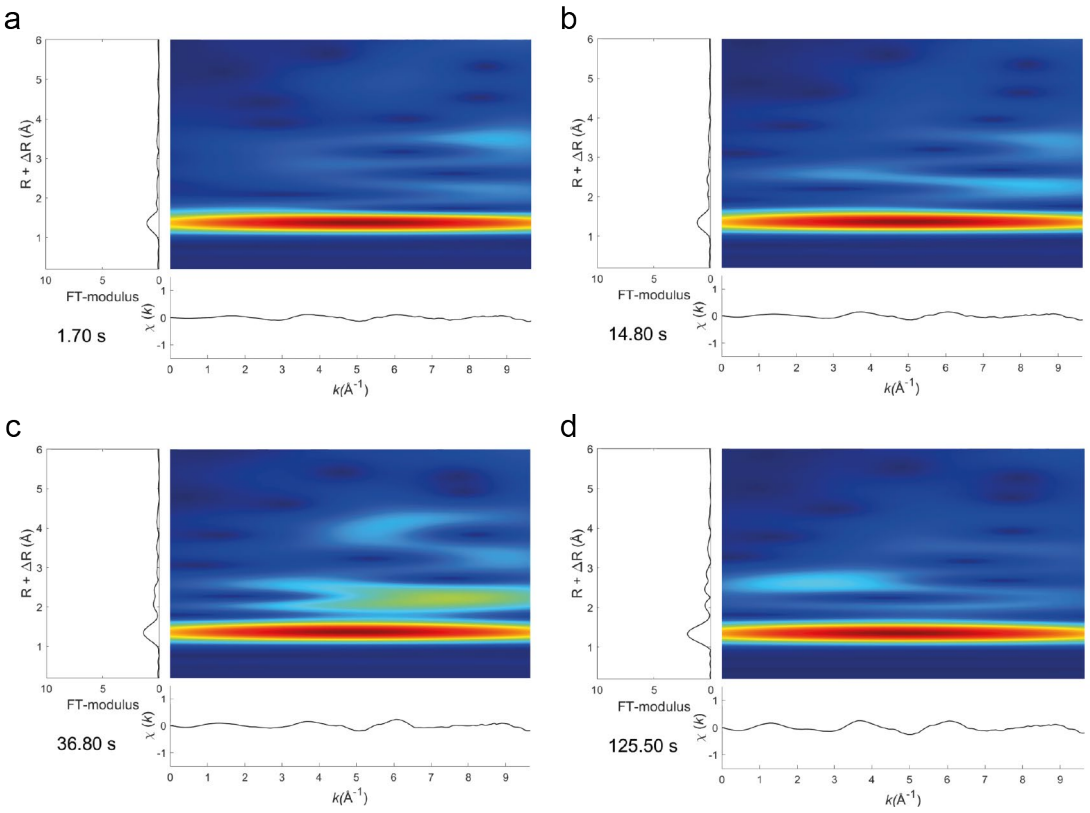

Figure 6.16 ***Wavelet Transform Time-Series during Cu(OAc)$_2$/DMF/AA.*** *Continuous Cauchy wavelet transforms combining the k-space (x-axis) and R-space (y-axis) Cu K-edge XAS data to form a heat map showing Cu(OAc)$_2$/DMF/AA reduction at 60ºC, at reaction times of (a) 1.7 s, (b) 14.8 s, (c) 36.8 s and (d) 125.5 s.*

The *in situ* XANES LCF of Cu(OAc)$_2$/DMF/AA reduction also shows a similar trend to Cu(OAc)$_2$/H$_2$O/AA, with reaction rate increasing with temperature (Figure 6.17). The shape of the curves match the sigmoidal shape of the WF two-step process.[46] In this case, the Cu^{1+} content is higher, with negligible formation of Cu^0 within the first 10 seconds of the reaction, as suggested by HR-XANES results. Reproducible LCF results for the first 10 seconds of the reaction were selected (Supplementary Figure 6.45).

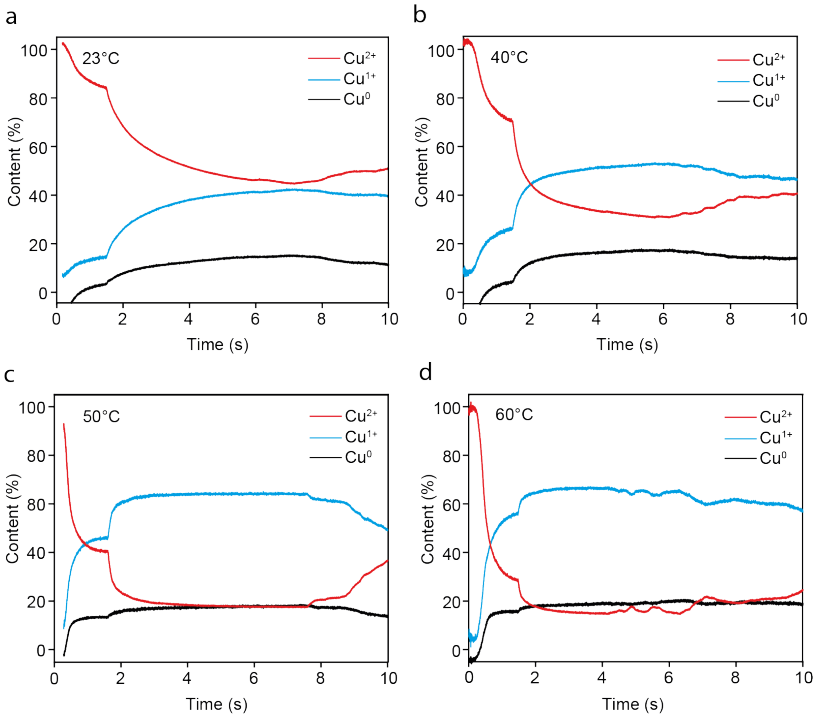

Figure 6.17 ***LCF Profile of Cu(OAc)$_2$/DMF/AA for a Temperature Range.*** *Cu K-edge XANES LCF results for Cu(OAc)$_2$/DMF/AA show the content of Cu^0 (black), Cu^{1+} (blue) and Cu^{2+} (red) at temperatures of (a) 23°C, (b) 40°C, (c) 50°C and (d) 60°C.*

The combined temperature series LCF results show an increasing trend (Figure 6.18 a-c), from which the initial regions are measured for the activation energy of the reaction. EXAFS refinement was performed for each spectrum, to observe the corresponding changes in Cu-Cu and Cu-O coordination during the reduction (Figure 6.18 d-f). Interestingly, no Cu-Cu coordination was observed in the EXAFS fitting, indicating that at this time-scale, the formation of metallic Cu species is either in small particles, or negligible.

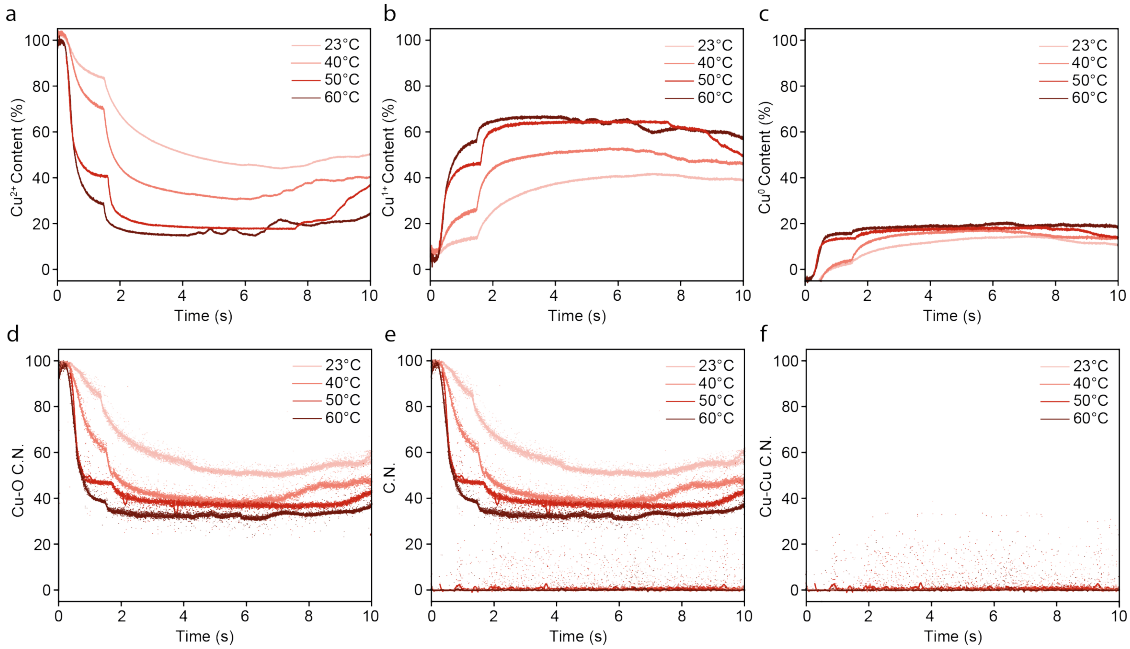

Figure 6.18 ***LCF for Temperature Series of Cu(OAc)$_2$/DMF/AA.*** *XAS data measured during Cu(OAc)$_2$/DMF/AA at the Cu K-edge are used to calculate the rate of change of (a) Cu^{2+} content, (b) Cu^{1+} content and (c) Cu^{0} content, from XANES LCF and (d) Cu-O C.N., (e) combined C.N. results and (f) Cu-Cu C.N. from EXAFS refinement, at temperatures of 23ºC (light pink), 40ºC (pink), 50ºC (red) and 60ºC (burgundy).*

Reaction rates of -0.0147 (23ºC), -0.02118 (40ºC), -0.03156 (50ºC), -0.06429 (60ºC) are calculated in Cu(OAc)$_2$/H$_2$O, compared to -0.01511 (23ºC), -0.03689 (40ºC), -0.1465 (50ºC) and -0.12032 (60ºC) in Cu(OAc)$_2$/DMF (Figure 6.19 a-d). An Arrhenius plot of both results (Figure 6.19 e, f) yields an activation energy of 27.169 ± 3.422 kJ.mol^{-1} for Cu(OAc)$_2$/DMF/AA reduction. The activation energy of formation of Cu^{1+} and Cu^{0} are calculated to be 28.465 ± 3.402 kJ.mol^{-1} and 22.986 ± 6.680 kJ.mol^{-1}, respectively. The results indicate that although the intermediate species may be similar in both cases, the reduction to Cu^{1+} is more rapid in Cu(OAc)$_2$/DMF than in Cu(OAc)$_2$/H$_2$O, while the formation of Cu^{0} occurs more readily in Cu(OAc)$_2$/H$_2$O, contrary to expectations.

The density and polarity of the DMF solvent may influence the reaction rate.[47,48] Hussain et al. also showed that increased polarity of solvent led to increased nanoparticle size, when comparing water-ethanol mixtures for Au nanoparticle growth.[48] This fits with the TEM observations of $Cu(OAc)_2$/DMF/AA nanoparticles.

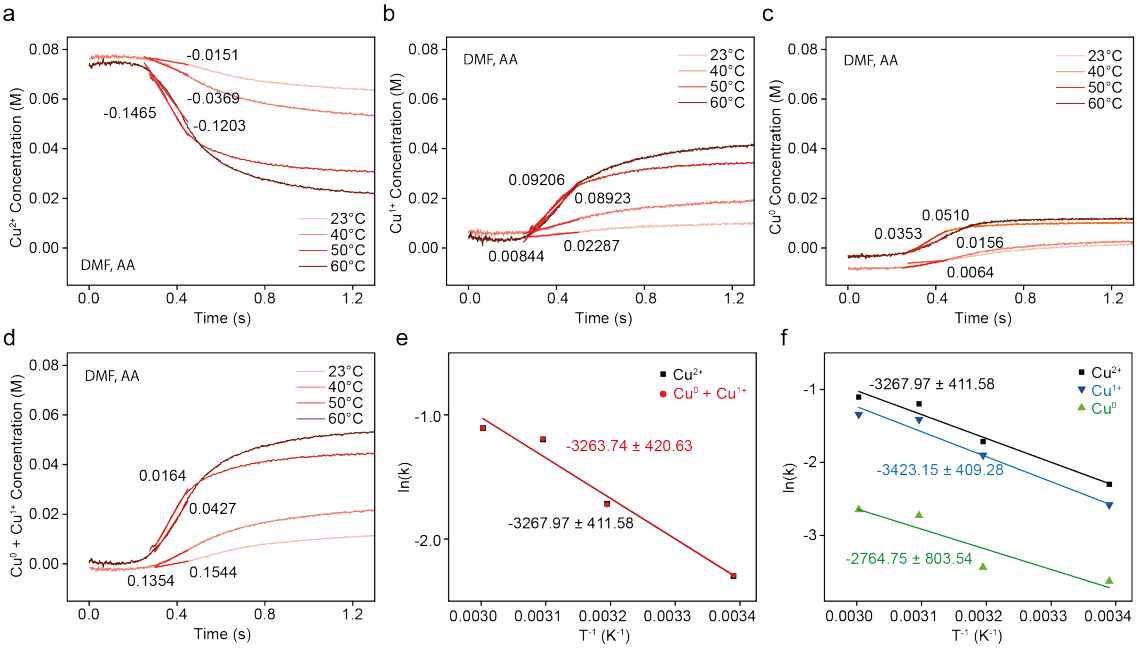

Figure 6.19 ***Rate and Arrhenius Plot for $Cu(OAc)_2$/DMF/AA.*** *Reaction rates (red) measured during $Cu(OAc)_2$/DMF/AA with temperatures of 23ºC (red), 40ºC (orange), 50ºC (turquoise) and 60ºC (purple) at the Cu K-edge for XANES LCF of (a) Cu^{2+} content, (b) Cu^{1+} content and (c) Cu^0 content and (d) Cu^0+Cu^{1+} content. (e) Arrhenius plot with slopes of -3263.74 K for Cu^0+Cu^{1+} (red) and -3267.97 K for Cu^{2+} (black) and (f) Arrhenius plot with slopes of -2764.75 K for Cu^0 (green), -3423.15 K for Cu^{1+} (blue) and -3276.97 K for Cu^0 (black).*

The same reaction was observed for 180 s (Supplementary Figure 6.46, Supplementary Figure 6.47), to better understand the changes after the initial 10 seconds. Up to 20% of the Cu content was converted to Cu^0 at 60ºC, although this was oxidised in the solution at longer reaction times. A majority of the Cu^{2+} was converted to Cu^{1+} and remains, without forming Cu^0 during the reaction time-

scale measured. The rate of reduction of Cu^{2+} measured for $Cu(OAc)_2/H_2O$/AA and $Cu(OAc)_2$/DMF/AA are shown in Table 6.2.

Table 6.2 ***Rate Measurement Results for $Cu(OAc)_2$/DMF/AA.*** *Nucleation rates ($mol.L^{-1}.s^{-1}$) are calculated from LCF results at each reaction temperature (K and ºC). Rate measurements are taken from the slope of the linear region, when concentration is plotted against reaction time.*

Temperature (ºC)	Temperature (K)	Nucleation Rate $Cu(OAc)_2/H_2O$ ($mol.L^{-1}.s^{-1}$)	Nucleation Rate $Cu(OAc)_2$/DMF ($mol.L^{-1}.s^{-1}$)
23	296.15	0.01056	0.00644
40	313.15	0.02121	0.01561
50	323.15	0.03172	0.05103
60	333.15	0.06571	0.03531

Thus, the major pathways in $Cu(OAc)_2/H_2O$/AA and $Cu(OAc)_2$/DMF/AA reduction are shown, which lead to similar nanoparticle structures. The characterization results demonstrate that although the Cu configuration is initially different in both materials, the Cu^{1+}-O formed during growth, attributed to an AA intermediate species, is identical and instrumental in determining the morphology of the particles, along with the interaction of the NP surface with the PVP surfactant. The reduction of Cu^{2+} to Cu^0 with AA therefore follows two steps, each with a single electron transfer. This is confirmed by the activation energy calculations and the size increase at increased temperatures in $Cu(OAc)_2/H_2O$, which is not the case in $Cu(OAc)_2$/DMF. The increased activation energy with DMF as a solvent can be attributed to the increased viscosity and interaction of the solvent with the metal salts, in comparison with H_2O.

6.2.4 Beam Induced Reduction: *In situ* TEM.

The *in situ* visualisation of growth of $Cu(OAc)_2/H_2O$ with PVP caused by beam damage is possible with *in situ* TEM measurements. Due to the high flux in the TEM, it is not possible to measure chemical reduction without a severe effect of beam interference. However, although the results are not directly comparable with the data observed under ascorbic acid or N_2H_4 reduction, the TEM visualisation of the growth process can give an indication of the nanoparticle morphology during growth.

The nanoparticles formed face a lag prior to nucleation into solid particles (Figure 6.20 a-l). Once particles begin to form, they are observed to have a variety of shapes and sizes. Restructuring is also observed to form a crystalline structure, with realignment of the nanoparticles. Nuclei emerge continuously throughout the reduction process, and some redissolve into the solution. The total reduced Cu area (Figure 6.20 m) corresponds with an estimate of the total reduced metal content. This calculation shows a quasi-linear increase after the initial nucleation, with nucleation events occurring continuously.

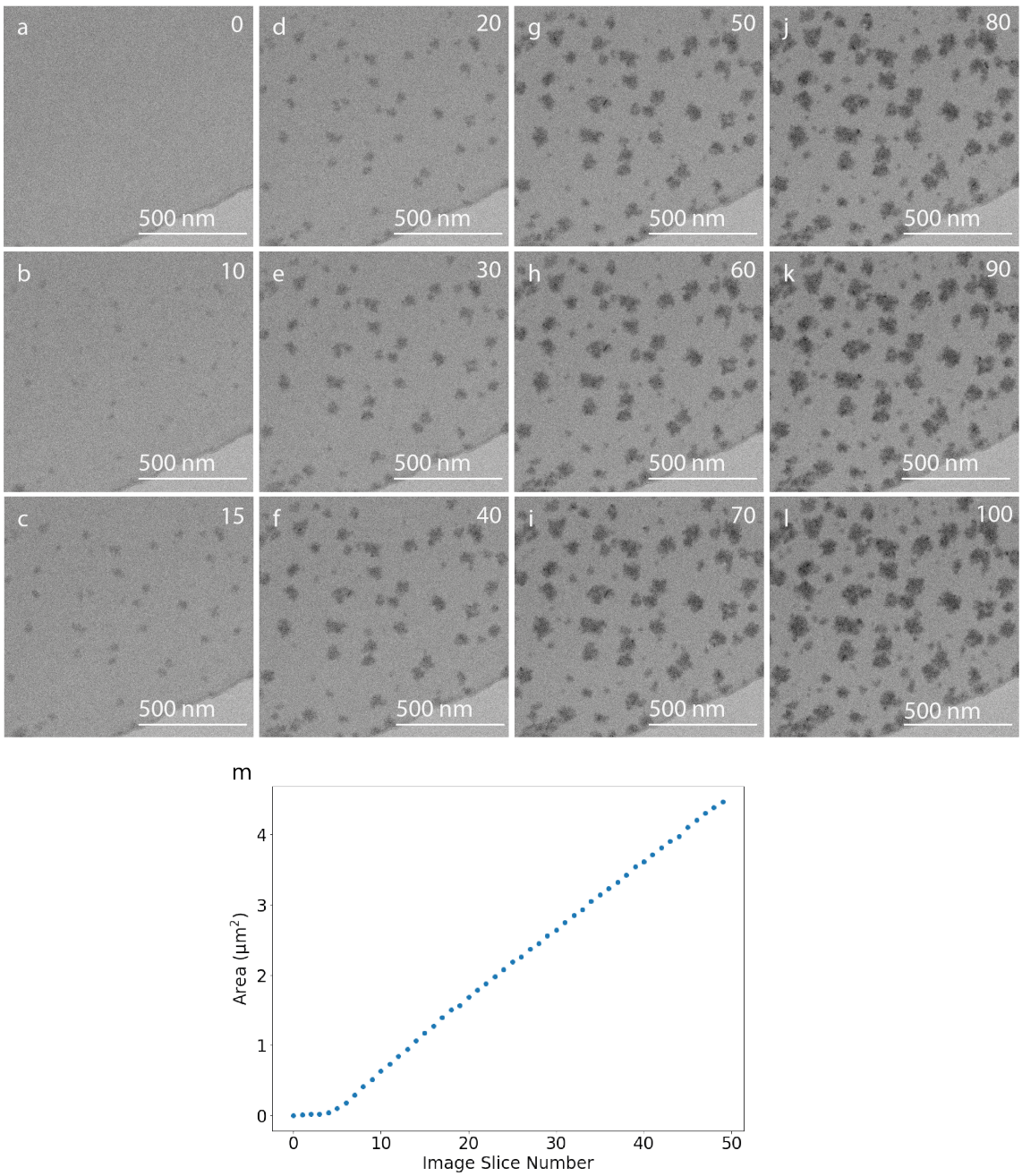

Figure 6.20 ***In situ TEM Images During Cu Nanoparticle Growth.*** *TEM images capture the growth of Cu nanoparticles in situ at 500 nm-scale at times of (a) 0 s, (b) 10 s, (c) 15 s, (d) 20 s, (e) 30 s, (f) 40 s, (g) 50 s, (h) 60 s, (i) 70 s, (j) 80 s, (k) 90 s and (l) 100 s, indicated in the top corner of the image. (m) The calculated total area of nanoparticles in each image captured.*

Based on these results, it appears that the growth of the nanoparticles follows an approximately spherical structure, with some redissolution and restructuring as

particles are formed. Smaller particles tend to redissolve in order for larger particles to grow, but this may be a side effect of the localised Cu concentration within the small beam-reduced area. Considering a case where the beam flux is uniform across the viewed surface, it is also seen that nucleation is continuous and reduction occurs directly on the nuclei, rather than nanoparticles growing *via* migration; again, a possible example of local concentration determining nanoparticle formation.

6.2.5 Hydrazine: Ligand Substitution

Based on the previous results, it seems that the reducing agent AA determines the intermediate species leading to a similar nanoparticle morphology within two different solvent systems. The formation of the Cu^{1+} intermediate is believed to be a key stage in these reactions. Next, we study the growth of $Cu(OAc)_2$/DMF/N_2H_4.

We show here that an intermediate species not captured by oxidation state changes, is responsible for determining nanoparticle morphology. Hydrazine hydrate ($N_2H_4.xH_2O$) as a reducing agent has been shown to lead to the faceted growth of nanoparticles.[18] The nanoparticle morphology produced by N_2H_4 reduction of $Cu(OAc)_2$/DMF show a faceted structure (Figure 6.21 a-c, Supplementary Figure 6.48). A lattice spacing of 0.200 nm was measured on the nanoparticle surface, indicating the presence of Cu(111) (Supplementary Figure 6.49).

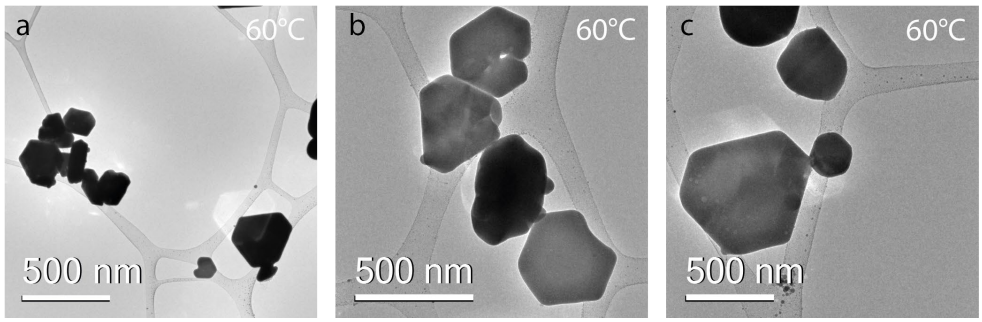

Figure 6.21 ***Morphology of $Cu(OAc)_2$/DMF/N_2H_4 Nanoparticles.*** *(a-c) TEM images show the faceted growth of Cu nanoparticles grown at 60ºC via $Cu(OAc)_2$/DMF/N_2H_4 reduction, with scalebars of 500 nm.*

Since the nanoparticle morphology observed with N_2H_4 reduction is considerably different to that observed with AA reduction, using the same solvent and reaction conditions ($Cu(OAc)_2$/DMF), it is apparent that the reducing agent is instrumental in determining the growth process.

The presence and structure of the species formed during the reaction are elucidated by temperature-controlled *in situ* EPR observation (Figure 6.22). Indeed, the asymmetric signal of an intermediate species is observed, which is distinct from the reacting species, since $Cu(OAc)_2$/DMF is EPR silent (Figure 6.22 a-c). Such a result can be attributed to a local change in the Cu^{2+} coordination environment, overcoming the clustering that caused the initial EPR silence. *In situ* EPR is performed at temperatures of 23ºC, 40ºC and 60ºC, to measure the rate of this intermediate species formation.

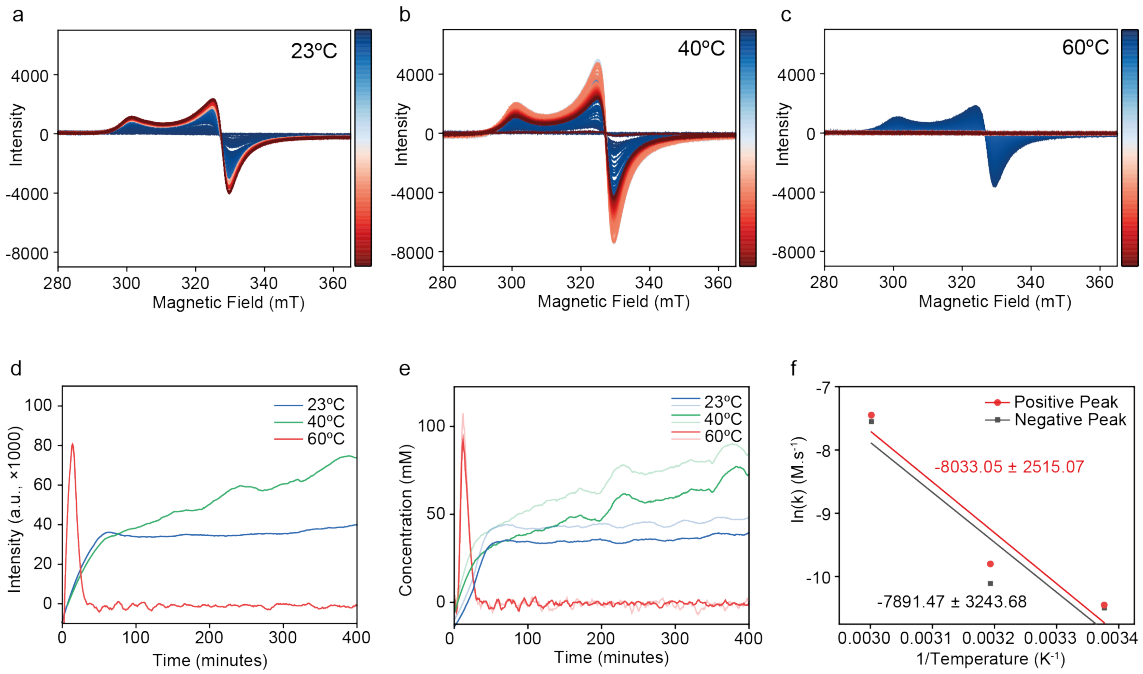

Figure 6.22 ***In situ EPR Results of Cu(OAc)$_2$/DMF/N$_2$H$_4$.*** *In situ EPR spectra tracks the formation of a Cu^{2+} intermediate during N_2H_4 reduction of $Cu(OAc)_2$/DMF at temperatures of (a) 23°C, (b) 40°C and (c) 60°C and (d) the corresponding profiles of intensity changes over time at 23°C (blue), 40°C (orange) and 60°C (red). (e) Calculated concentration of the intermediate species and (f) the corresponding Arrhenius plot.*

The rate of formation of the intermediate species, measured from the intensity of the positive and negative EPR peaks (Figure 6.22 d), could also be expressed in terms of concentration, using the $Cu(NO_3)_2$/DMF calibration curve (Figure 6.22 e). Although the shapes of the calibration EPR curves and those of the intermediate species are not identical, this provides an estimate of the concentration. The same data was used to calculate an estimated activation energy of the reaction (Figure 6.22 f), yielding a result of 66.787 ± 20.910 kJ.mol^{-1} for the positive peak and 65.609 ± 26.967 kJ.mol^{-1} for the negative peak. The average activation energy for intermediate formation can be estimated at 66.198

± 23.939 kJ.mol^{-1}. This analysis is only provided as an estimate, since the number of datapoints recorded is limited.

It can be noted from the EPR results of N_2H_4 reduction that the initial and final states of pure $Cu(OAc)_2$ and metallic Cu in nanoparticles are both EPR silent and appear as flat lines in the measurements; hence, when the *in situ* reduction is performed, the rate of formation of the EPR active intermediate can be monitored in isolation from initial $Cu(OAc)_2$ and subsequent Cu^0. This is not the case for $Cu(OAc)_2$/DMF/AA reduction, where the intermediate is EPR silent.

Visually, while initially colourless, the intermediate formed during $Cu(OAc)_2$/DMF/N_2H_4 is dark blue, comparable to a copper-ammonia complex. This observation fits closely with the similarity of EPR signals of a Cu^{2+}-ammonia complex (Figure 6.23 c) and the intermediate. EPR spectra of the intermediate species are more similar to $Cu(NH_3)_4$, than to Cu-O coordinated solutions like $Cu(NO_3)_2$ and $CuSO_4$ (Figure 6.23 a, b).

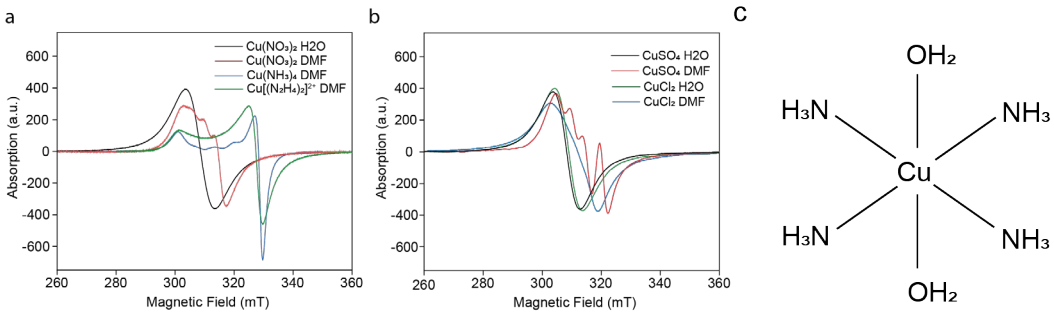

Figure 6.23 ***EPR of Copper Salts with Cu-O and Cu-N Configurations.*** *(a) EPR signals of $Cu(NO_3)_2/H_2O$ (black) and $Cu(NO_3)_2$/DMF (red) are compared with $Cu(NH_3)_4$/DMF (blue), and the Cu^{2+} intermediate ascribed to $Cu[(N_2H_4)_2]^{2+}.2AcO^-$ complex (green). (b) The EPR peaks of $CuSO_4/H_2O$ (black) and $CuSO_4$/DMF (red) resemble those of $Cu(NO_3)_2/H_2O$ and $Cu(NO_3)_2$/DMF, likely due to the similar Cu-H_2O coordination. $CuCl_2/H_2O$ and $CuCl_2$/DMF signals do not change significantly under different solvents. (c) Chemical configuration of $Cu(NH_3)_4/H_2O$ shows the coordination of Cu-N, which is likely similar to the $Cu[(N_2H_4)_2]^{2+}.2AcO^-$ complex.*

This intermediate species is attributed to a $Cu[(N_2H_4)_2]^{2+}.2AcO^-$ complex.[18] The hydrazine complex intermediate is also detected as a 600 nm peak (Figure 6.24 a) with *in situ* UV-vis with N_2H_4 reduction, which is notably absent in aqueous $NaBH_4$ reduction of $Cu(OAc)_2$/DMF (Figure 6.24 b). This metastable intermediate hydrazine complex peak continuously increases in intensity, since the complete N_2H_4 reduction of $Cu(OAc)_2$/DMF to metallic Cu does not occur at room temperature. The initial copper acetate peak signal at 700 nm is lost almost immediately in both cases, due to the high reduction rate.

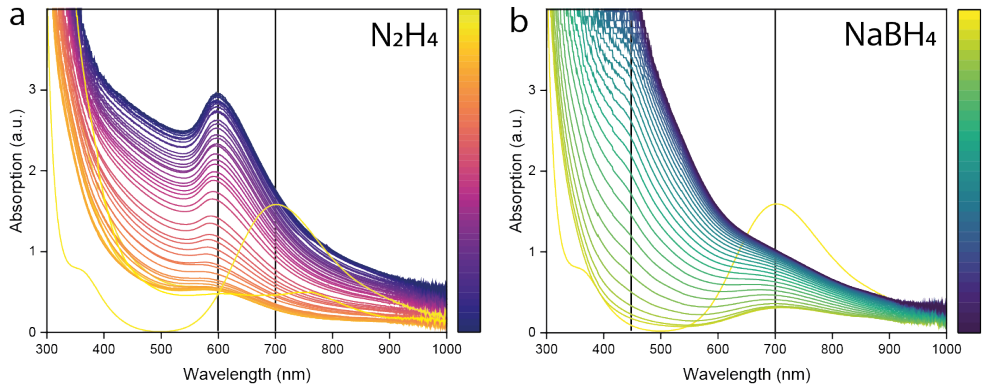

Figure 6.24 ***In situ UV-vis Results.*** *Time-resolved UV-vis spectra showing the key intermediate species formed, with significant peaks indicated with a black line for (a) 10 mM $Cu(OAc)_2$/DMF/N_2H_4 reduction and (b) 10 mM $Cu(OAc)_2$/DMF/$NaBH_4$ reduction at 23ºC. Both reductions are initally shown in yellow, gradually becoming dark blue.*

It can be noted from the *in situ* EPR that at room temperature, the conversion to $Cu(N_2H_4)_2^{2+}$ is incomplete as the concentration of the signal is significantly below that achieved at 40ºC. However, at both 23ºC and 40ºC the reduction to Cu^0 is incomplete and a significant concentration of $Cu(N_2H_4)_2^{2+}$ complex remains in the solution. Only at 60ºC is the total reduction achieved, shown as a final EPR silent signal. For this reason, the ideal reaction condition for the formation of Cu platelets follows the 40ºC complexation of $Cu(OAc)_2$ to $Cu(N_2H_4)_2^{2+}$, followed by reduction to Cu^0 at 60ºC,[18] since a more complete conversion to $Cu(N_2H_4)_2^{2+}$ intermediate at 40ºC, may lead to an increased control of Cu(111) faceted metallic nanoparticles formed at 60ºC.

The stages of ligand changes are shown in the VtC XES results, alongside the corresponding oxidation state changes from HR-XANES during N_2H_4 reduction in DMF (Figure 6.25 a-c). Clearly this reaction does not form a Cu^{1+} intermediate,

with Cu^{2+} in the $Cu[(N_2H_4)_2]^{2+}.2AcO^-$ complex being converted directly to Cu^0 (Figure 6.25 b, c).

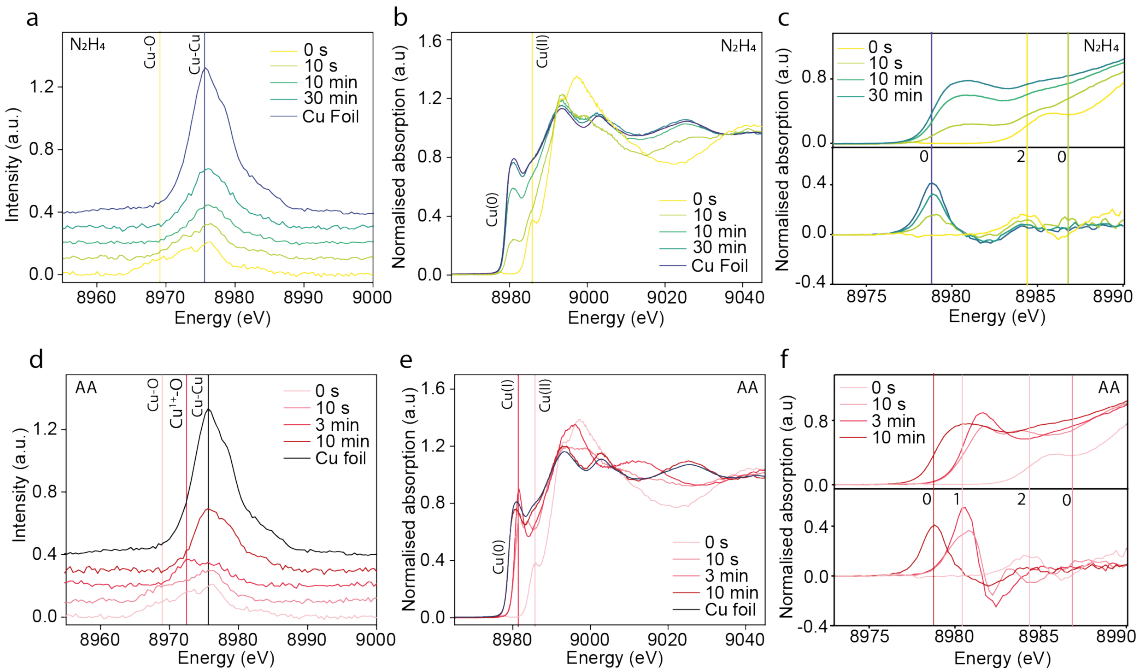

Figure 6.25 ***VtC XES and HR-XANES for Cu(OAc)$_2$/DMF Reduction.*** *Cu kβ$_{2,5}$ VtC XES, Cu K-edge XANES and differential-XANES results for (a-c) Cu(OAc)$_2$/DMF/N_2H_4 reduction (yellow to blue) and (d-f) Cu(OAc)$_2$/DMF/AA reduction (pink to red). Cu-O, Cu^{1+}-O and Cu-Cu VtC XES peaks are labelled, as well as Cu^{2+}(2), Cu^{1+} (1) and Cu^0 (0) for HR-XANES and the derivative.*

Copper VtC XES records the transition from Cu 1*s* to 3*d* shells and is therefore sensitive to ligands bonded to Cu atoms. However, from the Cu(OAc)$_2$/DMF VtC XES results, despite the clear formation of the intermediate species, it is impossible to distinguish the principal peak of Cu-N and Cu-Cu coordination directly from the VtC XES curves. Thus, the derivative of VtC XES curves, compared with standards (Figure 6.26 a, b), are shown for a reaction series at 23ºC and 60ºC (Figure 6.26 c-f), to differentiate the $Cu[(N_2H_4)_2]^{2+}.2AcO^-$ intermediate from metallic Cu.

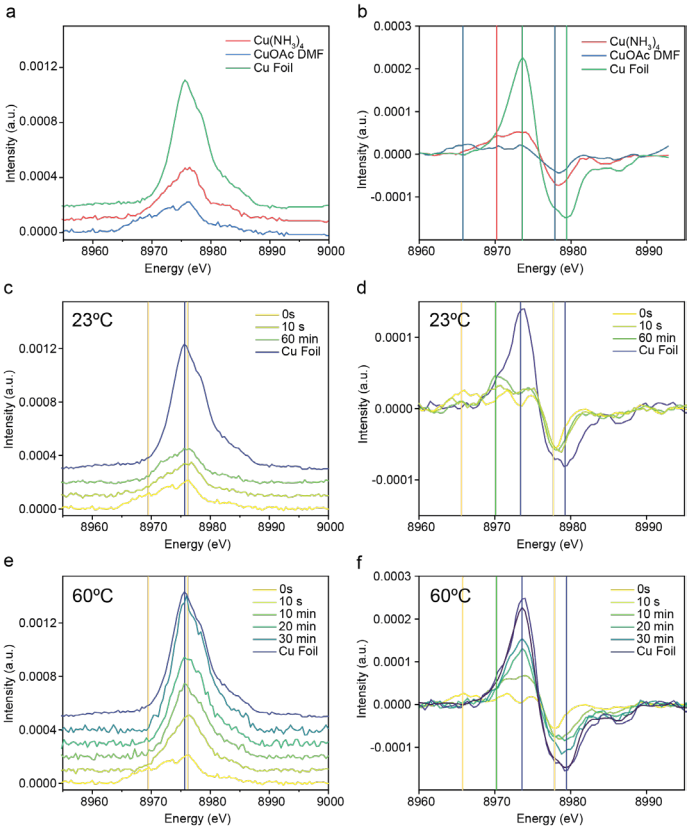

Figure 6.26 ***Cu(OAc)$_2$/DMF/N$_2$H$_4$ Differential VtC XES Spectra.*** *(a, c, e) VtC XES spectra measured for Cu kβ$_{2,5}$ peak and (b, d, f) their differentials are measured for (a, b) Cu(NH$_3$)$_4$, Cu(OAc)$_2$/DMF and Cu foil, and a time series of Cu(OAc)$_2$/DMF/N$_2$H$_4$ reduction at (c, d) 23ºC and (e, f) 60ºC.*

As the intermediate Cu[(N$_2$H$_4$)$_2$]$^{2+}$.2AcO$^-$ is stable during the 23ºC reduction, the corresponding Cu-N peak at 8970.5 eV can be seen more clearly during room-temperature reaction than in a Cu^{2+}-N standard (Figure 6.26 b, d). This transient intermediate complex is short-lived during 60ºC reduction, where it is observed within 10 s of N$_2$H$_4$ addition, substituting Cu-O with Cu-N coordination.

The formation of the Cu^{2+} intermediate and the subsequent 2e$^-$ reduction directly to Cu^0 illustrates the difference in reduction mechanisms of Cu(OAc)$_2$/DMF with hydrazine and AA. The absence of a Cu^{1+} peak (observed in Cu(OAc)$_2$/DMF/AA reduction) aligns with the literature for hydrazine reduction, where it is believed that the evolution of N$_2$ gas bubbles in the solution provides an inert atmosphere

for the reaction. The Cu^{2+}-N intermediate, formed within 10 seconds during 60ºC $Cu(OAc)_2$/DMF/N_2H_4 reduction directly reduces to Cu-Cu coordination within minutes. The content of the Cu^0, Cu^{1+} and Cu^{2+} can be quantified approximately using a linear combination fit (LCF) of the HR-XANES spectra, comparable with *in situ* XAS results (Supplementary Figure 6.50, Supplementary Figure 6.51).

The reaction profile is further measured with *in situ* XAS (Figure 6.27). This result was challenging to achieve due to the formation of N_2 bubbles during the reaction, as well as the high reactivity of N_2H_4, which should be held at a low temperature prior to use. However, ignoring the glitches caused by bubbles, the reaction would likely show a sigmoidal shape if the early seconds of the reaction were not missed. It is also clear from the LCF results that there are only two components for the fitting and that Cu^{1+} is not formed at any time during the measurement.

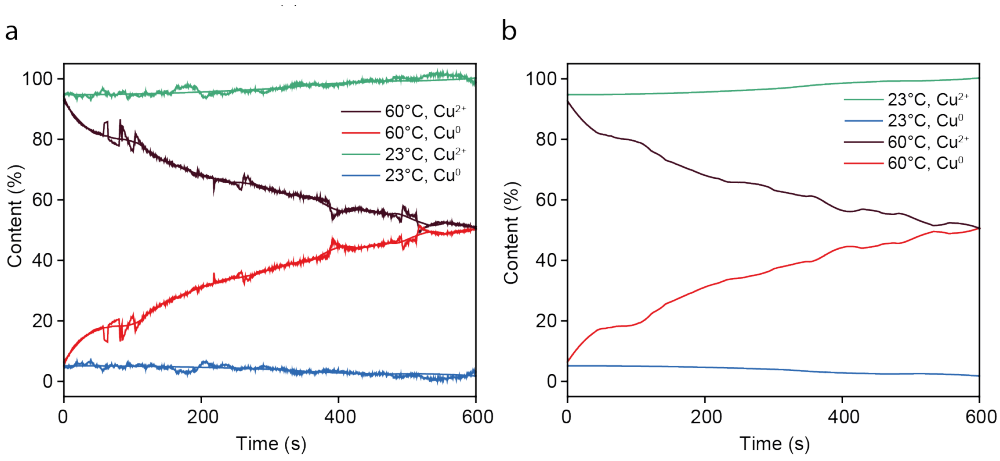

Figure 6.27 ***LCF of Temperature-Controlled Cu(OAc)₂/DMF/N₂H₄.*** *(a) Cu K-edge XANES LCF results show $Cu(OAc)_2$/DMF/N_2H_4 reduction content of Cu^{2+}(black) and of Cu^0 (red) at 60 ºC alongside Cu^{2+} (green) and Cu^0 (blue) at 23ºC that are (b) smoothed for clarity.*

The rate of the reaction is slower than that observed in AA reduction, consistent with general observations of crystalline nanoparticle growth. Since the reaction

profile was only successfully captured for two temperatures, the activation energy could not be calculated from *in situ* XAS data due to the difficulty of measurement.

6.3 Outcomes

The intermediates formed during Cu nanoparticle reduction were successfully identified and monitored in three different growth systems: $Cu(OAc)_2/H_2O/AA$, $Cu(OAc)_2/DMF/AA$ and $Cu(OAc)_2/DMF/N_2H_4$. The results show that the intermediate Cu complexes formed have a high degree of control over the final properties of the nanoparticle, including determining their morphology and crystallinity. *In situ* XAS measurements were recorded and batch-fitted to achieve ms-resolution, the highest achieved with XAS results during nanoparticle growth. The mechanisms of growth were determined for all three reactions using a combination of TEM, *in situ* EPR, VtC XES and *in situ* XAS.

$Cu(OAc)_2/H_2O/AA$ and $Cu(OAc)_2/DMF/AA$ are observed to follow a two-step reduction with the formation of a Cu^{1+} intermediate species. The rate of reduction to Cu^0 is rapid in the case of $Cu(OAc)_2/H_2O/AA$, compared to rates observed in $Cu(OAc)_2/DMF/AA$. The activation energy of Cu^{2+} reduction is also lower in $Cu(OAc)_2/H_2O/AA$ than in $Cu(OAc)_2/DMF/AA$ with values of 13.010 ± 3.231 $kJ.mol^{-1}$ and 27.169 ± 3.422 $kJ.mol^{-1}$ $kJ.mol^{-1}$, respectively. The reduction rate of the intermediate Cu^{1+} species is measured, for the first time, with an activation energy of 16.042 ± 3.235 $kJ.mol^{-1}$ in $Cu(OAc)_2/H_2O/AA$ and 28.465 ± 3.402 $kJ.mol^{-1}$ in $Cu(OAc)_2/DMF/AA$. This shows that the formation of Cu^{1+} species does take place with DMF as a solvent, with an increased stability compared to H_2O as a solvent. The formation of the intermediate species is therefore

considered to be a byproduct of ascorbic acid reduction, rather than solvent effects.

A comparison of $Cu(OAc)_2$/DMF/AA and $Cu(OAc)_2$/DMF/N_2H_4 elucidates the reaction mechanisms that determine morphology, from spherical to faceted nanoparticles. Within seconds of addition, N_2H_4 forms a Cu-complex which replaces Cu-O coordination observed in $Cu(OAc)_2$/DMF. This structured Cu^{2+} hydrazine complex is directly reduced to Cu^0, without forming a Cu^{1+} intermediate. However, the measured reduction rates of the intermediate species, recorded here for the first time, give a high calculated activation energy of 66.198 ± 23.939 $kJ.mol^{-1}$. Such a high value is possible since the reduction incomplete at 23ºC and 40ºC, where the intermediate species are stable. Heating to 60ºC, an *in situ* XAS observation shows the reaction profile with a typical sigmoidal shape, monitoring only the reduction of Cu^0, since the complexation cannot be distinguished in this case.

With these results, this work shows that within the first 10 s of the reaction, morphology-determining stages of the growth mechanism, such as complexation and intermediate formation, occur. The value of time-resolved data in observing the rate of reaction of intermediate species, as well as reactants and products, is significant for the prediction of nanoparticle formation in the future. Our research highlights the high time-resolution capabilities of the currently available characterization tools and the value of complementary techniques in assessing reaction mechanisms. The application of the experimental techniques used, and the data analysis techniques developed, contribute to the field of nanoparticle growth studies, and are applicable to other growth systems. The precise values and reaction stages observed experimentally can guide theoretical predictions of

Cu nanoparticle growth and provide a framework for the future measurement of similar systems.

6.4 Experimental Methods

6.4.1 Nanoparticle Synthesis

The synthesis method for nanoparticle growth is based on a published work, which describes the formation of Cu nanoplatelets.[18] In order to separate the effect of the solvent and the reactants, three different reduction methods were selected, with the same final concentration of Cu for XAS measurement. While selecting reaction conditions it was important to make the systems rigorously comparable by varying only a single reaction parameter with each iteration.

The first method, based on the cited paper, involves the spontaneously anaerobic growth of Cu nanoplatelets from solution. 10 µL of hydrazine hydrate (100% $N_2H_4.xH_2O$ (~64% w/w N_2H_4), Thermo Scientific) are added to 1 mL of 75 mM copper acetate ($Cu(CO_2CH_3)_2 \cdot H_2O$, ≥98%, Sigma Aldrich) solution with PVP (360,000 $g.mol^{-1}$) in dimethylformamide (DMF, 99+%, Fisher Scientific). The solutions were initially set to react for four minutes at 40ºC followed by a longer reduction at 60ºC to create platelets as described by Pastoriza-Santos et al.[18]

The same concentration of $Cu(OAc)_2$ is used for the second method in which 1 mL of 150 mM $Cu(OAc)_2$/DMF solution is reduced with 1 mL of 600 mM ascorbic acid dissolved in DMF. A condition of excess reducing agent is selected to achieve a quick and complete reaction. Replacing DMF as the solvent (in the second method) with H_2O gives the third method. Briefly, 1 mL of 150 mM $Cu(OAc)_2/H_2O$ is reduced with 1 mL of 600 mM ascorbic acid in H_2O.

Once the reaction solutions were selected, the conditions for growth were designed uniformly for comparison. The 75 mM concentration of $Cu(OAc)_2$ was selected for improved signal-to-noise during high time-resolution reactions, as described in Section 6.4.1. All measured reaction solutions had the same final copper content and had the same final concentration of PVP added. Reducing agents were dissolved in the same solvent as the copper acetate, to ensure uniformity of mixing and solvent behaviour. Each reaction was measured under a series of different temperatures between room temperature (marked here as average value of 23°C) and 70°C, to calculate rates and activation energy.

6.4.2 Lab-Based Characterization

TEM was operated on a JEOL-2100 (JEOL, Japan) with an acceleration range of 200 keV. Image analysis and lattice spacing measurements were performed on Gatan Digital Micrograph software (GMS3, GMS4) and compared with literature values. To prepare for **electron microscope imaging**, Cu nanoparticles at 3 minutes reaction time were centrifuged at 8000 rpm and washed thrice with ethanol and water. The residual nanoparticles were re-suspended in 1 mL ethanol *via* a ten-minute ultrasonication and drop-cast on a lacey carbon TEM grid.

UV-vis was recorded with the UV-2550, Shimadzu at UCL, with a wavelength range of 200 nm to 1000 nm and a slit width of 5 nm. A blank solution of PVP dissolved in DMF was used as a reference. Spectra were collected every 30 seconds during reduction of 10 mM Cu salts to observe reaction intermediate species. The measurements could not be taken directly for increased concentrations due to high attenuation (Figure 6.28).

The absorption spectrum of copper acetate was already saturated before reduction with the 30 mM solution, and so could only be measured for 10 mM solutions, using the cuvette pathlength of 10 mm available.

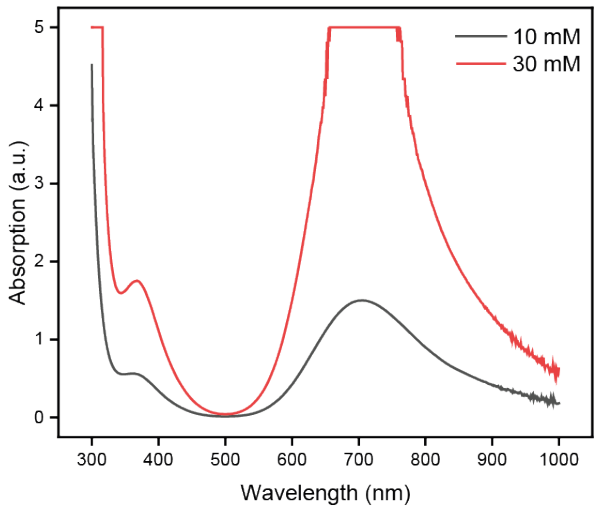

Figure 6.28 ***UV-vis Saturation at High Copper Concentrations.*** *UV-vis results of 30 mM $Cu(OAc)_2/H_2O$ (red) show saturation while 10 mM $Cu(OAc)_2/H_2O$ (black) is within the measurable range.*

EPR was recorded on a Magnettech ESR5000, Brucker with LN_2 temperature control by Freiberg Instruments. *Ex situ* data was measured for a range of 25 mT to 650 mT, with a modulation of 0.8 and a sweep time of 180 s for 3 accumulations. ESRStudio settings allowed automated temperature setting and batch data collection during *in situ* measurements. To reduce measurement time, *in situ* measurements were performed within a range of 280 mT to 365 mT with a sweep time of 30 s. Calibration curves with 5 mM to 50 mM $Cu(NO_3)_2$ linearly correlate the concentration of Cu salts with the area under the resulting EPR curve (Figure 6.29).

The EPR Cu concentration is calibrated by measuring eight $Cu(NO_3)_2$/DMF solutions with known Cu^{2+} content. The integral of the positive and negative peaks of first derivative EPR signal intensity shows the relationship between the

intensity and the Cu^{2+} concentration, used to extrapolate the Cu^{2+} concentration during *in situ* measurements. $Cu(NO_3)_2$/DMF is selected for its similarity to the reaction solutions.

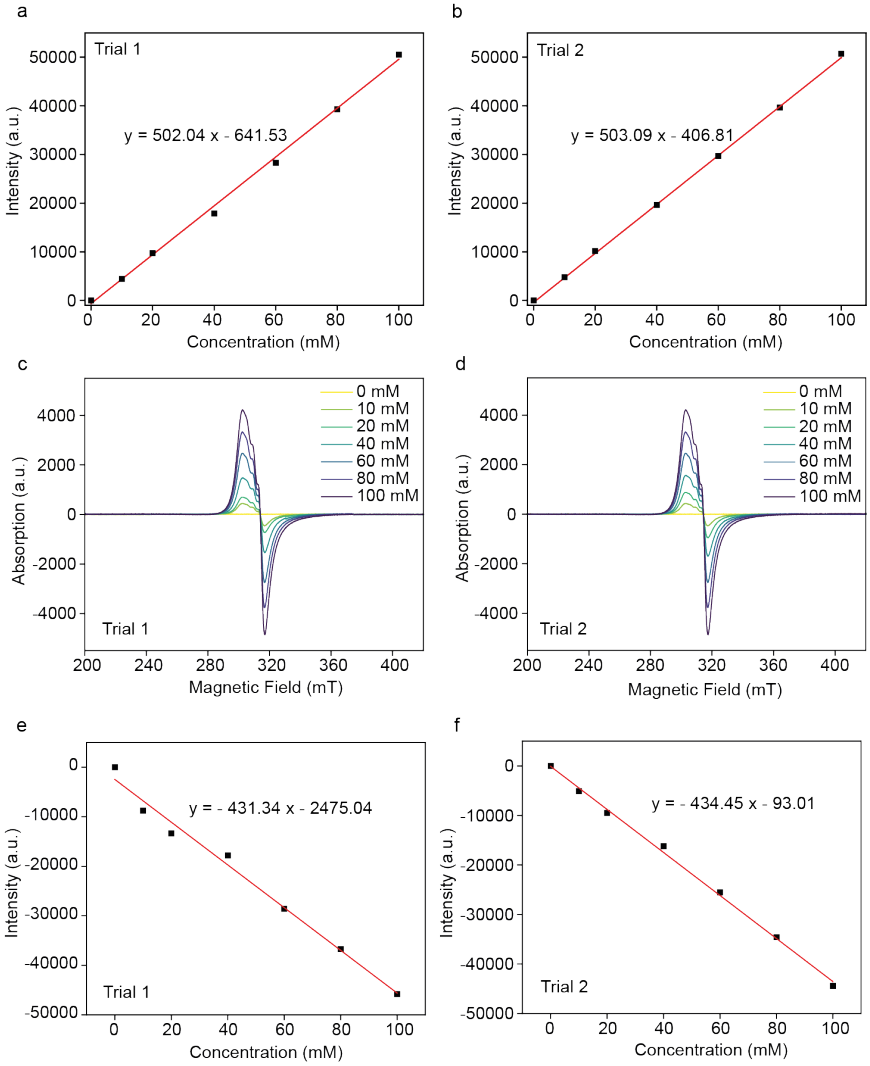

Figure 6.29 ***EPR Calibration with $Cu(NO_3)_2$/DMF Solution.*** *EPR calibration curves of $Cu(NO_3)_2$/DMF at concentrations of 0 to 100 mM are used to calculate Cu content using (a, b) a linear plot of the integrated intensity of the first peak (200 to 305 mT) and (e, f) the second peak (305 to 420 mT), measured from (c, d) the complete EPR data.*

Aside from the first-derivative peak areas, the g-value where first-derivative intensity is zero is also compared, to give an understanding of the material changes. These values were calculated with background subtraction for around

15,000 spectra using a python script. The reproducibility of the EPR concentrations measured during $Cu(OAc)_2$/DMF/N_2H_4 is assessed for each temperature, repeated three times (Figure 6.30). Variations are mostly attributed to inconsistent mixing and lab errors.

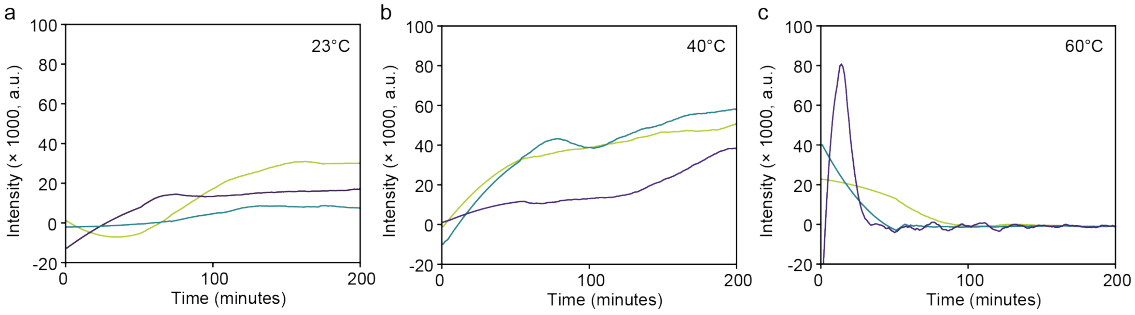

Figure 6.30 ***Reproducibility of Temperature-Controlled EPR.*** *EPR peaks are integrated to calculate Cu content for 200 minutes of reaction time at temperatures of (a) 23ºC, (b) 40ºC and (c) 60ºC for three repetitions, to show reproducibility of the results.*

6.4.3 Synchrotron Characterization

VtC XES and HERFD XANES were measured at I20-Scanning beamline while XAS was recorded at I20-EDE beamline, both at Diamond Light Source. Due to the differences in beamline requirements and measurement times, the experimental setup was adjusted for each beamline.

I20-Scanning

VtC XES, XES and HR-XANES measurements were performed at I20-Scanning, Diamond Light Source operating at 3 GeV with a current of 298.76 mA. Data was collected with a Medipix detector. 0.2 mm aluminium foil and 2 mm carbon filters were also inserted for long measurement times to reduce damage to the sample, while no filters were used with VtC XES measurements. XES was measured for

a range of 8890 to 8920 eV, with offset energy held at 9200 eV. VtC XES measurements were taken for a range of 8940 to 9000 eV, with monochromator energy held at 9050 eV. HR-XANES measurements were captured for a range of 8920 to 9200 eV, with analyser energy held at 8905 eV. Solid sample pellets were prepared with low Cu concentrations, by diluting with BN and cellulose powder and sealing with Kapton tape. Due to the significant beam damage caused over long measurement times (up to 30 minutes) and the increased sample stability in the beam path, samples were frozen solid prior to measurement. Liquid samples were reacted for a desired time at temperature, quenched in LN_2, and stored in dry ice to maintain the frozen state. These were maintained in a solid state with a 170 K cryojet, although ice crystals needed periodic removal from the vial surface (Figure 6.31).

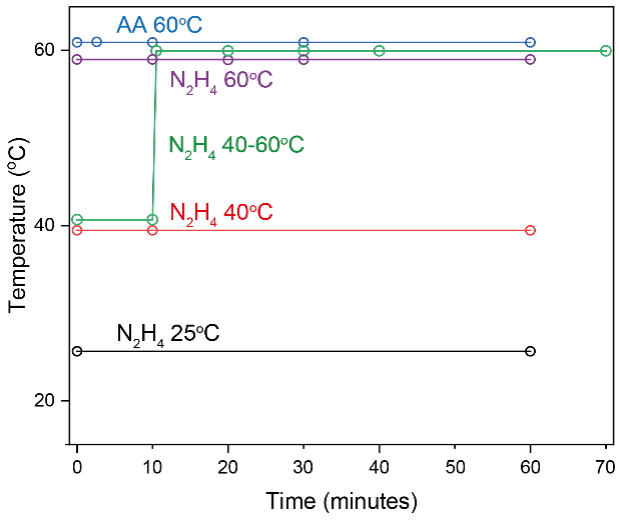

Figure 6.31 ***VtC XES and HR-XANES Reaction Conditions.*** *Experimental summary showing reaction conditions at which data is collected (circles) for* $Cu(OAc)_2/H_2O/AA$ *and* $Cu(OAc)_2/DMF/AA$ *(blue) and* $Cu(OAc)_2/DMF/N_2H_4$ *(black, red, green, purple). The progress of each experiment is connected by a line, with the sample history.*

Temperatures below -90°C were maintained to keep samples frozen especially for $Cu(OAc)_2$/DMF, observed to freeze around -78°C. The efficacy of freezing a solution to halt the reaction at a given time was confirmed by EPR measurements of the same samples before and after freezing. The reaction times measured (circles), temperatures and reaction history (connecting line) are given in Figure 6.31 (b). XANES and VtC are recorded at each circled point, along with XES spectrum for VtC background removal.

I20-EDE Measurements

EDE measurements were collected at I20-EDE, Diamond Light Source, using a Freelon detector and a Si(111) polychromator crystal. Spectra were measured at the Cu K-edge (8979 eV) within a range of 8760 eV to 9700 eV (k range= 14 $Å^{-1}$, clean to k = 12 $Å^{-1}$), with 1024 pixels collected per spectrum. The data energy was calibrated with Cu foil and calculated by pixel. 9100 spectra were collected during each reaction, for a total measurement time of 12 s, 45 s or 180 s. An I_0 background was measured for the solvent mixed with PVP. 400 μm of Al foil was inserted into the beam-path to attenuate the beam for longer experiments while 200 μm was applied for short timescales to improve data quality. For a 180 s measurement, 373 scans of 52.36 μs were merged to give a frame time of 0.02 s. During 45 s measurements 2 scans of 2 ms were merged for a frame time of 5.066 ms. For a 12 s measurement, 12 scans of 0.1 ms were merged for a frame time of 1.266 ms.

Foils, pellet standards and standard solutions were measured for longer time-period before loading the *in situ* cell. The SFM-4000 stop-flow cell, developed by Biokine (described in section 2.4.4), with a cell length of 10 mm was placed in the beam-path for *in situ* XAS measurements. The injection chambers were filled with H_2O, dilute HNO_3, reducing agent solution (AA or N_2H_4) and 75 mM Cu salt

solution. Solution injection and XAS measurements were triggered at the same moment, to ensure observation of initial reaction stages. The solution pathlength was 5 mm with a quartz capillary tube and concentrations for transmission measurement were adjusted accordingly.

Temperature control was achieved with a combination of stop-flow cell heating with a Lauda bath to hold the solutions at temperature prior to mixing, and a heat gun to maintain sample temperature during measurement. The Lauda bath and heat gun settings were selected to achieve the required temperature at the point measured with a thermocouple (Table 6.3).

Table 6.3 ***Temperature Settings for in situ Growth Measurements.*** *Temperature was measured by a thermocouple at the beam position before measurements. Reservoir temperature was controlled by the Lauda bath, while the cell temperature was maintained by the heat gun.*

Desired Temperature (ºC)	Lauda Bath Temperature (ºC)	Heat Gun Setting (Airflow)	Sample Position Temperature (ºC)	Hold Time (minutes)
23	23	0	23.0	20
30	30	44	30.0	20
40	40	72	40.0	20
50	50	100	50.3	10
60	60	130	60.3	10
70	70	159	70.3	16
80	83	181	80.3	12

9000 spectra were recorded for each measurement for a span of either 12 s, 45 s or 180 s, giving time-resolutions of 1.27 ms, 5.06 ms and 20 ms, respectively. Due to low data resolution with high time-resolution, it was necessary to repeat

reaction cycles and merge the results for EXAFS fitting. The reaction conditions and number of repeated measurements are given below (Table 6.4).

Table 6.4 ***Number of XAS Spectra Analysed.*** *Number of datasets collected at each temperature within the same session (No. Cycles) multiplied by the number of repeats in different sessions (x Repeats) where each dataset contains 9100 to 9500 spectra. The number of spectra obtained (Total No. Spectra) are calculated for each temperature condition of three $Cu(OAc)_2$ reduction routes. The sum of spectra analysed for this project, for all reduction routes, yields a total of 14,476,000 (14.476 million) spectra.*

Reaction, Time (s)		23ºC	30ºC	40ºC	50ºC	60ºC	Sum
H_2O, AA, 12 s	No. Cycles (x Repeats)	40 (x3)	39 (x2)	40 (x2)	59 (x2)	60 (x3)	576
	Total No. Spectra (x 1,000,000)	1.140	0.741	0.760	1.121	1.710	5.472
H_2O, AA, 45 s	No. Cycles (x Repeats)	25 (x1)	-	25 (x1)	25 (x1)	25 (x1)	100
	Total No. Spectra (x 1,000,000)	0.238	0	0.238	0.238	0.238	0.952
H_2O, AA, 180 s	No. Cycles (x Repeats)	13 (x1)	15 (x1)	10 (x3)	21 (x1)	14 (x2)	107
	Total No. Spectra (x 1,000,000)	0.124	0.143	0.095	0.200	0.266	0.828
DMF, AA, 12 s	No. Cycles (x Repeats)	59 (x1)	-	30 (x2)	58 (x2)	54 (x3)	397
	Total No. Spectra (x 1,000,000)	0.560	0	0.570	1.102	1.539	3.771
DMF, AA, 180 s	No. Cycles (x Repeats)	10 (x1)	-	14 (x2)	11 (x2)	18 (x2)	96

Reaction, Time (s)		23ºC	30ºC	40ºC	50ºC	60ºC	Sum
	Total No. Spectra (x 1,000,000)	0.095	0	0.266	0.209	0.342	0.993
DMF, N_2H_4, 12 s	No. Cycles (x Repeats)	56 (x1)	-	40 (x1)	39 (x1)	38 (x2)	173
	Total No. Spectra (x 1,000,000)	0.532	0	0.380	0.370	0.722	2.004
DMF, N_2H_4, 180	No. Cycles (x Repeats)	2 (x1)	-	2 (x1)	8 (x1)	12 (x3)	48
	Total No. Spectra (x 1,000,000)	0.019	0	0.019	0.076	0.342	0.456

All collected spectra were analysed, faulty experiments removed and repeats of the same experiment used to corroborate the results between the same conditions measured at different times.

6.4.4 Data Analysis

Due to the numerous large datasets involved, various data analysis techniques were employed to increase the speed and efficiency of calculations. The most time-consuming calculations were for *in situ* data analysis, which required some degrees of automation. Both XAS and EPR results were obtained *in situ* with 9500 and 1000 spectra per measurement, respectively. VtC XES and HR-XANES had significantly smaller datasets for processing, where background fitting and data analysis were performed in Origin(Pro).[49]

***In situ* EPR Data Processing**

EPR data was collected *in situ* for a time series, with 1000+ spectra collected under each reaction condition. First, the background noise was subtracted from

EPR data, using an empty EPR tube or blank solution. A linear correlation existed between the integrated area below the curve and the concentration of Cu species, explained further in calibration (Section 6.5.2). The calibration standards concentrations were applied to measurements of the positive and negative peak areas, using a python script. G-values were also calculated for all spectra, to indicate a change in species, as the point where the first derivative of the EPR spectrum crosses zero. The raw data was plotted to observe the trend of changes in the spectra, and the Cu concentration and g-value were used to plot the rate of the reaction and Cu salt transitions. The peaks in the EPR spectra were compared with literature values to identify the species present.

***Ex situ* XES Data Analysis**

The normalisation of the HR-XANES required a careful understanding of the polynomial order since the post-edge is not measured. The background in VtC XES was calculated by measuring the XES signal and removing a continuous fitted line from there. Since there was a gap between the measured VtC XES, the background subtraction line is extrapolated from XES results. A standard Cu foil was measured at the same session, under similar beamline setup to the samples, for calibration. Beam damage was tested and minimised before experiments.

***In situ* XAS Data Processing**

The analysis of large datasets applies similar processing steps to large batches of data. The script developed to help process large data sets, splits them into their component files for analysis and converts them to the required format. Data was formatted according to the parameters required for further analysis, such as configurations with only two columns of data, or specific headers required by pre-existing programs. Three separate stages of the XAS data processing are described briefly:

1. Data Cleaning and Selection – The removal of faulty datasets, merging of repeated cycles, cropping of regions of interest, energy calibration, removal of excessive noise, and normalisation of datasets for comparison are performed for each dataset in DAWN, to determine if valuable information has been obtained.[50] To select parameters for data processing, selected points from each dataset were first fitted individually with Athena from the Demeter Package (Bruce Ravel).[51] Files were formatted for batch XAS data analysis as nexus for processing in both DAWN-2.24[50] and the xraylarch 0.9.27[52] program with python. Scripts were written in Jupyter Notebook, with Anaconda package and made use of scipy[53] and Hyperspy.[54]
2. XANES Linear Combination Fitting – the mathematical fitting of selected standards to determine the combination of chemicals present within the sample gave further understanding of datasets in which the chemical reduction was unsuccessful, by monitoring oxidation state changes in Cu. Linear combination fittings were performed first with DAWN-2.24 and later in Larch, to adjust the fitting range.[50]
3. EXAFS fitting – processed data was divided into constituent spectra using a specially developed python script. These were later fitted using xraylarch script run on python and written to match with the fitting goals. These were compared with Artemis results to check the fit and select reasonable fitting parameters.[51] Scripts were written in Jupyter Notebook, and made use of scipy[53] and lmfit[55] for data fitting. K-range of 3 to 10 $Å^{-1}$ were used for the EXAFS fitting. Amplitude reduction factor was set as 0.9156 based on foil fitting. Data ranges were constrained between reasonable values.

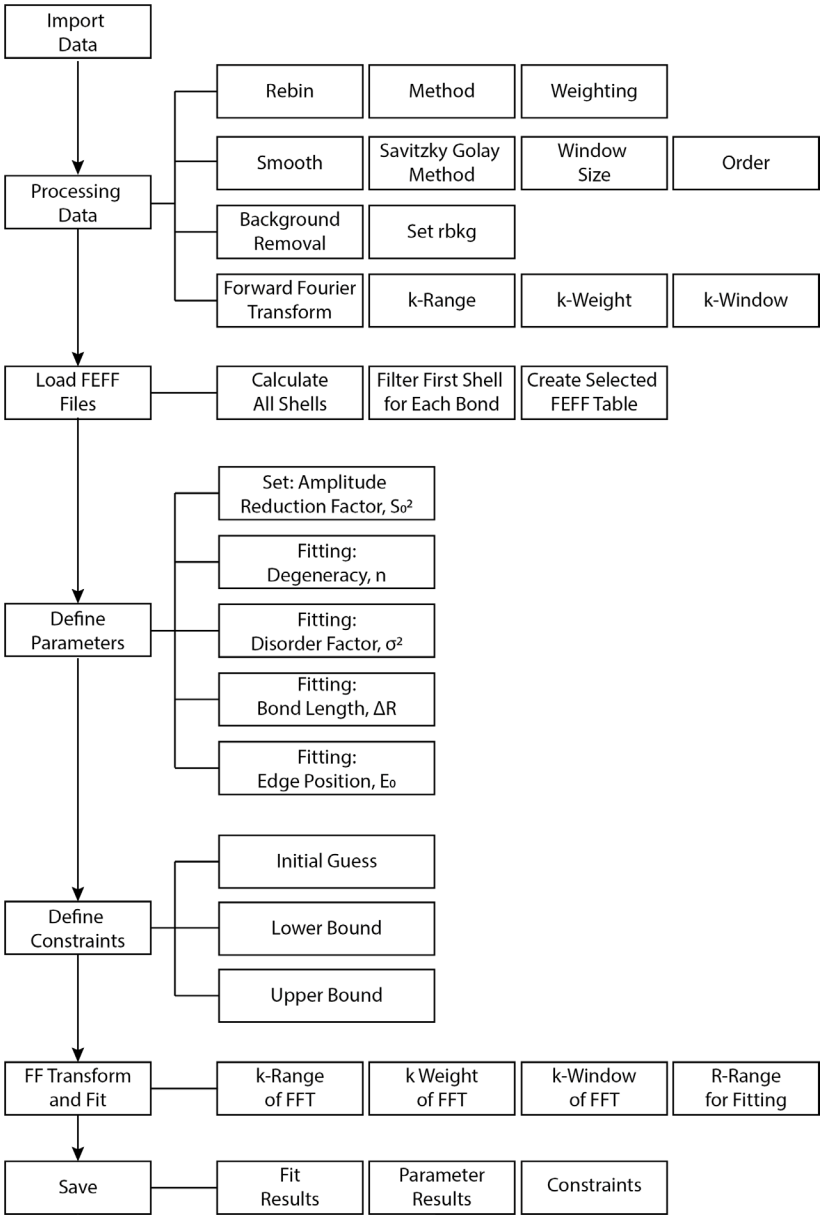

Figure 6.32 ***Script for Batch Data Analysis Flow Chart.*** *Flow chart outlining the process followed for batch EXAFS refinement of large datasets with 8500+ spectra. The major steps involve importing the data, processing to improve data quality, loading relevant FEFF files, defining fit parameters and constraints, fitting the data, and saving the results.*

FEFF File Selection

FEFF files are crystallographic data files which are used to simulate the spectrum or interactions within a given sample, based on where the atoms in the sample

are predicted to be located. These are often made by scientists based on experimental measurements and stored on a centralised database known as the Crystallographic Open Database. FEFF files have been selected in this work based on similarity to the studied system and reaction conditions, as well as their relevance and perceived accuracy.

The FEFF files selected in this work are:

Cu-Cu: 4105681, Smura, C.F. et al., Fm-3m, ccp

Cu-O: 9008961, Wyckoff, R.W.G., 1963, C 1 2/c 1

Python Scripts were used for the analysis of large datasets. In the case of this thesis, programmes were used for the analysis of time-resolved EPR and XAS data. All python scripts were tailored to the precise case for which they were applied. A general script is available upon request. Additional LCF and EXAFS fitting results from batch processing are too numerous to show in the Supplementary Information, but spectra and fitting parameters are available upon request.

Continuous Cauchy Wavelet Transform (CCWT)

CCWT is used for the visualisation of EXAFS data. It helps to distinguish the elements with lower and higher masses and gives an indication of the number of scattering paths required. The MATLAB script used is published by Munoz et al.[56] and adapted to give the desired output. The script is also tailored to create a video of the large dataset so that it could be easily viewed.

It has benefits both for seeing the different bond lengths formed during the reaction and noting the change in mass of bonding elements with similar bond-lengths.

6.5 Supplementary Information

6.5.1 Standards

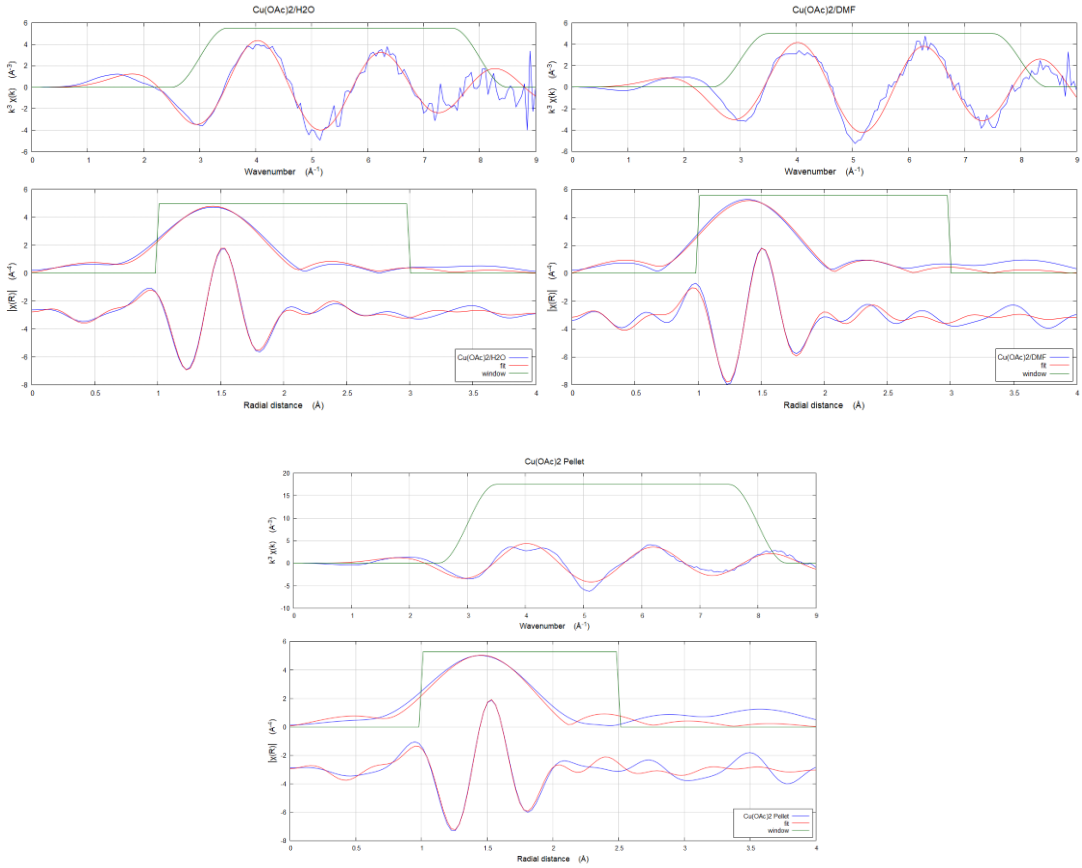

Figure 6.33 ***EXAFS Fit of Cu(OAc)$_2$ Standards.*** *k-space (0 to 9 Å^{-1}) and R-space (0 to 4 Å) results for Cu K-edge EXAFS fitting of Cu(OAc)$_2$/H$_2$O, Cu(OAc)$_2$/DMF and Cu(OAc)$_2$ powder. Fit is given in red, window in green and measured data in blue.*

6.5.2 TEM Images of AA Reduction

Table 6.5 ***Nanoparticle Size Measurements of AA-Reduction.*** *The measured sizes of nanoparticles formed during copper nanoparticle growth for $Cu(OAc)_2$/DMF and $Cu(OAc)_2/H_2O$ at temperatures of 23ºC and 60ºC.*

Temperature	Diameter (nm)	Error (nm)
23ºC, DMF	209.115	95.113
60ºC, DMF	223.981	111.673
23ºC, H_2O	213.315	61.058
60ºC, H_2O	408.467	60.344

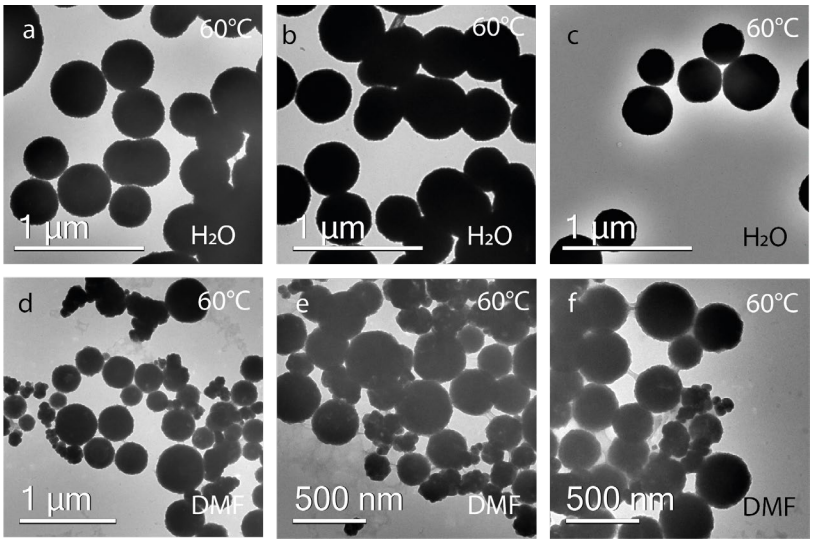

Figure 6.34 ***Morphology of 60ºC AA-Reduced Copper Nanoparticles.*** *TEM imaging of nanoparticles formed during 60ºC reduction of (a-c) $Cu(OAc)_2/H_2O$/AA and (d-f) $Cu(OAc)_2$/DMF/AA. Scalebars are given below images, ranging from 500 nm to 1 µm.*

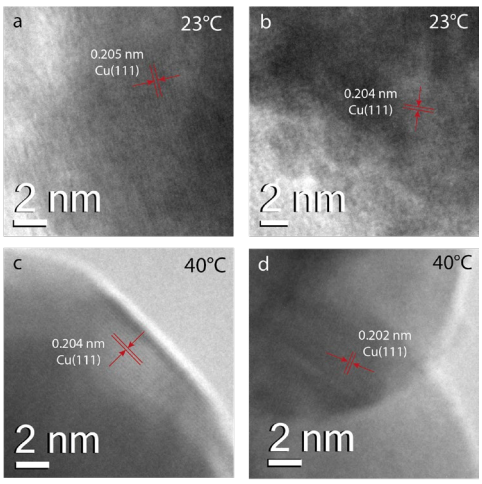

Figure 6.35 ***Lattice Spacing in $Cu(OAc)_2/H_2O/AA$.***

TEM images with 2 nm-scale of Cu nanoparticles formed by $Cu(OAc)_2/H_2O/AA$ reduction show lattice spacings of (a) 0.205 nm and (b) 0.204 nm at 23ºC and (c) 0.204 nm and (d) 0.202 nm at 40ºC, attributed to Cu(111).

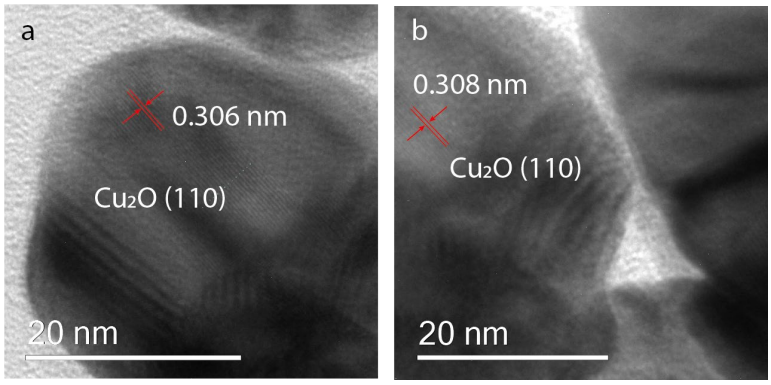

Figure 6.36 ***Lattice Spacing in $Cu(OAc)_2/DMF/AA$.***

Bright-field TEM images at the 20 nm-scale show Cu nanoparticles formed by $Cu(OAc)_2/DMF/AA$ reduction with lattice spacings of (a) 0.306 nm at 23ºC and (b) 0.308 nm at 60ºC, attributed to $Cu_2O(110)$, likely due to the formation of Cu_2O at the nanoparticle surface.

6.5.3 XAS Results AA Reduction

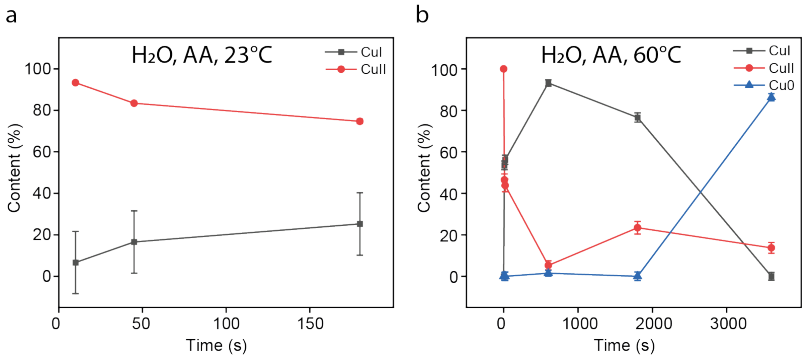

Figure 6.37 ***LCF of HR-XANES during Cu(OAc)$_2$/H$_2$O/AA Reduction.***

Cu K-edge HR-XANES LCF data shows the changing content of Cu^{2+} (red), Cu^{1+} (grey) and Cu^{0} (blue) during Cu(OAc)$_2$/H$_2$O/AA reduction at (a) 23°C and (b) 60°C.

The reproducibility of the XAS results is tested by 40 to 50 repeats for 12 second periods, but only 10 repeats for 180 second periods, due to the increased resolution from longer measurements.

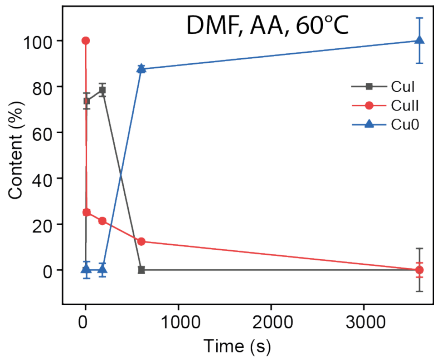

Figure 6.38 ***LCF of HR-XANES during AA-Reduction.*** *Cu K-edge HR-XANES LCF data shows the changing content of Cu^{2+} (red), Cu^{1+} (grey) and Cu^{0} (blue) during Cu(OAc)$_2$/DMF/AA reduction at 60°C. Standard error bars are given along y-axis.*

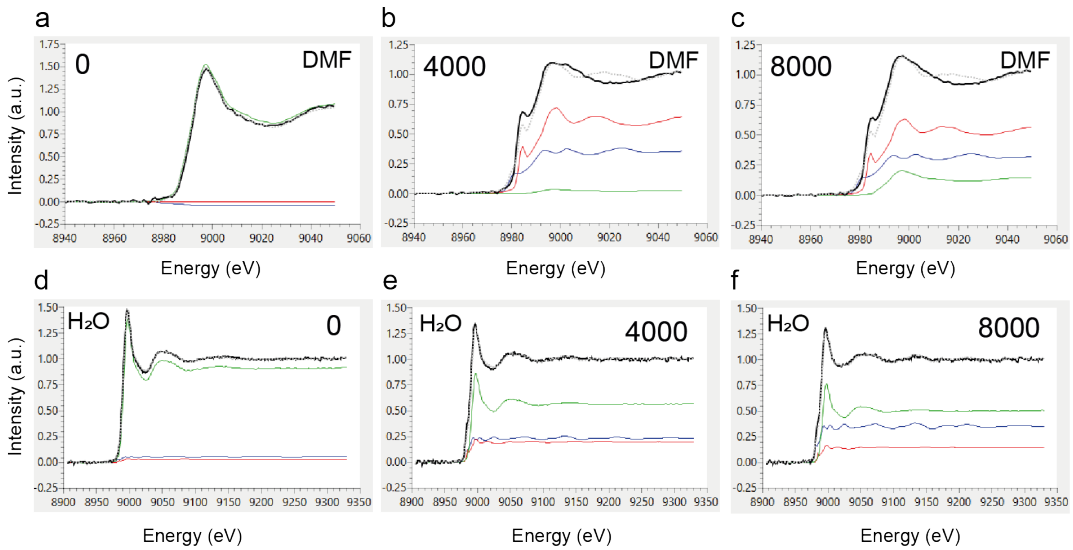

Figure 6.39 ***LCF Fit for Cu(OAc)$_2$/AA in H$_2$O and DMF.*** *Fit results of Cu K-edge XANES LCF are shown at scans 0, 4000 and 8000 for (a-c) Cu(OAc)$_2$/DMF/AA and (d-f) Cu(OAc)$_2$/H$_2$O/AA. Cu^0 (blue), Cu^{1+} (red) and Cu^{2+} (green) intensities are shown alongside the data (black) and the fitting (grey dash).*

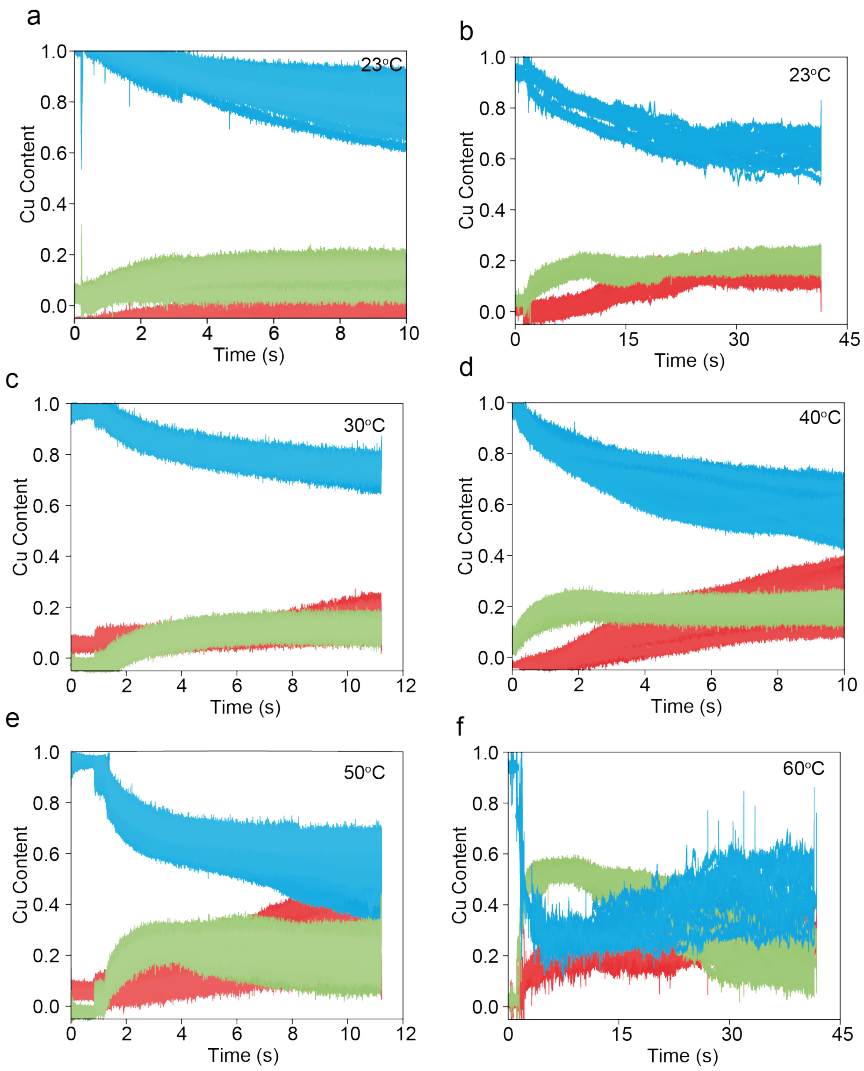

Figure 6.40 ***LCF Reproducibility of 12 s Cu(OAc)$_2$/H$_2$O/AA (Session 1).*** *Cu K-edge XANES LCF results show content of Cu^{2+} (blue), Cu^{1+} (green) and Cu^{0} (red) for Cu(OAc)$_2$/H$_2$O/AA reduction under (a) 23°C for 10 s, (b) 23°C for 45 s, (c) 30°C for 12 s, (d) 40°C for 10 s, (e) 50°C for 12 s and (f) 60°C for 45 s.*

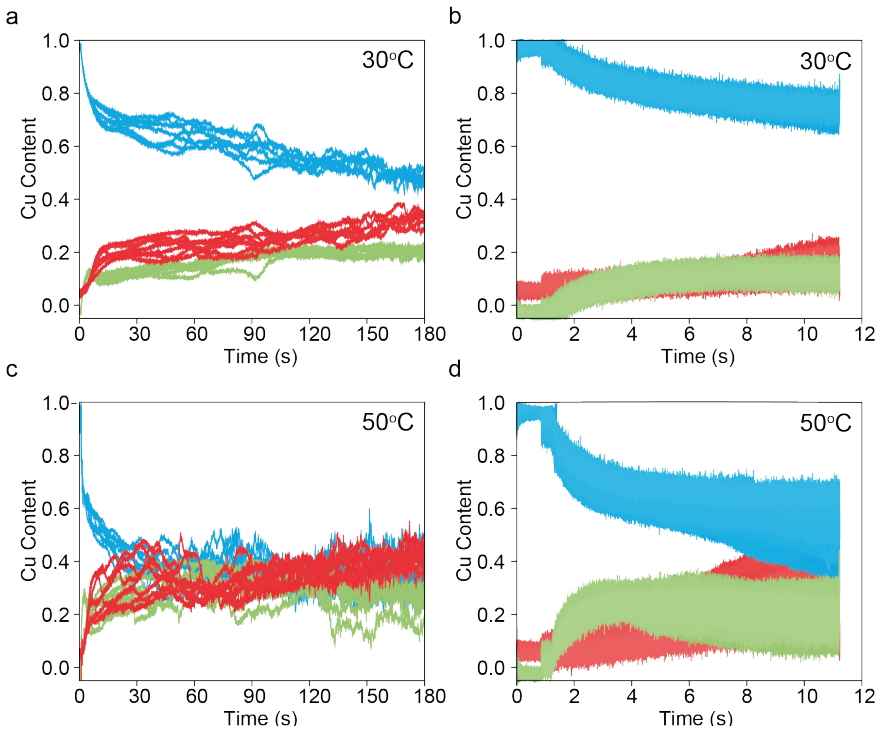

Figure 6.41 ***LCF Reproducibility of 12 s $Cu(OAc)_2/H_2O/AA$ (Session 2).*** *Cu K-edge XANES LCF results show content of Cu^{2+} (blue), Cu^{1+} (green) and Cu^0 (red) for $Cu(OAc)_2/H_2O/AA$ reduction under (a) 30°C for 180 s, (b) 30°C for 12 s, (c) 50°C for 180 s and (d) 50°C for 12 s.*

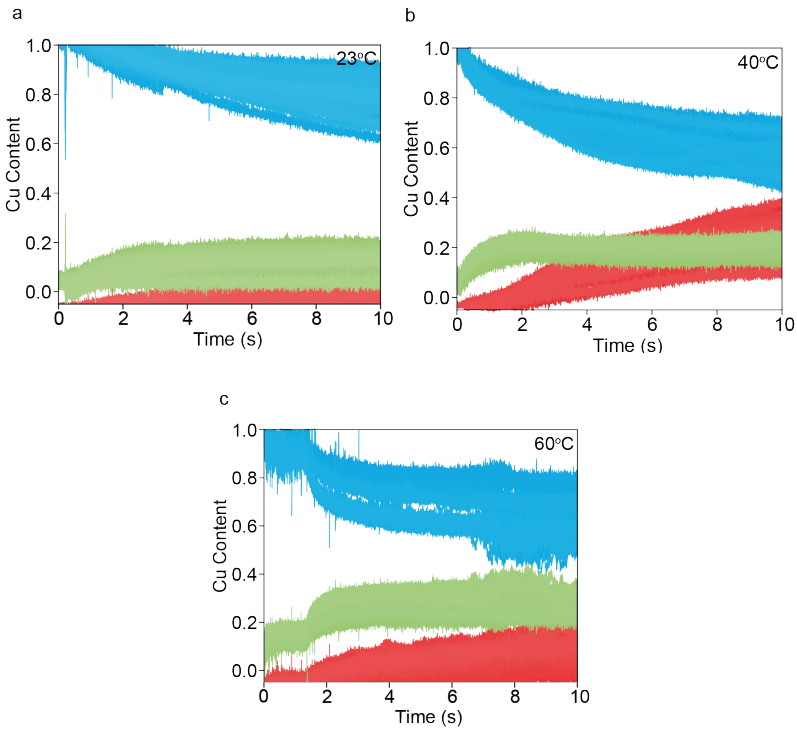

Figure 6.42 ***LCF Reproducibility of 180 s Cu(OAc)$_2$/H$_2$O/AA (Session 3).***

Cu K-edge XANES LCF results show content of Cu^{2+} (blue), Cu^{1+} (green) and Cu^0 (red) for Cu(OAc)$_2$/H$_2$O/AA reduction for 180 s at (a) 23ºC, (b) 40ºC and (c) 60ºC.

Table 6.6 ***Cu(OAc)$_2$/H$_2$O/AA LCF Results.*** *Cu K-edge Cu(OAc)$_2$/H$_2$O/AA LCF results were fitted with Athena at every 1000th spectra to confirm the batch analysis. The fitting range was between -20 eV and +30 eV from the edge position (E_0). Cu foil (Cu^0), Cu(OAc)$_2$/H$_2$O (Cu^{2+}) and Cu_2O (Cu^{1+}) XANES are used as fitting standards.*

	Time (s)	R-factor	Cu^{2+} (×100%)	Error (×100%)	Cu^0 (×100%)	Error (×100%)	Cu^{1+} (×100%)	Error (×100%)
23ºC	0	0.003	1.000	0.000	0.144	0.000	-0.144	0.000
	1000	0.001	0.916	0.011	0.129	0.026	-0.045	0.028
	2000	0.001	0.877	0.009	0.123	0.022	-0.000	0.024
	3000	0.001	0.854	0.008	0.146	0.019	-0.000	0.020

	Time (s)	R-factor	Cu^{2+} (×100%)	Error (×100%)	Cu^{0} (×100%)	Error (×100%)	Cu^{1+} (×100%)	Error (×100%)
	4000	0.001	0.827	0.009	0.166	0.021	0.007	0.022
	5000	0.001	0.811	0.009	0.192	0.020	-0.003	0.022
	6000	0.001	0.801	0.009	0.196	0.020	0.003	0.022
	7000	0.001	0.782	0.010	0.235	0.023	-0.017	0.025
	8000	0.002	0.769	0.013	0.269	0.029	-0.037	0.032
30ºC	0	0.002	0.947	0.013	0.083	0.030	-0.030	0.033
	1000	0.002	0.942	0.014	0.089	0.032	-0.031	0.035
	2000	0.001	0.870	0.009	0.123	0.022	0.007	0.024
	3000	0.001	0.829	0.010	0.144	0.023	0.027	0.025
	4000	0.001	0.796	0.010	0.188	0.024	0.016	0.026
	5000	0.001	0.786	0.010	0.201	0.024	0.013	0.026
	6000	0.001	0.777	0.010	0.202	0.024	0.021	0.026
	7000	0.002	0.761	0.011	0.228	0.026	0.012	0.028
	8000	0.002	0.753	0.011	0.234	0.025	0.013	0.027
40ºC	0	0.001	0.941	0.010	0.105	0.022	-0.046	0.024
	1000	0.001	0.772	0.007	0.133	0.017	0.095	0.019
	2000	0.001	0.691	0.009	0.222	0.022	0.087	0.024
	3000	0.002	0.625	0.011	0.334	0.027	0.041	0.029
	4000	0.003	0.566	0.013	0.413	0.031	0.021	0.034
	5000	0.003	0.542	0.013	0.432	0.031	0.026	0.033
	6000	0.003	0.513	0.014	0.470	0.032	0.017	0.035
	7000	0.003	0.492	0.014	0.495	0.032	0.012	0.035
50ºC	0	0.001	0.901	0.010	0.101	0.023	-0.002	0.026
	1000	0.001	0.847	0.010	0.165	0.024	-0.012	0.027
	2000	0.001	0.681	0.008	0.109	0.018	0.210	0.019
	3000	0.001	0.637	0.008	0.130	0.019	0.233	0.020
	4000	0.001	0.607	0.008	0.191	0.019	0.202	0.021
	5000	0.001	0.578	0.009	0.247	0.020	0.175	0.022
	6000	0.002	0.562	0.010	0.268	0.024	0.171	0.026
	7000	0.002	0.531	0.011	0.319	0.027	0.150	0.029
	8000	0.003	0.529	0.013	0.302	0.031	0.169	0.034

	Time (s)	R-factor	Cu^{2+} (×100%)	Error (×100%)	Cu^{0} (×100%)	Error (×100%)	Cu^{1+} (×100%)	Error (×100%)
60ºC	0	0.003	0.878	0.011	0.280	0.024	-0.158	0.026
	1000	0.002	0.685	0.008	0.286	0.019	0.029	0.021
	2000	0.003	0.380	0.008	0.287	0.019	0.333	0.020
	3000	0.004	0.294	0.009	0.348	0.021	0.358	0.023
	4000	0.005	0.241	0.011	0.388	0.025	0.371	0.027
	5000	0.006	0.205	0.011	0.436	0.026	0.358	0.028
	6000	0.006	0.180	0.011	0.488	0.025	0.332	0.028
	7000	0.006	0.174	0.011	0.498	0.026	0.328	0.028
	8000	0.006	0.182	0.012	0.469	0.026	0.349	0.029
	9000	0.006	0.166	0.011	0.506	0.026	0.328	0.029

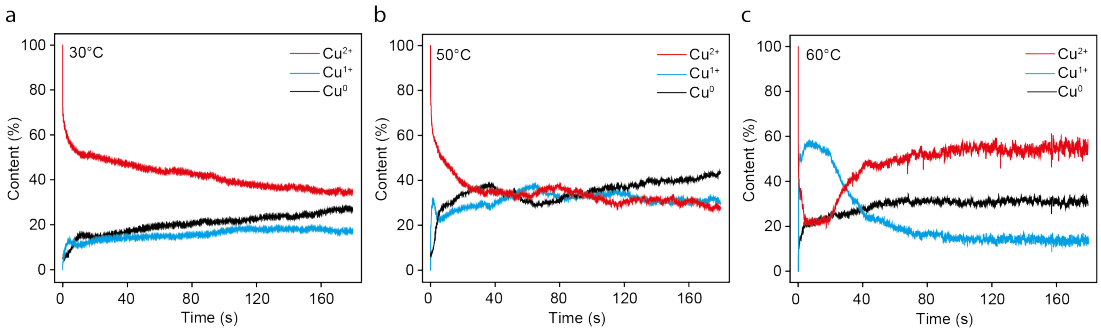

Figure 6.43 ***LCF Profile of 180 s Cu(OAc)₂/H₂O/AA.*** *Cu K-edge XANES LCF results show content of Cu^{2+} (red), Cu^{1+} (blue) and Cu^{0} (black) for $Cu(OAc)_2$/DMF/AA reduction measured for 180 s at (a) 30ºC, (b) 50ºC and (c) 60ºC.*

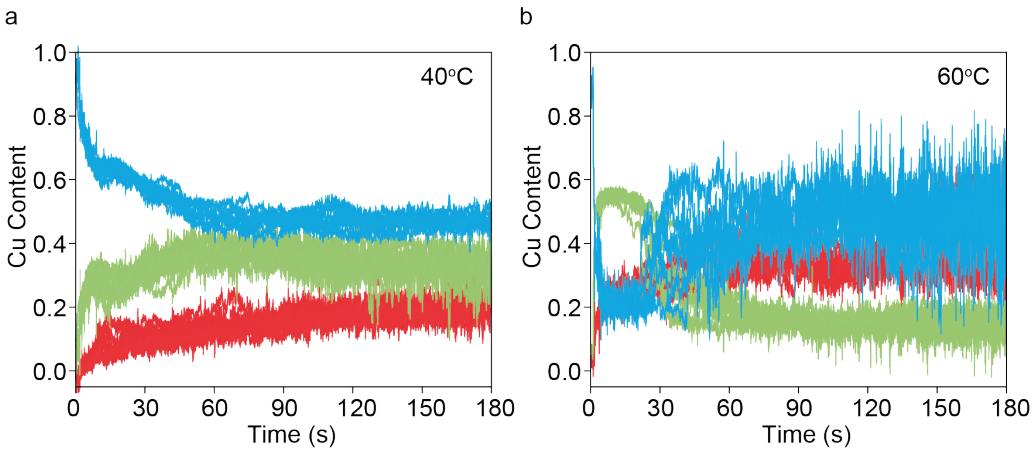

Figure 6.44 ***LCF Reproducibility of 180 s Cu(OAc)₂/H₂O/AA.*** *Cu K-edge XANES LCF results show content of Cu^{2+} (blue), Cu^{1+} (green) and Cu^{0} (red) for $Cu(OAc)_2/H_2O/AA$ reduction for 180 s at (a) 40°C and (b) 60°C.*

Table 6.7 ***Cu(OAc)₂/H₂O/AA EXAFS Results.*** *Cu K-edge $Cu(OAc)_2/H_2O/AA$ EXAFS results were fitted with Artemis at every 1000th spectra to confirm the batch analysis. The amplitude reduction factor was set at 0.9156, based on Cu foil fitting. To reduce the number of independent variables, σ^2 of Cu-O (R = 2.00 Å) and Cu-Cu (R = 2.44 Å) were tied for all datasets and calculated to be 0.00418 ± 6.2304E-4 and 0.0085 ± 9.2304E-4, respectively. Err. is short for Error.*

°C	Time (s)	Cu-Cu C.N.	Err.	ΔR Cu-Cu	Err.	Cu-O C.N.	Err.	ΔR Cu-O	Err.	ΔE_0	Err.
23	0	0	0	0	0	4.210	0.33	-0.036	0.01	-3.269	1.33
	1000	0.149	0.32	-0.229	0.15	3.785	0.39	-0.004	0.00	0	0
	2000	0.149	0.32	-0.229	0.15	3.886	0.44	-0.031	0.02	-2.259	2.61
	3000	0.240	0.44	0.046	0.13	3.979	0.45	-0.034	0.02	-2.217	2.68
	4000	0.367	0.41	-0.041	0.08	3.376	0.45	-0.032	0.02	-3.125	3.40
	5000	0.715	0.34	-0.033	0.04	3.163	0.38	-0.030	0.02	-2.830	3.16
	6000	1.150	0.40	-0.035	0.03	3.080	0.42	-0.021	0.03	-2.081	3.77
	7000	1.792	0.37	-0.018	0.02	3.014	0.38	0.004	0.02	1.222	3.15

ºC	Time (s)	Cu-Cu C.N.	Err.	ΔR Cu-Cu	Err.	Cu-O C.N.	Err.	ΔR Cu-O	Err.	ΔE_0	Err.
	8000	2.560	0.40	-0.039	0.02	2.872	0.41	-0.012	0.03	-1.815	3.79
	9000	3.185	0.43	0.026	0.00	2.938	0.50	0.005	0.01	0	0
30	0	0	0	0	0	3.751	0.20	-0.045	0.00	-3.446	1.03
	1000	0	0	0	0	3.524	0.25	-0.042	0.01	-3.600	1.23
	2000	0.431	0.34	0.062	0.05	3.485	0.28	-0.061	0.01	-5.891	1.96
	3000	0.504	0.33	0.080	0.04	3.356	0.26	-0.059	0.01	-5.502	1.88
	4000	0.504	0.33	0.080	0.04	3.354	0.25	-0.046	0.01	-3.008	1.75
	5000	0.436	0.31	0.086	0.05	3.279	0.23	-0.047	0.01	-2.779	1.69
	6000	0.436	0.31	0.086	0.05	3.279	0.23	-0.047	0.01	-2.779	1.69
	7000	0.623	0.29	0.022	0.03	3.229	0.23	-0.052	0.01	-3.600	1.23
	8000	0.667	0.27	0.011	0.03	3.131	0.22	-0.047	0.01	-2.595	1.76
40	0	0	0	0	0	3.970	0.21	-0.035	0.00	-3.424	0.94
	1000	0	0	0	0	3.725	0.22	-0.010	0.00	0.022	0.02
	2000	0	0	0	0	3.535	0.26	-0.030	0.01	-2.172	1.76
	3000	0	0	0	0	3.289	0.26	-0.038	0.01	-3.293	1.85
	4000	0	0	0	0	3.163	0.26	-0.036	0.01	-3.048	1.98
	5000	0.216	0.20	-0.044	0.07	3.088	0.21	-0.040	0.01	-3.309	1.66
	6000	0.518	0.25	-0.056	0.03	2.908	0.25	-0.037	0.01	-2.701	2.24
	7000	0.697	0.24	-0.016	0.02	2.860	0.20	-0.020	0.00	0.022	0
	8000	1.030	0.28	-0.014	0.02	2.747	0.24	-0.014	0.02	0.555	2.42
	9000	1.625	0.32	0.022	0	2.588	0.26	-0.010	0.02	-0.072	2.94
50	0	0.000	0.00	0.000	0.00	3.815	0.23	-0.067	0.00	-6.120	1.01
	1000	0.000	0.00	0.000	0.00	3.783	0.29	-0.073	0.01	-5.497	1.53
	2000	0.089	0.17	-0.073	0.13	3.181	0.28	-0.088	0.01	-7.138	2.20
	3000	0.245	0.20	-0.064	0.05	2.946	0.29	-0.082	0.02	-6.127	2.64
	4000	0.765	0.24	-0.066	0.02	2.765	0.29	-0.079	0.02	-5.663	3.11
	5000	1.004	0.27	-0.065	0.02	2.602	0.27	-0.073	0.02	-4.794	3.21
	6000	1.340	0.32	-0.055	0.02	2.496	0.26	-0.073	0.02	-4.822	3.21
	7000	1.539	0.35	-0.068	0.01	2.589	0.25	-0.087	0.01	-5.497	1.53
	8000	1.710	0.38	-0.074	0.02	2.463	0.26	-0.095	0.02	-6.118	3.24

ºC	Time (s)	Cu-Cu C.N.	Err.	ΔR Cu-Cu	Err.	Cu-O C.N.	Err.	ΔR Cu-O	Err.	ΔE_0	Err.
60	0	0	0	0	0	3.623	0.25	-0.052	0.00	-7.083	1.06
	1000	0	0	0	0	3.077	0.30	-0.047	0.01	-4.437	2.15
	2000	1.077	0.36	-0.034	0.03	1.975	0.26	-0.049	0.02	-2.287	3.84
	3000	1.117	0.39	-0.049	0.03	1.632	0.26	-0.084	0.03	-3.826	5.20
	4000	1.380	0.38	-0.020	0.02	1.509	0.20	-0.069	0.03	1.146	3.87
	5000	1.705	0.43	-0.014	0.02	1.412	0.19	-0.073	0.03	2.146	3.76
	6000	1.827	0.45	-0.001	0.02	1.364	0.19	-0.060	0.03	3.804	3.70
	7000	1.873	0.48	-0.001	0.02	1.337	0.21	-0.061	0.03	3.840	4.05
	8000	1.745	0.45	-0.003	0.02	1.342	0.20	-0.063	0.03	3.589	3.94
	9000	1.698	0.46	0.047	0.03	1.330	0.20	-0.068	0.03	3.061	4.38

6.5.4 $Cu(OAc)_2$/DMF/AA

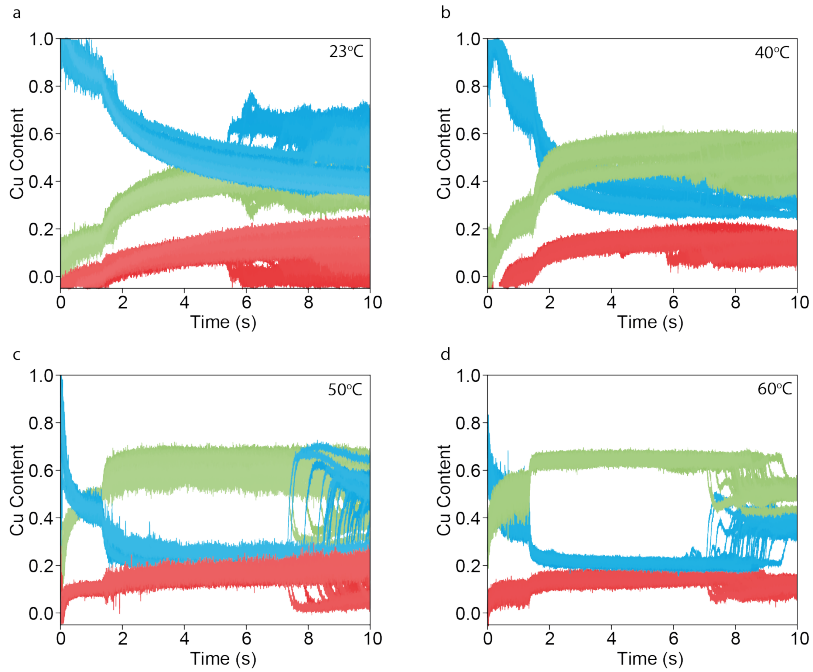

Figure 6.45 ***LCF Reproducibility of 10 s $Cu(OAc)_2$/DMF/AA.***

Cu K-edge XANES LCF results show content of Cu^{2+} (blue), Cu^{1+} (green) and Cu^0 (red) for $Cu(OAc)_2$/DMF/AA reduction under (a) 23ºC for 10 s, (b) 40ºC for 10 s, (c) 50ºC for 10 s and (d) 60ºC for 10 s.

Table 6.8 ***LCF $Cu(OAc)_2$/DMF/AA Results.*** *$Cu(OAc)_2$/DMF/AA LCF results were fitted with Athena at every 1000th spectra to confirm the batch analysis. The fitting range was between -20 eV and +30 eV from the edge position (E_0). Cu foil (Cu^0), $Cu(OAc)_2$/DMF (Cu^{2+}) and Cu_2O (Cu^{1+}) XANES are used as fitting standards.*

	Data	R-factor	Cu^{2+} (×100%)	Error	Cu^0 (×100 %)	Error	Cu^{1+} (×100 %)	Error
23ºC	0	0.0019	0.932	0.012	0.168	0.029	-0.101	0.032
	1000	0.0035	0.761	0.015	0.163	0.037	0.075	0.040
	2000	0.0042	0.529	0.016	0.289	0.037	0.181	0.040
	3000	0.0049	0.456	0.016	0.302	0.039	0.240	0.042
	4000	0.0053	0.425	0.017	0.296	0.041	0.277	0.044

	Data	R-factor	Cu^{2+} (×100%)	Error	Cu^{0} (×100 %)	Error	Cu^{1+} (×100 %)	Error
	5000	0.0054	0.413	0.017	0.290	0.041	0.296	0.045
	6000	0.0051	0.416	0.017	0.282	0.040	0.300	0.043
	7000	0.0039	0.452	0.014	0.261	0.034	0.286	0.037
	8000	0.0031	0.475	0.013	0.250	0.031	0.274	0.033
40ºC	0	0.0023	0.908	0.014	0.247	0.033	-0.155	0.036
	1000	0.0025	0.622	0.013	0.260	0.030	0.116	0.033
	2000	0.0092	0.365	0.022	0.183	0.051	0.450	0.056
	3000	0.0123	0.325	0.025	0.172	0.058	0.501	0.063
	4000	0.0140	0.311	0.026	0.163	0.062	0.525	0.067
	5000	0.0147	0.305	0.027	0.157	0.063	0.537	0.069
	6000	0.0120	0.343	0.024	0.146	0.057	0.509	0.062
	7000	0.0102	0.377	0.023	0.135	0.054	0.487	0.058
	8000	0.0091	0.386	0.021	0.145	0.051	0.468	0.055
50ºC	0	0.0013	0.866	0.010	0.188	0.025	-0.055	0.027
	1000	0.0090	0.400	0.022	0.202	0.053	0.397	0.057
	2000	0.0154	0.237	0.027	0.135	0.064	0.626	0.070
	3000	0.0167	0.225	0.028	0.148	0.067	0.625	0.073
	4000	0.0163	0.219	0.028	0.157	0.066	0.623	0.071
	5000	0.0166	0.220	0.028	0.151	0.066	0.628	0.071
	6000	0.0141	0.235	0.026	0.172	0.061	0.591	0.067
	7000	0.0097	0.298	0.022	0.185	0.052	0.516	0.057
	8000	0.0056	0.399	0.017	0.157	0.041	0.442	0.045
60ºC	0	0.0041	0.877	0.018	0.323	0.043	-0.209	0.047
	1000	0.0112	0.320	0.024	0.149	0.056	0.529	0.061
	2000	0.0192	0.214	0.030	0.123	0.070	0.661	0.076
	3000	0.0199	0.202	0.030	0.125	0.071	0.672	0.077
	4000	0.0180	0.206	0.028	0.149	0.067	0.643	0.073
	5000	0.0188	0.194	0.029	0.162	0.068	0.642	0.074
	6000	0.0178	0.252	0.029	0.121	0.068	0.626	0.074
	7000	0.0174	0.258	0.029	0.134	0.068	0.607	0.074
	8000	0.0166	0.304	0.028	0.092	0.067	0.603	0.073

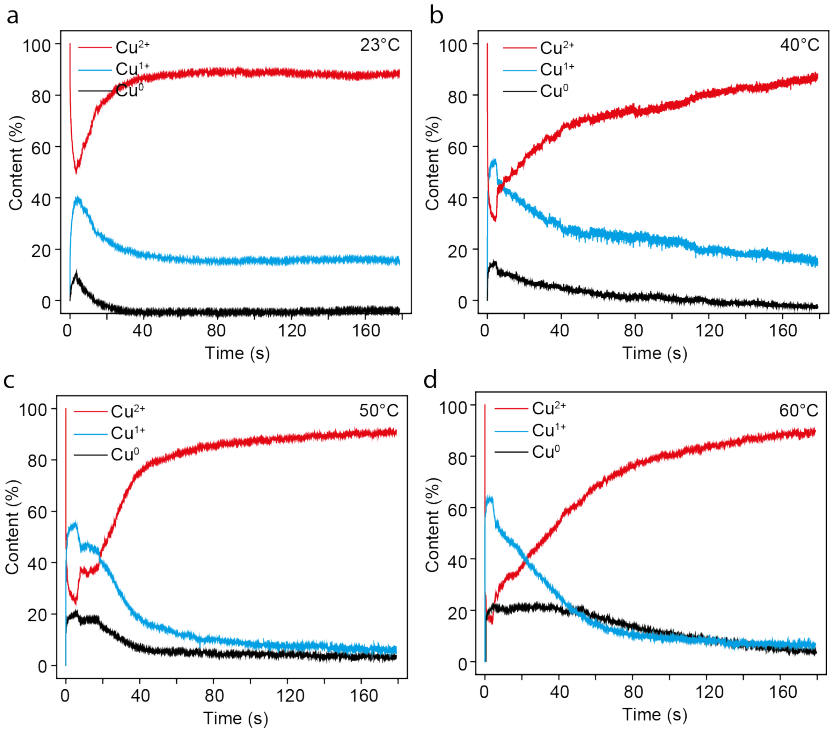

Figure 6.46 ***LCF Results for 180 s as a Temperature Range.*** *Cu K-edge XANES LCF results show content of Cu^{2+} (red), Cu^{1+} (blue) and Cu^{0} (black) for $Cu(OAc)_2$/DMF/AA reduction measured for 180 s at (a) 23°C, (b) 40°C, (c) 50°C and (d) 60°C.*

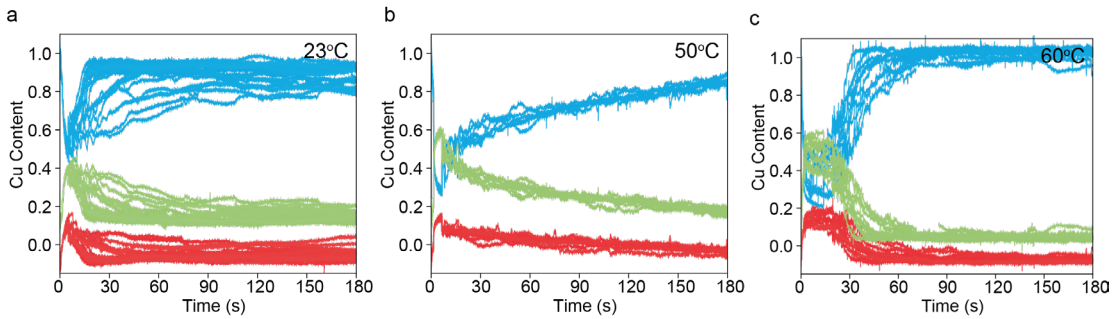

Figure 6.47 ***LCF Reproducibility of 180 s $Cu(OAc)_2$/DMF/AA.*** *Cu K-edge XANES LCF results show content of Cu^{2+} (blue), Cu^{1+} (green) and Cu^{0} (red) for $Cu(OAc)_2$/DMF/AA reduction for 180 s at (a) 23°C, (b) 50°C and (c) 60°C.*

Table 6.9 ***EXAFS Results for $Cu(OAc)_2$/DMF/AA Point Fitting.*** *$Cu(OAc)_2$/DMF/AA EXAFS results were fitted with Artemis at every 1000th spectra to confirm the batch analysis. The amplitude reduction factor was set at 0.9156, based on Cu foil fitting. To reduce independent variables, σ^2 of Cu-O (R = 2.00 Å) and Cu-Cu (R = 2.44 Å) were tied for all datasets and calculated to be 0.0098 and 0.0031, respectively.*

ºC	Time (s)	Cu-Cu C.N.	Error	ΔR Cu-Cu	Error	Cu-O C.N.	Error	ΔR Cu-O	Error	ΔE_0	Error
23	0	0.000	0.00	0.000	0.00	3.832	0.27	-0.068	0.00	-8.290	1.04
	1000	0.000	0.00	0.000	0.00	3.320	0.23	-0.068	0.00	-5.703	1.02
	2000	0.000	0.00	0.000	0.00	2.634	0.21	-0.090	0.01	-6.438	1.53
	3000	0.764	1.16	0.076	0.08	2.385	0.19	-0.090	0.01	-6.185	1.60
	4000	1.153	1.57	0.063	0.05	2.236	0.18	-0.097	0.01	-7.099	2.17
	5000	1.237	1.66	0.061	0.05	2.217	0.18	-0.097	0.01	-7.051	2.19
	6000	1.084	1.51	0.065	0.06	2.150	0.19	-0.093	0.01	-6.664	1.98
	7000	1.192	1.68	0.058	0.06	2.330	0.21	-0.093	0.01	-7.250	2.03
	8000	0.886	1.34	0.067	0.08	2.371	0.21	-0.093	0.01	-7.717	1.99
40	0	0.000	0.00	0.758	0.00	5.317	0.00	-0.081	0.01	2.133	1.02
	1000	0.000	0.00	0.683	0.00	4.691	0.00	-0.084	0.01	2.133	1.02
	2000	1.085	0.57	0.591	0.01	4.300	0.03	-0.091	0.01	2.133	1.02
	3000	1.912	0.85	0.580	0.04	3.819	0.02	-0.094	0.01	2.133	1.02
	4000	2.609	1.07	0.552	0.06	3.271	0.01	-0.091	0.01	2.133	1.02
	5000	2.941	1.16	0.525	0.06	3.086	0.01	-0.092	0.01	2.133	1.02
	6000	2.764	1.11	0.538	0.00	2.812	0.00	-0.005	0.01	2.133	1.02
	7000	2.898	1.14	0.515	0.00	2.737	0.00	-0.004	0.01	2.133	1.02
50	0	0.000	0.00	0.000	0.00	3.879	0.26	-0.047	0.00	-4.286	1.06
	1000	0.000	0.00	0.000	0.00	2.544	0.20	-0.098	0.01	-4.492	1.61
	2000	0.324	0.24	0.071	0.04	1.805	0.18	-0.098	0.01	-2.253	1.77
	3000	0.280	0.24	0.071	0.04	1.758	0.18	-0.101	0.01	-2.643	2.17
	4000	0.351	0.21	0.053	0.04	1.812	0.17	-0.101	0.01	-2.942	2.14

ºC	Time (s)	Cu-Cu C.N.	Error	∆R Cu-Cu	Error	Cu-O C.N.	Error	∆R Cu-O	Error	ΔE_0	Error
	5000	0.303	0.22	0.053	0.04	1.751	0.17	-0.102	0.01	-2.760	2.13
	6000	0.367	0.23	0.049	0.03	1.839	0.18	-0.102	0.01	-3.697	2.18
	7000	0.299	0.18	0.049	0.03	1.920	0.16	-0.080	0.01	-2.217	1.75
	8000	0.246	0.20	0.026	0.07	2.233	0.19	-0.080	0.01	-4.909	1.80
60	0	0.000	0.00	0.000	0.00	3.408	0.42	-0.044	0.00	-3.621	2.63
	1000	0.000	0.00	0.000	0.00	1.875	0.22	-0.102	0.00	-5.210	2.15
	2000	0.000	0.00	0.000	0.00	1.477	0.18	-0.102	0.00	-3.106	2.17
	3000	0.000	0.00	0.000	0.00	1.449	0.19	-0.109	0.00	-3.760	2.83
	4000	0.000	0.00	0.000	0.00	1.458	0.20	-0.109	0.02	-4.398	2.88
	5000	0	0.23	0.100	0.46	1.338	0.17	-0.091	0.01	-1.709	2.68
	6000	0.297	0.34	0.187	0.09	1.584	0.21	-0.091	0.01	-3.413	2.70
	7000	0	0.26	0.053	0.11	1.547	0.20	-0.067	0.02	-1.285	2.31
	8000	0	0.25	0.048	0.08	1.655	0.20	-0.067	0.01	-2.431	2.29

6.5.5 TEM images of N_2H_4 Reduction

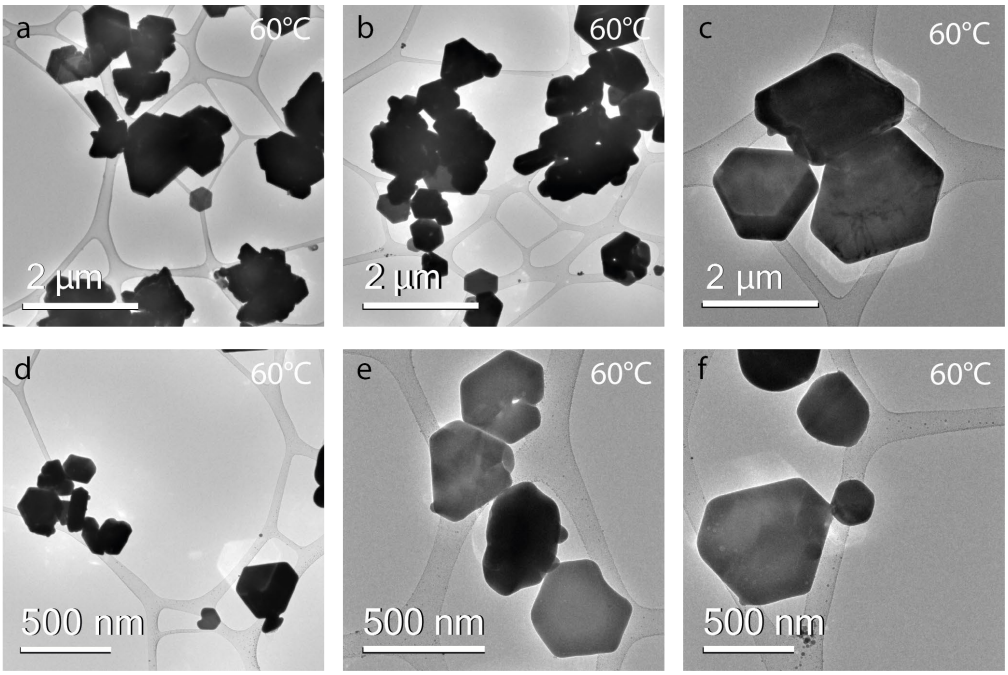

Figure 6.48 ***Cu(OAc)$_2$/DMF/N_2H_4 Nanoparticle Morphology.*** *TEM images show the faceted growth of Cu nanoparticles formed under Cu(OAc)$_2$/DMF/N_2H_4 reduction at 60°C with scalebar of (a-c) 2 µm and (d-f) 500 nm.*

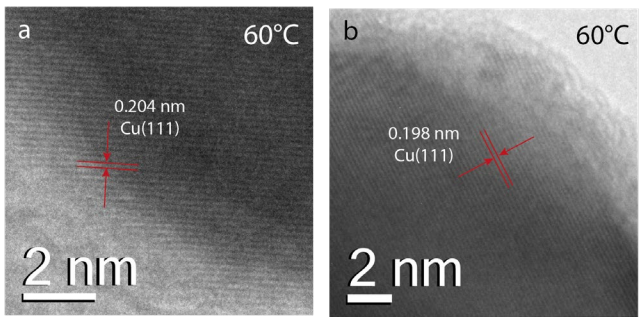

Figure 6.49 ***Lattice Spacing for Cu(OAc)$_2$/DMF/N_2H_4.*** *TEM results at 2 nm-scale show lattice spacing of Cu nanoparticles formed with Cu(OAc)$_2$/DMF/N_2H_4 reduction at 60°C of (a) 0.204 nm and (b) 0.198 nm, attributed to Cu(111) facets.*

6.5.6 $Cu(OAc)_2/DMF/N_2H_4$

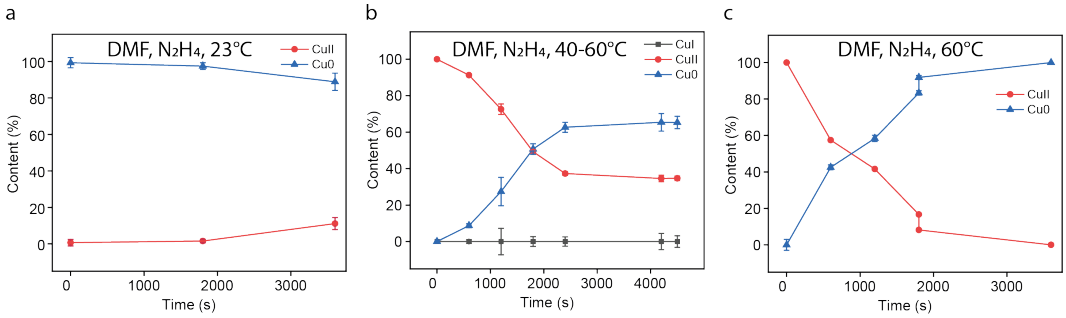

Figure 6.50 ***LCF of HR-XANES for $Cu(OAc)_2/DMF/N_2H_4$.*** *Cu K-edge HR-XANES LCF data shows the changing content of Cu^{2+} (red), Cu^{1+} (grey) and Cu^{0} (blue) during $Cu(OAc)_2/DMF/N_2H_4$ for reaction temperatures of (a) 23°C, (b) 40°C for 10 minutes, then increased to 60°C and (c) constant 60°C. Standard error bars are given along y-axis.*

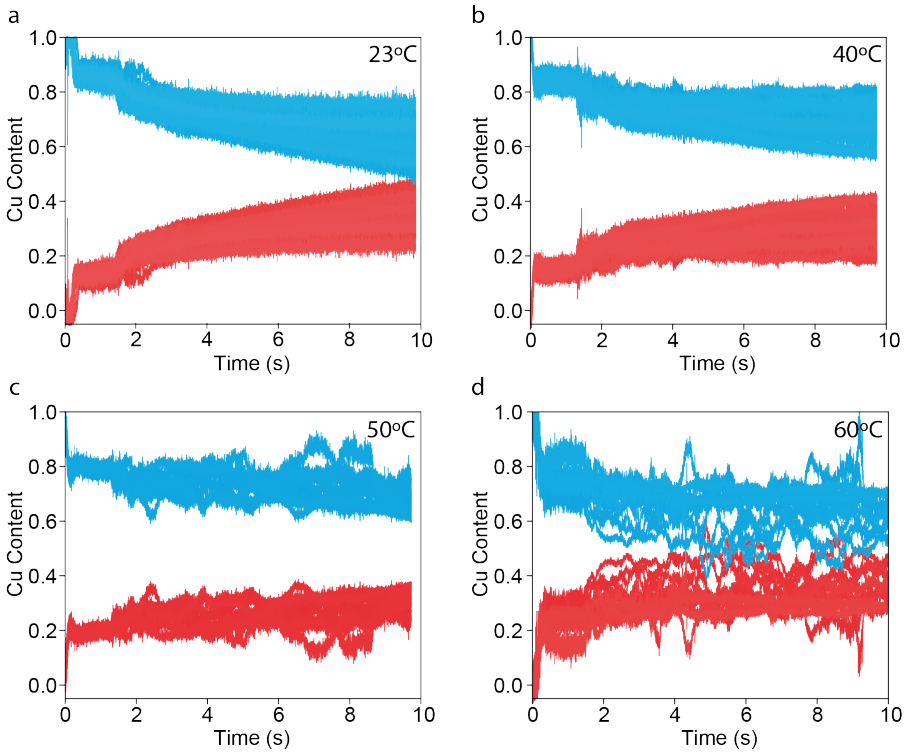

Figure 6.51 ***LCF Reproducibility of 10 s $Cu(OAc)_2/DMF/N_2H_4$.***

Cu K-edge XANES LCF results show content of Cu^{2+} (blue) and Cu^{0} (red) for $Cu(OAc)_2/DMF/N_2H_4$ reduction for 180 s at (a) 23°C, (b) 40°C, (c) 50°C and (d) 60°C.

6.6 References

1 Woldu, A. R., Huang, Z., Zhao, P., Hu, L. & Astruc, D. Electrochemical CO2 reduction (CO2RR) to multi-carbon products over copper-based catalysts. *Coordination Chemistry Reviews* **454** http://dx.doi.org/10.1016/j.ccr.2021.214340 (2022).

2 Wang, X. *et al.* Morphology and mechanism of highly selective Cu(II) oxide nanosheet catalysts for carbon dioxide electroreduction. *Nat Commun* **12**, 794, http://dx.doi.org/10.1038/s41467-021-20961-7 (2021).

3 Popovic, S. *et al.* Stability and Degradation Mechanisms of Copper-Based Catalysts for Electrochemical CO(2) Reduction. *Angew Chem Int Ed Engl* **59**, 14736-14746, http://dx.doi.org/10.1002/anie.202000617 (2020).

4 Thapa, S., Shrestha, B., Gurung, S. K. & Giri, R. Copper-catalysed cross-coupling: an untapped potential. *Org Biomol Chem* **13**, 4816-4827, http://dx.doi.org/10.1039/c5ob00200a (2015).

5 Jammi, S. *et al.* CuO Nanoparticles Catalyzed C−N, C−O, and C−S Cross-Coupling Reactions: Scope and Mechanism. *The Journal of Organic Chemistry* **74**, 1971-1976, http://dx.doi.org/10.1021/jo8024253 (2009).

6 Li, Z. *et al.* Mechanism Investigations on Water Gas Shift Reaction over Cu(111), Cu(100), and Cu(211) Surfaces. *ACS Omega* **7**, 3514-3521, http://dx.doi.org/10.1021/acsomega.1c05991 (2022).

7 Gokhale, A. A., Dumesic, J. A. & Mavrikakis, M. On the Mechanism of Low-Temperature Water Gas Shift Reaction on Copper. *Journal of the American Chemical Society* **130**, 1402-1414, http://dx.doi.org/10.1021/ja0768237 (2008).

8 Gawande, M. B. *et al.* Cu and Cu-Based Nanoparticles: Synthesis and Applications in Catalysis. *Chem Rev* **116**, 3722-3811, http://dx.doi.org/10.1021/acs.chemrev.5b00482 (2016).

9 Jardón-Maximino, N. *et al.* Oxidation of Copper Nanoparticles Protected with Different Coatings and Stored under Ambient Conditions. *Journal of Nanomaterials* **2018**, 1-8, http://dx.doi.org/10.1155/2018/9512768 (2018).

10 Vazquez-Vazquez, C., Banobre-Lopez, M., Mitra, A., Lopez-Quintela, M. A. & Rivas, J. Synthesis of small atomic copper clusters in microemulsions. *Langmuir* **25**, 8208-8216, http://dx.doi.org/10.1021/la900100w (2009).

11 Oka, H., Kitai, K., Suzuki, T. & Obora, Y. N,N-Dimethylformamide-stabilized copper nanoparticles as a catalyst precursor for Sonogashira–Hagihara cross coupling. *RSC Advances* **7**, 22869-22874, http://dx.doi.org/10.1039/c6ra27910d (2017).

12 Deraedt, C. *et al.* Sodium borohydride stabilizes very active gold nanoparticle catalysts. *Chem Commun (Camb)* **50**, 14194-14196, http://dx.doi.org/10.1039/c4cc05946h (2014).

13 Sood, A., Arora, V., Shah, J., Kotnala, R. K. & Jain, T. K. Ascorbic acid-mediated synthesis and characterisation of iron oxide/gold core–shell nanoparticles. *Journal of Experimental Nanoscience* **11**, 370-382, http://dx.doi.org/10.1080/17458080.2015.1066514 (2015).

14 Kim, H. S. *et al.* Concentration Effect of Reducing Agents on Green Synthesis of Gold Nanoparticles: Size, Morphology, and Growth

Mechanism. *Nanoscale Res Lett* **11**, 230, http://dx.doi.org/10.1186/s11671-016-1393-x (2016).

15 Langille, M. R., Personick, M. L., Zhang, J. & Mirkin, C. A. Defining rules for the shape evolution of gold nanoparticles. *J Am Chem Soc* **134**, 14542-14554, http://dx.doi.org/10.1021/ja305245g (2012).

16 Xiong, J., Wang, Y., Xue, Q. & Wu, X. Synthesis of highly stable dispersions of nanosized copper particles using l-ascorbic acid. *Green Chemistry* **13** http://dx.doi.org/10.1039/c0gc00772b (2011).

17 Ramos, A. R. *et al.* Effects of reaction temperatures and reactant concentrations on the antimicrobial characteristics of copper precipitates synthesized using L-ascorbic acid as reducing agent. *Journal of Science: Advanced Materials and Devices* **4**, 66-71, http://dx.doi.org/10.1016/j.jsamd.2018.12.009 (2019).

18 Pastoriza-Santos, I., Sánchez-Iglesias, A., Rodríguez-González, B. & Liz-Marzán, L. M. Aerobic Synthesis of Cu Nanoplates with Intense Plasmon Resonances. *Small* **5**, 440-443, http://dx.doi.org/10.1002/smll.200801088 (2009).

19 Watzky, M. A. & Finke, R. G. Nanocluster Size-Control and “Magic Number” Investigations. Experimental Tests of the “Living-Metal Polymer” Concept and of Mechanism-Based Size-Control Predictions Leading to the Syntheses of Iridium(0) Nanoclusters Centering about Four Sequential Magic Numbers. *Chemical Materials* **9**, 3083-3095, (1997).

20 Nayak, C. *et al.* Insight into growth of Au-Pt bimetallic nanoparticles: an in situ XAS study. *J Synchrotron Radiat* **24**, 825-835, http://dx.doi.org/10.1107/s1600577517006257 (2017).

21 Nayak, C., Bhattacharyya, D., Jha, S. N. & Sahoo, N. K. In Situ XAS Study on Growth of PVP-Stabilized Cu Nanoparticles. *ChemistrySelect* **3**, 7370-7377, http://dx.doi.org/https://doi.org/10.1002/slct.201801358 (2018).

22 Yao, S. *et al.* Insights into the Formation Mechanism of Rhodium Nanocubes. *The Journal of Physical Chemistry C* **116**, 15076-15086, http://dx.doi.org/10.1021/jp302471p (2012).

23 Harada, M. & Ikegami, R. In Situ Quick X-ray Absorption Fine Structure and Small-Angle X-ray Scattering Study of Metal Nanoparticle Growth in Water-in-Oil Microemulsions during Photoreduction. *Crystal Growth & Design* **16**, 2860-2873, http://dx.doi.org/10.1021/acs.cgd.6b00173 (2016).

24 Godfrey, I. J., Dent, A. J., Parkin, I. P., Maenosono, S. & Sankar, G. Following the Formation of Silver Nanoparticles Using In Situ X-ray Absorption Spectroscopy. *ACS Omega* **5**, 13664-13671, http://dx.doi.org/10.1021/acsomega.0c00697 (2020).

25 Kong, Q. *et al.* Microsecond time-resolved energy-dispersive EXAFS measurement and its application to film the thermolysis of (NH(4))(2)[PtCl(6)]. *Sci Rep* **2**, 1018, http://dx.doi.org/10.1038/srep01018 (2012).

26 Chang, S. Y. *et al.* Energy dispersive-EXAFS of Pd nucleation at a liquid/liquid interface. *Journal of Physics: Conference Series* **712**, 012058, http://dx.doi.org/10.1088/1742-6596/712/1/012058 (2016).

27 Wojnicki, M., Fitzner, K. & Luty-Blocho, M. Kinetic studies of nucleation and growth of palladium nanoparticles. *J Colloid Interface Sci* **465**, 190-199, http://dx.doi.org/10.1016/j.jcis.2015.11.066 (2016).

28 Perala, S. R. & Kumar, S. On the two-step mechanism for synthesis of transition-metal nanoparticles. *Langmuir* **30**, 12703-12711, http://dx.doi.org/10.1021/la503199m (2014).

29 Watzky, M. A. & Finke, R. G. Gold Nanoparticle Formation Kinetics and Mechanism: A Critical Analysis of the "Redox Crystallization" Mechanism. *ACS Omega* **3**, 1555-1563, http://dx.doi.org/10.1021/acsomega.7b01772 (2018).

30 Amirjani, A. & Haghshenas, D. F. Modified Finke-Watzky mechanisms for the two-step nucleation and growth of silver nanoparticles. *Nanotechnology* **29**, 505602, http://dx.doi.org/10.1088/1361-6528/aae3dd (2018).

31 Lu, R. *et al.* A simple method for the synthesis of copper nanoparticles from metastable intermediates. *RSC Adv* **13**, 14361-14369, http://dx.doi.org/10.1039/d3ra01082a (2023).

32 Liu, Q.-m., Yasunami, T., Kuruda, K. & Okido, M. Preparation of Cu nanoparticles with ascorbic acid by aqueous solution reduction method. *Transactions of Nonferrous Metals Society of China* **22**, 2198-2203, http://dx.doi.org/10.1016/s1003-6326(11)61449-0 (2012).

33 Garribba, E. & Micera, G. The Determination of the Geometry of Cu(II) Complexes: An EPR Spectroscopy Experiment. *Journal of Chemical Education* **83**, 1229, http://dx.doi.org/10.1021/ed083p1229 (2006).

34 Husáriková, L. *et al.* Unusual EPR Spectra with Inverse Axial g values of Chlorosalicylate–Cu(II)–2,6-Pyridinedimethanol Complex in Frozen Water–Methanol Solution. *Applied Magnetic Resonance* **44**, 571-582, http://dx.doi.org/10.1007/s00723-012-0431-9 (2013).

35 Tsybizova, A. *et al.* Speciation Behavior of Copper(II) Acetate in Simple Organic Solvents – Revealing the Effect of Trace Water. *European Journal of Inorganic Chemistry* **2014**, 1407-1412, http://dx.doi.org/10.1002/ejic.201400036 (2014).

36 Mikuriya, M. *et al.* Copper(II) Carboxylates with 2,3,4-Trimethoxybenzoate and 2,4,6-Trimethoxybenzoate: Dinuclear Cu(II) Cluster and μ-Aqua-Bridged Cu(II) Chain Molecule. *Magnetochemistry* **7** http://dx.doi.org/10.3390/magnetochemistry7030035 (2021).

37 Günter, T. *et al.* The SCR of NOx with NH3 Examined by Novel X-ray Emission and X-ray Absorption Methods. *Topics in Catalysis* **59**, 866-874, http://dx.doi.org/10.1007/s11244-016-0561-7 (2016).

38 Zhang, R., Li, H. & McEwen, J.-S. Chemical Sensitivity of Valence-to-Core X-ray Emission Spectroscopy Due to the Ligand and the Oxidation State: A Computational Study on Cu-SSZ-13 with Multiple H2O and NH3 Adsorption. *The Journal of Physical Chemistry C* **121**, 25759-25767, http://dx.doi.org/10.1021/acs.jpcc.7b04309 (2017).

39 Persson, I. *et al.* EXAFS Study on the Coordination Chemistry of the Solvated Copper(II) Ion in a Series of Oxygen Donor Solvents. *Inorg Chem* **59**, 9538-9550, http://dx.doi.org/10.1021/acs.inorgchem.0c00403 (2020).

40 Fulton, J. L., Hoffmann, M. M. & Darab, J. G. An X-ray absorption fine structure study of copper(I) chloride coordination structure in water up to 325°C. *Chemical Physics Letters* **330**, 300-308, http://dx.doi.org/https://doi.org/10.1016/S0009-2614(00)01110-6 (2000).

41 Wang, J., Su, F. & Shi, L. Crystal structure of tetrakis[μ-2-(methoxycarbonyl)benzoato-κ2O1:O1′]bis[(N,N-dimethylformamide-

κO)copper(II)](Cu—Cu) dimethylformamide disolvate. *Acta Crystallographica Section E Crystallographic Communications* **74**, 691-694, http://dx.doi.org/10.1107/s2056989018005893 (2018).

42 van Niekerk, J. N. & Schoening, F. R. L. A new type of copper complex as found in the crystal structure of cupric acetate, Cu2(CH3COO)4.2H2O. *Acta Crystallographica* **6**, 227-232, http://dx.doi.org/doi:10.1107/S0365110X53000715 (1953).

43 Anh-Nga, N. T., Tuan-Anh, N., Thanh-Quoc, N. & Ha, D. T. (2018).

44 Lai, T. *et al.* in *2018 19th International Conference on Electronic Packaging Technology (ICEPT)*. 1702-1705.

45 Bai, Y., Yang, T., Gu, Q., Cheng, G. & Zheng, R. Shape control mechanism of cuprous oxide nanoparticles in aqueous colloidal solutions. *Powder Technology* **227**, 35-42, http://dx.doi.org/10.1016/j.powtec.2012.02.008 (2012).

46 Bentea, L., Watzky, M. A. & Finke, R. G. Sigmoidal Nucleation and Growth Curves Across Nature Fit by the Finke–Watzky Model of Slow Continuous Nucleation and Autocatalytic Growth: Explicit Formulas for the Lag and Growth Times Plus Other Key Insights. *The Journal of Physical Chemistry C* **121**, 5302-5312, http://dx.doi.org/10.1021/acs.jpcc.6b12021 (2017).

47 Liu, J. *et al.* Understanding the Solvent Molecules Induced Spontaneous Growth of Uncapped Tellurium Nanoparticles. *Sci Rep* **6**, 32631, http://dx.doi.org/10.1038/srep32631 (2016).

48 Hussain, M. H. *et al.* Synthesis of Various Size Gold Nanoparticles by Chemical Reduction Method with Different Solvent Polarity. *Nanoscale Res Lett* **15**, 140, http://dx.doi.org/10.1186/s11671-020-03370-5 (2020).

49 Origin(Pro). Version 2023. *OriginLab Corporation, Northampton, MA, USA*.

50 Basham, M. *et al.* Data Analysis WorkbeNch (DAWN). *J Synchrotron Radiat* **22**, 853-858, http://dx.doi.org/10.1107/S1600577515002283 (2015).

51 Ravel, B. & Newville, M. ATHENA, ARTEMIS, HEPHAESTUS: data analysis for X-ray absorption spectroscopy using IFEFFIT. *J Synchrotron Radiat* **12**, 537-541, http://dx.doi.org/10.1107/S0909049505012719 (2005).

52 Newville, M. Larch: An Analysis Package for XAFS and Related Spectroscopies. *Journal of Physics: Conference Series* **430**, 012007, http://dx.doi.org/10.1088/1742-6596/430/1/012007 (2013).

53 Virtanen, P. *et al.* SciPy 1.0: fundamental algorithms for scientific computing in Python. *Nat Methods* **17**, 261-272, http://dx.doi.org/10.1038/s41592-019-0686-2 (2020).

54 Francisco de la Peña, Eric Prestat, Tonaas, V., Fauske & Pierre Burdet, J. L., Petras Jokubauskas, Tom Furnival, Magnus Nord, Tomas Ostasevicius, Katherine E. MacArthur, Duncan N. Johnstone, Mike Sarahan, Joshua Taillon, Thomas Aarholt, Vadim Migunov, Alberto Eljarrat, Jan Caron, Carter Francis,Håkon Wiik Ånes. hyperspy/hyperspy: v1.7.6 (v1.7.6). *Zenodo* http://dx.doi.org/10.5281/zenodo.10151686 (2023).

55 Newville, M., Stensitzki, T., Allen, D. B. & Ingargiola, A. *LMFIT: Non-Linear Least-Square Minimization and Curve-Fitting for Python*. (2014).

56 Muñoz, M., Farges, F. & Argoul, P. Continuous Cauchy wavelet transform of XAFS spectra. *Physica Scripta* **2005**, 221, http://dx.doi.org/10.1238/Physica.Topical.115a00221 (2005).

Chapter 7. Rate of Electrochemical Cu Oxidation with Fast-Switching

The carbon dioxide reduction reaction (CO_2RR) is an important reaction, commercial and environmentally, for the conversion of CO_2 to value-added chemicals and the removal of CO_2 from the atmosphere. To date, the synthetic products formed during CO_2RR are difficult to predict, and the product conversion and selectivity are often not commercially viable. Cu foil and Cu nanoparticles are currently the most effective and widely-reported catalysts. The improved catalytic activity observed with Cu for the formation of C_{2+} reaction products, has been linked to the oxidation state of the Cu surface.

We present a study of the formation of Cu^0, Cu^{1+} and Cu^{2+} oxidation states, measured with microsecond (μs) time-resolved *in situ* X-ray absorption spectroscopy (XAS), induced by electrochemical square-wave (SW) cycling within a CO_2RR setup. The oxidation state changes in Cu foil during electrochemical Cu oxidation in a 0.5 M KOH electrolyte are measured to understand the limitations of high-speed switching for oxidation and the rate of formation of oxidised Cu species at the surface. This chapter is a preliminary study, to explore fundamental aspects of Cu oxidation for potential use in CO_2RR. Such ultra-high-speed switching and the subsequent observations will inform future experiments for the controlled oxidation of copper, as well as providing a framework for the study of other active CO_2RR catalysts.

Notable Contributions

Contributions were made by Luke Keenan in batch XAS data fitting procedure and Ryan Wang in experimental design. Additional experimental support from Hao Gu, Jay Yan and Manxi Gong.

7.1 Introduction

The rate of oxidation is important for the Cu in the CO_2RR due to the role of oxidation states in the adsorption and reaction, leading to different selectivity for various products formed.[1] Studies of the oxidation state of the Cu catalyst determining reaction products show that a combination of Cu^0 and Cu^{1+} is most effective in selective formation of C_{2+} products during CO_2RR.[2-4] Such controlled surface oxidation states can be achieved within the same electrochemical setup by cycling the catalyst under set conditions before the reaction.

Previously published results of Cu oxidation in 0.5 M KOH, are in agreement about the Cu oxidation states corresponding to the peaks measured in the cyclic voltammetry (CV) profile.[5]

Based on the peaks in the CV, the Cu oxidation and reduction pathways have been suggested with one- and two-electron transfer stages suggested, with some stages remaining in dispute. The mechanisms and surface species may also change depending on the scan rate, electrolyte concentration, electrolyte composition, and other factors that affect the Cu surface. A combination of three processes is considered likely for the Cu oxidation reaction – (1) Cu_2O formation (peak A), (2) $Cu(OH)_4^{2-}$ and $Cu(OH)_2$ formation (peak B_1), and (3) CuO and $Cu(OH)_2$ formation (peak B_2).

Before peak A, $Cu(OH)_2$ is believed to occur either directly (Equation 7.1) or *via* the two-step process with intermediate formation of Cu_2O (Equation 7.2).

$$2Cu + 2OH^- \rightarrow Cu(OH)_2^- + e^- \qquad \textit{Equation 7.1}$$

$$2Cu + 2OH^- \rightarrow Cu_2O + H_2O + 2OH^- \rightarrow 2Cu(OH)_2^- + H_2O \qquad \textit{Equation 7.2}$$

Next, in peak A the formation of Cu_2O may follow the first stage of Equation 7.2, or Equation 7.3 has also been suggested as a reaction pathway.[6]

$$2Cu(OH) \leftrightarrow Cu_2O + H_2O \qquad \textit{Equation 7.3}$$

For peak B_1, a combination of Equations 7.4 and 7.5 are considered likely, forming a combination of $Cu(OH)_2$ and $Cu(OH)_4^{2-}$, proposed by Ambrose et al., with low KOH concentrations (such as 0.1 M).[5,6]

$$Cu + 2OH^- \rightarrow Cu(OH)_2 + 2e^- \qquad \textit{Equation 7.4}$$

$$Cu_2O + H_2O + 6OH^- \rightarrow 2Cu(OH)_4^{2-} + 2e^- \qquad \textit{Equation 7.5}$$

And in peak B_2, Equations 7.6 and 7.7 give rise to $Cu(OH)_2$ and CuO species.

$$Cu(OH)_4^{2-} \rightarrow Cu(OH)_2 + 2OH^- \qquad \textit{Equation 7.6}$$

$$Cu(OH)_2 \rightarrow CuO + H_2O \qquad \textit{Equation 7.7}$$

For the reverse scan, peak C is attributed to a partial reduction of oxide species formed in peak B_2. Since CuO reduction has higher driving force than $Cu(OH)_2$ reduction, this is considered the most likely reaction. Peak D may correspond to the reduction of remaining oxide species, including those formed during peak B_1.[5]

Previous research has correlated changes in the crystalline surface structure with CV results using *in situ* GIXRD.[7] This *in situ* observation found that the transition of Cu^0 to Cu^{2+} formed a crystalline Cu_2O (cuprite) intermediate, measured in 0.2 M KOH electrolyte. *In situ* shell-isolated nanoparticle-enhanced Raman spectroscopy (SHINERS) was further able to confirm the formation of an OH species before Cu_2O formation in KOH electrolyte.[8] The rate of this Cu oxidation could be further ascertained by an *in situ* XAS observation, proposed in this work.

We present the experimental measurement of Cu oxidation rate measured with ultra-high time-resolved *in situ* XAS. 5 μm Cu foil was selected as the Cu surface

of interest due to the large surface area and uniform structure. Oxidation was measured in 0.5 M KOH to follow the applied CO_2RR conditions in previous publications.[9,10] The potential was varied for fast-switching square-wave measurements with three different ranges, to induce the formation of the various Cu oxidation states.

The study of oxidation state changes alongside electrochemical response provides a framework for the prediction of Cu oxidation control using an applied potential, and hence improved selectivity for desirable CO_2RR products. In addition, electrochemical Cu oxidation provides an ideal system for high time-resolution measurements since the reduction and oxidation are potential controlled and are not physically limited by the mixing rate of solutions. This time-scale and high rate of switching are recorded to test the limits of characterization tools and determine the rate of the physical oxidation response.

7.2 Results and Discussion

The changes in the foil surface oxidation state were mainly observed in the case of 1 s hold between potential switching, with a square-wave measurement. The working electrode was a commercially produced 5 µm Cu foil (Goodfellow, product code: CU00-FL-000150), with high purity, and crystalline structure.[11] The Cu foil was placed in a three-electrode flow cell, at the working electrode, with an Au contact wire and a Pt wire as a counter electrode. A reversible hydrogen electrode (RHE) was used as the reference electrode. 0.5 M KOH was the electrolyte[5] in which a complete cyclic voltammogram was measured to select the square-wave switching parameters.

7.2.1 Electrochemical Behaviour

First, the total Cu oxidation state changes on a CV curve were observed (Figure 7.1). The shape of the curve corresponds with the literature values,[5,7] although the peak intensity is lower, likely due to resistance within the cell setup. Relevant peaks are labelled 1 to 9, to further explain the results and the expected Cu oxidation states.

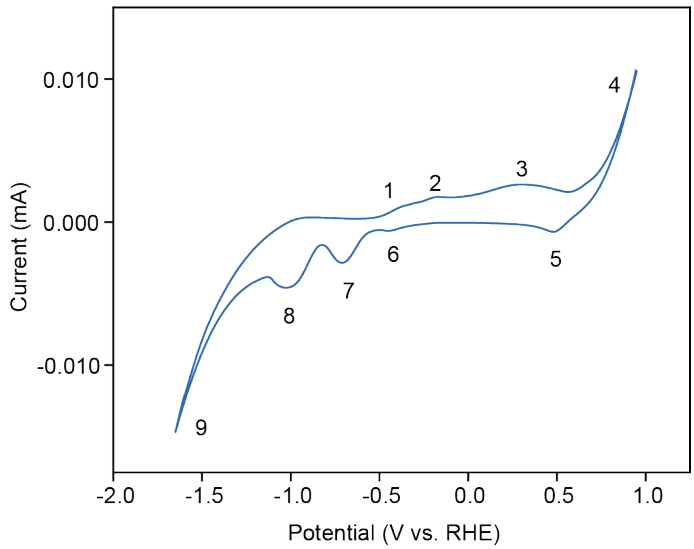

Figure 7.1 ***Experimental Observation of Copper CO_2RR CV Peaks.*** *Cu oxidation CV peaks observed experimentally with a 5 µm thick Cu foil working electrode in 0.5 M KOH electrolyte, measured at a scan rate of 50 mV.s^{-1}. The principal peaks labelled 1 to 9 correspond with (1) preliminary $Cu(OH)_2$ formation, (2) Cu_2O and $Cu(OH)_2$ formation, (3) $Cu(OH)_2$ and CuO formation, (4) end of CV scan range, (5) small extra peak for discussion, (6, 7) Cu from CuO, (8) Cu from $Cu(OH)_2$ and remaining CuO, and (9) beginning of scan range and oxygen evolution reaction.*

The peak positions show the potentials at which the various Cu oxidation states are formed (Table 7.1). Positions 1 and 2 are believed to indicate the formation of Cu^{1+} species, while Cu^{2+} species are formed at position 3. After initiating the reverse cycle, Cu^{2+} oxides are first reduced to metallic Cu at position 6 and 7, followed by Cu^{1+} reduction to Cu^0 at position 8. Position 5 is a minor peak observed during CV, which is attributed to the early reduction of Cu species.

Table 7.1 ***Peak Positions in CO_2RR CV.*** *Brief descriptions of the various peaks are given, alongside the voltage for switching which is selected at a value beyond the peak position.*

Peak No.	Voltage (V)	Voltage for Switching (V)	Description	Cu Oxidation State Transitions
1	-0.500	-	$Cu \rightarrow Cu(OH)_2$	($Cu^0 \rightarrow Cu^{1+}$)
2	-0.190	(-0.285)	$Cu \rightarrow Cu_2O$ or $Cu(OH)_2$	($Cu^0 \rightarrow Cu^{1+}$)
3	0.290	(0.500)	Cu_2O and $Cu(OH)_2 \rightarrow CuO$	($Cu^{1+} \rightarrow Cu^{2+}$)
4	1.000	-	End of Scan Range	-
5	0.500	-	Small Peak of Interest	-
6, 7	-0.695	(-0.800)	$CuO \rightarrow Cu$	($Cu^{2+} \rightarrow Cu^0$)
8	-1.000	(-1.550)	$Cu(OH)_2 \rightarrow Cu$	($Cu^{2+} \rightarrow Cu^0$)
9	-1.650	-	OER, region for CO_2RR	-

Of the labelled positions, three potential ranges were selected to study Cu oxidation behaviour. Aiming to switch between two oxidation states of interest, potential ranges for $Cu^0 \leftrightarrow Cu^{1+}$, $Cu^0 \leftrightarrow Cu^{2+}$ and $Cu^{1+} \leftrightarrow Cu^{2+}$ are given in Table 7.2. The Cu foil was cycled to reset the surface between measurements. Similar

square-wave oxidation performed in concentrated KOH, switching between Cu^0 (-0.75 V) and Cu^{1+} (-0.45 V) potentials, showed significant oxidation.[12]

Table 7.2 ***Voltages Selected for Square-Wave Measurements.*** *The experimental conditions selected for the square-wave switching of a 5 μm thick Cu foil in Ar-purged 0.5 M KOH.*

Sr. No.	Low Voltage (V)	High Voltage (V)	Description
1	-1.550	-0.285	$Cu^0 \leftrightarrow Cu^{1+}$
2	-1.550	0.500	$Cu^0 \leftrightarrow Cu^{2+}$
3	-0.800	0.500	$Cu^{1+} \leftrightarrow Cu^{2+}$

While applying the desired potential, the XAS measurements were recorded, automatically triggered at the same time as electrochemical switching, to reduce error in aligning the two datasets.

7.2.2 Rate of Cu Oxidation

The *in situ* XAS results are compared for 1 s and 10 ms hold time between potential switching. The first observation, before normalisation, is a set of peaks observed at 1.25 second intervals under each reaction condition (Figure 7.2). However, this changing intensity is also apparent in the pre-edge region and is therefore expected to be an artefact of the experimental setup. Further evidence that the peaks are background noise is that they do not directly correspond with the electrochemical switches applied to the Cu foil.

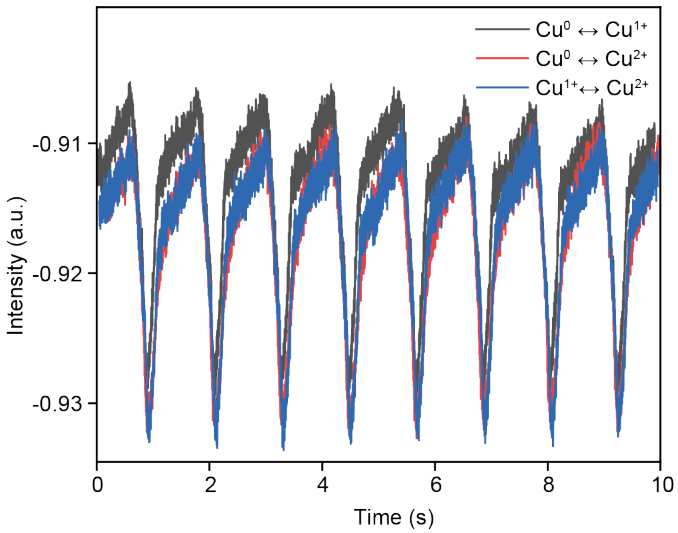

Figure 7.2 ***Cu Oxidation Background Peaks.*** *An initial Cu K-edge XANES LCF provides a similar trend of peaks under all cycling conditions. Peaks in condition 1 (grey), condition 2 (red) and condition 3 (blue) are attributed to background variations in XAS absorption, likely due to a pressure build-up within the electrochemical flow cell.*

After normalisation, these peaks disappear, and the data can be analysed directly to observe changes in the Cu oxidation state. A profile of intensity over time at 8955 eV shows that the normalisation has set the pre-edge linear region at a constant value (Figure 7.3 a), removing the noise signal. When the profile is observed at the edge position of 8983 eV, a clear trend of changing intensity over 10 switches is apparent (Figure 7.3 b). These correspond with the expected oxidation state changes during potential switching.

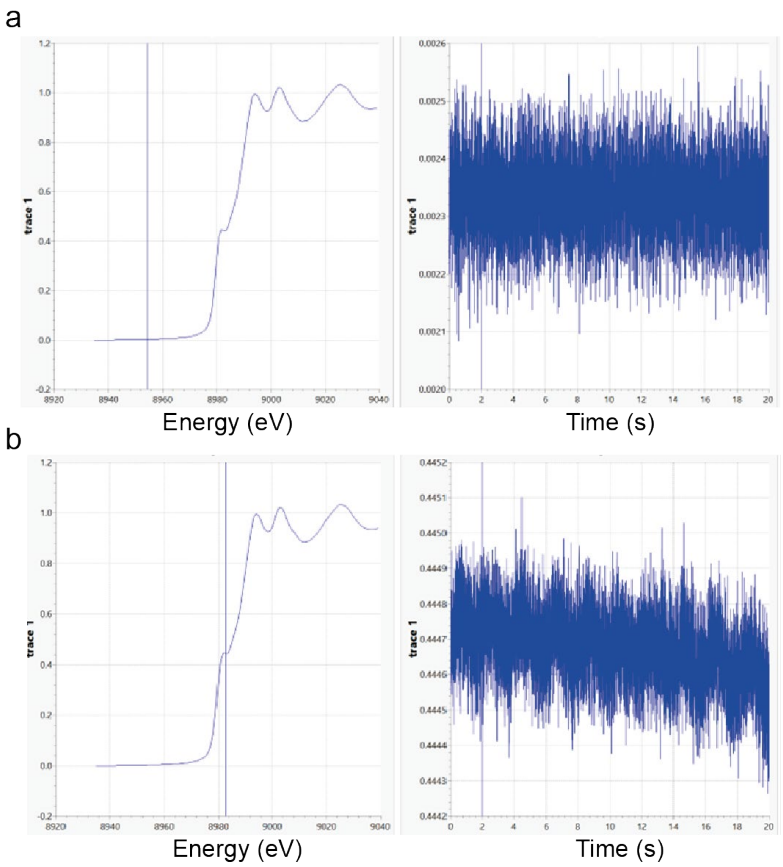

Figure 7.3 ***Normalisation Enhanced Oxidation State Changes.*** *Normalised Cu K-edge XANES show (a) no background changes, while (b) 10 distinct cycles are observed at the edge position, for Cu foil in 0.5 M KOH under a potential switching between -1.55 V to 0.5 V, likely due to surface oxidation.*

Based on the change in absorption, the transition between oxide species could be estimated from the peak intensity, measured at the same energy for all three cases of switching potentials. From standard Cu K-edge XANES spectra of Cu^{0}, Cu^{1+} and Cu^{2+} standards, measured for Cu foil, Cu_2O and CuO, respectively (Figure 7.4), the trend of intensity changes at 8983 eV are determined. As shown, the highest intensity at this position is measured for Cu_2O, while the lowest intensity is in CuO. Assuming that the surface initially contains Cu^{0} (due to cycling before the reaction), then an increase in intensity can be seen as oxidation to Cu^{1+} and reduced intensity as the oxidation to Cu^{2+}.

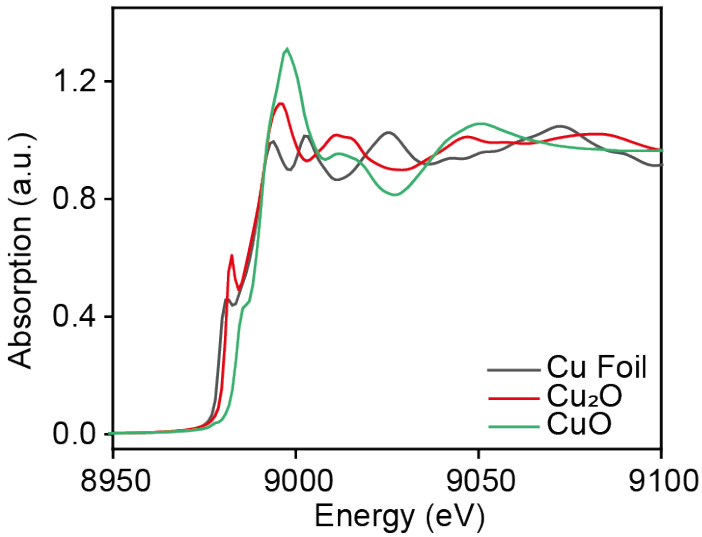

Figure 7.4 ***XANES Spectra of Cu Standards.*** *Cu K-edge XAS results show normalised XANES spectra of CuO (green), Cu_2O (red) and Cu foil (black) standards between 8950 and 9100 eV.*

To further compare the results obtained for different oxidation state switches, the rate of the oxidation was observed from changes in the XANES region for three different square-wave (SW) cycled experiments (Figure 7.5 a-c). Smoothing of the resulting data gives a clearer visualisation of the oxidation state changes observed to correspond with the electrochemical switches. The electrochemical data, captured simultaneously, also shows a reversible trend of current response (Figure 7.5 d-f).

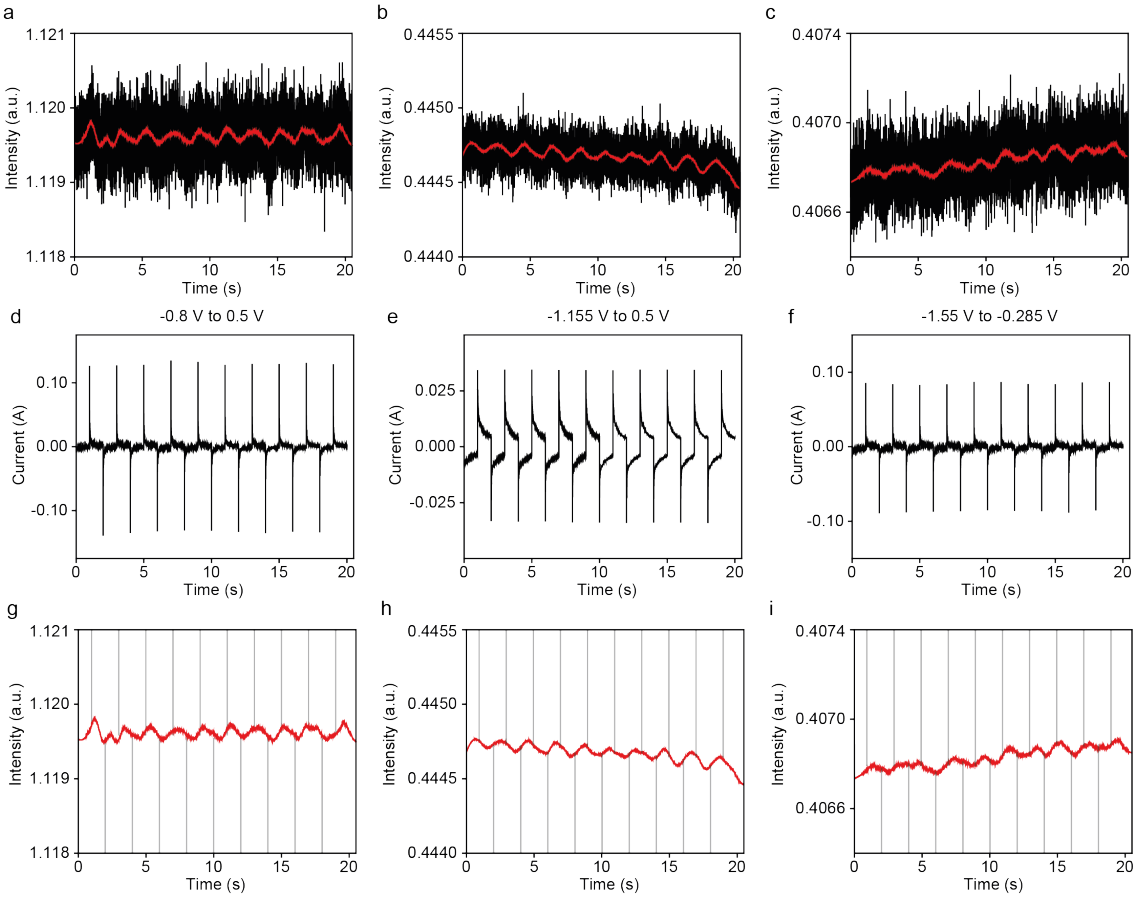

Figure 7.5 ***XANES Cu Oxidation Peaks for 1 s SW Switches.*** *Cu K-edge XANES oxidation peaks, measured as change in intensity of edge position are shown for (a) -0.8 V to 0.5 V switch ($Cu^{1+} \leftrightarrow Cu^{2+}$), (b) -1.55 V to 0.5 V switch ($Cu^{0} \leftrightarrow Cu^{2+}$) and (c) -1.55 V to -0.285 V switch ($Cu^{0} \leftrightarrow Cu^{1+}$) are shown above (d-f) their corresponding electrochemical results for 1 s square-wave switches and (g-i) the combined visualisation of XANES variations with switching times.*

A temporal comparison of the current response peaks and the XAS results indicate that there is a lag in the oxidation state changes. For the case of -0.8 V to 0.5 V switch, an average lag of 0.358 ± 0.191 s is observed between the electrochemical switch and the oxidative response. Similar average lag times of 0.602 ± 0.172 s and 0.355 ± 0.209 s were measured for -1.55 V to 0.5 V and -1.55 V to -0.285 V, respectively (Table 7.3).

Table 7.3 ***Lag Times in XAS Response to Potential Switches.*** *The lag time in the Cu K-edge XAS response is measured from the zero-crossing in the derivative, which corresponds to the turning points between oxidation states. These are compared to current peaks measured in the electrochemical response.*

Potential Switch Range (V)	Number of switches	Mean Lag Time (s)	Error (s)	Minimum (s)	Maximum (s)
-0.8 to 0.5	20	0.35788	0.19087	0.04842	0.65871
-1.55 to 0.5	20	0.60215	0.17241	0.0145	0.86301
-1.55 to -0.285	20	0.35509	0.20926	-0.23888	0.71666

The rate of oxidation can also be measured from the slope of the XANES peaks. Rates are measured for peak ascent and descent, for comparison of the oxidation and reduction rates (Figure 7.6). It can be assumed that the ascent, starting from Cu^0, measures the formation of Cu^{1+} and descent the oxidation to Cu^{2+}. In the case of

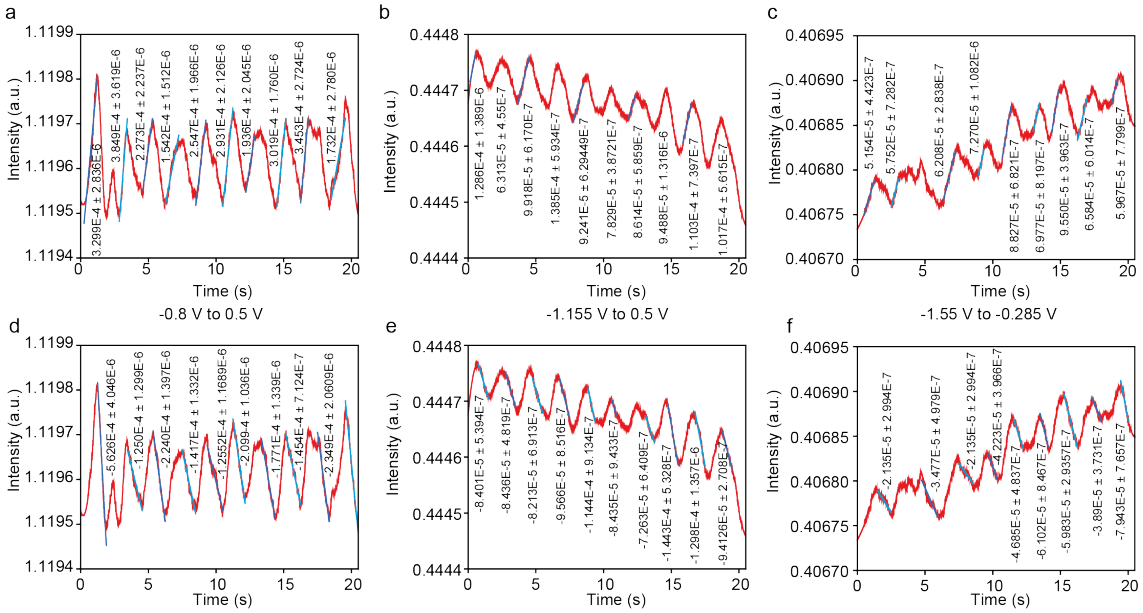

Figure 7.6 ***Rate of Change of XANES Cu Oxidation Peaks at 1 s.*** *The rate of change of each peak is measured using a linear fit (blue) on the data (red), for (a-c) oxidation and (d-f) reduction of Cu for (a, d) -0.8 V to 0.5 V switch, (b, e) -1.55 V to 0.5 V switch and (c, f) -1.55 V to -0.285 V switch. Noisy data was not measured, and the calculated slope values are given beside the peak.*

The rate of oxidation measured at each condition is compared in Table 7.4. These results can be taken as the rate of $Cu^{1+} \leftrightarrow Cu^{2+}$ (-0.8 V to 0.5 V), $Cu^{0} \leftrightarrow Cu^{2+}$ (-1.55 V to 0.5 V) and $Cu^{0} \leftrightarrow Cu^{1+}$ (-1.55 V to -0.285 V) switches between holding potentials for 1 second. The average rates of oxidation in the ascending peaks are 265.864 ± 2.361 s^{-1}, 80.718 ± 0.714 s^{-1} and 71.294 ± 0.652 s^{-1} for $Cu^{2+} \rightarrow Cu^{1+}$, $Cu^{2+} \rightarrow Cu^{0}$ and $Cu^{0} \rightarrow Cu^{1+}$, respectively. The corresponding descending peaks have average rates of -225.827 ± 1.599 s^{-1}, -98.591 ± 0.722 s^{-1} and -48.726 ± 0.512 s^{-1}, attributed to $Cu^{1+} \rightarrow Cu^{2+}$, $Cu^{0} \rightarrow Cu^{2+}$ and $Cu^{1+} \rightarrow Cu^{0}$, respectively.

Table 7.4 ***Measured Rates of XANES Cu Oxidation.*** *Table of rates measured for the rising (climb) and falling (descent) slopes of Cu K-edge XANES data, corresponding to $Cu^{1+} \leftrightarrow Cu^{2+}$, $Cu^{0} \leftrightarrow Cu^{2+}$ and $Cu^{0} \leftrightarrow Cu^{1+}$ reactions, with their calculated averages.*

	-0.8 V to 0.5 V (s^{-1})		-1.55 V to 0.5 V (s^{-1})		-1.55 V to -0.285 V (s^{-1})	
Climb	$Cu^{2+} \rightarrow Cu^{1+}$	Error	$Cu^{2+} \rightarrow Cu^{0}$	Error	$Cu^{0} \rightarrow Cu^{1+}$	Error
1	329.930	2.837	128.667	1.389	51.546	0.442
2	384.923	3.620	63.136	0.456	57.521	0.728
3	227.386	2.237	-84.515	0.424	62.082	0.284
4	154.259	1.513	99.184	0.617	72.705	1.083
5	254.740	1.966	138.577	0.593	88.279	0.682
6	293.152	2.126	92.414	0.629	69.780	0.820
7	193.646	2.046	78.297	0.387	95.501	0.396
8	301.994	1.760	86.149	0.586	65.850	0.601
9	345.326	2.724	94.881	1.317	59.670	0.780
10	173.279	2.781	110.386	0.740	88.000	0.700
Average	265.864	2.361	80.718	0.714	71.294	0.652
Descent	$Cu^{1+} \rightarrow Cu^{2+}$	Error	$Cu^{0} \rightarrow Cu^{2+}$	Error	$Cu^{1+} \rightarrow Cu^{0}$	Error
1	-562.686	4.047	-84.014	0.539	-23.761	0.402
2	-125.052	1.300	-84.368	0.482	-34.770	0.498
3	-224.040	1.398	-82.136	0.691	-21.351	0.299
4	-141.732	1.333	-95.663	0.852	-42.236	0.397
5	-125.529	1.169	-114.475	0.913	-46.483	0.484
6	-209.950	1.037	-84.355	0.943	-61.022	0.847
7	-177.115	1.339	-72.635	0.641	-59.834	0.294
8	-145.463	0.712	-144.318	0.533	-38.931	0.373
9	-234.972	2.061	-129.817	1.358	-79.434	0.766
10	-311.727	1.599	-94.127	0.271	-46.483	0.484
Average	-225.827	1.599	-98.591	0.722	-48.726	0.512

The discrepancy in rates indicates that the oxidised species formed at the surface may not be entirely reversible, especially in the case of Cu^{1+} formation. $Cu^{2+} \leftrightarrow Cu^{1+}$ show an average descending slope (reduction) 40.037 ± 3.960 s^{-1} lower than the ascending slope (oxidation). This indicates that Cu^{1+} is more readily formed at the surface and reduces reluctantly. Similarly, $Cu^{1+} \leftrightarrow Cu^{0}$ switching shows an averaged descending slope (reduction) 22.568 ± 1.164 s^{-1} lower than the ascending slope (oxidation). In the case of $Cu^{2+} \leftrightarrow Cu^{0}$, the ascending slope ($Cu^{2+}$ reduction to Cu^{0}) is 17.873 ± 1.436 s^{-1} lower than the descending slope (oxidation). Thus, it could be generally confirmed from these results that the oxidation at the surface occurs more readily than reduction.

To test the limit of oxidation rate measurements, a similar experiment was recorded 100 times faster at the µs-scale (Figure 7.7). The resulting XANES data shows a similar response to the applied voltage, but the resolution is not sufficient to measure rate information. In addition, the oxidation and reduction peaks have some offset from the electrochemical results, likely due to switching faster than the stabilisation time of the oxidation state.

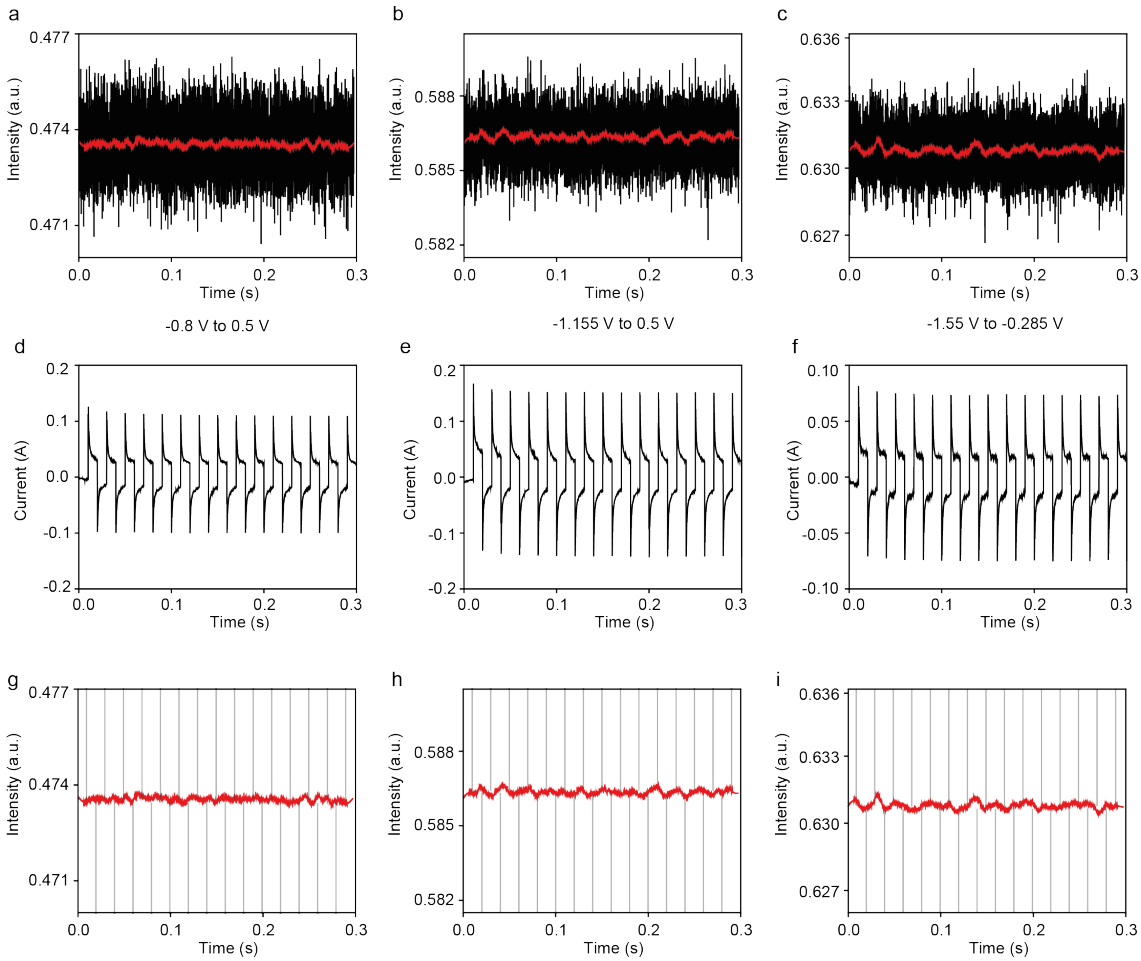

Figure 7.7 ***XAS Cu Oxidation Peaks for 10 ms SW Switches.*** *Cu K-edge XANES oxidation peaks, measured as change in intensity of edge position for (a) -0.8 V to 0.5 V switch, (b) -1.55 V to 0.5 V switch and (c) -1.55 V to -0.285 V switch are shown above (d-f) their corresponding electrochemical results for 1 s square-wave switches and (g-i) the combined visualisation of XANES variations with switching times.*

7.3 Outcomes

In this work, we show that the rates of formation of Cu oxide species, of fundamental interest for potential CO_2RR applications, can be controlled by electrochemical modulation at the µs time-scale. Ultra-high time-resolution *in situ* XAS measurement results show the rates of Cu oxidation at the µs-scale. The

formation of oxide species is found to closely follow the electrochemical response, although often with a lag. Cu oxidation rates of 265.864 ± 2.361 s^{-1}, 80.718 ± 0.714 s^{-1} and 71.294 ± 0.652 s^{-1} are measured for $Cu^0 \leftrightarrow Cu^{1+}$, $Cu^0 \leftrightarrow Cu^{2+}$ and $Cu^{1+} \leftrightarrow Cu^{2+}$ conversions, respectively, while holding potentials for 1 second. This indicates that the formation of Cu^{1+}species occurs more readily than Cu^{2+}.

These results show that the formation of oxide species at the surface could be modulated with fast switching within a desired potential range before measuring a reaction, for improved catalytic activity. For a combination of Cu^{1+} and Cu^0 at the surface, as suggested for CO_2RR, a potential range of -0.8 V to 0.5 V with fast square-wave switching (as applied in this work) would increase Cu^{1+} formation at the surface.

The same cycles recorded with 10 ms switching, show poor a match between the electrochemical response and oxidation states, indicating that there may not be sufficient time for stabilisation of an oxidised Cu species at the surface.

These preliminary results would benefit greatly from further research, to answer questions such as:

1. How does the oxidation rate change with the voltage range selected? This could be experimentally measured by comparing time-resolved data at different voltages and calculating the rate in each case, to find the optimal switching for Cu^{1+} formation.
2. How does the electrolyte determine the oxidation state at the surface? Measurements could be performed under a range of electrolytes, to observe which is most conducive to each oxidation state.

3. Does the oxidation-state-controlled surface show improved CO_2RR activity? And how does this work? This could be explored through the investigation of controlled surfaces and observing *in situ* changes during catalytic activity.

The current study confirms surface oxidation with fast-switch square-wave electrochemistry and indicates that Cu^{1+} stabilisation would be most readily possible while switching between the Cu^{2+} and Cu^{1+} oxidation states. Such an observation also shows the value of high time-resolution *in situ* studies, to test the limits of characterisation tools and to better understand chemical behaviours at these time-scales.

7.4 Experimental Methods

7.4.1 Cu Foil and Electrochemical Setup

A 5 μm thick Cu foil, made by Goodfellow (product code: CU00-FL-000150) was used for the study of oxidation state change. This foil had a high purity with 100 ppm of Pb and K, 25 ppm Ca and less than 10 ppm of other metals.[11] The foil is highly crystalline with face centred cubic structure and is composed of majority metallic Cu^0. Electrochemical measurements were taken within a glass chamber first, and later in the electrochemical flow cell. The electrolyte was 0.5 M KOH with DI water, both purified by cycling with a Cu sheet beforehand at extreme conditions to remove impurities of Fe within the system. This was selected based on the literature setup of similar reactions.[12-16]

7.4.2 Beamline Setup

I20-EDE Beamline at Diamond Light Source was used to record high time-resolution measurements using an XH detector, recorded at the Cu K-edge. The energy was calibrated for EDE using Cu foil. A trigger program was set up between the XAS collection software (GDA 9.26.0) and the Gamry potentiostat, to auto-align the initialisation of the measurements. Background I_0 was measured in air. XAS spectra were measured for an energy range of 8760 eV to 9705 eV (k range of 14 $Å^{-1}$), collecting 1024 pixels, converted to energy points.

The electrochemical measurements were set up with an *in situ* flow-cell designed by Yue Wen at EIL, UCL (Section 2.5.4). The cell has a continuous flow of Ar-purged 0.5 M KOH electrolyte through the inlet, allowing simultaneous Ar flow through the electrolyte to remove oxygen. A Kapton window seals the front of the cell, and the electrolyte makes contact with the Au wire and Cu foil at the working electrode connection, the Pt wire at the counter electrode and a reversible hydrogen electrode at the reference electrode. The flow of electrolyte was controlled by an external Watson-Marlow peristaltic pump was paused to prevent pressure build-up during measurements. A 1 cm^2 square of Cu foil sheet was applied at the working electrode. As the foil is not super-smoothed, surface defects are present and a combination of crystal facets are likely exposed to the electrolyte. The foil was handled carefully to avoid contamination or deformation prior to insertion into the cell.

7.4.3 Data Analysis

As the data was recording minor changes at the foil surface with high time-resolution, pushing the limitations of the instrument, a description of the data

clean-up and analysis techniques will support the results. Data analysis was initially performed with DAWN, for batch processing of large datasets.[17]

First, the cyclic data was normalised, to remove the background signal before merging. A relative normalisation was performed with a pre-edge range to -20 eV before the edge and post-edge from 100 eV after the edge, with a polynomial order of 2, “flattened”. Normalised data was merged, and noisy datasets were removed, determined using a principal component analysis (PCA) to see if the noise was greater than the signal. A PCA and XY-profile fitting were used to analyse the XANES region oxidation state changes.

Electrochemical data was compared with the XANES XY-profile data in Origin(Pro), and time lag was measured from the derivative of XANES, against the switch times. Savitsky-Golay smoothing filter for 200 points was applied to reduce noise. Slope value measurements and data analysis were performed with Origin(Pro).[18]

This separated normalisation was performed carefully to prevent reinforcement of background noise. A repetitive background signal was uniformly seen across all cases, which was later removed by the normalisation of the curves. It is believed that part of this signal could remain and be reinforced by the noise in the data, which is able to pick up and amplify such signals. Meaningful signals were obtained both through the interpretation of the changes in the data, which should not be exclusively from noise signals, and from the correspondence with the electrochemical changes introduced to the sample.

7.5 References

1 Wang, X. *et al.* Morphology and mechanism of highly selective Cu(II) oxide nanosheet catalysts for carbon dioxide electroreduction. *Nat Commun* **12**, 794, http://dx.doi.org/10.1038/s41467-021-20961-7 (2021).

2 Wang, S. *et al.* Synergistic Cu+/Cu0 on Cu2O-Cu interfaces for efficient and selective C2+ production in electrocatalytic CO2 conversion. *Science China Materials* **66**, 1801-1809, http://dx.doi.org/10.1007/s40843-022-2344-2 (2023).

3 Lv, X. *et al.* Grain refining enables mixed Cu+/Cu0 states for CO2 electroreduction to C2+ products at high current density. *Applied Catalysis B: Environmental* **324** http://dx.doi.org/10.1016/j.apcatb.2022.122272 (2023).

4 Li, H. *et al.* High-Rate CO(2) Electroreduction to C(2+) Products over a Copper-Copper Iodide Catalyst. *Angew Chem Int Ed Engl* **60**, 14329-14333, http://dx.doi.org/10.1002/anie.202102657 (2021).

5 Giri, S. D. & Sarkar, A. Electrochemical Study of Bulk and Monolayer Copper in Alkaline Solution. *Journal of The Electrochemical Society* **163**, H252-H259, http://dx.doi.org/10.1149/2.0071605jes (2016).

6 Ambrose, J., Barradas, R. G. & Shoesmith, D. W. Investigations of copper in aqueous alkaline solutions by cyclic voltammetry. *Journal of Electroanalytical Chemistry and Interfacial Electrochemistry* **47**, 47-64, http://dx.doi.org/https://doi.org/10.1016/S0022-0728(73)80344-4 (1973).

7 Scherzer, M. *et al.* Electrochemical Surface Oxidation of Copper Studied by in Situ Grazing Incidence X-ray Diffraction. *The Journal of Physical Chemistry C* **123**, 13253-13262, http://dx.doi.org/10.1021/acs.jpcc.9b00282 (2019).

8 Bodappa, N. *et al.* Early Stages of Electrochemical Oxidation of Cu(111) and Polycrystalline Cu Surfaces Revealed by in Situ Raman Spectroscopy. *J Am Chem Soc* **141**, 12192-12196, http://dx.doi.org/10.1021/jacs.9b04638 (2019).

9 Endrodi, B. *et al.* Operando cathode activation with alkali metal cations for high current density operation of water-fed zero-gap carbon dioxide electrolyzers. *Nat Energy* **6**, 439-448, http://dx.doi.org/10.1038/s41560-021-00813-w (2021).

10 Ding, J. *et al.* Atomic high-spin cobalt(II) center for highly selective electrochemical CO reduction to CH(3)OH. *Nat Commun* **14**, 6550, http://dx.doi.org/10.1038/s41467-023-42307-1 (2023).

11 Goodfellow. Copper Foil 0.005 mm Specifications.

12 Li, J. *et al.* Electroreduction of CO(2) to Formate on a Copper-Based Electrocatalyst at High Pressures with High Energy Conversion Efficiency. *J Am Chem Soc* **142**, 7276-7282, http://dx.doi.org/10.1021/jacs.0c00122 (2020).

13 Zhang, X. *et al.* Selective and High Current CO(2) Electro-Reduction to Multicarbon Products in Near-Neutral KCl Electrolytes. *J Am Chem Soc* **143**, 3245-3255, http://dx.doi.org/10.1021/jacs.0c13427 (2021).

14 Jaster, T. *et al.* Electrochemical CO(2) reduction toward multicarbon alcohols - The microscopic world of catalysts & process conditions. *iScience* **25**, 104010, http://dx.doi.org/10.1016/j.isci.2022.104010 (2022).

15 Li, T., Yang, C., Luo, J.-L. & Zheng, G. Electrolyte Driven Highly Selective CO2 Electroreduction at Low Overpotentials. *ACS Catalysis* **9**, 10440-10447, http://dx.doi.org/10.1021/acscatal.9b02443 (2019).

16 Li, L., Yang, J., Li, L., Huang, Y. & Zhao, J. Electrolytic reduction of CO2 in KHCO3 and alkanolamine solutions with layered double hydroxides intercalated with gold or copper. *Electrochimica Acta* **402** http://dx.doi.org/10.1016/j.electacta.2021.139523 (2022).

17 Basham, M. *et al.* Data Analysis WorkbeNch (DAWN). *J Synchrotron Radiat* **22**, 853-858, http://dx.doi.org/10.1107/S1600577515002283 (2015).

18 Origin(Pro). Version 2023. *OriginLab Corporation, Northampton, MA, USA*.

Chapter 8. Conclusions

The measurement of oxidation and reduction rates in a range of experiments has provided valuable insights into the fundamental chemistry behind the synthesis and oxidative behaviour of metal nanoparticles. The experiments carried out in this work, measured with *in situ* characterisation tools at increasing time-resolutions, have provided an understanding of the transient states of the system, as well as the reaction mechanisms occurring, which have not been reported before. Each chapter presents a different aspect of the advancements made possible by the *in situ* study of chemical reactions, and their combinations. These results are collated here for a unified perspective on the research, followed by a brief discussion of the outcomes and challenges faced in this field, and possible future research directions.

8.1 Research Summary

8.1.1 Pd Nanoparticle Growth with CTAC

The combination of 500 ms-resolved *in situ* XAS and *in situ* SAXS in Chapter 3 gave a multi-faceted observation of the rates and stages of nano-dendritic Pd nanoparticle growth. By comparing temporal changes in 2,400 XANES and EXAFS fittings under each condition, it was logically inferred that a reduced chlorine-coordinated Pd^0 growth species, with a measurable concentration, existed in solution rather than forming directly at the metal surface.

Captured for a 20 minute term, Pd nanoparticle growth *via* the ascorbic acid reduction of aqueous K_2PdCl_4 in the presence of CTAC displayed stages of reduction, nucleation, growth and reoxidation. *In situ* XANES (Pd oxidation state) fitting provided reduction rates at a series of temperature conditions enabling the

calculation of an activation energy of 22.59 kJ.mol^{-1} for Pd nucleation before rapid growth. *In situ* EXAFS (Pd-Pd, Pd-Cl/O C.N.) and SAXS (nanoparticle radius) fittings captured the simultaneous increase in nanoparticle size and polydispersity in the system.

The Pd growth profile observed for seeded growth (Pd, 2 to 4 nm) showed the clear obviation of the nucleation stage, irrespective of the seed concentrations introduced (ranging three orders of magnitude). The uniformity of growth profiles obtained in the presence of seeds emphasised their value for a reproducible, controlled synthesis.

This work provides three major contributions to the field of nanoparticle growth studies. First, the *in situ* measurement of effects of environmental controls (temperature, seed solution) on Pd nanoparticle synthesis provides data which could be used to train models and predict of Pd nanoparticle growth under new conditions. Second, it illustrates the value of combining characterization tools to extrapolate further mechanistic information, in this case the presence of a soluble Pd^0-Cl growth species. Lastly, it provides a methodology and successful batch-fitting results for 2400 spectra per reaction condition, for both XANES and EXAFS. Such high time-resolution observations, with a subsequent increase in data storage and analysis will likely continue to grow in future, and benefit from the development of batch methodologies.

8.1.2 Pt-Pd Alloy Nanoparticles in ORR

Such Pd nanoparticles, and their extreme ratio alloys with Pt were studied in Chapter 4. *In situ* XAS was used to explore two interesting research questions surrounding extreme ratio alloys for ORR – 1. The role of Pt-Pt coordination in

determining ORR mechanisms and activity and 2. A comparison of the *in situ* surface oxidation behaviour of a typical alloy and a low Pt-Pt C.N. alloy.

For the first, it was found that the addition of dispersed Pt sites within the Pd matrix of Pt_1Pd_{493}/C led to an increase in ORR activity (halfwave potential of 0.80 V), compared with a pure Pd/C nanoparticle (halfwave potential of 0.77 V). The increase in Pt content thereafter (Pt_1Pd_{142}, Pt_1Pd_{22}) showed little or no improvement, indicating the higher efficiency of low Pt-Pt C.N. sites. An in-depth DFT study of the theoretical response of Pt monomers and dimers in a Pd matrix concluded that the dissociative ORR mechanism would explain high activity in such materials, compared with the associative mechanism observed in bulk Pt.

Next, to compare behaviour during catalysis, an *in situ* XAS observation of Pt surface during ORR showed 12.4% oxidation in $Pt_1Pd_{2.4}$ while Pt_1Pd_{142} had a negligible oxidative response to the applied potential.

In the context of this thesis, this Chapter explored the value of *in situ* XAS, successfully captured for a challenging system (with extremely low Pt content), as a tool to provide mechanistic insights and identify descriptors for ORR activity. The rate of oxidation, here associated with passivation of the reacting surface was minimised through material design, linking material properties (such as Pt coordination environment) to the observed catalytic response. Further observation of surface changes in extreme alloys during ORR is an avenue worth exploring for future ORR catalyst materials and with *in situ* XAS this is possible for a range of alloy systems.

8.1.3 Pd Nanoparticle Growth with CTAB

While the Pd nanoparticles formed in Chapter 3 showed a nano-dendritic structure, replacing the surfactant CTAC with CTAB in Chapter 5 was found to produce a faceted block morphology. CTAB-capped growth was studied with *in situ* XAS to compare the growth profile and experimental results accompanying the new nanoparticle morphology.

In situ XAS results showed a different profile for CTAB capped growth, where rapid reduction occurred immediately and in two stages, followed by slow continuous growth, without reoxidation. The duration of each growth stage was temperature-dependent. Reduction rate measurements for a temperature series 30ºC to 60ºC resulted in a calculated activation energy of -8.20 $kJ.mol^{-1}$. This negative value is attributed to limited adsorption caused by CTAB interaction at the metal surface (which determines growth facets) competing with increased reduction rates at high temperature. The rate of growth under a range of AA concentrations showed a non-linear dependence, decreasing at high concentrations. Interestingly, under all reaction conditions for CTAB-capped growth the concentration of Pd^0-Br remained negligible, indicating a direct surface reduction, rather than in solution, contrary to CTAC-capped growth.

In the wider context, this short study showed the significance of comparing reaction systems with *in situ* measurement, to pinpoint the mechanistic differences that determine morphology. The effect of Br^- ions in comparison to Cl^- ions is in blocking the nanoparticle surface, causing an unusual growth profile, and reducing directly at the metal surface without etching at long reaction times. The same methodology would be ideal to study a wider range of surfactants and determine their effect on growth mechanisms.

8.1.4 Cu Nanoparticle Growth

The advantage of increased time-resolution for *in situ* characterisation was explored in Chapter 6, studying the growth rates and intermediate species formed during the synthesis of Cu nanoparticles. Measured with ultra-high time-resolution, the first 10 seconds of the reaction were monitored *in situ* to show the rapid formation of intermediate species at the early stages.

First, the Cu coordination and molecular structure of standard solutions of $Cu(OAc)_2$ in H_2O and DMF were studied with EPR, XAS, VtC XES and HR-XANES. It was determined that both solvents led to Cu-O coordination but Cu clustering in DMF made the solution EPR silent. Next, the study of AA reduction of $Cu(OAc)_2$ using a combination of VtC XES, HR-XANES and *in situ* XAS at two different solvent conditions showed the role of AA in forming an intermediate Cu^{1+} species, and the effect of the solvent in determining the reaction rates. The ascorbic acid reduction of $Cu(OAc)_2$ in H_2O and DMF yielded activation energies of 13.010 ± 3.231 $kJ.mol^{-1}$ and 27.169 ± 3.422 $kJ.mol^{-1}$, respectively.

A third reaction condition, the hydrazine reduction of $Cu(OAc)_2$/DMF was introduced to observe the effect of the reducing agent on intermediates formed and the resulting faceted platelet Cu nanoparticle morphology. This reaction maintained high Cu^0 content by an immediate $2e^-$ reduction, without the formation of a Cu^{1+} intermediate. Moreover, the intermediate coordination complex described as $Cu[(N_2H_4)_2]^{2+}$ acetate has Cu-N coordination and takes on an EPR active structure. The activation energy for formation of the intermediate was estimated from *in situ* EPR measurements to be 66.198 ± 23.939 $kJ.mol^{-1}$.

The overall result of this work is a presentation the data analysis of over 150,000 XAS spectra and 90,000 EPR spectra, combined with a unique combination of characterization tools to propose a reaction mechanism, generally expanding the

possibilities for *in situ* observations. The capture of the rate of change of various Cu oxidation states, Cu-Cu and Cu-O bonding, and the formation of intermediate species during three $Cu(OAc)_2$ reduction reactions has been performed for the first time and paves the way for the wider study of rate of intermediate formation. The time-resolutions of measurements were improved further, reaching the limits of current time-resolved EDE characterization for such systems, and achieving a time-resolution higher than previously reported for nanoparticle growth.

8.1.5 Cu Oxidation

The highest time-resolution achieved in this work is in the study of Cu oxidation under the influence of electrochemical switching. Three different potential ranges showed different oxidative responses, due to the formation of different Cu species at the surface. The rate of oxidation of the Cu surface was found to be 265.864 ± 2.361 s^{-1}, 80.718 ± 0.714 s^{-1} and 71.294 ± 0.652 s^{-1} for $Cu^0 \leftrightarrow Cu^{1+}$, $Cu^0 \leftrightarrow Cu^{2+}$ and $Cu^{1+} \leftrightarrow Cu^{2+}$ switches. This was not the same as the measured reduction rate for the same, which were measured to be -225.827 ± 1.599 s^{-1}, -98.591 ± 0.722 s^{-1} and -48.726 ± 0.512 s^{-1} for $Cu^0 \leftrightarrow Cu^{1+}$, $Cu^0 \leftrightarrow Cu^{2+}$ and $Cu^{1+} \leftrightarrow Cu^{2+}$, respectively. In addition, a lag in response time of 0.358 ± 0.191 s, 0.602 ± 0.172 s and 0.355 ± 0.209 s was observed for $Cu^0 \leftrightarrow Cu^{1+}$, $Cu^0 \leftrightarrow Cu^{2+}$ and $Cu^{1+} \leftrightarrow Cu^{2+}$. Based on these results, we conclude that the Cu^{1+}species forms and reduces more readily than Cu^{2+}. For a combination of Cu^{1+} and Cu^0 at the surface, as suggested for CO_2RR, a potential range of -0.8 V to 0.5 V with fast square-wave switching (as applied in this work) would increase Cu^{1+} formation at the surface.

This work serves as an initial study of the rate of surface oxidation, giving rate insights into the formation of electrochemically induced oxide species within a

reaction setup, for practical applications. Such measurements are valuable in the wider control of electrochemical surfaces for catalysts, to improve activity and selectivity. The preliminary observations could be further pursued to gain a better understanding of the surface chemistry for different oxidation states, and impact on the catalytic selectivity at the Cu surface. The time resolution of these measurements are also measured close to the nanosecond scale, reaching the limitations of observation.

8.2 Outcomes and Challenges

As a result of the research shown here, three manuscripts have been prepared for publication, with the two shorter projects requiring deeper investigation. These projects aim to further the scientific study of chemical mechanisms with advanced characterisation tools, which are versatile in their applications and valuable for future research in this rapidly-expanding field.

- Millisecond-Resolved *in situ* XAS and SAXS Study of CTAC-Capped Pd Nanoparticle Growth (Chapter 3)
- Engineering the Pt-Pt Coordination Environment to Enhance the Four-Electron Oxygen Reduction Reaction (Chapter 4)
- 1.27 ms-Resolved XAS Study of the Role of Intermediate Species in Cu Nanoparticle Growth (Chapter 6)

Some of the key innovations presented in this work, which will benefit the research community, are the use of programming for batch data-analysis (indispensable for high-resolution measurements which yield increasingly large datasets) and the exploration of the scope of *in situ* measurements on a range of characterization tools, under various reaction conditions. However, as with any

research at the boundary of technological advancement, this work has scientific limitations and challenges.

A general limitation of this research is the balance of time-resolution versus data quality. Moreover, while detailed data has been carefully collected for a range of reactions, there is a continued need to apply the results with modelling and theoretical observations for wider application of the results. This could be achieved retrospectively, but constitutes a valuable aspect of the research goal, to achieve a rational design and predict growth behaviour. Some of the practical and scientific challenges faced while carrying out this work are discussed in more detail.

The first challenge, which has been mitigated where possible, is the phenomenon of beam-induced reduction or beam-damage. Generally XAS is a non-destructive measurement tool but, when high time-resolved measurements are required, increased flux is necessary to achieve high data quality. During the *in situ* TEM visualisation (Chapter 6), Cu reduction was entirely beam-induced and was therefore considered unfeasible for a reduction reaction measurement. In this work, beam damage was limited by irradiating a solution for long periods, with a particular attenuation, and finding a condition where the effect was negligible. A secondary impact of aiming for high time-resolution characterization was the necessity for increased concentrations of solutions. Achieving quality data at high time-resolution was challenging in systems where concentration was low, so the results in this thesis may not be directly applicable to dilute lab-based synthesis techniques.

In the case of oxidation studies, the key challenge was the difficulty of isolating active sites, or even the surface of the samples using XAS. Currently, the resulting data is an average of the whole system. Furthermore, a detailed *in situ*

measurement of the reaction mechanism was made impossible by the low loading, an effect observed in Chapter 3 where Pt loading was minimal. Further investigation and experimental design with FTIR and surface-sensitive XAS is required for the direct visualisation of reaction mechanisms and oxide adsorption occurring at the surface of single atom alloys, and other extreme ratio structures which reduce the use of platinum group metals.

A final challenge worth mentioning was the use of large datasets, on the scale of millions, which required particular care in storage, management and analysis. First, the collection of data required pre-planning, since the available servers and data-capture programs were often not accustomed to holding such large files. During analysis, missteps in running batch analysis could be time consuming, and often the error could only be understood after the whole set had been run. The analysis ranges and settings were therefore trialled on single datasets before batch fitting. Faulty data was only stored for a limited time before deletion, in order to manage storage. Such analyses will become more manageable as data analysis software attunes to larger datasets and memory space increases. The batch analysis programs used in this work will also be available on GitHub for public use.

8.3 Future Work

The projects forming this thesis have some common themes which we believe are important avenues of research for the future of environmental chemistry and nanoparticle use. Outlined are some key areas of future work, related to the projects in this thesis.

In situ Characterization

The combining of *in situ* and *ex situ* characterization tools has been shown to provide valuable information about the chemical changes during a reaction leading to the confirmation of theoretical results and the observation of previously un-recorded phenomena.

From the research in Chapter 4, it is clear that further study and comparison of extreme alloys with different materials (e.g. PtNi, PtCo, etc.) and different nanoparticle morphologies would be beneficial to understanding atomic-scale behaviour in catalytic reactions. Further study of the oxidation species at the surface using *in situ* measurements and potentially FTIR, would enable measurement of the reaction species and could confirm a reaction pathway experimentally. Such works would provide a further understanding of the materials, for development of more exposed active sites in catalytic reactions, with increased stability.

The preliminary study of Cu oxidation in Chapter 7 leads naturally into future research of the products formed during CO_2RR with various loadings of different Cu oxidation states. An *in situ* study may also benefit the fundamental understanding of CO_2RR, as the knowledge surrounding the selectivity and active sites remains limited. The chemical oxidation of Cu foil may be crucial in the formation of longer-chain hydrocarbons from CO_2.

High Time-Resolution

The projects described focus largely on the increase of time-resolution for the various measurements in order to improve our understanding of the stages and mechanisms of reactions. While these are not always necessary, the development of data analysis strategies and high time-resolution techniques will

lead to more detailed measurements in future. These important features of reaction chemistry cannot be explored experimentally without high-resolution instruments, and we further believe that this could particularly help in the quest for a more complete understanding of the nucleation stage of particle growth.

Some of the faster reactions, and especially the very early stages of these, may be better observed by the use of a continuous flow set-up, where observations can be taken at various points from the initial mixing onwards. The continuous flow has the added benefit of reducing beam-damage to the solution. While this would use more materials, it might provide valuable insights into the early stages of nucleation.

Pd nanoparticle growth, explored in Chapters 3 and 5, could benefit from measurement under more reaction parameters and within different systems to find the effects on nanoparticle morphology. Further SAXS data has already been collected during the seeded growth, which remains to be analysed. In particular, time-resolved measurements of the nucleation stages and kinetically limited reactions are ideal systems for high time-resolution measurements.

The high-time-resolution achieved in Chapter 6 could be further increased with the development of new detectors and beamline setups. During the period of this research, DAWN software has already been upgraded to enable batch processing of large datasets, continually adding new features; beamlines are being further advanced to host *in situ* experiments, due to their integral research value. The SWIFT (Spectroscopy WithIn Fast Timescales) beamline under development at Diamond Light Source bodes well for the future of high time-resolution studies.

Chemical Reasoning and Rate Measurement

The application of various characterisation tools enables us to draw scientific conclusions by collecting evidence of reaction rates and intermediates. The calculation of rates and activation energies during a wide range of reactions can enable improved theoretical prediction and assist in the rational design of nanoparticles in the future. This is important in systems where improved materials, with reduced cost or increased catalytic potential are needed, so that these materials can be fine-tuned for their respective applications. The development of more precise reaction rate and activation energy determination coupled with accurate intermediate identification will provide an ever-improving framework for the comparison, understanding and prediction of chemical behaviour, as tools to engineer a sustainable future.

In conclusion, the development and understanding of environmental materials is a key area for scientific application in the future. Experimental measurements of nanoparticle synthesis and catalytic behaviour, a necessary foundation for the ‘rational design’ of catalysts, will continue to shed insights into this fundamental area of environmental chemistry. This research lays a foundation for such work and encourages a continuation of this field of studies.

Chapter 9. Additional Materials

9.1 List of Figures

Figure 1.1 Conventional and Rational Catalyst Design Routes. 21
Figure 1.2 'Rate determination' Literature Survey. 24
Figure 1.3 "Nanoparticle" Literature Survey. 28
Figure 1.4 Oxygen Reduction Reaction Pathways. 32
Figure 1.5 Summary of Nanoparticle Synthesis Methods..... 45
Figure 1.6 Free Energy with Nanoparticle Radius. 50
Figure 1.7 Stages and Concentration Profile of LaMer Growth. 53
Figure 1.8 Classical Growth Theory. 55
Figure 1.9 Sigmoidal Finke-Watzky Two-Step Growth. 57
Figure 1.10 Nanoparticle Ripening and Coalescence. 59
Figure 1.11 Growth Control Parameters..... 62
Figure 1.12 Controlling Nanoparticle Morphology. 67
Figure 2.1 X-ray Interactions with Matter..... 100
Figure 2.2 The Diamond Light Source Synchrotron. 102
Figure 2.3 Transmission and Fluorescence Mode XAS. 105
Figure 2.4 Transmission and Fluorescence Mode XAS. 106
Figure 2.5 XANES and EXAFS Region. 107
Figure 2.6 Background Subtraction for EXAFS. 109
Figure 2.7. k-Weighting EXAFS Data. 111
Figure 2.8 XAS Experimental Setup..... 113
Figure 2.9 Energy Dispersive EXAFS Setup. 115
Figure 2.10 Damping and Reproducibility in XAS Standards. 117
Figure 2.11 XAS Beam Damage in Cu Solution. 118
Figure 2.12 HR-XANES Measurement Setup. 120
Figure 2.13 VtC XES Measurement Setup. 121
Figure 2.14 SAXS Measurement Setup and Spectrum. 122
Figure 2.15 XPS Working Diagram. 126
Figure 2.16 Bragg's Law Values from XRD. 127

Figure 2.17 Spin Orbital Splitting Enables EPR Measurement. 131
Figure 2.18 EPR Spectrum, First Derivative and Concentration Effects. 132
Figure 2.19 UV-vis Working Diagram. 134
Figure 2.20 MP-AES Working Diagram. 136
Figure 2.21 Cryojet Setup for VtC and HR-XANES Measurements 141
Figure 2.22 SFM-4000 Stop-Flow Cell Working Diagram. 143
Figure 2.23 Concentration Profile of Reactants During Injection. 145
Figure 2.24 Three-Electrode Electrochemical Cell. 147
Figure 2.25 Typical ORR Sigmoidal LSV Result 151
Figure 2.26 Three-Electrode in situ Fluorescence-XAS Cell 155
Figure 2.27 Three-Electrode in situ Transmission-XAS Liquid Flow Cell 156
Figure 2.28 Determining Rate and Order of a Reaction. 157
Figure 2.29 Free Energy Diagram and Arrhenius Plot. 159
Figure 3.1 EDE Setup for Time-Resolved Spectra. 176
Figure 3.2 Time-Resolved Nanoparticle Morphology 178
Figure 3.3 Nanoparticle Growth Stages and Early Reduction 179
Figure 3.4 Temperature-Controlled LCF and EXAFS Fit Results. 181
Figure 3.5 Characterization Results for a Temperature Range. 182
Figure 3.6 Calculated Pd^0-Cl Coordination for a Temperature Range. 183
Figure 3.7 Combined Characterization Results for Seeded Growth. 185
Figure 3.8 EXAFS and LCF Fit Results for Seeded Growth. 186
Figure 3.9 Pd^0-Cl Coordination for Seed Concentration Range 187
Figure 3.10 Nanoparticles formed at different temperatures 200
Figure 3.11 Initial and Final Nanoparticle Morphology 201
Figure 3.12 XRD Results 202
Figure 3.13 Lattice spacing in crystalline Pd nanoparticles. 202
Figure 3.14. Time-Resolved MP-AES Results. 203
Figure 3.15 LCF Results for a Temperature Range 203
Figure 3.16 Reproducibility of LCF Results for a Temperature Range. 204
Figure 3.17 LCF and kLCF for a Temperature Range. 205
Figure 3.18 Time-Resolved EXAFS Fit Parameters for Pd NP Growth. 206
Figure 3.19 Reduction Rates and Arrhenius Plot 207

Figure 3.20 Time-Resolved SAXS for a Temperature Range..... 211
Figure 3.21 Temperature-Controlled Initial and Final SAXS Data. 212
Figure 3.22 P(r) Results of Seeded Growth. 214
Figure 3.23 Reproducibility of LCF Results by Seed Concentrations. 215
Figure 3.24 Selected LCF Results for Seed Concentration Range. 216
Figure 3.25 LCF and kLCF Results for Seed Concentration Range. 217
Figure 3.26 Time-Resolved EXAFS Parameters for Seeded Growth. 218
Figure 4.1 Average Nanoparticle Diameter. 229
Figure 4.2 Morphology of Pt-Pd particles over carbon. 230
Figure 4.3 XRD Results. 231
Figure 4.4 Ex situ EXAFS Fit Results..... 232
Figure 4.5 Pt coordination and PtO_2 content resolved with XAS. 235
Figure 4.6 XPS Fit Results. 236
Figure 4.7 ORR Performance..... 238
Figure 4.8 Durability Testing. 240
Figure 4.9 DFT Free Energy Calculation..... 242
Figure 4.10 In situ XAS during CV. 245
Figure 4.11 R-Space Fit Results. 246
Figure 4.12 Additional TEM Images of Pt_xPd_y/C Nanoparticles..... 257
Figure 4.13 Lattice Spacing in Pd/C nanoparticles..... 258
Figure 4.14 Nitrogen Sorption Isotherms of NP Loaded Carbon Black..... 258
Figure 4.15 CV, LSV and Tafel Results of Pt_xPd_y/C Nanoparticles. 259
Figure 4.16 EXAFS Fitting of Pt/C, Pd/C and Pt_xPd_y/C Nanoparticles..... 263
Figure 4.17 Water/Ice Bilayer Over Pt_xPd_y Slab Configurations. 272
Figure 4.18 ORR Intermediates Top-Down View. 274
Figure 4.19 Optimised O_2 Dissociation Transition States. 276
Figure 5.1 Chemical Structure of CTAB and CTAC..... 283
Figure 5.2 Morphology of CTAB- and CTAC-Capped Nanoparticles..... 287
Figure 5.3 Aggregated Small CTAB-Capped Nanoparticles..... 288
Figure 5.4 Lattice Spacing of Pd Nanoparticles with CTAB..... 288
Figure 5.5 Reaction Profile of CTAB-Capped Growth. 290
Figure 5.6 Temperature-Controlled CTAB-Capped XAS Results. 291

Figure 5.7 LCF for CTAB-Capped Temperature Range. 292
Figure 5.8 Rate Calculation and Arrhenius Plot..... 293
Figure 5.9 AA-Controlled CTAB-Capped XAS Results..... 294
Figure 5.10 Full Series LCF for CTAB AA Concentration. 295
Figure 5.11 Growth Rate for AA Concentration Range..... 296
Figure 5.12 Temperature-Controlled Pd^0 Content with CTAC and CTAB..... 297
Figure 5.13 Wavelet Transform of CTAB-capped Pd NP growth..... 298
Figure 5.14 Wavelet Transforms of CTAC-capped Pd NP growth..... 299
Figure 5.15 Morphology of CTAB-Capped Nanoparticles at 60ºC and 23ºC. . 305
Figure 5.16 Reproducibility of LCF Results for a Temperature Range. 306
Figure 5.17 Temperature-Controlled CTAB-capped LCF. 307
Figure 5.18 Reproducibility of LCF for an AA Concentration Range..... 308
Figure 5.19 AA Concentration CTAB-capped LCF. 308
Figure 6.1 Merging Repeated XAS Data. 320
Figure 6.2 Cu Growth Stages and Characterization Methods..... 323
Figure 6.3 EPR Results of Cu Salts with H_2O and DMF..... 324
Figure 6.4 HR-XANES Spectra for $Cu(OAc)_2$ Standards..... 325
Figure 6.5 HR-XANES Comparison for Cu^0, Cu^{1+} and Cu^{2+} Standards..... 326
Figure 6.6 VtC XES Spectra of $Cu(OAc)_2$ and Cu^{2+} Standards. 327
Figure 6.7 Chemical Structure of $Cu(OAc)_2$..... 328
Figure 6.8 Morphology of AA-Reduced Copper Nanoparticles..... 330
Figure 6.9 In situ EPR Results of $Cu(OAc)_2/H_2O$/AA Reduction..... 331
Figure 6.10 VtC XES and HR-XANES Results of AA-Reduction..... 332
Figure 6.11 XAS of Standards of Cu^0, Cu^{1+} and Cu^{2+}..... 333
Figure 6.12 Time-Resolved Wavelet Transforms of $Cu(OAc)_2/H_2O$/AA Reduction.
..... 334
Figure 6.13 LCF Time-Series of $Cu(OAc)_2/H_2O$/AA..... 335
Figure 6.14 XAS results for Temperature-Series of $Cu(OAc)_2/H_2O$/AA. 336
Figure 6.15 Arrhenius Plot from $Cu(OAc)_2/H_2O$/AA. 337
Figure 6.16 Wavelet Transform Time-Series during $Cu(OAc)_2$/DMF/AA. 339
Figure 6.17 LCF Profile of $Cu(OAc)_2$/DMF/AA for a Temperature Range..... 340
Figure 6.18 LCF for Temperature Series of $Cu(OAc)_2$/DMF/AA. 341

Figure 6.19 Rate and Arrhenius Plot for $Cu(OAc)_2$/DMF/AA. 342
Figure 6.20 In situ TEM Images During Cu Nanoparticle Growth..... 345
Figure 6.21 Morphology of $Cu(OAc)_2$/DMF/N_2H_4 Nanoparticles.. 347
Figure 6.22 In situ EPR Results of $Cu(OAc)_2$/DMF/N_2H_4..... 348
Figure 6.23 EPR of Copper Salts with Cu-O and Cu-N Configurations. 350
Figure 6.24 In situ UV-vis Results. 351
Figure 6.25 VtC XES and HR-XANES for $Cu(OAc)_2$/DMF Reduction..... 352
Figure 6.26 $Cu(OAc)_2$/DMF/N_2H_4 Differential VtC XES Spectra. 353
Figure 6.27 LCF of Temperature-Controlled $Cu(OAc)_2$/DMF/N_2H_4. 354
Figure 6.28 UV-vis Saturation at High Copper Concentrations. 359
Figure 6.29 EPR Calibration with $Cu(NO_3)_2$/DMF Solution. 360
Figure 6.30 Reproducibility of Temperature-Controlled EPR..... 361
Figure 6.31 VtC XES and HR-XANES Reaction Conditions..... 362
Figure 6.32 Script for Batch Data Analysis Flow Chart..... 369
Figure 6.33 EXAFS Fit of $Cu(OAc)_2$ Standards. 371
Figure 6.34 Morphology of 60ºC AA-Reduced Copper Nanoparticles. 372
Figure 6.35 Lattice Spacing in $Cu(OAc)_2$/H_2O/AA. 373
Figure 6.36 Lattice Spacing in $Cu(OAc)_2$/DMF/AA. 373
Figure 6.37 LCF of HR-XANES during $Cu(OAc)_2$/H_2O/AA Reduction. 374
Figure 6.38 LCF of HR-XANES during AA-Reduction. 374
Figure 6.39 LCF Fit for $Cu(OAc)_2$/AA in H_2O and DMF. 375
Figure 6.40 LCF Reproducibility of 12 s $Cu(OAc)_2$/H_2O/AA (Session 1)..... 376
Figure 6.41 LCF Reproducibility of 12 s $Cu(OAc)_2$/H_2O/AA (Session 2)..... 377
Figure 6.42 LCF Reproducibility of 180 s $Cu(OAc)_2$/H_2O/AA (Session 3)..... 378
Figure 6.43 LCF Profile of 180 s $Cu(OAc)_2$/H_2O/AA. 380
Figure 6.44 LCF Reproducibility of 180 s $Cu(OAc)_2$/H_2O/AA..... 381
Figure 6.45 LCF Reproducibility of 10 s $Cu(OAc)_2$/DMF/AA..... 384
Figure 6.46 LCF Results for 180 s as a Temperature Range. 386
Figure 6.47 LCF Reproducibility of 180 s $Cu(OAc)_2$/DMF/AA..... 386
Figure 6.48 $Cu(OAc)_2$/DMF/N_2H_4 Nanoparticle Morphology. 389
Figure 6.49 Lattice Spacing for $Cu(OAc)_2$/DMF/N_2H_4..... 389
Figure 6.50 LCF of HR-XANES for $Cu(OAc)_2$/DMF/N_2H_4. 390

Figure 6.51 LCF Reproducibility of 10 s $Cu(OAc)_2$/DMF/N_2H_4..... 390
Figure 7.1 Experimental Observation of Copper CO_2RR CV Peaks..... 400
Figure 7.2 Cu Oxidation Background Peaks..... 403
Figure 7.3 Normalisation Enhanced Oxidation State Changes..... 404
Figure 7.4 XANES Spectra of Cu Standards..... 405
Figure 7.5 XANES Cu Oxidation Peaks for 1 s SW Switches..... 406
Figure 7.6 Rate of Change of XANES Cu Oxidation Peaks at 1 s..... 408
Figure 7.7 XAS Cu Oxidation Peaks for 10 ms SW Switches..... 411

9.2 List of Tables

Table 1.1 Time-Resolution of in situ Measurements by Chapter..... 75
Table 2.1 Summary of X-ray Characterization Techniques..... 124
Table 2.2 SFM-4000 Stop-Flow Cell Dead Times and Volumes..... 144
Table 3.1 Temperature Settings for Pd Nanoparticle Growth with XAS..... 200
Table 3.2 Average Nanoparticles Sizes..... 201
Table 3.3 LCF Results for Temperature-Controlled Pd Growth..... 208
Table 3.4 EXAFS Results for Temperature-Controlled Pd Growth (1)..... 209
Table 3.5 EXAFS Results for Temperature-Controlled Pd Growth (2)..... 210
Table 3.6 Activation Energy Calculation..... 211
Table 3.7 SAXS Results for Temperature-Controlled Pd Growth..... 212
Table 3.8 Temperature-Controlled Peak Pd^0-Cl Concentration..... 213
Table 3.9 EXAFS Fit Results of Pd Seeds on Carbon..... 213
Table 3.10 Pd^0-Cl Peak Concentration for Seed-Controlled Growth..... 219
Table 4.1 MP-AES Results..... 228
Table 4.2 Ex situ EXAFS Fit Results..... 232
Table 4.3 J-value Calculations..... 234
Table 4.4 Electrochemical ORR Performance..... 239
Table 4.5 Free Energies of Adsorption..... 243
Table 4.6 Held-Potentials EXAFS Fitting..... 247
Table 4.7 Average Nanoparticle Size Results..... 258
Table 4.8 EXAFS Fitting Results for Pt_xPd_y/C Nanoparticles..... 264

Table 4.9 LCF of Pt L_3-edge data. 264
Table 4.10 LCF Results During $Pt_1Pd_{2.4}$/C CV. 265
Table 4.11 LCF Results During Pt_1Pd_{142}/C CV. 266
Table 4.12 LCF Results During Pt_1Pd_{142}/C Held Potentials. 267
Table 4.13 LCF Results During $Pt_1Pd_{2.4}$/C Held Potentials. 268
Table 4.14 Free Energies of Reaction at U = 1.23 V. 275
Table 4.15 Activation Barriers of Dissociation. 276
Table 5.1 Nanoparticle Size Measurements in CTAB-capped growth. 306
Table 5.2 Temperature Series LCF CTAB-Capped Pd Growth. 309
Table 5.3 EXAFS Temperature Series CTAB-Capped Pd Growth. 310
Table 5.4 AA Concentration Series LCF CTAB-Capped Pd Growth. 312
Table 5.5 EXAFS AA Concentration Series CTAB-Capped Pd Growth. 313
Table 6.1 EXAFS Refinement of $Cu(OAc)_2$ Standards. 329
Table 6.2 Rate Measurement Results for $Cu(OAc)_2$/DMF/AA. 343
Table 6.3 Temperature Settings for in situ Growth Measurements. 364
Table 6.4 Number of XAS Spectra Analysed. 365
Table 6.5 Nanoparticle Size Measurements of AA-Reduction. 372
Table 6.6 $Cu(OAc)_2/H_2O$/AA LCF Results. 378
Table 6.7 $Cu(OAc)_2/H_2O$/AA EXAFS Results. 381
Table 6.8 LCF $Cu(OAc)_2$/DMF/AA Results. 384
Table 6.9 EXAFS Results for $Cu(OAc)_2$/DMF/AA Point Fitting. 387
Table 7.1 Peak Positions in CO_2RR CV. 401
Table 7.2 Voltages Selected for Square-Wave Measurements. 402
Table 7.3 Lag Times in XAS Response to Potential Switches. 407
Table 7.4 Measured Rates of XANES Cu Oxidation. 409
Table 9.1 Selected Absorption Edge Energy for XAS Calibration. 437
Table 9.2 Symbol, Atomic Mass and Density of Elements Used. 437
Table 9.3 List of Constant Values. 438
Table 9.4 Synchrotron Facilities and Beamlines Attended. 438
Table 9.5 Conferences, Workshops and Poster Sessions. 439

Standard Values for Calculation

Table 9.1 ***Selected Absorption Edge Energy for XAS Calibration.***

Element	Atomic Mass (amu)	Edge	Absorption Energy (eV)
Palladium	106.42	K	24350
Platinum	195.084	L_3	11564
Copper	63.546	K	8979

Table 9.2 ***Symbol, Atomic Mass and Density of Elements Used.***

Element	Symbol	Atomic Mass	Density g/cm^3 at 20°C
Hydrogen	H	1.01	0.000084
Boron	B	10.81	2.370
Carbon	C	12.01	1.700
Nitrogen	N	14.01	0.0012
Oxygen	O	15.99	0.0013
Sodium	Na	22.99	0.971
Chlorine	Cl	35.45	0.003
Potassium	K	39.10	0.862
Nickel	Ni	58.69	8.902
Copper	Cu	63.55	8.960
Ruthenium	Ru	101.07	12.4
Palladium	Pd	106.42	12.0
Platinum	Pt	195.08	21.5

Table 9.3 ***List of Constant Values.***

Constants	Symbol	Value	Units
Molar Gas constant	R	8.3145	$J.mol^{-1}.K^{-1}$
Pi	π	3.1416	-
Avogadro's Number	N_A	6.022×10^{23}	mol^{-1}
Atomic Mass Constant	amu	1.6605×10^{-27}	kg
Faraday Constant	F	9.6485×10^{4}	$J.mol^{-1}$
Planck's Constant	h	6.6261×10^{-34}	J.s

9.3 Academic Activities

This section will detail additional experimental work carried out, in collaboration, through the course of the thesis.

Table 9.4 ***Synchrotron Facilities and Beamlines Attended.***

Synchrotron Facility	**Beamlines Attended**
Diamond Light Source, Harwell, UK	E-02
	B-07B
	B-07C
	B-18
	I-20 EDE
	I-20 Scanning
	I-22
BESSY II, Berlin, Germany	ISISS, soft X-ray beamline
DESY, Hamburg, Germany	P64
PAL, Pohang, South Korea	8A2 AP-XPS, soft X-ray beamline
SPring-8, Sayo, Japan	BL01B1, hard X-ray beamline

Table 9.5 ***Conferences, Workshops and Poster Sessions.***

Event	**Year**	**Capacity**
Cardiff Catalysis Conference	2019	Attendee
Toyota-visit Poster Session, MCL	2019	Poster Presentation
SElectrochem Conference	2019	Poster Presentation
UK Catalysis Conference	2020	Oral Presentation
XAFS workshop (Diamond Light Source)	2020	Attendee
ISE conference 2020 (online)	2020	Poster Presentation
Hyperspy workshop (online)	2021	Attendee
UCL ChemEng Poster and 3MT Competition	2021	Poster Presentation
IXS Conference	2022	Poster Presentation

9.4 Publications with Authorship Contributions

The following papers were published in which authorship contributions were made.

Adsorption and Activation of Molecular Oxygen over Atomic Copper(I/II) Site on Ceria,[1] Nature communications, 2020, Vol.11 (1), p.4008-4008 by Kang, L; Wang, B; Bing, Q; Zalibera, M ; Büchel, R; Xu, R; Wang, Q; Liu, Y; Gianolio, D; Tang, C; Gibson, E; Danaie, M; Allen, C; Wu, K; **Marlow, S**; Sun, L; He, Q; Guan, S; Savitsky, A; Velasco-Vélez, J; Callison, J; Kay, C; Pratsinis, S; Lubitz, W; Liu, J and Wang, F

Frontispiece: The Electrophilicity of Surface Carbon Species in the Redox Reactions of CuO-CeO_2 Catalysts,[2] Angewandte Chemie, 2021, Vol.133 (26) by Kang, L; Wang, B; Güntner, A; Xu, S; Wan, X; Liu, Y; **Marlow, S**; Ren, Y; Gianolio, D; Tang, C; Murzin, V; Asakura, H; He, Q; Guan, S; Velasco-Vélez, J; Pratsinis, S; Guo, Y and Wang, F

Improving the ORR Performance by Enhancing the Pt Oxidation Resistance,[3] Journal of Catalysis, 2022, Vol. 416, p. 311-321 by Xu, R; Kang, L; Papanikolaou, K; Wang, B; **Marlow, S**; He, Q; Zhang, P; Wang, J; Brett, D; Stamatakis, M and Wang, F

Designing Reactive Bridging O^{2-} at the Atomic Cu–O–Fe Site for Selective NH_3 Oxidation,[4] ACS Catalysis, 2022, Vol. 12, p. 15207-15217 by Guan, X; Han,

R; Asakura, H; Wang, Z; Xu, S; Wang, B; Kang, L; Liu, Y; **Marlow, S**; Tanaka, T; Guo, Y and Wang, F

Reversible Lithium Storage in sp^2 Hydrocarbon Frameworks,[5] Journal of Energy Chemistry, 2022, Vol. 66, p. 161-167 by Hao, Z; Feng, J; Liu, Y; Kang, L; Wang, B; Gu, J; Sheng, L; Xu, R; **Marlow, S**; Brett, D; Huang, Y and Wang, F

Lessons from Countries Implementing Find, Test, Trace, Isolation and Support Policies in the Rapid Response of the COVID-19 Pandemic: A Systematic Review,[6] BMJ open, 2021, Vol.11 (7) by Chung, S; **Marlow, S**; Tobias, N; Alogna, A; Alogna, I; You, S; Khunti, K; McKee, M; Michie, S and Pillay, D

9.5 Bibliography

The following books are fundamental to this work and are recommended for further reading.

Electrochemical Methods by Bard and Faulkner

Fundamentals of XAFS by Matt Newville

XAFS for Everyone by Calvin Scott

Sustainability Without the Hot Air by David McKay

Inorganic Chemistry by Housecroft and Sharpe

PEM Fuel Cell Testing and Diagnosis by Jianlu Zhang, Huamin Zhang, Jinfeng Wu, Jiujun Zhang

Handbook of advanced methods and processes in oxidation catalysis : from laboratory to industry, Edited by Daniel Duprez and Fabrizio Cavani

9.6 References

1 Kang, L. *et al.* Adsorption and activation of molecular oxygen over atomic copper(I/II) site on ceria. *Nat Commun* **11**, 4008, http://dx.doi.org/10.1038/s41467-020-17852-8 (2020).

2 Kang, L. *et al.* The Electrophilicity of Surface Carbon Species in the Redox Reactions of CuO-CeO(2) Catalysts. *Angew Chem Int Ed Engl* **60**, 14420-14428, http://dx.doi.org/10.1002/anie.202102570 (2021).

3 Xu, R. *et al.* Improving the ORR performance by enhancing the Pt oxidation resistance. *Journal of Catalysis* **416**, 311-321, http://dx.doi.org/10.1016/j.jcat.2022.10.025 (2022).

4 Guan, X. *et al.* Designing Reactive Bridging O(2-) at the Atomic Cu-O-Fe Site for Selective NH(3) Oxidation. *ACS Catal* **12**, 15207-15217, http://dx.doi.org/10.1021/acscatal.2c04863 (2022).

5 Hao, Z. *et al.* Reversible lithium storage in sp2 hydrocarbon frameworks. *Journal of Energy Chemistry* **66**, 161-167, http://dx.doi.org/10.1016/j.jechem.2021.07.019 (2022).

6 Chung, S. C. *et al.* Lessons from countries implementing find, test, trace, isolation and support policies in the rapid response of the COVID-19 pandemic: a systematic review. *BMJ Open* **11**, e047832, http://dx.doi.org/10.1136/bmjopen-2020-047832 (2021).